UNIVERSITAT POLITÈCNICA DE CATALUNYA BARCELONATECH

PhD program in Environmental engineering

Formation and Evolution of Carbonate Phases upon Accelerated Carbonation of Mg-Oxides and Silicates

Doctoral thesis by:

Kwon Rausis

Thesis advisor:

Ignasi Casanova

Enginyeria de Camins, Canals I Ports de Barcelona

Barcelona, July 2020

This work was supported in part by:

PhD fellowship of
University, research center and hospital foundation grants for the contracting of new research staff (FI-2017) of Catalonia government

Contract number: 2017 FI_B00129e

To Claire, Neil & Laura

“Tell your son to stop trying to fill your head with science,
for to fill your heart with love is enough”

Richard Feynman

Acknowledgments

Firstly, I would like to express my greatest thanks to my thesis supervisor Prof. Ignasi Casanova and to Generalitat de Catalunya for giving me the opportunity to research on the emerging field of mineral carbonation.

Very special thanks go to Dr. Agnieszka Ćwik for all her friendly support and for all the countless constructive discussions.

I am grateful to Prof. Jordi Llorca for all his enthusiastic encouragement, useful critiques and support.

I would like to thank the extended technical assistance of Dr. Trifon Trodorov and Dra. Montserrat Dominguez.

Prof. Alissa Park and Mr. Guanhe Rim for constructive discussions and technical guidance.

I am also grateful to all the people in the Institut of Energy Technologies for their tireless working spirit and their enthusiastic support during all these years: Ander, Serafin, Anthea, Natalia, Gerardo, Alejandra, Yufen, Xenia and Ilaria.

Finally, I am particularly grateful to my family for their unconditional support. Without them I certainly would have not been able to put this work together.

Table of contents

List of figures

Chapter 1. Why CCUS and NETs?

Chapter 2. Mineral carbonation

Chapter 3. Methodology

Chapter 4. Steam-mediated carbonation of brucite

Chapter 5. Phase formation and evolution of Mg-carbonate phases.

Chapter 6. Carbonation of activated lizardite

Chapter 7. Carbonation of brucite-bearing serpentinized dunite

Chapter 8. Raman study of Mg-carbonate minerals

Chapter 9. Direct-carbonation of enstatite and forsterite single crystals

List of tables

Chapter 1. Why CCUS and NETs?

Chapter 2. Mineral Carbonation

Chapter 3. Methodology

Chapter 4. Steam-mediated carbonation of brucite

Chapter 6. Carbonation of activated lizardite

Chapter 8. Raman study of Mg-carbonate minerals

Chapter 9. Direct-carbonation of enstatite and forsterite single crystals

Abbreviations

a	Atmospheric absorption
A95	Commercial Aldrich brucite (>95%)
A99	Commercial Aldrich brucite (>99%)
ÅA Route	Åbo Akademi Mineral Carbonation process
ACC	Amorphous Ca-carbonate
ACC-Mg	Amorphous Ca-carbonate with Mg
A_{geo}	Theoretically derived geometric specific surface area
AGS	Acid Generation Substances
AMC	Amorphous Mg-carbonate
AOD	Argon decarburization slag
APC	Air pollution control
AR	Afforestation and Reforestation
AS610	Activated lizardite at 610ºC
AS650	Activated lizardite at 650ºC
AS710	Activated lizardite at 710ºC
ATR	Attenuated total reflection
BE	Binding energy
BECCS	Bioenergy with CCS
BF	Blast furnace slag
BHC	Blended Hydraulic Slag Cement
BM	Building materials
BOF	Basic Oxygen Furnace slag
Bru	Brucite
BW	Ambient groundwater
capex	Capital Expenditures
CBD	Cement Bypass Dust

cc	Cubic centimeter
CC	Concentrated CO2
CCHH	Ca-carbonate hemihydrate
CCS	Carbon Capture and Storage
CCU	Carbon Capture and Utilization
CCUS	Carbon Capture Utilization and Storage
CKD	Cement Kiln Dust
CLC	Chemical Looping Combustion
CLR	Chemical Looping Reforming
CR	Ratio of of CO2 capture to the carbon per unit of produced biofuels
d	average particle diameter
D_{3h} symmetry	Symmetry of a tricapped trigonal prism
DAC	Direct Air Capture
DC	Direct carbonation
DGS	Direct Gas solid
DIC	Dissolved Inorganic Carbon
DSP	Dead sea periclase
dTG	Differential mass change
Dyp	Dypingite
EAF	Electric Arc furnace slag
ECBM	Enhanced Coal-Bed Methane Recovery
EDTA	Ethylenediaminetetraacetic acid
EDTA	Ethylenediaminetetraacetic acid
EDX	Energy Dispersive X-ray spectroscopy
EGS	Enhanced Geothermal Systems
EJ	10^{18} J
el	Electricity
EOR	Enhanced Oil Recovery
EW	Enhanced weathering
Ext-cw	Extract-cold wash
Ext-hb	Extract – hot bath
FA	Fly Ash
Fa	Fayalite
FG	Flue gas
FIB	Focused ion beam
Fo	Forsterite

FTIR	Fourier Transformed Infrared Spectrometer (FTIR)
FWHM	Full Width Half Maximum
GHG	Greenhouses Gases
GLiM	Global Lithological Map
Gt	10^9 tonnes
ha	Hectares
HCFA	High-Ca fly ash
HK12	CarbFix Monitoring well, see figure 2.8
HK13	CarbFix Monitoring well, see figure 2.8
Hmg	Hydromagnesite
HN2	CarbFix injection well
HN4	CarbFix Monitoring well, see figure 2.8
HT	High temperature
HT’	Heat treated
IC	Indirect carbonation
IGCC	Integrated Gasification Combined Cycle
IPCC	Intergovernmental Panel for Climate Change
IS	Injected fluid
L/S	Liquid/solid ratio
LDH	Layer Double Hydroxides
LF	Ladle Furnace slag
LT	Low temperature
LW	Longwave outgoing radiation *R*
Mag	Magnesite
MC	Mineral Carbonation
MC	Mineral Carbonation
MEA	Diethanolamine
MgC	Mg-carbonates
Mg_{st}	Mg that substituted Ca in the monohydrocalcite structure
Mha	10^6 ha
MHC	Monohydrocalcite
MKM	Mount Keith Nickel Mine
MSA	Moisture Swing Adsorption
MSW	Municipal Solid Wastes
MSWI	Municipal Solid Waste Incineration
MSWI BA	Bottom Ash from Municipal Solid Waste Incineration

MtC	Million tonnes of CO_2
nCIE	Negative Carbon Isotope Excursion
NETL	US National Energy Technology Laboratory
NETs	Negative Emission Technologies
NiMT	Nickel mine tailings
NMR	Nuclear magnetic resonance
n_{Si}	Si number of moles in one mole of the respective mineral or glass
Nsq	Nesquehonite
PCC	High-purity calcium carbonate
PCO2	CO_2 partial pressure
Per	Periclase
PETM	Paleocene-Eocene Thermal Maximum
PgC	Petagrams of carbon
PGE	Platinum group elements
PMSP	Precipitated Mg-silicate phases
PMW	Paper mill Waste
PSCC	Point Source Carbon Capture
r^2	Correlation coefficient
RCO2	Carbonation potential
$\mathbf{r}_{geo}$	Silicate dissolution rate normalized to the theoretically derived geometric specific surface area
RH	Relative humidity
RM	Red mud
rT	Room temperature
R_X	Extent of reaction
Rx(max)	Maximum R_x obtained in the reaction series
SEM	Scanning Electron Microscopy
SFG	Simulated flue gas
SI	Saturation Index
SMD	Stirred media detritor
STP	Standard Temperate and Pressure
SW	Short-wave incoming radiation I
t	Tonnes
TCD	Thermal conductivity detector
T_E	Earth's Surface temperature
TEM	Transmission Electron Microscopy

TGA	Thermogravimetric analysis
th	Thermal
TPD	Temperature programmed desorption
TSA	Temperature Swing Adsorption
UMT	Ultramafic mine tailings
UMC	Unknown Mg carbonate phase
WAXS	Wide angle X-ray Scattering
X	Fraction of the injected solution in the extracted water sample
XCO_2	CO_2 wt%. In the reaction products
XPS	X-ray photoelectron spectroscopy
XRD	X-ray Diffraction
XRF	X-ray fluorescence spectroscopy
α_a	Atmospheric reflection
α_L	Ice-free land albedo
α_{LI}	Land ice albedo
α_o	Ocean albedo
α_p	Planetary albedo
α_s	Surface albedo
α_{SI}	See ice albedo
Γ	Raman vibrational activity
$\delta^{26}Mg_{DSM3}$	Isotopic ratio as per mil deviation of the $^{26}Mg/^{24}Mg$ ratios from the DSM3 international reference materials
$\delta^{44}Ca$	Isotopic ratio as per mil deviation of the $^{44}Mg/^{40}Mg$ ratios
ΔR	Radiative forcing (W m^{-2})
$\Delta T_{E,P}$	Temperature anomalies of the Planck feedback
ε_a	Percent weight gain assuming 100% stoichiometric conversion of the available Ca^{2+}, Mg^{2+} and Fe^{2+} to carbonates
ν_{1sym}	ν_1 symmetric stretching mode
$\nu_{1symcar}$	ν_1 symmetric stretching mode of the carbonate ion
ν_{as}	Antisymmetric stretching modes
ρ	Density of the solid

Abstract

This work discloses new insights into the formation and evolution of Mg-carbonates as well as carbonation processes of Mg-rich oxides and silicates with the aim of providing a safe and permanent anthropogenic CO_2 storage, helping to tackle the worst effects of climate change. Carbonation reactions were carried in a purpose-built steam-mediated carbonation system at temperature and pressure ranges between 50-205ºC and 1 to 10 bar, respectively.

A hydrated amorphous Mg-carbonate was identified upon carbonation of Mg-rich silicates and oxides at 50ºC. Such material might have similar composition and thermal dehydration behavior as nesquehonite. Results from this thesis provided new insights into the enigmatic and yet unconstrained transition of such phase to less hydrated phases. The evolution of Mg-carbonate phases is mainly controlled by the slow dehydration kinetics of Mg^{2+} rather than evolving to a thermodynamically more stable or structurally similar phase. Despite it has been predicted that such material could straightforward transform into magnesite, it is strongly argued that such transition is greatly inhibited due to preferential nucleation pathways to less hydrated Mg-carbonate phases. Phases within the group $Mg_5(CO_3)_4{\cdot}(OH)_2{\cdot}XH_2O$ ($11 \leq X \leq 4$) allows a progressive dehydration whereas the $MgCO_3{\cdot}nH_2O$ ($n \geq 0$) seemingly not. It is proposed that the transition between hydrated amorphous Mg-carbonate to highly disordered dypingite-like phases could occur progressively as it dehydrates and crystallizes, forming dypingite-like phases.

The progressive evolution of dypingite-like phases is controlled by the removal of molecular water, inducing cell-shrinkage as well as ordering the internal structure heterogeneity, resulting in a crystalline hydrated structure with the name of hydromagnesite. This might explain the inconsistencies in the solubility and decomposition behavior data reported in the literature for such carbonate phases. No further dehydration is allowed within this group, entailing a significant kinetic barrier in order to allow the transition from hydromagnesite to magnesite.

Results from this work shed light into the yet enigmatic evolution of Mg-carbonate phases. The understating of such processes is of paramount importance to accelerate the transition and/or dehydration kinetics among such phases and possibly unlocking preferential nucleation pathways.

Brucite carbonation was observed to occur at feasible conversion rates even under simulated flue gas conditions, highlighting the potential of mineral carbonation processes for direct combined CO_2 capture and storage/utilization.

Carbonation of Mg-rich silicates remained a challenging field under the studied conditions, even for activated serpentine, despite its partial high-reactivity attributed to the presence of a highly-reactive amorphous Mg-rich phase. It was also found the presence of a poorly-reactive Mg-rich amorphous phase (formed upon activation of lizardite) which remained seemingly unreacted upon carbonation. Such observation might provide new insights into the yet unanswered low carbonation efficiencies for direct-carbonation of activated serpentine.

Similar carbonation yields were observed for brucite-bearing serpentinized dunite when compared to activated lizardite. Strategically sourcing serpentinized rocks with higher brucite contents will potentially increase the carbonation potential of such materials. Coexisting lizardite and/or forsterite were also observed to be partially carbonated.

Carbonation of enstatite and forsterite were also individually studied under conditions relevant to localized early Martian conditions. Enstatite dissolution was observed by the formation of a Si-rich passivating layer, where Si and Mg are heterogeneously distributed. Such observation is consistent with morphological changes within this layer, strongly suggesting an intergrowth of nucleating and growing Mg-carbonates with Si-rich phases.

Resum

Aquest treball mostra noves percepcions sobre la formació i l'evolució dels carbonats de Mg, així com els processos de carbonatació d'òxids i silicats rics en Mg amb l'objectiu de proporcionar un emmagatzematge segur i permanent d'antropogènic CO_2, ajudant a fer front als pitjors efectes del canvi climàtic. Les reaccions de carbonatació es van dur a terme en un sistema de carbonatació dissenyat específicament per al desenvolupament d'aquesta tesi. Els experiments s'han realitzat a intervals de temperatura i de pressió entre 50-205 ºC i 1 a 10 bar, respectivament.

Un carbonat de Mg amorf hidratat es va identificar després de la carbonatació de silicats i òxids rics en Mg a 50 ºC. Aquest material pot tenir una composició i un comportament de deshidratació tèrmica similars a la de la nesquehonita. Els resultats d'aquesta tesi van aportar una visió nova de la transició enigmàtica d'aquesta fase amorfa a fases menys hidratades. L'evolució, via deshidratació, de les fases de carbonat de Mg és controlada principalment per la lenta deshidratació de Mg^{2+} en lloc d'evolucionar cap a una fase termodinàmicament més estable o estructuralment similar. Tot i que s'ha previst que aquest material es podria transformar directament en magnesita, es defensa que aquesta transició està inhibida a causa de les vies de nucleació preferents a les fases de Mg-carbonat menys hidratades. Les fases del grup $Mg_5(CO_3)_4(OH)_2 \cdot X$H2O ($11 \leq X \leq 4$) permeten una deshidratació progressiva mentre que $MgCO_3 \cdot$nH2O ($n \geq 0$) aparentment no.

L'evolució progressiva de les fases semblants a la dypingita es controla mitjançant l'eliminació d'aigua molecular. A mesura que es deshidrata es produeix la contracció de l'estructura interna, donant com a resultat una estructura hidratada cristal·lina amb el nom d'hidromagnesita. Això podria explicar les incoherències en les dades de solubilitat i de descomposició tèrmica per a aquestes fases.

Els resultats d'aquest treball van donar llum a l'encara enigmàtica evolució de les fases de carbonat de Mg. L'enteniment d'aquests processos és d'importància per accelerar la cinètica de transició i/o deshidratació entre aquestes fases i possiblement desbloquejar vies de nucleació preferents.

S’ha observat que la carbonatació de la brucita succeeix ràpidament, fins i tot en condicions de gasos de combustió simulades, recalcant el potencial dels processos de carbonatació mineral per a la captació i l'ús d'emmagatzematge de CO_2.

La carbonatació de silicats rics en Mg és encara un camp difícil en les condicions estudiades, fins i tot per a la serpentina activada, malgrat la seva alta reactivitat atribuïda a la presència d'una fase rica en Mg amorfa altament reactiva. No obstant això, també es va observar la presència d'una fase amorfa poc reactiva, formada després de l'activació de la lizardita. Aquesta observació podria aportar noves visions sobre la baixa carbonatació directa de la serpentina activada, la qual encara és desconeguda.

Es van observar rendiments similars de carbonatació per a dunitas serpentinitzades en comparació amb la lizardita activada. L’obtenció estratègica de dunites serpentinitzades amb un contingut més elevat de brucita augmentarà el potencial de carbonatació d’aquests materials.

La carbonatació de cristalls d’enstatita i forsterita també es va estudiar individualment a condicions rellevants a l’antic Mars. La dissolució de l’enstatita es va observar inequívocament mitjançant la formació d’una capa passivadora rica en Si, on Si i Mg es distribueixen de forma heterogènia. Aquesta observació és coherent amb els canvis morfològics dins d'aquesta capa.

Introduction

Global warming is considered the most serious of all environmental problems and is mainly driven by the ever-increasing anthropogenic CO_2 emissions. It is likely that climate change (due to global warming) is occurring at such rate that many marine and terrestrial species will not be able to adapt, resulting in a widespread future extinction of several species. Significant global warming mitigation efforts must be rapidly implemented to prevent such associated effects of climate change by aiming to limit global warming under 1.5ºC above pre-industrial levels, as proposed in the Paris Agreement by the United Nations. However, it seems increasingly unlikely that a significant reduction of CO_2 emissions will occur in the near future. Therefore, providing a safe and permanent CO_2 storage is critical to prevent the worst effects of climate change. Failing to implement such technologies in a timely manner will endanger people and nature future. Moreover, an extremely large investment will be required to partially remediate climate change consequences. Therefore, it seems more reasonable to currently invest for a progressive transition from fossil-fuel to clean energy-based society.

Passive weathering of Mg and Ca-rich silicate rocks are known to sequester significant amounts of CO_2 trough mineral carbonation, although it suffers from slow kinetics, despite their thermodynamically-driven reactions. Several studies have proposed to engineered mineral carbonation process in order to accelerate the carbonation of Mg and Ca-oxides and silicates in an anthropic timescale. This is mainly justified by (i) the exothermic-nature of such reactions, (ii) the CO_2 storage potential of such widely abundant Mg/Ca-rich oxides and silicate on Earth's crust far exceeds the total CO_2 that can be produced by burning fossil fuels, (iii) it is among the safest and more permanent among all the CO_2 storage technologies and (iv) reaction products might be profitable (for ex-situ mineral carbonation processes). However, the kinetics of such reactions are generally limited, requiring extreme carbonation conditions (150 bar, 185ºC) to achieve reasonable

conversion rates. Such reaction conditions stray far from reality of post-combustion flue-gas conditions, making them currently industrially unfeasible.

This thesis aims to provide new insights on direct mineral carbonation of Mg-silicates and oxides as well as to shed light into the yet enigmatic formation and evolution of Mg-carbonates under moderately low temperature and pressure conditions (50-185ºC, ≤10 bar) in the presence of water vapor for both concentrated CO_2 and flue gas streams. If sufficient reaction yields and rates are obtained at such experimental conditions, such processes could be easily implemented on large-scale projects, providing a permanent anthropogenic CO_2 storage. Moreover, reaction products can be utilized for several industrial applications, lowering the costs associated with carbonation processes.

Results of this work highlight the importance of disordered precursors during the formation and evolution of hydrated Mg-carbonates. Understanding such mechanisms is of paramount importance, since it might provide new insights on the accelerated carbonation mechanisms, which are strongly controlled by preferential nucleation and growth of several hydrated precursors, driven by the slow dehydration nature of Mg^{2+}.

Alteration of Mg-rich silicates was observed to suffer from slow kinetics under the studied conditions. The slowly-driven direct-carbonation reactions combined with the fate of silica provides significant challenges, limiting their industrial applications.

Results presented on this thesis are aimed to contribute to the joined efforts for tackling climate change in order to help people and nature thrive.

General objectives

- Study the direct moist carbonation of Mg oxides and silicates under moderately low temperature and pressure conditions (≤10 bar; ≤200ºC) using simulated flue gas and concentrated CO_2.
- Provide insights on the role of disordered and crystalline hydrated Mg-carbonate precursors during accelerated carbonation reactions.
- Identification of limiting factors that reduces the direct carbonation efficiency of activated serpentine.
- Evaluate the carbonation potential of serpentinized dunites as an alternative to the carbonation of activated serpentine.

1. Why Carbon Capture, Utilization and Storage (CCUS) and Negative Emissions Technologies (NETs)?

1.1. Anthropogenic CO_2 emissions and global warming

The global warming is caused by the unbalanced radiative equilibrium between the incoming short wave (SW) radiation *I* from the sun reaching the Earth and the outgoing long-wave (LW) radiation *R*, following the Stefan-Bolts-Mann law ($R_0=\alpha \cdot T_E^4$, $\alpha=5.67 \cdot 10^{-8}\ Wm^{-2}\ K^{-4}$, R_0, α and T_E stands for radiative balance, Stefan-Boltzmann constant and Earth's equilibrium temperature, respectively) [1]. The incoming radiation *I* is mainly determined by the solar constant S, but also depends on the Earth's orbital configurations [2]. Almost a third of the incoming radiation is reflected back to space, determined by the planetary albedo of $\alpha_p = 0.3$ [3]. The atmospheric albedo constitutes >75% of the planetary albedo [4]. The main interaction of outgoing radiation *R* is with greenhouses gases (GHG), absorbing about 40% to the total outgoing radiation [5,6]. Fig. 1.1 summarizes the global annual mean radiative budget of Earth's atmosphere.

Water vapor (the most important GHG) absorbs about 60% of the LW radiation absorbed by GHG [6]. The other main GHG (CO_2, CH_4 and N_2O) absorbed the remaining 40%. During the last 800 kyr the CO_2 concentration in the atmosphere has estimated to vary between 170 and 300 ppm, meanwhile, CH_4 and N_2O concentration variations are three order of magnitude smaller [7–12] (Fig. 1.2) . However, the impact of this latter GHG on the radiative balance per mol gas is larger than CO_2, following these simplified equations 1.1 – 1.5 [13]. CO_2 concentration variations are directly related to episodes of Earth' surface warming and cooling during the las 800kyr.

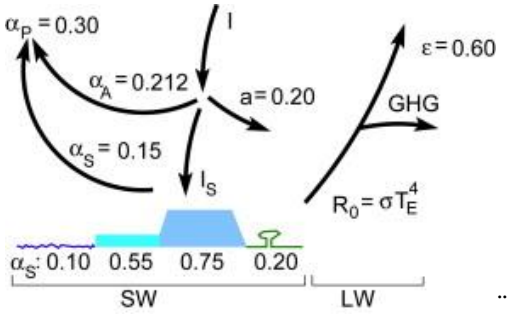

Fig. 1.1. Global annual mean radiative budget of Earth's atmosphere. SW: short-wave incoming radiation *I*; LW: long-wave outgoing radiation *R*, which is dependent of Earth's surface temperature (T_E); atmospheric reflection (α_a: 0.212) and absorption (a=0.2); Is: SW dependent on the solar constant; the planetary albedo (α_p: 0.3) combines αa and the surface albedo (α_s=0.15) which itself is divided into: ocean albedo (α_o= 0.1), sea ice albedo (α_{SI}= 0.55) land ice albedo (α_{LI}: 0.75) and ice-free land albedo (α_L:0.2). ε is the effective emissivity of the earth, accounting to 0.6. of the total outgoing *R* radiation. Figure from Köhler et al., 2010 [1].

$$\Delta R_{CO_2}(W\,m^{-2}) = 5.35 \cdot \ln\left(\frac{CO_2}{CO_{2,0}}\right) \quad (1.1)$$

$$\Delta R^0_{CH_4} = 0.036 \cdot \left(\sqrt{CH_4} - \sqrt{CH_{4,0}}\right) \quad (1.2)$$

$$\Delta R_{CH_4}(W\,m^{-2}) = 1.4 \cdot \Delta R^0_{CH_4} \quad (1.3)$$

$$\Delta R^0_{N_2O}(W\,m^{-2}) = 0.12 \cdot \left(\sqrt{N_2O} - \sqrt{N_2O_0}\right) \quad (1.4)$$

$$\Delta R_{N_2O}(W\,m^{-2}) = 0.12 \cdot \left(\Delta R_{CO_2} + R_{CH_4}\right) \quad (1.5)$$

Where ΔR's are the radiative forcing of the respective GHG and are given in W m^{-2}. CO_2, CH_4 and N_2O are the estimated concentrations for CO_2 (ppm), CH_4 (ppb) and N_2O (ppb). $CO_{2,0}$, $CH_{4,0}$ and N_2O_0 are the concentration reference values accounting for 278 ppm, 742 ppb and 272 ppb, for CO_2, CH_4 and N_2O, respectively. ΔR_{N_2O} and ΔR_{CH_4} are the optimized parameters relative to the $\Delta R^0_{N_2O}$ and $\Delta R^0_{CH_4}$. ΔR_{CH_4} taking into account the indirect effects of CH_4 on stratospheric H_2O and tropospheric O_3 [14] which accounts to an additional 40% relative to $\Delta R^0_{CH_4}$[15]. ΔR_{N_2O} linearly estimate the radiative forcing of N_2O based on the combined effect from CO_2 and CH_4 [15]. The uncertainties for each estimated ΔR's are described in Köhler et al., 2010 [1]. Temperature anomalies ($\Delta T_{E,P}$) of the Plank feedback caused by these three GHG. As discussed by Köhler et al., 2010 [1], the feedback processes (i.e.: water vapor, lapse rate, clouds) were not considered in detail, which enlarges the temperature anomalies.

CO_2 concentration in the atmosphere are increasing at an alarming rate, currently exceeding 400ppm, which is significantly higher than those estimated during the last 800 kyr [16]. This problem is widely considered to be one of the most serious of all environmental problems. The challenges associated with the stabilization of atmospheric CO_2 levels becomes increasingly difficult as the problem matures. Therefore, forecasting the response of the Earth' systems to the ever-increasing emission rates is of paramount importance [17]. Geologic analogues from past climates

provides invaluable information on the impacts of massive carbon release on the Earth systems [18,19]. The fastest known carbon released occurred during the Cenozoic (past 66 Myrs) at the onset of the Paleocene-Eocene Thermal Maximum (PETM; ~56Myr ago) [17,20], associated with a surface warming of~5 ºK.

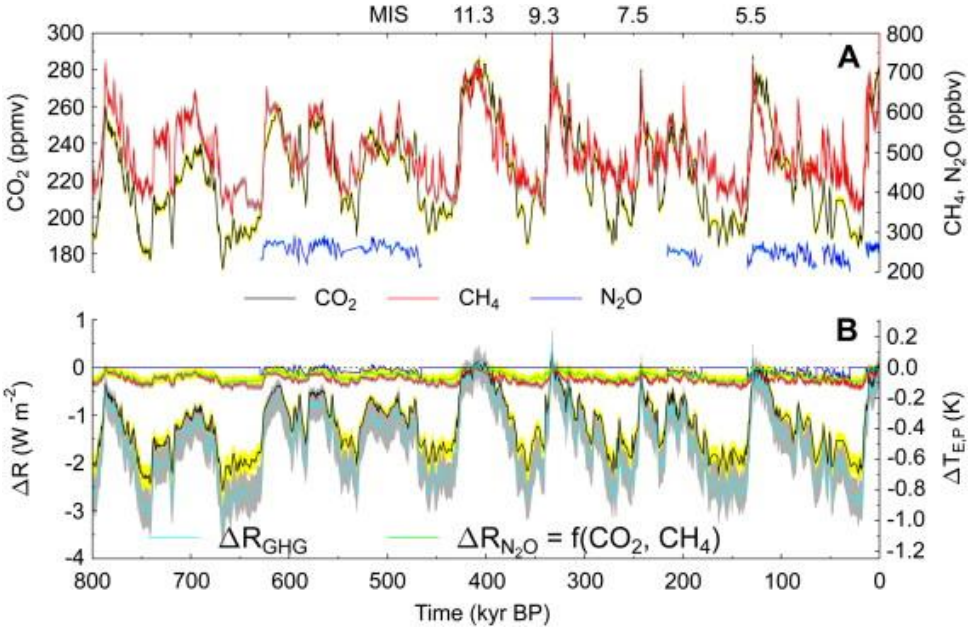

Fig. 1.2. (a) Variation of atmospheric CO_2, CH_4 and N_2O concentrations and **(b)** perturbation in the radiative budget due to the CO_2, CH_4 and N_2O concentrations and the total GHG forcing. The right y-axis shows the temperature anomalies ($\Delta T_{E,P}$) of the Planck feedback. Figure from Köhler et al., 2010 [1].

The marine depositional environment from Millville, New Jersey has paleorecords from the PETM and cm-resolution bulk isotope records, including well-constrained age foraminiferal isotope data [17]. Such sediments have potentially the highest-fidelity recording isotopic data of the onset [21,22]. Oxygen and carbon isotope records are important tools used to reconstruct past ocean and climate conditions. $\delta^{13}C$ and $\delta^{18}O$ tracks the timing of the carbon release and the climate response to CO_2 and other forcings, respectively [17]. The~3‰ negative carbon isotope excursion (nCIE) as well as the~1‰ $\delta^{18}O$-drop at Millville is consistent with other pelagic sequences and foraminifer isotope data of the onset at Bass River and Wilson Lake [17] (Fig. 1.3). Several nCIE in the geological record are interpreted as episodes of massive carbon release and are evidence for past global warming and/or ocean acidification [23], known as the Suess effect [24,25]. The isotopic data of the onset is consistent with a global surface warming of ~5 ºK [17,26]. Analogously, due to current anthropogenic CO_2 emissions from burning depleted $\delta^{13}C$ and $\delta^{14}C$ fossil fuels, the $\delta^{13}C$ composition of atmospheric CO_2 has declined by ~1.5‰ [23].

Zeebe et al., 2016 [17] have estimated an initial carbon release (accounting to 2500 – 4000 Pg C) occurred during the PETM onset occurred over at least 4000 yr. Thus, the carbon release rate was estimated to be of 0.6 – 1.1 Pg C yr^{-1}. The unprecedent current anthropogenic carbon release rate is

estimated to be ~ 10 Pg C yr^{-1} which defines it as an era of no-analogue state, which represents challenges regarding the projection of future climate. These current vast amounts of released carbon are extremely alarming, leading a rapid climate change and ocean acidification [27–29]. It is extremely likely that such changes are occurring at such rate that many species will not be able to adapt [30,31], resulting in a widespread future extinctions for both marine and terrestrial species, significantly exceeding those estimated at the PETM [32]. The possible known consequences caused by anthropogenic-induced fast climate changes have been extensible discussed elsewhere [16,33,34].

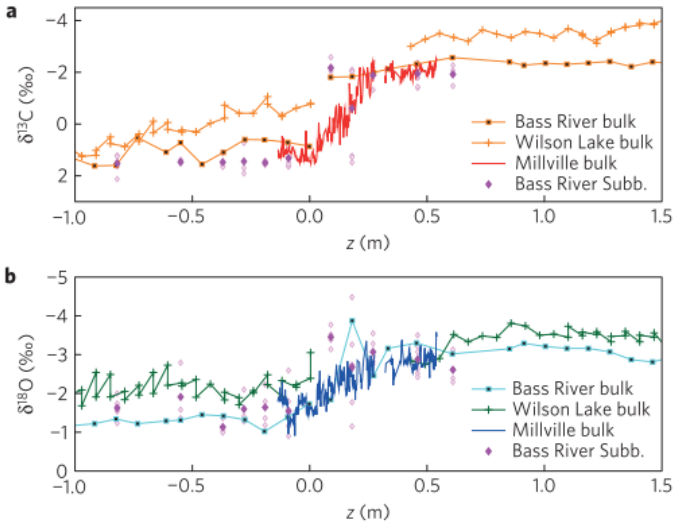

Fig. 1.3. (a) $\delta^{13}C$ and **(b)** $\delta^{18}O$ stable isotope records from New Jersey margin sections across the PETM onset relative to the position in the core (z=0m alignment is arbitrary). Diamonds shows the foraminifer isotopic data. Figure from Zeebe et al., 2016 [17].

In view of this alarming data, the Paris agreement was signed with objective to limit the global warming preferably bellow 1,5ºC and maximum up to 2ºC above pre-industrial levels, thus, avoiding the worst probable scenarios related associated with global warming [35]. The Intergovernmental Panel for Climate Change (IPCC) have modelled different scenarios where such goal could be obtained [16]. In a "business as usual" scenario, the global warming is more likely to overpass the 1,5ºC goal between 2030 and 2050. The scenario that is more likely to be successful requires that a decline of CO_2 emissions, reaching net zero by 2040 and the non-CO_2 radiative forcing have to be reduced by 2030[16]. It seems increasingly unlikely that a rapid reduction in the anthropogenic carbon emissions will occur in the near future [36]. Therefore, such optimistic scenario is subjected to extremely difficult challenges.

Different IPCC scenarios for the reduction of CO_2 emissions were carried out taking into account Carbon Capture, Utilization and Storage (CCUS) processes and emerging Negative Emissions Technologies (NETs), such as Direct Air Capture (DAC) [16,37,38] (Fig. 1.4a). All the scenarios are strongly dependent on the successful implementation of CCUS technologies. P1 shows the most

optimistic scenario, where no CO_2 have to be removed from the atmosphere. It has been foreseen that CCUS will contribute to 19% of the total estimated CO_2 emission reduction (Fig. 1.4b) [39]. However, scenario P4 is more both realistic and worrying, where up to 20 Gt of CO_2 per year have to be removed from the atmosphere per year. An important question arises concerning the development rate for NETs, whether they will be able or not to achieve and sustain such goals [38].

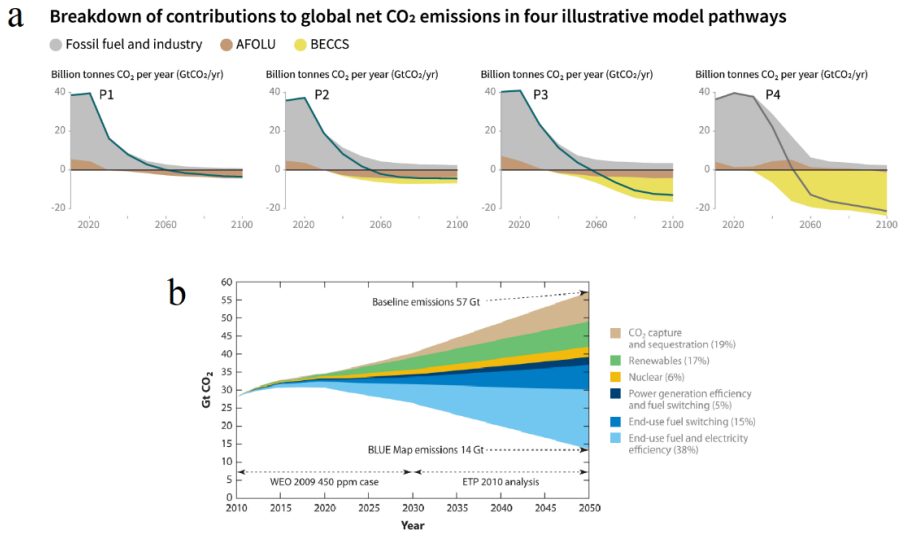

Fig. 1.4. (a) Model pathways for CO_2 emission reduction. Fossil fuels and industry also include the successful implementation of CCUS technologies. Agricultural, Forestry and Other Land Uses (AFOLU). Bio-Energy with Carbon, Capture and Storage (BECCS), including the successful implementation of Negative Emission Technologies (NETs). Figure from IPCC, 2018 [16]. **(b)** CO_2 emissions in a "business as usual scenario" and with the successful implementation of a portfolio of solutions. Figure from Geerlings et al., 2013 [39].

Figure 1.5 shows the carbon flows between atmospheric, land, ocean and geological reservoirs derived from CO_2 emissions upon fuel combustion (Fig. 1.5a), bioenergy (Fig. 1.5b), CCS (Fig. 1.5c) and NETs (Fig. 1.5d-h). Bioenergy processes have no CO_2 footprint since all the CO_2 that is being realized into the atmosphere via biomass energy generation is capture once again by re-growing bioenergy feedstocks. CCS aims to capture anthropogenic CO_2 and return it to a geological or ocean reservoirs. NETs remove CO_2 from the atmosphere. There are several NETs options such as: biological uptake (mainly afforestation and ocean fertilization), uptake by biological or industry processes combined with CCS, such as DAC (which aims to capture atmospheric CO_2) and BECCS [38]. An overview of this technologies is presented in the upcoming sections.

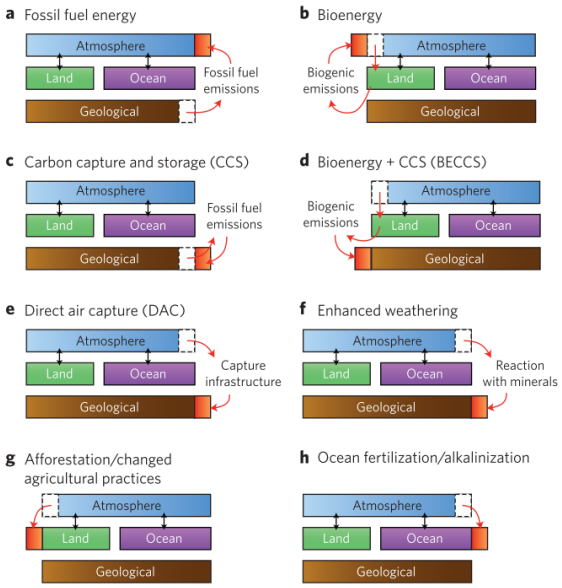

Fig. 1.5. Scheme of the carbon flows among atmospheric, land, ocean and geological reservoir by several processes. Figure from Smith et al., 2016 [38].

1.2. Carbon Capture, Utilization and Storage (CCUS)

CCUS technologies are aimed to capture anthropogenic CO_2 emissions from point sources (i.e.: power plants and industrial processes) in order to prevent its release into the atmosphere [40]. Generally, CO_2 is separated from gaseous waste streams (process known as CO_2 capture). Once is captured, CO_2 can be either stored/sequestered (CCS) or utilized (CCU). For CCS, CO_2 have to be transported to storage locations and then, indefinitely isolated from the atmosphere [41,42]. CCS technologies face several technical and economic (since they are currently unprofitable and requires large capital investment) barriers that must overcome for large-scale industrialization [43].

CCU has been recently proposed for turning waste CO_2 emissions into valuable products, such as chemical fuels and carbonates [40,44]. Moreover, CO_2 could be considered as a renewable source, low cost and non-toxic [45]. However, chemical and fuel synthesis from CO_2 is energy intensive, mainly due to the thermodynamic stability of CO_2 The successful implementation of such process, with current demand of chemicals, will not contribute significantly to the reduction of the current CO_2 emissions (34.5 Gt/yr) [46]. Fuel and chemical synthesis will only delay the CO_2 emissions rather than removing them [40]. [43,45].

On the other hand, the synthesis of carbonates is driven by thermodynamically-favored exothermic-reactions. The energy-produced from such processes could help to overcome the reaction energy requirements [40,47]. Moreover the carbonate products are thermodynamically stable, environmental benign and could sequester CO_2 over geological timescales [48–50].

Moreover, CCUS processes should also be assessed on a life cycle basis, avoiding the environmental burdens shifts from one cycle to another [40]. Fig. 1.6 summarizes the different CCUS options.

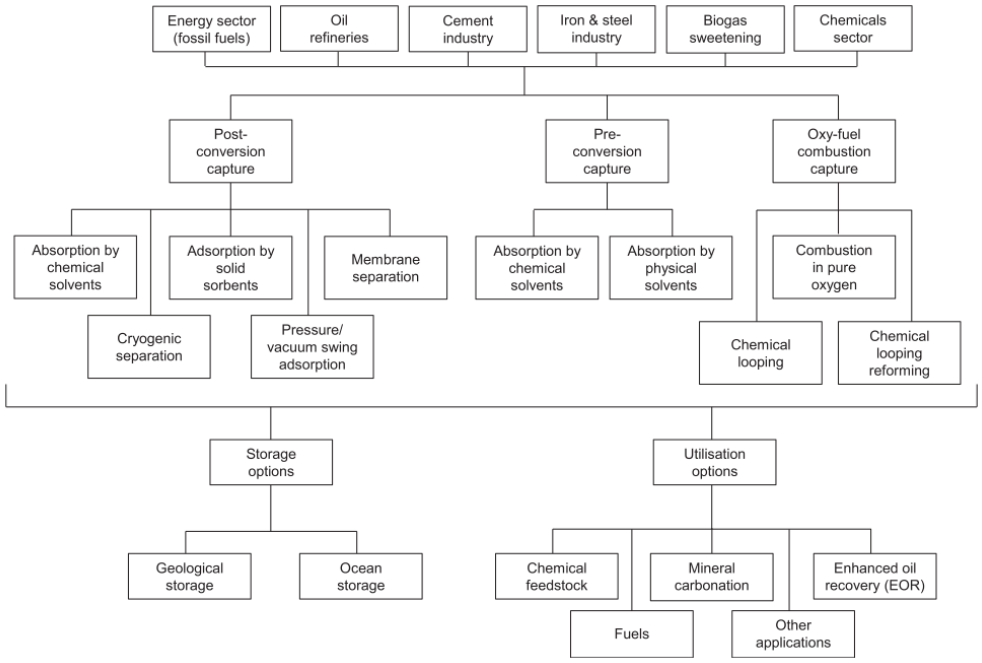

Fig. 1.6. Summary of the different CCUS processes. Figure from Cuéllar-Franca et al., 2015 [40].

1.2.1. CO_2 capture

The main industrial sources of CO_2 are: power plants, oil refineries, biogas sweetening and production of ammonia, ethylene oxide, cement, iron and steel production[43]. Fossil-fuel fired power plants makes up to 40% of the total anthropogenic CO_2 emissions [51]. Such options are the main candidates for carbon capture processes [40].

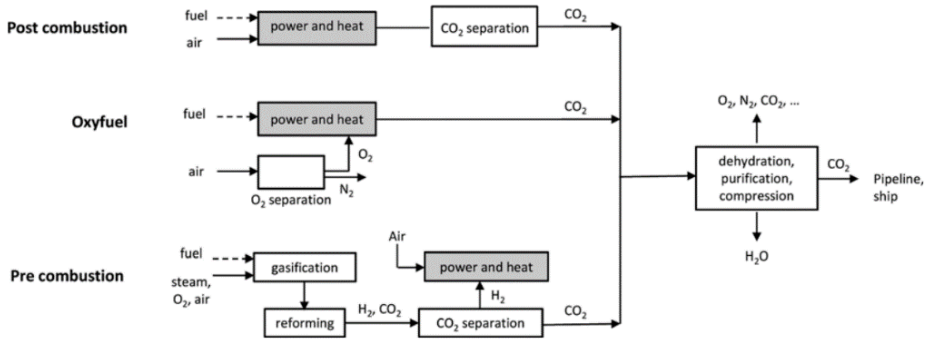

Fig. 1.7. Scheme of the main CO_2 capture processes: (i) post-combustion capture, (ii) pre-combustion capture and (iii) oxy-fuel combustion. Figure from Markewitz et al., 2012 [51].

Carbon capture processes can be divided within three main categories: (i) post-conversion , (ii) pre-conversion and (iii) oxy-fuel combustion [52–54]. It should be also noted that there are emerging

integrated processes, where CO_2 is capture by profitable products, an no prior CO_2 capture processes are needed, such as flue gas carbon mineralization [44,55–57] an biomass fixation of CO_2 [53]. However, such processes are (arguably) associated with CCU [40]. A summary of such processes is shown in Fig. 1.6 and Table 1.1.

Table 1.1. Carbon Capture processes, technologies and applications. [a]mature technology, [b]commercially available, [c]may become available in long term (>2030). Adapted from Cuéllar-Franca et al., 2015 [40] and Markewitz et al., 2012 [51].

Capture option	Separation technology	Method	Applications
Post-conversion	Absorption by chemical solvents[a]	• Amine-based solvent, i.e.: MEA[b], diethanolamine (DEA), and hindered amine (KS-1) • Alkaline solvents, e.g. NaOH and $Ca(OH)_2$ • Ionic liquids	Power plants; cement, iron and steel industry
	Absorption by solid sorbents	• Amine-based solid sorbents • Alkali earth metal-based solid sorbents, i.e.: $CaCO_3$ • Alkali metal carbonate solid sorbents, i.e.: Na_2CO_3 and K_2CO_3 • Porous organic frameworks – polymers	No application reported
	Membrane separation	• Polymeric membranes, i.e.: polymeric gas permeation membranes[b] • Inorganic membranes, i.e.: zeolites • Hybrid membranes	Power plants; natural gas sweetening
	Cryogenic separation	• Cryogenic separation	Power plants
	Pressure/vacuum swing adsorption	• Zeolite[b] • Activated carbon[b]	Power plants; cement, iron and steel industry
Pre-conversion	Absorption by physical solvents	• Selexol, rectisol	Power plants (Integrated gasification combined cycle)
	Absorption by chemical solvents	• Amine-based solvent, i.e.: MEA	Ammonia production
	Adsorption by porous organic frameworks	• Porous organic frameworks membranes	Gas separations Power
Oxy-fuel combustion	Separation of oxygen from air	• Oxy-fuel process	Power plants; iron and steel industry; cement industry[c]
		• Chemical looping combustion	Power plants
		• Chemical looping reforming	Power plants; syngas production and upgrading
		• Membranes	Power plants

1.2.1.1. Post-conversion capture

This process is characterized by the separation of CO_2 form waste gas streams after the conversion of the carbon source to CO_2 (i.e.: Fossil-fuel fired power plants, production of ethylene oxide, cement, iron and steel production) (Fig. 1.7). When such process is used in power-plants its known as post-combustion capture [54].

Several methods are being developed for such processes (Table 1.1). The absorption in liquid solvents have been industrially tested and widely applied due to the obtained high purities and degree

of separation [51]. The absorption by monoethanolamine (MEA) is the most commonly used [58,59]. However, such method is too costly for large-scale deployments mainly due to the energy required during the absorption-desorption cycle, as MEA regeneration requires high-heat consumption [40,51].

As summarized by Markewitz et al., 2012 [51], post-combustion advantages are: (i) absorption processes are well known, (ii) there is high optimization potential for reducing energy losses, (iii) easily-adapted to a diversity of power-plants and (iv) CO_2 purity (>99.99%), the highest among all carbon capture processes. The disadvantages are: (i) high costs, (ii) large environmental impact and (iii) a flexible operation mode has not yet been demonstrated.

1.2.1.2. Pre-conversion capture

This carbon capture option refers to such processes that captures the un-desired CO_2 generated during intermediate reactions of a conversion process, such as the production of ammonia and coal gasification in power plants [41,54,60]. After the CO synthesis by catalytic conversion of cleaned coal or heavy oil, CO is reacted with steam as oxidant to form CO_2 and H_2 (CO-shift reaction)[51]. The capture of CO_2 takes place after both the fuel gas synthesis and the conversion of CO to CO_2 and H_2 [51]. CO_2 must be separated from H_2 before ammonia synthesis or in an integrated gasification combined cycle (IGCC) power plant, this is commonly carried via MEA absorption [41,61] and by physical solvents such as selexol and rectisol [54,62]. Similarly to post-combustion processes, regeneration of chemical/physical solvents produces energy penalties which are higher for chemical solvents than physical solvents, as this latter are regenerated by reducing pressure rather than by heat [40]. When such process is used in power-plants its known as pre-combustion capture [54].

As summarized by Markewitz et al., 2012 [51], pre-combustion advantages are: (i) high efficiency potential, (ii) flexibility due to the poly-generation of electricity and H_2. The disadvantages are: (i) elevated investment costs, (ii) low availability and reliability and (iii) less mature compared with conventional power plant technologies.

1.2.1.3. Oxy-fuel combustion capture

It refers to direct carbon capture processes by combustion of carbon-fuels with pure oxygen, producing a CO_2-rich flue gas (89%) and free form N_2 and concomitants NO and NO_2. By condensing water vapor from the flue gas, pure CO_2 flue gas is obtained. However, the prior O_2 separation from air is expensive due to the energy intensive treatments which also emits CO_2 [51,63]. Generally, oxygen is separated from air by means of cryogenic air separation (due to O_2 condensation at < - 182ºC).

Alternatives to such processes are: chemical looping combustion (CLC), chemical looping reforming (CLR) and O_2-selective membranes [40,51]. CLC and CLR use a metal oxide to selectively transfer O_2 from an air reactor to a fuel combustor (Fig. 1.8). In CLR, O_2-containg air oxidizes reduced metal oxide. Then, this metal oxide is reduced in a fuel reactor by reacting with hydrocarbon fuel, releasing CO_2 and $H_2O_{(g)}$. The reduced metal oxide is then carried to a steam reactor, upon reaction with steam it produces H_2. Reduced metal is once again feed it to the air reactor [64]. However, operating such system at high pressures (which will give equivalent efficiencies to those obtained by state-of-the-art oxy-fuel and post-combustion processes) is still challenging [51,65]. The handling of ash and the application to solid fuels during CLC processes also remains challenging [65].

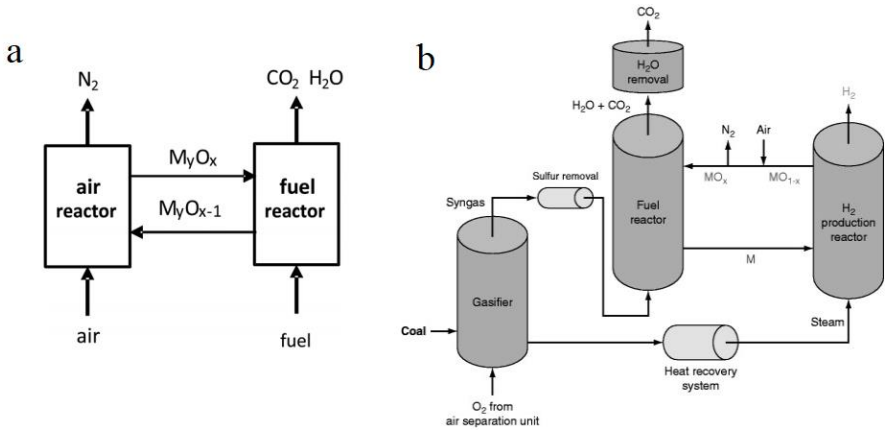

Fig. 1.8. (a) Scheme of the CLC and **(b)** CLR processes. Figures from Markewitz et al., 2012 [51] and Lackner et al., 2010 [66], respectively.

As summarized by Markewitz et al., 2012 [51], Oxy-fuel combustion advantages are: (i) low environmental impacts, (ii) cryogenic O_2 separation is a mature technology and (iii) has high potential for reducing energy losses. The disadvantages are: (i) modification of burners and boilers are required, (ii) retrofitting is probably not possible and (iii) its high costs.

1.2.2. Carbon Capture and storage (CCS)

Once CO_2 is captured, it is compressed and transported to CO_2 storage locations either in the ground, ocean or as mineral carbonate [40,41,58]. Fig. 1.9 summarizes the natural and mad-made CO_2 storage options as well as their characteristic storage time and carbon storage capacity. Ground CO_2 storage, commonly known as geological storage, consist on the injection of compressed CO_2 into geological formations such as depleted oil and gas reservoirs, deep saline aquifers and coal bed formations (to depths between 800 to 1000m). CO_2 remains stored by trapping mechanisms, characteristic of the geological formation, such as being trapped bellow “caprocks”, characterized by impermeable layers containing fine to ultrafine particle sizes (i.e.: clays, shales and mudstones), and in-situ CO_2 absorption by fluids and organic matter [41]. Depending on the reservoir properties,

pressurized CO_2 can be stored as gas, liquid or in a supercritical condition (31.1ºC and 73.8 bar). When CO_2 is stored this latter condition, it is denser and makes a better use the formation pore space, decreasing the associated leaking risks [67,68].

Currently, geological storage is probably one of the most promising routes to sequestration due to the vast and mature experience by oil and gas industry [50]. Moreover, it has been proven its suitability for large-scale implementation [69]. Several CCS projects, at pilot and commercial scale, are currently operating around the world, including the Weyburn-Midale in Canada, In Salah in Algeria, the Salt Creek in USA and the Sleipner and Snøhvit projects in Norway [41,52]. Industry have been injecting CO_2 for more than four decades in oil gas and coal-bed methane reservoirs in order to enhance the extraction of hydrocarbons. Such process are known as Enhance Oil Recovery (EOR) and enhanced coal-bed methane recovery (ECBM), respectively [41,70,71]. Such processes can be considered as both CCS and CCU options [40,58]. For the purpose of this thesis, this process will be considered to be an CCU option and will be discussed further in the CCU section. Oil and gas reservoir have limited CO_2 storage capacity, compared to the vast amounts of anthropogenic CO_2 that needs to be stored.

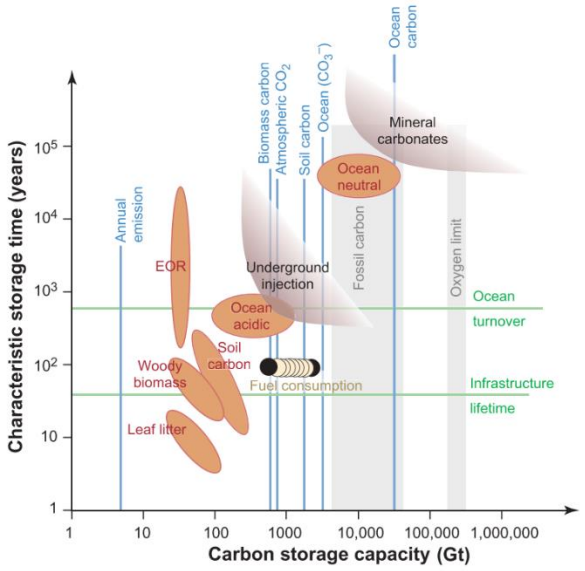

Fig. 1.9. Estimated CO_2 storage capacities and times for different sequestration options. Figure from Lackner et al., 2003 [50].

Deep saline aquifers also represent a suitable and easy way to sequester CO_2, as demonstrated by the energy company Statoil, where removed CO_2 from natural gas has been injected under the North Sea [72]. The CO_2 storage capacity is estimated to be of 700-900 Gt [41]. However, uncertainties regarding the storage time due to seismic activity and potential migration of buoyant CO_2, a specific study have to be performed to guarantee the long-term integrity of the stored CO_2. Further explorations on the injection of CO_2 on coal-bed formation are required for them to be

considered as safe storage option [41]. Oceans-bed have vast storage capacity when CO_2 is injected at great depths. However, such storage option have not yet been tested on the large-scale [41,58].

Although CO_2 storage in considered to be the most promising route, it has great risks associated with the possible leaks of vast amounts of CO_2 and the related damage to the environment. Fig. 1.10i summarizes the possible CO_2 leakages pathways in geological reservoirs and the respective remedial measures. The annual leakages are reported to be from 0.00001 % to 1%. Generally, stored CO_2 could escape from the geological CO_2-reservoir through: (i) the pore system in caprocks if the capillary pressure at which CO_2 may enter the caprock is exceeded, (ii) displacements/openings in fracture, faults and the caprock and (iii) poorly-completed and/or abandoned pre-existing wells [41]. This last option is considered to be the most probable leakage pathway [73]. Fig. 1.10ii summarizes the possible leakages pathways in an abandoned well. It should also be taken into account the possible increase of pressure caused by the injection and CO_2, which might exceed the maximum allowed pressure for the specific geological formation, thus, causing fracturing of the caprock and/or reactivating faults [74].

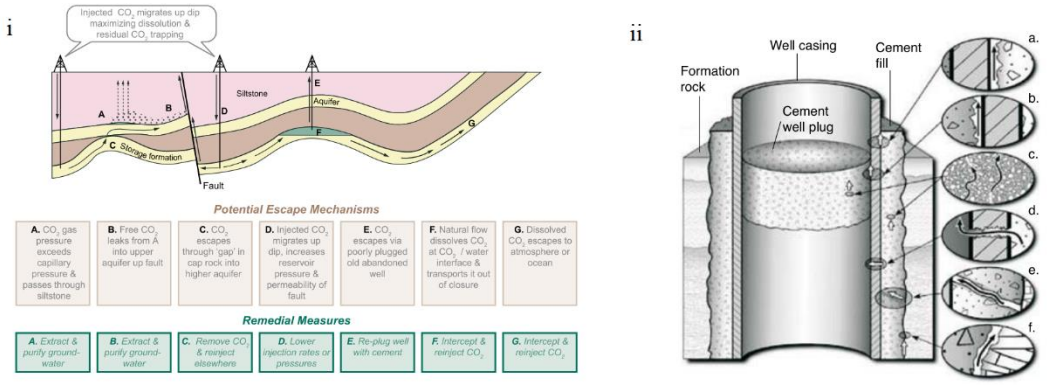

Fig. 1.10. Potential CO_2-stored leakages pathways from **(i)** saline formations and **(ii)** abandoned well. (a, b) between casing and cement wall and plug, respectively; trough (c) cement plugs, (d) casing and (e) cement wall; (f) between then cement wall and rock. Figure adapted from Metz et al., 2005 [41].

As observe in Fig. 1.9, the formation of carbonates represents the safer and with more storage capacity than any other sequestration option [50,75]. However, it is more expensive than the above mentioned options [50] (Table 1.2). Such process accelerated the neutralization reaction between CO_2-rich fluids and alkaline Ca/Mg-bearing rocks (Na/K-bearing rocks are also candidates for mineralization; however, such reserves are far less common than Ca/Mg-bearing rocks). Such reactions are exothermic and thermodynamically favored, and the reaction products are stable and commonly found in nature. This process is known as “In-situ mineral carbonation” [48].

The storage capacity of vast and widespread reserves of Mg-rich silicates in the Earth’s crust far exceeds the total CO_2 that can be produced by burning the estimated remaining fossil fuel reserves [50]. Recently, the CarbFix project in Iceland have demonstrated the permanent disposal of CO_2 by

accelerated carbonation of Ca-rich basaltic rocks into carbonates, where 95% of the total CO_2 injected has been mineralized in less than 2 years [76].

Table 1.2. Summary of advantages and disadvantages of different CCS technologies. *Does not include capture costs. Table adapted from Bobicki et al., 2012 [42]

Storage Method	Advantages	Disadvantages	Cost* (US$/t$CO_2$ stored)
Geological sequestration	• Feasible on a large scale • Substantial storage capacity • Low cost	• Requires monitoring • Possible CO_2 leakages	0.5 – 8.0 (Storage) 0.1-0.3 (Monitoring)
Ocean carbon sequestration	• Large storage capacity	• Temporary storage • Potential harmful effects on aquatic microbes and biota	6 – 31 (Pipeline) 12- 16 (Tanker)
Industrial use	• CO_2 incorporated into valuable products	• Limited storage capacity • Short storage time • High cost	-
In-situ mineral carbonation	• Only known form of permanent storage • Vast and widespread reserves of reactive feedstock, capable of binding all CO_2 released upon combustion of the fossil-fuel reserves •Carbonation products are stable and environmentally benign	• Energy intensive • High costs	50 - 100

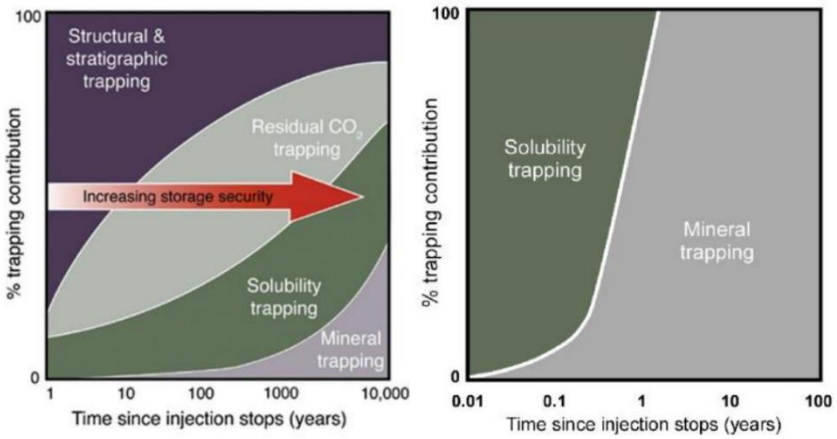

Fig. 1.11. Schematic of the different trapping mechanisms of **(left)** traditional geological storage in sedimentary basins and **(right)** CarbFix approach for geological storage. Figure from Grandia et al., 2014 [77].

Comparison of the CO_2-trapping mechanisms between the traditional geological storage in sedimentary basins with traditional in-situ mineral carbonation processes is shown on Fig 1.11. Stratigraphic and structural trapping refers to the trapping mechanisms where CO_2 is trapped via impermeable caprock or folded/fracture rocks, and in some cases, faults can also act as poorly-permeable barriers or other cases a potential leakages pathways [78]. Residual CO_2 trapping occurs in saline formation that do not have a closed trap, however, when CO_2 is injected in a saline formation where the fluids migrate very slowly over long distances, it migrated buoyantly upwards

(since it is less dense than the formation water)[79]. Eventually, CO_2 gets trapped in local structural or stratigraphic traps within the formation or as residual CO_2 saturation. Solubility trapping occurs by the dissolution of CO_2 in the formation water. Mineral trapping refers to the CO_2-rich fluids that has reacted with dissolved formation rock to form stable carbonates.

Mineral trapping in a traditional geological storage is partially attained after prolonged times after CO_2 injection. However, in CarbFix site have been demonstrated that such mechanisms could be the only CO_2 trap of all the injected CO_2 after only 1 year after the CO_2 injection (Fig. 1.11) [77,80].

Mineral carbonation can also be considered as an CCU option, since the carbonate products can be profitable [44], especially in the construction industry [81,82]. Such approach belongs to the so called "Ex-situ Mineral Carbonation" processes [83]. A detailed and technical description of such processes will be described in Chapter 2.

1.2.3. Carbon Capture and Utilization (CCU)

An extensive diversity of CCU options are being improved and developed in order to utilize the vast amounts of captured CO_2. The CO_2 utilization potential should meet the proportionate scale of future CO_2 capture technologies. Captured CO_2 can be utilized for the production of valuable products such as: food and drink industry, EOR & ECBM, chemical, fuel & carbonate synthesis, Enhance Geothermal Systems (EGS), and to cultivate microalgae, which it is later used for the production of biofuels [40,84–86]. The potential CO_2 utilization market demand is shown in Table 1.3. The main CCU options are described in the upcoming sections.

Table 1.3. Potential CO_2 market demand. Million metric tonnes per year (MPTA). Table from Brinckerhoff et al., 2011 [87].

CO_2 Utilization method	Potential CO_2 demand (MTPA)	CO_2 utilization method	Potential CO_2 demand (MTPA)
EOR, and ECBM	30 -300	Horticulture	1 - 5
Mineralization	>300	Pulp and paper processing	< 1
Fuel & Chemical synthesis	>300	Inerting	< 1
Biofuel from algae	>300	Steel manufacture	< 1
EGS	5-30	Metal working	< 1
Beverage carbonation	~14	$ssCO_2$ as solvent	< 1
Food processing, packaging	~15	Electronics	< 1
Power generation (CO_2-working fluid)	< 1	Pneumatics	< 1
Water treatment	1 - 5	Welding	< 1
Wine making	< 1	Refrigerant gas	< 1
Coffee decaffeination	1 – 5	Fire suppression technology	< 1
Pharmaceutical processes	< 1		

1.2.3.1. Direct CO_2 utilization

Captured CO_2 can be directly utilized in the food and drink industry, commonly as carbonating agent, preservative, packaging gas and as a solvent for extraction of flavor and in the decaffeination process [40]. It can be also directly utilized in the pharmaceutical industry as a respiratory stimulant of for drug synthesis [40,45]. Generally, the CO_2 source for such processes are from the CO_2 waste streams from ammonia production, due to its high CO_2 purity.

1.2.3.2. EOR and ECBM

Such processes are used to extract unrecoverable hydrocarbon reserves. EOR can recover up to 60% more of the originally available crude. However, the industrial source of CO_2 used by those projects is extracted from underground reservoirs [50], and it is often used because its cheap and widely abundant [71]. Most of the CO_2 is extracted with concomitant pumped crude, and it is recycled in order to continue the loop, although some CO_2 is released in the atmosphere. Moreover, if CO_2 is injected in its supercritical condition, it decreases the crude viscosity, increasing the extraction yields [88]. The combined CO_2 storage with EOR and EGR could potentially provide additional revenues from oil and gas recovery and partially offset the costs of CO_2 capture processes.

1.2.3.3. Biofuels from microalgae

CO_2 can be utilized to cultivate microalgae. This latter is used for the production of biofuels [85,86]. This option does not require prior CO_2 capture processes, since algae have the ability to fix CO_2 and N_2 from flue gas waste streams [43,89]. Generally, the cultivation of microalgae is carried out in open raceway ponds (this requires large land area and process control is challenging) and photo-bioreactors [89,90]. This latter more expensive than the former but it does not require large land lands and it offers a better control of the reaction processes. Flat-panel reactors were recently developed offering low-cost and energy requirements [91,92].

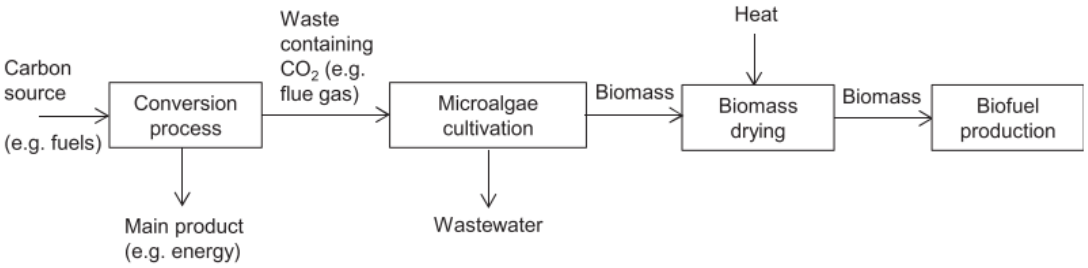

Fig. 1.12. Scheme of the CO_2 utilization for biofuels synthesis from microalgae. Figure from Cuéllar-Franca et al., 2015 [40].

Before the conversion from the microalgae biomass to fuels, it should be harvested and dried (Fig. 1.12). Then, after thermochemical (i.e.: gasification, liquefaction and pyrolysis) and biochemical (i.e.: anaerobic digestion, fermentation and esterification) conversion processes, syngas

is produced, followed by the production of fuels [85,90]. A large-scale production of such processes is yet not available because of the high production costs, mainly due to the energy requirements during harvesting [85,86].

1.2.3.4. Chemical and fuel synthesis

The utilization of CO_2 has received considerable attention as a possible way to manufacture chemicals, since it cheap and abundant [45,93,94]. CO_2 has a lower energy level than the desired chemicals and fuels. In order to use CO_2 for the synthesis of such products, energy and high-selectivity catalyst are required, since CO_2 is thermodynamically highly stable (Fig. 1.13). However, it has been suggested that the central carbon can be easily attacked by nucleophiles due to its electrophilic properties [95]. The energy required for breaking the CO_2 molecule can be supplied by energy-rich reactants or as heat, light or electricity. From a life-cycle perspective, it should be taken into account the CO_2 emitted from the energy supply required to carry-out the reaction. Therefore, for such processes, the utilization of renewable energy resources may significantly reduce its CO_2-footprint [40,51].

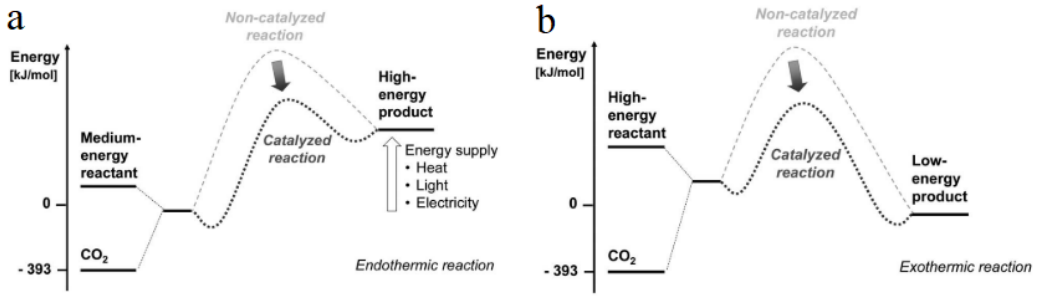

Fig. 1.13. Energy balance for the reaction of CO_2 with **(a)** medium-energy and **(b)** high-energy reactants. Adapted from Markewitz et al., 2012 [51].

Generally, chemicals synthesis from CO_2 is achieved through carboxylation reactions, where CO_2 is used as a precursor for organic compounds (i.e.: carbonates, acrylates and polymers) or reduction reactions where C=O bonds are broken to produce chemicals (i.e.: methane, methanol, syngas, urea and formic acid) [45,51,81]. A summary of the most common chemical produced from CO_2 is summarized in Fig. 1.14. CO_2 can also be utilized to produce fuels, such as the Fischer-Tropsch process, where after syngas is produced, CO is converted into different types of fuels [96,97].

Moreover, CO_2 stored by chemical and fuels have only limited storage periods due to their very-short life spans, which is generally less than 6 months. Therefore, capture and utilized CO_2 is quickly released into the atmosphere before the benefits of CO_2 capture can be observed [40]. Therefore, future research should focused on material synthesis with longer lifespans, such as carbonates that can be used in construction [41].

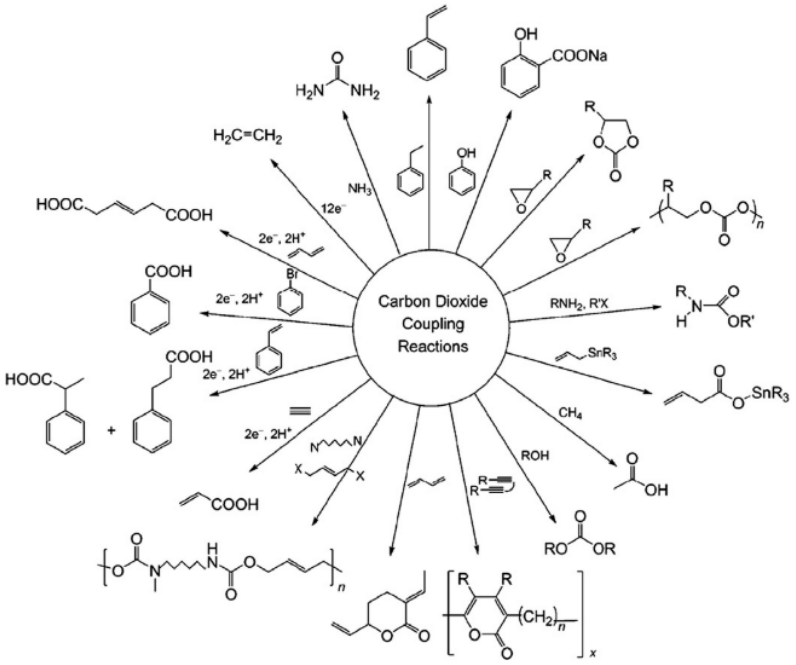

Fig. 1.14. CO_2 coupling reactions to produce a variety of chemicals. Figure from Li et al., 2013 [58].

1.2.3.5. Mineral carbonation

CO_2 utilization to produce carbonates are within the so called "Ex-situ mineral carbonation" processes [83]. Such process is based on the chemical reaction of CO_2 with alkaline earth-containing minerals (such as serpentine, olivine and wollastonite) to form environmental benign and permanent carbonates [41,98], without risks of CO_2 leakage [41]. This reaction is driven by exothermic thermodynamically favorable reactions (Fig 1.13b), and it has been suggested that the heat produced by this reactions could sustain the reaction with no further energy inputs [48]. Those characteristics makes this CCU option a suitable and promising alternative to chemical and fuel synthesis.

Moreover, CO_2 does not have to be separated from N_2 and impurities (i.e.: NO_x) since this gas species does not interfere with the carbonation reaction [55,99,100]. Therefore, prior CO_2 capture processes are not strictly needed.

This technology offers several advantages when compared to other CCUS options. Its CO_2 utilization demand market is on the rise. However, is not fully developed for large-scale applications as the costs and energy penalty are currently too high (including mining, transportation, mineral pretreatments and carbonation treatments). Moreover, there is a huge potential for optimizing the efficiency and the energy requirements for pretreatments and carbonation reactions, as well as targeting cheap and widely available reactive feedstocks sources [40,84,101]. For the purpose of this thesis, a detailed and technical description of such processes will be described in Chapter 2.

1.3. Negative CO_2 Emissions Technologies (NETs)

In order to achieve the 1,5ºC goal [35], the scenarios for the reduction of CO_2 emissions are beginning to rely on the successful implementation of NETs alongside with CCUS (Fig. 1.4a) [102]. Generally, CO_2 capture processes can be applied from CO_2 emitting point sources, such as flue gas from conventional power plants. However, the average CO_2 capture rates are between 50-94%, the residual CO_2 is emitted to the atmosphere [103]. CO_2 capture cannot be applied to the vast amounts and widespread small emitters, especially in the transport sector (accounting to 50% of the total GHG emissions) [104].

NETs have been proposed to capture CO_2 directly from the atmosphere, thus, indirectly capturing the CO_2 that cannot be captured in-situ [37]. NETs have higher CO_2 separation costs when compared to traditional CO_2 capture processes. However, they offer particular advantages: (i) CO_2 can be captured from any emitting source at different time and location, (ii) the location of the capture units can be placed near the storage site, thus, avoiding the associated transportation costs and (iii) such processes are not influenced by other pollutants (i.e.: nitrogen and sulphur oxides). Such technologies should not be considered as the solution for the delay implementation of anthropogenic CO_2 mitigation policies, but as complementary to other solutions [105].

Table 1.4. Land energy, water, nutrients and investment requirements as well as the albedo impact f NETs to meet the 2ºC target. *Mean (and maximum) potential is given along for each impacts and requirements. Table adapted from Smith et al., 2016 [38].

NET	Global Carbon removal (Gt Ceq yr^{-1} in 2100)	Mean (max.) land requirements (Mha in 2100)	Estimated Energy requirement (EJ yr^{-1} in 2100)	Mean (max.) water requirement (km^3 yr^{-1} in 2100)	Nutrients impact (kt N yr^{-1} in 2100)	Albedo impact in 2100	Investment needs (BECCS for electricity/biofuel; US$ yr^{-1} in 2050)
BECCS	3.3	380-700	-170	720	Variable	Variable	138 billion/123 billion
DAC	3.3	Very low (unless solar PV is used for energy)	156	10-300	None	None	>>BECCS
EW*	0.2 (1.0)	2 (10)	46	0.3 (1.5)	None	None	>BECCS
AR*	1.1 (3.3)	320 (970)	Very low	370 (1040)	2.2 (16.8)	Negative, or reduced GHG	<<BECCS

Plants have been doing such processes naturally, however, they are not able to neutralize the increasing anthropogenic CO_2 emissions [106]. There are a variety of NETs options such as: (i) BECCS [107], (ii) DAC [108], (iii) enhanced weathering of minerals (EW) [109], (iv) afforestation and reforestation (AR) [110,111], (v) carbon uptake by the ocean, either biologically-driven such as fertilizing nutrient-limited areas [112,113] or chemically via enhancing alkalinity [114], (vi) altered

agricultural practices such as increased carbon storage in soils [115] and (vii) biomass conversion to recalcitrant biochar in order to be used as a soil amendment [116]. For the purpose of this thesis, an overview of AR, BECCS, DAC and EW will be provided since this are the main NETs processes [38]. A summary of the land, energy and water requirements of AR, BECCS, DAC and EW technologies in order to meet the IPCC scenarios to limit global warming bellow 2ºC in shown in Fig. 1.15 and Table 1.4.

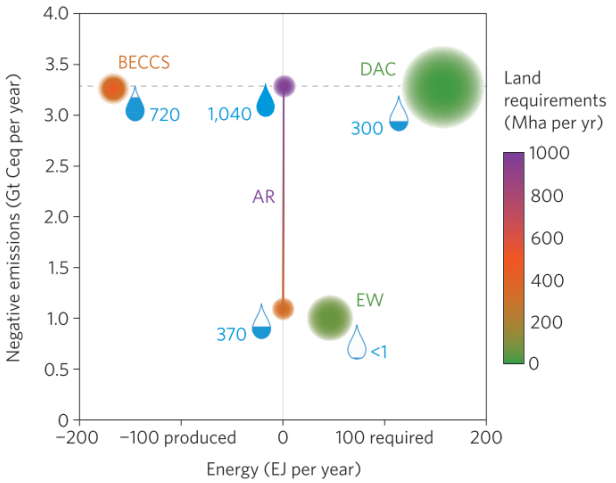

Fig. 1.15. Foreseen CO_2 negative emissions of different NETs (BECCS, DAC, Afforestation and Restoration and Enhanced Weathering) in order to meet the 2ºC target as well as the expected energy requirements or production, land and water requirements, respectively. Water requirements is shown as water droplets ($km^3\ yr^{-1}$). Investment need are represented by the circle area, see table 1.4. Figure from Smith et al., 2016 [38].

1.3.1. Afforestation and Reforestation (AR)

Afforestation and the restoration of trees it still one of the most effective strategies to mitigate climate change. Recent studies have estimated the global tree cover potential and the role it will play in the carbon cycle [117,118]. A total of 4.4 billion ha of canopy could be supported under the current climate conditions, occupying 1.6 to 2.8 billion ha more when compared to the current tree cover [117]. However, only 0,9 billion ha are free of cropland and urban regions [117,119].

The IPCC models [16] include a forest restoration target of 1 billion ha. Bastin et al., 2019 [117] have reported that such goal is undoubtedly achievable under current climate. This vegetation will be able to store an additional 205 Gt of carbon. The biomass stocks of the current vegetation are of ~ 450 PgC (Fig. 1.16a). The potential biomass stock of potential vegetation is estimated to be ~ 916 PgC, doubling the actual biomass stocks, as evidenced by the almost doubled potential biomass stock per area when compared to the actual stock (Fig. 1.16b). The estimated biomass stock potential is also almost double for each of the world's major biomes (Fig. 1.16c). Moreover, this different land-use type could have significantly higher biomass stocks within the same occupied area [118]

(Fig. 1.16b, d). Therefore, this might indicate the huge global tree restoration potential, in addition to those estimated by Bastin et al., 2019 [117] (if afforestation of an additional 0,9 billion ha occurs). Moreover, AR is relatively inexpensive when compared to other NETs (Fig. 1.15 and table 1.4).

It should also be noted that such processes might threat biodiversity, water and food security, due to their vast land requirements (Fig. 1.15, Table 1.4) [38] and issues might rise for land competition with BECCS [120,121]. It is also important to take into account the unintended impacts of AR, since alt high latitudes, an increased evapotranspiration would increase the atmospheric water vapor content, a therefore, limiting the effectiveness for tackling climate change. Analogously, the increased water requirements are another important trade-off, especially for dry regions.

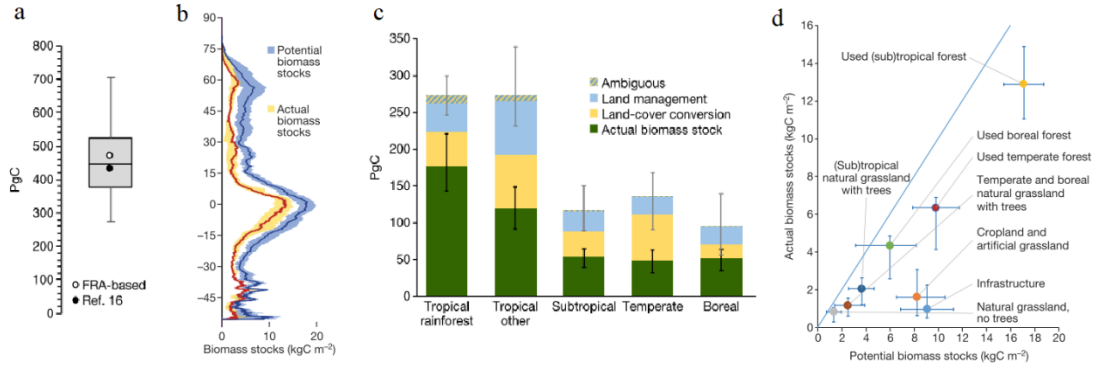

Fig. 1.16. (a) Estimated current biomass stock of the current vegetation. **(b)** Latitudinal profile of actual and potential biomass stock estimates. Line and shades show the estimated respective median and range. **(c)** Actual and potential biomass stocks from vegetation in the world major biomes. **(d)** Ranges of potential and actual biomass stocks by different land-use types. The diagonal line indicates de 1:1 that the actual biomass stock meets the its estimated potential. Figure adapted from Erb et al., 2018 [118].

1.3.2. Bioenergy with Carbon Capture and Storage (BECCS)

Pants and microorganisms capture and utilize CO_2 through photosynthesis, producing biomass. This latter can be used to produce electricity in a thermoelectric power plant releasing the capture CO_2. Therefore, biomass is considered to be a clean energy source. If the CO_2 released upon biomass combustion is utilized or stored, the atmospheric carbon balance is negative. Consequently, BECCS technologies are foreseen as an interesting option for producing energy and reducing the CO_2 concentration in the atmosphere simultaneously [108,122]. Not all the heat is recovered upon electricity production from biomass combustion and generally, CO_2 capture efficiency is of 90% [105]. Recent studies have proposed that heat waste can be potentially use to increase the efficiency of amine-based CO_2 capture, by its utilization during amine regeneration, tackling simultaneously both issues [123].

Scenarios to limit global warming bellow 2ºC relative to preindustrial level, has emphasized the role of NETs, particularly the large-scale deployment of BECCS, such as the RCP2,6 scenario

[16,120,124]. However, large-scale BECCS deployment have potential trade-offs, particularly regarding land and water requirements, which might threat biodiversity, water and food security, analogously to AR (Fig. 1.15, Table 1.4)[38,120]. To remove 1Gt of CO_2 by current BECCS approaches, 1 – 1.7 ha of land is required [105].

Kato and Yamagata, 2014 [120] have estimated the land requirements for large-scale BECCS deployment including conventional bioenergy crops (including the bioethanol production and post-combustion CO_2 capture of biofuels from sugarcane, sugar beet, maize and rapeseed) for three different scenarios in order to meet the RCP2,6 goals (Fig. 1.17, Table 1.5). All the results indicate a significant land deployment increase before 2055 for any scenario. The scenario with the highest ratio of CO_2 capture to the carbon per unit of produced biofuels (CR) and capture efficiencies of 90% also requires a significant increase on the land use for each of the biomass stocks, however the land requirements are significantly reduced when compared to scenarios with the lowest CR.

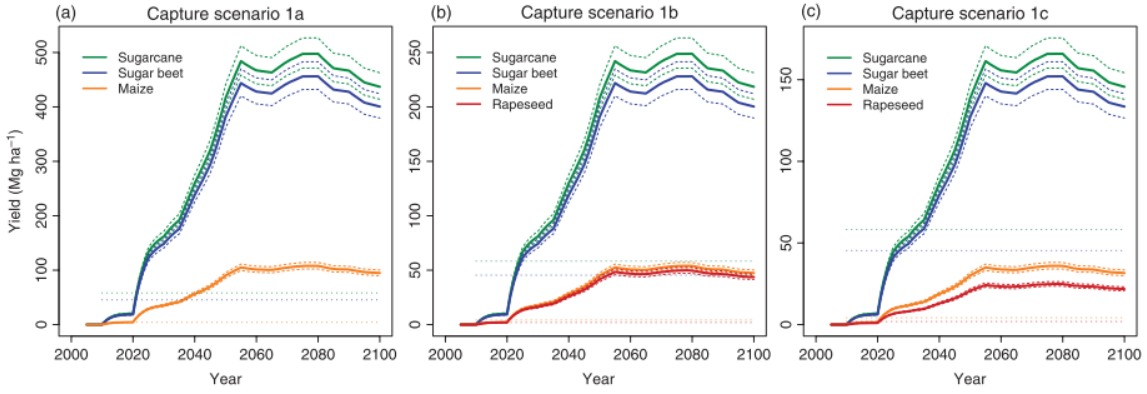

Fig. 1.17. Estimated land requirements required to achieve the BECCS of RCP2.6 for conventional bioenergy crops, including bioethanol production from sugarcane, sugar beet, maize and rapeseed. **(a)**, **(b)** and **(c)** corresponds to the different scenarios summarized in Table 1.5. Solid line represents the estimated land requirements considering 90% CCS efficiency for each crop. Dashed lines represent the ranges estimated with 85-95% CCS efficiency for each crop. Dotted lines correspond to the actual average yields in 2010 for each crop. Figure from Kato and Yamagata, 2014 [120].

Table 1.5. CO_2 capture scenarios for conventional bioenergy. Table adapted from Kato and Yamagata, 2014 [120].

Scenario	Technological options of CO_2 capturing systems	CR
1a	Fermentation process of bioethanol production	0.5
1b	1a + 50% post-combustion CO_2 capture of biofuels	1.0
1c	1a + 100% post-combustion CO_2 capture of biofuels	1.5

Moreover, biomass have higher moisture content and lower heating value than coal, but it has low SO_x and NO_x emissions upon calcination than the latter [105]. The large-scale BECCS deployments are also subjected to significant uncertainties [125,126], and currently is only used in some demonstration-projects. On the other hand, CCUS technologies are not commercially established. Such approach may also be limited by nutrient demand and/or increased water use [38].

1.3.3. Direct Air Capture (DAC)

The concept of capturing CO_2 from the atmosphere has been applied for decades in close environments, such as submarines and spacecrafts [127]. It was until 1999 when Lackner et al. [128], proposed that such process could be applied for climate change mitigation. The current DAC costs and energy requirements are too high for its quick development (Fig. 1.15 and Table 1.4) [38].

DAC processes have limited applications of the conventional PSCC of concentrated streams (i.e.: flue gas) since the energy required for such processes will be excessively high if applied for capture of ultra-diluted CO_2 in the atmosphere. The application of aqueous solutions of strong bases (see also Table 1.1; commonly used in Point Source Carbon Capture, PSCC) to DAC have been extensible studied [37]. Comparative studies with BECCS have suggested that aqueous solutions-based are the feasible option in the near term [129]. However, the high desorption temperatures (900ºC) limit the scalability of such processes due to its respective high costs.

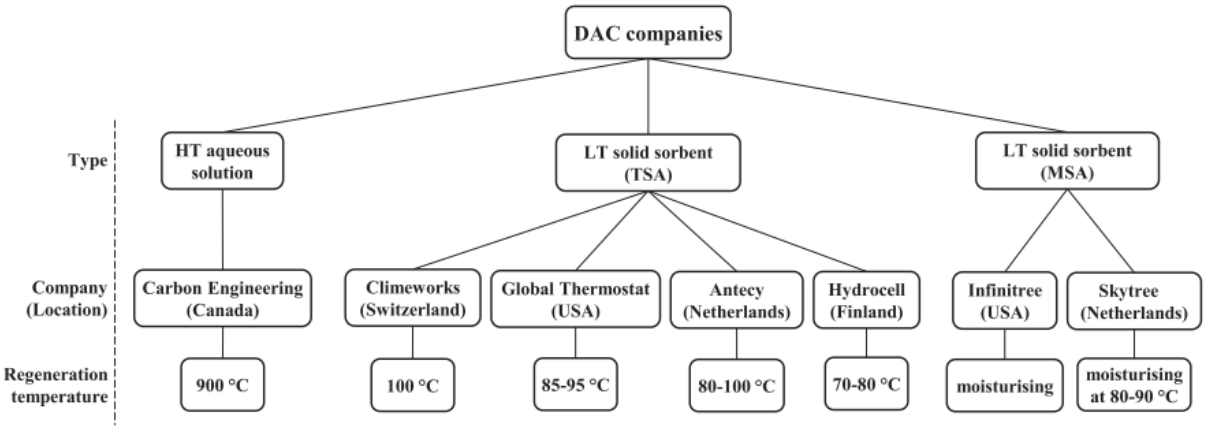

Fig. 1.18. Main DAC methods with its specific regeneration solvent/sorbent temperature and the current active companies on the field. HT: high-temperature, LT: low temperature. Figure adapted from Fasihi et al., 2019 [37]

As result, different approaches have been focusing on feasible options that can be applied to DAC, which include the utilization of sorbents and solvents that can be regenerated at low temperature. Currently, two main approaches stand-out: Temperature Swing Adsorption (TSA) and Moisture Swing Adsorption (MSA). For both methods, the regeneration of the solid-sorbent is carried at ≤100ºC [130,131]. Fig. 1.18 summarizes the main DAC method and current active companies in the field. An overview of high temperature aqueous solutions and low temperature solid sorbent processes will be presented in the following sections.

Fasihi et al., 2019 [37] have estimated the DAC capital expenditures (capex) as well as its CO_2 capacity demand until 2050 assuming two different scenarios: conservative (CS) and base case (BS). The first assumes only 50% realization of the cumulative DAC capacity demand caused by the delayed implementation of measures from the Paris Agreement. The latter assumes the punctual

execution of the Paris Agreement, which assumes DAC implementation by 2020. Such target is currently attained by different companies and it is expected that DAC technologies will meet the long-term targets.

The annual CO_2 DAC capacity demand is estimated to steeply grow from 3 MtC yr^{-1} (2020) to 470 MtC yr^{-1} (2030), 4,7 GtC yr^{-1} (2040) and 15 GtC yr^{-1} (2050). Moreover, it is expected that the DAC capex will be significantly reduced from 2030. At such costs DAC will be competitive to PSCC. It should be also taking into account the lower transportation costs of DAC, since such capturing units can be located near CCUS sites. DAC's versatility and the expected capex drop increases the competitiveness of DAC vs CCUS projects.

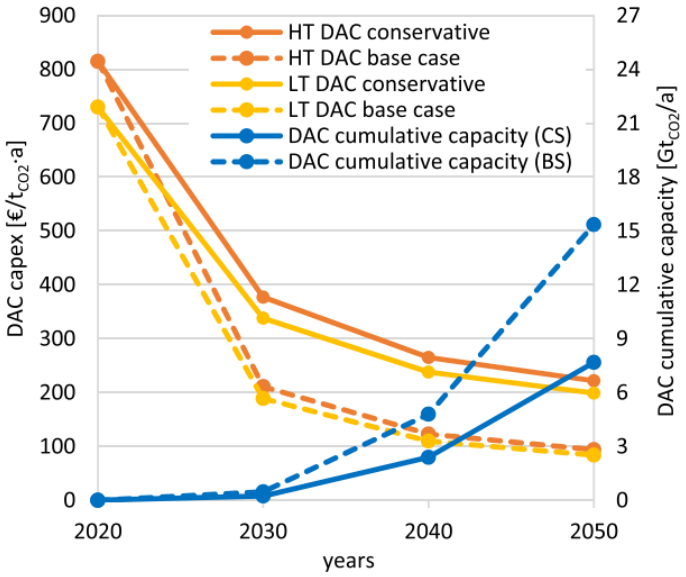

Fig 1.19. Estimated DAC capital expenditures development for LT and HT systems following conservative (CS) and base case scenarios (BS). Figure from Fasihi et al., 2019 [37]

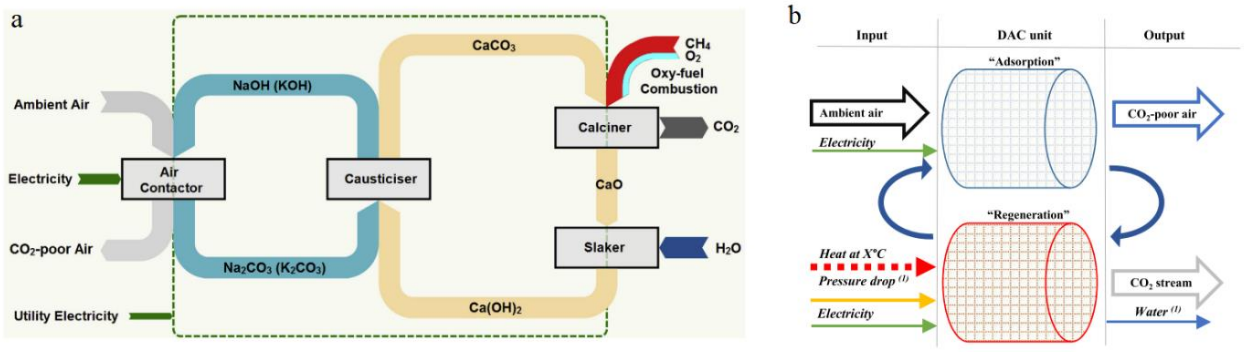

Fig. 1.20. Scheme of the fundamental processes of **(a)** high temperature aqueous solutions and **(b)** low temperature solid sorbents, (i)depends on the system. Figure adapted from Fasihi et al., 2019 [37] and Keith et al., 2018 [132].

Table 1.6. Technical specification of HT aqueous solutions and LT solid sorbent. Table adapted from Fasihi et al., 2019 [37].

DAC	Solvent/ Sorbent	CO_2 con.	Absorption	Desorption		Energy demand		CO_2 purity	Reference
		ppm	T (ºC)	T (ºC)	P (bar)	kWh_{el}	kWh_{th}	%	
HT aqueous solution	• $KOH/Ca(OH)_2$	400	ambient	900	1	1535	-	> 97	Fasihi et al., 2019 [37]
	• $KOH/Ca(OH)_2$	400	ambient	900	1	-	2450	97.1	Keith et al., 2018 [132]
LT solid sorbent	• Amine-based	400	ambient	100	0.2	200-300	1500-2000	99.9	Climeworks, data obtained from Fasihi et al., 2019 [37]
	• Amino-polymer	400	ambient	85-95	0.5-0.9	150-260	1170-1410	> 98.5	Ping et al., 2018 [133]
	• TRI-PE-MCM-41	400	ambient	110	1.4	218	1656	88	Kulkarni and Sholl, 2012 [134]

1.3.3.1. High Temperature (HT) aqueous solution

Generally, such processes consist of two simultaneous cycles. In the first cycle, absorption, air is brought into contact with an aqueous solution containing sodium hydroxide (NaOH). This latter reacts with CO_2 from atmospheric air at room temperature and ambient pressure to form sodium carbonate (Na_2CO_3). Then, the solution is transported to the second cycle, regeneration. In this process, Na_2CO_3 is mixed with calcium hydroxide, $Ca(OH)_2$, in the causticiser unit, where calcium carbonate ($CaCO_3$) is formed, regenerating the solvent. The solvent is then sent back to the absorption unit. $CaCO_3$ is calcined at 900ºC to release pure CO_2 [132]. Figure 1.20a shows a fundamental example of such processes. The calcination of calcite is the most energy intensive process requiring 1420-2250 kWh_{th} per ton of CO_2 [37]. Electrical power is also needed for blowing air through the contactor, spraying the aqueous solutions with NaOH, moving the solution through the absorption and regeneration unit and CO_2 compression. The energy required for such purposes is estimated to be of 366-764 kWh_{el} [37]. A summary of the different HT aqueous solutions systems and energy requirements are described in Table 1.6.

1.3.3.2. Low Temperature (LT) solid sorbent

This processes usually happens in a single unit where the absorption and desorption happen in two different steps. In the first step, ambient air (either by natural flow or helped by fans) is in contact with the filters containing the solid sorbents. CO_2 from the air binds chemically to the solid sorbent. Once the sorbent is CO_2-saturated, ambient air is no longer allowed to flow through the filters and the inlet valve is closed. The remaining air is swept either by pressures drop or be flowing steam through the system. In the second step, the system is heat up to a specific temperature, depending on the CO_2-desorption temperature of the solid sorbent. In TSA systems, the desorption of the solid sorbent is carried only by increasing the temperature to (80-100ºC) [130]. In MSA systems, the regeneration of the sorbent is carried by moisturizing and temperature increase up to 90ºC [131,135]

(Fig. 1.18). The release CO_2 is collected and transported for purification and compression. Before starting another loop, the system should be cooled down to ambient conditions. Figure 1.20b shows a fundamental example of such processes. Different sorbents have been proposed for such processes. The main sorbents and the system energy requirements for their respective system are described in Table 1.6.

1.3.4. Enhanced weathering (EW)

This approach, similar to mineral carbonation, consists of the acceleration of the natural weathering of silicate rock, releasing cations that can fix atmospheric CO_2 [136,137]. Generally, such process is carried out by displacing rock powder to suitable application areas to increase the natural weathering rates [138,139]. A common example is the dissolution of forsterite (Mg_2SiO_4) in contact with CO_2 and water (eq. 1.6). Dissolution of suck rock releases cations that then react with dissolved CO_2 to form bicarbonate and carbonate ions. These latter are eventually transported to the ocean. Naturally occurring weathering is able to sequester about 1 Gt of atmospheric CO_2 per year [140]. It has been estimated that if a 4mm thick layer of forsterite spread over the entire terrestrial land is weathered, could consume all the atmospheric CO_2 [109]. Moreover, carbonate minerals may precipitate, more likely fixing CO_2 for millions of years [141].

$$Mg_2SiO_4 + 4CO_2 + 4H_2O \rightarrow 2Mg_2^+ + 4HCO_3^- + H_2SiO_4 \quad (1.6)$$

Ultramafic igneous rocks are foreseen as possible feedstocks for EW [142–144] and mineral carbonation [101,145,146] due their vast and widespread abundance and their large carbon sequestration capacity. Current approaches for mineral carbonation of ultramafic rocks requires elevated temperatures and pressures. This elevates the capital investment required and may limit its large-scale deployment [47]. EW occurs at ambient pressure and temperature, using the soil as reactor, eluding some of the capital expenditure associated with mineral carbonation [147].

EW key technologies are mature and already used on regional scale for fertilization and pH regulation of agricultural and forest soil [147,148]. However, scaling-up such processes might have possible drawbacks such as increasing river's pH [149] or the release of metals (which is associated with the source rock composition) [150]. Moreover, land availability and suitability might be a major limiting factor [122], which is highly dependent on infrastructure requirements of transporting large volumes of rock, compounded by the fact that the estimated potential for atmospheric CO_2 removal is lower than other NETs [38] (see also Fig. 1.15).

Moreover, soil and plant productivity in agriculture have been improved using EW. Silicon, product of silicate weathering, is a beneficial nutrient for many plants [151,152]. Additionally, trace content of phosphorous and other elements could increase the productivity of some agricultural areas. However, metals (also released upon weathering) could potentially inhibit plant growth and

use [153]. Currently, the potential effects of EW on agricultural productivity need more research. [154].

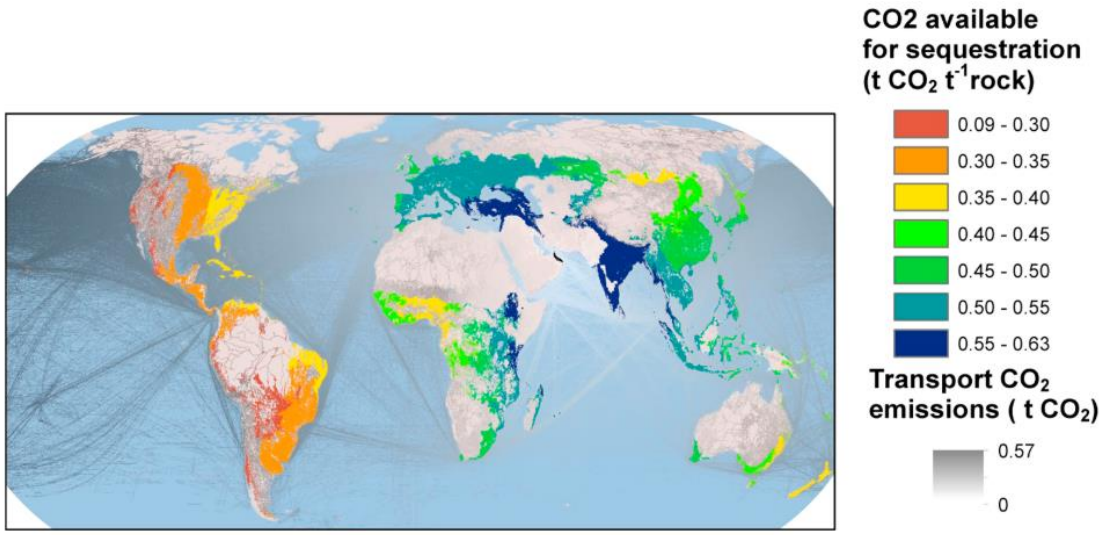

Fig. 1.21. Estimated EW removal capacity and their correspondent CO_2 emissions associated with feedstock preparation and transportation using only the Samail Ophiolite as source rock (marked in black) taking into account a conservative scenario (subtracting the pessimistic values from estimated optimistic value), see Table 1.7. Figure from Moosdorf et al., 2014 [147].

Table 1.7. Factor affecting the EW CO_2 removal capacity and their associated CO_2 emissions due to feedstock preparation and transportation. Negative values indicate CO_2 emissions; positive values indicate CO_2 removed from the atmosphere. t^{-1} refers to tonnes of rock. Table adapted from Moosdorf et al., 2014 [147].

Theme	CO_2 budget reference	Optimistic scenario		Pessimistic scenario	
		Condition	Value	Condition	Value
Source material	-	Ultramafic rocks	736 10^3 km^2	Ultramafic rocks	736 10^3 km^2
CO_2 removal capacity	10	Upper limit value form model (see figure 1.21 and 1.22)	1.1	Lower limit value form model (see figure 1.21 and 1.22)	0.8
Mining	9	Estimated energy requirement	-0.007 tCO_2 t^{-1}	Estimated energy requirement	-0.007 tCO_2 t^{-1}
Communication	10	0.6 GJ t^{-1} energy demand	-0.07 tCO_2 t^{-1}	2 GJ t^{-1} energy demand	-0.22 tCO_2 t^{-1}
Roads	32	Lower estimate	-59 tCO_2 t^{-1}	Upper estimate	-109 tCO_2 t^{-1}
Railroads	32	Lower estimate	-7 tCO_2 t^{-1}	Upper estimate	-26 tCO_2 t^{-1}
Trails	32	Lower estimate	-59 tCO_2 t^{-1}	Upper estimate	-109 tCO_2 t^{-1}
Rivers	32	Lower estimate	-28 tCO_2 t^{-1}	Upper estimate	-35 tCO_2 t^{-1}
Buffer: 5km around roads, railroads, trails and rivers	32	Lower estimate	-59 tCO_2 t^{-1}	Upper estimate	-109 tCO_2 t^{-1}
Shipping lines	35	Lower estimate	-5 tCO_2 t^{-1}	Upper estimate	-20 tCO_2 t^{-1}
Application emissions	35	1 t per ha, 80 ha per field	-0.0011 tCO_2 t^{-1}	3 t per ha, 1 ha per field	-0.004 tCO_2 t^{-1}
Arable land	-	Upper estimate of proportion on cells, outside polar or arid climates	14.7 10^6 km^2	Lower estimate of proportion on cells, outside polar or arid climates	11.8 10^6 km^2

The Samail Ophiolite in Oman has been suggested as the geological location for in-situ mineral carbonation [48]. Additionally, some studies have also suggested to mine and grind this geological unit for EW applications [147]. The global EW CO_2 sequestration capacity, if Samail Ophiolite are used as the only source rock, has been modelled as well as the CO_2 emissions due to the transportation of this large volumes of rock (Fig. 1.21). The average Mg% content of Harzburgites from Samail is of 25%, which it translates to a maximum CO_2 sequestration capacity of 0.89 tCO_2 t^{-1} (tones of CO_2 per tones of rock) (see also Table 1.7) [155]. In a conservative scenario (taking into account pessimistic scenario conditions, see Table 1.7), large agricultural areas in Europe and most part of Southeast Asia will be able to sequester 0.5 tCO_2 t^{-1} [147]. However, if such rocks are transported to North America, the CO_2 emissions associated with transportation and material preparation will significantly reduce the net EW CO_2 sequestration capacity accounting to values bellow 0.3 tCO_2 t^{-1}.

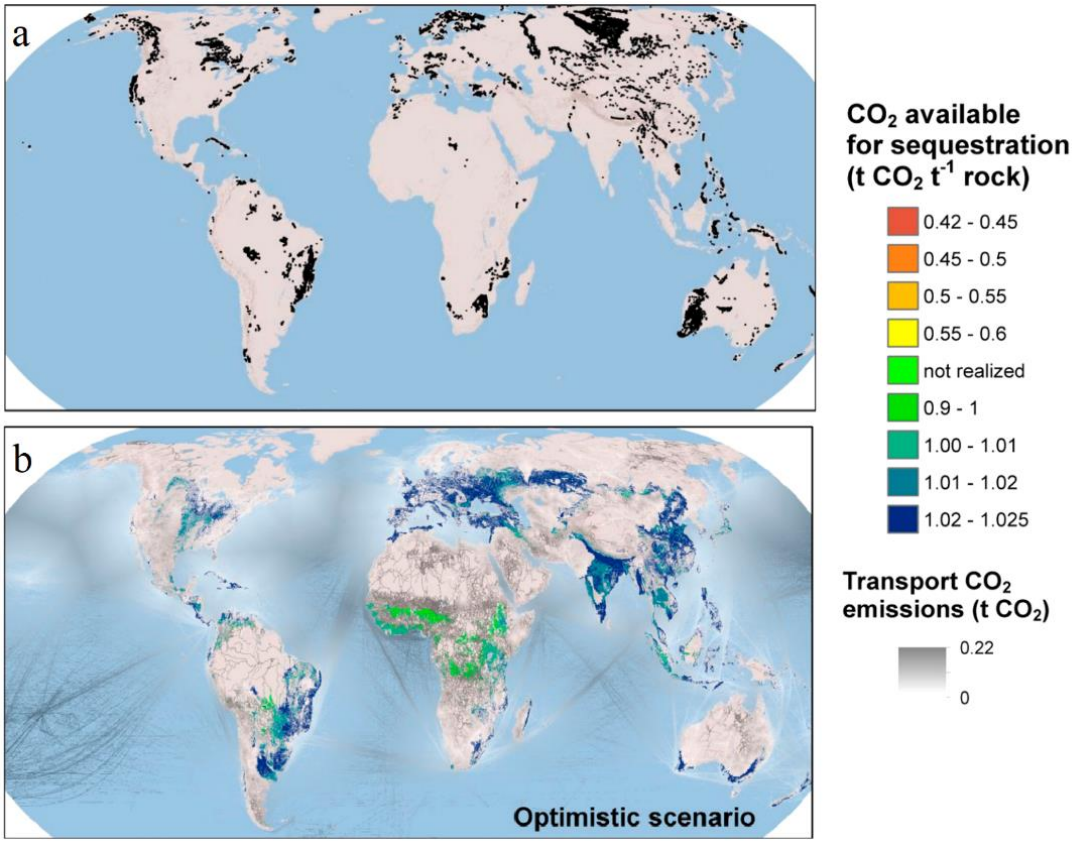

Fig. 1.22. (a) Source rock location according to the GLiM (marked in black). **(b)** EW removal capacity and their correspondent CO_2 emissions associated with feedstock preparation and transportation using only the different ultramafic source rock from the GLiM, taking into account an optimistic scenario, see Table 1.7. Figure adapted from Moosdorf et al., 2014 [147].

Different available and widespread ultramafic rock sources can be used for EW. Within the Global Lithological Map (GLiM), 736000 km^2 of ultramafic rock unit occur. However, the GLiM does not include all ultramafic rocks globally. Moosdorf et al., 2014 [147] have also modelled the

EW CO_2 removal capacity taking into account the ultramafic rock occurrence within the GLiM (Fig. 1.22a). The CO_2 removal capacity is greatly increased for both pessimistic and optimistic scenarios when compared to the model where only Samail Ophiolites were used (Fig. 1.21). The transport cost and their associated CO_2 emissions are, thus, not a major constraint for the global EW application. If the unrepresented ultramafic rock in the GLiM are also used, it will increase further the EW CO_2 removal capacity as the transport routes and their associated CO_2 emissions will be reduced.

In any case, the associated CO_2 emissions from transportation and material preparation do not exceed the CO_2 removal potential for the majority of application areas (even under pessimistic scenario conditions). However, when the CO_2 removal potential approaches zero, higher unit cost are associated. The estimated total energy requirements of terrestrial enhanced weathering are 1.6 (pessimistic scenario) and 9.9 (optimistic scenario) GJ tCO_2^{-1}. The huge logistic requirements for large-scale global application limit the CO_2 removal capacity of EW. Therefore, such technologies could only be one part of the puzzle in the efforts to mitigate climate change [147].

2. Mineral carbonation

The main advantages of mineral carbonation (MC) for CCUS and NETs applications have been described in Chapter 1. This chapter will provide a detailed and technical summary of the different MC processes, their applications and implications for climate change mitigation.

Accelerated CO_2 mineralization mimics the naturally occurring weathering of Ca/Mg-rich silicate rocks in an anthropic timescale [42,48,50]. This alternative to tackle the ever-increasing anthropogenic CO_2 emissions to the atmosphere was firstly proposed by Seifritz, 1990 [136]. Lackner et al., 1995 [156] presented the first detailed study of such processes, which main advantages are: (i) the CO_2 storage capacity of vast and widespread reserves of Mg/Ca-rich minerals far exceeds the total CO_2 that can be produced in all the fossil fuel reserves are consumed (Figure 1.9) [50]; (ii) the carbonation products are geologically stable and can store CO_2 over millions of years, without monitoring (see also Table 1.2) [50,157]; (iii) profitable pure carbonates and silica can be produced [44,87]; (iv) exothermic reactions could provide sufficient heat to sustain the reaction without any addition of energy [48,156]. However, such processes are kinetically challenging and current approaches are energy intensive, requiring high temperatures and pressure treatment in specialized reactor vessels, increasing significantly the associated costs [42,145,146]. It has been predicted that such process can be simplified and eventually energy required can be reduced for obtaining efficient carbonation yields, however it remains a challenging field [156,158,159]. Carbonate rocks represent the world's biggest carbon reservoir [160]. Due to the vast amount of naturally-occurring carbonates in the lithosphere, an enormous MC potential can be expected (Table 2.1)[161].

Calcium and Magnesium are the most abundant alkaline earth metals. Therefore, due to their high carbonation potential are generally considered for MC [157]. Ca and Mg oxides are the ideal carbonation feedstocks, as the reaction of these minerals with CO_2 generates the most heat and is not as kinetically limited as silicate carbonation (eq. 2.1, 2.2). However, only scarce abundance of

this minerals are found in nature, mainly due to their relatively high reactivity with CO_2 and solubility [41,162,163]. However, Ca and Mg are abundant in silicate rocks, but their exothermic reaction with CO_2 is more kinetically challenging and less energy is released than Mg and Ca oxides (eq. 2.3, 2.4, 2.5). Ultrabasic rocks have the highest CaO + MgO (%) among other silicates, and therefore, they have the higher carbonation potential (Figure 2.1) [164]. The common natural-occurring Ca/Mg-rich silicate minerals feedstock for MC include wollastonite ($CaSiO_3$) , Mg-olivine (Mg_2SiO_4; forsterite) and Mg-serpentine ($Mg_3Si_2(OH)_4$) [157,165]. Wollastonite is more reactive than the other silicates, however it is not as abundant as olivine and serpentine [98].

$$CaO + CO_2 \rightarrow CaCO_3 + 179\ kJ/mol \quad (2.1)$$

$$MgO + CO_2 \rightarrow MgCO_3 + 118\ kJ/mol \quad (2.2)$$

$$CaSiO_3 + CO_2 \rightarrow CaCO_3 + SiO_2 + 90\ kJ/mol \quad (2.3)$$

$$Mg_2SiO_4 + 2CO_2 \rightarrow 2MgCO_3 + SiO_2 + 89kJ/mol \quad (2.4)$$

$$Mg_3Si_2(OH)_4 + 3CO_2 \rightarrow 3MgCO_3 + 2SiO_2 + 2\ H_2O + 64\ kJ/mol \quad (2.5)$$

Table 2.1. Distribution of C on earth. Table from Dunsmore, 1992 [161].

Source	Amount (10^{15} kg)	Relative amount (%)
Ca-carbonate	35000	46.64
Ca/Mg-carbonate	25000	33.31
Carbonates	60000	79.99
Sedimentary C (i.e.: graphite)	15000	19.99
Fossil fuels	4	0.0053
Other geological C	15004	19.99
Total C in the lithosphere (“dead C”)	75004	99.94
Oceanic HCO_3^- and CO_3^{2-}	42	0.056
Dead surficial C (i.e.: hummus)	3	0.0040
Atmospheric CO_2	0.72	0.00095
All life	0.56	0.00074
Total non-geological C (“live C”)	46.28	0.06

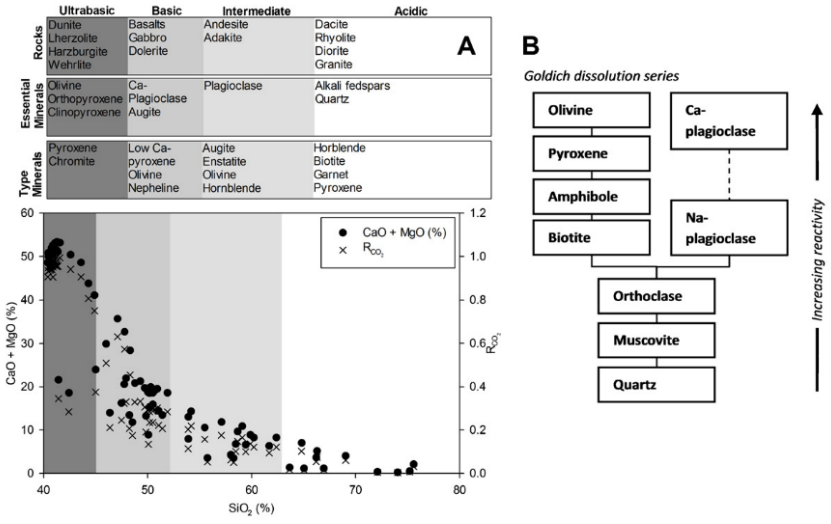

Fig. 2.1. (a) Ca/Mg-bearing rocks with their respective composition as week as their maximum CO_2 capture potential (R_{CO_2}). **(b)** Goldich dissolution series [166]. Figure from Renforth 2012 [164].

Vast amounts of silicate ore are required to fix a significant amount of anthropogenic CO_2, thus, the environmental impact on costs associated with the large-scale carbonation of such rocks would be substantial. Moreover, the current MC approaches for CCUS are energy intensive due to the feedstock preparation, processing, purification/disposal of the carbonate products. Reaction carried at high-temperatures and pressures in aqueous-mediated system as well as energy intensive pretreatments (i.e: grinding, heat activation[‡] and chemical activation[§]) are required to obtain elevated conversion yields. The estimated amount of energy required for such processes is of 30-50% of power plant output. Therefore, such elevated costs with the current approaches have prevented this option from large-scale deployment [41,167]. Mining and preparation of sustainable MC silicate rocks has to be also accounted. Previous studies have been estimated to be: 10 US$/t CO_2 stored with 2% of additional CO_2 emissions [41].

A summary of MC studies using different reactive feedstock and their respective pretreatments as well as the MC reaction conditions and the obtained reaction yield and carbonation potential is shown in Table 2.2. The carbonation potential is expressed as $1/R_{CO_2}$ where R_{CO_2} corresponds to the mass of ore that needs to be mined in order to store a unit mass of CO_2; higher $1/R_{CO_2}$ indicate higher carbonation potential, following the eq. 2.6 [145,168].

$$\frac{1}{R_{CO_2}} = \left(\frac{y_{Mg}}{MW_{Mg}} + \frac{y_{Ca}}{MW_{Ca}} + \frac{y_{Fe}}{MW_{Fe}}\right) \cdot MW_{CO_2} \quad (2.6)$$

Where y is the Mg/Ca/Fe mass fraction and MW is the molecular weight of respective alkaline metal species and CO_2.

Table 2.2. Summary of MC studies. [a] Direct and [b] indirect carbonation. Modified after Gadikota and Park, 2015 [98]. EDTA: ethylenediaminetetraacetic acid.

Mineral and rocks	Composition (wt%.)	$\frac{1}{R_{CO_2}}$	Carbonation yield (%)	Reaction conditions				Ref.
				Pretreatment	Reaction-phase	P_{CO_2}, T, reaction time	Chemical additives	
• Brucite $Mg(OH)_2$	MgO: 68	0.77	60	None	Gas-solid[a]	40 bar, 510ºC, 6h	None	[169]
			>97	None	Steam-mediated[a]	10 bar, 120ºC, 4h	None	[55]
• Olivine $(Mg,Fe)_2SiO_4$	Mg: 30.2 Fe: 6.5	0.63	55	Attrition grinding	Aqueous[a]	152 bar, 185ºC, 1h	2.5 M $NaHCO_3$	[101]
	CaO: 0.2 MgO: 47.3 FeO: 12.3	0.59	73	None	Aqueous[a]	141 bar, 185ºC, 3h	1.0 M NaCl + 0.64 M $NaHCO_3$	[146]
	Ca: 0.1 Mg: 27,9 Fe: 6.1	0.56	38	Attrition grinding	Aqueous[a]	152 bar, 185ºC, 1h	1.0 M NaCl + 0.64 M $NaHCO_3$	[168]
• Serpentine $(Mg,Fe)_3(OH)_4Si_3O_5$	Mg: 27,1 Fe: 4.3	0.53	65	Aqueous with pH swing	Aqueous[b]	1 bar, 70ºC, 1h	Orthophosphoric acid (1 vol%) + oxalic acid (0.9 wt%) + EDTA (0.1 wt%)	[170]

[‡] Thermal amorphization of serpentine minerals, see section 2.3.1.3.2
[§] Also known as indirect carbonation, see section 2.3.2

Mineral and rocks	Composition (wt%.)	$\frac{1}{R_{CO_2}}$	Carbonation yield (%)	Reaction conditions				Ref.
				Pretreatment	Reaction-phase	P_{CO_2}, T, reaction time	Chemical additives	
• Serpentine $(Mg,Fe)_3(OH)_4Si_3O_5$	Mg: 27,1 Fe: 4.3	0.53	42	Aqueous with pH swing	Aqueous[b]	1 bar, 70ºC, 1h	1.4 M $(NH_4)_2SO_4$	[170]
	Mg: 24.6 Fe: 2.4 (Antigorite)	0.48	43	Attrition grinding (<38 µm) + heat activation (630ºC, 2h)	Aqueous[a]	152 bar, 185ºC, 1h	1.0 M NaCl + 0.64 M $NaHCO_3$	[170]
	CaO: 0.1 MgO: 38.7 Fe_2O_3: 4.9	0.48	60	Magnetic separation + steam activation	Aqueous[a]	128 bar, 155ºC, 1h	1.0 M NaCl + 0.64 M $NaHCO_3$	[171]
	MgO:~40	0.43	30	None	Gas-solid[a]	340 bar, 300ºC	None	[169]
	Ca: 0.1 Mg: 27.9 Fe: 6.1 (Lizardite)	0.4	41	Attrition grinding (<38 µm) + heat activation (630ºC, 2h)	Aqueous[a]	152 bar, 185ºC, 1h	1.0 M NaCl + 0.64 M $NaHCO_3$	[172]
• Wollastonite $CaSiO_3$	Ca: 31.6 Mg: 0.3 Fe: 0.5	0.38	82	Attrition grinding	Aqueous[a]	152 bar, 185ºC, 1h	1.0 M NaCl + 0.64 M $NaHCO_3$	[168]
			100	Attrition grinding	Aqueous[a]	40.5 bar, 100ºC, 1h	None	[168]
• Fayalite Fe_2SiO_4	Ca: 0.6 Mg: 0.3 Fe: 44.3	0.36	66	Attrition grinding	Aqueous[a]	152 bar, 185ºC, 6h	1.0 M NaCl + 0.64 M $NaHCO_3$	[173]
• Talc $Mg_3Si_4O_{10}(OH)_2$	Ca:2.2 Mg: 15,7 Fe: 9.2	0.36	15	Attrition grinding	Aqueous[a]	152 bar, 185ºC, 0.5h	1.0 M NaCl + 0.64 M $NaHCO_3$	[173]
• Anorthite $CaAl_2Si_2O_8$	Ca: 10.3 Mg: 4.8 Fe: 3.0	0.23	9	Attrition grinding	Aqueous[a]	152 bar, 185ºC, 6h	1.0 M NaCl + 0.64 M $NaHCO_3$	[173]
• Magnetite Fe_3O_4	Ca: 0.6 Mg: 0.3 Fe: 21.9	0.13	8	None	Aqueous[a]	152 bar, 155ºC, 6h	1.0 M NaCl + 0.64 M $NaHCO_3$	[173]
• Labradorite ((Ca, Na)(Al, Si)$_4O_8$)	Ca:0.6 Mg: 0.2 FeO: 1.0	0.09	33	None	Aqueous[a]	141 bar, 185ºC, 3h	1.0 M NaCl + 0.64 M $NaHCO_3$	[174]
Anorthosite, Mixed Rock	CaO: 10.2 MgO: 8.7 FeO: 8.7	0.26	17	None	Aqueous[a]	141 bar, 185ºC, 3h	1.0 M NaCl + 0.64 M $NaHCO_3$	[174]
Basalt, Mixed rock	Ca: 6,7 Mg: 4.3 Fe: 6,7	0.2	15	Attrition grinding	Aqueous[a]	152 bar, 185ºC, 1h	1.0 M NaCl + 0.64 M $NaHCO_3$	[174]
Basalt from Columbia River, Mixed Rock	Ca: 6,7 Mg: 4.3 Fe: 6,7	0.19	5	None	Aqueous	141 bar, 185ºC, 3h	1.0 M NaCl + 0.64 M $NaHCO_3$	[174]

Most of the carried studies on MC of naturally-occurring Mg/Ca-rich silicates have been performed at elevated temperatures and pressures in aqueous-slurry systems (Table 2.2). This conditions are relevant to in-situ MC, however the energy requirements for ex-situ carbonation processes are currently too high for large-scale industrialization [42]. Different approaches have

been carried out in order to unlock both the ex-situ and in-situ MC potential for CCUS applications [42,98,99,175,176]. It is expected that the combination of different MC technologies will be able to sequester 1GtC yr^{-1} (Fig. 2.2) [176]. MC of natural rock is expected to contribute up to 55% of the MC carbon sequestration stabilization wedge. The remaining reactive feedstock is expected to come from industrial wastes. A technical summary of this options is presented in the upcoming sessions.

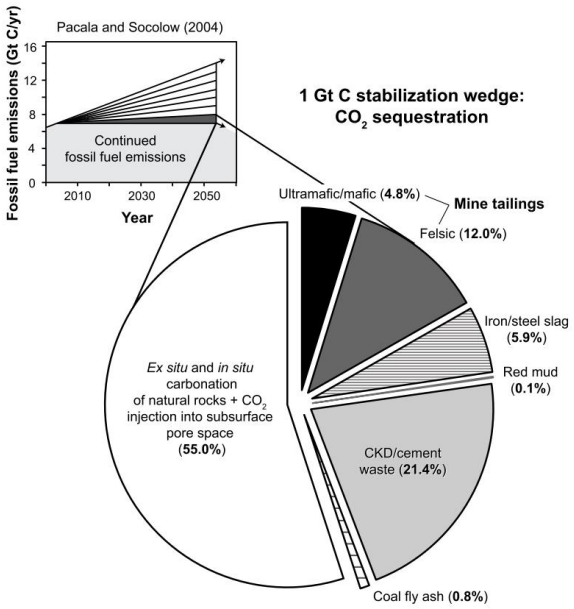

Fig. 2.2. Contribution of the different MC technologies towards a 1 GtC yr^{-1} ("stabilization wedge"). CKD stands for cement kiln dust. Figure from Power et al., 2013 [176]

2.1. MgO-CO_2-H_2O system

In the system MgO-CO_2-H_2O at 0-60ºC, the known stable phases at very low CO_2 partial pressures are brucite and magnesite, the most stable Mg-carbonate [177,178]. At mild-low temperatures (≤200ºC), the formation of magnesite is kinetically inhibited by the kinetically preferential formation of a variety of hydrous Mg-carbonate phases. This behavior is mainly attributed to the high hydration energy of Mg^{2+}[178]. Among the hydrous Mg-carbonate phases, hydromagnesite is the only mineral that is stable at atmospheric CO_2 pressures and temperatures [179]. Moreover, several hydromagnesite-like phases exist, differing in unit cell parameters and waters of crystallization [179]. The relationship between this minerals and the formation mechanism of these phases remains unclear [179]. This might explain the discrepancies regarding hydromagnesite solubility data reported in the literature [177].

Another common hydrated carbonate is nesquehonite which forms at *ca.* 10-50ºC and atmospheric CO_2 partial pressures or higher [179] (Fig. 2.3). However, this mineral is unstable at near surface conditions (different than hydromagnesite). Several experiments have observed a

transition between nesquehonite to hydromagnesite in aqueous media at 52-65ºC [180,181]. This transition follows one or more dissolution-precipitation step(s) of intermediate and short-lived phases, including hydromagnesite-like phases such as dypingite, $Mg_5(CO_3)_4(OH)_2 \cdot 5H_2O$ [180,182]. Thus, nesquehonite acts as precursor of less hydrated carbonate phases. This formation is greatly dependent on temperature and to less extent of CO_2 partial pressure [177]. However, the crystallization mechanisms between hydrated Mg-carbonates continues to be a challenging field of study [179].

Several distinct crystalline Mg-carbonate phases have been identified (Fig. 2.3). The group characterized by $Mg_5(CO_3)_4 \cdot (OH)_2$ have different amounts of water of crystallization per units (4 to 11): heavy hydromagnesite, $Mg_5(CO_3)_4 \cdot (OH)_2 \cdot 5H_2O$; light hydromagnesite, $Mg_5(CO_3)_4 \cdot (OH)_2 \cdot 4H_2O$ [183,184]; dypingite $Mg_5(CO_3)_4 \cdot (OH)_2 \cdot$5-6 H_2O [185]; giorgiosite $Mg_5(CO_3)_4 \cdot (OH)_2 \cdot 6H_2O$ [185], an unnamed mineral with formulae $Mg_5(CO_3)_4 \cdot (OH)_2 \cdot 8H_2O$ [186]; and protohydromagnesite, $Mg_5(CO_3)_4 \cdot (OH)_2 \cdot 11H_2O$ [180,183]. This groups follows a constant relation from protohydromagnesite to hydromagnesite, depending on their MgO-CO_2-H_2O (Fig. 2.3).

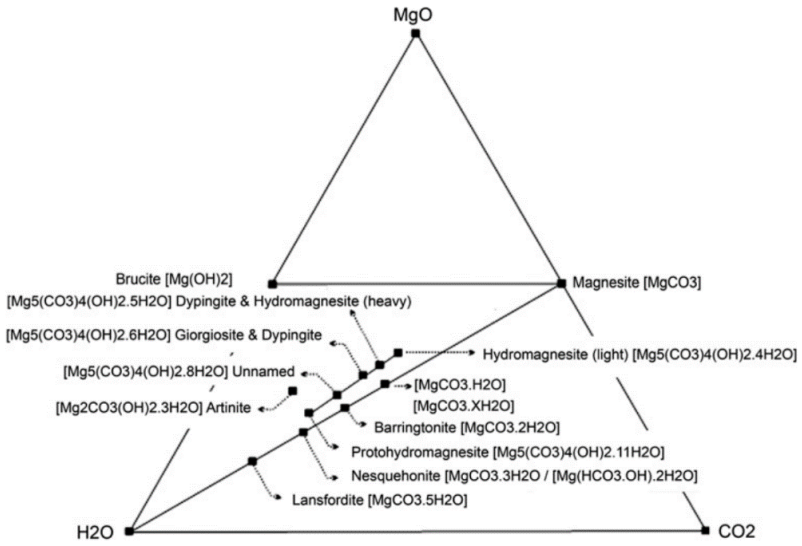

Fig. 2.3. Crystalline basic and hydrous Mg-carbonate phases. Specified values of *X* in synthetized $MgCO_3 \cdot XH_2O$ phases are between 0.3-1.3. Dypingite might have 5 or 6 H_2O molecules per unit. The status for giorgiosite remains questionable. Unnamed mineral, $Mg_5(CO_3)_4 \cdot (OH)_2 \cdot 8H_2O$, is not listed. Figure from Hopkinson et al., 2012 [179].

Within the group $MgCO_3 \cdot XH_2O$, the known natural occurring phases are: landsfordite, $MgCO_3 \cdot 5H_2O$; nesquehonite, $MgCO_3 \cdot 3H_2O$ (also represented as $Mg(HCO_3 \cdot OH) \cdot 2H_2O$); and barringtonite, $MgCO_3 \cdot 2H_2O$ (Fig. 2.3). Nesquehonite and landsfordite are commonly found in caves and are associated with weathered Mg-rich rocks at low temperatures and CO_2 partial pressure at least 10 times higher than atmospheric CO_2 [187]. Experiments carried at 1 bar and temperatures 10

± 2ºC showed that landsfordite spontaneously transforms irreversibly to nesquehonite. This latter mineral has also been observed in similar environments as hydromagnesite and dypingite [188]. Natural occurrence of barringtonite are associated with nesquehonite precipitates derived from weathered basalts [189]. Upon heating nesquehonite to 100ºC, an unidentified $MgCO_3 \cdot 2H_2O$ was observed [190]. A variety of $MgCO_3 \cdot XH_2O$ phases (X < 3) have been synthetized under different experimental conditions [181]. Moreover, some minerals such as nesquehonite and dypingite might have variable amounts of water, and in some cases such variability might be associated with structural isomers of such minerals [191]. A more detailed study of the reaction mechanisms is needed to shed light on the differentiation and formation of such minerals.

Among the phases of this group, natural-occurrences of hydromagnesite are the most common, resulting from the weathering of Mg-rich rocks as deposits in lakes, alkaline wetlands and evaporitic basins [188,192]. Dypingite is significantly less common than hydromagnesite, although it has been observed often coexisting with hydromagnesite [185,188,192], which might indicate that such minerals have similar formation mechanisms and/or dypingite might be precursor of hydromagnesite. Far less common is giorgiosite and the unnamed mineral, whose occurrences are associated with weathered volcanics [186]. Protohydromagnesite has not been identified in nature, but it has been synthetized [180,182].

Vibrational spectra of these phases are undocumented, with the exception of dypingite and hydromagnesite. However, both minerals have nearly undistinguishable CO_3^{2-}infrared-active vibration modes [185,187]. It has also been reported that upon heating dypingite it rapidly transforms to hydromagnesite [184,185].

2.1.1. Magnesite formation

Magnesite formation at low temperatures is often observed to occur upon the transformation of hydrate Mg-carbonates, such as hydromagnesite. The direct formation of magnesite under low temperature conditions (>100ºC) is virtually impossible within an anthropic timescale due to the kinetically preferred formation of intermediate and metastable carbonate phases [179,193]. Nonetheless, some studies have reported on the formation of magnesite at low temperature without an hydrous crystalline precursor, but with limited formation rate [194,195]. Farhang et al., 2016 [196] suggested that hydromagnesite formation hinders magnesite nucleation and crystal growth. The latter is likely due to the slower formation rate of magnesite nucleation and crystal growth relative to hydromagnesite [197]. The main formation mechanisms of magnesite is crystal growth rather than nucleation of more crystals [197,198]. In order to overcome the nucleation-limitation of magnesite, Swanson et al., 2014 [197] investigated the use of seed magnesite and inert alumina

particles (Fig. 2.4). It was concluded that difficulties associated with the nucleation of magnesite were significantly reduced with the addition of magnesite particles.

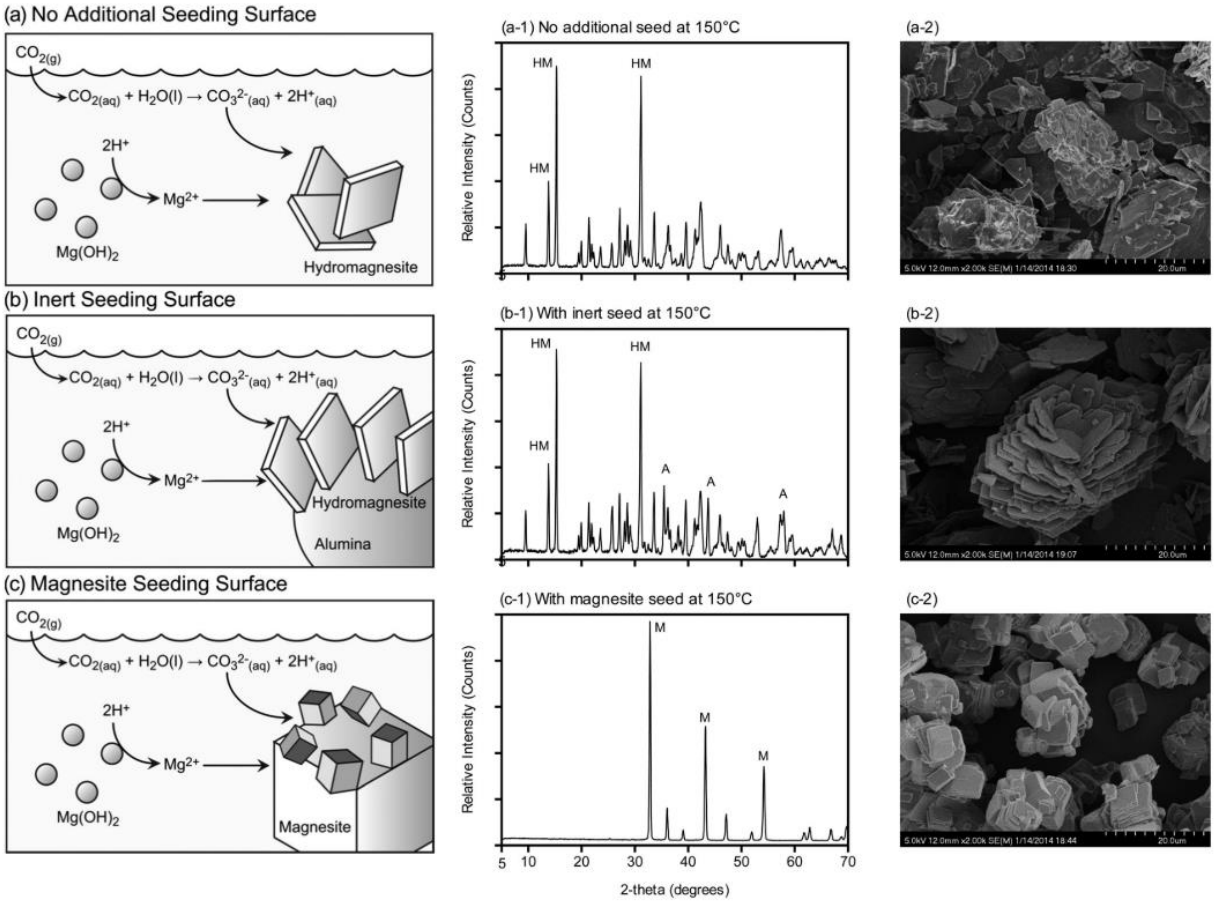

Fig. 2.4. (a, b, c) Schematic of alumina and magnesite seeded slurry carbonation reactions, including (a) homogeneous nucleation of hydromagnesite from brucite, **(b)** heterogeneous nucleation of hydromagnesite on the surface of inert alumina seeds and **(c)** growth of magnesite on the surface of seeded magnesite particles. **(a-1, b-1, c-1)** XRD and **(a-2, b-2, c-2)** Scanning Electron Microscopy (SEM) analysis of the dried slurry products, confirming the process shown in the scheme (a, b, c), as evidenced by the characteristic rhombohedral magnesite crystals and hydromagnesite plates, together with their characteristic X-ray diffractograms. HM: hydromagnesite; M: magnesite; A: Alumina. Figure adapted from Swanson et al., 2014 [197].

Magnesite is the most stable Mg-carbonate under Earth surface conditions and has the highest CO_2 sequestration capacity (Mg/C=1). Moreover, magnesite is a profitable product and could be used in the construction industry [199]. Its formation from aqueous slurries requires elevated temperatures and CO_2 partial pressures (100ºC, ~100 bar) and/or may require extended reaction times [178,179,197,200]. Di Lorenzo et al., 2014 [201] reported that magnesite was formed from the transformation of hydromagnesite at CO_2 partial pressures below 10 bar at 120 over several days. Different studies have reported that increasing the pressure significantly enhances (>100 bar) the magnesite yield, achieving a complete hydromagnesite to magnesite conversion in 90 minutes at 120ºC [178,196]. Moreover, increasing the temperature (≥150ºC) while keeping elevated pressures

enhances further the formation of magnesite [196,201,202]. However, increasing the temperature and pressure elevates the MC costs [197]. Studies carried via steam-mediated DC have also reported that magnesite formation requires elevated temperatures and pressures (>120ºC, >10 bar) [203,204]. Montes-Hernandez et al., 2020 [199] have estimated the formation rate of hydromagnesite (120 kg/m^{3}h) and magnesite (40 kg/m^{3}h) from in-situ Raman measurements from aqueous carbonation experiments carried at 90ºC and 50 bar (Fig. 2.5).

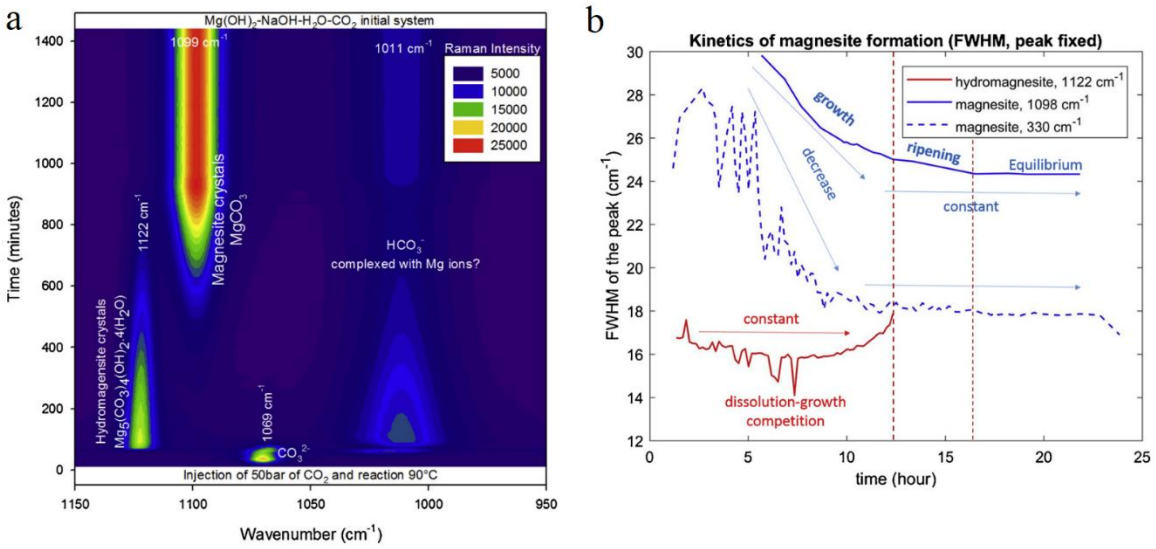

Fig. 2.5. (a) In-situ Raman analyses of slurry carbonation of $Mg(OH)_2$ at 90ºC under anisobaric conditions (50 bar). **(b)** Calculated Full Width Half Maximum of hydromagnesite and magnesite Raman peaks in function of reaction time. Figure from Montes-Hernandez, 2020 [199].

2.2. In-situ Mineral Carbonation

This approach attempts to mimic the weathering of ultrabasic-basic (specially peridotites and basalts) rocks in an anthropic timescale. Such approach could permanently sequester billions of tCO_2 y^{-1} [48,205,206]. Natural weathering of peridotite produces alkaline springs that forms vast travertine deposits as well as carbonate-filing fractures and veins (Fig. 2.6) [48,207] and carbonate chimneys at submarine hydrothermal vents [208]. The carbonation of the Samail Ophiolites in Oman alone consumes ~10^3 tCO_2 km^{-3} yr^{-1} [48]. Analogously, natural carbonation of basalts (by interaction with CO_2-rich fluids in hydrothermal and surface weathering systems) consumes ~1.8 10^8 tCO_2 y^{-1} globally [209,210]. As it was shown in Fig. 1.9 and 1.11 in-situ MC offers several advantages when compared to traditional geological storage, however, it has higher associated costs (Table 1.2)

Kelemen and matter, 2008 [48] proposed the engineering acceleration of natural weathering in situ in tectonically exposed peridotite massifs. The authors estimated that carbonation can be enhanced by a factor of ~10^6 relative to the natural carbonation rates by increasing the peridotite

temperature while injecting CO_2-rich fluids (Fig. 2.7). There is an optimal temperature for olivine carbonation (~ 185ºC), at higher temperatures, the chemical potential that drives the reaction is diminished as it approaches the equilibrium phase boundary of the reacting phases [48]. The reaction enhancement is also greatly increased with pressure (from $4 \cdot 10^{-4}$ to 75 bar). Further increase of pressure yields to no significant further enhancement, coinciding with the $ssCO_2$ point of CO_2. Undesired olivine serpentinization rate occurs significantly slower than carbonation and higher temperatures are needed. The volume increase by formation of carbonates (and minor serpentines) more likely will produce rock fracturing [211,212], which could further enhance the carbonation by a factor of ~10^9. With such enhancement rate, in-situ carbonation of peridotites in Oman could sequester $2 \cdot 10^9$ tCO_2 km^{-3} yr^{-1}[48].

Fig. 2.6. Photographs of **(A)** actively-depositing travertine and altered peridotite in the background. **(B, C)** White carbonate veins in altered peridotite. Figure from Kelemen and Matter, 2008 [48]

Moreover, the exothermic nature of the carbonation reactions could potentially maintain the temperatures of peridotite in-situ CO_2 injecting system (where the reaction-heat produced is equal to cooling due to diffusive heat loss of cold surroundings), thus, reducing the energy requirements. It should be also taken into account the geothermal gradient (10-20ºC km^{-1}) [213], which will also contribute to reduce the overall energy requirements. Eventually, reaction-surface areas may become carbonate-depleted, and if no reaction-driven cracking occurs, it might be necessary to induce hydraulic fracturing or pumped into and adjacent area to start a new process [48].

The key limitations for in-situ carbonation are: (i) decrease in the density of the rock unit and mass gain (due to the sequestered CO_2), increasing the risks of compaction, (ii) precipitation of carbonates/Si-rich phases in fractures and pore spaces [214,215], formation of passivating layer surrounding reactive material, inhibiting their possible reaction [176].

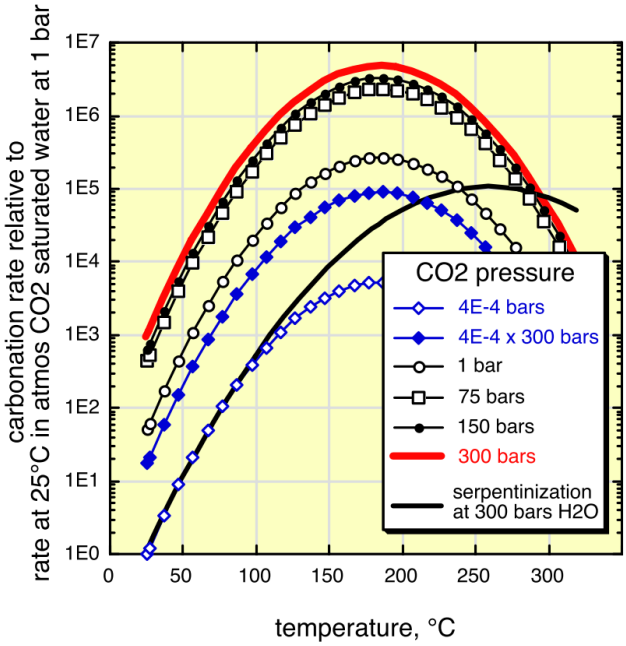

Fig. 2.7. Carbonation rate enhancement relative to the estimated natural weathering of olivine as function of temperature and pressure. Olivine serpentinization is also shown. Figure from Kelemen and Matter, 2008 [48].

Generally, peridotite contains 40-50 wt% MgO±CaO±FeO, higher than basalt (20-25 wt% MgO±CaO±FeO). Moreover, the dissolution of forsterite (which forms 60-5% of peridotite) dissolves at a faster rate than the dominant compositional type of plagioclases, labradorite, which forms 50-70% of crystalline basalt (Fig. 2.8). Results from experiments performed with crystalline basalt with composition ~ 60% plagioclase and 40% olivine + pyroxene exhibit faster dissolution rates than plagioclase alone [208].

Similar dissolution rates are observed for forsterite with basaltic glass under similar experimental conditions. Forsterite dissolution at high pressures (150 bar) in a highly-concentrated bicarbonate solution ($NaCl+NaHCO_3^-$/ $KHCO_3^-$) occurs 100 to 1000 times faster than the dissolution of forsterite and basalt without high bicarbonate concentrations (Fig. 2.8) [168,216]. This could be attributed to the delayed formation of a passivating Si-rich layer on unreacted forsterite grains, inhibiting further carbonation [168,216]. On the other hand, the effect of high bicarbonate-concentration in the carbonation of basalt is yet unknown [79].

Figure 2.9 shows the dissolution rates (normalized by the geometric surface area) of silicate minerals and glasses (natural and synthetic) in function of the Si:O ratio as estimated by Wolff-böenisch et al., 2006 [217]. Such dissolutions rates are adjusted to linear regression fits and correlation coefficients (r^2), whose equation is 2.7 and 2.8. Faster dissolution rates (at least 1.6 order of magnitude faster) are observed for silicate-glasses than their respective crystalline counterpart. This difference is particularly evident for minerals with high Si:O ratios (Si:O ≥0.39). Upon

increasing Si-content (Si≤0.28) the difference between crystalline and their respective no-crystalline counterpart do not differ. Moreover, the dissolution rates for both mineral and glasses reduces with increasing Si-content. As discussed by the authors, this might be attributed to the effect of crystallinity on the degree of Si:O polymerization. The rate limiting step for both minerals and glasses with Si≤0.28 is the breaking of Si-O bonds. This might explain the relative inertness of Si-rich rocks (i.e.: granite and rhyolites), compared to basalt. Therefore, weathering and hydrothermal alterations of Si-rich rocks play only a minor role in the carbon cycle. Anorthite, forsterite and wollastonite do not reflect the rate of Si-O breaking, probably indicating that the dissolution mechanisms follow the breaking bonds other than Si-O.

$$\log\left(\frac{\mathbf{r}_{geo}}{\mathrm{n_{Si}}}\right)\mathrm{glass}\left(\frac{\mathrm{mol}}{\mathrm{m^2/_s}}\right) = -6.91 - 6.77\,(\mathrm{Si{:}\,O});\ \ \mathrm{r^2} = 0.71 \tag{2.7}$$

$$\log\left(\frac{\mathbf{r}_{geo}}{\mathrm{n_{Si}}}\right)\mathrm{mineral}\left(\frac{\mathrm{mol}}{\mathrm{m^2/_s}}\right) = -5.15 - 15.43\,(\mathrm{Si{:}\,O});\ \ \mathrm{r^2} = 0.47 \tag{2.8}$$

$$\boldsymbol{A}_{\mathrm{geo}} = \frac{6}{\rho \cdot d} \tag{2.9}$$

Where $\mathbf{r}_{\mathrm{geo}}$ is the dissolution rate normalized to the theoretically derived geometric specific surface area ($\boldsymbol{A}_{\mathrm{geo}}$) (equation 2.9; [218]), ρ is the density of the solid, d is the average particle diameter, $\mathrm{n_{Si}}$ is the Si number of moles in one mole of the respective mineral or glass and r^2 is the correlation coefficient.

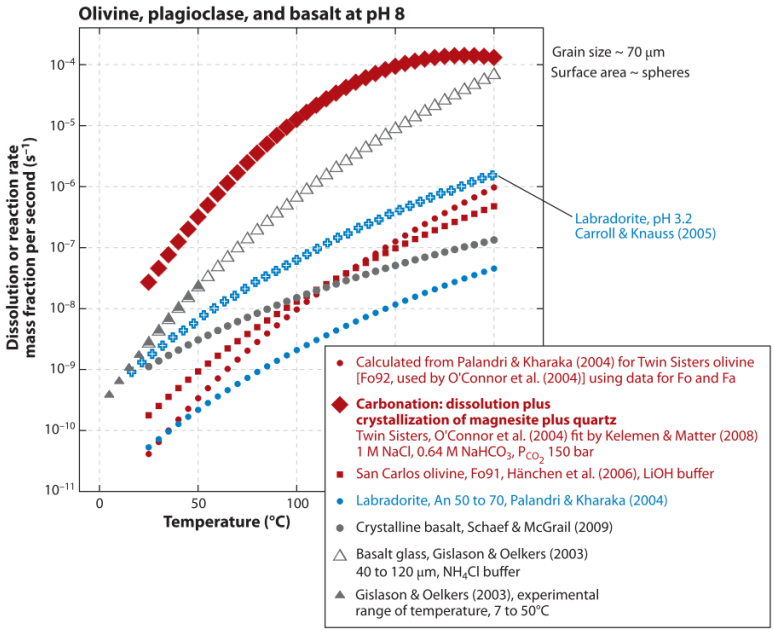

Fig. 2.8. Compilation of dissolution rates (expressed in mass fraction per second as a function of temperature of olivine, labradorite, basalt (crystalline and glass) with grain size ~ 70µm and semi-spherical surface area. References within the figure: Palandri and Kharaka, 2004 [219]; O'Connor et al., 2005 [168]; Kelemen and Matter, 2008 [48]; Hänchen et al., 2006 [220]; Schaef and McGrail, 2009 [221]; Gislason and Oelker, 2003 [222]. Figure from Kelemen et al., 2011 [223].

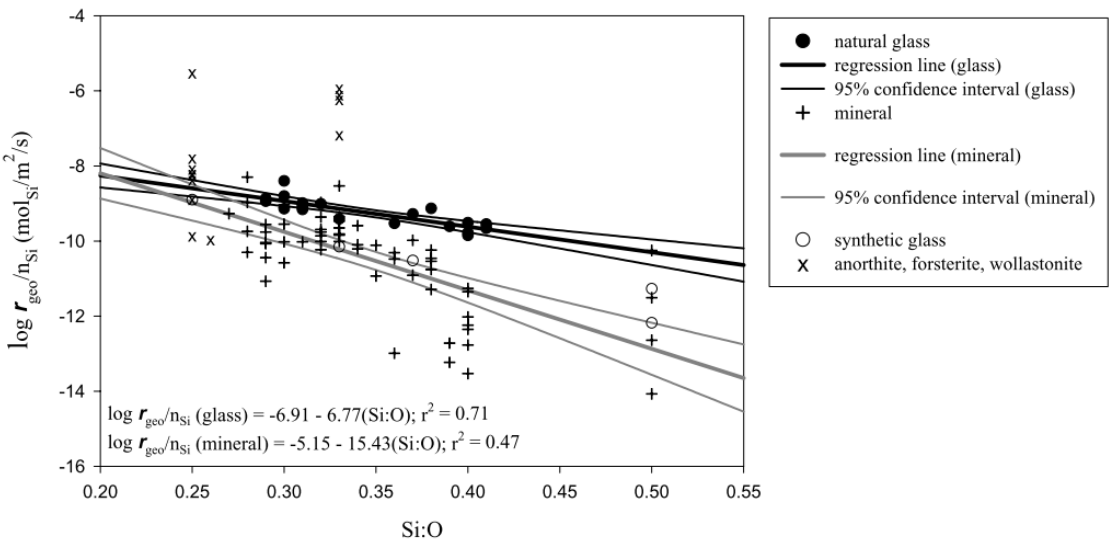

Fig. 2.9. Logarithm dissolution rates normalized by the geometric surface area of silicate glasses and minerals at pH 4 and 25ºC as function of the molar ratio of silicon to oxygen in the structure (Si:O). Bold black and gray lines represent the linear regression fit of mineral and glass data. Thin lines represent the interval of 95% data confidence. Anorthite, forsterite and wollastonite do not follow the same trends as other silicates, associated with the breaking bonds other than Si-O during dissolution. Figure from Wolff-Boenisch et al., 2006 [217].

The dissolution of basalt glass occurs 10 to 1000 times faster than their respective crystalline counterpart (Fig. 2.8) [217]. However, natural basic silicate glasses are not abundant due to their quick hydration and recrystallization during hydrothermal alteration and weathering. Nevertheless, there might be local strata where natural glass remains abundant [79]. Despite crystalline basalt have seemingly lower dissolution rates than peridotite, basalt is the most abundant rock type in Earth's crust, therefore, in-situ carbonation of basalt is also a promising option.

Iceland has large volumes of basalt flows and volcanic breccias formed upon a rapid quenching (hyaloclastites), associated with the local strong volcanic and geothermal activity. Large deposits of basaltic andesitic tephra, mainly composed of highly-reactive volcanic glass [224]. There are several occurrences of natural carbonation of basalt within the island [225,226]. It was estimated that this natural carbonation analogs store up to 70kg$CO_2 \cdot m^{-3}$[226]. High alkaline meteoric waters (pH from 7.7 - 9.3) due to the presence of Ca^{2+} and Mg^{2+} from the dissolution of basaltic rocks, feed a series of springs. Comparison of the CO_2 partial pressure (P_{CO_2}) and the pH of the spring waters shows that P_{CO_2} systematically diminishes with pH (Fig. 2.10a). The springs waters are CO_2 supersaturated relative to the CO_2 concentration in the atmosphere at pH<8.4. However, at lower pH the waters are CO_2 undersaturated. Analogous trend is observed with the measured dissolved inorganic carbon (DIC; Fig. 2.10b). This is consistent with the precipitation of carbonates from the alkaline meteoric waters.

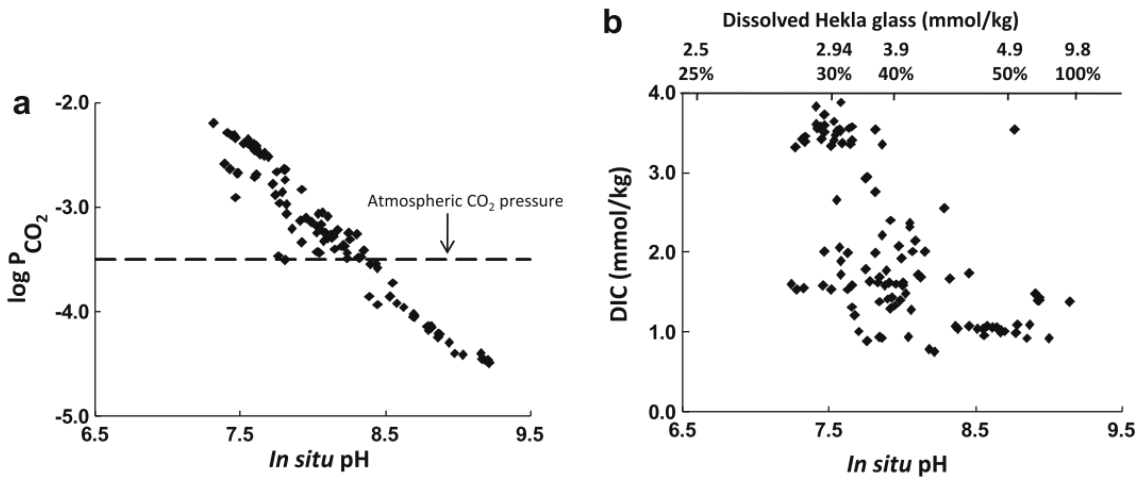

Fig. 2.10. (a) Estimated P_{CO_2} using PHRREQC 2.1 4.2 and the measured pH of the spring waters (*in istu pH).* **(b)** DIC concentration as a function of the measured pH of the spring waters. An estimation of the dissolved Hekla glass to reach the measured pH is shown in the secondary *x*-axis. Figure from Flaathen et al., 2009 [225].

Moreover, the dissolution of basalt also liberates heavy metals ions that are mobilized by the spring waters. Such metals are partially to fully immobilized as they are incorporated in precipitating carbonates and Fe (III) oxyhydroxides [225]. Such behavior have also been observed during the accelerated carbonation of ultramafic rock, where the precipitation of nesquehonite, $Mg(HCO_3)(OH)\cdot 2H_2O$, is also able to sequester transitions metals [227]. Thus, carbonate precipitation also helps to reduce the risk of environmental pollution[225].

2.2.1. CarbFix project

In view of this vast carbonation potential, the project CarbFix (located in Iceland) emerged [228]. Such project aims to assess the feasibility of injecting CO_2 into reactive basalt. A gas mixture of 98% CO_2 and 2% H_2S are injected into the basaltic aquifer originated from the emissions at the Hellisheidi power plant [229]. The hosting basalt rock are ultrabasic to basic (45 – 49% SiO_2) basalt flows and hyaloclastites of olivine-tholeiite composition [230]. Figure 2.8 shows the NE-SW cross-section of the injection site with the location of injection and monitoring wells. Crystalline lava flows were deposited after the last glacial age. Hyaloclastites originated during rapid quenching during the last glaciations (between 116000 and 1500 years ago) under the ice cover [224,229,231]. The originated geo-structure is a sequence of permeable lava flows (hosting a shallow aquifer), separated and isolated from the deeper aquifer by a low-permeability layer of hyaloclastites [224,232]. The degree of basalt alteration increases with depth [232].

The shallow aquifers (above 400m) has a pH and temperature range of 7.7 – 8.4 and 8-12ºC, respectively, a P_{CO_2} near to atmospheric CO_2 pressure and undersaturated with respect to calcite. The

ground waters are between 400 and 800 m depth (where approximately the injection takes place [80]) with a pH range from 8.4 - .9.4, temperatures between 18-33ºC [230], a lower P_{CO_2} with respect to atmospheric CO_2 pressure and are at saturation with calcite [232]. The target injection formation consists of basaltic lavas and hyaloclastites with calcite and Ca-zeolites (formed upon alteration of the hosting basaltic rocks). The permeability is highest between 400 and 500m. At depths below 800 meters, the permeability is greatly decreased.

A novel and specific CO_2 injection system was designed in order to avoid the high risks of CO_2 gas leakage through fractures, particularly since the shallow depth of the target storage reservoir. Such system consists on dissolving CO_2 into down-flowing water in the well during injection. Trapping (initially) all the injected CO_2 by solubility trapping (Fig. 1.11), which makes it no longer buoyant and immediately starts to react with basaltic rocks [233].

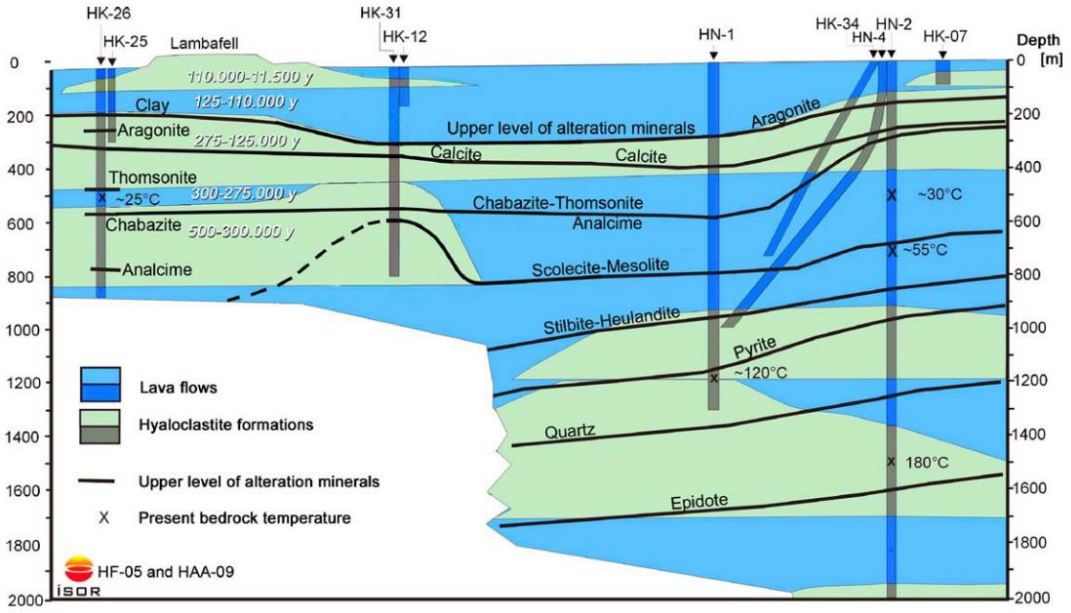

Fig. 2.11. NE-SW cross-section of the CarbFix injection site with the location of injection (HN-2) and monitoring wells (HN-4 is the first monitoring well). Figure from Gislason et al., 2010 [232].

Modelling of the mineral precipitation at the injection site estimates that the precipitation of secondary minerals will occur at a significant distance from the injection well, therefore the clogging due to calcite and other alteration mineral precipitation in the vicinity of the injection well should not be a problem [234].

Model calculations estimate the fraction of minerals that will be formed upon accelerated basalt alteration under specific pressure and temperature injection conditions. Fig. 2.12 shows the estimated mole fractions of alteration minerals formed upon basaltic glass dissolution and precipitation at 25ºC and 2, 10 and 30 bars of CO_2. Ca-Fe-Mg divalent and trivalent cations upon basalt dissolution could be fixed by carbonates or by undesired reactions such as the formation of

mixed clays and zeolites, since they fix a fraction of the available Ca-Fe-Mg% without sequestering CO_2 [235]. Aradóttir et al., 2012 [234] has predicted the clay minerals and oxyhydroxides will compete with magnesite-siderite precipitation and zeolites compete with calcite for the dissolved Ca.

It is estimated that at elevated CO_2 partial pressure the carbonation efficiency of the system is enhanced, as evidenced by the highest yield of Ca^{2+} precipitated as carbonates. Note that the precipitation of Si-Al minerals in unavoidable, however those minerals do not fix any of the divalent and trivalent cations that could be used to sequester CO_2. Nevertheless, the formation of such minerals reduces the density and increases the volume and solid mass (due to hydration) relative to unaltered basalt. This might increase the risks of compaction [176].

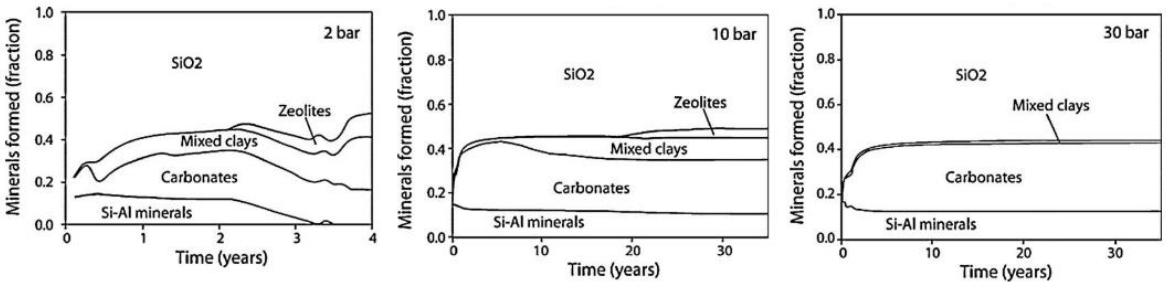

Fig. 2.12. Estimated mole fraction of secondary minerals formed upon accelerated groundwater alteration of basaltic glass under CO_2 and H_2S injection conditions at 25ºC and 2, 10 and 30 bar CO_2. Mixed clays include celandonite, Ca-Fe-Mg smectites and chlorites. Carbonates include magnesite, calcite, dolomite, siderite and Mg-Fe carbonate. Si-Al minerals include allophanes, imogolite and kaolinite. Figure from Gysi and Stefánson, 2008 [235].

Conventional well monitoring methods are not able to detect dissolved or mineralized CO_2. Therefore, the injected CO_2 was enriched with ^{14}C to monitor its mobility and reactivity [232]. $^{14}CO_2$ and $^{12}CO_2$ have almost identical physical and chemical behavior, minimally differing by isotope fraction during phase transitions [236], providing accurate monitoring of dissolved and mineralized CO_2. Non-reactive and volatile sulfur hexafluoride (SF_6) and trifluoromethyl sulfur pentafluoride (SF_5CF_3) were additionally co-injected to monitor the transport of the injected CO_2-rich fluids.

In 2012, two injection tests were performed: (phase I) 175 tCO_2 were injected from January to March 2012 and (phase II) a gas mixture composed of 55 tCO_2 and 18 tH_2S were injected from June to August [80]. Table 2.3 summarized the composition and characteristics of the injected fluids of these two phases. The ^{14}C, tracers and DIC concentrations as well as the pH from fluid samples were measured without degassing at the injection (HN2; Fig. 2.11) and monitoring wells (HN4, located at~70m downstream from HN2) with help of a specially designed in-situ syringe sampler [237].

Upon Phase I injection, the arrival of the injected fluids to the monitoring well HN4 was confirmed, as evidenced by an increase of SF_6, DIC and ^{14}C concentrations and a significant decrease

of pH (Fig. 2.13), especially after 56 days after injection [80]. Slightly decreased in the SF_6 concentration were observed after the plume arrival to HN4 before increasing significantly, reaching peak concentration after 406 days after injection. Analogous behavior was observed for the SF_5CF_3 tracer during phase II injection. This double tracers concentrations peak are an indicative that the basaltic aquifer has relatively homogenous porosity with intersected low-volume and fast flowing paths, where about 3% of the plume volume was mobilized faster than the remaining plume between HN2 to HN4 [238]. ^{14}C and DIC concentrations decreased after phase I injection followed by a subsequent increase due to phase II injection, coinciding with a small drop in pH. After CO_2 injections, ^{14}C and DIC concentrations remained stable during the monitoring period.

Table 2.3. Summary of the ^{14}C and traces concentrations, injection rates, DIC and pH of origin basaltic reservoir of injection phase I and II. *Conditions of the basaltic reservoir prior injection. STP (Standard Temperate and Pressure).

Phase	^{14}C concentrations [80]	Tracers (ccSTP/cc) [80]		Injection rates (g/s) [233]		DIC (mol/L) [80,232]	pH (20ºC) [80,232]
	$^{14}C/^{12}C$	SF_6	SF_5CF_3	CO_2	H_2O		
Basaltic reservoir*	$1.68 \cdot 10^{-13}$	-	-	-	-	0.2	8.4 - .9.4
I	$2.16 \cdot 10^{-11}$	$2.33 \cdot 10^{-8}$	-	70	1800	0.82	3.85
II	$6.5 \cdot 10^{-12}$	-	$2.24 \cdot 10^{-8}$	10-50	417-2082	0.43	4.03

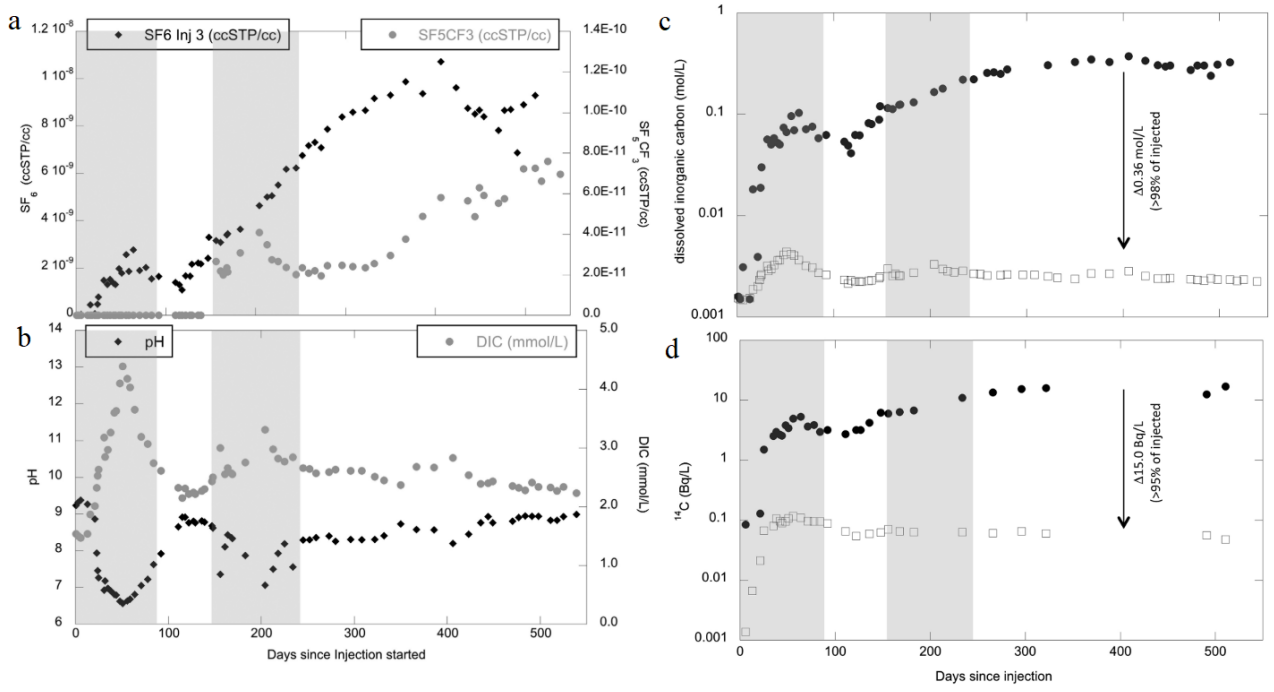

Fig. 2.13. Measured **(a)** SF_6 and SF_5CF_3 tracer concentrations, **(b)** pH and DIC concentration changes during 550 days from phase I injection in the monitoring well HN4. **(c, d)** Calculated (open squares) and measured (solid circles) DIC and ^{14}C concentration in monitoring well HN4 as function of monitoring time. Shaded areas indicate the phase I and II injection periods. Figure from Matter et al., 2016 [80].

DIC and ^{14}C mass balance calculations (eq 2.9, 2.10, 2.11) were performed to assess the fate of the injected CO_2 [80], following the procedure in Assayag et al., 2009 [239]. The calculated DIC and ^{14}C concentrations due to the mixing of injected solutions with ambient groundwater are much higher than the measured. This strongly suggest a significant loss of ^{14}C and DIC between HN2 and HN4 (Fig. 2.13c, d). Among the alternative options in the context of basalt dissolution and precipitation of secondary minerals [240] that explain the consumption of ^{14}C and DIC, the precipitation of calcite is the most plausible [80]. Calculated data estimates that over 95% of the injected CO_2 has mineralized between HN2 and HN4 within 2 years [80]. This observation is also corroborated by (i) calculation of the monitoring fluids, which were found to be in saturation and supersaturation with respect to calcite, (ii) X-ray Diffraction (XRD) and Energy Dispersive X-ray spectroscopy (EDX) analysis of solid samples collected from the clogged submersible pump in HN4 and (iii) collected calcite has similar ^{14}C concentration to the enriched ^{14}C injected [80].

$$[SF_6]_i = X[SF_6]_{IS} + (1 - X)[SF_6]_{BW} \quad (2.9)$$

$$DIC_{mix} = X \cdot DIC_{IS} + (1 - X) \cdot DIC_{BW} \quad (2.10)$$

$$^{14}C_{mix} = X \cdot {}^{14}C_{IS} + (1 - X) \cdot {}^{14}C_{BW} \quad (2.11)$$

Where, X is the fraction of the injected solution in the extracted water sample; i represents the calculated concentration for each extracted water sample. IS and BW stands for injected solution and ambient groundwater, respectively.

Released cations upon hosting basaltic rock dissolution were also measured during injection phases and monitoring from fluid samples obtained at the monitoring well HN4 [241] (Fig. 2.14). Ca, Mg and Fe concentrations rapidly increased after each of the injection phases followed by a subsequent gradual decline. Analogously to the calculated and measured ^{14}C and DIC concentrations, measured Ca, Mg and Fe concentrations were significantly higher than the calculated if the injection and ambient groundwater fluids mixed without the dissolution and precipitation of hosting basaltic rock (Fig. 2,11a, b, c). This strongly suggest that the hosting rock dissolved, enriching the fluids with divalent cations followed by their mineralization. The presence of calcite was verified [80] and together with ^{14}C and DIC observations it is more likely that all (or mostly all) dissolved Ca precipitated into Calcite. Several studies have provided insights into the fate of the other dissolved and precipitated cations [241,242]. Moreover, the measured dissolved Si concentrations were constant throughout the monitoring period (Fig 2.1d). This could be explained by the rapid or subsequent precipitation of Si-rich phases upon silicate dissolution [101,243].

Saturation indices (SI) for calcite, magnesite and siderite were calculated using PHREEQC. Calcite was saturated before and after injection phase I and II (Fig. 2.15a) [241]. However, this latter mineral remained undersaturated right after the injection phases, in correlation with the significant decrease of pH after injection phase I (Fig 1.20b). The fluid samples attained saturation with respect

to calcite when the pH increased to >8. An analogous behavior was observed for aragonite ($CaCO_3$) and solid solutions of Ca, Mg and Fe carbonates such as dolomite $CaMg(CO_3)_2$ and particularly ankerite, $CaFe(CO_3)_2$, (Fig. 2.15b). This latter mineral, despite being supersaturated, was not identified to precipitate. However, Gysi and Stefánson, 2012 [244] reported on the formation of ankerite during basaltic-glass in contact with CO_2-rich waters at 75ºC and McGrail et al., 2006 [206] identified its formation during basalt carbonation with ssCO_2-rich fluids at 75ºC.

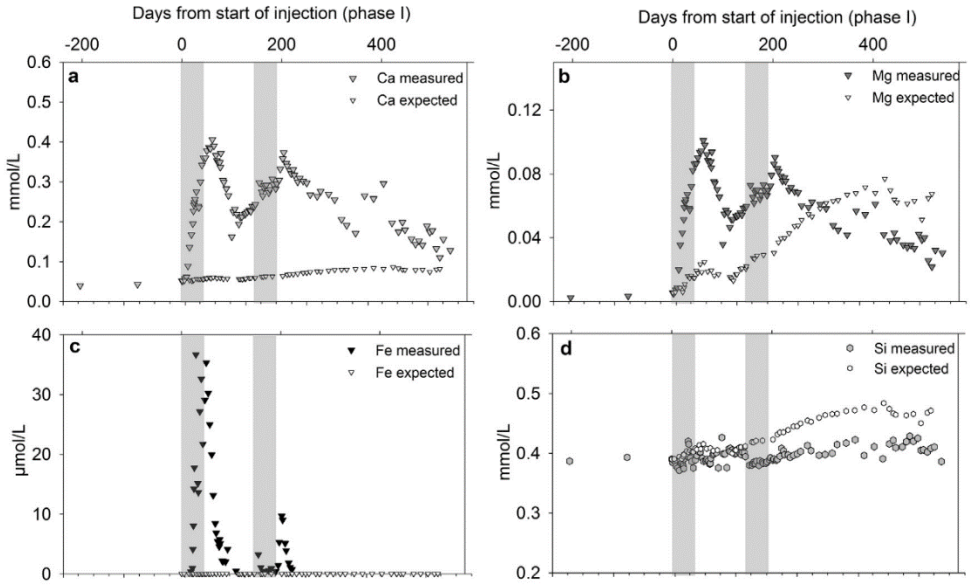

Fig. 2.14. (a) Ca, **(b)** Mg, **(c)** Fe and **(d)** Si concentrations of montitoring fluids from HN4 prioir and after phase I and II injection phases (which its times its characteristic time is gray-highlighted). Figure from Snæbjörnsdóttir et al., 2017 [241].

On the other hand, the monitoring samples were saturated with respect to siderite after the injection phases, without being influence by the decrease of the pH and magnesite was strongly undersaturated throughout the monitoring time (Fig 2.15a). Magnesite and siderite were not observed to precipitate in the onset. These latter minerals have been observed in drill-cuttings from Svartsengi saline high-temperature geothermal field in Iceland [241].

Sulphur-bearing minerals could also precipitate due to the injection of H_2S together with CO_2. Their respective saturation indices are shown in Fig. 2.15c. The monitoring fluids were undersaturated with respect to native sulphur and at equilibrium with pyrrhotite, $Fe_{1-x}S$ (x= 0 – 0.17), mackinawite, $(Fe,Ni)S_{0.9}$. Pyrite, FeS_2, was estimated to be supersaturated in the monitoring fluids. Calcite was the only precipitate on the clogged pump from HN4. However, samples collected from the HN2 confirmed the presence of pyrite after phase II injection. The other S-containing minerals were not identified in HN2. The identification of pyrite on the injection well but not on the monitoring well evidences the rapid precipitation of this mineral an suggest that its precipitation was essentially complete before arriving to HN4 [241]. The success of both CO_2 and H_2S mineralization indicates that the injection of mixed gases could be a cost-effective approach [228,241].

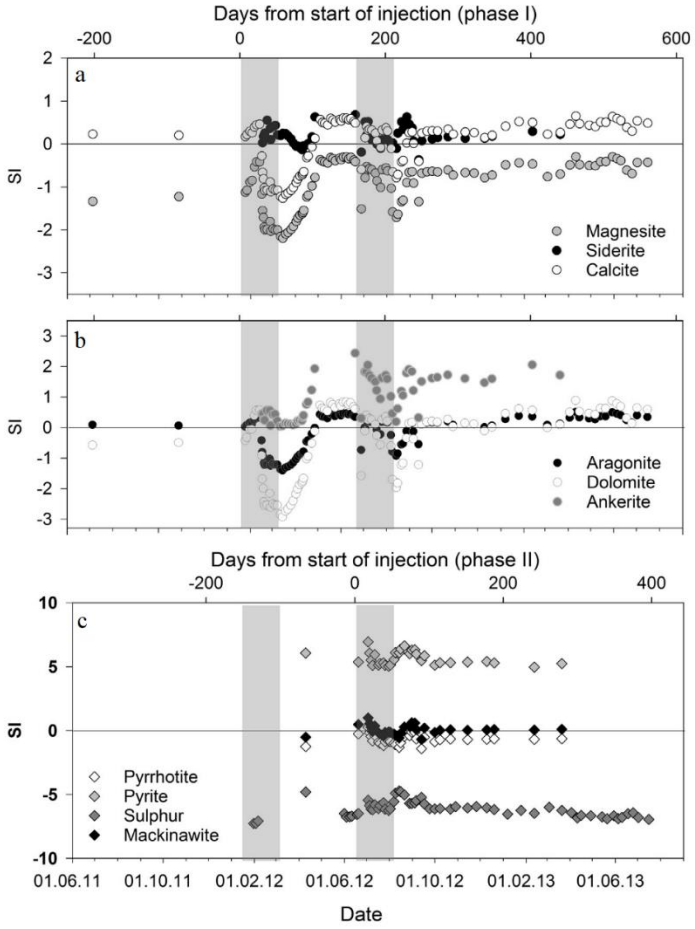

Fig. 2.15. Estimated saturation indices (SI) based on the cation concentration and onset injection conditions of sampled monitoring fluids from HN4 with respect to **(a)** magnesite, siderite and calcite; **(b)** aragonite, dolomite and ankerite; **(c)** pyrrhotite, pyrite, Sulphur and mackinawite. The injection periods of phase I and II are indicated in grey bars. Positive and negative and zero SI value corresponds to sampled fluids are supersaturated, undersaturated and at equilibrium with the specific mineral. Figure from Snæbjörnsdóttir et al., 2017 [241].

Oelkers et al., 2019 [242] measured the Mg isotope composition of the monitoring fluids collected from HN4 in order to provide more insights on the fate of dissolved Mg^{2+}. Fig. 2.16 shows the evolution of $\delta^{26}Mg_{DSM3}$ (isotopic ratio as per mil deviation of the $^{26}Mg/^{24}Mg$ ratios from the DSM3 international reference materials) composition of the fluids collected from HK-12, HK-13 and HK-25 (drilled at depths of 130, 210 and 310m, respectively; Fig. 2.11) prior injection and from HN4 during and after the injection. It was concluded that the Mg isotope composition of the monitoring fluids were lighter than the dissolved host basalts. This is consistent with the formation of clays which tend to fix isotopically heavier Mg, rather than the formation of carbonates which often fixes isotopically light Mg. Mg-smectites are commonly found as secondary minerals in altered basalts at low temperature instead of Mg-carbonate phases. The formation of Mg-clay minerals is seemingly relatively slow. Mass balance calculation estimates that 12% of the dissolved Mg remains to be precipitated after 2 years. Despite the slow precipitation of such minerals, their formation may

limit significantly the CO_2 mineralization efficiency as discussed by Rigopoulos et al., 2018 [245] during EW of peridotites and basalts.

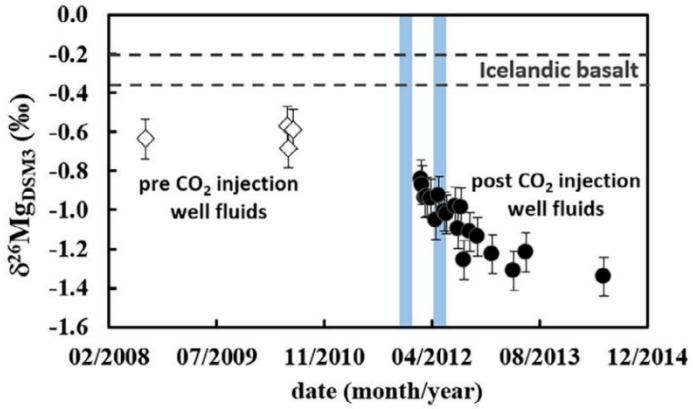

Fig. 2.16. $\delta^{26}Mg_{DSM3}$ composition of the fluids from the CarbFix site (pre-injection fluids from HK12, HK13 and HK25, represented as open diamonds; pots CO_2 injections fluids from HN4, represented as solid circles). The horizontal lines represent the composition of the hosting basaltic rocks. Blue bars represent injection phase I and II, respectively. Figure from Oelkers et al., 2019 [242].

The injected carbon mineralization efficiency is limited by the permeability and porosity of the hosting basaltic rock and their ability of cations to form carbonates instead of zeolites and clays. Therefore, the precipitation of this latter minerals such be avoided. This could be achieved by (i) raising the pCO_2 (Fig. 2.12) and (ii) keeping the pH high enough to be favorable for carbonate formation at a distance from the injection well. Snæbjörnsdóttir et al., 2018 [246] estimated that the precipitation of carbonates is more efficient at pH from 5.2 to 6.5 at low temperatures (20-50ºC).

Analogously to $\delta^{26}Mg$ isotopic measurements, $\delta^{44}Ca$ (isotopic ratio as per mil deviation of the $^{44}Mg/^{40}Mg$ ratios) isotope composition of the monitoring fluids from HN4 was measured [76]. Prior CO_2 injection, the $\delta^{44}Ca$ values of the ambient groundwater is of 1.89 – 1.95 ‰. After injection $\delta^{44}Ca$ varies significantly between 0.8 – 2.1 ‰ (Fig. 2.17). As discussed previously, there are two periods of calcite undersaturation (Fig. 2.15, 2.17), coinciding with the injection periods of phase I and II due to pH decrease [241]. Nevertheless, calcite remained supersaturated during the rest of the post-injection periods, where it precipitated [80]. Post-injection $\delta^{44}Ca$ values correlate with calcite saturation, and therefore is associated with calcite precipitation. Mass balance calculation based on isotopic measurements from the fluid estimates that 93% of Ca has been fixed by carbonates, similar to 95% estimated by Matter et al., 2016 [80].

The in-situ MC success of the pilot scale CarbFix project [80], as determined by independent methods, has motivated to upscale this process toward mineralizing all CO_2 and H_2S emitted gases from the Hellisheioi geothermal power plant in the CarbFix 2 site [247]. Such gases are captured by a cost-saving capture approach by dissolving them in water and separate them from the non-soluble gases in water. Therefore, only water and electricity are needed for this process, lowering

significantly their associated costs (estimated to be 21.3$/t). The estimated transport, injection of combined CO_2 and H_2S and monitoring costs are significantly lower than the capture process (1.3, 1.3 and 0.9 $/t, respectively). The overall cost of in-situ MC in CarbFix2 is estimated to be 24.8$/t [247]. Moreover, the estimated sequestration capacity of subsurface basaltic rocks in Iceland is up to 2500 GtC [248], 25 times greater to those required for in-situ MC to meet the 2ºC target [47].

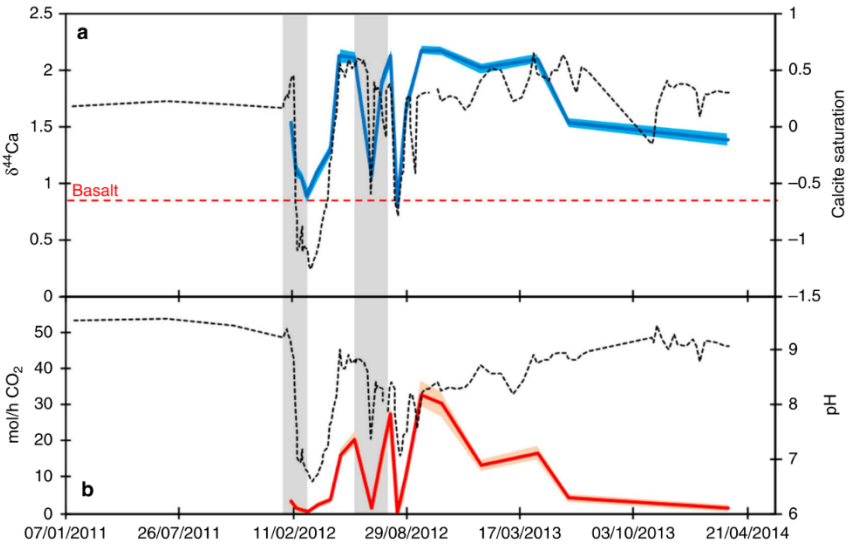

Fig. 2.17. (a) Relation between the estimated calcite saturation index (dotted black line) and measured $\delta^{44}Ca$ (blue line) from the monitoring fluids sampled at HN4 as a function of time. Blue shaded area represents the analytical uncertainty on isotopes measurements. **(b)** pH changes (dotted black line) and the calculated CO_2 precipitation rate based on mass balance calculation of Ca isotopes (red line) prior and post-injections. Red shaded area represents the uncertainties of calcite precipitation rates. The injection periods of phase I and II are shown in grey areas, respectively. Figure from Pogge von Strandmann, et al., 2019 [76].

At such low prices, in-situ MC is a promising option to help the joined efforts to mitigate CO_2 emissions. Such process could be implemented in different locations around the world where permeable basaltic rocks and water are abundant. On plausible option is the ocean floor which is mostly comprised of basaltic rocks and an inexhaustible supply of water [206,248–250]. This latter property will make this storage location favorable to many continental coastlines and on volcanic islands. Nevertheless, the application of the CarbFix approach to such location has to take into account: (i) CO_2 solubility is lower in seawater than in fresh water [247,251] and (ii) the transportation of captured gases to the injection sites and their associated costs [247]. Moreover, Wolff-Boenisch et al., 2011 [249] have concluded that the CO_2 mineralization of basaltic glass is accelerated using CO_2-charged seawater instead of CO_2 charged fresh water, due to faster dissolution rates.

Basaltic subsea floor of the Juan de Fuca plate, characterized by a basaltic bedrock composed of pillow lavas and massive flows covered by fine-grained turbiditic sequences and clay sediments, with porosity greater than 10% and pore volume of 7800 km^3, has a CO_2 sequestration potential of 920 GtC [250]. The Hook permeable basaltic basin offshore New Hersey has a porosity of 15% and a pore volume of 1 km^3 with a CO_2 sequestration potential of 900 MtC [252]. The estimated overall CO_2 storage potential in offshore basaltic subsea floor (with average porosity of 10%) is of 8238 GtC [205].

2.3. Ex-situ Mineral Carbonation

Ex-situ MC refers to the above-ground carbonation processes of raw mined minerals and alkaline industrial wastes through chemical processes (Fig. 2.18). As summarized in table 2.2, Ca/Mg-bearing minerals have been the studied as potential MC reactive feedstocks. Moreover, cheap and widely available alkaline industrial wastes rich in Ca and Mg-rich material and near to the CO_2 emission source have been also predicted as potential CO_2 sinks. Nevertheless, their total amounts are considered to be too small, thus, they have very-limited CO_2 storage capacity. However, the implementation of this technologies has been foreseen as a key step in the development of an economically viable MC processes of natural minerals. Among the alkaline industrial wastes, steelmaking slags, concrete wastes, mining and mineral processing wastes, combustion waste ashes and alkaline paper mill wastes have been considered for ex-situ MC [42,224]. A key advantage of ex-situ MC is that the reaction products could have profitable value [44]. Particularly, the carbonated products of steel slags, fly ash, bottom ash and cement kiln can be used in the construction industry [82,253–256].

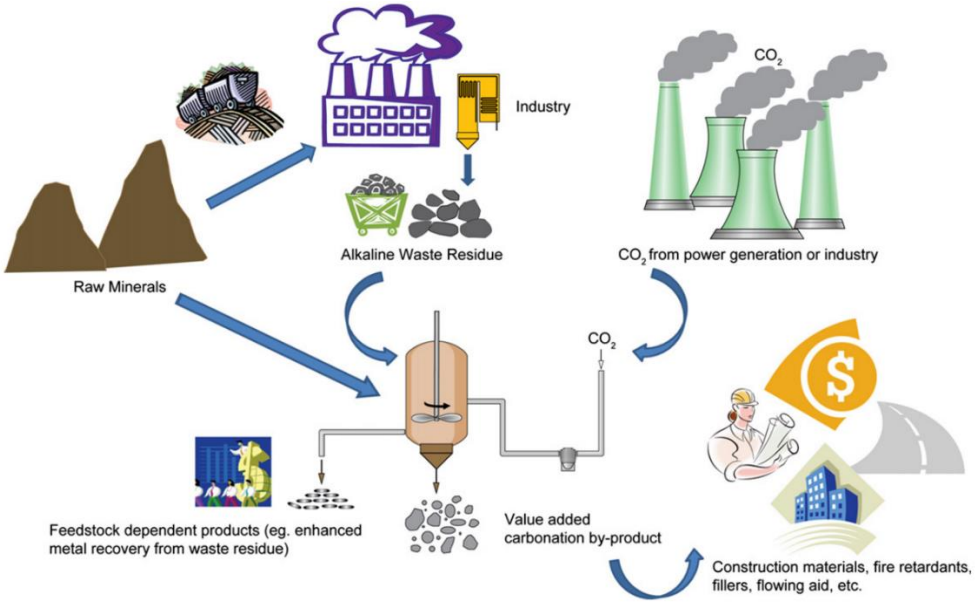

Fig. 2.18. General scheme of ex-situ MC processes. Figure from Bobicki et al., 2012 [42].

A variety of processes have been developed for ex-situ MC with acceptable reaction kinetics. Generally, such processes can be divided into two main categories: (i) Direct Carbonation (DC) and (ii) Indirect Carbonation (IC). DC processes is characterized by carbonation is carried in a single process that can be achieved by (i) direct gas-solid (DGS) reactions or (ii) via mineralization in aqueous solutions. In IC reaction schemes, reactive oxides are chemically separated from alkaline wastes or natural rocks, and then such oxides are carbonated in a different step. Figure 2.19 summarizes aqueous DC and IC processes.

Table 2.4. Summary of Ex-situ carbonation reaction schemes for DC and IC processes. Table from Bobicki et al., 2012 [42].

Method	Characteristic
Gas-solid	• CO_2 reacts with mineral in Gas-solid reaction • Simplest approach for MC • Pre-treatment is required (grinding, thermal activation**) • Currently, not feasible for silicate minerals
Aqueous (See Fig. 2.19)	• CO_2 is dissolved in water and reacts with minerals in aqueous solution • Pre-treatment is required (grinding, thermal activation**) • Most promising technique

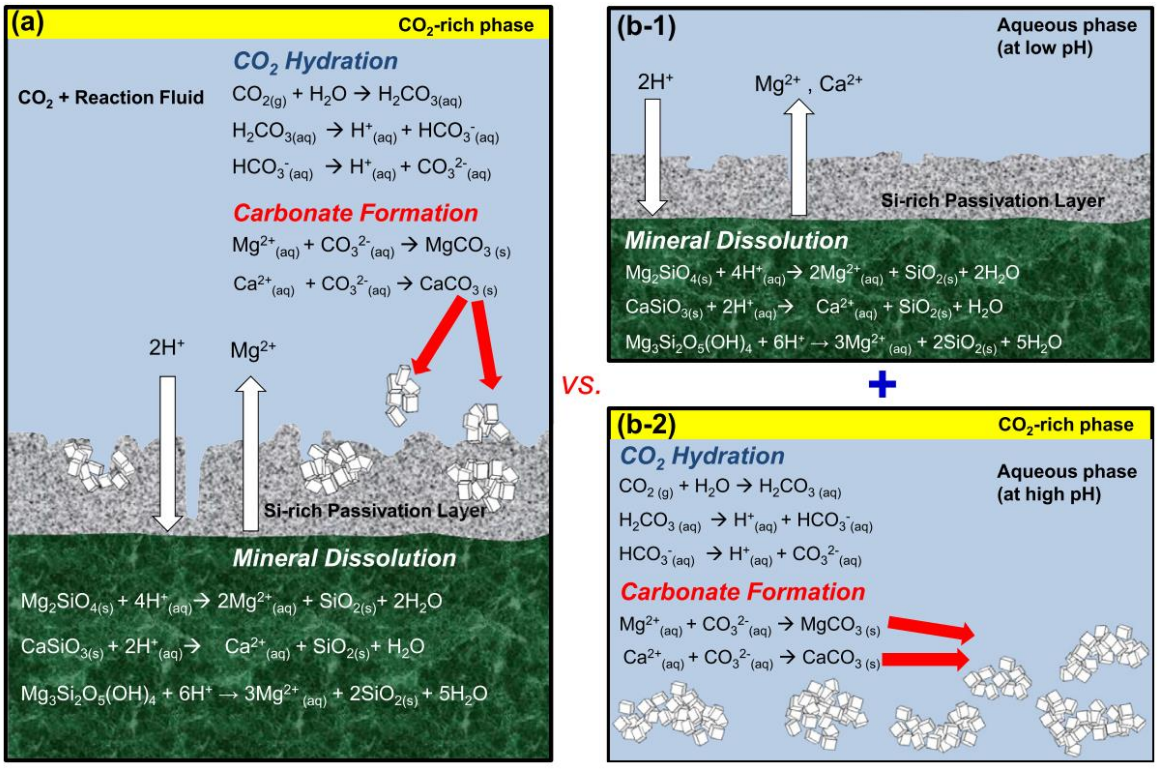

Fig. 2.19. Schematic of ex-situ MC processes via **(a)** DC in aqueous media where silicate dissolution and carbonate precipitation occurred concurrently and **(b)** two-step IC in aqueous media which consist of (b-1) dissolution of silicate minerals, releasing Mg^{2+} and Ca^{2+} and **(b-2)** their subsequent carbonation in a separate step. Figure from Gadikota and Park, 2015 [98].

** Thermal amorphization of serpentine minerals, see section 2.3.1.3.2

2.3.1. Direct Carbonation

DC is the simplest MC approach and can be achieved via reaction of Ca/Mg-rich minerals with CO_2 either in a DGS or aqueous reaction scheme (Fig. 2.19). Ca and Mg oxides and hydroxides are the most reactive MC feedstocks, however, the have limited abundance. Therefore, Ca/Mg-rich silicates and industrial wastes have been targeted for MC [41]. Serpentine, olivine and less abundant wollastonite have receive more attention due to their fast reaction kinetics and abundance [168]. However, such minerals require some mineral pretreatments (grinding and heat-treatment[††]) prior carbonation in order to unlock their carbonation potential, but do not require the extraction of reactive metal oxides from Mg/Ca-rich silicates prior carbonation. Table 2.2 summarizes representative MC studies on different Ca/Mg-rich minerals.

DC reactions can be significantly enhance by the following key parameters: (i) reducing the particle size increases significantly the reaction rates and yields since diffusion can occur in a larger surface area [224], (ii) temperature, which influences the dissolution of CO_2 (lower at higher temperatures) in water as well as the dissolution of silicates (higher at higher temperatures) [257,258] and (iii) high pressure treatments (40-150 bar) enhance both the dissolution of CO_2 in water and the diffusion of carbonic acid into the silicate [224].

Recent research has emphasized the importance to implements ex-situ MC as an integrated CCUS process [44,56,57,99,100]. This route will simplify significantly the MC reaction since prior CO_2 capture processes are not required. Similar carbonation mechanisms are expected using concentrated CO_2 (CC) and flue gas (FG). However, some studies reported slower reaction rates using FG rather than CC [55,254].

2.3.1.1. Direct gas solid carbonation

DGS carbonation of Ca/Mg-minerals is the simplest and economically viable MC approach, however these reactions take place over geological timescales (eq. 2.1 – 2.5; Table 2.4) [157]. Some studies have suggested that such reaction mechanisms are not an efficient mechanism for MC, despite their thermodynamically favored reactions [259–261], requiring elevated CO_2 pressures (100-150 bar) to obtain reasonable reaction rates

Dacosta et al., 2012 [262] reported a DGS carbonation of silicate rock using FG obtaining an olivine carbonation yield of 12%. Moreover, with the addition of water vapor, the obtained carbonation yield reached 18% [259]. Several studies have reported that DGS reactions are greatly enhanced with the addition of water vapor, aiming to unlock the economically desired DGS carbonation potential [204,263,264]. It has been suggested that water vapor plays a crucial role during DGS, allowing the formation of reactive hydrated carbonate phases [265,266].

[††] Thermal amorphization of serpentine minerals, see section 2.3.1.3.2

Early studies reported on the carbonation of portlandite, $Ca(OH)_2$, and brucite, $Mg(OH)_2$ is significantly improved in the presence of high pressure steam [203,267]. However, the utilization of pressurized steam increases significantly the reaction energy requirements. Recent research obtained reasonable carbonation yields of portlandite and brucite by working near the vicinity of liquid-vapor equilibrium point of water (Relative Humidity, RH,: 100%) with reaction carried at ≤150ºC and at moderately low pressures (≤10 bar) [55,204,268]. Larachi et al., 2012 [269] reported a significant increase of the carbonation yield during activated chrysotile[‡‡] (up to 70% at 130º) with decreasing temperature, most likely attributed to the increase of relative humidity. Bhardwaj et al., 2016 [270] also reported high carbonation extents (up to 50% at 120ºC) of activated serpentine[§§] with moist CO_2.

2.3.1.2. Aqueous carbonation

This route is generally carried at elevated pressures (100-160 bar) and temperatures (>100ºC), involving: (i) the dissolution of CO_2 in water, decreasing the pH to about 5 -5.5 at elevated CO_2 partial pressures (eq. 2.12); followed by (ii) the dissolution of silicate minerals, releasing Mg^{2+} and Ca^{2+} from the silicate matrix (eq. 2.13); and the subsequent (iii) Mg^{2+} and Ca^{2+} reaction with bicarbonate, precipitating carbonates (eq. 2.14; Fig. 2.19a)[98,224]. Dissolution of silicate and carbonate precipitation occurs simultaneously, thus, a successful reaction is greatly dependent on the internal pH swing and the formation of passivating Si and Fe-rich layers [98]. As summarized in section 2.2, the addition of bicarbonates ($NaHCO_3$) to the aqueous solution significantly increases the obtained reaction yield as it serves as a pH buffer and a source of carbon [145,146,168,216], see also Table 2.2.

$$CO_{2(g)} + H_2O_{(l)} = H_2CO_{3(aq)} = H^+_{(aq)} + HCO^-_3 \quad (2.12)$$

$$Mg_2SiO_{4(s)} + 4H^+_{(aq)} = 2Mg^{2+}_{(aq)} + SiO_{2(s)} + 2H_2O_{(l)} \quad (2.13)$$

$$Mg^{2+}_{(aq)} + HCO^{3-}_{(aq)} = MgCO_{3(s)} + H^+_{(aq)} \quad (2.14)$$

Energy intensive pretreatments and carbonation reactions due to the slow dissolution of silicate minerals have limited the large-scale deployment of such technologies [41,271]. The dissolution process is mainly controlled by the following sequential steps: (i) diffusion processes between a fluid film on the particle surface, (ii) diffusion through a reaction solid product on the surface of the particle and (iii) chemical reactions on the particle surface [224]. Several studies were performed on the dissolution of serpentine and particularly olivine [220,272–274]. The rate-limiting step is the formation of a Si-rich inert passivating layer product of the dissolution of both olivine and serpentine, which reduces significantly the diffusivity between the reactive mineral and CO_2

[‡‡] Thermal amorphization of serpentine minerals, see section 2.3.1.3.2
[§§] Thermal amorphization of serpentine minerals, see section 2.3.1.3.2

[101,275]. Carbonate precipitation on silicate grains might also play a role on the passivation of the reaction. However, some studies suggested that carbonate precipitation allows ions from the dissolving mineral to be rapidly transported to the bulk fluid [276].

Both serpentinites and dunites generally contains up to 15% of iron oxides. The presence of such minerals upon carbonation often resulted in the formation of an Fe-rich passivating layer on silicate grains, significantly limiting the carbonation reaction [44,146,171]. Therefore, separation of magnetic minerals is often carried out prior carbonation. Moreover, such processes significantly increase the extent of MC and relatively pure and profitable magnetic minerals are obtained [44,168]. Nevertheless, it also increases the energy requirements of such processes.

The liquid-solid ratio (L/S) is another important parameter for aqueous DC. Generally, at L/S lower than 2, the autoclave reactor cannot be stirred sufficiently, reducing the carbonation efficiency [277]. The majority of aqueous DC experiments is carried at a higher L/S to enhance the carbonation efficiency [278].

Aqueous-route DC with mineral pretreatment is considered as the most successful approach [224]. However, reaction yields are low, often requiring elevated CO_2 partial pressures and temperatures. Some pretreatments have been proposed in order to enhance the obtained reaction yields [157], as summarized in following sections.

2.3.1.3. Silicate mineral pretreatment

Two major processes have been developed for increasing the reactivity of silicate minerals: (i) high energy mechanical grinding processes, increasing the diffusive surface area and (ii) amorphization of serpentine minerals by thermal treatments, known as thermal activation.

2.3.1.3.1. Mechanical grinding

This approach aims to increase the reactivity of silicate minerals by aiming to destroy or disorder the mineral lattice, increasing the surface area [224]. Such method has been extensively studied by the US National Energy Technology Laboratory (NETL). Firstly, the minerals are crushed, reducing their particle sizes to <300μm, followed by wet grinding, obtaining grain sizes bellow 75 or 38 μm. The energy requirements for optimal grinding processes were assessed for different silicate minerals. The reactivity of olivine is significantly and steadily increased with diminishing particle size, reaching a reaction extent over 80% (Fig. 2.20), however the concomitant energy requirements for only grinding also significantly increases, besides the high carbonation energy requirements. Wollastonite was found to be the more reactive (Fig 2.20a) with reaction extents over 80% without the need of ultrafine gridding processes. Wollastonite and olivine carbonation were greatly influenced by the increased of surface area. The higher reactivity of wollastonite is attributed to the higher precipitation rates of $CaCO_3$ when compared to $MgCO_3$ (four times lower than $CaCO_3$) [279].

Nevertheless, hydrated Mg-carbonate phases have precipitation rates much higher than $MgCO_3$, but their formation is inhibited at elevated temperatures (≥200ºC) [55,197,199,204]. More detailed explanation of hydrated Mg-intermediate carbonate phases will be given in Chapter 3.

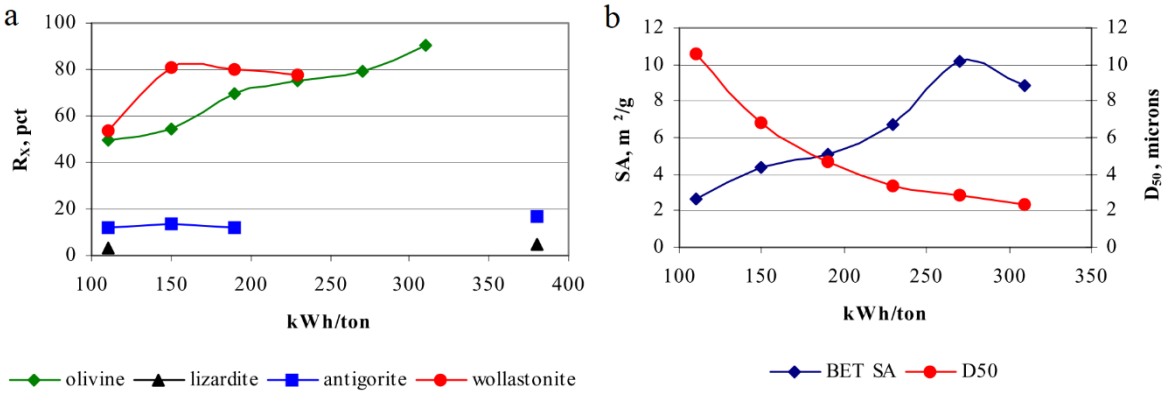

Fig. 2.20. (a) Grinding energy requirements and the obtained extent of reaction, R_X (see eq. 2.15), for olivine, lizardite, antigorite and wollastonite. **(b)** Relationship between surface area and particle size in function of grinding energy requirements for olivine grinding. D_{50} represents 50% of the particle sizes are finer than 50μm. Figure from O'Connor et al., 2005 [168].

$$R_x = \frac{X_{CO_2}}{\varepsilon_A(1 - X_{CO_2})} \tag{2.15}$$

Where X_{CO_2} is the CO_2 wt%. in the solid product and ε_A is the percent weight gain assuming 100% stoichiometric conversion of the available Ca^{2+}, Mg^{2+} and Fe^{2+} to carbonates.

Un-activated analyzed serpentine minerals (antigorite and lizardite) were significantly less reactive than olivine and wollastonite, especially for lizardite, indicating that such minerals require additional pretreatments in order to unlock their carbonation potential. This is mainly justified by the large abundance of this latter minerals in the earth's crust [145,168].

Similar experiments were carried by Fabian et al., 2010 [280] and Haug et al., 2010 [272], where the mechanical activation was found to be effective for olivine. Rashid et al., 2019 [281], recently proposed a concurrent (in operando) grinding process where the carbonation at high temperatures (155- 180ºC) and pressures (65-130 bar), with the addition of 0.64M $NaHCO_3$, and grinding takes places simultaneously. The carbonated material is brucite-rich serpentinized dunite, mainly composed of lizardite (Fig. 2.21a). It was observed that partial carbonation of un-activated lizardite, obtaining a magnesite yield above 60% after 8 hours of reaction. The carbonation extent of such material without concurrent grinding was found to be below 20%, mainly attribute to the presence of lizardite (Fig. 2.21b). The carbonation of lizardite was significantly enhanced, providing a new option for activation of lizardite. However such pretreatment costs require too much energy for CCUS purposes (see table 2.5) [224].

Additionally, ultrasonic and wet grinding in caustic solutions have been also tested but no significant enhancement was obtained [224], however they increase the pretreatment energy-requirements, which is the main drawback of such technologies. Table 2.6. summarizes the specific pretreatment energy requirements for different minerals and the obtained extent of reaction.

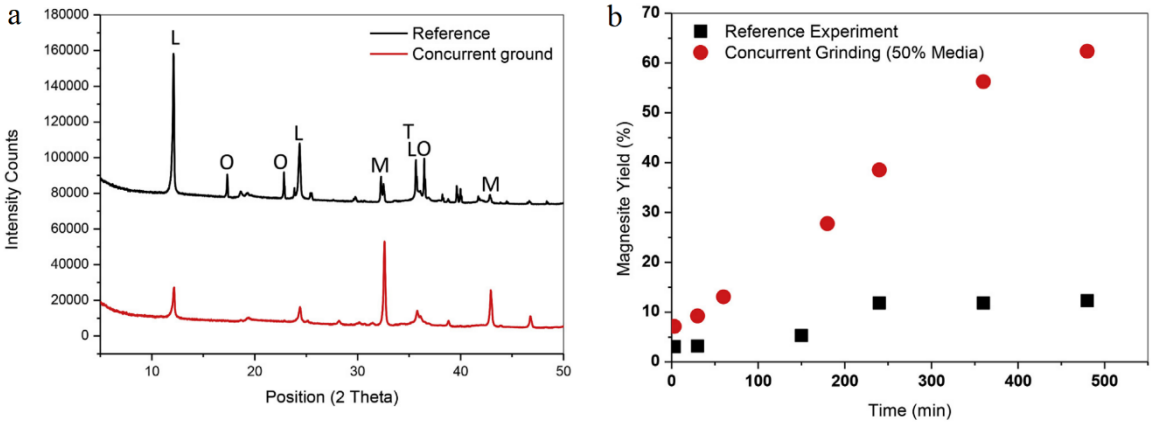

Fig. 2.21. (a) XRD analyses and **(b)** magnesite yield (%) of concurrent grinding experiments and reference experiments carried at 180ºC, 15wt% slurry solid using 0.64M $NaHCO_3$ and 130 bar of pressure. O: Olivine, L: Lizardite, M: Magnesite and T: Magnetite. Figure from Rashid et al., 2019 [281].

Table 2.5. Estimated pretreatment energy requirements for olivine, lizardite, antigorite and wollastonite as well as the R_x at optimal high pressures and temperature conditions. SMD mill: Stirred media detritor. Bene: beneficiation step (i.e.: gravity separation)Table adapted from Gerdemann et al., 2007 [145].

Feed material		Pretreatments energy consumption, $kW \cdot h \cdot t^{-1}$							
				Grinding			Heat		
Mineral (grade)	Pretreatment methodology	Crush	Bene	Stage 1	Stage 2	Stage 3	treatment	Total	R_x
Olivine, 100%	Ball mill (- 75µm)	2	-	11	-	-	-	13	16
	Ball mill (- 38µm)	2	-	11	70	-	-	83	61
	SMD mill	2	-	11	70	150	-	233	81
Serpentine	Ball mill (- 75µm)	2	-	11	-	-	-	13	9
Lizardite (100%)	Heat treatment (- 75µm)	2	-	11	-	-	326	339	40
Olivine, 70%	Ball mill (- 75µm)	2	2	15	-	-	-	19	16
	Ball mill (- 38µm)	2	2	15	70	-	-	89	61
	SMD mill	2	2	15	70	150	-	239	81
Serpentine	Ball mill (- 75µm)	2	-	11	-	-	-	13	12
Antigorite (100%)	Heat treatment (- 75µm)	2	-	11	-	-	293	306	62
	Heat treatment (- 38µm)	2	-	11	70	-	293	376	92
Wollastonite,	Ball mill (- 38µm)	2	4	21	70	-	-	97	43
50%	SMD mill	2	4	21	70	70	-	167	82

2.3.1.3.2. Thermal activation

Upon heat treating serpentine minerals, their hydroxyl content is partially to fully removed, increasing significantly their reactivity [282,283]. Mckelvy et al., 2004 [49] reported that the reactivity of activated materials is highly dependent on the remaining OH content. Thermal activation of lizardite occurs between 580ºC to 800ºC. At 580ºC, lizardite undergoes partial dehydration, losing structural order, becoming partially amorphous. At this temperature a new phase

emerges as evidenced by the X-ray scattering at 2θ=6º, suggesting that it has longer range-ordering than lizardite and is likely associated with a doubling of the 7.336 Å interlamellar spacing (~14.7 Å corresponds to 2θ ~6º) along the <001> plane. This phase is commonly called the "α component" and is observed to coexist with structurally-ordered lizardite (Fig.2.22). This might suggest that the dehydration of lizardite occurs via lamellar nucleation and growth, similarly to the dihydroxylation of brucite [49,284].

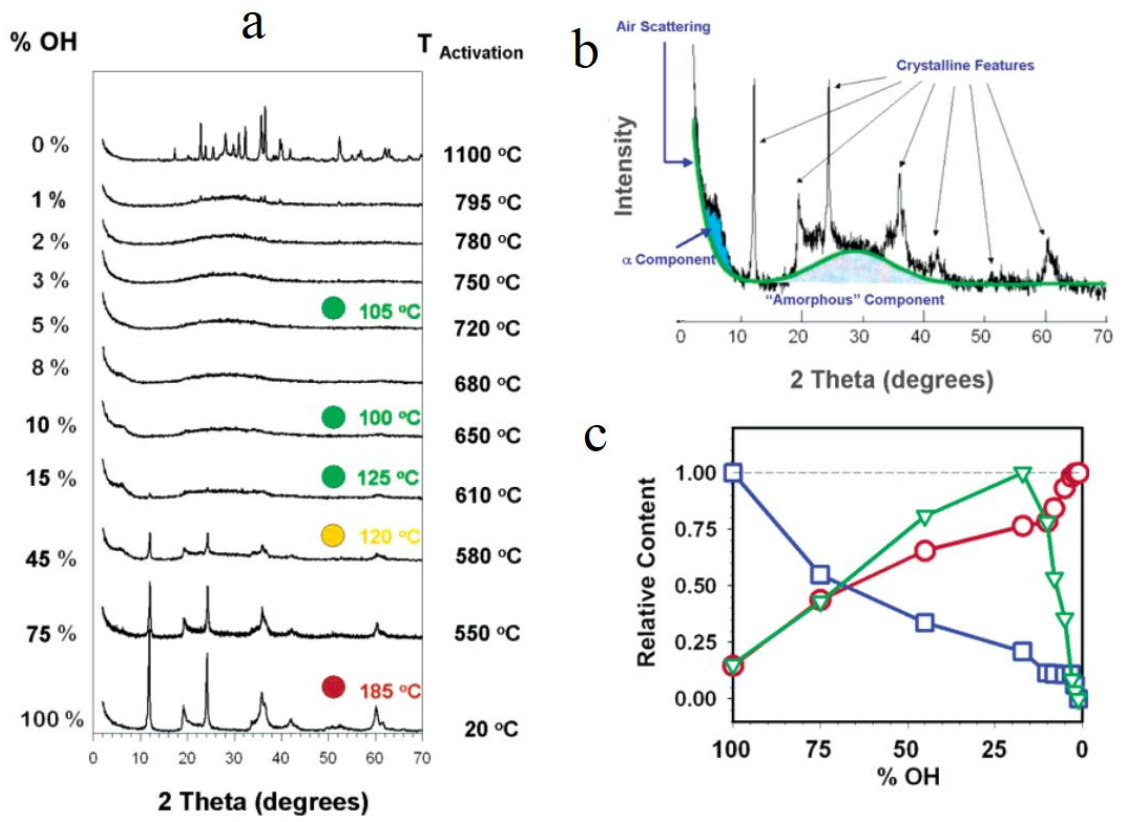

Fig. 2.22. (a) XRD analyses of heat activated materials activated from 550 – 1100ºC, as well as their residual OH content (wt%). Colored circles indicate no (red), trace (yellow) and substantial (green) carbonation as observed with in-situ synchrotron XRD carbonation analysis. The onset carbonation temperatures are shown alongside the colored circles. Carbonation was performed at elevated CO_2 pressures (150 bar) in an aqueous solution containing 0.64M $NaHCO_3$ + 1M NaCl. **(b)** XRD phase analysis of activated lizardite at 580ºC, where residual lizardite crystalline features are observed coexisting with "α component" and an "amorphous component". **(C)** Relative content of both intermediate phases (α: green, amorphous: red) and residual crystalline lizardite (blue) as function of the residual OH content. Figure from McKelvy et al., 2004 [49].

At 650ºC, the residual OH content reaches 10%. Lizardite sharp features disappears as an XRD an "amorphous component" emerges, as evidenced by an XRD plateau centered at 2θ ≈ 28° (Fig.2.22a, b). As the temperature increases the "α component" is diminishing. At 750ºC, the α component have disappeared and only the "amorphous component" remains. At 780ºC, nucleation of forsterite begins to occur, followed by enstatite, $MgSiO_3$ (at 790ºC). At 1100ºC, the "amorphous component" has disappeared and only forsterite and enstatite are observed.

When the residual OH content is between 8-25%, a significant enhancement of the reaction extent is obtained relative to those obtained with un-activated lizardite (Fig. 2.23) [285,286]. In particular, when the OH residual contents reaches 16%, the obtained reaction extents are nearly 100%, coinciding with the highest proportion of the amorphous component, relative to the other intermediate phases (Fig 2.22c). Previous studies have suggested that the reactivity of activated serpentines is primarily due to the highly-disordered nature of the intermediate phases [49,287].

Moreover, it is also observed that when serpentine minerals are fully dehydroxylated, the carbonation yield is reduced, indicating that there is an optimal temperature for serpentine activation [286]. This is likely attributed to the nucleation of forsterite and particularly enstatite from the intermediate phases, consuming the available amorphous reactive phases [49,287]. This is in agreement with in-situ synchrotron XRD analysis of activated lizardite carbonation, where the optimal carbonation was obtained with materials activated at 650ºC (associated with 10% of residual OH; Fig. 2.22a) [49]. The transition from lizardite to forsterite and enstatite follows a topotactic transformation, where the rate transition rates decreases with increasing degree of disorder [287].

Dihydroxylation of antigorite and lizardite possess similar reactivity as evidenced by the similar trends observed in Fig. 2.23. However, both minerals have different thermal stability, being antigorite the more thermally stable. Therefore, each mineral has an optimal activation temperature [287].

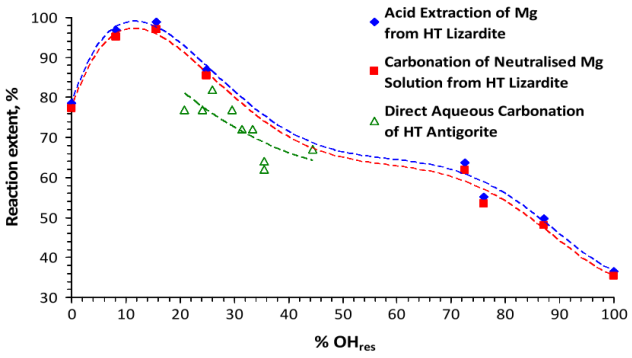

Fig. 2.23. Obtained reaction extent upon carbonation of heat activated lizardite and antigorite as function of the residual OH content. Activated lizardite carbonation was performed by introducing simulated flue gas into the alkalized leachate until a neutral pH was reached, then the solution was heated at 85ºC for 15 min. Direct carbonation of antigorite was carried at >155ºC and 150 bar of CO_2 in an aqueous solution with 0.64M $NaHCO_3$ + 1M NaCl. HT' refers to heat activated. Figure from Dlugogorski and Balucan, 2014 [287].

Gerdemann et al., 2007 [145] have compared the reactivity of olivine, wollastonite and activated serpentine at analogous experimental conditions (Fig 2.24). Since the reaction rate is greatly dependent on the particle size, comparison of different material with different pretreatments is difficult. The authors proposed to compared the obtained R_x, normalized by the maximum R_x obtained in the reaction series ($R_{x(max)}$). Therefore, the mineral-specific variations partially due to

different pretreatments are not taken into account in the comparison [168]. The actual maximum R_x values were 49.5, 81,8 and 73.5 for olivine, wollastonite and heat treated (HT) serpentine, respectively (Fig. 2.24) [145]. Heat treated serpentine is more reactive than olivine, requiring lower temperature and pressures to obtained maximum carbonation yields. This demonstrates that HT plays a crucial role on the enhancement of serpentine reactivity. However, the maximum reaction yield obtained in any set of experiments at elevated temperatures and pressures conditions is of 49.5, significantly lower than olivine and wollastonite. The possible explanation for this behavior as well as a more detailed description together with a performed experimental campaign will be extensively discussed in Chapter 5. Wollastonite remained more reactive than the other compared materials, requiring moderately low pressures (40 bar) and temperatures (100ºC), without the addition of 0.6M $NaHCO_3$ + 1M NaCl to the aqueous solution, to obtain its maximum carbonation yield.

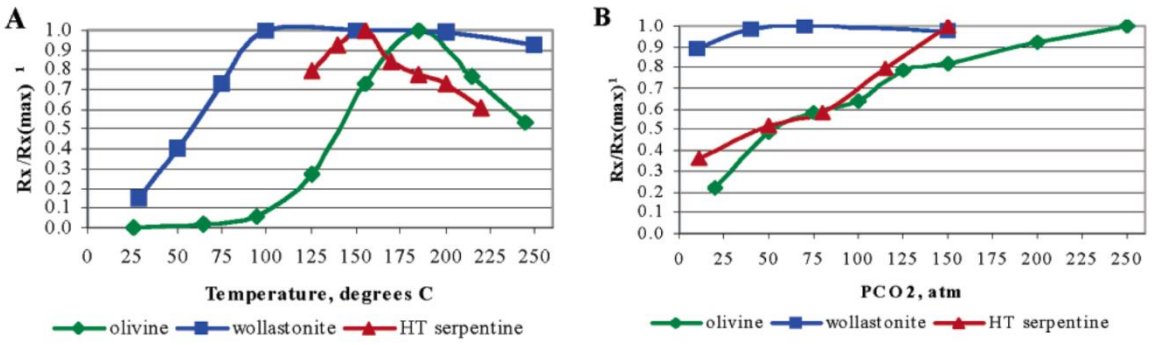

Fig. 2.24. (A) Obtained R_x normalized by $R_{x(max)}$ of carbonation series of olivine, HT serpentine and wollastonite, performed at: (a) 25-250ºC and 185 bar of CO_2; **(B)** 185ºC and 10-250 bar of CO_2. Figure from Gerdemann et al., 2007 [145].

Sanna et al., 2013 [288] suggested that the energy requirement for activation at 610ºC during 0,5h could be reduced to 245 $kW \cdot h \cdot t^{-1}$. Mg extracted was higher compared to those reported in a different study for activation at 640-700ºC, during 1h [289]. Moreover, other studies have suggested that if thermal heat is used instead of electrical energy, the activation energy requirements could be reduced up to 60% [290]. Orica (an Australian company) have proposed to reduce the energy requirements for activation by using exothermic heat from carbonation reactors (operated at elevated CO_2 pressures and temperatures) as well as low grade heat from the power plant that provides the flue gas [291]. It has been estimated that such process could be economically viable and has a CO_2 storage capacity of 14.1 Mt y^{-1} from a conventional pulverized fuel-based electricity generation plant [87,291]. Activation pretreatments are more effective than mechanical grinding processes but the energy requirements are still too high to CCUS large-scale implementation [280,288].

2.3.2. Indirect carbonation

It refers to the ex-situ MC process that takes more than one step, decoupling dissolution of minerals and extracting reactive components (Table 2.7) and carbonation processes as two different steps. This is based on the differences in the pH that favors mineral dissolution (acidic) and carbonation (basic). The individual steps can be better optimized than a couple MC process, achieving lower reaction temperature during the carbonation step [292,293]. Moreover, high-purity and profitable carbonate products can be obtained if an additional step is added between mineral dissolution and carbonation [42,294]. The most relevant extraction method will be summarized in the following sections.

Table 2.7. Summary of extraction of metal ions from silicates processes prior carbonation. Table from Bobicki et al., 2012 [42].

Metal oxide extraction methods	Characteristic
Acid extraction (See Fig. 2.19)	• Mineral dissolution via HCl or other acid • Alkaline metals precipitate as a hydroxide for carbonation • Acid can be recovered • Energy intensive if acid is recovered • Multiple steps allow the separation of carbonate pure phases
Molten salt	• Molten NaCl is used to extract metal ion from silicates • Alkaline metals precipitate as a hydroxide for carbonation • Molten NaCl is highly corrosive • The associate chemical cost is prohibitive
Bioleaching	• Chemolithotrophic bacteria combined with acid generating substances and silicate minerals to extract metal ions • Passive and inexpensive
Ammonia extraction	• Ammonia salts are used to extract metal ion from silicates • Selective leaching of alkaline earth metals • Reagent recovery is possible • Reasonable conversion rates obtained
Caustic extraction	• Caustic solid used to extract metal ions from silicates • Not a promising technique

2.3.2.1. Acid extraction

Generally, HCl, H_2SO_4 and HNO_3 are used to dissolve silicate rocks [42,274,295]. Eq. 2.16-2.19 summarizes the reaction involving IC by HCl extraction. Among these acids, H_2SO_4 was found to extract Mg from silicates more effectively, followed by HCl [274]. Lin et al., 2009 [295] tested the dissolution of serpentine with HCl at 150ºC over prolonged times. The precipitate brucite was then carbonates at 325ºC and atmospheric pressure for 2. Another approach tested the dissolution of serpentine minerals with H_2SO_4 at 20-65ºC during 3-12 hours, producing magnesium sulfate, which subsequently reacted with sodium hydroxide, precipitating brucite. This latter mineral was then carbonated at 20ºC and 40 bar. H_2SO_4 was regenerated after reaction between CO_2 and $MgSO_4$ [171]. However, the energy intensive regeneration of such acids prohibits the current development of such approach [42].

Organic acids, such as acetic acid (CH_3COOH) and formic acid (HCOOH) dissolve significantly serpentine minerals and their utilization is proposed to avoid the high energy requirements associated with strong acids [274]. Krevor and Lackner, 2009 [296] reported that sodium salts of citrate, oxalate, and EDTA significantly dissolved serpentine minerals under weakly acidic conditions. Park et al., 2003 & 2004 [170,293] reported that a mixture of 0.1% EDTA, 0.9wt% oxalic acid and 1vol% of orthophosphoric acid enhanced Mg leaching from serpentine minerals at 70ºC and 1 bar. SiO_2 residue was then filtered from the slurry. The Mg^{2+} and Fe^{2+}-rich filtrate was subjected to carbonation by bubbling CO_2 at ambient temperature, achieving 65% conversion.

$$Mg_3Si_2O_5(OH)_{4(s)} + 6HCl_{(aq)} + H_2O \xrightarrow{100ºC} 3MgCl_2 6H_2O_{(aq)} + 2SiO_{2(s)} \quad (2.16)$$

$$MgCl_2 6H_2O_{(aq)} \xrightarrow{250ºC} MgCl(OH)_{(aq)} + HCl_{(aq)} + 5H_2O \quad (2.17)$$

$$2MgCl(OH)_{(aq)} \xrightarrow{\text{cooling}} Mg(OH)_{2(s)} + MgCL_{2(aq/s)} \quad (2.18)$$

$$Mg(OH)_{2(s)} + CO_{2(g)} \rightarrow MgCO_{3(s)} + H_2O \quad (2.19)$$

2.3.2.2. Ammonia extraction

The first approach of using ammonium salts for serpentine dissolution (known as pH swing process) was reported by Wang and Maroto-Valer, 2011 [257]. It was reported that 100% Mg was leached from serpentine after 3h at 100ºC in a solution containing 1,4M NH_4HSO_4. The complete process consists of five steps (Fig. 2.25; eq. 2.20-2.24): (i) NH_3 is used to capture CO_2, forming NH_4HCO_3; (ii) separately, a solution containing 1.4M NH_4HSO_4 is used to leach Mg^{2+} from serpentine minerals with grain sizes between 75-125 µm; (iii) the solution is then neutralized by adding NH_4OH and the solution is filtered to removed SiO_2 residues and Fe-rich minerals from serpentine dissolution; (iv) Mg^{2+}-rich filtrate is reacted with NH_4HCO_3 (from the CO_2 capture step), precipitating nesquehonite, $Mg(HCO_3)(OH)\cdot 2(H_2O)$, which is then transformed in-situ into hydromagnesite $Mg_5(CO_3)_4(OH)_2\cdot 4(H_2O)$. The resulting solution, after carbonate precipitation mainly contains $(NH_4)_2SO_4$; (v) the last step consists of the regeneration of the additive by decomposition of $(NH_4)_2SO_4$ at 330ºC, producing NH_3 and NH_4HSO_4 [278,297] One of the main advantages of this process is that the different products (carbonates, iron oxides and silica) can be separated [274,275,293,294,297]. Chilled ammonia can also be utilized in such processes, increasing the CO_2 capture efficiency to more than 90% with overall estimated energy penalty of 477 $kW\cdot h\ t^{-1}$ [224]. One of the main drawbacks of this process is the salts regeneration step. Wang and Maroto-Valer, 2013 [298] proposed to reduce the water usage in the system, due to its high evaporation energy penalty. However, the CO_2 sequestration efficiency was greatly decreased and larger amounts of reactants (ammonia salts and serpentine) were required.

$$NH_3 \cdot H_2O + CO_2 \rightarrow NH_4HCO_3 \quad (2.20)$$

$$Mg_3Si_2O_5(OH)_4(Fe^{2+},Fe^{3+})_{(s)} + 6NH_4HSO_{4(aq)} \xrightarrow{heat} 3MgSO_4(Fe^{2+},Fe^{3+})_{(aq)} + 2SiO_2 + 3(NH_4)_2SO_{4(s)} + 5H_2O \quad (2.21)$$

$$3MgSO_4(Fe^{2+},Fe^{3+})_{(aq)} + 8NH_4OH_{(aq)} \xrightarrow{\text{pH to 8.5}} \frac{Fe_2O_3}{FeO}_{(s)} + 3MgSO_4 + 8NH_4^+ + 4H_2O \quad (2.22)$$

$$6MgSO_4 + 6(NH_4)_2SO_{4(aq)} + {}^{24}/_{5}\ CO_{2(g)} + 12NH_4OH_{(aq)} \rightarrow {}^{6}/_{5}\,(4MgCO_3 \cdot Mg(OH)_2 \cdot 5H_2O)_{(s)} + 12(NH_4)_2SO_{4(s)} \quad (2.23)$$

$$4(NH_4)_2SO_{4(s)} \xrightarrow{320ºC} NH_4HSO_{4(aq)} + NH_{3(g)} \quad (2.24)$$

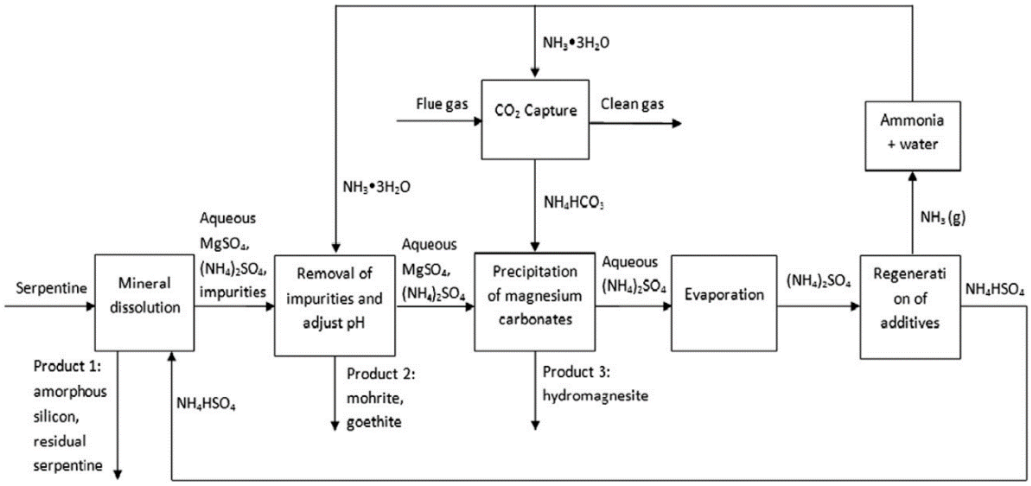

Fig. 2.25. Scheme of pH-swing CO_2 MC process using ammonium salts looping. Figure from Wang and Maroto-Valer, 2011 [257].

Fagerlund et al., 2009 [299] proposed a modified version of the Mg extraction by ammonium salts (known as the ÅA Route, from Åbo Akademi), involving two-steps (Fig. 2.26; eq. 2.25, 2.26): (i) a slurry containing a mixture of serpentine feedstock with NH_4HSO_4 is heated to 450 -550ºC, producing $MgSO_4$. By adjusting the pH using ammonium hydroxide or ammonia, brucite precipitates; (ii) brucite is carbonated in the dry phase in a fluidized bed at 20 bar and 500-550ºC,where 50% Mg conversion was achieved in 10 minutes [267]. However, modest Mg recovery yields of this technologies (50-60%) limits the large-scale deployment of this technology[204]. The main advantages of this method are: (i) highly reactive brucite is produced and (ii) there is high potential for heat recovery due to the exothermic carbonation reactions.

$$Mg_3Si_2O_5(OH)_{4(s)} + 3(NH_4)_2SO_{4(s)} \xrightarrow{heat} 3MgSO_{4(s)} + 2SiO_2 + NH_3 \quad (2.25)$$

$$3MgSO_{4(s)} + 2NH_4OH_{(aq)} \rightarrow Mg(OH)_{2(s)} + (NH_4)_2SO_{4(aq)} \quad (2.26)$$

Hunwick, 2008 (123) developed another multi-step IC process via ammonia extraction from power station flue gases: (i) Mg/Ca-silicates were mixed with ammonia to produce an aqueous slurry

containing 30% solids; (ii) the slurry was then pressurized with CO_2 to 100 bar an heated to 225ºC, precipitating magnesite; (iii) ammonia recovery.

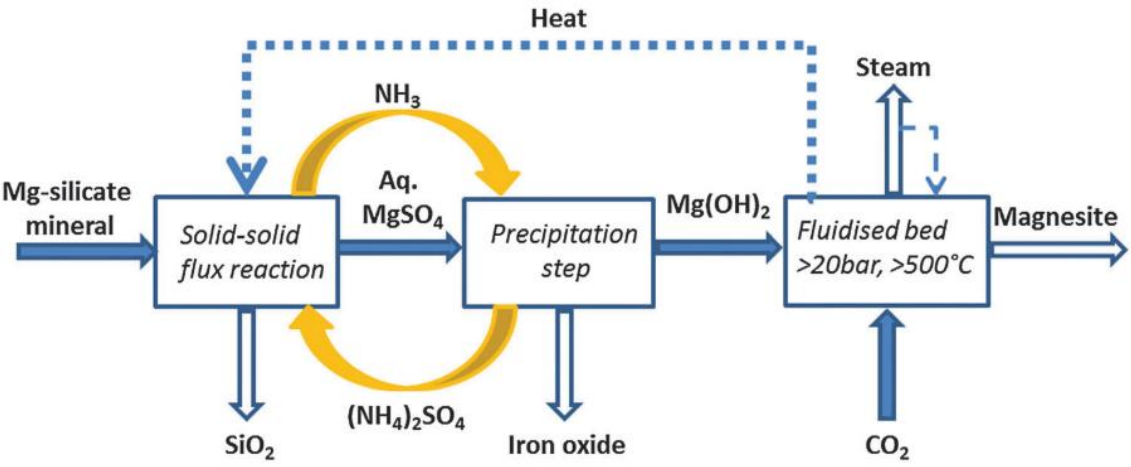

Fig. 2.26. Scheme of ÅA route among the IC processes. Figure from Sanna et al., 2014 [224]

2.3.2.3. Molten Salt processes

This process was developed as an alternative to HCl extraction with lower energy requirements. The process is very similar to HCl extraction, varying in the extraction agent used: molten salt, $MgCl_2 \cdot 3.5H_2O$ instead of HCl (eq. 2.27-2.30) [157]. Despite having less energy requirements than HCl extraction, molten salt is extremely corrosive, and it need a continuous production of such compound. It has been estimated that even with an attained commercial supply of $MgCl_2$, such process will remain unaffordable. Therefore, it has received less attention over the last two decades [42].

$$Mg_3Si_2O_5(OH)_{4(s)} + 3MgCl_2 \cdot 3.5H_2O_{(aq)} \xrightarrow{200ºC} 6Mg(OH)Cl_{(aq)} \quad (2.27)$$

$$Mg(OH)Cl_{(aq)} + nH_2O_{(aq)} \xrightarrow{150ºC} MgCl_2 \cdot nH_2O_{(aq)} + Mg(OH)_{2(s)} \quad (2.28)$$

$$MgCl_2 \cdot nH_2O_{(aq)} \xrightarrow{120ºC} MgCl_2 \cdot 3.5H_2O_{(aq)} + (n-3.5)H_2O \quad (2.29)$$

$$Mg(OH)_{2(s)} + CO_{2(g)} \rightarrow MgCO_{3(s)} + H_2O \quad (2.30)$$

2.3.2.4. Bioleaching

It refers to the process when bacteria are utilized to extract metals from minerals [300]. Such process has been adapted to extract Ca and Mg from silicates, following natural analogues [301]. Silicate weathering can be artificially enhanced with a combined utilization of Acid Generation Substances (AGS; i.e.: sulphides and sulfur) and chemolitothrophic bacteria such as: *Acidithiobacillus (A.) ferrooxidans* and *A. thiooxidants* [302]. Both bacteria generate H_2SO_4 during their metabolism process (which leaches metal ions from silicates) and feed on AGS. Moreover,

both species also utilizes atmospheric CO_2 as a source of carbon for producing new cell material [300,302]. Such process has been studied on the accelerated carbonation of passive MC of mine tailings (Fig. 2.27). However, such process has not yet been optimized to achieve significant metal leaching rates from silicates, since only limited amounts of AGS can be utilized in order to avoid the formation of acidic leachate [302]. Currently, the metal extraction obtain by this method cannot compared to those obtained in the other methods described, due to their characteristic slow kinetics. Nonetheless, it is and innovative, sustainable, low cost and passive approach which intends to utilizes waste products for MC purposes. It is foreseen that such method could play an important role on CO_2 mitigation efforts [42].

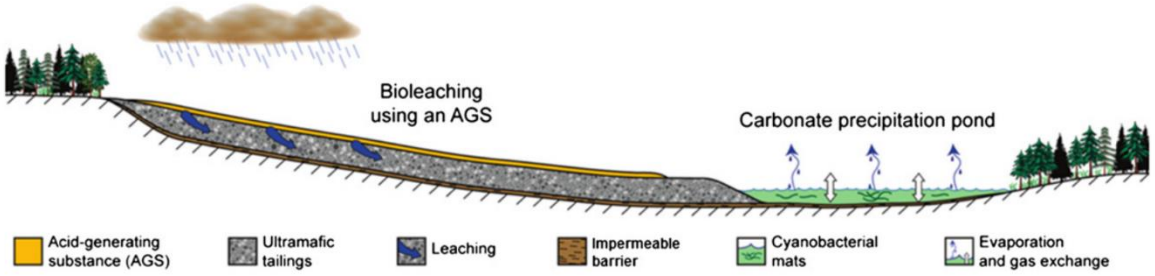

Fig. 2.27. Schematic of enhanced passive metal leaching from mine tailings by utilizing combined AGS and chemolithotrophic bacteria. Figure from Power et al., 2010 [302].

2.3.3. Carbonation of alkaline industrial wastes

There is an increasing interest for the utilization of both CO_2 and wastes materials for CCUS purposes. Such wastes often elevated Ca, Mg, Al and Fe contents. Unlike Ca/Mg-rich silicates, alkaline wastes are primarily composed of reactive oxides and hydroxides [98]. The main advantages of utilizing alkaline industrial wastes for MC instead of natural minerals are: (i) mining is not required and consumption of raw material is avoided, as well as their associated environmental impacts [303]; (ii) generally, no additional milling is required to increase their reactivity [145]; (iii) such material are widely available and cheap [157]; (iv) generated near the PSCC, potentially avoiding transportation costs; (v) generally, do not require pre-treatments due to their high reactivity; (vi) upon carbonation, such wastes are potential neutralized, allowing to stored them more safely, reutilized and value is added due to the generation of profitable by-products [253,304,305]. However, the available quantity of alkaline wastes (estimated to have a CO_2 storage capacity of 200-300Mt yr^{-1}) is significantly smaller than known Ca/Mg-rich silicate reserves [224]. Despite their limited CO_2 storage, their successful implementation is foreseen as a key step in the development and industrialization of MC technologies [41,303].

Alkaline residues can be classified in three major categories: (i) wastes from power generation, such as: fly ash, bottom ash, Air Pollution Control (APC) residues and oil shale wastes); (ii) cement, building material and paper production, such as: kiln dust, asbestos and paper mill waste; (iii) steel

an aluminum production, such as: steelmaking slag [98]; (iv) mine tailings, such as: asbestos, cooper, nickel, platinum deposits, etc. [224]. The availability of fly ashes far exceeds the other alkaline wastes (Fig. 2.28). However, steel slag has significantly higher Ca content [98]. The average Mg content of the residues shown in Fig. 225 is generally low. Nevertheless, ultramafic mine tailing have significantly higher Mg contents (up to 40% MgO) and are generally poor in CaO [224]. Generally, APC wastes and waste ashes from fuel combustion contains significant amounts of reactive free lime. Its carbonation is driven by exothermically and fast kinetics in DC via aqueous carbonation (eq. 2.31 - 2.35) [306–308] and steam mediated [82,268].

$$CaO_{(s)} + H_2O_{(l)} \rightarrow Ca(OH)_{2(s)} \quad (2.31)$$

$$Ca(OH)_{2(s)} \rightarrow Ca^{2+}_{(aq)} + 2OH^{-}_{(aq)} \quad (2.32)$$

$$CO_{2(g)} + H_2O_{(l)} \leftrightarrow H_2CO_{3(aq)} \leftrightarrow H^{+}_{(aq)} + HCO^{-}_{3\,(aq)} \quad (2.33)$$

$$HCO^{-}_{3\,(aq)} + OH^{-}_{(aq)} \leftrightarrow CO^{2-}_{3\,(aq)} + H_2O_{(l)} \quad (2.34)$$

$$Ca^{2+}_{(aq)} + CO^{2-}_{3\,(aq)} \rightarrow CaCO_{3\,(nuclei)} \rightarrow CaCO_{3\,(s)} \quad (2.35)$$

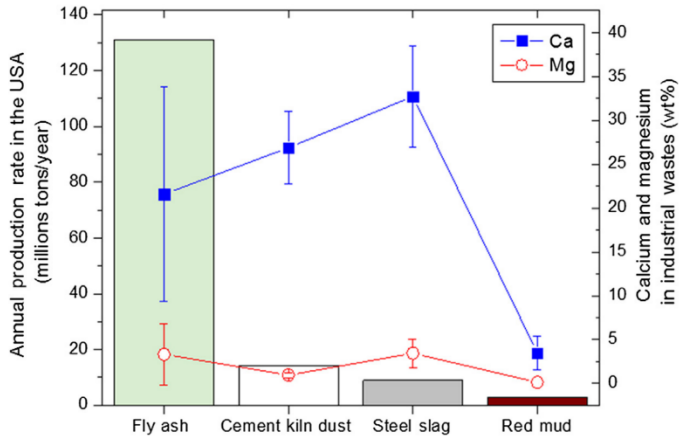

Fig. 2.28. Annual production rate (Mt yr^{-1}) in the USA and their average Ca and Mg concentration in fly ash, CDK, steel slag and red mud, see table 2.8. Figure from Gadikota and Park, 2015 [98].

Several wastes, such as steel slags, have high CaO contents, however, Ca is mainly bounded to silicates, instead of highly reactive oxides and hydroxides. The carbonation of such silicates follows the general equation 2.36 and 2.37 [224]. Different studies have reported that Ca leaching from silicates in alkaline wastes is enhanced by increasing temperature, pressures and surface area [145,306,309].

$$Ca(\text{or } Mg)\text{ silicate}(s) + 2H^{+}_{(aq)} \rightarrow Ca^{2+}(\text{or } Mg^{2+})_{(aq)} + SiO_{2(s)} + H_2O_{(l)} \quad (2.36)$$

$$Ca^{2+}(\text{or } Mg^{2+})_{(aq)} + HCO^{-}_{3\,(aq)} \rightarrow Ca(\text{or } Mg)CO_{3(s)} + H^{+}_{(aq)} \quad (2.37)$$

Industrial materials containing hazardous materials such as heavy metals, their carbonation should be carefully assessed, particularly in DC via aqueous media, since leaching of such metals

can be enhanced. Some studies have reported that such metals could be fixed within the precipitated carbonate matrix [227]. A summary of MC studies of different waste materials is shown in Table 2.8. The main MC routes for alkaline wastes will be summarized in the following sections.

Table 2.8. Summary of MC carbonation studies of different alkaline industrial wastes and their reaction conditions and reactive feedstocks Ca and Mg content. MSWI: Municipal Solid Waste Incineration; BM: Building materials; UMT: Ultramafic mine tailings; PMW: Paper Mill Waste; LF slag: Ladle Furnace slag; BOF slag: Basic Oxygen Furnace slag; BHC: blended hydraulic slag cement. [a]Indirect Carbonation Table adapted from Gadikota and Park, 2015 [98] and Bobicki et al., 2012 [42].

Material type		Composition (wt%.)	CO_2 Storage capacity $\left(\frac{kg_{CO_2}}{kg_{waste}}\right)$	R_x (%)	Reaction conditions			Ref.
					Reaction phase	P_{CO_2}, T, reaction time	Chemical additives	
Fly ash	Coal	CaO: 9.3	0.07	86	Aqueous	40 bar, 30ºC, 1h	NaCl	[310]
	Coal	CaO: 4.1	0.03	82	Aqueous	1 bar, 30ºC, 18h	None	[307]
	Coal	CaO: 55.44 MgO: 1.04	N/A	81	Gas-solid	80 vol% CO_2, 800ºC, 1h	None	[311]
	MSWI	CaO: 36.3	N/A	N/A	Aqueous	3 bar, 8-42ºC, 3d	None	[312]
	MSWI	CaO: 53.02	N/A	N/A	Aqueous	1 bar, 25ºC, 10 d	None	[255]
	Lignite	CaO: 15.72-29.28 MgO: 0.78-4.47	0.04-0.09	N/A	Aqueous	10 bar, 25ºC, 10d	None	[313]
	Lignite	Ca: 28.4 Mg: 9.2	0.21	53	Aqueous	0.15 bar, 25ºC, 2h	None	[314]
Bottom ash	MSWI	N/A	N/A	N/A	Gas-solid	1 bar, 50ºC, 2h	None	[254]
	MSWI	CaO: 16.3 MgO: 2.6	24L CO_2/kg	N/A	Gas-solid	17 bar, 25ºC, 3h	None	[315]
APC residues	APC	CaO: 35 Mg: 0.0084	0.25	67	Aqueous	3 bar, 30ºC, 5h	None	[316]
	MSWI APC	Ca: 308.07 mg/kg Mg: 29.243 mg/kg	0.20	N/A	Aqueous	1 bar, 20ºC, 3h	None	[317]
Oil shale waste	Oil shale	CaO: 50,75 MgO: 15.19	0.17	N/A	Aqueous	1 bar, 25ºC	None	[318]
	Oil shale	CaO: 50,75%	N/A	N/A	Aqueous	1 bar, 25ºC	None	[319]
CKD	CKD	CaO: 34,5 MgO: 2.1	0.19	71	Gas-solid	1 bar, 25ºC, 12d	None	[253]
	CKD	CaO: 34.5 MgO: 2.1	0.20	75	Gas-solid	1 bar, 25ºC, 3.4 d	None	[253]
	CKD	CaO: 34.5 MgO: 2.1	0.26	94	Gas-solid	1 bar, 25ºC, 4,9d	None	[253]
Asbestos (BM)	HT Chrysotile	CaO: 0.5 MgO: 39.7	N/A	0.7 mol CO_2/mol Mg	Gas-solid	32 bar, 260ºC, 1h	None	[263]
	HT asbestos	CaO: 35.4% MgO: 5.12	0.14 - 0.18	N/A	Aqueous	55 bar, 22ºC, 1h	None	[320]
UMT	Nickel tailings	Ca: 3.4 Mg: 21.8	0.43	94	Aqueous[a] via HCl, HNO_3 and H_2SO_4	1 bar, 30ºC, 40m	None	[321]

Material type		Composition (wt%.)	CO_2 Storage capacity $\left(\frac{kg_{CO_2}}{kg_{waste}}\right)$	R_x (%)	Reaction conditions: Reaction phase	Reaction conditions: P_{CO_2}, T, reaction time	Reaction conditions: Chemical additives	Ref.
PMW	Ca mud	CaO: 83.2	0.22	85	Aqueous	10 bar, 30ºC, 2h	None	[322]
Steel slag	Steel slag	CaO: 31.7 MgO: 6.0	0.25	74	Aqueous	19 bar, 100ºC, 0.5h	None	[303]
	LF slag	CaO: 58.1 MgO: 6.2	0.25	N/A	Aqueous	1 bar (15 vol% CO_2), 25ºC, 40 h	None	[323]
	Blast furnace slag	CaO:40.6 MgO: 6.2	0.23	90	Aqueous[a] via (pH-swing)	1 bar, 30ºC, 2h	NaOH + CH_3COOH	[304]
	Converter slag	N/A	N/A	80	Aqueous[a] via (pH-swing)	0.07 bar (13 vol% CO_2), 40ºC, 1h	NH_4Cl	[275]
	Stainless steel slag	Ca: 40 -5 0 Mg: 2.2 - 4.5	0.13	N/A	Aqueous	3 bar, 50ºC, 2h	None	[324]
	BOF slag	CaO: 51.1 MgO: 4.2	0.23	57	Aqueous	1 bar, 70ºC, 2h	None	[325]
	BOF slag	CaO: 42.2 MgO: 9.2	0.29	93	Aqueous	1.47 bar, 60ºC, 30 min	None	[326]
	BHC	CaO: 54.2 MgO: 4	0.19	44	Aqueous	1 bar, 70ºC, 2h	None	[325]
	BHC	CaO: 52.8 MgO: 4,7	0.29	69º	Aqueous	48.3 bar, 160ºC, 12h	None	[327]
	BHC	CaO: 52.8 MgO: 4,7	0.24	59	Aqueous	89.6 bar, 160ºC, 1h	None	[327]
Red mud	Bauxite residue	Ca: 4.8 Mg: 0.1	0.02	N/A	Aqueous	1 bar, 30d	None	[328]
	Red mud	CaO: 2.99	0.05	N/A	Aqueous	3.5 bar, 25ºC, 3.5h	NaOH	[329]

2.3.3.1. Metallurgical Slag

Significant amounts CO_2 is emitted from steel production, accounting for 6-7% of global CO_2 emissions [304]. Slags are a by-product of steelmaking process, formed upon interaction of impurities (mainly silica) and lime during steelmaking processes [42]. Different types of slags are produced depending on the steelmaking process: (i) basic oxygen furnace (BOF), which constitutes 62% of the total steel slags; (ii) electric arc furnace (EAF; 22%); (iii) ladle slag (LS; 9%); (iv) blast furnace slag (BF), which is generated as a by-product of iron production via ore gangue melting together with coke ashes and siliceous and aluminous residues from reduction and separation of iron from starting ore. Moreover, refinement process for stainless steel production also produces LS and argon decarburization slag (AOD) [330,331].

Generally, steelmaking slags consists mainly of Ca, Mg, Al-silicates and oxides with CaO and MgO contents between 31.7 -58.1 and 3.97 – 10.7 wt%, respectively (Fig. 2.28) [303,323,325]. Their estimated CO_2 storage capacity is of 130 – 289kg CO_2 t^{-1} of slag [324,327]. In order to achieve reasonable conversion rates to carbonates, grinding pretreatments are often required [42]. Table 2.8

summarized representative steel slags studies. Such process is mostly carried via aqueous DC at ambient and elevated pressures and temperatures [224], similarly to the carbonation of natural Ca-silicates, but with lower energy requirements [303,323]. Steel slags that contains higher free lime instead of Ca-silicate contents were observed to be more reactive [323]. The experimental CO_2 uptake upon steel slag carbonation varies between 1.7-28.9 wt% as reported by different studies [224]. Generally, carbonation kinetics were greatly improved by experiments carried at elevated temperatures and pressures, but also are associated with increased costs [331,332]. Due to the high Ca content of steel slags, studies have studied the possibility to synthetize commercial-grade high-purity euhedral scalenohedral precipitated $CaCO_3$ (PCC) in order to reduce the carbonation costs [271,275,304].

IC of steel slags via acid extraction has also been studied. It has been reported a rapid dissolution of Ca-silicate from BOF and EAF with HNO_3, achieving a CO_2 storage capacity of 0.26-0.38 tCO_2/t_{slag}.[333]. When using NH_4Cl, 0.16 tCO_2/t_{slag} was attained upon carbonation [275]. In general, when using weaker acids, high temperatures and prolonged reaction times, a selective Ca-extraction is obtained, allowing the formation of high-purity PCC [304]. However, the associated costs of producing PCC from steel slag is still too high, with an actual cost of 1990€/t $CaCO_3$ when using acetic acid as dissolvent agent [224]. IC via ammonia extraction route has also been applied to steel slags, obtaining a carbonation efficiency of 59-74 % [334].

2.3.3.2. Municipal solid waste incinerator (MSWI) ashes

Resulting from the incineration of Municipal Solid Wastes (MSW), which reduces the MSW mass and volume up to 70 and 90%, respectively, as well as disinfection and potential energy recovery. Upon incineration, bottom ash is produces (MSWI BA; 80%) and APC residues (20%), as well as CO_2 emissions [42,98,224].

MSWI BA is considered as a non-hazardous waste. Such material is mainly composed of Ca, Si, Al-silicates, sulfates, carbonates, reactive oxides (portlandite, magnetite, hematite) and chlorides [42,335]. However, their Ca and Mg content are generally limiting its CO_2 storage capacity, and MC processes are mainly focused on chemically neutralizing such wastes (reducing its alkalinity and trace metal mobility [336,337]) for different applications [42,315]. Their experimental CO_2 storage capacity ranges between 3-6.5 wt% [315,335]. This carbonation is mainly associated with reacting portlandite [254,315]. However, it is likely that Ca, Mg-silicates were also involved but with significantly slower reaction rates [303,335].

APC residues are generated during the process of flue gas treatment. Generally, they contain a mixture of fly ashes, unburned carbon and residual lime. These residues are considered as hazardous due to their elevated alkalinity and high concentrations of heavy metals (Zn, Pb, Cd, Cr, Cu, Hg, Ni), soluble salts and chlorinated compounds [42,334]. Nonetheless, the elevated lime contents make

these materials appealing for MC (Table 2.8). Moreover, this latter process reduces their alkalinity to acceptable regulatory limits (pH <9.5) [338,339], and could also fix heavy metals into carbonates [227], however, MC could also contribute to enhance the leaching of such metals [98]. Their carbonation potential is of 0.07-0.25tCO_2 t^{-1}APC [42,224,331]. The comparison of the DC via aqueous media or dry-DGS was performed by Bacciochi et al., 2009 [258]. Faster reaction kinetics were observed for DGS compared to aqueous DC.

2.3.3.3. Power plant ashes

Coal-fired power plants provide nearly 40% of the world's electricity demand [307], producing 600Mt y^{-1} of Fly Ash (FA) and 12000 $MtCO_2$ yr^{-1} (23, 25). Up to 30% of coal FA are generally utilized in the construction industry. FA composition varies significantly depending on the mineral content of fuel. Generally, FA consist of a mixture of aluminosilicate glass, silica, cristobalite and mullite. This carbonation of this material does not need further grinding, as their grain size ranges between 10-15µm [331].

The MC of oils shale FA, which contains low-grade fossil fuel, have been investigated since it contains an elevated content of highly reactive free-lime (12-30%) [308]. Analogously, MC of co-fired wood and coal power plant FA have also received attention, since it contains about 45% CaO [340]. FA from Ca-rich lignite coal combustion have a CO_2 storage potential of 43-49% [82,268,341]. On the other hand, the resulting FA from bituminous coal combustion has a relatively low CaO content and CO_2 storage potential [82,307,331]. Carbonation of such material is usually carried out by aqueous DC at mild conditions (Table 2.8) [224]. It has been estimated that capture 90% of the emitting CO_2 from a 532MW coal fired power plant would cost between \$11-21/tCO_2, assuming a FA CO_2 storage capacity of 0.1-0.2 tCO_2/t FA [342]. However, FA CO_2 storage capacity is limited and could only sequester 0.25% of CO_2 from coal fired power plants [42,307,331].

2.3.3.4. Cement wastes

The production of Portland cement and lime (responsible for 5% of anthropogenic CO_2 emissions) from high-temperature rotary kiln generates fine-grained 0.2t of Cement Kiln Dust (CDK)/t cement as a by-product [42,331,343,344] and, in minor quantities, Cement Bypass Dusts (CBD). This latter is generated as a by-product during kiln firing. The global annual production of CDK is 2.8 Gt and it is expected to increase to 4.0Gt [42]. Due to its high alkalinity, CDK is considered as potential hazardous material [42,343]. Generally, it contains 38-48% CaO and 1.5-2.1% MgO [42,331,344]. CDK is already 46-57% carbonated due to its high reactivity and fine grain sizes [344]. CBD have a much lower carbonate content and, therefore, higher carbonation potential (0.5 tCO_2/t CBD) compared to CDK [340]. Experimental studies on CDK carbonation have reported a CO_2 uptake up to 0.08 - 0.25 tCO_2/t CDK (Table 2.8) [340,344]. It has been estimated that CDK could potential store up to 42 $MtCO_2$ yr^{-1}, equivalent to 0.1% of global CO_2 emissions [42].

Waste cement has similar properties as CDK and it is a by-product generated during the aggregate recycling process, where waste concrete (obtained mainly from demolished buildings) is grinded and classified, separating aggregates from waste cement. This latter is can be reused for construction applications without any treatments. However, the majority of this waste material is disposed. The CO_2 storage capacity of this material is estimated to sequester up to 42 $MtCO_2$ yr^{-1}, taking into account the total produced waste concrete (1100 Mt yr^{-1} in the USA, EU and China) [42].

$CaCO_3$, the reaction product, is significantly less hazardous than CD and waste cement and can be reused in the cement manufacturing, avoiding mining and calcining limestone, and their associated CO_2 emissions or in other industrial processes. Therefore, MC of such materials contributes to mitigate the building of CO_2 in the atmosphere and to neutralizes potential hazardous materials [253,309].

Some studies have evaluated the possibility of producing high-purity $CaCO_3$ by aqueous IC [309,345]. Ca^{2+} was performed using pressurized CO_2 (30 bar), followed by carbonation (which was performed at a CO_2-rich atmospheric pressure) (Fig. 2.29). It was concluded that 98% pure $CaCO_3$ was possible to produce at a cost of US$ 136 t^{-1}, significantly lower than the market price for $CaCO_3$ (US$400 t^{-1}) [345].

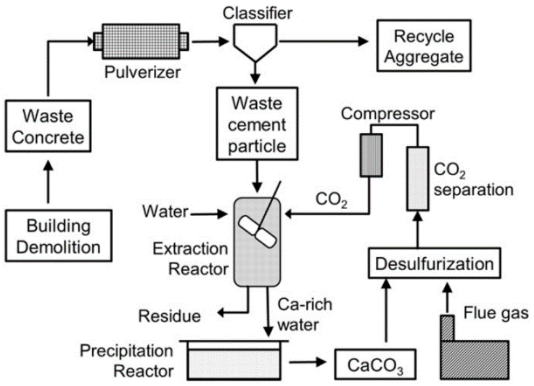

Fig. 2.29. Scheme of the high-purity $CaCO_3$ production from aqueous IC of waste cement. Figure from Katsuyama et al., 2005 [345].

2.3.3.5. Mine tailings

These wastes are desirable for MC purposes, since they are already mined feedstock, and in the case of mineral processing (metal extraction), they have already grinded to a suitable size for MC [266,302,346]. Generally, deposits that are hosted in ultramafic rocks produces suitable MC feedstocks, including: asbestos, cooper-nickel-PGE (platinum group elements), diamondiferous kimberlites and podiform chromite deposits, hosted by dunites, serpentines and gabbronorites. [346,347]. Another common type of mine waste is bauxite residue (known as red mud) generated during the alumina extraction [323,329,348]. Particularly for red mud and asbestos, MC processes not only stores CO_2 but also improves the properties of the waste, enabling a safer landfilling or

reuse. The CO_2 sequestration capacity of such tailings is generally exceeding the CO_2 emissions from the ore processing site. It is expected that MC will become another revenue stream for mining and milling operations upon new incentives to reduce carbon emissions[42].

2.3.3.5.1. Asbestos tailings

Globally, 20t of tailings are generated upon the production of 1t of asbestos. Tailings produced after chrysotile processing are associated with residual asbestos, therefore, are classified as hazardous materials [42]. These wastes are suitable for MC due to their high MgO contents (up to 40%), they have already been grinded and their asbestiform hazardous nature is destroyed upon MC [145]. Natural weathering of such piles has extensively studied [346,349]. It has been estimated that natural carbonation of chrysotile has a carbonation rate of 0.3% yr^{-1}. This rate could be enhanced by optimizing the grain surface area and by bioleaching processes (see section 2.3.2.4) [346]. Larachi et al., 2010 [266] have investigated dry and moist DC at low pressures and high temperatures of chrysotile mine tailings, obtaining significantly higher carbonation yield for humid experiments compared to dry experiments (Table 2.8). Generally, chrysotile MC processes requires pretreatment and elevated temperature and pressures, as described in section 2.3.

2.3.3.5.2. Nickel tailings

Ni-industry have focused on low-grade sulphide resources, commonly found in ultramafic rocks, since high-grade sulphide Ni-deposits are almost depleted and laterites requires energy intensive and complex processes. The processing of ultramafic rocks generates grinded Mg-rich tailings, suitable for MC. The valorization of such tailing could provide additional revenue for Ni-projects. Teir et al., 2007 & 2009 [274,321] have studied the aqueous IC via HCl and HNO_3, obtaining a carbonation yield of 94%, as well as relatively high-purity (93-99%) individual and profitable by-products: silica, iron oxides and hydromagnesite [274]. However, the utilization of chemicals alone has an estimated cost of US$600 – 1600/$tCO_2$, currently unfeasible [321]. The integration of MC processes with nickel mining operation needs further developments, including a sufficiently high carbon price [42].

2.3.3.5.3. Red Mud

Red mud (RM) caustic waste is generated upon bauxite ore processing for alumina extraction. Generally, 1-1.5t red mud is produced per tonne of alumina [329,350]. The global production of RM is 70 Mt yr^{-1}. RM is rich in iron (Fe_2O_3: 30 – 60%) and Na (2-10%). On the other hand, it is relatively poor on Ca and Mg (2-8 %, Fig. 2.28). It generally contains a wide range of Na, Ca, Al, Si, S, Fe-rich minerals [323]. Carbonation of such wastes not only sequesters CO_2 but also reduces its toxicity and the leaching of heavy metals [329,350]. Neutralized RM can be reused for various applications [323].

The carbonation of RM is generally carried via DC at ambient pressure and temperature conditions [323,329,348], with a CO_2 storage capacity of 0.04-0.05 $tCO_2\ t^{-1}$ RM (Table 2.8). MC

processes have been estimated to costs: US$147 t^{-1} CO_2. RM main alkaline source is NaOH, which also are the main products upon carbonation [348]. However, Na-carbonate are significantly more soluble than Ca-Mg-carbonates. Therefore, RM MC provides a less permanent CO_2 storage. Dilmore et al., 2007 [350] and Johnston et al., 2010 [351] proposed the mixing of RM with brine solutions (containing hydrated Ca and Mg-chlorides) prior carbonation in order to provide a more permanent CO_2 storage as well as providing an increased CO_2 storage capacity (Fig. 2.30). It has been estimated that >100 Mt CO_2 have been fixed via natural weathering of cumulated RM stockpiles [352].

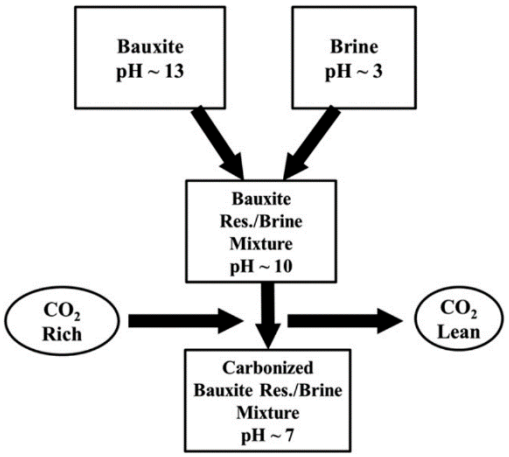

Fig. 2.30. MC scheme of mixed brine and RM to obtain neutralized and reusable material as well as sequestering CO_2. Figure from Dilmore et al., 2007 [350].

2.3.3.6. Alkaline paper mill wastes

Several types of alkaline paper mill wastes (PMW) are produced from cellulose pulp production for paper production, containing elevated free lime contents (45-82%) [322,340]. This material is highly suitable for MC purposes. Moreover, pulp mills generate also CO_2 which can be used for on-site MC, avoiding transportation costs. Elevated high-Ca contents of PMW eases the production of high-purity and valuable $CaCO_3$. This can be utilized in the pulp and paper industry or for other various applications [322]. Their carbonation is mainly carried via aqueous DC obtaining high reaction yields (85%) at mild conditions (Table 2.8) due to the highly-reactive nature of free lime [42,322]. Despite these favorable properties, the research on PMW is limited [42]

3. Methodology

3.1. Analytical methods

3.1.1. X-ray Diffraction (XRD)

X-ray scattering of the reaction products were obtained by XRD, using a Bruker D8™ diffractometer with Cu Kα radiation. The 2θ deg analyzed range was of 5 to 80°, with a step-size of 0.01° and measuring time of 1 second per step.

3.1.2. Raman spectroscopy

Micro-Raman spectra were obtained with an inVia Qontor™ confocal Raman microscope, equipped with a green laser (532.1 ± 0.3 nm) with a nominal 100 mW output power directed through a specially adapted Leica DM2700 M microscope (x50 magnification). Spectra were acquired in the range 100-1350 cm^{-1} with an exposure time of 1 s, 0.05 % of laser maximum power and 60 repetitions. Given the substantial heterogeneity of phase distribution at the microscale of the analyzed samples, Raman spectra was recorded by mapping a region acquiring a total of 40 measurements. The Raman results presented below correspond to the average of 40 measurements on each sample in order to obtain representative results. Raman results presented in chapter 9 shows point analysis.

3.1.3. Fourier Transformed Infrared Spectroscopy (FTIR)

FTIR spectra was acquired by FTIR Nicolet 6700™. An attenuated total reflection (ATR) module was used to record ATR spectra on a germanium crystal of the carbonated samples. Transmission spectra of the starting materials were acquired for analysis of the OH vibration modes. The samples (~3% total mass) were mixed with KBr (~97%) and pressed into pellets.

3.1.4. X-ray Fluorescence Spectroscopy (XRF)

Data were acquired using 64 scans and 2 data point spacing. Bulk chemical compositions were determined by XRF by the fusion bead method on a UniQuant® apparatus from Thermo Fisher Scientific™.

3.1.5. Thermogravimetric analysis (TGA)

The mass losses upon decomposition of phases obtained upon carbonation were estimated by TGA system (TA Instruments Q50™). Data were acquired at a heating rate of 10ºC/min, from room temperature to 900ºC, under a N_2 flow of 60mL/min.

3.1.6. Temperature Programmed Desorption of CO_2 and H_2O (CO_2, H_2O-TPD)

CO_2, H_2O-TPD analysis was acquired by BELCAT-M™ instrument equipped with Thermal Conductivity Detector (TCD), where CO_2 and H_2O wt% of the analyzed samples was measured. Data were acquired at a heating rate of 10ºC/min from room temperature to 850ºC, under a He flow of 50mL/min. Calibration of the CO_2 signal of the TCD was carried out on the basis on measuring the moles of CO_2 from different known gas mixtures composition varying the CO_2/He proportions (0.34; 0.18; 0.10). Calibration of the water vapor signal was carried out by measuring the moles of water vapor originated from calcining brucite (>99% BioUltra CAS number: 1309-42-8), using a heating rate of 10ºC/min.

3.1.7. Scanning Electron Microscopy and Focused Ion Beam (SEM-FIB)

SEM-FIB imaging of single crystals was carried out with a cross-beam work station Zeiss Neon 40™, equipped with an INCAPentaFET energy dispersive X-ray system for elemental analysis, operated at 5keV.

3.1.8. X-ray Photoelectron Spectroscopy (XPS)

X-ray photoelectron spectra (XPS) was acquired at room temperature on an SPECS system equipped with a XR50 source operating at 250 W and a Phoibos 150 MCD-9 detector, using Mg K_α ($h\nu$=1253 eV) X-ray soruce. The pass energy of the hemispherical analyzer and the energy step of high-resolution spectra were set at 20 eV and 0.05 eV, respectively. The pressure in the analysis chamber was kept below 10^{-12} bar. Peak deconvolution was performed with the CasaXPS software. Binding energy (BE) of the C1s core level from adventitious carbon was used as reference to calibrate acquired XPS spectra. Acquired carbon 1S spectra were deconvoluted following the procedure explained by Larachi et al., 2010 [266].

3.1.9. Particle size measurements

The particle size distribution of samples was measured by a Malvern Panalytical MasterSizer 3000.

3.2. Purpose-built carbonation reactor

For the purpose of this thesis, the author designed, built and calibrated a purpose-built steam-mediated carbonation stainless-steel reactor for continuous flow and batch configurations (Figs 3.1, 3.2). The system allows pressurization up to 20 bar in continuous flow configuration and up to 100 bar in batch. Ćwik et al., 2019 [82] explored the possibilities of such configuration in the carbonation of High-Ca FA. In continuous flow configurations, pressure was controlled by using pressure reducers and back-pressure regulators, achieving a constant pressure at a given flux. The pressure of the reactor was measured by two manometers located prior and after the reactor. The pressure drift was measured under operando conditions in pressurized continuous flow configuration and corresponds to a maximum of ± 0.2 bar. A thermocouple was placed inside the reactor, allowing accurate temperature measurements. The maximum measured temperature drift was 1ºC. The gas volumetric income was regulated by specifically-adapted flowmeters for the regulated gas. Prior CO_2 enters the reactor, if flows through a heated bubbler containing water, allowing an accurate mixture of incoming gases with water vapor. Different RH can be obtained by adjusting the bubbler temperature. The CO_2 dilution with water vapor was estimated following the saturated water vapor pressure Antoine equation (Eq. 3.1) and Raoult's law (3.2).

$$P = 10^{A-\frac{B}{C+T}} \tag{3.1}$$

$$P_{i,(g)} = X_{i(l)} \cdot P_{i,sat}(T) \tag{3.2}$$

Where P is the water vapor pressure, T is the temperature and A, B & C are constant specific for different components. $P_{i,(g)}$ is the partial pressure of the component, $X_{i(l)}$ is the vapor pressure of the pure component and X_i is the dissolvent molar fraction.

To avoid possible gas mixture changes due to the dissolution of CO_2 in the bubbler water, a continuous flow of the desired gas mixture (CO_2, N_2) at the specific temperature and pressure conditions of each experiments was maintained for at least 30 min, saturating the water on the bubbler with CO_2 prior each experiment. During heating and cooling, N_2 was used as a carrier gas, allowing repeatability of the experimental conditions.

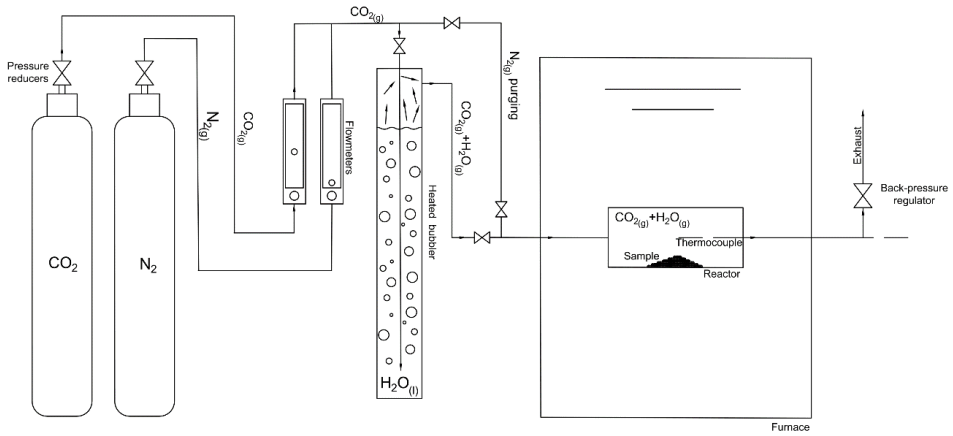

Fig. 3.1. Schematic of the purpose-built steam-mediated carbonation reactor. Figure from Rausis et al., 2020 [55].

Fig. 3.2. Picture of the purpose-built steam-mediated carbonation reactor. Picture taken by K. Rausis.

3.3. Materials

3.3.1. Brucite

In this thesis, pure commercial brucite (>99%, Sigma-Aldrich^{TM}, CAS # 1309-42-8) was obtained for carrying several experiments and as reference material.

3.3.2. Serpentine

Lizardite was obtained from the Hispaniola Island, located in the orogenic complex at the northern edge of the Caribbean plate (Fig. 3.3). XRD analysis confirmed that the obtained material was mainly composed of lizardite, as evidence by its characteristic X-ray scatterings (Fig. 3.4a) [49,287,353], as well as minor magnetite ($Fe^{3+}{}_2\ Fe^{2+}\ O_4$, often found in serpentines, reaching up to

15wt%). Other serpentine phases were not observed. was identified. Oxide composition was determined by XRF (Table 3.1). Loss on ignition was also determined, accounting for 12.24wt%. Such values are slightly lower than reference stoichiometric lizardite (13.04 wt%). The calculated (Mg/(Mg+Fe)) ratio accounted for 0.805.

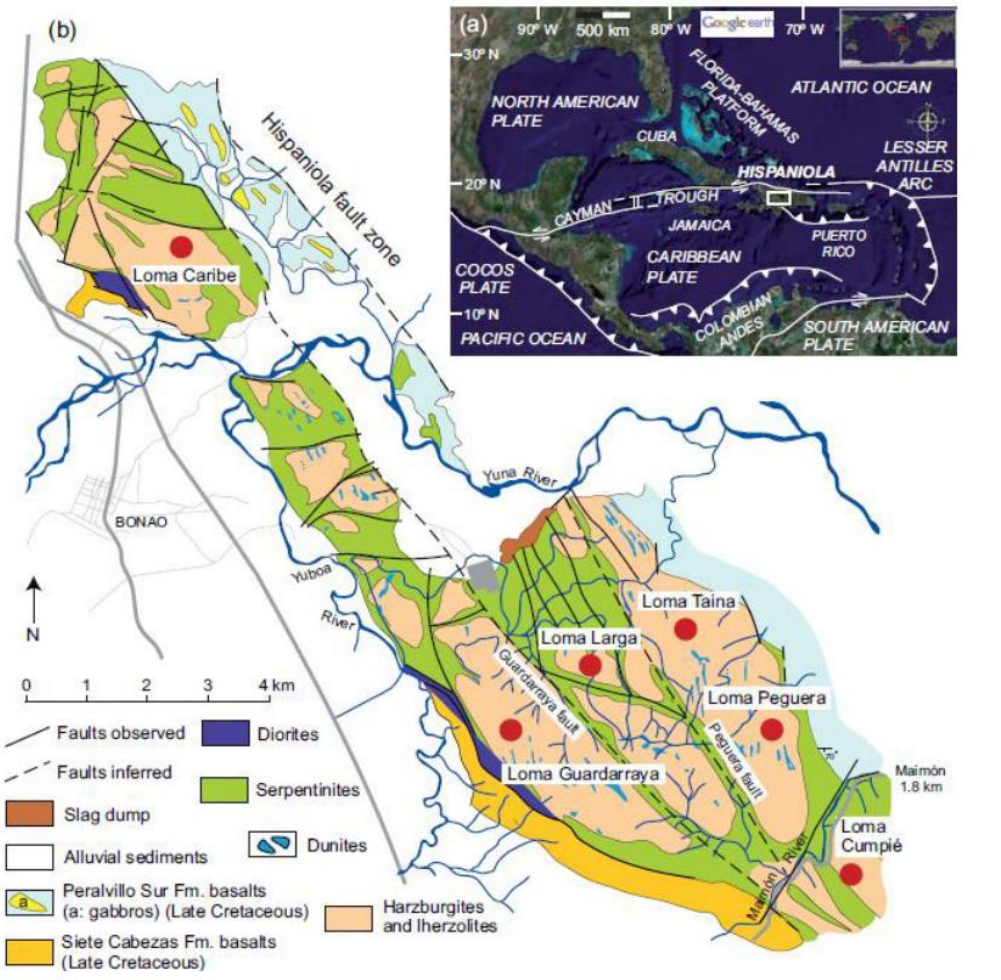

Fig. 3.3. Geological province of the Caribbean region with location of modern plate boundaries and major tectonic elements. White box shows the location of the sampled location. (b) Geological units of the sampled area. Figure from Marchesi et al., 2016 [354].

Table 3.1. Chemical analysis of the tested serpentinite.

Compound	% Content
SiO_2	41.45
MgO	35.98
Fe_2O_3	8.71
Al_2O_3	0.59
MnO	0.11
CaO	0.1
TiO_2	0.01

FTIR analysis of this serpentine shows absorption bands at 3705, 3690, 3650, 1086, 958, 610 and 570 cm^{-1} (Fig. 3.4b). The first three bands are associated with the vibration modes of the inner

(3690 and 3705 cm^{-1}) and outer (3650 cm^{-1}) OH groups attached to octahedral Mg-sheets, characteristic of lizardite [49,101]. Bands at 1086 and 958 cm^{-1} are attributed to the out of planes and in plane vibration of Si-O bonds, respectively. The 610 cm^{-1} is associated with the deformation modes of OH. The last band (570 cm^{-1}) is characteristic to the Mg-O out of plane vibrations of lizardite [355,356].

Fig. 3.4c shows the Raman analysis of un-activated serpentine, exhibit bands at 3705, 3684, 3648, 1098, 689, 618, 383, 328 and 229 cm^{-1}. The first three bands, analogously to FTIR observations are associated with the inner (3705 and 3684 cm^{-1}) and outer (3648 cm^{-1}) O-H stretching modes [287,357]. The band at 1098 cm^{-1} is associated with the antisymmetric stretching modes (ν_{as}) of the Si-O_{nb} groups, characteristic of lizardite. The 689 cm^{-1} absorption band is attributed to the ν_{sym} of the Si-O_b-Si groups. The 618 cm^{-1} band is characteristic to the antisymmetric translation modes of the Oh-Mg-OH groups. The 382, 348 and 229 cm^{-1} are associated with the ν_{sym} modes of the SiO_4 groups, symmetric vibration of the Mg-Oh groups and to the vibrations of O-H-O groups, respectively [357,358].

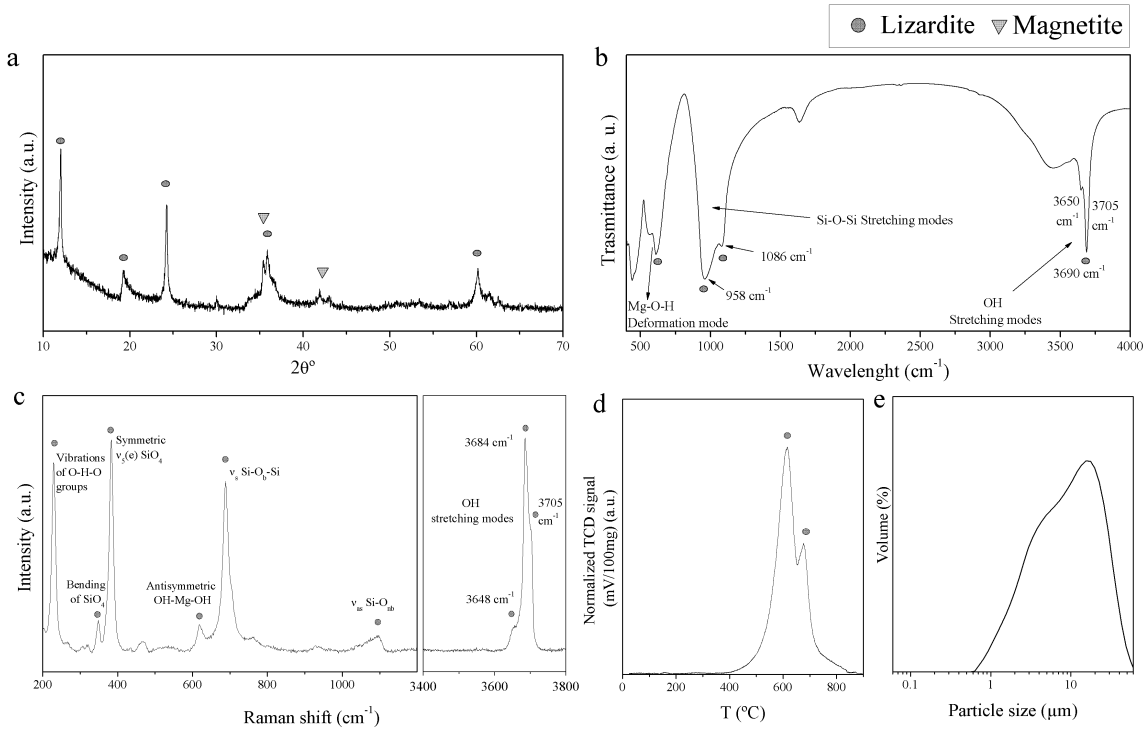

Fig. 3.4. (a) XRD, **(b)** FTIR, **(c)** Raman, **(d)** TPD analysis as well as (e) particle size distribution of sampled serpentinite prior and after activation.

TPD-CO_2-H_2O analysis shows that the starting material contains 11.85 wt%, associated with the chemically bond inner (450-680ºC) and outer (580-840ºC) OH groups (Fig. 3.4d).

3.3.3. Serpentinized dunite

Brucite-bearing serpentinized samples were obtained from the same geological setting to those described in section 6.2. (Fig. 3.3). Table 3.2 shows the oxide composition of the analyzed material as determined with the aid of XRF. The obtained loss on ignition was 13.71 wt%. Atomic Mg/(Mg+Fe) ratio was estimated accounting to 0.86.

Table 3.2. Chemical analysis of the tested serpentinized dunite.

Compound	% Content
MgO	44.72
SiO_2	35.04
Fe_2O_3	6.03
MnO	0.1
CaO	0.05
Al_2O_3	0.03
TiO_2	0.02

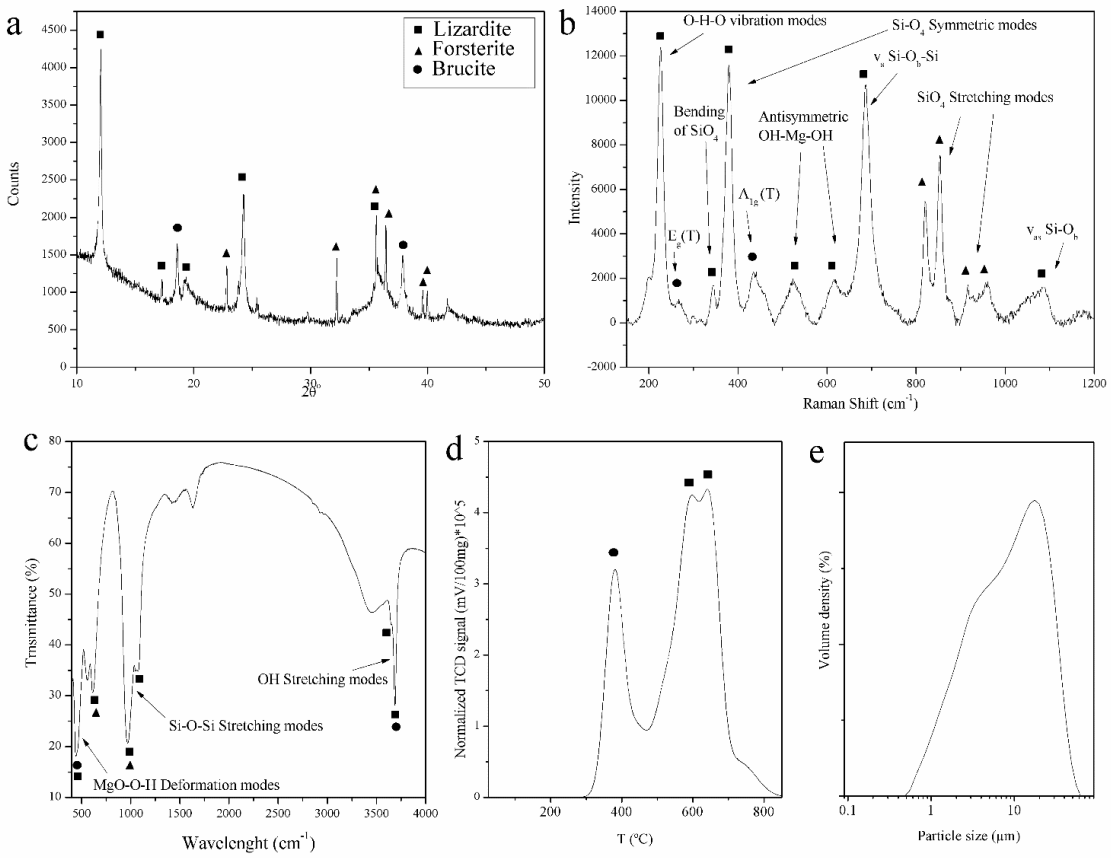

Fig. 3.5 (a) XRD, **(b)** FTIR, **(c)** Raman, **(d)** TPD analyses as well as **(e)** particle size and distribution of the grinded and sieved brucite-bearing serpentinized dunite. $E_1(T)$ and A_{1g} (T) indicate the parallel and perpendicular vibrations of the brucite OH groups.

Fig. 3.5. shows XRD, FTIR, Raman, TPD analysis as well as particle size distribution of the analyzed material. Forsterite, lizardite and brucite were identified by its characteristic XRD, Raman and FTIR features (Fig. 3.5a, b, c) [179,198,359,360]. Quantification of brucite and lizardite contents were estimated by measuring the H_2O moles released upon thermal dehydration of such phases

[204,263,264,270,356] and taking into account their stoichiometric compositions, as determined with TPD (Fig. 3.5d) and corroborated with TGA (Fig. 3.6). The estimated brucite and lizardite contents are 9.4 and 68 wt%, respectively. Moreover, it is possible that magnetite is also present in the starting material, as serpentinites often contains magnetite contents up to 15wt%. However, this latter mineral was not identified. It is plausible that such mineral exists in such low abundance that it was not detected by XRD. Forsterite, lizardite and brucite were the only observed phases, therefore the remaining 22.6wt% content (based on TPD and TGA data) might be attributed to forsterite and possibly minor magnetite. The material was grinded to powder and sieved to obtain grain sizes smaller than 45 μm (Fig. 3.5e).

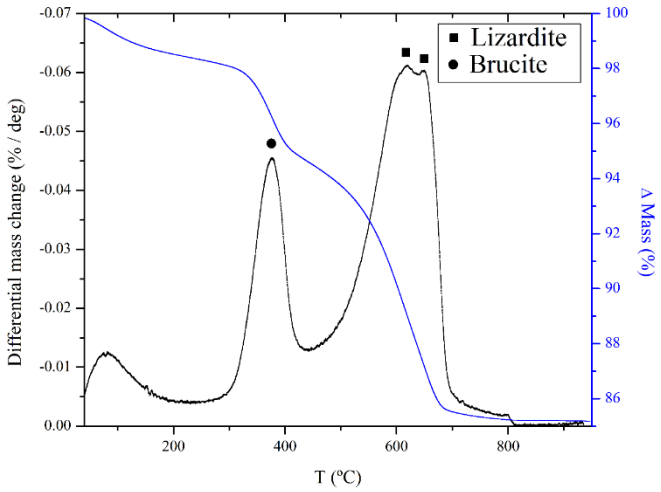

Fig. 3.6. TGA analysis of starting material, corroborating TPD analysis.

3.3.4. Enstatite and forsterite single crystals

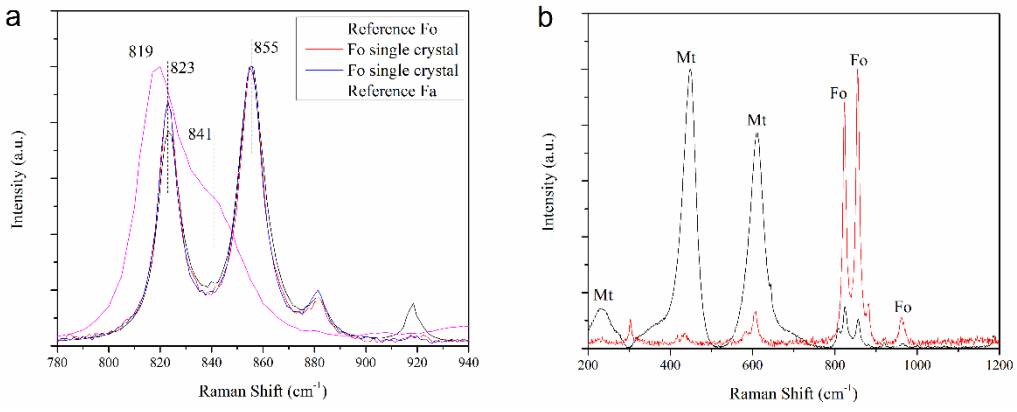

Fig. 3.7. Micro-Raman analysis of **(a)** forsterite (Fo) single crystal, compared to reference Fayalite (Fa) and Fo; **(b)** Rare magnetite occurrence along the forsterite crystal. Dashed lines show the relevant peak positions. Raman data of reference minerals were obtained from Lafuente, et al., 2015 [361]. Mt: Magnetite.

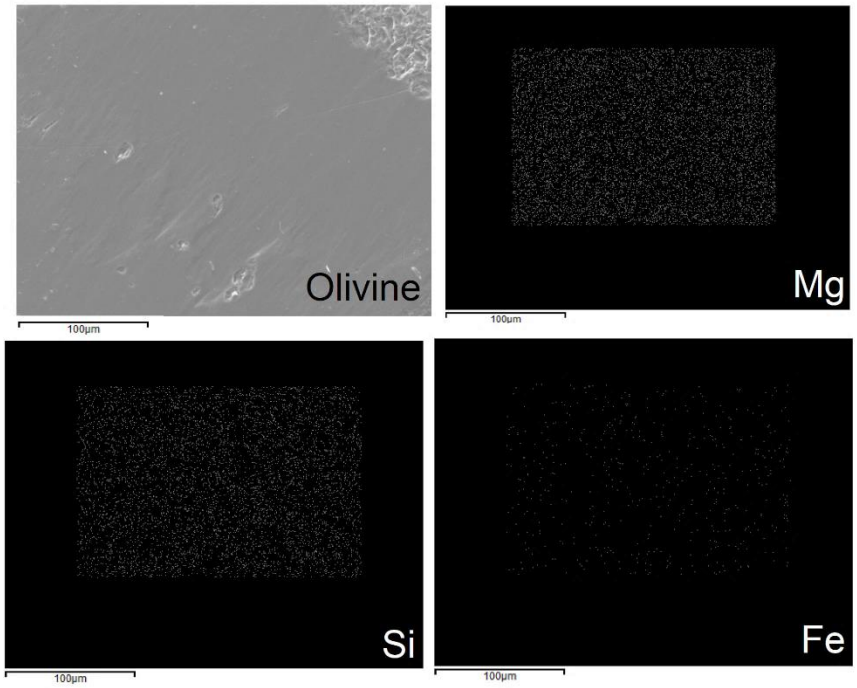

Fig 3.8. SEM image of unreacted surface of forsterite and their respective EDS analysis.

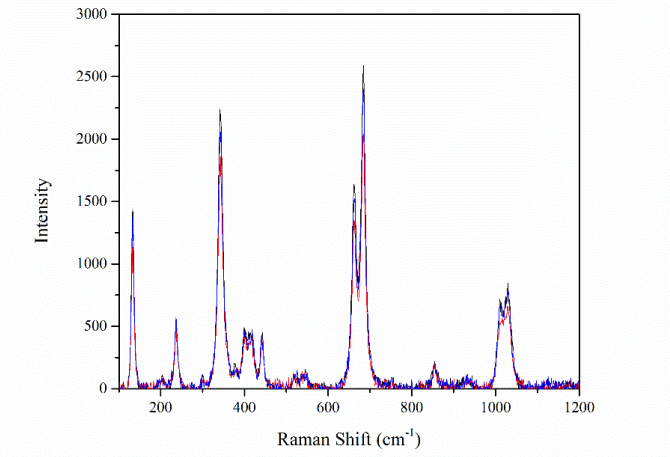

Fig. 3.9. Raman analysis of enstatite single crystal. Blue and black lines represent the average between 40 surface measurements. Red line is the reference data for enstatite. Unmarked peaks are respective to enstatite Raman features obtained from Lafuente, et al., 2015 [361].

Single crystals of enstatite and forsterite were provided by the University of Barcelona. Raman analysis confirmed that olivine single crystal is mainly composed by forsterite, as its Raman features are consistent with reference forsterite instead of fayalite (Fe_2SiO_4; Fig. 3.7a) [362]. Some occurrences of magnetite were observed along the forsterite crystal (Fig. 3.7b). Quantitative EDS analysis of forsterite single crystal exhibit that it is mainly composed of Mg and Si. However, Fe is uniformly distributed across the analyzed surface, indicating that a small amount of Fe is incorporated into olivine crystal accounting to $Mg_{1.9}Fe_{0.1}SiO_4$ (Fig. 3.8). Enstatite crystal is only composed by this mineral phase, as evidenced with Raman spectroscopy [363](Fig. 3.9).

3.4. Carbonation Experiments

The specific carbonation conditions from chapters 4-9 are described as following:

3.4.1. Chapter 4

Samples of 600mg brucite were loaded inside the reactor. Table 3.3 summarizes the carried brucite carbonation experiments as well as the specific experimental conditions of each experiment. A constant mixture of CO_2 with water vapor was 80% P_{CO_2} and 20% P_{H_2O} was used in each experiment in the temperature range 120-205ºC. At 50 and 90ºC, the P_{H_2O} far exceeds the dew-point of water at chosen experimental conditions, therefore, the mixture was adjusted at the maximum allowed for such experiments (RH: >90%).

Table 3.3. Summary of the carried experiments as well as the estimated CO_2 and H_2O partial pressures.

	Temperature						
Pressure	50ºC	90ºC	120ºC	145ºC	165ºC	185ºC	205ºC
7 bar	4h, 16h P_{CO_2}: 6.87 P_{H_2O}: 0.13	4h, 16h P_{CO_2}: 6.3 P_{H_2O}: 0.7	4h, 16h P_{CO_2}: 5.6 P_{H_2O}: 1.4	4h, 16h P_{CO_2}: 5.6 P_{H_2O}: 1.4	4h, 16h P_{CO_2}: 5.6 P_{H_2O}: 1.4	4h, 16h P_{CO_2}: 5.6 P_{H_2O}: 1.4	4h, 16h P_{CO_2}: 5.6 P_{H_2O}: 1.4
10 bar	4h, 8h, 16h P_{CO_2}: 9.87 bar P_{H_2O}: 0.13 bar	4h, 8h, 16h P_{CO_2}: 9.3 bar P_{H_2O}: 0.7 bar	4h, 8h, 16h P_{CO_2}: 8 bar P_{H_2O}: 2 bar	4h, 8h, 16h P_{CO_2}: 8 bar P_{H_2O}: 2 bar	4h, 8h, 16h P_{CO_2}: 8 bar P_{H_2O}: 2 bar	4h, 8h, 16h P_{CO_2}: 8 bar P_{H_2O}: 2 bar	4h, 8h, 16h P_{CO_2}: 8 bar P_{H_2O}: 2 bar

3.4.2. Chapter 5

Table 3.4. Summary of the carried experiments. Results are presented and discussed in section 5.2.1 (*), 5.2.1.1 (♦) and 5.2.4 (▪). Table from Rausis et al., 2020 [55].

	Concentrated CO_2 (Relative Humidity > 90%)		Simulated Flue Gas
	Temperature		
Pressure	50ºC	120ºC	120ºC
1 bar	4, 8, 16h*	4, 8, 16h*	4, 8, 16h▪
4 bar	4, 8, 16h*	4, 8, 16h*	4, 8, 16h▪
7 bar	4, 8, 16h*	4, 8, 16h*	4, 8, 16h▪
10 bar	0.125, 0.25,0.5, 1, 2, 4, 8, 16, 24, 48, 120h*,♦	4, 8, 16h*	4, 8, 16h▪

Samples of 600 mg brucite (>99%, Sigma-Aldrich™, CAS # 1309-42-8) were treated via steam-mediated DC at 50 and 120ºC in the pressures range 1 to 10 bar using concentrated CO_2 (CC) and simulated flue gas (SFG). Table 3.4 summarizes the carried experiments. Flue gas composition was simulated with a 85% N_2 – 15% CO_2 mixture, following previous research [56,364–366]. The relative humidity of each experiments was adjusted by regulating the temperature on the bubbler, obtaining 5 and 90% RH for SFG and CC experiments. Table 3.5 summarizes the specific estimated partial pressures for CO_2 and H_2O during each carried experiment (▪).

Table 3.5. Estimated CO_2 (P_{CO2}), $H_2O_{(g)}$ ($P_{H2O(g)}$), N_2 (P_{N2}) partial pressure of the carried experiments (Table 4.1). CO_2 dilution with water vapor (relative humidity > 90% and 5% for concentrated CO_2 and simulated flue gas experiments, respectively) was estimated following the saturated water vapor pressure Antoine equation and Raoult's law. $P_{T(m)}$ refers to the total pressure measured during the experiments. * shows the estimated P_{CO2} and $P_{H2O(g)}$ of experiments carried at 120ºC and 1 bar taking into account the proportion between calculated P_{CO2} and $P_{H2O(g)}$ and the measured total pressure, since the carbonation system consists on a pressurized continuous flux reactor that does not allow the increase of pressure above the set-pressure. Table from Rausis et al., 2020 [55].

	Concentrated CO_2 (Relative Humidity > 90%)		Simulated Flue Gas
	Temperature		
Pressure	50ºC	120ºC	120ºC
1 bar	P_{CO2}: 0.89 $P_{H2O(g)}$: 0.11	P_{CO2}: 0.36* $P_{H2O(g)}$: 0.64*	P_{CO2}: 0.14 $P_{H2O(g)}$: 0.01 P_{N2}: 0.85
4 bar	P_{CO2}: 3.97 $P_{H2O(g)}$: 0.028	P_{CO2}: 3.54 $P_{H2O(g)}$: 0.45	P_{CO2}: 0.58 $P_{H2O(g)}$: 0.04 P_{N2}: 3.38
7 bar	P_{CO2}: 6.98 $P_{H2O(g)}$:0.016	P_{CO2}: 6.74 $P_{H2O(g)}$:0.26	P_{CO2}: 1.01 $P_{H2O(g)}$: 0.07 P_{N2}: 5.91
10 bar	P_{CO2}: 9.98 $P_{H2O(g)}$: 0.011	P_{CO2}: 9.81 $P_{H2O(g)}$:0.18	P_{CO2}: 1.45 $P_{H2O(g)}$: 0.1 P_{N2}: 8.45

3.4.3. Chapter 6

Table 3.6. Specific experimental conditions and the identified carbonate phases for each experiment. Relative humidity was estimated following the saturated water vapor pressure Antoine equation and Raoult's law. P_{CO2}: CO_2 partial pressure; $P_{H2O(g)}$: H_2O vapor partial pressure, Nsq: Nesquehonite; Dyp: Dypingite; Hmg: Hydromagnesite; Mag: Magnesite; AMC: possibly an amorphous hydrous Mg carbonate.

Activated material	**Time (h)**	**50ºC**	**90ºC**	**120ºC**
		P_{CO2}: 5.9; $P_{H2O(g)}$: 0.1	P_{CO2}: 5.4; $P_{H2O(g)}$: 0.6	P_{CO2}: 4.2; $P_{H2O(g)}$: 1.8
AS610	0.5	Nsq	Dyp, AMC	Hmg
	1	Nsq	Dyp	Hmg
	2	Nsq	Dyp	Hmg, Mag
	4	Nsq	Dyp	Hmg, Mag
AS650	0.5	Nsq	Dyp, AMC	Hmg
	1	Nsq	Dyp	Hmg
	2	Nsq	Dyp	Hmg
	4	Dyp, AMC	Dyp	Hmg, Mag
AS710	0.5	Nsq	Dyp, AMC	Hmg
	1	Nsq	Dyp, AMC	Hmg
	2	Nsq	Dyp	Hmg
	4	Dyp, AMC	Dyp	Hmg, Mag

Serpentinite was heat treated at 610 (AS610), 650 (AS650) and 710ºC (710ºC) during 16h at the desired temperature. To avoid exceeding temperature to those defined due to thermal inertia a heating rate of 1ºC/min was used, generating an activated Mg-rich due to the partial amorphization

of lizardite [49,196,266]. The material was ground to a powder and sieved to obtained grains of size smaller than 45 µm, prior heat activation.

Heat activated serpentine was loaded into the stainless-steel reactor and then it was heated to 50, 90 and 120ºC, respectively. Once the temperature was reached a mixture of CO_2 and water vapor (RH>90%) was introduced into the system. The pressure was increase to 6 bar at a constant given flux (20ml/min). Carbonation treatments were performed individually from 30 min to 4h. After experiments, CO_2 and water pressure were released and carried away from the reactor with N_2, while cooling, inhibiting further carbonation. Table 3.6. summarizes the performed experiments as well as the CO_2 and H_2O estimated partial pressures for each experiment.

3.4.4. Chapter 7

600mg of grinded serpentinized dunite were loaded in the reactor. Experiments were carried in the temperature range from 50 to 185ºC at 10 bar in the presence of steam (≥90% RH). A summary of the carried experiments, as well as the estimated CO_2 and H_2O partial pressure for each experiment, is shown in Table 3.7.

Table 3.7. Performed experiments and the estimated CO_2 and H_2O partial pressures as well as the identified carbonate phases.

T(ºC)	P (bar)	Time (h)				
		2	4	8	16	60
50	P_{CO2}: 9.8 $P_{H2O(g)}$: 0.2		Nsq> AMC~ Dyp			
90	P_{CO2}: 9.4 $P_{H2O(g)}$: 0.6		Dyp > AMC			
120	P_{CO2}: 8.2 $P_{H2O(g)}$: 1.8		Hmg > AMC			
145	P_{CO2}: 6.2 $P_{H2O(g)}$: 3.8		Mag			
165	P_{CO2}: 3.7 $P_{H2O(g)}$: 6.3	Mag>Hmg	Mag	Mag	Mag	Mag
185	P_{CO2}: 0.3 $P_{H2O(g)}$: 9.7	Hmg>Mag	Hmg>Mag	Mag>Hmg	Mag>Hmg	Mag

3.4.5. Chapter 9

Forsterite and enstatite single crystals were sonicated for 1h in ethanol solution, immediately after they were dried at 75ºC for 24h in an N_2 atmosphere. Then, samples were analyzed with XPS and Raman. Once this XPS spectra of untreated crystals were acquired, they were placed in the

carbonation reactor, following the experimental procedure explained in chapter 3. Single crystals were treated individually at 185ºC and 5 bar from 8h to 2 weeks. Experiments were carried with the addition of water vapor, where RH was always maintained below 1% (simulating possible local conditions on early Mars [367]. Immediately after carbonation experiments, samples were analyzed with XPS, Raman spectroscopy and SEM-FIB. Crystals were always transported from analysis to experiments and vice-versa with a N_2 desiccator.

4. Steam-mediated carbonation of brucite: the formation of distinct Mg-carbonate phases

4.1. Introduction

Brucite is a common product of the serpentinization of ultramafic rocks [368]. So far it has not been one of the main materials of interest for CCS technologies due to its limited natural abundance. Nevertheless, its reactivity towards CO_2 sequestration is higher than Mg-rich silicates [369]. The presence of brucite in Mg-rich silicate rocks plays a key role in the carbonation of serpentine mine tailings [370,371] and natural carbonation [368], improving its CCS efficiency. The CO_2 fixation capacity via brucite carbonation alone from the total mine tailing residues stockpiles (with ~1.8wt% Brucite) at Black Lake mine in Quebec is 27Mt of CO_2 [371]. Moreover, brucite can also be extracted from widely abundant serpentine minerals by metal leaching via acid extraction processes, such as the ÅA route (see section 2.3.2.2). However a significant energy penalty is associated [42].

Direct carbonation of $Mg(OH)_2$ is under intense academic scrutiny [170,175,372–376,203,204,261,264,267,368,370,371] because of its known fast carbonation kinetics in slurry phase [170,264,371,373].

At temperatures ≤200ºC, brucite carbonation is driven by the formation of metastable hydrated carbonates, selectively produced at different temperatures [264]. Still, an optimal process where the formation of these intermediate phases is controlled and in consequence the carbonation is accelerated has not yet been reported [267].

From a CCS perspective, the formation of anhydrous magnesium carbonates is preferred. Compared to hydrated Mg-based carbonates, magnesite is less soluble and has less molar volume and mass yielding to lower cost on transportation and processing [264]. Although the direct

carbonation reaction of brucite to anhydrous magnesium carbonate is difficult because the carbonation and dihydroxylation occur simultaneously in similar temperature ranges, but reaction of CO_2 with MgO is reported to be much slower than with $Mg(OH)_2$ [203,204,377]. The reaction mechanism of slurry-phase $Mg(OH)_2$ carbonation is currently poorly understood for CCS applications [264].

Previous research has stated that the gas-solid carbonation of both MgO and $Mg(OH)_2$ takes place at very slow kinetic rate [169,203,204,261,378]. Recent work has emphasized the role of relative humidity in such reactions, which is a key factor to accelerate the reaction rate [204,263,266,270]. The carbonation reaction is favored by working near the vapor/liquid equilibrium of water [204]. Highfield et al., 2016 [204] reported a promising moisture carbonation process at moderate conditions of $Mg(OH)_2$ to metastable hydrated carbonates, which spontaneously transforms in route to the desired anhydrous magnesium carbonate ($MgCO_3$) over longer reaction times (Table 4.1).. Generally, the reaction rate was increased upon reducing the temperature from 350 to 100ºC, as the RH increased. Magnesite yield was observed to be higher for middle temperatures (125 and 200ºC), as low temperatures (<125ºC) induced rapid formation of hydrous phases, but their transformation to magnesite was greatly reduced. On the other hand, at higher temperatures (>200ºC), the RH is greatly reduced as well the stability of rapidly forming hydrous phases, therefore only anhydrous carbonate phases were formed as a product of an uncomplete carbonation of reactive materials.

Table 4.1. Steam-mediated carbonation of periclase and brucite at specified conditions and the main product phases after 5 hours of reaction. A95, A99: Commercial Aldrich brucite (>95, >99%); Ext: extracted from Finnish serpentine. Ext-cw: extract-cold wash; Ext-hw: extract – hot bath; DSP: dead sea periclase. Table from Highfield et al., 2016 [204].

	Conditions				
Sample	T (ºC)	P_{CO_2}	RH (%)	R_x	Main phases (XRD)
MgO	350	40	2	68	Magnesite, periclase
MgO	300	40	5	61	Magnesite, periclase
MgO	250	40	10	58	Magnesite, periclase
MgO	200	40	25	75	Magnesite
MgO	125	40	>100	84	Magnesite
MgO	125	20	85	90	Hydromagnesite ≈ magnesite
MgO	100	10	~100	98	Hydromagnesite
$Mg(OH)_2^{A95}$	150	40	85	96	Hydromagnesite >> magnesite ≈ brucite
$Mg(OH)_2^{A99}$	150	40	85	85	Hydromagnesite > brucite
$Mg(OH)_2^{Ext}$	150	40	85	82	Magnesite > hydromagnesite
$Mg(OH)_2^{Ext-cw}$	150	40	85	92	Hydromagnesite
$Mg(OH)_2^{Ext-hw}$	150	40	85	93	Hydromagnesite >> magnesite
$Mg(OH)_2^{DSP}$	150	40	85	32	Brucite > hydromagnesite
$Mg(OH)_2^{A95}$	100	10	~100	98	Hydromagnesite >> brucite
$Mg(OH)_2^{A95}$	100	5	50	93	Hydromagnesite >> brucite

In this work, an experimental campaign on the carbonation of brucite under moderate temperatures and pressures (50-205ºC, 7 – 10 bar) was carried out in order to provide further insights on phase formation and evolution of distinct carbonate phases upon steam-mediated brucite carbonation processes, which still remains a challenging field [179].

4.2. Results and discussion

4.2.1. Role of temperature

Raman and XRD analysis of the reaction products of brucite steam-mediated carbonation from 50-205ºC at 10 bar from 4 to 16 hours are shown in Figs. 4.1 and 4.2. Brucite was observed as the only phase in the starting materials, as evidenced by its characteristic peaks 443 and 279 cm^{-1} [203,379]. At 50ºC, a partial carbonation of brucite was observed as well as the emergence of two distinct peaks (1093.11 and 1122.3 cm^{-1}) within the characteristic ν_1 symmetric stretching mode (ν_{1sym}) of the carbonate ion (CO_3^{2-}) [380,381]. The 1122.3 cm^{-1} has similar position to reference hydromagnesite and dypingite, being closer to dypingite [179,382]. Dypingite is similar in composition to hydromagnesite, but it has a more disordered structure and variable amount of waters of crystallization [180,183,185]. The 1093.11 cm^{-1} has a ν_{1sym} peak position similar to that of magnesite, but it lacks the characteristic peak of magnesite within the lattice vibration region at 324 cm^{-1}, suggesting that the phase responsible for the 1093.11 cm^{-1} peak is distinctive of magnesite. It remains unknown which is the (carbonate) phase responsible for such peak. It should be noted that there might be several unnamed or highly-disordered precursors that could possibly be forming during our experiments [179]. XRD results shows the presence of a hydromagnesite-like phase (such as dypingite), as also suggested by Hövelmann et al., 2012 [373]. XRD patterns do not show any additional crystalline phase in addition to from residual brucite. This might suggest that the phase responsible for the 1093.11 cm^{-1} Raman peak is either low in abundance (since Raman and XRD have different detection limits) or it is a highly-disordered phase. Since this phase cannot be associated with any known Mg-carbonate phase, it will be referred as Unknown Mg-carbonate (UMC).

Raman results from treatments performed at 90ºC show the emergence of only one peak within ν_{1sym} (1118.9 cm^{-1}). Such peak is slightly shifted with respect to that observed at 50ºC (1122.3 cm^{-1}), approaching the reference Raman data for hydromagnesite. XRD results shows a clear crystalline pattern, suggesting that the phase responsible for the 1118.9 cm^{-1} has a more ordered structure to that observed at 50ºC. This is consistent with the possible presence of hydromagnesite-like phases [373]. Upon raising the temperature to 120ºC, the Raman ν_{1sym} peak (1117.64 cm^{-1}) and their associate X-ray diffractograms strongly suggest the presence of hydromagnesite.

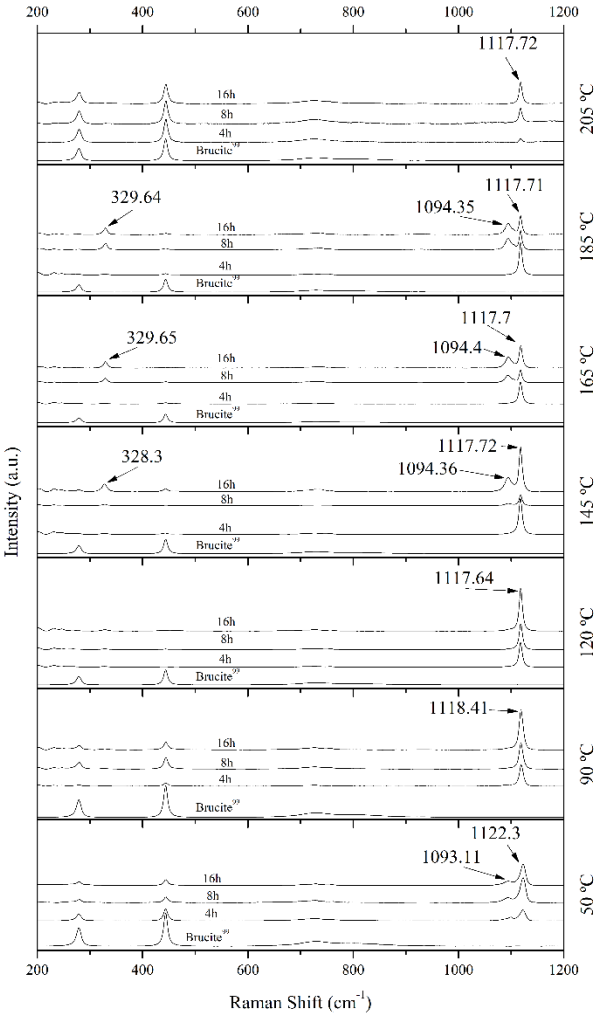

Fig. 4.1. Raman analysis of the reaction products obtained from treatments at 50-205ºC, 10 bar during 4 to 16 hours in the presence of steam.

At 145ºC, hydromagnesite was the only phase identified after 4h of reaction. However, after 8 and 16h, a new ν_{1sym} Raman peak emerged (1094.36 cm^{-1}). The presence of this peak is associated with the emergence of the 328.3 cm^{-1}. Such peaks are characteristic of magnesite [380,383,384]. Such observation is corroborated by the identification of magnesite by XRD. The formation of magnesite is accelerated at 165ºC and 185ºC with respect to 145ºC. However, at 205ºC, magnesite is no longer identified, leaving hydromagnesite as the only identified carbonate phase. Moreover, residual brucite is significantly more abundant than at lower temperatures (50-185ºC), indicating slower carbonation kinetics at 205ºC. Such behavior has been extensively documented for activated serpentine and olivine. It has been observed that increasing the temperature above 185ºC, the carbonation yield is significantly reduced [48,145]. This is attributed to the chemical potential that

drives the reaction is significantly reduced as it reaches the equilibrium between serpentine or carbonate mineral stability [48,145].

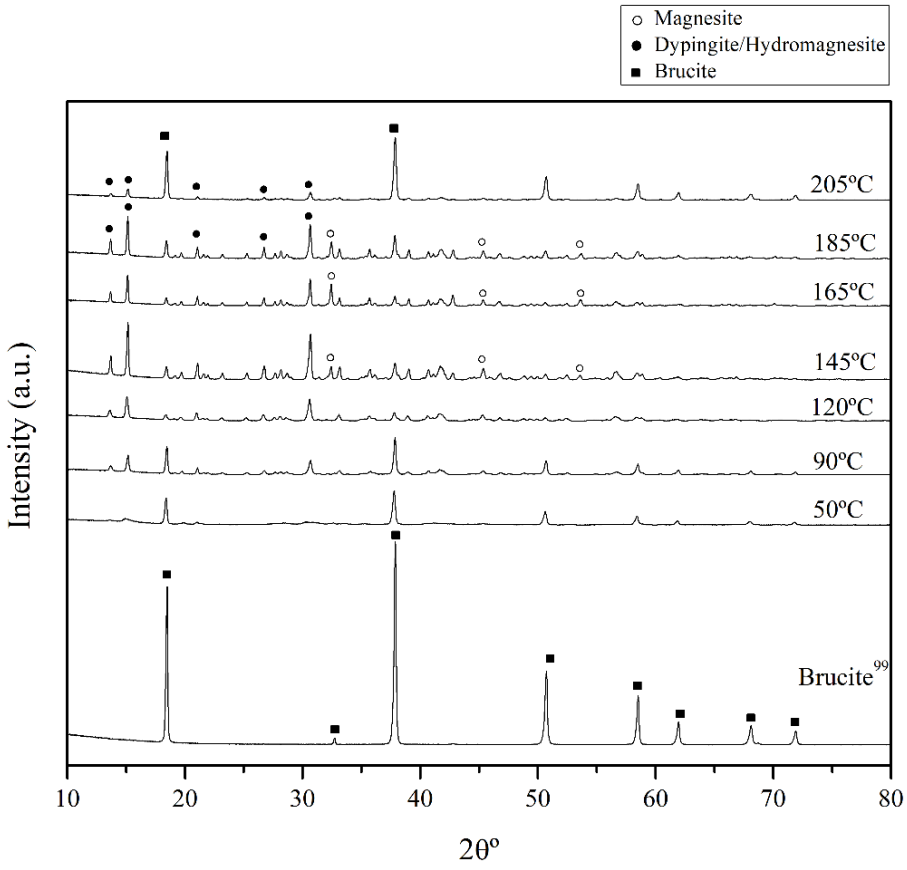

Fig. 4.2. XRD analysis of the reaction products obtained from treatments at 50-205ºC, 10 bar during 4 to 16 hours in the presence of steam.

In a recent study it was suggested that the formation of magnesite is strongly dependent on the formation of hydromagnesite (see chapter 6), where the formation of magnesite is greatly accelerated in a hydromagnesite-saturated environment [385]. This might explain the inexistence of magnesite at 205ºC, due to the significantly slower formation of hydromagnesite relative to 50-185ºC experiments, concurrently, delaying the formation of magnesite.

The direct formation of magnesite at moderately-low temperatures is inhibited by the formation of hydrated intermediate Mg-carbonate phases, and is often observed from the transformation of such phases [179,193,196]. However, magnesite could directly form without a hydrous precursor over extended reaction times [194,195]. Therefore, it remains unclear if magnesite formed directly from brucite or passed through a hydrous precursor.

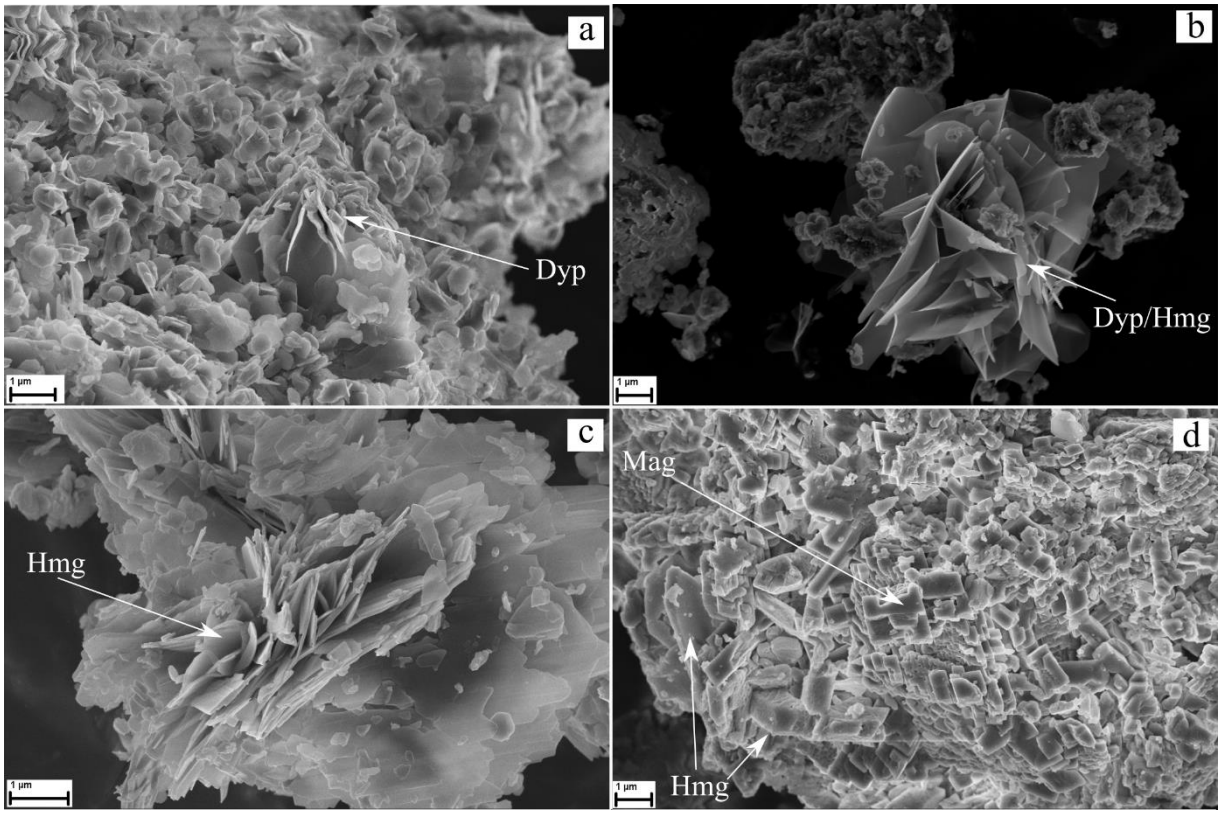

Fig. 4.3. Representative SEM images of the reaction products of brucite carbonation at 10 bar and (a) 50, (b) 90, (c) 120 and (d) 165ºC, during 16h. Dyp: dypingite; Hmg: hydromagnesite; Mag: Magnesite.

The evolution of the carbonate reaction at different temperatures was also observed by SEM. At 50ºC, platy dypingite crystals organized in agglomerates (≤1 μm; Fig 4.3a) [188,386]. Rosette crystal arrangements consisting of thicker plates to those observed at 50ºC crystals (≥1 μm; Fig. 4.3b) were observed at 90ºC. Comparison of Raman and XRD results strongly suggest the presence of a hydromagnesite or a hydromagnesite-like phase with very similar composition and structural order to hydromagnesite. At 120ºC, a rosette crystal arrangement of thicker plates than those observed at 50 and 90ºC, consistent with the presence of hydromagnesite (Fig. 4.3c) [171,179,182,194]. At 165ºC, euhedral hydromagnesite thick plates (≤0,5μm) as well as characteristic magnesite rhombohedral crystals (≤1μm; Fig. 4.3d) [387].

4.2.2. Role of pressure

Additional experiments were carried at 7 bar, in order to assess the role of pressure during brucite carbonation. Figs. 4.4 and 4.5 show the Raman and XRD analysis of the reaction products obtained at 50-185ºC, 7 bar during 4 and 16h. The obtained carbonate phases at 50ºC are analogous to those obtained at 10 bar. At 90ºC, the Raman ν_{1sym} peak is slightly shifted from such observed at 10 bar. XRD analyses of the reaction products obtained at 7 bar shows the presence of a hydromagnesite-like phase, with significantly broader peaks to those observed at 10 bar, strongly suggesting that the

carbonate phase observed at 7 bar have a more disordered structure, consistent with the presence of a hydromagnesite-like phase.

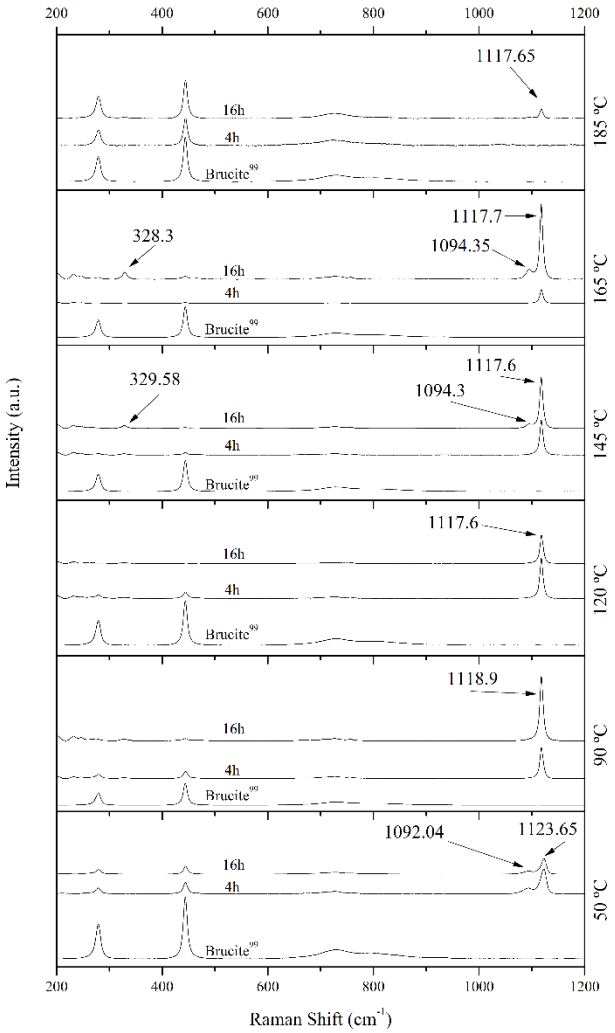

Fig. 4.4. Raman analysis of the reaction products obtained from treatments at 50-205ºC, 7 bar during 4 and 16 hours in the presence of steam.

Experiments carried from 120 to 165ºC at 7 bar yielded the formation of identical carbonate phases to those observed at 10 bar. However, magnesite is significantly less abundant during 7 bar experiments at 145 and 165ºC relative to analogous experiments carried at 10 bar.

Significant differences are observed from 185ºC experiments carried at 7 and 10 bar. The yield of carbonation is significantly reduced and magnesite is no longer observed in the 7 bar relative to the 10 bar experiments. This is consistent with the slower brucite carbonation to hydromagnesite kinetics of the 7 bar experiments, delaying the formation of magnesite. I should be noted that the enhanced carbonation is highly dependent on combined temperature and pressure.

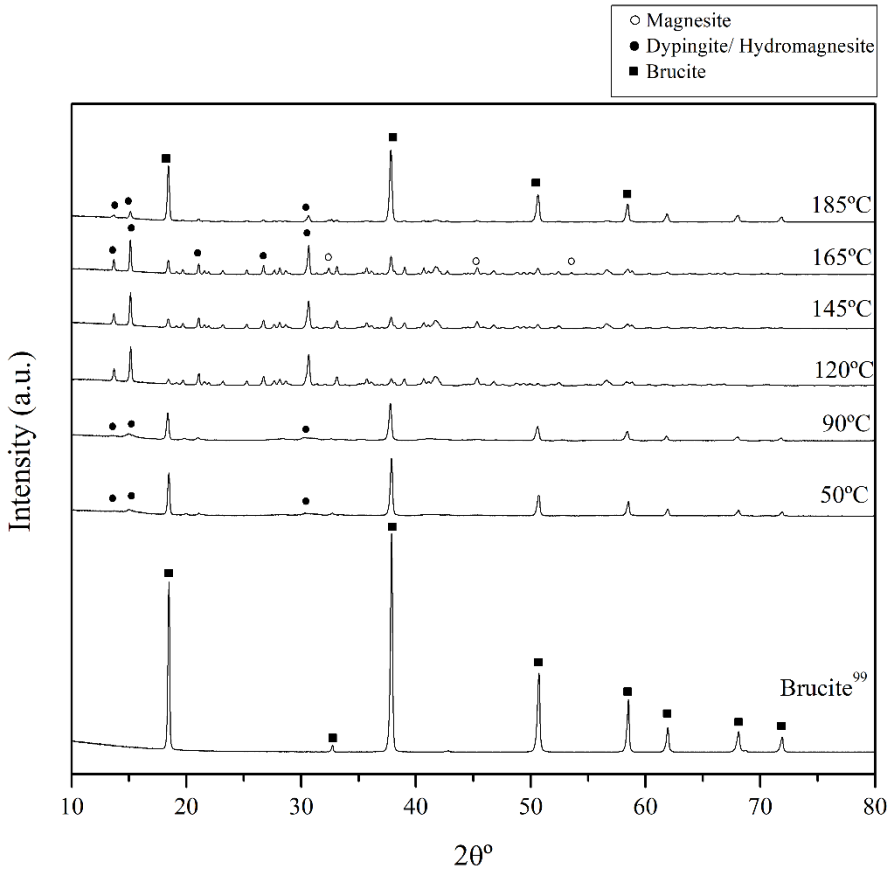

Fig. 4.5. XRD analysis of the reaction products obtained from treatments at 50-205ºC, 7 bar during 4 and hours in the presence of steam.

4.2.3. Phase equilibrium of the MgO-CO_2-H_2O system

Phase equilibrium boundaries of the reaction systems involving brucite and periclase (MgO) carbonation through metastable intermediates were calculated based on phase equilibrium in reacting systems that contain solid and gas phases [388–390] for the experimental conditions used in this study. The standard potential of gases refers to pure ideal gases at temperature T and standard pressure P_o = 0.1 MPa. The thermodynamic properties used for the calculations are summarized in Table 4.2.

Defining enthalpy of reaction ($\Delta_r H_{298}$), entropy of reaction ($\Delta_r S_{298}$) and volume of reaction ($\Delta_r V_{298}$) as:

$$\Delta_r H_{298} = \sum_i \left(\nu_i H_{298,i}\right)_{\text{Products}} - \sum_i \left(\nu_i H_{298,i}\right)_{\text{Reactants}} \quad (4.1)$$

$$\Delta_r S_{298} = \sum_i \left(\nu_i S_{298,i}\right)_{\text{Products}} - \sum_i \left(\nu_i S_{298,i}\right)_{\text{Reactants}} \quad (4.2)$$

$$\Delta_r V_{298} = \sum_i \left(\nu_i V_{298,i}\right)_{\text{Products}} - \sum_i \left(\nu_i V_{298,i}\right)_{\text{Reactants}} \quad (4.3)$$

where ν_i is the stoichiometric coefficient of species i.

The standard Gibbs free energy of reaction which contains solids and gases phases is described as follows:

$$\Delta_r G_{P,T} = \Delta_r G_{P,T}^{o,s} + \Delta_r G_{P,T}^{o,g} + RT\ln K_q^{s,g} \quad (4.4)$$

Where $\Delta_r G_{P,T}$, K_q designates Gibbs free energy and thermodynamic equilibrium constant, respectively. The superscripts s and g stands for solid and gas phases respectively. The equilibrium constant referring to solids equals to 1, due to the solid components are considered pure phases. On the other hand, the equilibrium component that refers to the gas phases activities does not equal 1. The reaction activities are approximately the value of the partial pressures of each gas phases divided by the standard pressure:

$$K_q = \sum_j \nu_j \ln \frac{P_j}{P_o} \quad (4.5)$$

where P_j and P_o refers to the partial pressure of gas j and standard pressure respectively.

The enthalpy and entropy of such reactions will be expressed by:

$$\Delta_r H_{298} = \Delta_r H_{298}^s + \Delta_r H_{298}^g \quad (4.6)$$

$$\Delta_r S_{298} = \Delta_r S_{298}^s + \Delta_r S_{298}^g \quad (4.7)$$

If temperature and pressure dependence of the enthalpy, entropy and volume of reaction is not considered, Gibbs free energy of reaction reads:

$$\Delta_r G_{P,T} = \Delta_r H_{298} - T\Delta_r S_{298} + \Delta_r V_{298}^s (P - P_o) + RT \sum_j \nu_j^g \ln \frac{P_j}{P_o} \quad (4.8)$$

where T stands for temperature. A system in thermodynamic equilibrium $\Delta_r G_{P,T}$ equals zero.

Table 4.2. Thermodynamic properties of the observed mineral phases in the Mg-CO_2-H_2O system. $\Delta_f H_{298}$, S_{298}, V_{298} stands for the standard enthalpy, entropy and volume respectively. Values taken from Robie & Hemingway, 1995 [390] and Holland & Powell, 1990 [388].

Phase	$\Delta_f H_{298}$ [kJmol^{-1}]	S_{298} [Jmol^{-1}]	V_{298} [cm^{3}mol^{-1}]
Brucite	-924.5	63.20	24.60
Periclase	-601.6	26.9	11.25
$CO_{2(g)}$	-393.51	213.79	0
$H_2O_{(g)}$	-241.29	188.84	0
Magnesite	-1112.48	65.7	28.02
Hydromagnesite	-6514.9	503.7	211.10
Nesquehonite	-1977.3	195.6	75.47

Brucite exothermic carbonation is favored under high temperatures ≥800ºC (depending on the water vapor and CO_2 partial pressures, as well as the total pressure), exceeding the stability boundary of brucite dihydroxylation and magnesite decarbonation. Phase boundary of brucite carbonation to form hydromagnesite and nesquehonite at studied CO_2 and H_2O partial pressures (P_{CO_2}/P_{H_2O}: 4) is found to be 259ºC and 134ºC respectively at 10 bar and 247ºC and 129ºC respectively at 7 bar.

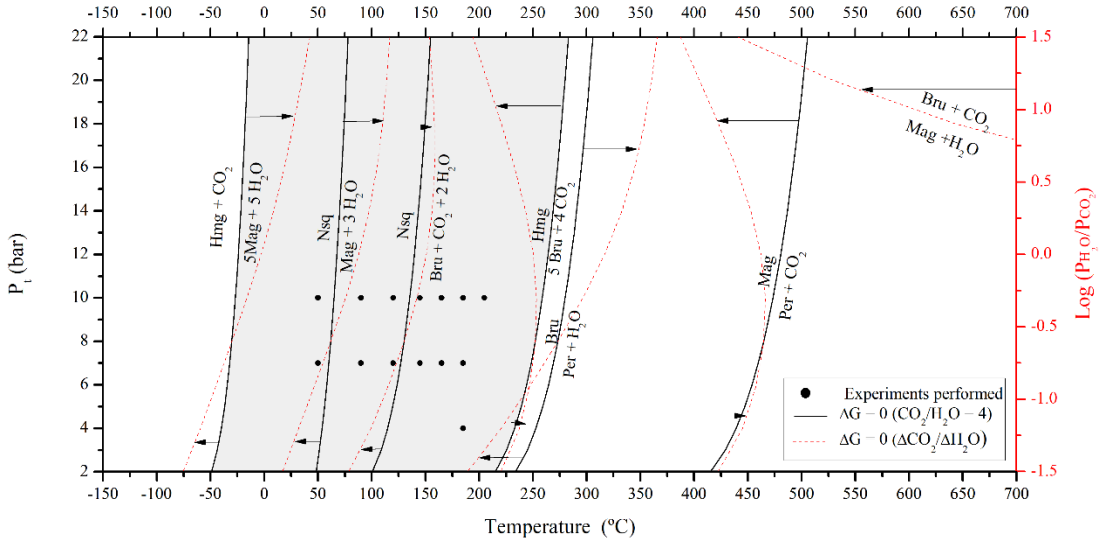

Fig. 4.6. (Solid lines, left axis) Calculated phase diagram of observed reactions from the system Mg-CO_2-H_2O with a gas mixture relation of (CO_2/H_2O = 4). (Dotted lines, right axis) Calculated phase diagram from the system Mg-CO_2-H_2O with varying CO_2/H_2O relation. Bru, Per, Mag, Hmg and Nsq stands for brucite, periclase, magnesite, hydromagnesite and nesquehonite respectively. ΔG = 0 represents that Gibbs free energy equals zero. Dots refers to the experiments performed. Arrows represents the thermodynamic equilibrium curve changes due to variations of H_2O/CO_2 relative to the gas mixture of (CO_2/H_2O = 4). Gray area indicates the pressure and temperature range where the reaction of brucite to a hydrous carbonate phase is exothermic and concurrently, the transformation of such hydrous phase to magnesite is also exothermic. Note that all the carried experiments are withing this gray area.

The obtained experimental results are in agreement with the calculations performed. Carbonation processes are only observed when the reacting system is in the stability yield of hydrated carbonates relative to brucite carbonation. Concurrently, the transition between hydrated carbonates (nesquehonite and hydromagnesite) to magnesite is estimated to be exothermic at these experimental conditions (Fig. 4.6, gray area). It should be noted that the equilibrium boundaries of dypingite (which is more hydrated than hydromagnesite and less than nesquehonite) are not estimated due to their thermodynamic properties have not been well stablished ¡[177].

It has been reported that the presence of water is a key factor to prevent the dihydroxylation of brucite and catalyzing the carbonation reaction [267]. The latter is reflected on Fig. 4.6, where at higher $H_2O_{(g)}$ partial pressures, the thermal stability of brucite is increased. The stability of hydromagnesite and magnesite are greatly influenced by the water vapor partial pressure. Generally, dehydration-induced reactions have greater thermal stability with increasing water vapor pressure.

The Mg-CO_2-H_2O system is strongly influenced by the reaction-pathway [391], selectively induced by temperature, leading to major variations in reaction kinetics[391]. Considering a 2-step reaction process (involving brucite carbonation through a hydrated reactive intermediate, followed by spontaneous dehydration to form an anhydrous magnesium carbonate) within one reaction system seems to be a CO_2 fixation mechanism that fits into the experimental observations. Two-step reaction through an intermediate hydrated reactive carbonate is more optimal than direct synthesis of magnesite (since the reaction temperatures and pressures are considerably lower [203,267]).

Experiments carried at higher temperatures (185 and 205ºC) are approaching the phase equilibrium boundary between hydromagnesite and brucite. Moreover, it was observed slower reaction kinetics at 185 and 205ºC, compared to lower temperatures (50-165ºC). This is consistent with previous studies regarding where a decreased carbonation yield is observed upon approaching the equilibrium phase boundaries between reacting phases [48,145]. This also might suggest that the preferred brucite-carbonation path is through the formation of hydromagnesite, followed by its transformation to magnesite (at 145-185ºC), inhibiting the direct formation of magnesite. At lower temperatures (50 and 90ºC), a different behavior is observed. At this temperatures dypingite coexisting with a not known carbonate phase are observed. These phases could be possibly be products of intermediate precursor, thus, distinct processes are associated [178,179].

These simplified thermodynamic estimations mainly express the exothermic or endothermic nature of certain reactions. The actual reaction mechanisms, which unequivocally occurs at the mineral-CO_2-H_2O interfaces [392] might include complicated reaction pathways that may not follow predictions based on equilibrium thermodynamics including diffusion mechanisms thought a condensate water-film on the surface reacting mineral. This water film could also be generated from surface brucite dihydroxylation and the presence of water might play a crucial role to prevent evaporation of such film. Moreover, unnamed and highly-disordered Mg-carbonate phases might be evolving and transforming during our experiments. The formation of hydrous Mg-carbonate mineral assemblages often do not follow predictions based on thermodynamic equilibrium, as expressed by the Ostwald rule, where the transformation of phases often evolves to a structurally similar phase rather than a thermodynamically more stable phase [393].

4.2.4. Thermogravimetric analysis

TGA analysis was performed to quantitatively asses the CO_2 sequestration efficiency of the solid products obtained from the reaction in the 50-185ºC temperature range at 7 and 10 bar for 16h (Fig.4.7). The differential thermogravimetric (dTG) approach has been used in this work to represent the velocity at which mass change occurs upon thermal decomposition. Results from the treatments at 7 bars at different temperatures shows significant differences relative to the starting material. Characteristic dihydroxylation of $Mg(OH)_2$ at ~360 ºC [204,264] is observed in the starting material.

Decomposition of residual brucite is observed in the results from reactions performed at different temperatures.

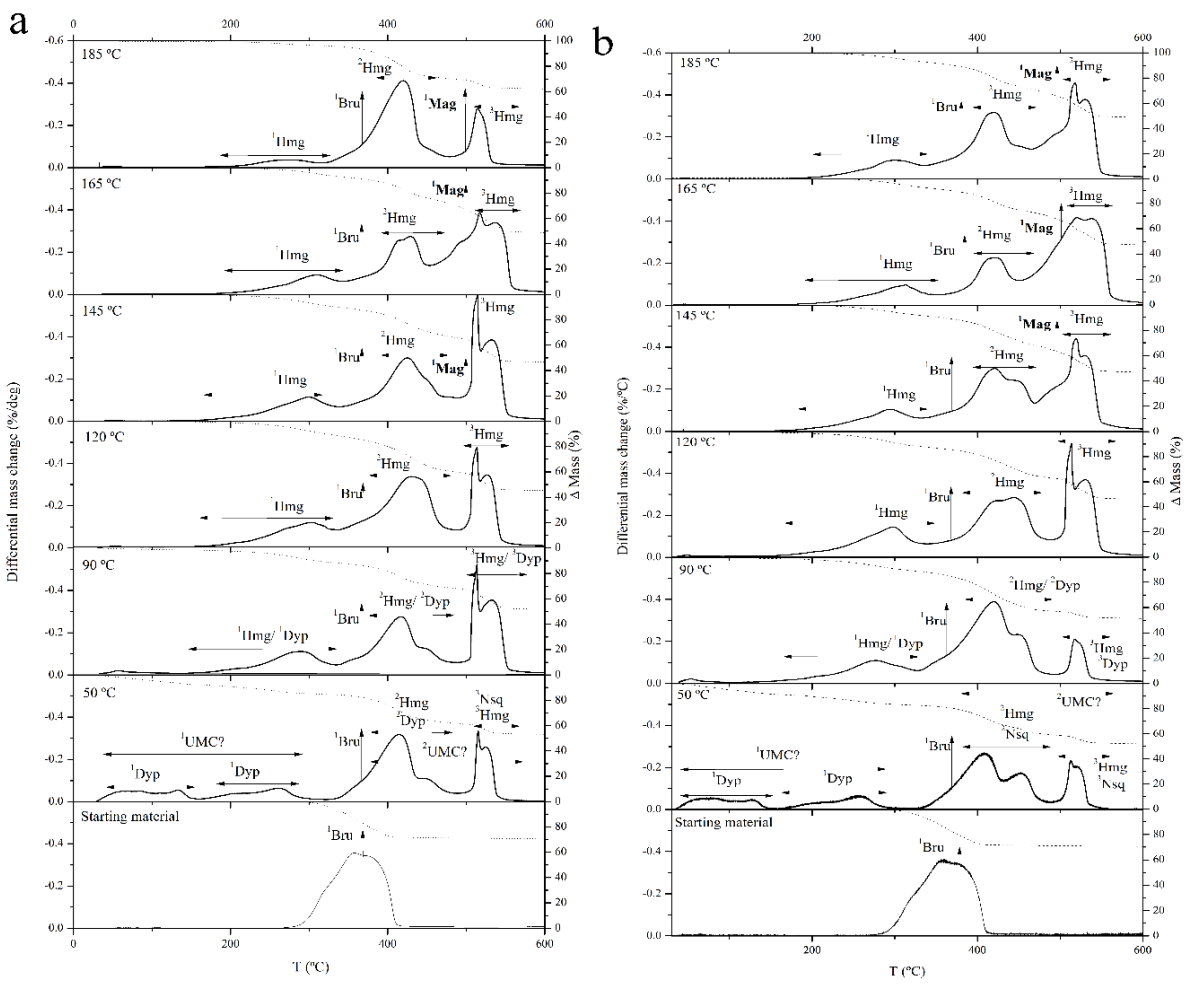

Fig. 4.7. Differential thermogravimetric analysis (dTG) of mass change upon thermal decomposition at 50-185ºC, **(a)** 7 and **(b)** 10 bar during 16h. (Solid line) dTG (%/ ºC), (Dash line) peak fitting cumulative, (Doted line) mass loss upon thermal decomposition. The decomposition ranges of relevant and reference Mg-carbonate phases are shown with double ended arrows. ^{1}Bru: brucite dihydroxylation; ^{1}Mag: magnesite decarbonation; ^{1}Hmg: hydromagnesite dihydroxylation and dehydration; ^{2}Hmg: hydromagnesite decarbonation; ^{3}Hmg; magnesite decarbonation (produced from hydromagnesite decomposition); ^{1}Dyp: Dypingite dehydration; ^{2}Dyp and ^{3}Dyp: Dypingite decarbonation; ^{1}UMC?: possible dehydration range of the unknown Mg-carbonate phase; ^{2}UMC?: possible decarbonation range of the unknown Mg-carbonate phase.

Results obtained from treatment at 185ºC, 10 bar exhibits new decomposition peaks due to the loss of water molecules from hydromagnesite with peak position ~283ºC [394,395]. Followed by the characteristic dihydroxylation of residual brucite. Immediately following, two decomposition peaks with center in ~422ºC and ~452ºC. Those peaks can be attributed to the decarbonation of the dehydrated/hydroxylated hydromagnesite respectively [395]. Magnesite decomposition with peak position (~503ºC) [204,264,395,396] is observed afterwards. Finally, two sharp peaks are observed with peak position ~514ºC and ~540ºC, respectively. The 514ºC peak can be attributed to a sudden

release of CO_2 that is trapped in the remaining magnesium carbonates from hydromagnesite decomposition, which exothermically recrystallizes to form a more thermally stable structure [397]. The latter decomposition is immediately followed by the release of the remaining CO_2 trapped into the recrystallized magnesium carbonate [397].

dTG of materials treated at temperatures 145-165ºC are akin to the one observed at 185ºC. The major difference is that magnesite is significantly more abundant at 145-165ºC relative to 185ºC. The amount of water lost from residual brucite seems to decrease as the carbonation temperature diminished from 185 to 120ºC, achieving its minimum at 120ºC. Further decrease of the reaction temperature (90 and 50ºC) leads to higher amounts of residual brucite. It can be concluded that treatments performed at 120ºC undergo a more efficient brucite carbonation, although the only carbonate phase of the reaction is hydromagnesite. Increasing temperature reduces the hydromagnesite formation efficiency, but leads to an increased yield of magnesite formation.

Dypingite, as observed with Raman and XRD from 50 and 90ºC treatments, has dehydration temperatures that starts at room temperature (rT) to 380ºC. Different studies reported that dypingite has differing dehydration behavior within this temperature range. It is plausible that coexistence of different dypingite-like phase and highly disordered Mg-carbonate phases might be accountable for discrepancies in dehydration behavior for dypingite [398–400]. The possible dehydration and decarbonation temperature ranges of UMC are shown in Fig 4.7, which are likely overlapping with those of the identified carbonate minerals, and therefore, making difficult their differentiation.

Treatments performed at 7 bar exhibit similar dTG profiles to those obtained at 10 bar. The main difference is observed from carbonation treatments at 145ºC to 185ºC, where magnesite decomposition peaks are significantly lower.

4.2.5. CO_2 sequestration efficiency

Quantification of total CO_2 sequestration efficiency (CO_2 wt%) was estimated by area calculation of the dTG deconvoluted peaks within the 350-550ºC region, since Mg-carbonates decarbonate within this temperature range [395–400]. It should be taken into account that residual brucite have a dehydration temperature range of 275ºC – 420ºC, which overlaps with the decarbonation temperature ranges of hydrated Mg-carbonates. Therefore, the area of the deconvoluted peak associate with residual brucite dehydration was not added to the calculated area associated with the decarbonation of Mg-carbonate phases (Fig. 4.8).

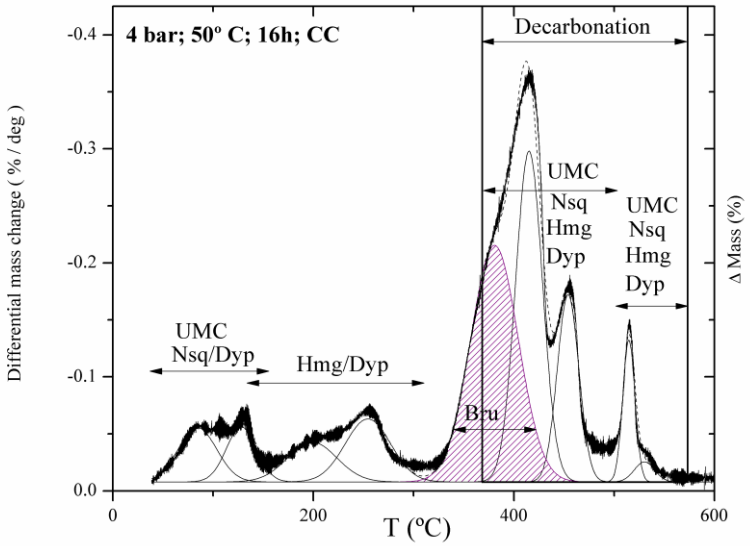

Fig. 4.8. Peak deconvolution of differential thermogravimetric analysis (dTG) of mass change upon thermal decomposition of carbonation products at 50 ºC and 4 bar, maintained for 16h using concentrated CO_2 (RH > 90%). Solid and dashed curves represent the differential mass change (% / deg) and cumulative peak fitting curve, respectively. Thermal decomposition temperature ranges of Bru: brucite (filled area), nesquehonite (Nsq), hydromagnesite (Hmg), dypingite (Dyp) and possibly "Unknown Mg-carbonate" (UMC) are indicated with double-ended arrows. The dehydration of such phases occurs from room temperature to 270 ºC and decarbonation (350-550 ºC). Figure from Rausis et al., 2020 [55].

CO_2 sequestration efficiency was found to be optimal for treatments at 7 and 10 bar within temperature range 120-165ºC and 120-185ºC respectively (Fig. 4.9). Achieving, at both studied pressures, the highest CO_2 sequestered value at 165ºC, accounting to ~39 and ~ 41 CO_2 wt%, respectively for 7 and 10 bar. Respectively, at this temperature is observed the highest CO_2 efficiency due to its high hydromagnesite and magnesite yield (magnesite have greater CO_2 storage capacity than hydromagnesite). Hydromagnesite formation is optimal in reaction temperature range 90-165ºC at both studied pressures, reaching its highest value at 120ºC. Nevertheless, magnesite yield is negligible at 120ºC, leading to lower CO_2 sequestration efficiency. Yet, the extent of the reaction is almost complete under these conditions, as evidenced by the lack of brucite features. Treatment at 50ºC exhibits lower CO_2 sequestration efficiency compared to the ones obtained within the temperature range 120-165ºC, associated with the slower reaction kinetics at low temperatures.

Pressure increase from 7 to 10 bar exhibits higher CO_2 sequestration efficiencies at 10 relative to 7 bar experiments (~5%). Crucial differences are observed from treatments at 185ºC with varying pressure. Further pressure increase (>10 bar) will probably enhance the kinetics of hydromagnesite and magnesite formation, which will reduce the synthesis times. Further optimization regarding the experimental conditions should be studied in order to improve the CO_2 sequestration efficiency.

Different water vapor partial pressures should be studied in order to find an optimal CO_2/H_2O relation at different temperatures and pressures for an efficient brucite carbonation.

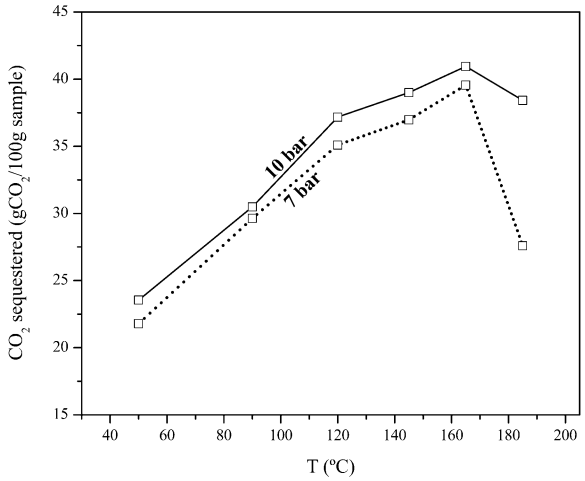

Fig. 4.9. CO_2 sequestered in g/100g of sample at different temperatures (50-185ºC) with varying pressure (Dotted line) 6 and (Solid line) 10 bar (CO_2/H_2O = 4) for 16h.

Brucite carbonation efficiency with water vapor saturation is found to be similar to the one obtained from slurry phase carbonation proposed in Fricker and Park, 2014 [264]. This process, similar to the "non-immersive" approach [204], is found to optimize water utilization for such processes. This work proposes a mechanism to sequester CO_2 through a very simple reaction system for brucite carbonation. Besides, the proposed reaction set-up is cost-effective due to the used moderate pressures, low temperatures and H_2O/CO_2 gas mixtures.

Research interest in moist carbonation processes is continuously increasing because it is potentially a cost-saving approach [204]. Recent work has been focused on claiming the proof-of-principle of such processes [203,204,263,266,270]. Highfield et al., 2016[204] showed evidence of nearly complete carbonation of $Mg(OH)_2$ at 150ºC and 40 bar (humid) through a "non-immersive" approach was attained at 1h.

4.3. Conclusions

Brucite carbonation in the presence of steam yielded to the formation of hydrated and anhydrous Mg carbonates, and their formation is selectively dependent on temperature. At 50ºC, highly-disordered dypingite was observed as well as an unknown Mg-carbonate phase. The relative inexistence of this phase in XRD analysis might be explained by either low abundance of this phase or that it may have a very disordered internal structure. Nevertheless, the nature of this carbonate phase remains unclear as well as its composition. Further research is needed to narrow down the

characteristic of this phase for its correct identification and its possible association to other carbonate phase reported in literature.

At 90ºC and 7 bar dypingite was observed. However, upon raising the pressure to 10 bar, a carbonate phase more similar to hydromagnesite than dypingite was observed, as evidence by a more ordered internal structure and thicker crystal plates as observed by XRD and SEM, respectively. Hydromagnesite and magnesite were observed in treatments performed at different temperatures (120-185ºC). The relative proportions of these minerals are highly dependent on temperature, pressure and reaction time. The formation of magnesite is more likely to occur via transformation of hydromagnesite. Brucite carbonation yield increases with temperature until 165 and 185ºC is reached at 7 and 10 bar, respectively. Significantly slower reaction rates were observed at higher temperatures (185 and 205ºC for 7 and 10 bar, respectively). This might be attributed to the chemical potential is reduced as the reacting phases approached the equilibrium phase boundaries. The slower kinetics were evidenced by the significantly lower hydromagnesite yield at these temperatures compared to lower temperatures (50-165º and 50-185ºC for 7 and 10 bar, respectively). The slower formation of hydromagnesite might also delay the formation of magnesite, explaining its relatively inexistence in the experiments carried at 185 and 205ºC for 7 and 10 bar, respectively.

Almost complete carbonation of brucite is reported in this work. Laboratory observations reveal that 165ºC was the optimal temperature for carbonation; at this temperature combined hydromagnesite and magnesite formation was identified to be more efficient. The maximum CO_2 sequestered is 39wt%. and 41wt%. for 7 and 10 bar, respectively. Results from the 10 bar experiments shows a slightly better CO_2 carbonation efficiency when compared to the 7 bar experiments.

5. Phase formation and evolution of Mg-carbonate phases upon carbonation of brucite under concentrated CO_2 and simulated flue gas conditions

5.1. Introduction

An extended experimental campaign of brucite carbonation was carried out in order to provide more insights on the nature of Mg-carbonate phases mentioned in Chapter 4, particularly to the chemical composition, dehydration behavior and vibrational spectra of UMC as well as to assess the carbonation efficiency under moderately low pressures and temperature conditions (1-10 bar, 50 and 120ºC) under concentrated CO_2 and simulated flue gas conditions.

A successful MC process should be able to reach effective conversion rates when working at temperatures and pressures near to those of flue gas emissions [56,204]. Recent studies are focusing on the possibility of using MC processes as an integrated alternative to CO_2 capture [44,57,99,100,200]. The advantages of such processes are: (i) initial CO_2 capture processes are avoided as well as their associated costs, significantly simplifying the overall MC processes and (ii) high-purity and profitable carbonate products might be obtained. Some studies have observed that carbonation mechanisms are similar when using flue gas and captured CO_2, indicating the high carbonation potential of flue gas carbonation [99,100].

However, the formation of Mg-carbonates under these conditions remains a challenging field os study [179] (see chapter 4), providing challenges on understanding the formed phases and their reaction mechanisms, the stability of such carbonates and their long-term storage capacity. The

identification of the Mg-carbonate phases that formed upon conditions relevant to the utilization of industrial flue gas streams are of paramount importance since it might provide a better understanding of the carbonation steps and mechanisms of intermediate phases, which is a key aspect for engineered ways to accelerate carbonation kinetics [199] and to the preferential nucleation of specific carbonate phases [401].

5.1.1. Amorphous Ca and Mg carbonates

Amorphous Ca/Mg carbonates (ACC/AMC) are precursors to crystalline phases and they play an important role on the formation of hydrated and anhydrous carbonate phases. Such reactions have been widely exploited by nature in a variety of processes [402–404]. Research has mainly focused on studying the stability of ACC and their transition to crystalline Ca-carbonates [401,405–407]. The formation of AMC, their stability and transition to crystalline Mg-carbonate phases have received less attention and have been mainly discussed in the context of mixed Ca/Mg amorphous carbonate phases [401,407–409], since the presence of Mg plays a crucial for stabilizing natural and artificial ACC [410,411]. Moreover, the stability of amorphous materials is known to depend on size and water content [412]. The presence of Mg^{2+} plays a key role on the formation kinetics of ACC and its transition to crystalline phases, most likely due to the slow dehydration kinetics of Mg^{2+} [413], inhibiting the formation of anhydrous calcite and vaterite crystallization [414–416]. Research interest on the formation of Mg-carbonate is continuously increasing since such processes are foreseen to play an important role on climate change mitigation efforts [50,417].

An example being the formation of both natural and synthetic monohydrocalcite (MHC), which occurs from the transition of ACC with Mg (ACC-Mg), requiring the presence of high concentration of Mg relative to Ca in the precipitating solution [192,418]. The crystalline phase (MHC) formed from the transition of ACC-Mg is controlled by its Mg content. Pure ACC crystallizes to vaterite [416], 10% ACC-Mg crystallizes to calcite [411], 30% ACC-Mg crystallizes to MHC [408,419], 50% ACC-Mg crystalizes to protodolomite/dolomite, although it requires higher temperatures [408]. This might be explained by the energy required to desolvate Mg is higher than Ca, therefore, higher temperature is needed to crystalize Ca-Mg / Mg carbonates, such as dolomite and magnesite [408].

Nishiyama et al., 2013 [420] reported that MHC can only form from a solution saturated with respect to nesquehonite, indicating that MHC formation may require the paragenesis of nesquehonite. However, this latter mineral was not observed in the XRD results. According to the crystallographic structure of MHC, Ca in this mineral gas eight-fold coordination[401]. On the other hand, Mg in solution do not take eight-fold coordination, which makes difficult the substitution between Ca and Mg into MHC structure. However, Rodriguez-Blanco et al., 2014 [408] observed changes on the MHC structure depending on the Mg content, which was interpreted as the structural

incorporation of Mg since MHC structure is open an less dense compared to calcite and aragonite. This conclusion was corroborated by the lack of nesquehonite formation as evidence with XRD.

This two latter studies have significant inconsistencies, which are more likely attributed to the solid phase speciation of Mg in MHC which remains unknown [401]. Currently, two main uncertainties exist: (i) the possibility of Mg incorporation into the MHC structure or not. This has remained challenging due to the possible precipitation of Mg carbonate phases during MHC formation. Nishiyama et al., 2013 [419] and Rodriguez-Blanco et al., 2014 [408] reported the formation of hydromagnesite after aging of MHC (Fig. 5.1). However, instead of hydromagnesite, it is more likely that a hydromagnesite-like phase was formed (such as dypingite), as the X-ray scattering features resembles the broad feature of dypingite, instead of sharp hydromagnesite features [55,179,373]; (ii) the possible formation of AMC associated with MHC nucleation, instead of nesquehonite. Wang et al., 2015 [421] suggested the presence of an amorphous material with high Mg content, suggesting that the assumed nesquehonite formation [419] might correspond to AMC. This is consistent with the observations of Rodriguez-Blanco et al., [408], where no crystalline phases were identified, based mainly on diffraction techniques, insensitive to amorphous materials. More recently, Fukushi et al., 2017 [401] estimated that a limited amount of Mg^{2+} can be incorporated into MHC structure. Such substitution was found to be almost constant at 0.057 $Mg_{st}/(Ca+Mg_{st})$, where Mg_{st} stands for Mg that substituted Ca in the MHC structure. It was also suggested that values exceeding >0.06 were consistent with the presence of AMC. Fig. 5.2. shows the proposed speciation of Mg associated with MHC and the discussed inconsistencies between different studies.

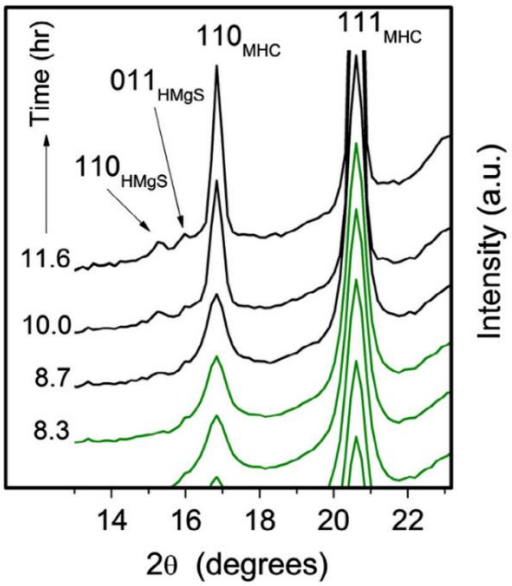

Fig. 5.1. Wide angle X-ray Scattering (WAXS) analysis of aged MHC, exhibiting the formation of a hydromagnesite-like phase after 8.7h. Figure from Rodriguez-Blanco et al., 2014 [408].

High-Mg MHC have needle-like morphology. On the other hand, low-Mg MHC exhibit spherical morphology. Nishiyama [419] et al., 2013 and Wang et al., 2015 [421] have observed that the elemental distribution of Ca and Mg in HMC is micro-homogeneous, in agreement with Fukushi et al., 2017 [401]. A different study had observed the presence of a Mg-rich layer in MHC spherules [422], which then latter was interpreted by Fukushi et al., 2017 [401], which suggested that such layer is very likely to be AMC. The presence of AMC played a key role on the nucleation of MHC, where AMC coats MHC surface, inhibiting its ability to form spherical surface, keeping a needle-like shape. Moreover, this hydrated AMC layer also prevents MHC transformation to anhydrous calcium carbonates [401]. This is consistent with the relative inexistence of Mg-carbonate phases upon MHC formation, as there were characterized with XRD. However, the aging of MHC yielded the formation of hydromagnesite [408,419]. Instead of hydromagnesite, it is more likely that a hydromagnesite-like phase was formed (such as dypingite) [55,179,373]. It can be assumed that such hydrous Mg-carbonate phase formed upon crystallization of AMC, based on Fukushi et al., 2017 [401] observations. This strongly suggest that the properties and presence AMC, AMC-Mg and ACC plays a key role on the nucleation of crystalline phases. Therefore, it is of paramount importance to characterize such amorphous phases and their nucleation pathways in order to understand the formation mechanisms of crystalline phases.

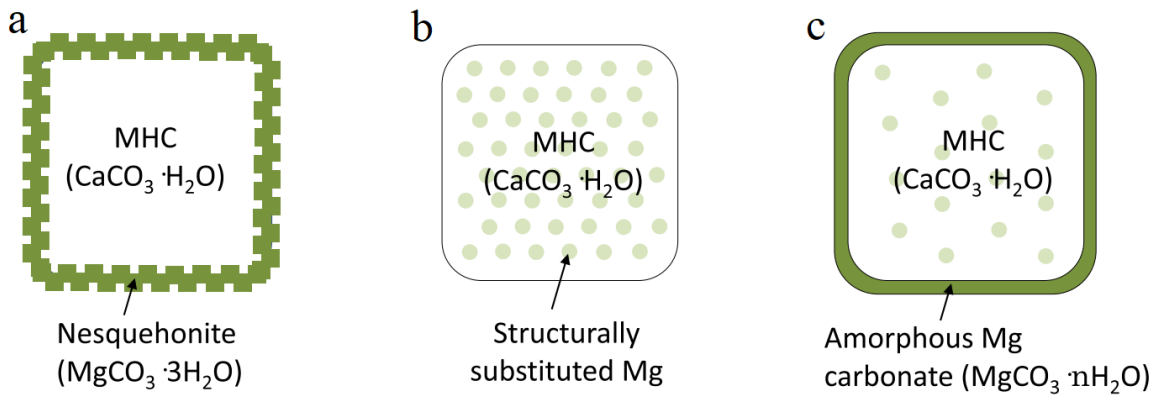

Fig. 5.2. Schematic of the discussed fate of Mg during the formation of MHC by **(a)** Nishiyama et al., 2013 [419], **(b)** Rodriguez-Blanco et al., 2014 [408] and Fukushi et al., 2017 [401]. Solid circles represent Mg_{st}. Figure from Fukushi et al., 2017 [401].

Zou et al., 2019 [423] have reported the formation of a new discovered hydrated Ca-carbonate phase: calcium carbonate hemihydrate (CCHH) with composition $CaCO_3 \cdot 1/2H_2O$, exhibiting needle-like morphology. Such phase was formed during crystallization of ACC-Mg (with 5-9% of Mg content) and it is precursor of MHC (Fig. 5.3). Upon the crystallization of ACC-Mg to CCHH, a significant decreased in the $Mg_{st}(Ca+Mg_{st})$ molar ratio is observed, greatly limiting the amount of Mg_{st} within the CCHH structure. This also control the amount of Mg_{st} in the MHC structure. Upon formation of CCHH, the expulsed Mg form ACC-MG is more likely to form AMC, coating the surface of CCHH and eventually of MHC. This provides new insight on the nucleation processes of

ACC-Mg to crystalline phases, as well as the fate of Mg during CCHH and MHC formation (Fig. 5.4).

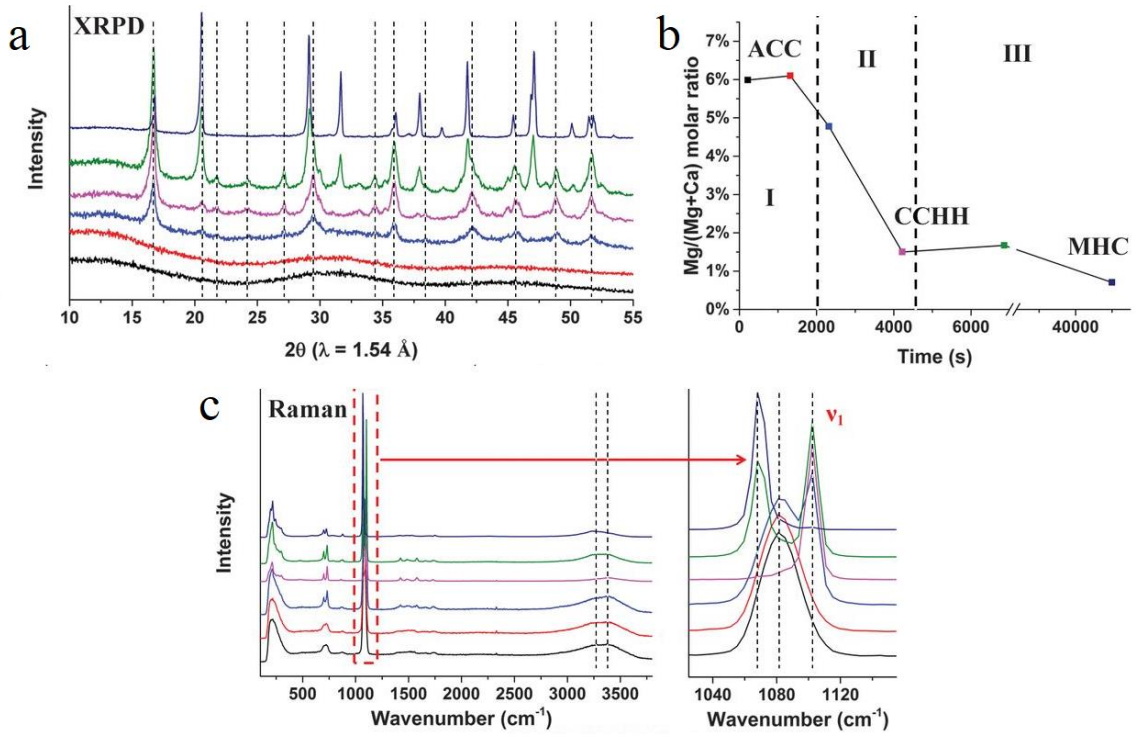

Fig. 5.3. (a) XRD and **(C)** Raman analysis of the evolution of AMC-Mg (black and red lines) to CCHH (dark blue, purple and green lines) and the transition of CCHH to MHC (blue line). **(C)** $Mg_{st}(Ca+Mg_{st})$ molar ratio variations in function of the AMC-Mg aging. Figure adapted from Zou et al., 2019 [423].

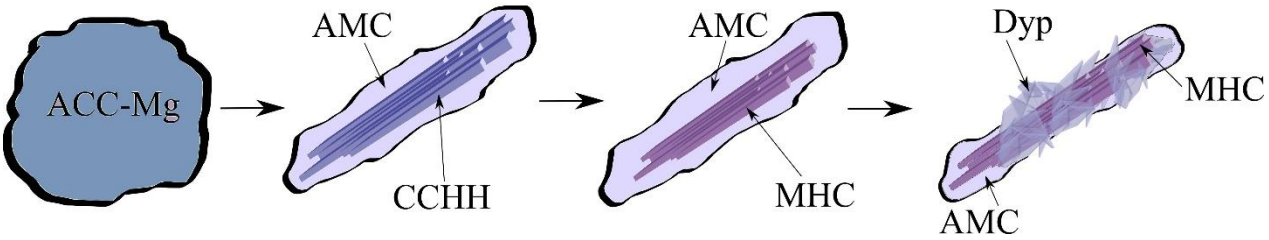

Fig. 5.4. Proposed schematic of the transition of ACC-Mg to CCHH and AMC and the subsequent transformation of CCHH to MHC, followed by Dypingite crystallization from AMC.

AMC has been recently synthetized from mixing solutions of $MgCl_2$ and Na_2CO_3 [401,424]. The precipitates and their evolution over time (1 – 48h) are shown in Fig. 5.5. AMC presence is evidence by two broad humps at 18 and 31º in the XRD patterns of precipitates sampled at 1 to 12h. The position of this humps are almost identical to those observed from ACC-Mg [408]. Moreover, no crystalline features are observed. At 24h, new peaks emerged at 15, 21 and 42ºC, which are associated with a hydromagnesite-like phase, followed by a more pronounced hydromagnesite-like phases crystallization at 48h. AMC is more durable than ACC. This latter phase transforms almost instantaneously to crystalline Ca-carbonates [413].

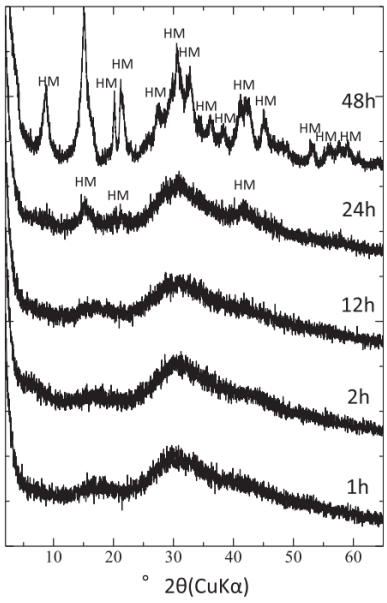

Fig. 5.5. XRD patterns of synthetized AMC and its progressive transformation to hydromagnesite-like phases (HM). Figure from Fukushi et al., 2017 [401].

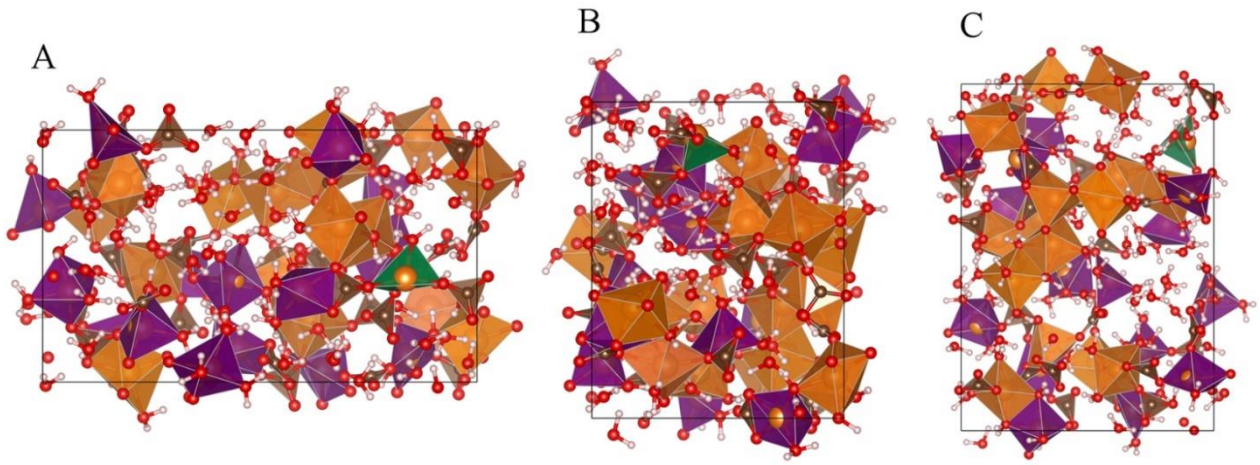

Fig. 5.6. Estimated atomic structure of hydrated AMC, where H_2O-rich regions ("small pores") are interspersed with regions rich in Mg^{2+} and CO_3^{2-}. (A, B, C) shows the structure viewed from different axes. Figure from White et al., 2014 [424].

White et al., 2014 [424] suggested that the stoichiometric composition of AMC is $MgCO_3 \cdot 3H_2O$, similar to reference nesquehonite. Moreover, the atomic structure of hydrous AMC was also proposed. It was suggested the distribution of H_2O molecules in AMC is not distributed homogeneously. In fact, there are H_2O-rich regions, called "small pores" interspersed with regions rich in Mg^{2+} and CO_3^{2-}. This might indicate that H_2O-molecules from the small pores is less tightly bound in the $MgCO_3$ matrix, making it relatively easy to be removed from the AMC structure (Fig. 5.6). Zhang et al., 2018 [425] have also identified a hydrated AMC with dehydration behavior similar to reference nesquehonite.

5.2. Results and discussion

5.2.1. Concentrated CO_2 experiments

Raman spectra of the reaction product obtained upon brucite carbonation using CC at 50 and 120ºC, in the pressure range of 1 to 10 bar from 4 to 16 hours are shown in Fig. 5.7. Distinctive brucite Raman features are observed in the starting materials, as evidenced by its characteristic peaks at 443 and 279 cm^{-1} [203,379]. The reaction products obtained at 50ºC shows the emergence of two distinct peaks at 1093.3 ± 1.1 and 1122.3 ± 0.1 cm^{-1} within the ν_1 symmetric stretching mode (ν_{1sym}) of the carbonate ion (CO_3^{2-}) [380,381]. The intensity of the brucite peaks progressively diminishes as the ν_{1sym} peaks increase. At 120ºC, two distinct ν_{1sym} Raman peaks are observed at 1094.6 ± 0.1, and 1118.1 ± 0.5 cm^{-1}. Moreover, an additional peak is observed at 328.3 ± 0.1, especially at 7 and 10 bar.

The presence of carbonates is corroborated by FTIR analysis, which exhibits the characteristic peaks of the CO_3^{2-} and HCO_3^- ν_3 asymmetric stretching mode at 1405, 1470 and 1515 cm^{-1} (Fig. 5.8) [182,356,360]. Nonetheless, overlapping features between the different Mg-carbonate phases makes difficult their correct distinction. Moreover, Mg-carbonates cannot be easily distinguished by the sole observation of optical methods, such as Raman and FTIR [380].

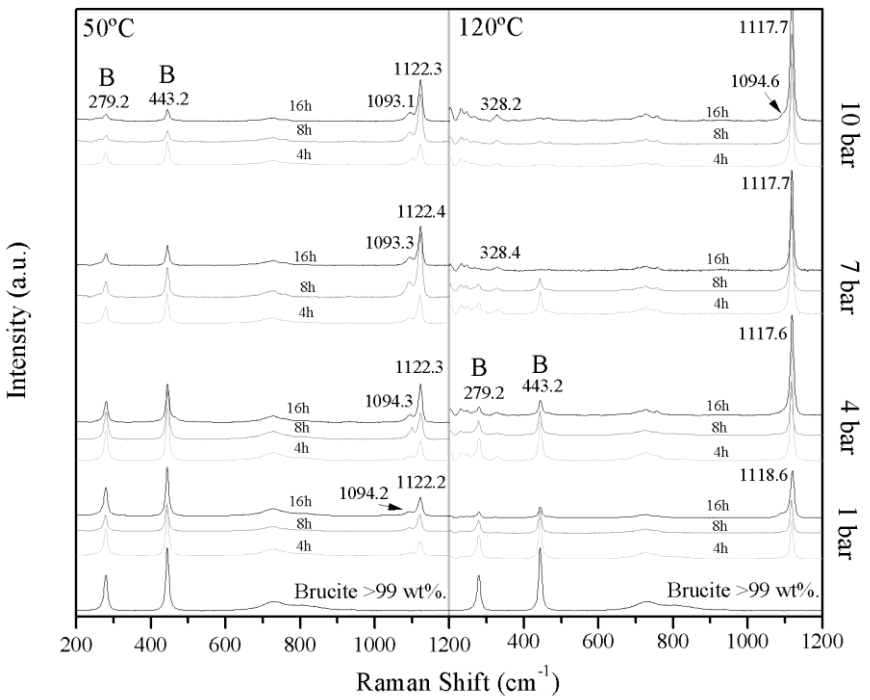

Fig. 5.7. Raman spectra of phase evolution after thermal treatments (50 – 120ºC) in the 1-10 bar range (RH > 90%) from 4 to 16 hours. B: Brucite. Figure from Rausis et al., 2020 [55].

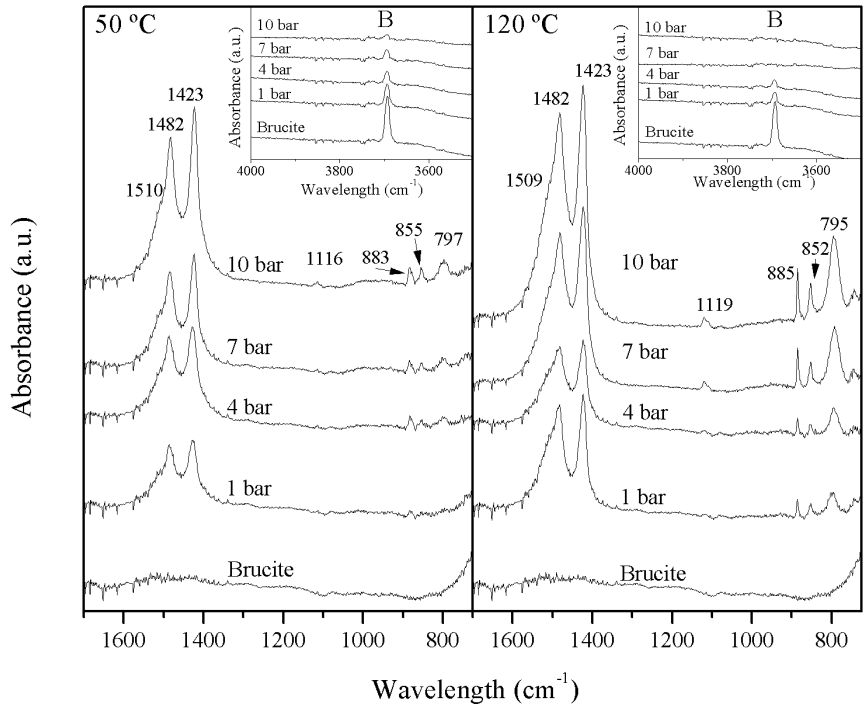

Fig. 5.8. FTIR-ATR of the starting and carbonated materials at 50 and 120ºC and 1 to 10 bar, maintained for 16h (RH = 100%). B: Brucite. Figure from Rausis et al., 2020 [55].

In view of this, an XRD analysis was carried out in order to provide more insights on the differentiation of the distinct carbonate phases formed upon brucite carbonation (Fig. 5.9). Brucite is clearly observed in the starting materials. Its relative intensity is progressively reduced upon carbonation from 1 to 10 bar. Characteristic XRD peaks of hydromagnesite are observed at 120ºC. At 50ºC, broader peaks with similar position to such of hydromagnesite are observed, probably suggesting the presence of a hydromagnesite-like phase, such as dypingite (Fig. 5.10; see also section 4.2.1), as also observed by Hövelmann et al., 2012 [373]. It has been reported that the formation of hydromagnesite might be kinetically inhibited by the preferential formation of highly hydrated Mg-carbonate phases at temperature ≤50ºC (such as nesquehonite and dypingite) [188,346,426].

Comparison of the baseline from the XRD patterns shows no differences between the starting material with the reaction products from 120ºC and 10 bar treatments (Fig. 5.10b). However, a plateau is observed from 24 to 54 2θº and with center near 31 2θº the XRD baseline when comparing the baselines between the carbonated products obtained at 50 and 120ºC and 10 bar (Fig. 5.10c). This plateau is very similar to the one observed for AMC with chemical composition $MgCO_3 \cdot nH_2O$ [401,427–429]. This strongly suggest the coexistence of an amorphous phase with poorly-ordered dypingite [49,405,423,428]. Analogous comparison was applied to the XRD results obtained at lower pressures, where the presence of this amorphous component is clearly observed (Fig. 5.11).

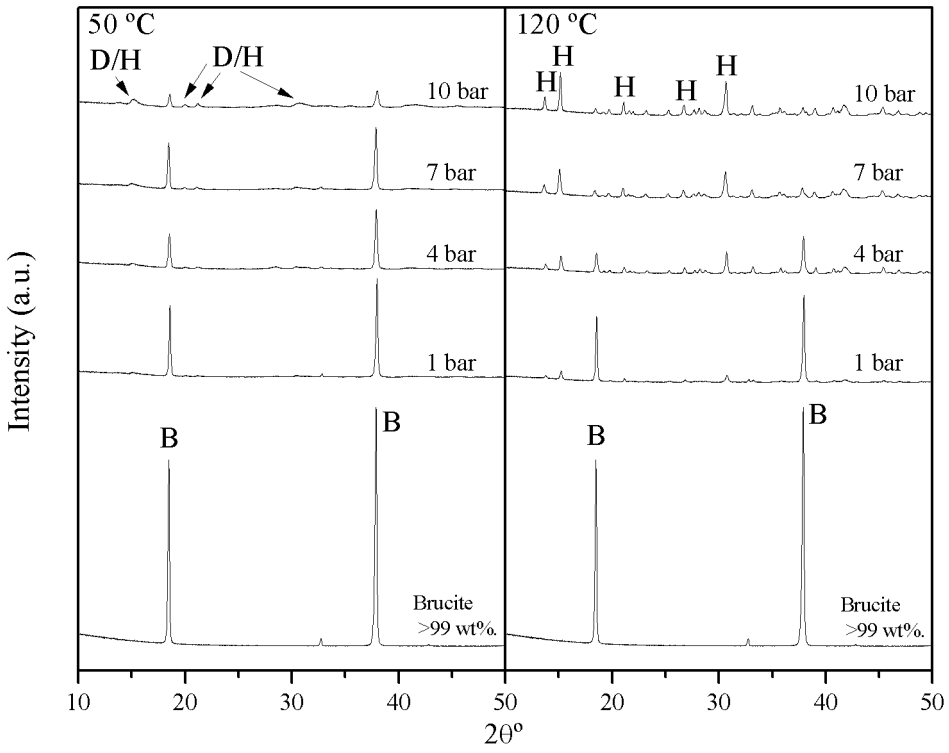

Fig. 5.9. XRD of samples after thermal treatments at 50 and 120ºC and 1 to 10 bar, maintained for 16h (RH > 90%). D/H: Dypingite/Hydromagnesite phase, H: Hydromagnesite, B: Brucite. Figure from Rausis et al., 2020 [55].

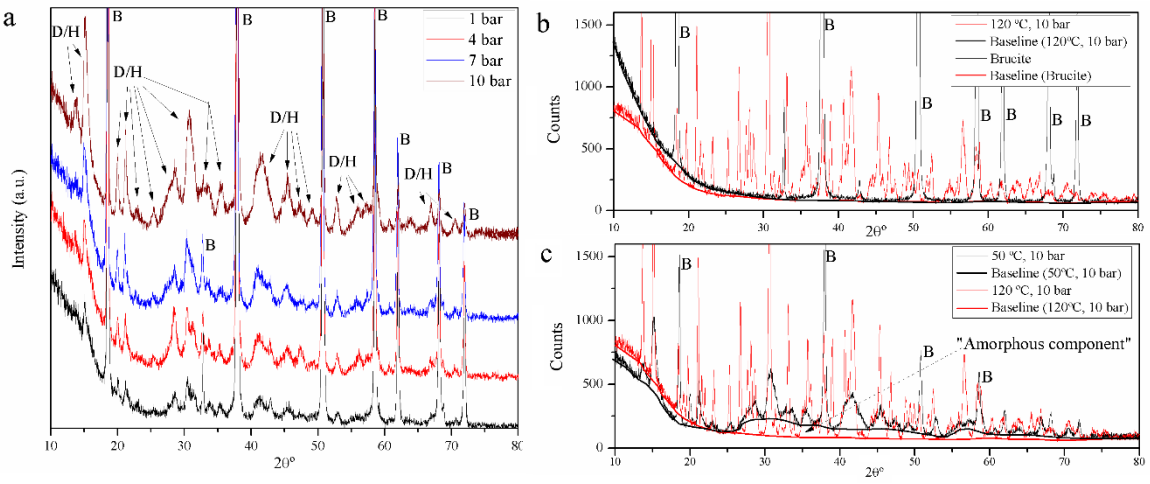

Fig. 5.10 (a) XRD data showing the low intensity and broad peaks of the reaction products from treatments at 50 and 120ºC and 1 to 10 bar, maintained for 16h (RH > 90%). D/H: Dypingite/Hydromagnesite phase, H: Hydromagnesite, B: Brucite. **(b)** XRD data baseline comparison between the starting materials and the reaction products obtained at 120ºC and 10 bar. **(c)** XRD data baseline comparison between the reaction products obtained at 50 and 120ºC, 10 bar. “Amorphous component” refers to the observed plateau between 24 to 54 2θº and with center near 31 2θº. Figure from Rausis et al., 2020 [55].

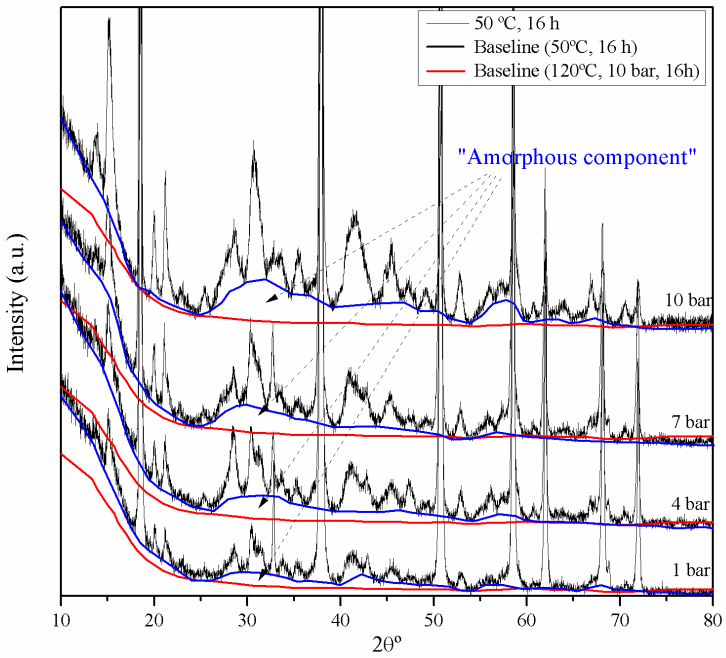

Fig. 5.11. XRD data showing the low intensity and broad peaks of the reaction products from treatments at 50 from 1 to 10 bar, maintained for 16h (RH > 90%) and their XRD baseline comparison with treatments performed at 120ºC and 10 bar. "Amorphous component" refers to the observed plateau between 24 to 54 2θº and with center near 31 2θº. Figure from Rausis et al., 2020 [55].

In order to provide more insight on the nature of the observed carbonates, comparison of FWHM and position of the ν_{1sym} Raman peaks as well as the two more intense XRD peaks of the carbonated products was carried out (Fig. 5.12). Calculated Raman and XRD data from 120ºC treatments fits very well with reference data for hydromagnesite, suggesting a well-defined structure. Moreover, the calculated data for the minor ν_{1sym} Raman peak at 1094.6 ± 0.1 cm^{-1} fits very well with reference data for magnesite. The presence of this peak is associated with the concomitant emergence of the 328.3 ± 0.1 cm^{-1} Raman peak, which is also characteristic of magnesite [380,383,384]. Moreover, only traces amounts of this later mineral were observed, which might explain its relative inexistence in the XRD patterns (Fig. 5.9, 120ºC treatments). The possible origin of magnesite is from the transformation of hydromagnesite or directly formed from brucite [193,203,382].

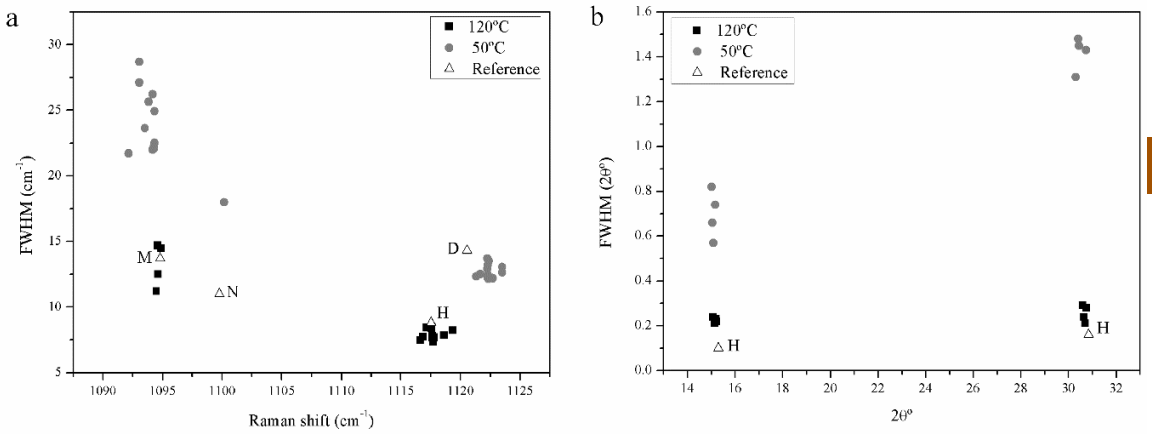

Fig. 5.12. FWHM vs peak position of **(a)** Raman ν_{1sym} peaks and **(b)** two more intense XRD peaks of the carbonated products reacted at 50 and 120ºC, 1-10 bar. M: Magnesite, N: Nesquehonite, H: Hydromagnesite, D: Dypingite. The FWHM and peak position of reference minerals were calculated from Lafuente, et al., 2015 [361]. Figure from Rausis et al., 2020 [55].

Calculated Raman data from 50ºC experiments shows that the 1122.3 ± 0.1 ν_{1sym} Raman peak fits well with reference data for dypingite. Accordingly, the XRD calculated data shows that the two more intense scattering peaks have very similar position to reference hydromagnesite but they are significantly wider, which is in agreement with a more disordered structure, as discussed previously (see section 2.1. and 4.2.1.). However, the 1093.3 ± 1.1 cm^{-1} ν_{1sym} Raman peak has a much higher FWHM than the represented carbonate phases as well as higher peak position variability, indicating that such phase might have a disordered structure. Some studies have previously observed this peak, and its presence is often related to dypingite [179,430]. Nonetheless, the semi-disordered to disordered structure of dypingite puts some challenges on acquiring good quality Raman spectra [430]. Moreover, the possible coexistence of semi-ordered dypingite-like phases with a possible amorphous phase further increases the difficulties on obtaining Raman spectra of pure dypingite phases. It remains unclear if the 1093.3 ± 1.1 cm^{-1} ν_{1sym} Raman peak belong to dypingite-like phases or it is prompted by the excitation of an amorphous Mg-carbonate phase [179,430]. The nature of the phase responsible for this peak is yet unknown, and therefore it will be referred to as unknown Mg-carbonate (UMC). UMC might be associated with the amorphous component observed with XRD (Figs. 5.10, 5.11).

Morphology of the formed Mg-carbonates have been studied with the aid of SEM (Fig. 5.13). The starting material is consists of well-defined characteristic hexagonal crystal of brucite (< 1µm; Fig. 5.13a), as also observed by Pang et al., 2011 [431]. Upon carbonation at 50ºC and 10 bar, sub-euhedral brucite grains are observed as well as an irregularly-shaped massive material (Fig. 5.13b). Such phase might be associated with UMC. Energy dispersive spectrometry (EDS) reveals that such material is a carbonate-phase, different from the carbon-free starting material (Fig. 5.14).

Characteristic hydromagnesite plates of maximum sizes of ~1 μm are observed at 120ºC and 4 bar (Fig. 5.13c), resembling features identified by Zhang et al., 2006 [181]. As pressure reaches 10 bar, fully developed hydromagnesite plates (Fig. 5.13d) are observed as well as minor rhombohedral magnesite (Fig. 5.13d, inset) [387].

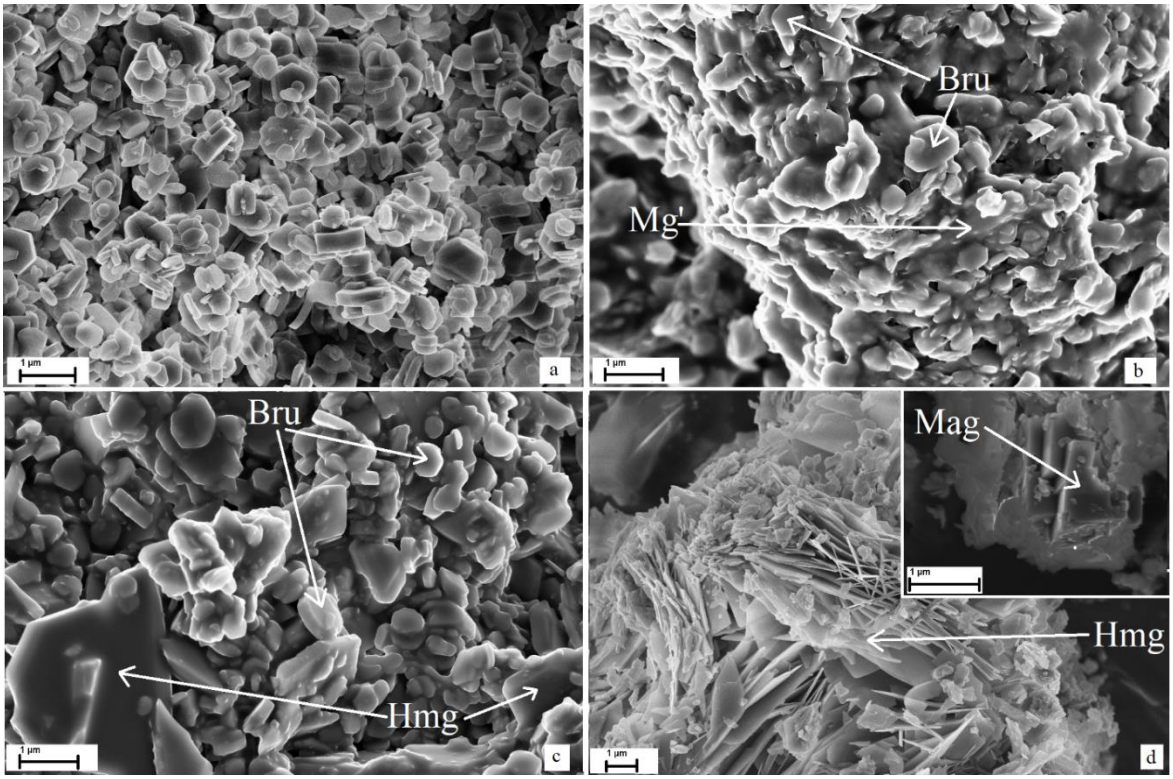

Fig. 5.13. Representative SEM images of the progressive carbonation stages, from (a) brucite starting material (euhedral hexagonal crystals ≤1μm) to (b) relict subhedral brucite immersed in a massive carbonate matrix formed at 50ºC, (c) well developed hydromagnesite plates (~1 μm) appearing at 120ºC with some residual brucite and (d) euhedral hydromagnesite plates (≤10 μm) and rhombohedral magnesite (≤1μm) formed at 120ºC and 10 bar. Bru: Brucite, Mg': massive irregularly shaped carbonate, Hmg: Hydromagnesite, Mag: Magnesite. Figure from Rausis et al., 2020 [55].

Carbonate products from 120ºC treatments are composed of crystalline carbonate phases and residual brucite. However, at 50ºC a possible amorphous phase and semi-ordered dypingite-like phases are observed. These later phases provide challenges for predicting and controlling the long-term CO_2 storage capacity, since the properties of such phases are not well stablished [391].

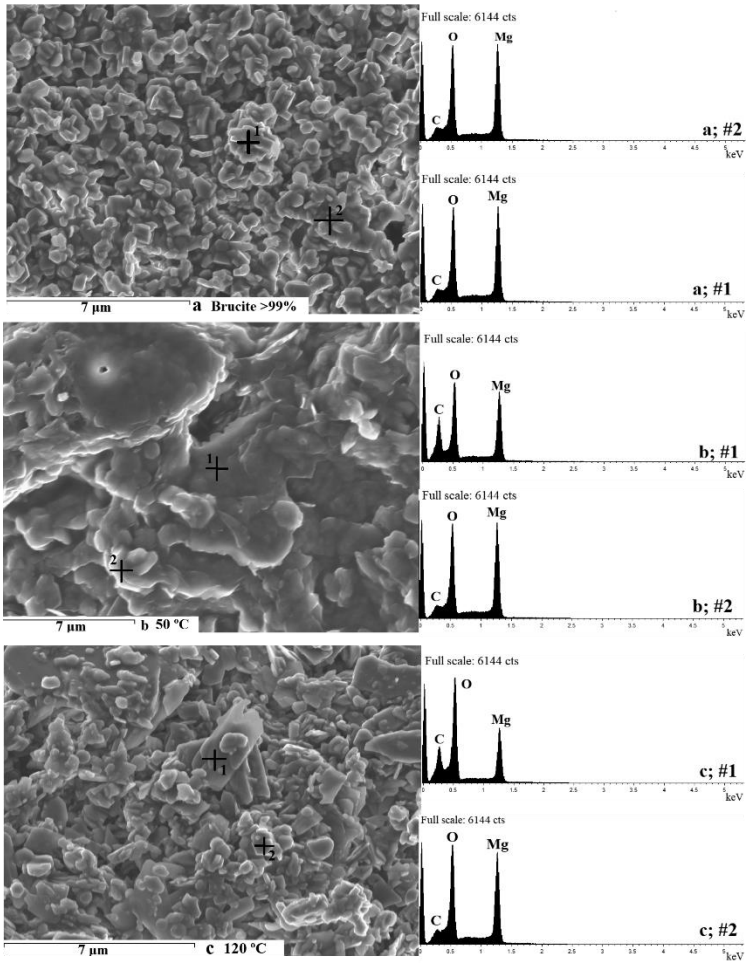

Fig. 5.14. SEM images (left) of the progressive carbonation stages from the solid products of the experiments at 4 bar (RH > 90%), maintained for 16h with varying temperature (50 and 120ºC). Qualitative EDS analysis (right) of single points shown on the SEM images **(a)** Brucite hexagonal crystals (≤1µm); **(b)** Residual brucite surrounded by a poorly crystalline material with no associated shape (50ºC); **(c)** Hydromagnesite plates and residual brucite (~1 µm; 120ºC). Figure from Rausis et al., 2020 [55].

5.2.1.1. Evolution of carbonate phases at 50ºC

Additional experiments were carried at 50ºC and 10 bar over from 7 min to 120h in order to provide additional insights on the identification of different carbonate phases (Fig. 5.15). Fig. 5.16 shows the variation of ν_{1sym} Raman peak for carbonate products as well as starting and residual brucite as a function of reaction time. After only 7 minutes, dypingite is already identified as well as UMC. From 15 min to 2 h, a new ν_{1sym} Raman peak with position 1101.1 cm^{-1} emerges (Fig. 5.15a) as well as concomitant XRD features (Figs. 5.15b, 5.17a), which are characteristic of nesquehonite [178,182]. UMC and dypingite were also identified (Figs. 5.15, 5.18). An analogous comparison of the XRD baselines from section 5.2.1. (Figs. 5.10, 5.11) shows the presence of an amorphous component in each of the carbonated products (Fig. 5.17b, c).

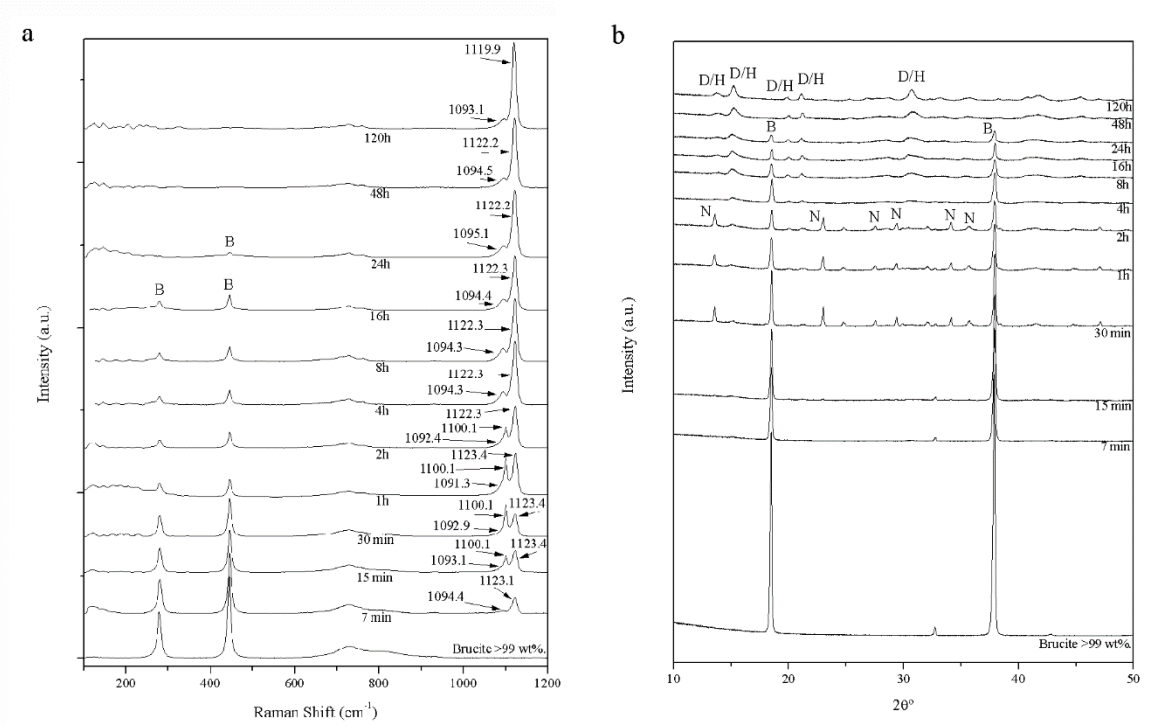

Fig. 5.15. (a) Raman and **(b)** XRD analysis of the carbonated product of reactions from 7 minutes to 120 hours. B: Brucite, D/H: Dypingite/Hydromagnesite phase, N: Nesquehonite. Figure from Rausis et al., 2020 [55].

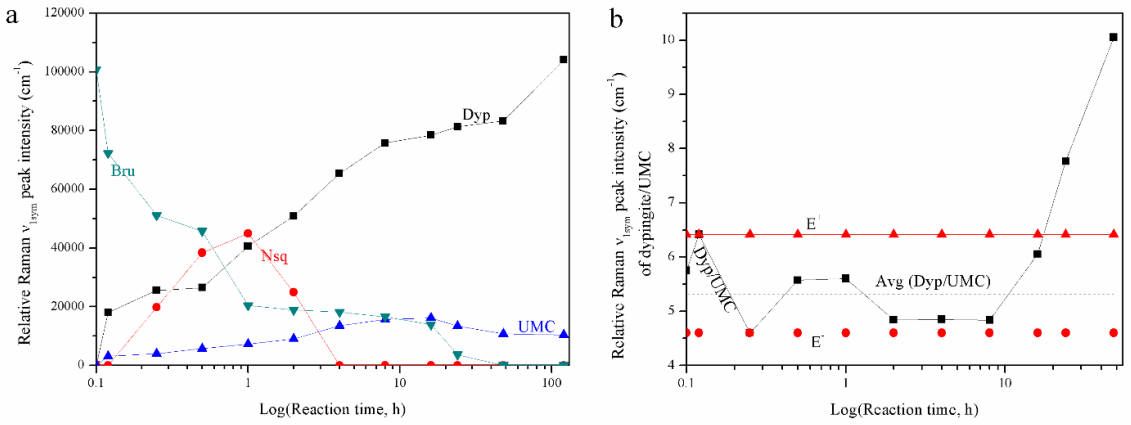

Fig. 5.16. (a) Raman semi-quantitative intensities of the Raman characteristic peaks of different phases **(b)** Raman semi-quantitative ratio intensities of the characteristic Raman peaks of Dypingite/UMC. Bru: Brucite, Nsq: nesquehonite, Dyp: dypingite, UMC: "Unknown Mg carbonate", Avg(Dyp/UMC) shows the average Dypingite/UMC Raman v_{1sym} peak intensity ratio of the experiments carried from 7 minutes to 24 hours, E^+ and E^- represent the estimated error of the Dypingite/UMC Raman v_{1sym} peak intensity ratio considering both highest and lowest ratio value within the 7 minutes to 24 hour treatments, respectively. Figure from Rausis et al., 2020 [55].

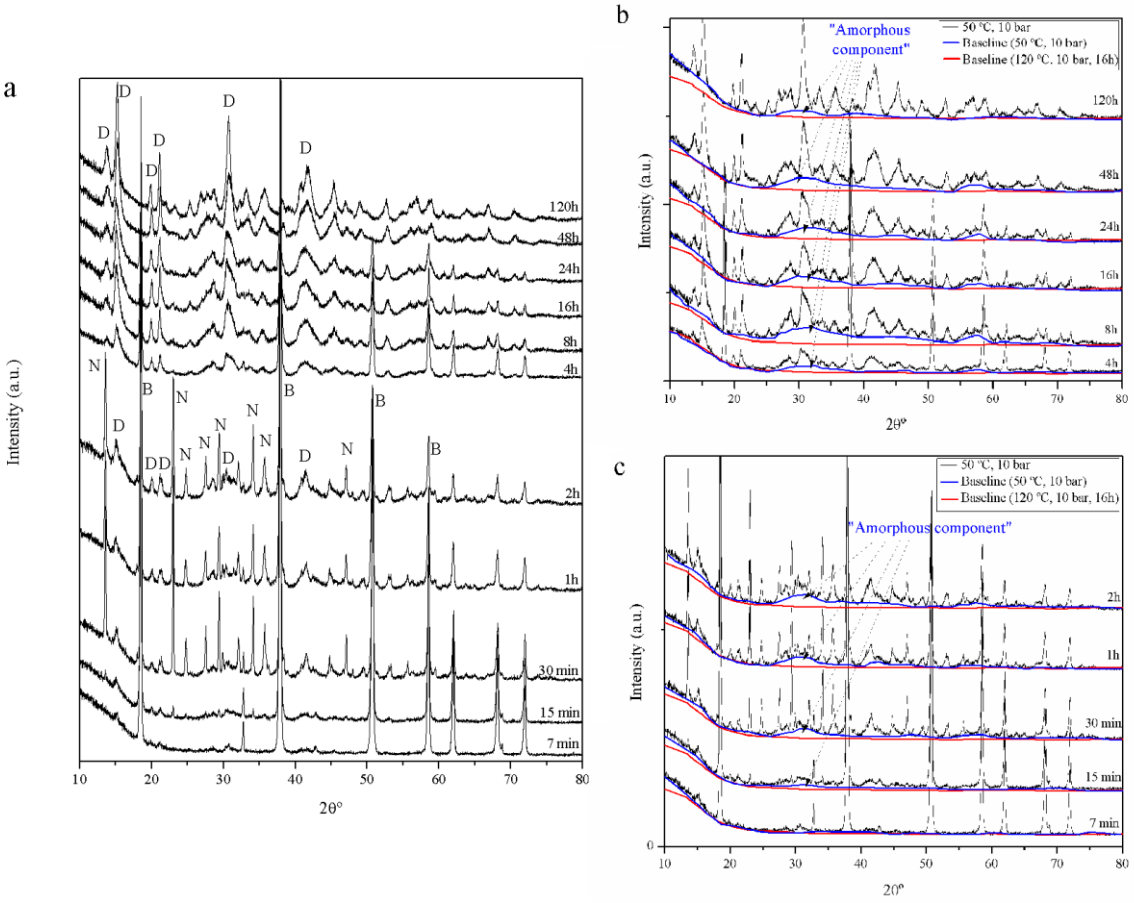

Fig. 5.17. (a) XRD data showing the low intensity and broad peaks of the reaction products from treatments at 50 and 10 bar, maintained from 7 minutes to 120 hours (RH > 90%). D/H: Dypingite/Hydromagnesite phase, H: Hydromagnesite, B: Brucite; XRD data baseline comparison between the reaction products from **(b)** 4 to 120 hour treatments and **(c)** 7 minutes to 2 hour treatments with reaction products obtained at 120ºC and 10 bar. "Amorphous component" refers to the observed plateau between 24 to 54 2θº and with center near 31 2θº. Figure from Rausis et al., 2020 [55].

Dypingite-like phases and UMC are the only identified phases at 4 hours of reaction, implying that nesquehonite is precursor of one of both phases (Figs. 5.15, 5.17). It is known the precursor nature of nesquehonite to form hydromagnesite or hydromagnesite-like phases [179,180]. Such transformation may occur via an amorphous precursor [376]. It remains uncertain the if nesquehonite was formed upon the crystallization of an amorphous precursor or was directly formed from brucite. However, it is clearly observed that nesquehonite is precursor of UMC and/or less hydrated dypingite-like phases.

A complete carbonation of brucite is observed after 48h, as evidenced by the lack of residual brucite peaks. However, the intensity of the ν_{1sym} Raman peak keeps increasing as UMC and the amorphous component observed with XRD are diminishing. Calculated dypingite/UMC ν_{1sym} Raman peak intensity ratio exhibits a similar formation rate for both dypingite and UMC at ≤24h (Fig. 5.16).

However, at longer reaction times (≥48h), dypingite formation is significantly increased relative to UMC. This might suggest that UMC is nourishing the late-growth of dypingite. Moreover, the differential behavior also suggests that UMC ν_{1sym} Raman peak is not characteristic of dypingite, as Hopkinson et al., 2012 [179] suggested, instead these two peaks might be respective to two distinct phases.

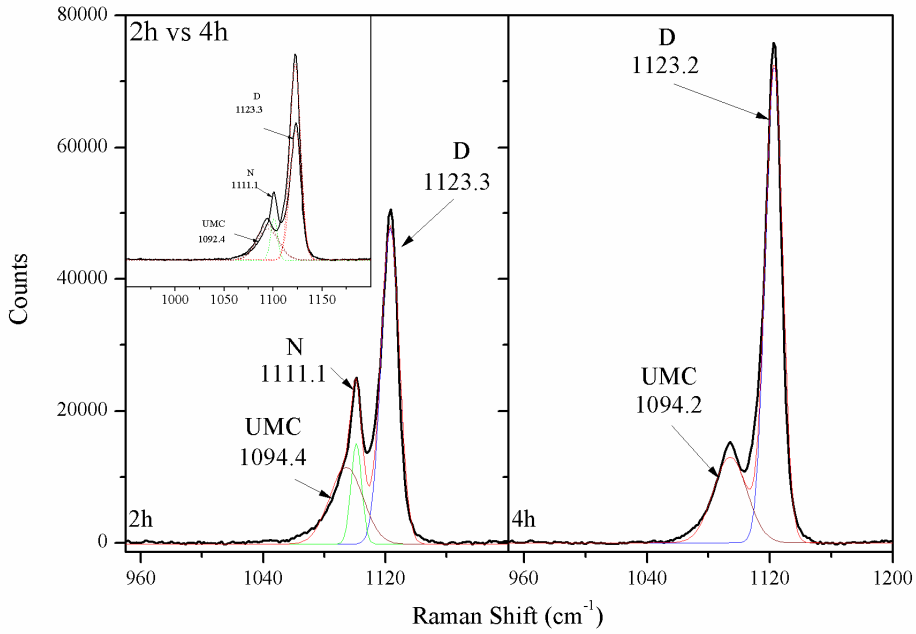

Fig. 5.18. Deconvoluted Raman ν_{1sym} peak comparison between the reaction products obtained from treatments at 50ºC, 10 bar for (left) 2 and (right) 4 hours. Inlet shows the overlapping and differentiating features among both analyses. N: nesquehonite, D: dypingite, UMC: "Unknown Mg Carbonate". Figure from Rausis et al., 2020 [55].

Brucite carbonation under these experimental conditions probably proceeds through the formation of an amorphous precursor, followed by the progressive crystallization of this latter phase to highly-disordered dypingite, which over time it becomes more structurally organized. This behavior is consistent with the Ostwald step rule [393].

Fig. 5.19 shows the FWHM vs peak position comparison between ν_{1sym} Raman peak and the two more intense X-ray scattering peaks of the carbonate products. Calculated data for the peaks associated with nesquehonite fits very well with the reference data. Dypingite peaks are progressively approaching the reference data for hydromagnesite as the carbonation reaction proceeds, indicating that dypingite becomes structurally more ordered and with less molecular water per unit. This might indicate a slow and progressive transformation of highly-disordered dypingite to semi-ordered dypingite and finally to hydromagnesite. Calculated UMC data is observed to have similar position as observed in Fig. 5.12 (1093 ± 2.05 cm^{-1} ν_{1sym} Raman peak).

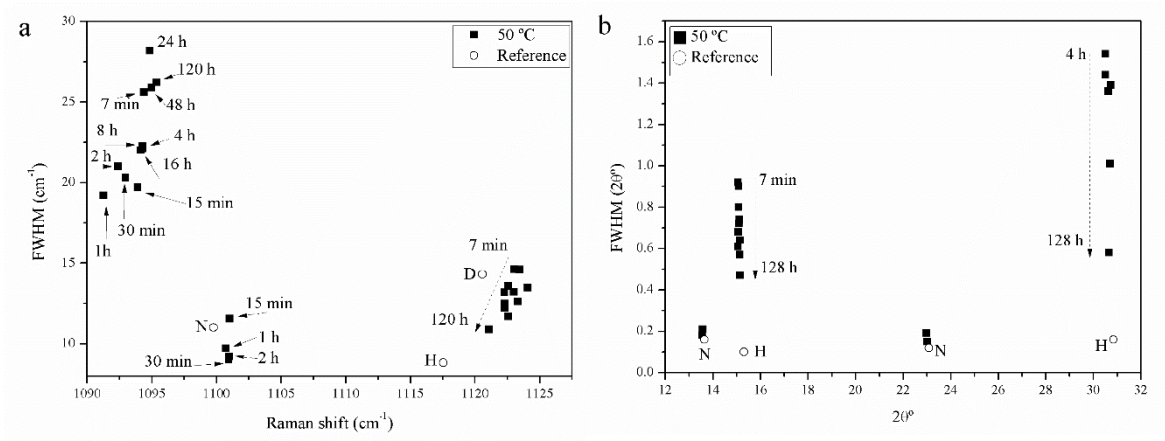

Fig. 5.19. FWHM vs peak position of **(a)** Raman ν_{1sym} peaks and **(b)** two more intense XRD peaks of the carbonated products reacted at 50 ºC, 10 bar from 7 minutes to 120 hours. N: Nesquehonite, H: Hydromagnesite, D: Dypingite. The FWHM and peak position of reference minerals were calculated from Lafuente, et al., 2015 [361]. Dashed line represents the evolution of different phases over time. Figure from Rausis et al., 2020 [55].

Previous studies have identified the rapid formation of AMC with Raman, as reported by the emergence of ν_{1sym} Raman peak with position 1082 cm^{-1} and FWHM 8cm^{-1} [382]. However, this peak have a very low FWHM (often associated with crystalline phases [423]) and its peak positions is lower from any known Mg-carbonate phase and very similar to Ca-carbonate phases, which often have a lower ν_{1sym} Raman peak position than Mg-carbonates [380]. Moreover, it should be noted that there are several disordered precursors and unnamed Mg-carbonate phases, which might be forming and evolving differently in this study and in Montes-Hernandez et al., 2016 [382].

A SEM study was performed to provide additional insights on the evolution of the carbonation reaction at 50ºC (Fig. 5.20). The reaction products obtained at 30 minutes form agglomerated of platy crystals, characteristic of dypingite (≤1μm) [188,386] coexisting the hexagonal brucite crystals (Fig. 5.20a). Large rod crystals (~ 10μm), characteristic of nesquehonite, are observed after 1h of reaction. Moreover, this crystal have etch pits and overgrowths of platy dypingite crystals, producing a "house of cards" texture (Fig. 5.20b) [179,432]. Well developed "house of cards" texture is observed at 2 hours of reaction (Fig. 5.20c). On the residual uncovered nesquehonite rod is observed a massive carbonate layer with an irregular interface between both minerals (Fig. 5.20c inset). This layer has a similar morphology to that observed by an hydrated AMC identified by Zhang et al., 2019 [425]. This might suggest that such layer is amorphous and might be related with the presence of UMC.

The "house of cards" texture have been previously observed and has been interpreted as resulting from a dissolution-recrystallization self-assembly growth mechanism. Moreover, the overgrowths of dypingite eases the nucleation of more dypingite crystals [179,432]. It is probable that upon dissolution of nesquehonite a hydrated AMC is formed, which then is recrystallized to highly-

disordered dypingite [179]. Such behavior is consistent with the Ostwald step rule [393]. Fig. 5.20d shows a former nesquehonite rod-like structure which has been replaced by dypingite plate and its partially covered by a massive and probably amorphous carbonate layer.

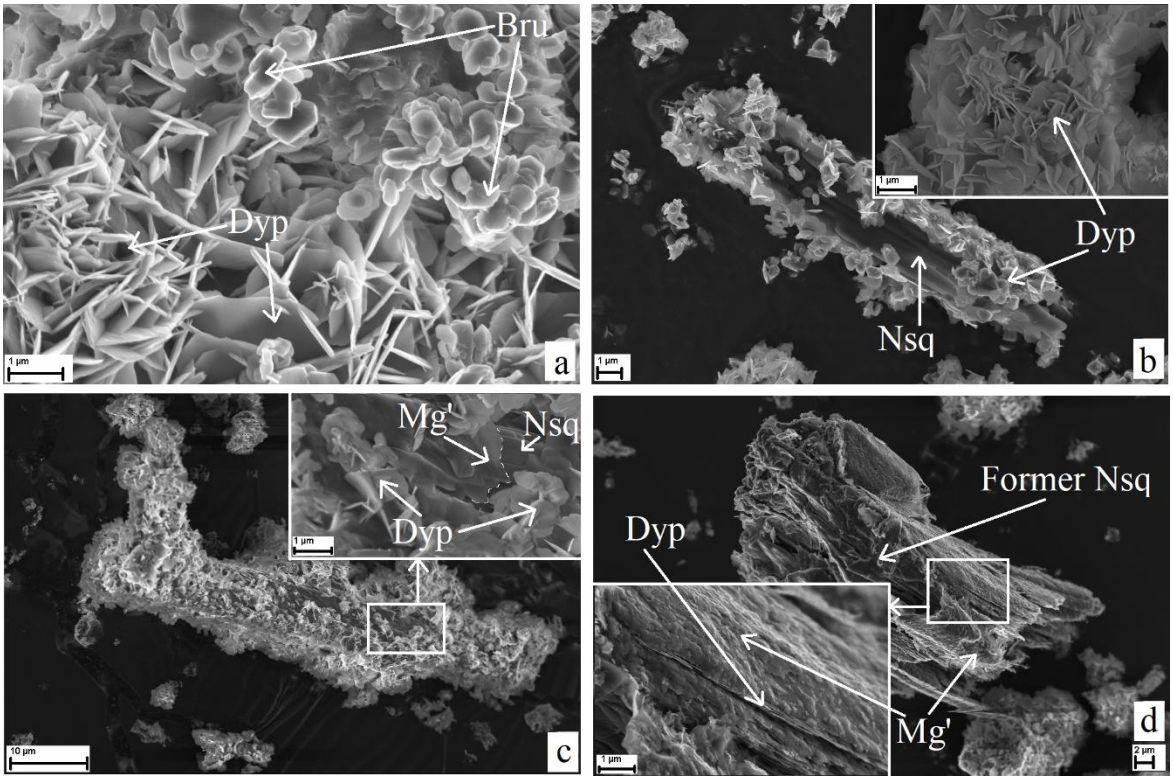

Fig. 5.20. Representative SEM images of the progressive carbonation stages performed at 50ºC and 10 bar. **(a)** brucite euhedral hexagonal crystals (≤1µm) and dypingite characteristic plates (30 min); **(b)** nesquehonite rod crystal (~10µm) showing etch pits and overgrowths of platy dypingite crystals ~10µm, producing a "house of cards" texture (1h); **(c)** well developed "house of card texture", inlet shows a naked section of nesquehonite being covered by a massive and irregularly shaped carbonate (Mg'; 2h); **(d)** former nesquehonite rod that has been replaced with dypingite plates, which itself is covered by a massive carbonate matrix (4h). Bru: brucite, Nsq: nesquehonite, Dyp: dypingite and Mg': massive irregularly shaped carbonate. Figure from Rausis et al., 2020 [55].

5.2.2. Thermogravimetric analysis

Brucite carbonation yield and carbonate contents were assessed with the aid of TGA analysis. Fig. 5.21, 5.22 and 5.23 shows the dTG profiles of the reaction products obtained using CC at 50 and 120ºC for 16, 8 and 4h.

The starting material ,brucite, dehydration occurs from 275 to 420ºC, losing 31wt% of its total mass, in agreement with its stochiometric water content [204,264]. The dehydration and decarbonation of hydromagnesite (formed during 120ºC treatments) were observed to occur in the temperature range of 165-340ºC and 350-550ºC, respectively, which is consistent with previous studies [365,394,395].

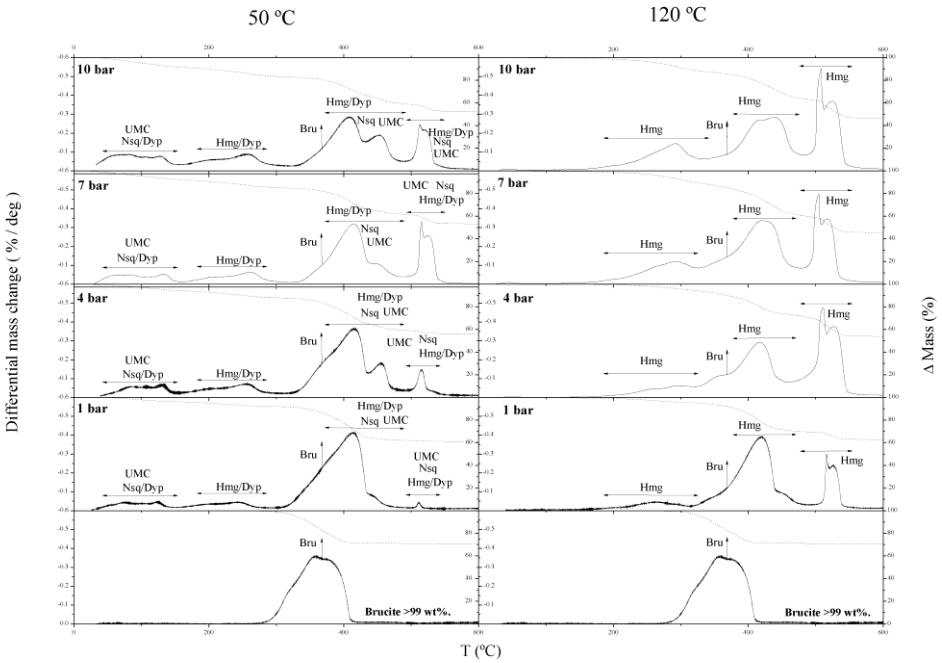

Fig. 5.21. Differential thermogravimetric analysis (dTG) of mass change upon thermal decomposition of carbonation products at 50 **(left)** and 120ºC **(right)**, from 1 to 10 bar carried during 16 hours using concentrated CO_2. Solid and dotted curves represent, respectively, the differential change (mass % per degree) and the mass variation upon thermal decomposition. Thermal decomposition temperature ranges of brucite (bru), nesquehonite (Nsq), hydromagnesite (Hmg), dypingite (Dyp) and possibly "Unknown Mg-carbonate" (UMC) are indicated with double-ended arrows. The dehydration of such phases occurs from room temperature to 270 ºC) and decarbonation (350-550 ºC). Figure from Rausis et al., 2020 [55].

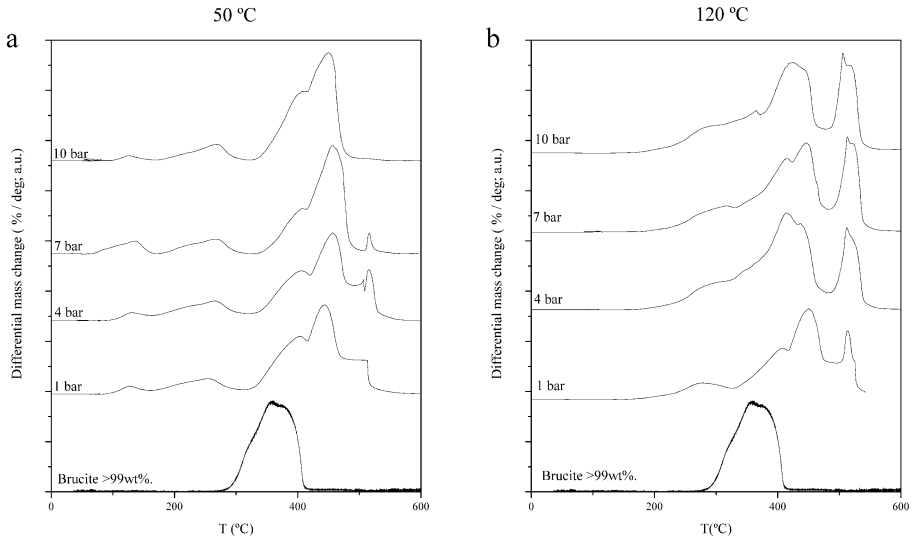

Fig. 5.22. Differential thermogravimetric analysis (dTG) of mass change upon thermal decomposition of carbonation products at 50 **(left)** and 120ºC **(right)**, from 1 to 10 bar carried during 8 hours using concentrated CO_2. Figure from Rausis et al., 2020 [55].

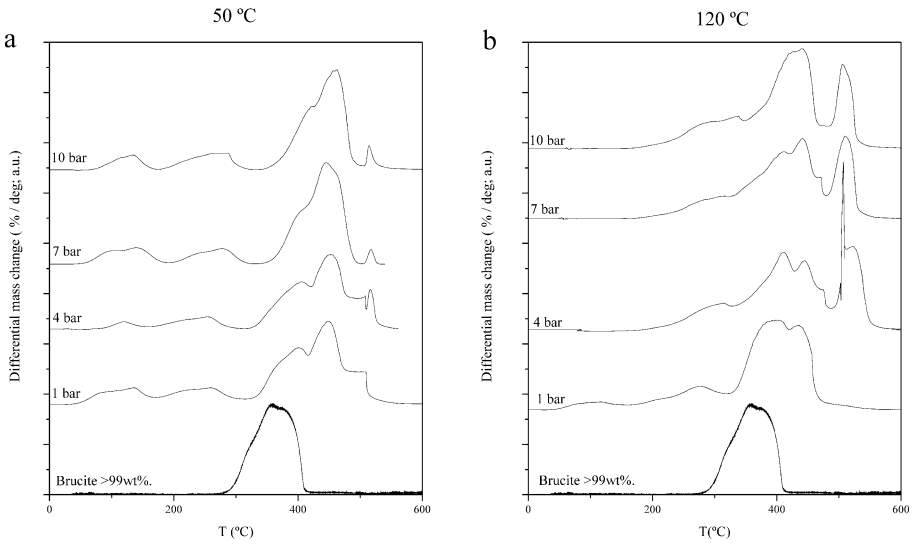

Fig. 5.23. Differential thermogravimetric analysis (dTG) of mass change upon thermal decomposition of carbonation products at 50 **(left)** and 120ºC **(right)**, from 1 to 10 bar carried during 4 hours using concentrated CO2. Figure from Rausis et al., 2020 [55].

Reaction products obtained at 50ºC exhibit and additional dehydration temperature range between rT to 150ºC. This mass loss might be interpreted as the dehydration of dypingite-like phases [398–400], nesquehonite [396] and possibly an amorphous carbonate phase with the same decomposition behavior as nesquehonite as observed by Zhang et al., 2018 [425]. Moreover, further dehydration occurs between 165 and 270ºC associated with the dehydration of hydromagnesite and dypingite-like phases.

The decarbonation and dehydration of all the identified and possible carbonate phases occurs between 350 and 550ºC and rT to 340ºC, respectively [365,394–396,398–400,425]. Therefore, it is easy to determine the CO_2 and H_2Owt% of the reaction products. However, the CO_2 and H_2Owt% content of each phase cannot be determined due to overlapping features. Remnant brucite is also identified in the reaction products for both 50 and 120ºC treatments. The dehydration of this phase overlaps with the decarbonation of the identified and possible carbonate phases. Therefore, the overlapping mass los associated with the dehydration of brucite should not be taken into account in order to estimated correctly the CO_2 wt% of the carbonate products. This was performed following the procedure explained in section 4.2.5 (Fig.4.8).

Fig. 5.24 shows the dTG patterns of the reaction products from experiments carried at 50ºC, 10 bar from 7min to 120h. Dehydration of the carbonate phases occurs between rT to 380ºC. The phases responsible for such behavior are nesquehonite, dypingite-like phases and UMC. However, discrepancies between the dehydration temperatures of dypingite-like phases are reported in

literature [398–400]. This might be attributed to the possible coexistence of dypingite phases with different level of structural order and hydrated amorphous phases.

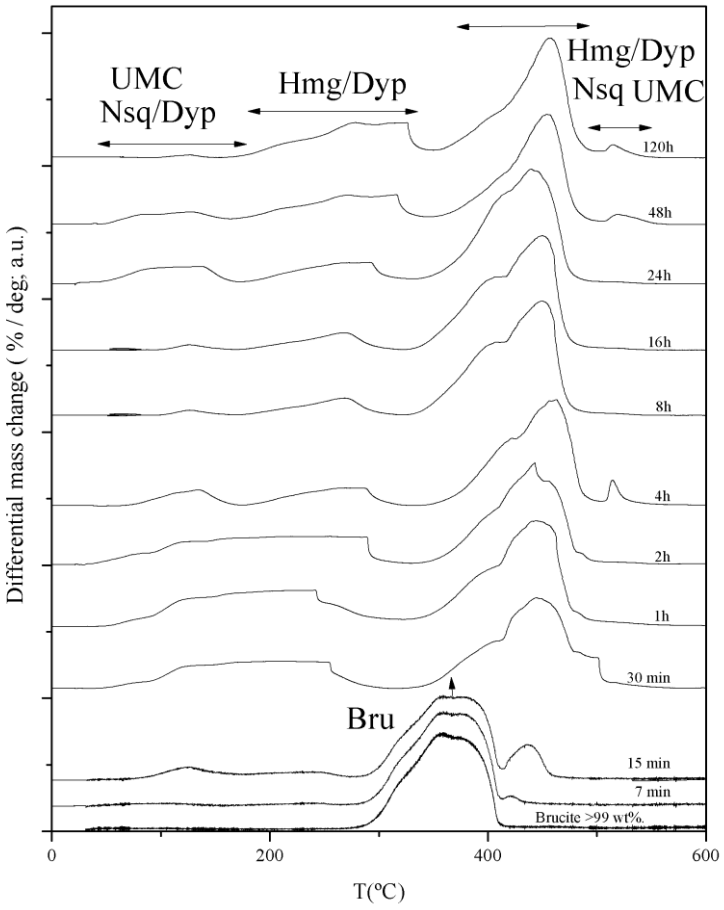

Fig. 5.24. Differential thermogravimetric analysis (dTG) of mass change upon thermal decomposition of carbonation products obtained at 50ºC, 10 bar during 7 minutes to 120 hours using concentrated CO_2. Thermal decomposition temperature ranges of brucite (bru), nesquehonite (Nsq), hydromagnesite (Hmg), dypingite (Dyp) and possibly "Unknown Mg-carbonate" (UMC) are indicated with double-ended arrows. The dehydration of such phases occurs from room temperature to 270 ºC) and decarbonation (350-550 ºC). Figure from Rausis et al., 2020 [55].

The mass loss from rT- 180ºC is generally decreasing as the mass loss from 180-380ºC increases. Comparison of Raman, XRD and TGA suggest that there is a relation between the initial mass loss (rT-180ºC) and the relative peak intensity of UMC ν_{1sym} Raman peak as well as with the amorphous component. Therefore, UMC associated with the observed amorphous component might have dehydration temperatures between (rT-180ºC), which are also characteristic of nesquehonite [396]. Zhang et al., 2018 have reported that a hydrous AMC with similar dehydration behavior as nesquehonite. Moreover, White et al., 2014 [424] reported a hydrous AMC with very similar water content as nesquehonite.

5.2.2.1. CO_2: H_2O wt% ratio

The CO_2:H_2O wt% ratio was possible to estimate since the dehydration and decarbonation Mg-carbonate phases have different temperature ranges. Fig. 5.25 shows the CO_2:H_2O wt% ratio of the carbonated products discussed on section 5.2.1 (Fig. 5.25a) and 5.2.1.1 (Fig. 5.25b). Reaction products obtained at 120ºC have water content similar to stoichiometric hydromagnesite (Fig. 5.25a). The overall water content of all the carbonate phases observed at 50ºC generally have the hydration level of dypingite, and in some cases it reaches the hydration level of nesquehonite.

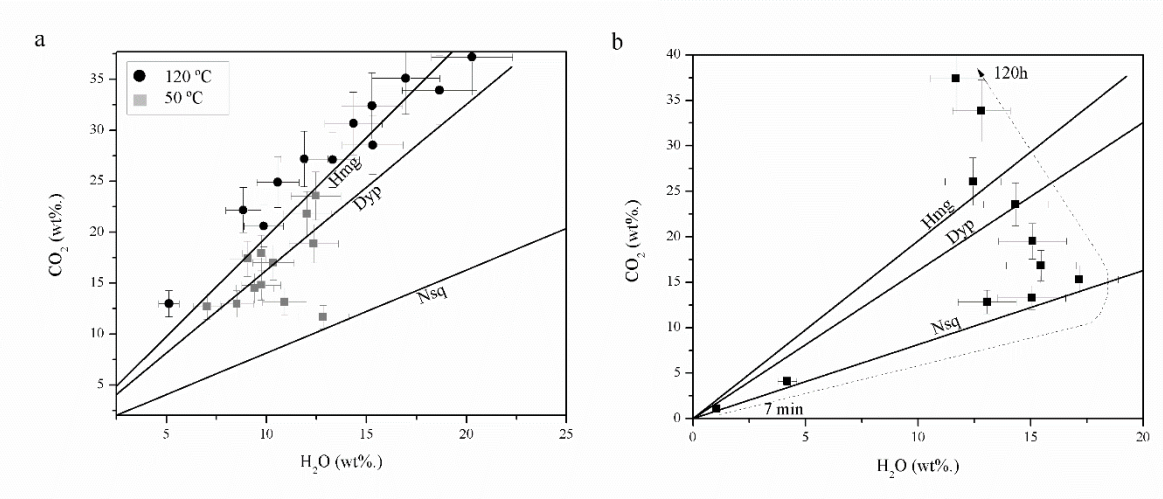

Fig. 5.25. (a) CO_2:H_2O (wt%.) ratios as estimated with TGA of the solid product of reaction at (a) 50 – 120 ºC, 1 - 10 bar from 4 to 16 hours and at **(b)** 50ºC, 10 bar, 7 minutes to 120 hours. Error bars were estimated on the average of three different experiments. Dashed line represents the evolution of the CO_2:H_2O (wt%.) ratio from reaction performed at 7 minutes until 120 hours. Figure from Rausis et al., 2020 [55].

Moreover, carbonate products from 50ºC, 10 bar from 7min to 120h treatments (Fig. 5.25b) shows that early carbonate products have a hydration level very similar to stoichiometric nesquehonite. However over longer reaction times, they start to dehydration, reaching hydration levels below stoichiometric hydromagnesite (48 to 120h). Such partial dehydration is consistent with the progressive structural organization of dypingite-like phases (Fig. 5.19) as well as the consumption of UMC and the amorphous component. This suggest that dypingite-like phases underwent a cell shrinkage as the reaction proceeded with less waters of crystallization.

5.2.3. CC experiments summary

The identified highly-ordered with semi-ordered dypingite-like phases are probably coexisting with an amorphous component. Comparison of TGA, Raman, XRD and SEM analysis of the reaction products suggests that the wide UMC ν_{1sym} Raman peak is strongly associated with the observed amorphous component, and it might have dehydration behavior akin to nesquehonite as well as similar composition. It remains unclear if early dypingite was formed from this probable hydrous AMC or was formed directly from brucite. However, it was observed that the possible AMC

nourished the late growth of dypingite. An analogous behavior was reported during the transformation of AMC to hydromagnesite-like phases [401,413].

The possible AMC was observed to play an important role during the formation and evolution of dypingite-like phases. White et al., 2014 [424] suggested that the atomic structure of AMC is heterogeneous, where there are regions rich in Mg^{2+} and CO_3^{2-} interspersed with H_2O-rich regions (Fig. 5.6). Water molecules within this H_2O might be relatively easy to be removed from the disordered matrix. As discussed by the authors, this property might play a crucial role on the dehydration mechanisms responsible to a prograde transition of hydrous AMC to anhydrous AMC. Based on the observation for this study, such heterogeneity might play an important role on the crystallization of highly-disordered dypingite-like phases, since the region rich in Mg^{2+} and CO_3^{2-} might tend to have a more organized structure and less tightly bound water might tend to scape, resulting in the progressively and partial crystallization of highly-disordered dypingite-like phases. Moreover, the partial crystallization of dypingite only accounts for partial dehydration of AMC, which is consistent with the slow dehydration nature of Mg^{2+}[413].

Over extended reaction times, a progressive and slow shrinkage of dypingite occurs as controlled by the on-going partial dehydration, producing a more ordered structure. This slow process might be resulting in the slow transition between dypingite-like phases to hydromagnesite. The kinetics of such dehydration are controlled by the dehydration nature of Mg^{2+}[413]. Therefore, increasing the temperature will significantly enhance such transformation [408]. This might explain the appearance of only hydromagnesite at 120ºC, since it is the last step of a progressive crystallization from an AMC.

On the other hand, the early formation of nesquehonite remains unclear. However, nesquehonite also played an important role on the crystallization of dypingite and possibly AMC via dissolution-reprecipitation self-assembly growth mechanism. The transition od nesquehonite to dypingite-like phases is more likely to have a precursor intermediate. Such processes are consistent with the Ostwald rule. The proposed reaction mechanism is shown in Fig. 5.26.

Research on brucite carbonation in the presence of steam have speculated on the formation of hydrated AMC coexisting with Mg-carbonate minerals [203,204,263]. However, several challenges are associated with the characterization of coexisting amorphous with crystalline phases [401,408,419]. Our results provide new insights on the formation and evolution of Mg-carbonate phases upon accelerated carbonation of brucite at moderately low temperature and pressure conditions. A hydrated AMC was probably formed upon carbonation and played an important role on the evolution of the observed carbonate phases.

It is known that amorphous carbonate precursors play a key role on the nucleation of different hydrated and anhydrous crystalline carbonates. An example is the formation of MHC. Fukushi et

al., 2017 [401] that AMC coats MHC surface. Such process inhibits the ability of MHC to form spherical morphology as well as it prevents the transformation of MHC to more stable Ca-carbonate phases (see section 5.1.1). Recent research highlighted the importance of amorphous precursor and their crucial role for the nucleation of specific phases, such as CCHH [423]. Understanding the reaction steps and mechanisms during accelerated carbonation might provide insightful observations in order to enhance such reactions ways as well as to selectively nucleate preferential phases with the aim of providing long-term safe CO_2 disposal.

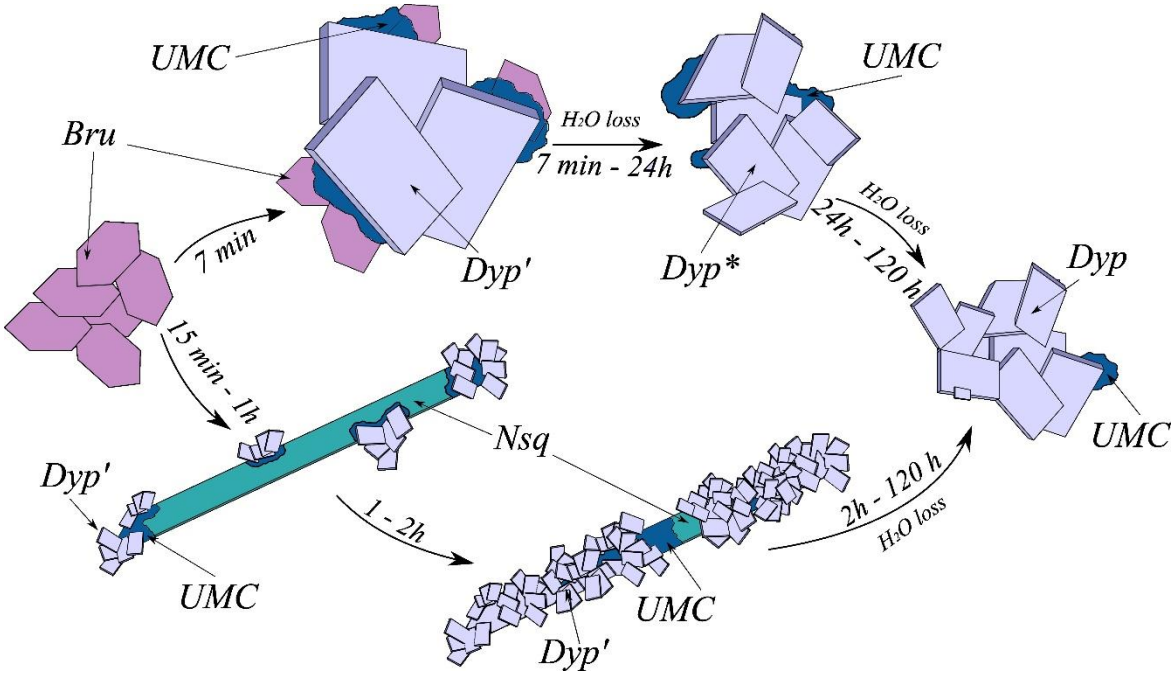

Fig. 5.26. Scheme of the carbonate phases evolution during carbonation reactions performed at 50ºC, 10 bar during 7 minutes to 120 hours. Bru: Brucite, Dyp', Dyp* and Dyp represent the evolution of dypingite-like phases from early highly disordered to late semi-ordered, Nsq: nesquehonite, UMC: possible amorphous Mg carbonate that might have played an important role on the nucleation and/or partial crystallization of semi-ordered dypingite. Figure from Rausis et al., 2020 [55].

5.2.4. Flue gas experiments

Fig. 5.27 shows the solid product of reactions carried at 120ºC using simulated flue gas (SFG) at 1 to 10 bar during 4 to 16h. It is observed a similar mineralogy to that observed when using CC, being hydromagnesite the only identified phase, as also evidence by the FHWM and peak position comparison (Fig. 5.28). Brucite was identified after each set of experiments. Trace amounts of hydromagnesite were observed from experiments carried at atmospheric pressure (Fig. 5.27a), which explain the relative inexistence on the XRD patterns (Fig. 5.27b). Pressure increase (from 1 to 10 bar) significantly increases the carbonation yield, as evidence by the progressive formation of hydromagnesite.

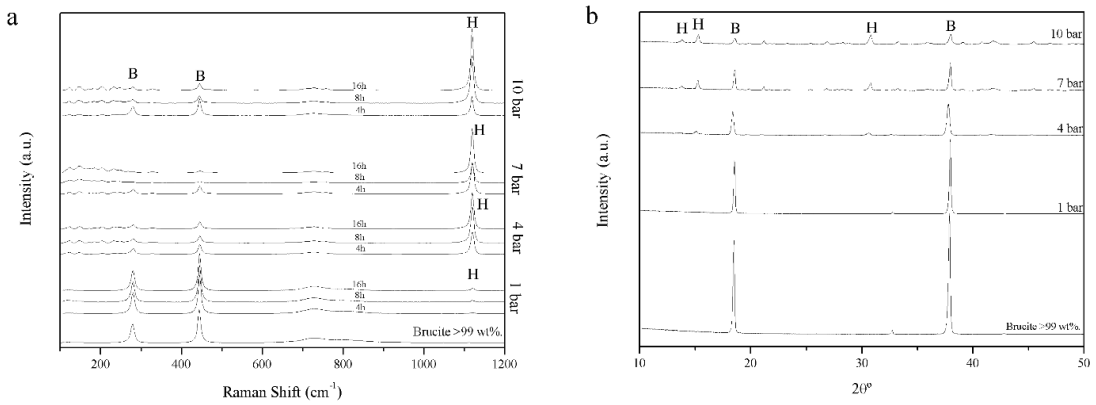

Fig. 5.27 (a) Raman and **(b)** XRD analysis of phase evolution treatments at 120ºC, 1 and 10 bar using SFG. H: hydromagnesite, B: Brucite. Figure from Rausis et al., 2020 [55].

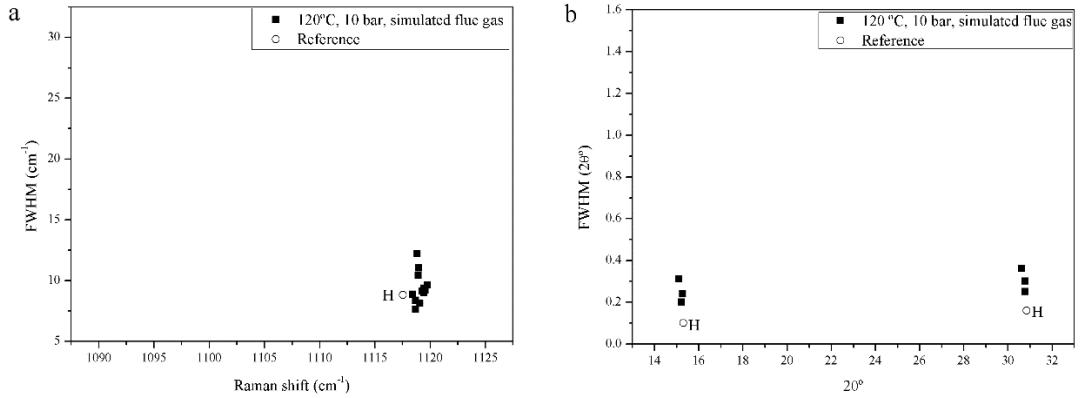

Fig. 5.28. FWHM vs peak position of **(a)** Raman v_{1sym} peaks and **(b)** two more intense XRD peaks of the carbonated products reacted at 120ºC, 10 bar from 4 to 16 hours using simulated flue gas. H: Hydromagnesite. The FWHM and peak position of reference minerals were calculated from Lafuente, et al., 2015 [361]. Figure from Rausis et al., 2020 [55].

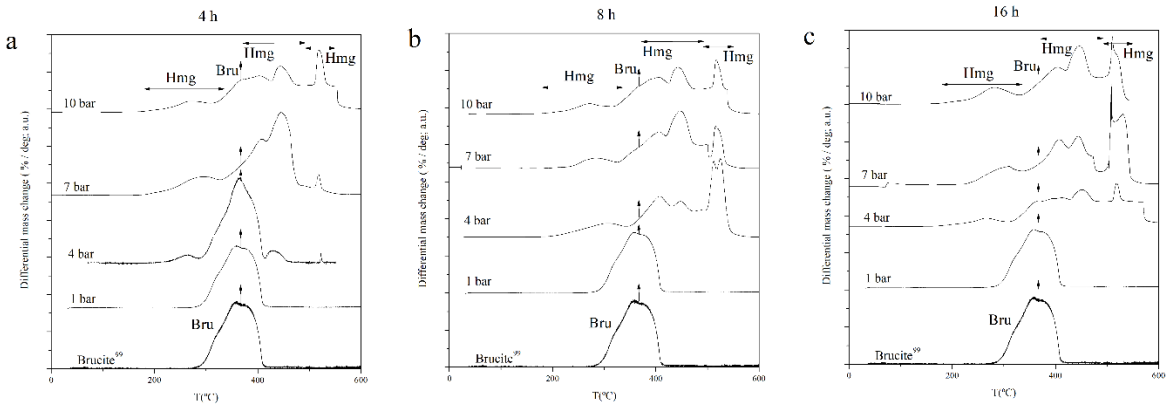

Fig. 5.29. Differential thermogravimetric analysis (dTG) of mass change upon thermal decomposition of carbonation products at 120ºC, from 1 to 10 bar carried during **(a)** 4, **(b)** 8 and **(c)** 16 hours using simulated flue gas. Thermal decomposition temperature ranges of brucite (bru) and hydromagnesite (Hmg) are indicated with double-ended arrows. Figure adapted from Rausis et al., 2020 [55].

Fig 5.29 shows the dTG data obtained from SFG experiments. The decomposition of residual brucite and hydromagnesite are observed, following observations from section 5.2.2. Analogously to CC experiments, CO_2:H_2O ratio was possible to estimate due to the different dehydration and decarbonation temperature ranges of hydrated carbonates and excluding the mass loss associated with the overlapped dehydration of brucite with the decarbonation of hydromagnesite (see section 4.2.5; Fig. 5.30). The SFG reaction products are less hydrated than those obtained when using CC as well as with stoichiometric hydromagnesite.

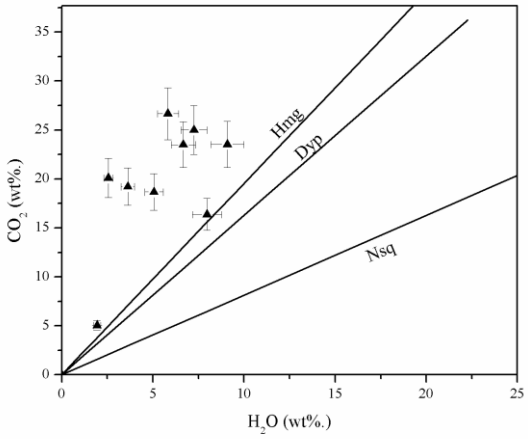

Fig. 5.30. CO_2:H_2O (wt%.) ratios as estimated with TGA of the solid product of reaction at 120 ºC, 1 - 10 bar from 4 to 16 hours uing simulated flue gas. Error bars were estimated on the average of three different experiments. Figure from Rausis et al., 2020 [55].

5.2.5. Time-resolved carbonation efficiency

Fig. 5.31 shows the CO_2 wt%. and the estimated carbonate content attained during CC and SFG experiments. Experiments carried at 120ºC yielded to higher amounts of CO_2 contents than 50ºC experiments using CC (Fig. 5.31). At both temperatures, the increase of pressure always enhanced the carbonation reaction, particularly from 1 to 4 bar. SFG experiments yielded to similar amounts of CO_2 sequestered as the 50ºC CC experiments. SFG treatments carried at atmospheric yielded to negligible CO_2 wt%. On the other hand, carbonation at atmospheric pressure when using CC yielded to a total of 11.5 and 22.1 CO_2 wt% for 50 and 120ºC, respectively, indicating a successful carbonation.

Fig. 5.32 shows the comparison of normalized sequester CO_2 wt% by CO_2 partial pressure among the carried experiments. CC experiments at ≥4 bar have lower CO_2 fixation capacity per unit of pressure when compared to atmospheric treatments. This might indicate that the carbonation reaction is very efficient (defined as the capacity to fix CO_2) at atmospheric pressure and is significantly reduced when increasing the pressure. CC experiments show higher CO_2 wt% than SFG experiments. Nonetheless, treatments carried using SFG have higher CO_2 fixation capacity per

unit of pressure when compared to the CC experiments in the pressure range from 4 to 10 bar. It should also be noted that carbonation using direct SFG at 4 bar was successful. Our results highlight the importance of the effect on CO_2 partial pressure during carbonation reaction, particularly at moderately low pressures and temperatures. This might provide new insights on the direct utilization of industrial gas waste streams via MC as an alternative to implement an integrated CCUS process.

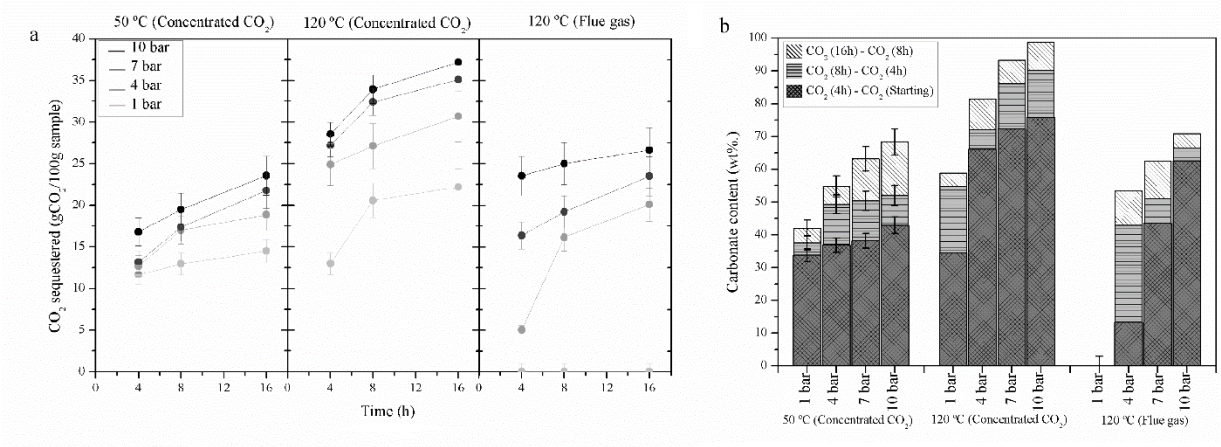

Fig. 5.31. (a) CO_2 sequestered (gCO_2/100g sample) of experiments carried using concentrated CO_2 (50, 120ºC) and simulated flue gas (120ºC) from 1 to 10 bar at 4, 8 and 16 hours. Error bars estimate the average between three analogous experiments **(b)** calculated carbonate content based on the sequestered CO_2. Error bars represent the estimated carbonate content based on the different carbonate mineralogy. Figure from Rausis et al., 2020 [55].

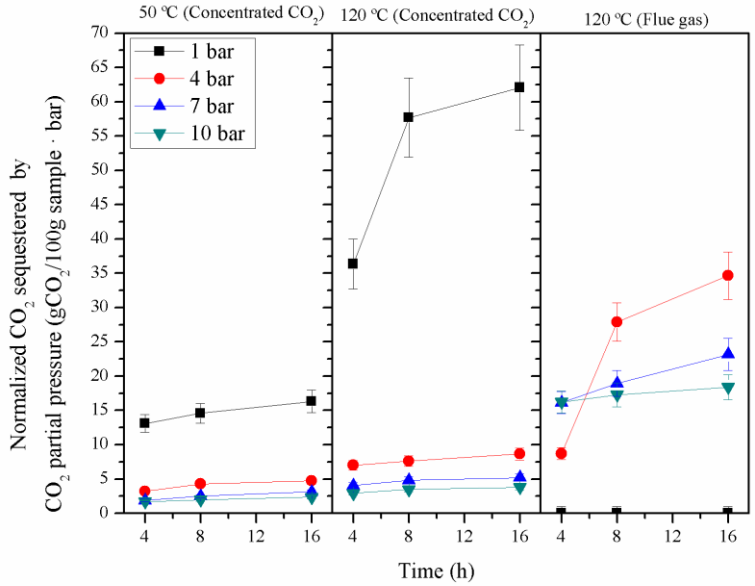

Fig. 5.32. CO_2 sequestered (gCO_2/100g sample) normalized by the partial pressure (bar; Table 3.7) of experiments carried using concentrated CO_2 (50, 120ºC) and simulated flue gas (120ºC) from 1 to 10 bar at 4, 8 and 16 hours. Error bars estimate the average between three analogous experiments. Figure from Rausis et al., 2020 [55].

Moreover, the reaction proceeded similarly or both CC and SFG experiments, as observed in section 5.2.4., in agreement with previous observations [99,100]. Nonetheless, faster reaction kinetics were observed during CC than SFG experiments, particularly within the pressure range from 1 to 4 bar. Previous studies on brucite carbonation in the presence of steam have suggested that such reaction is favored when working near 100% RH (see also section 4.1) [204]. Therefore, the lower reaction kinetics observed during SFG experiments might be associated with the lower RH when compared to CC experiments (see section 3.3.2.). Moreover, it has been also reported different CO_2 sequestration efficiencies when using different CO_2 partial pressure during carbonation of heat activated serpentine [44], suggesting that there is an optimal CO_2 partial pressure for carbonation of heat activated serpentine.

Carbonate contents were estimated based on the stoichiometric composition of nesquehonite and/or hydromagnesite, since these phases represent the maximum and minimum hydration level of the obtained carbonate products, respectively. The carbonate content ranges shown in the 50ºC experiments (Fig. 5.31b) represent either the respective carbonate content considering all the observed carbonate phases nesquehonite (higher value) or all hydromagnesite (lower value), since the exact proportions of this phases is unknown, due to the overlapping dehydration and decarbonation behavior, as observed with TGA.

CC experiments carried at 120ºC, 10 bar during 16 hours yielded to an almost complete brucite carbonation (>98%), obtaining high-purity hydromagnesite as reaction product. Such material could be profitable and may contribute to overcome the carbonation processing costs, which has been partially reduced by the utilization of moderately low pressures and temperatures. The maximum carbonate content obtained during SFG experiments was 53 to 70%, depending on pressure conditions. Similar carbonation yields were observed upon brucite CC carbonation at 50ºC. Further SFG carbonation enhancement is required in order to obtain profitable high-purity carbonate products. The carbonation yields obtained in this study are similar to those reported by Highfield et al., 2016 [204].

Fig. 5.33 shows the CO_2 wt% and the carbonate content % from 50ºC and 10 bar CC treatments during 7min to 120h. A progressive increment on the CO_2 wt% is observed as the reaction proceeds until it reaches 48h of reaction. At this reaction time a complete carbonation of brucite was attained. It should be noted that 40% of the carbonation occurred in less than 2 hours, and it took over 46 hours to attained to reach the remaining 60%.

Typical temperature of flue gas waste streams from coal-burning power plants is between the range from 160 to 180ºC [433]. Therefore, this indicate that no additional heating will be required for the direct utilization of flue gas for MC, considering the results obtained in this work. SFG experiments at atmospheric pressure shows high carbonation potential, however they require

significant acceleration. It should be noted that the SFG experiments were carried at lower temperatures than typical flue gas. Moreover, typical flue gas has higher RH% than 5% (this study). Therefore, increasing the temperature (to a maximum of 180ºC) as well as the RH% (to a maximum of 15%) could potentially provide significant carbonation enhancement and might unlock the SFG carbonation potential at atmospheric pressure, without any additional costs [261,265,378]. The successful implementation of such processes will utilize direct flue gas to produce valuable carbonate products, without the need of heating large amounts of water (as required by the MC aqueous routes).

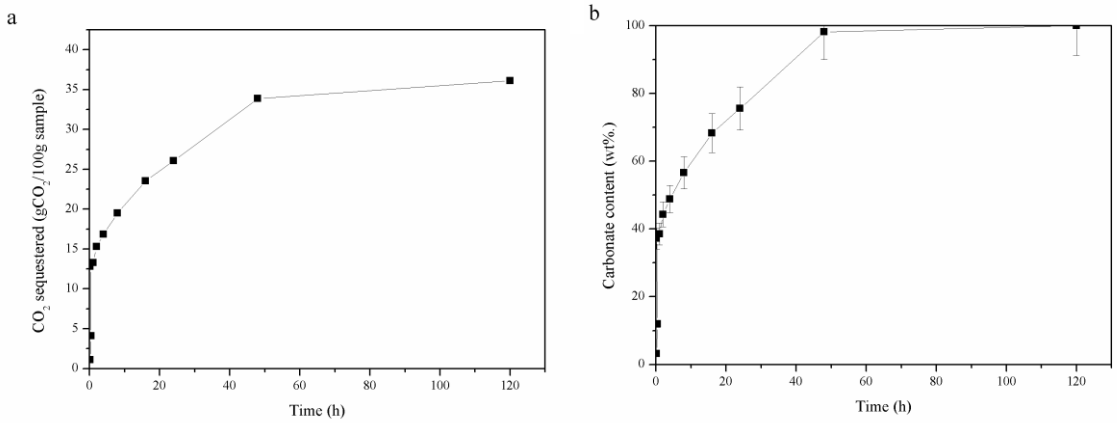

Fig. 5.33. (a) CO_2 sequestered (gCO_2/100g sample) of experiments carried using concentrated CO_2 at 50ºC, from 1 to 10 bar from 15 minutes to 120 hours. **(b)** calculated carbonate content based on the sequestered CO_2. Error bars represent the estimated carbonate content based on the different carbonate mineralogy. Figure from Rausis et al., 2020 [55].

It should also be noted that only traces amount of magnesite was formed at 120ºC. This mineral is the preferred Mg-carbonate for CCUS purposes due to its higher stability, least soluble, lighter and with the highest CO_2 storage capacity, which might reduce the transportation and processing costs [264]. However, its formation under condition near to those of flue gas is kinetically challenging and inhibited by the preferential formation of hydrated carbonates [197,204] (see section 2.1.1.). Further research is needed to acceleration the formation of magnesite under these specified conditions. Swanson et al., 2014 [197] demonstrated that magnesite growth can occur at condition where normally hydrated carbonates will formed by seeding the reaction with magnesite crystals, reducing the difficulties for magnesite nucleation. It should be expected that an increase of the temperature (up to 180ºC) will significantly enhance the magnesite yield as discussed in section 4.2. Moreover, the formation of high-purity hydrated carbonates is also valuable, and it should be considered if increasing the temperature (which generally increases processing costs) to obtain magnesite or to optimize the experimental condition to obtain high-purity hydrated carbonates at the lowest possible costs [44].

5.3. Conclusions

Phase formation and evolution during brucite carbonation using concentrated CO_2 (CC) and simulated flue gas (SFG) in the temperature and pressure range from 50 to 120ºC and 1 to 10 bar was experimentally studied. Hydromagnesite was identified during 120ºC treatments as well as trace amounts of magnesite. Experiments carried at 50ºC yielded the formation of nesquehonite, highly-disordered to semi-ordered dypingite-like phases as well as a possible hydrated amorphous Mg-carbonate (AMC). This latter phase was associated with a wide Raman peak with position at 1093 ± 2.05 cm^{-1} and might have similar composition to nesquehonite as well as similar dehydration behavior. It remains unclear if early dypingite was formed form the nucleation of an AMC precursor or if it formed directly from brucite. However, the possible observed AMC nourished the late growth of dypingite, in agreement with the Ostwald rule. The origin of nesquehonite remains unclear. However, this latter phase was precursor to less hydrated dypingite-like phases and possibly to an AMC. It is proposed that an AMC precursor partially nucleated to highly-disordered and less hydrated dypingite-like phases and as, the reaction proceeded, dypingite became more structurally ordered as cell shrinkage occurs due to partial and progressive dehydration, becoming hydromagnesite after prolonged reaction times.

CC experiments yielded to higher carbonation yields compared to SFG experiments, attaining a maximum of 37 CO_2 wt%. (equivalent to a carbonate content of >98%) at 120ºC, 10 bar during 16h. However, SFG experiments show higher carbonation potential by unit of pressure, particularly in the pressure range from 4 to 10 bar. Treatments performed at 120ºC for both SFG and CC yielded to the formation of only crystalline phases (mainly hydromagnesite). Further research in needed to unlock the economically-desired SFG reactions at atmospheric pressures. Results from this work provides additional insights on the direct utilization of industrial gas waste streams via mineral carbonation in order to obtain valuable carbonate products as well as contributing to the CO_2 mitigation efforts.

6. Carbonation of activated lizardite: the identification of a highly-reactive amorphous Mg-rich phase

6.1. Introduction

It is well stablished that serpentine requires heat activation for DC processes. Lizardite has the simplest structure compared to antigorite and chrysotile [434]. The activation of chrysotile has been extensively studied [283,435–437]. Chrysotile dihydroxylation products have been described to be largely disordered [435], partially disordered [436] and semi-amorphous while preserving some of the original structure [437]. The discrepancies among those studies is mainly due to the difficulties associated with the characterization of different coexisting crystalline with poorly ordered phases as well as highly disordered amorphous phases, often exhibiting overlapping feature in many spectroscopy techniques. Readers are referred to section 2.3.1.3.2. as it gives a general overview of serpentine activation processes.

Mackenzie and Meinhold et al., 1994 [283] studied the phase formation and evolution of Mg-rich phases upon thermal activation of chrysotile by an nuclear magnetic resonance spectroscopy (NMR) study. Such analysis is very sensitive to local coordination of individual silica tetrahedral. Depending on the possible silica tetrahedral polymerization, a characteristic chemical shift is observed, which can be assigned to five possible silica tetrahedral arrangements (Fig. 6.1) [101]. Where Q_0 consist on isolated silicon tetrahedral with no oxygen share with any other silica tetrahedral, such crystal arrangement is characteristic of nesosilicates, such as olivine, where the negatively charged individual silica tetrahedral is balanced by 2 Fe^{2+} and/or Mg^{2+} cations. On the other hand, Q_4 species occurs when each oxygen within the silica tetrahedral is shared with other silica tetrahedral, characteristic of tectosilicates, such as silica (SiO_2). In this case the negatively

charged $(SiO_4)^{-4}$ silica tetrahedral are balanced by sharing oxygen with neighboring silica tetrahedral. Such detailed analysis of the silica tetrahedral coordination changes upon heat activation provided invaluable new insights on such processes. Results from such studies has suggested the activation of chrysotile is significantly more complex to those previously postulated [283]. Table 6.1 summarizes the different silica tetrahedral configurations and their associated NMR chemical shifts for activated lizardite and chrysotile.

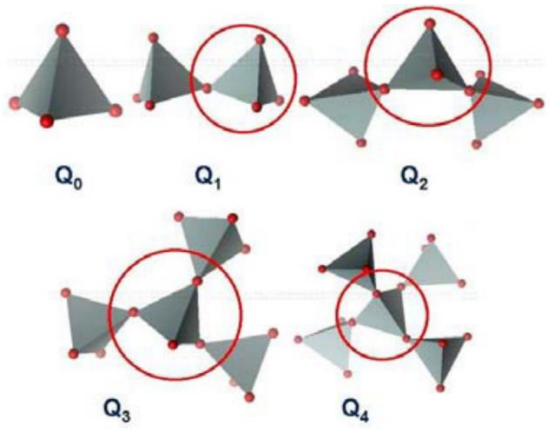

Fig. 6.1. Schematic of individual silica tetrahedral coordination as represented from Q0-Q4. Oxygen atoms are represented as red spheres and silicon atoms are located at the center of each tetrahedron. Figure from Chizmeshya et al., 2006 [101].

Table 6.1. 29Si NMR peak positions of activated chrysotile and lizardite and their associated SiO4-4 polymorph association, as well as the associated silicate phase.

Q-assignment	Peak position (ppm) [101,438]	Associated Mg-rich phase [283]
Q_0	-~64	Forsterite (~ - 64 ppm)
Q_1	-~73	Dehydroxylate I (~ - 73 ppm)
Q_2	-~85	Enstatite (~ - 83 ppm)
Q_3	-~95	Chrysotile (~ - 92 ppm)
Q_3'	-~99	Dehydroxylate II (~ - 97 ppm)
Q_4^*	-~110 to - 120	Silica (~ - 110 ppm)

Upon heat treatment of serpentine minerals, the progressive formation of forsterite and enstatite occurs with increasing activation temperature. The formation of forsterite always precedes the formation of enstatite, since the formation of forsterite do not require full dehydration and enstatite seemingly does, following the general equations [287]:

$$2Mg_3Si_2O_5(OH)_{4(s)} \xrightarrow{<800ºC} 3Mg_2SiO_{4(s)} + SiO_{2(s)} + 4H_2O_{(g)} \quad (6.1)$$

$$2Mg_3Si_2O_5(OH)_{4(s)} \xrightarrow{>800ºC} Mg_2SiO_{4(s)} + MgSiO_{3(s)} + 2H_2O_{(g)} \quad (6.2)$$

However, intermediate phases were observed upon activation of chrysotile as evidence by the emergence of two new NMR peaks with position -73 and -97ppm (see table 6.1). The material

responsible for the broad resonances with peak position at -73ppm have been suggested to be amorphous due to its low degree of Si-polymerization (Hartman and Millard, 1990). Due to the presence of different tetrahedral configurations, as evidence by the broadness of this peak, incipient formation of forsterite and enstatite cannot be distinguished due to overlapping features. Such Mg-rich amorphous phase is commonly referred as Q_1 dehydroxylate I [283]. The -97ppm resonance peak is significantly thinner than such observed for dehydroxylate I, and its presence its related to a phase that still contains elements of the original silicate structure, called Q_3 dehydroxylate II [283]. This phase has been strongly associated with the "α component" observed in McKelvy et al., 2004 [49] (Fig. 2.22). The proposed thermal dehydration sequence of chrysotile as well as the distribution of Si-polymorphism upon chrysotile activation as function of activation temperature are shown in Fig. 6.2.

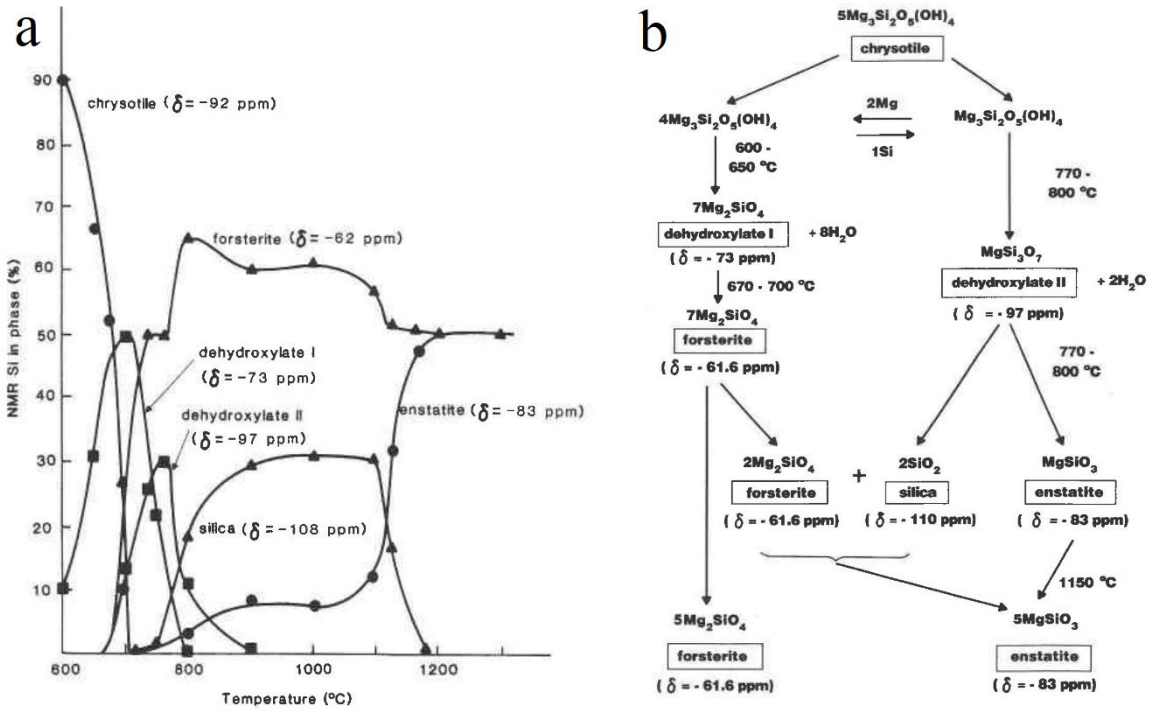

Fig. 6.2. (a) Distribution of silicate phases during dehydration of chrysotile as function of the activation temperature, as determined by ^{29}Si NMR analysis. **(b)** Schematics of the proposed dehydration sequence of chrysotile dehydration. Figure from Mackenzie and Meinhold, 1994 [283].

Upon chrysotile activation, amorphous dehydroxylate I is firstly formed, followed by the formation of both forsterite and semi-ordered dehydroxylate II (Fig. 6.2a). Upon increasing the temperature, dehydroxylate I and II nourished the growth of forsterite and the formation of silica. At >1100ºC, two oxygen atoms are shared between silica and forsterite, forming enstatite as evidenced by the appearance of a Q_2 structure, characteristic of inosilicates. The formation of enstatite is inhibited upon the consumption of available silica [283].

An intriguing question was raised upon chrysotile dehydration which yielded to two different dehydroxylate intermediate phases (Fig. 6.2b). It was proposed that chrysotile underwent two on-going decomposition processes: (i) dehydration-induced amorphization of the silicate structure, however its Mg coordination remained largely intact; (ii) chrysotile was able to largely maintained its Q_3 silicate structure upon partial dehydration [283].

Analogously, the dehydration of lizardite has recently received research interest within the context of MC, since it has been observed that intermediate phases appearing during serpentine dehydration are highly reactive in a CO_2-rich environment. This elevated reactivity is mainly attributed to the presence of amorphous phases during activation [101]. This study also analyzed the changes of the local silica tetrahedra upon dehydration with aid of ^{29}Si NMR, as well as their association with XRD results (Fig. 6.3).

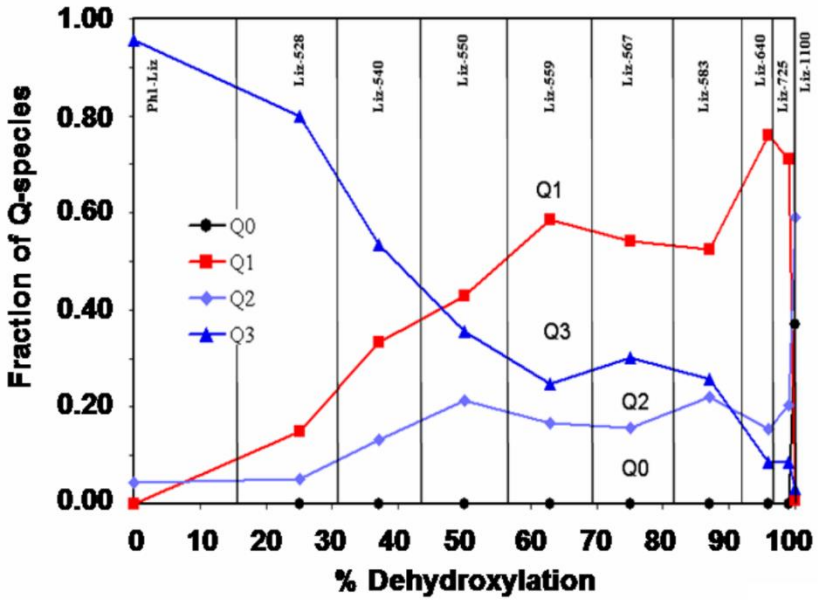

Fig. 6.3. Distribution of silicate phases during dehydration of lizardite as function of the residual OH content %, as determined by ^{29}Si NMR analysis. The respective at which lizardite was activated is represented as Liz-T(ºC). Figure from Chizmeshya et al., 2006 [101].

Q_1 dehydroxylate I as well as a Q_2 silicate phases are formed upon lizardite amorphization. Comparison with XRD results of lizardite activated at 580ºC (Figs. 2.22 and 6.3), where an amorphous component was observed as well as the "α component". This latter phase is strongly associate to a Q_3 dehydroxylate II due to their silicate structure remained largely unaltered upon Q_3 lizardite dehydration. It should also be noted that Q_3 dehydroxylate II ("α component") have overlapping features with Q_3 lizardite [283]. Therefore, the presence of "α component" in the XRD data indicated that Q_3 from Fig. 6.3 represent both lizardite consumption as well as "α component" formation. Q_1 dehydroxylate I amorphous phase and a Q_2 silicate phase are forming as lizardite dehydrates. Comparison with the XRD data where only "α component" and residual brucite showed

crystalline X-ray scattering, strongly suggesting that Q_2 phase is also amorphous [101]. Such inosilicate-like phase might be precursor of enstatite. In summary, upon lizardite activation three intermediate phases might have formed. Among such phases, two are amorphous (Q_1 dehydroxylate I and Q_2, precursor to enstatite) and the remaining is crystalline (Q_3 dehydroxylate II). Such intermediate phases are precursors for enstatite and forsterite.

A possible dehydration mechanism that explain the relationships between the different formed phase upon lizardite activation have been discussed based on the OH vibration changes upon dehydration as observed with FTIR [49,101]. It was observed that the reactivity of inner OH was higher than outer layer "brucite-like" hydroxyls, suggesting that the dehydration process starts form the inner OH. Inner hydroxyls start to react with Q_3 lizardite and protons are liberated. Then, these protons react with outer OH and forming water, which is liberated from the silicate structure. Local Q_3 now have a charged oxygen, which induces the tearing of Q_3 to Q_3'("α component"), Q_2 and Q_1 (Fig. 6.4). The proposed resulting structure is shown in Fig. 6.5. Resulting amorphous Q_1 dehydroxylate I share only one oxygen with Q_3' dehydroxylate II. Such arrangement is rare for silicates[101]. Therefore, both their amorphous nature and their rare silicate coordination might indicate that Q_1 dehydroxylate I is highly reactive.

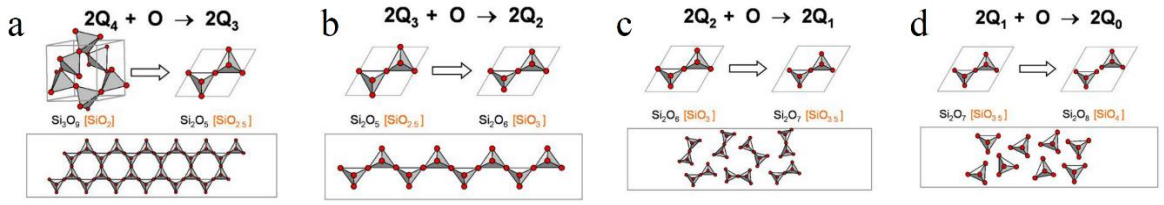

Fig. 6.4. Schematic of inter-relationships between Q species. Conversion of **(a)** Q_4 to Q_3, **(b)** Q_3 to Q_2, **(c)** Q_2 to Q_1 and **(d)** Q_1 to Q_0. Figure from Chizmeshya et al., 2006 [101].

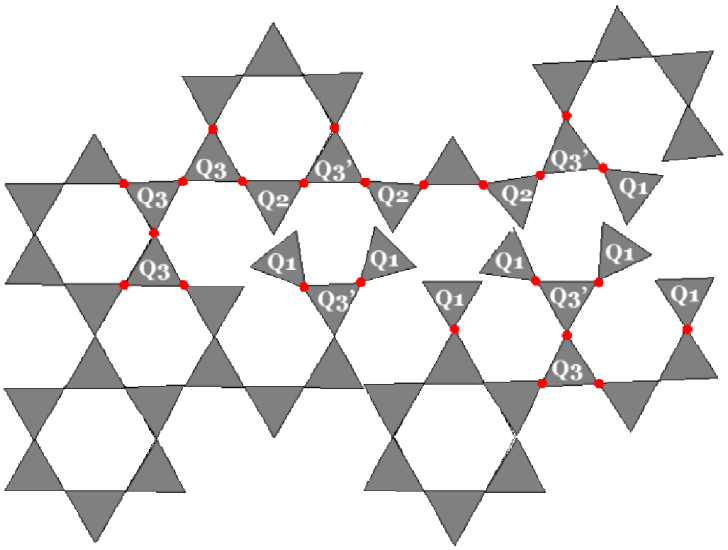

Fig. 6.5. Proposed structure of partially-activated lizardite by tearing of the Q_3 silicate phases to intermediate Q_3', Q_2 and Q_1 phases. Figure from Chizmeshya et al., 2006 [101].

The high reactivity towards MC of such intermediate phases (Fig. 2.24) and the vast amounts of serpentinites reserves, makes this process (heat activation) a promising option for MC. Moreover, numerous worldwide and large mining sites produces large amounts of finely-ground, cheap and easy-accessible ultramafic mine wastes [269,346,439–441]. Serpentinites are, among such wastes, the most abundant.

An experimental campaign was carried out in order to provide more insights on the role of partial dehydration of lizardite, by an extensive characterization of the intermediate phases formed upon activation as well as their reactivity towards MC. Different activated lizardites were carbonated via in a continuous flow at 6 bar and 50 to 120ºC in the presence of steam. The results obtained provides insights on the differentiation of the evolved intermediate phases upon lizardite activation and their role towards MC.

6.2. Results and discussion

6.2.1. Mg-rich silicate phases analysis upon lizardite activation

A complete transformation of lizardite was observed upon activation, as its characteristic XRD, Raman and FTIR features are no longer observed (Fig. 6.6a, b, c). The formation of forsterite and minor hematite ($Fe_3^{+2}O_3$) were observed in all activated materials. With increasing temperature from 610 to 710ºC, a prograde formation of both forsterite and hematite was observed.

Moreover, XRD analysis shows the presence of a plateau in the 2θº range between17 to 43 in all activated materials, strongly suggesting the presence of an amorphous component (Figs. 6.6a, 6.7) [49,401,405]. As summarized in the introduction (section 6.1), different studies have observed different Mg-rich intermediate phases upon activation of lizardite [101,438]. There are three known intermediate precursors upon lizardite activation: two amorphous phases(Q_1 dehydroxylate I and Q_2 Mg-rich phase) and one crystalline phase (Q_3 dehydroxylate II "α component") [101,283,438]. This intermediate crystalline phase is not identified in our results, as its characteristic X-ray scattering at 2θº ≈ 6.0º are not observed (Fig.6.7) [49,101].

Q_1 and Q_2 Mg-rich phases might be responsible for the amorphous component observed with XRD (Fig. 6.7). The residual OH content was estimated with TPD for each activated material, accounting for 8.47, 4.92 and 1.93% for AS610, AS650 and AS710, respectively (Fig. 6.6d). According to Chizmesya et al. 2006 [101], Q_3 "α component" is no longer observed when the residual OH content reaches >90% and the amorphous phases (Q_1 and Q_2 Mg-rich silicate phases). Such observation is in agreement with our results.

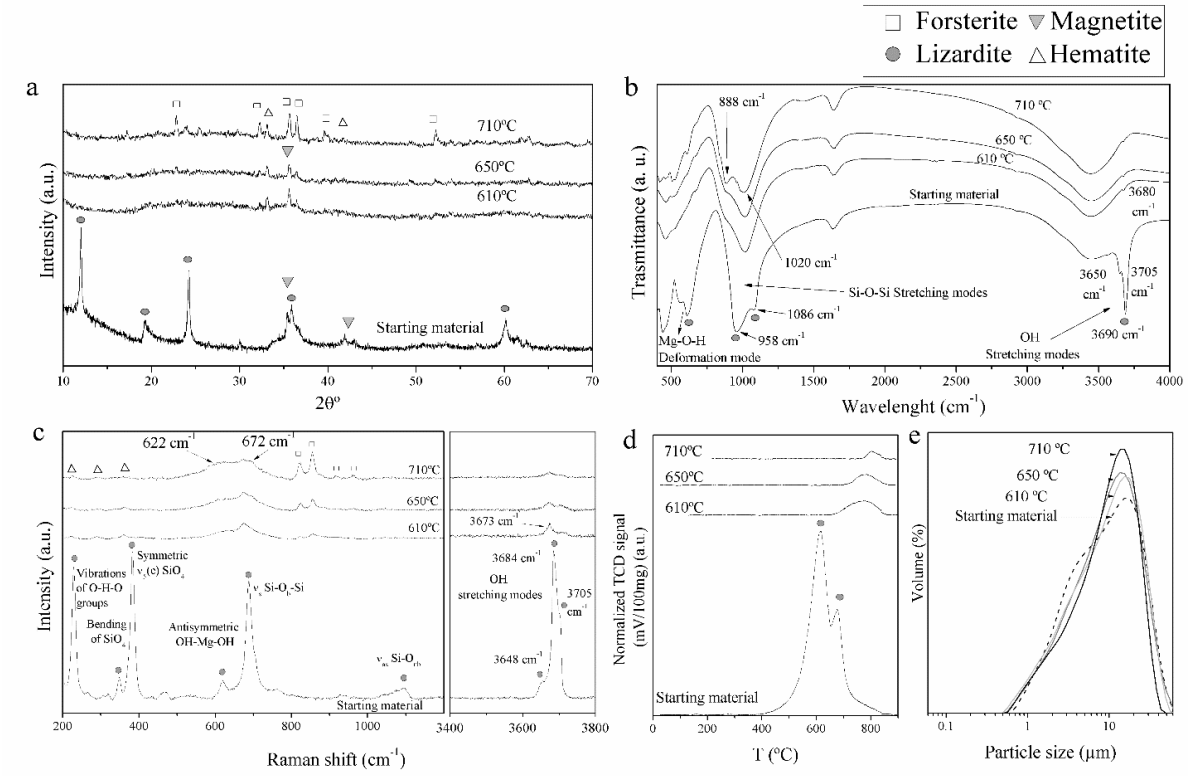

Fig. 6.6. (a) XRD, **(b)** FTIR, **(c)** Raman, **(d)** TPD analysis as well as (e) particle size distribution of sampled serpentinite prior and after activation. Figure adapted from Rausis et al., 2020 [385].

Farhang et al., 2016 [196] conducted an experimental study on the carbonation of activated lizardite at elevated pressures and temperature (150ºC, 140 bar). It was observed that the Q_3 dehydroxylate phase was poorly reactive as it remained seemingly unreacted upon carbonation. This might indicate that in order to increase the reactivity of activated serpentine, a complete transformation of such phase to amorphous phases should be attained. Our results indicate that at 610ºC a complete transformation of lizardite is observed as well as a complete (or almost complete) transformation of Q_3 dehydroxylate II to amorphous and more reactive intermediate phases, while only minor and less reactive forsterite was formed. Moreover, lower activation times might inhibit the formation of forsterite. However, it might also decrease the conversion yield of Q_3 dehydroxylate II to amorphous intermediate phases, as well as the transformation of lizardite, as observed by McKelvy et al., 2004 [49]. Therefore, this suggest that there is an optimal combined temperature and time for obtaining the maximum yield of amorphous phases upon a complete transformation of lizardite.

Upon activation, only the 3680 cm^{-1} OH Raman and FTIR band remained detectable, however it is barely recognizable due to the partial dehydration of lizardite (Fig. 6.6b, c). The intensity of such band decreases as the activation temperature increases from 610 to 710ºC (Fig. 6.6b, c, d). The local OH bonding environment remained largely unaltered upon activation as evidenced by the minimal frequency shifts of the OH bands, in agreement with Mckelvy et al., 2004 [10].

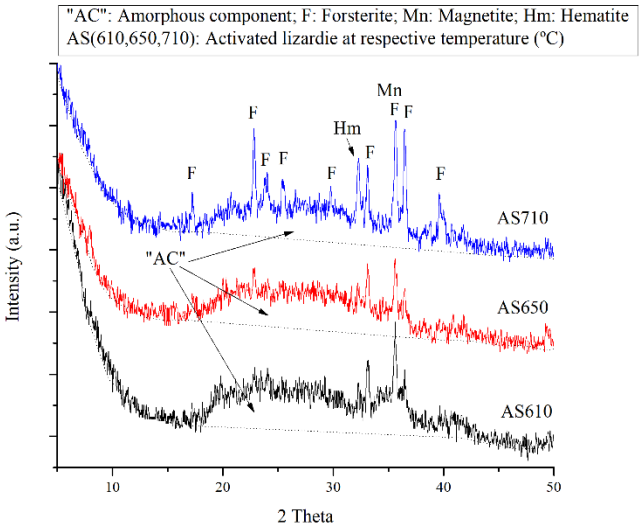

Fig. 6.7. XRD analysis of activated materials at 610, 650 and 710ºC during 16 hours. Figure from Rausis et al., 2020 [385].

The characteristic 1086, 958, 610 and 570 cm^{-1} FTIR bands disappeared upon activation and two new distinct broad and less intense peaks are observed at 1020 and 888 cm^{-1}, which is in agreement with a complete transformation of lizardite. These latter peaks are associated with the presence of intermediate Mg-rich silica phases [353,442].The band at 1020 cm^{-1} overlaps with incipient forsterite formation. Benhelal et al., 2019 [353] discussed that the 888 cm^{-1} band might be associated with the Si-OH bending vibration of free silanol groups. The relative proportion of these two new peaks formed upon activation is different for each activated material.

Raman analysis also confirmed a complete transformation of lizardite and the incipient formation of forsterite and hematite, as well as the emergence of two broad peaks at 622 and 672 cm^{-1}. Broad Raman peaks are often associated with highly-disordered materials [55]. Analogous to FTIR discussion, these emerged Raman bands (622 and 672 cm^{-1}) are associated with intermediate phases. Moreover, it should be noted that forsterite Raman peaks does not overlapped with the peaks of these intermediate phases, which makes easier the differentiation of intermediate Mg-rich silicate phases.

Particle size changes were also measured upon activation. It was observed that the smaller grain from the starting material have acquired a slightly bigger size upon activation (Fig. 6.6e). The size progressively increases with higher activation temperatures.

6.2.2. Steam-mediated carbonation

The emergence of carbonate phases where observed upon reaction of AS610, AS60 and AS710. Fig. 6.8 shows the Raman analysis of the solid products of carbonation performed at 50, 90 and 120ºC and 6 bar during 30min to 4h. The appearance of two different Raman peak at 1094.2 ± 0.4,

1116.6 ± 0.3 cm^{-1}) were observed. within the region of the ν_{1sym} of the carbonate ion (CO_3^{2-}; $\nu_{1symCar}$) [380,381] for all three activated materials. The 1094.2 ± 0.4 cm^{-1} Raman peak appears with concomitant 324.9 ± 0.5 Raman peak within the lattice vibration region (100-500 cm^{-1}). The identification of these peaks is particularly evidence for the AS610 materials. The concomitant emergence of those two peaks might suggest the presence of magnesite (see chapter 4 and 5).

FWHM and peak position comparison of the $\nu_{1symCar}$ Raman peaks is shown in Fig. 6.9. Calculated data of $\nu_{1symCar}$ Raman peaks from experiments carried at 120ºC shows that the observed 1094.2 ± 0.4 cm^{-1} Raman peak fits well with reference magnesite for all three activated materials. The second peak (1116.6 ± 0.3 cm^{-1}) fits well with reference hydromagnesite, particularly for AS610 materials. The calculated data for this same Raman peak observed for the AS650 and AS10 is approaching the reference data for dypingite.

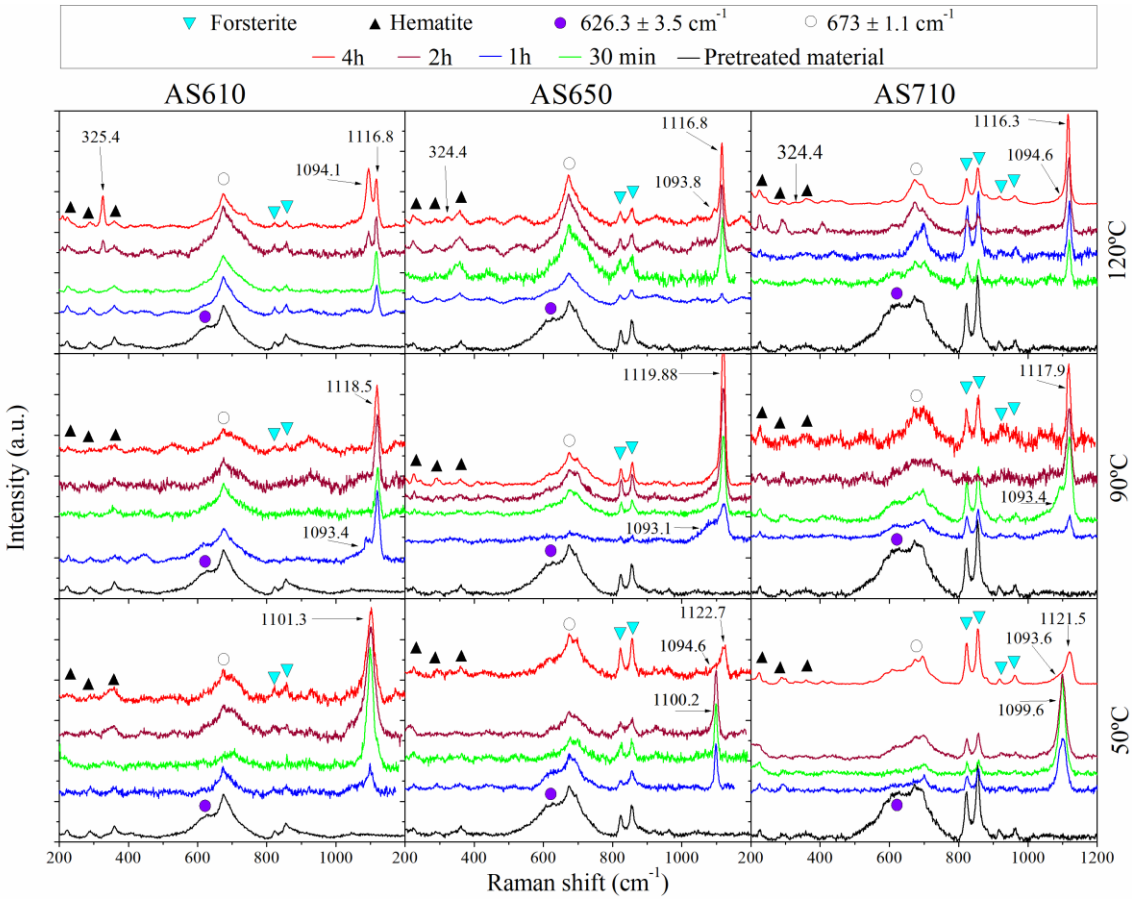

Fig. 6.8. Raman spectra of activated materials (AS610, AS650, AS710) and their respective reaction products from 30 minutes to 4 hours. Figure from Rausis et al., 2020 [385].

Treatments performed at 90ºC exhibit the emergence of two $\nu_{1symCar}$ Raman peaks at 1093.4, 1118.9 ± 1 cm^{-1}). The position of these peaks does not vary as the carbonation reaction proceeds. The 1093.4 cm^{-1} peak, despite having similar position as reference magnesite, it does not emerge with the concomitant magnesite peak at 324.9 ± 0.5, suggesting that the phase responsible for

the1093.4 cm^{-1} is different from magnesite. The calculated FWHM vs peak position data shows that this peak does not correlate with any represented Mg-carbonate phase. Moreover, previous studies have observed the presence of a very similar peak [55], which was associated with the presence of an hydrous AMC with composition and dehydration behavior akin to nesquehonite. The presence of this peak was only observed at 30min of reaction for AS610 and AS650. However, it was observed only during the first hour of reaction for the AS710 materials. The disappearance of this peak upon longer reaction times (2 to 4h) for all activated materials indicates that this possibly AMC is precursor to the phase responsible for the 1118.9 ± 1 cm^{-1} peak. This latter peak is observed to be slightly shifted from the phase observed from 120ºC treatments (1116.6 ± 0.3 cm^{-1}). The comparison between FWHM and peak position shows this phase might be dypingite (See chapter 4 and 5).

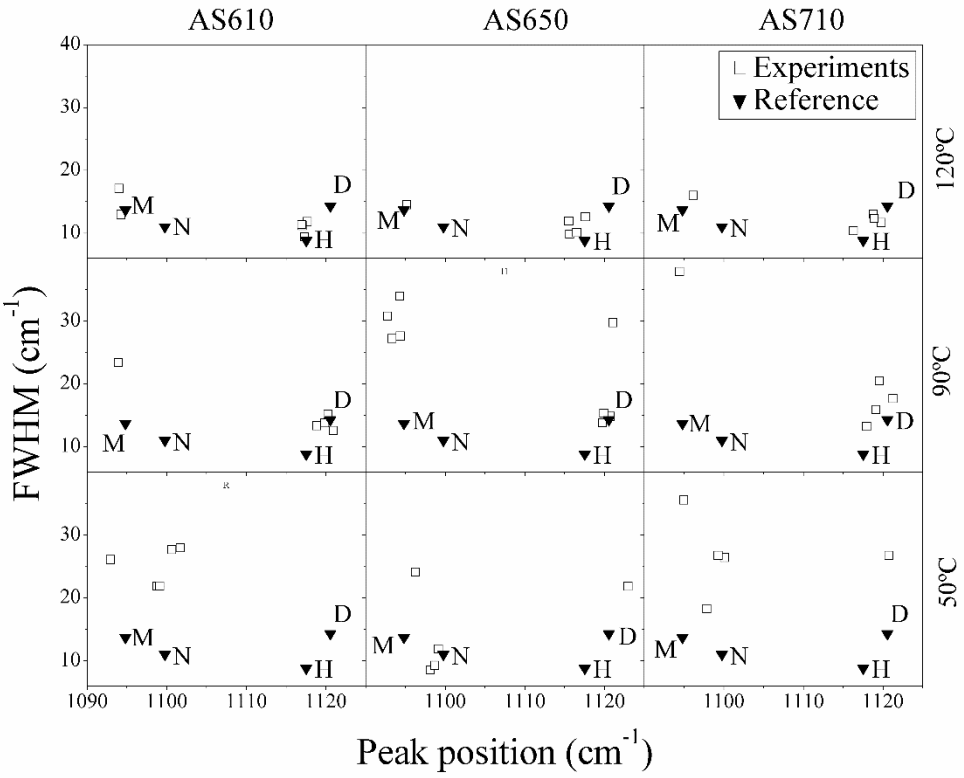

Fig. 6.9. FWHM vs peak position of Raman v_{1sym} peaks emerged upon carbonation of AS610, AS650 and AS710. M: Magnesite; N: Nesquehonite; H: Hydromagnesite; D: Dypingite. FWHM and peak position of reference minerals were calculated following Lafuente, et al., 2015 [85]. Figure from Rausis et al., 2020 [385].

Treatments performed at 50ºC shows the emergence of three $v_{1symCar}$ Raman peaks at 1094.1 ± 0.5, 1100.5 ± 0.9, 1122.1 ± 0.6 cm^{-1}. Clear differences on the emergences of these carbonates associated peaks are observed among the different activated materials. The first peak 1094.1 ± 0.5 cm^{-1} is similar to that observed at 90ºC, which might be associated with an AMC, following observations reported by Rausis et al., 2020 [55]. The calculated data for the 1100.5 ± 0.9 Raman peak fits well with reference nesquehonite only for AS650. However, for AS610 and AS710 such

peak keeps the same position but it has significantly higher FWHM. Additionally, the AS610 shows only the presence of this peak at any reaction time. However, this peak is only identified from 30min to 2h for AS650 and AS710. At 4h of reaction, two $\nu_{1symCar}$ Raman peaks emerges at 1094.1 ± 0.5 and 1122.1 ± 0.6 cm^{-1}. This indicated that the 1100.5 ± 0.9 cm^{-1} nourished the late growth of the two emerged peaks at 4h. Analogous behavior was reported in a recent study [55]. The emergence of the broad 1094.1 ± 0.5 cm^{-1} might be associated with the presence of a hydrous AMC, as previously discussed. The calculated FWHM vs peak position of the 1122.1 ± 0.6 cm^{-1} band shows a good correlation with dypingite, but with higher FWHM, suggesting a highly-disordered structure [55].

Results are in agreement with observation from previous studies, where it has been observed that the formation of hydromagnesite at ≤ 50 ºC is kinetically inhibited by the preferential formation of more hydrated phases such as dypingite, nesquehonite and possibly an hydrous AMC [188,346,426]. This behavior is analogous to the inhibition of magnesite formation by hydromagnesite at higher temperatures [193,264,369], probably due to the slow dehydration kinetics of Mg^{2+} [413]. Raman observation are suggesting the presence of different Mg-carbonate phases with different amount of molecular water, whose formation is significantly controlled by the reaction temperature. However, such phases cannot be easily distinguished with the sole observation of the Raman associated peaks due to overlapping features [380].

Additionally, changes upon carbonation are observed on the emerged 622 and 672 cm^{-1} peaks (Fig. 6.6c) from activation of lizardite, particularly for the 622 cm^{-1} peak (Fig. 6.8). These bands are possibly associated with the presence of an amorphous Mg-rich phases since only forsterite and hematite were the only crystalline observed phases (taking into account that semi-ordered Q_3 dehydroxylate II was not identified). The intensity of the 622 cm^{-1} Raman band is diminishing as the carbonation proceeds, probably indicating that this phase is partially of fully nourishing the growth of carbonate phases. On the other hand, the broad band at 672 cm^{-1} remained relatively unreacted upon carbonation. Therefore, this observation might suggest that two Raman peaks are associated with two distinct amorphous intermediate Mg-rich phases (probably Q_1 dehydroxylate I and Q_2 Mg-rich phase, see section 6.1.), where the phase associated with 622 cm^{-1} Raman band is significantly more reactive. Similar observations were also suggested by Benhelal et al., 2018 [438].

Previous studies have reported a partial recrystallization of antigorite from the intermediate phases upon high-pressure treatments [353]. As discussed by the authors, such recrystallization is undesired since not only partially disactivate the reactive nature of meta-serpentines, fixing available reactive Mg within stable serpentine structure, but also increases the energy penalty of the overall reaction. The recrystallization of lizardite did not occur in this study as evidenced by the lack of lizardite characteristic Raman feature upon carbonation. Such observation is in agreement with Benhelal et al., 2019 [353].

Forsterite was not observed to carbonate under the experimental conditions used in this work, as evidenced by the relatively unchanged forsterite Raman features upon carbonation. Gerdemann et al., 2007 [145] observed higher carbonation yields for forsterite rather than activated serpentine from carbonation treatments at elevated temperatures and pressures (185ºC and 150 bar). However, at pressures <25 bar, forsterite remained largely unaltered while activated serpentine was significantly carbonating (see section 2.3.1.3.2.), in agreement with results from this study.

FTIR-ATR analysis of the activated materials and carbonated materials was carried out in order to provide additional information on the differentiation of carbonate phases as well as intermediate Mg-rich phases (Fig. 6.10), since both Raman and FTIR are commonly used for identifying amorphous and semi-ordered materials [443,444]. Upon formation of carbonates tree absorbance bands appeared at 797 ± 3, 853 ± 2, 883 ± 3, 1418,9 ± 8.2, 1480.6 ± 5.3 and 1516 ± 3.2 cm^{-1}. The bands at 1418,9 ± 8.2, 1480.6 ± 5.3 and 1516 ± 3.2 cm^{-1} are characteristic of ν_3 asymmetric stretching mode of the CO_3^{2-} and HCO_3^- functional groups [182,356,360]. The latter band (1516 ± 3.2 cm^{-1}) is often attributed to the presence of nesquehonite or hydromagnesite-like phases. The 883 ± 3 cm^{-1} is attributed to the out-of-plane ν_2 CO_3^{2-} bending mode, characteristic of magnesite and hydromagnesite-like phases [182,356,376]. The 853 ± 2 cm^{-1} FTIR peak is associated with the out of plane ν_2 HCO_3^- bending mode, characteristic of hydromagnesite-like phases, nesquehonite and possible to an hydrous AMC [55,182,376]. The 797 ± 3 cm^{-1} band is characteristic of the in-plane ν_4 CO_3^{2-} bending modes, commonly observed in hydromagnesite-like phases [182,376].

The 883 ± 3 cm^{-1} FTIR peak is not observed from the reaction products obtained at 50ºC for AS650 and AS710 (up to 4h). The absence of this peak might discard the presence of hydromagnesite-like phases and magnesite. Therefore, the more plausible Mg-carbonate phases that might explain the absence of this peak are nesquehonite and probably AMC. The transformation of a nesquehonite-like phase to a hydromagnesite-like phase was observed with Raman at 50ºC (Fig. 6.8), which occurred at 4 hours for both AS650 and AS710 is also observed with FTIR, as evidence by the 883 ± 3 cm^{-1} peak emergence as well as a peak shift from 1411.3 ± 1 to 1426.1 ± 1 cm^{-1} [182,376]. The differentiation of magnesite and hydromagnesite-phases is difficult due to overlapping FTIR features.

Changes on the Si-O-Si stretching modes are observed upon carbonation. Upon carbonation two peaks are observed at 1019 ± 8.5 and 1073.55 ± 3.95 cm^{-1}. The first peak (1019 ± 8.5 cm^{-1}, which is overlapped between forsterite and probably an intermediate Mg-rich phase) is also observed in the activated materials and it remained seemingly unchanged upon carbonation, suggesting that the phases responsible for this peak did not react. Such behavior was also observed by Benhelal et al., 2019 [353]. Moreover, the broad peak observed upon activation at 883 ± 3 cm^{-1} is no longer identified upon carbonation; instead a characteristic thin peak of hydromagnesite-like phases and/or magnesite is identified in a very similar position. The intermediate and probably amorphous phase

Mg-rich phase responsible for this peak is partially or fully nourishing the growth of carbonation. A combined observation of Raman (Fig. 6.8) and FTIR (Fig. 6.10) results suggest that the intermediate and probably amorphous Mg-rich silicate phase responsible for the 888.1 cm^{-1} and 626.3 ± 3.5 cm^{-1} FTIR and Raman broad peaks, respectively, is highly-reactive. In a similar way, the 673 ± 1.1 cm^{-1} Raman peak is associated with a less reactive and possibly amorphous Mg-rich phase partially responsible for the overlapped peak at 1019 ± 8.5 cm^{-1} FTIR peak. The inexistence of the characteristic lizardite peaks upon carbonation suggest the recrystallization of lizardite did not occur, in agreement with Raman observations.

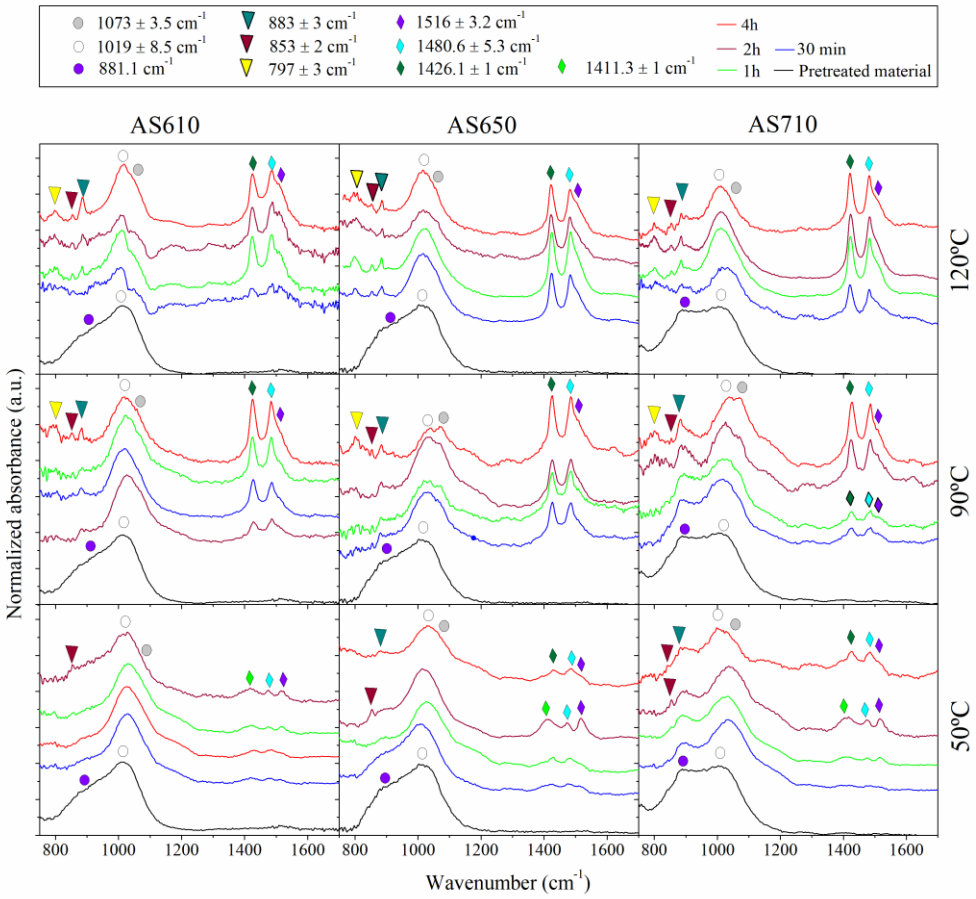

Fig. 6.10. FTIR-ATR analysis of activated materials (AS610, AS650 and AS710) and their respective reaction products. Figure from Rausis et al., 2020 [385].

Moreover, our results suggests that the observed highly-reactive amorphous intermediate Mg-rich silicate phases is different from the poorly-reactive precipitated Mg-silicate phases (PMSP) observed upon carbonation, associated with a similar FTIR band, as observed by Benhelal et al., 2019 [353]. This might indicate that PMSP might be associated with another FTIR band and might not contain silanol groups (as discussed by Benhelal et al., 2019 [353]), or might have overlapping features with the highly-reactive phase observed in this study. In this study, upon carbonation the characteristic peak of hydromagnesite-like phases and magnesite was the only emerged peak within

this discussed FTIR region. This could also suggest that PMSP were not formed in this study, since the activation process as well as the carbonation conditions were different to those reported by Benhelal et al., 2019 [353]. Therefore, it is not clear if PMSP were formed in this study or if it should be assigned to different FTIR features.

Analogously, the 888.1 cm^{-1} FTIR band associated with the intermediate and possible amorphous silicate phases might not contain silanol groups, as both this latter functional group as well as siloxane and Si-O-Al^{2+}/Na^{2+}/Mg^{2+} groups are associated with the emergence of a Si-rich passivating layer [101,445–447], which is incoherent with the high-reactivity of this phase.

The emergence of the 1073.55 ± 3.95 cm^{-1} band, formed upon carbonation and different from the un-activated lizardite FTIR features (Fig. 6.6), might suggest that this phase contains siloxane groups [353] or amorphous silica [448]. The appearance of this Si-rich phases, formed upon Mg liberation, are known to passivate carbonation reactions [449,450]. Moreover, it was recently found that such Si-rich phases can also retain a fraction of Mg, reducing the available Mg fraction to form carbonates and therefore reducing the carbonation yield [353].

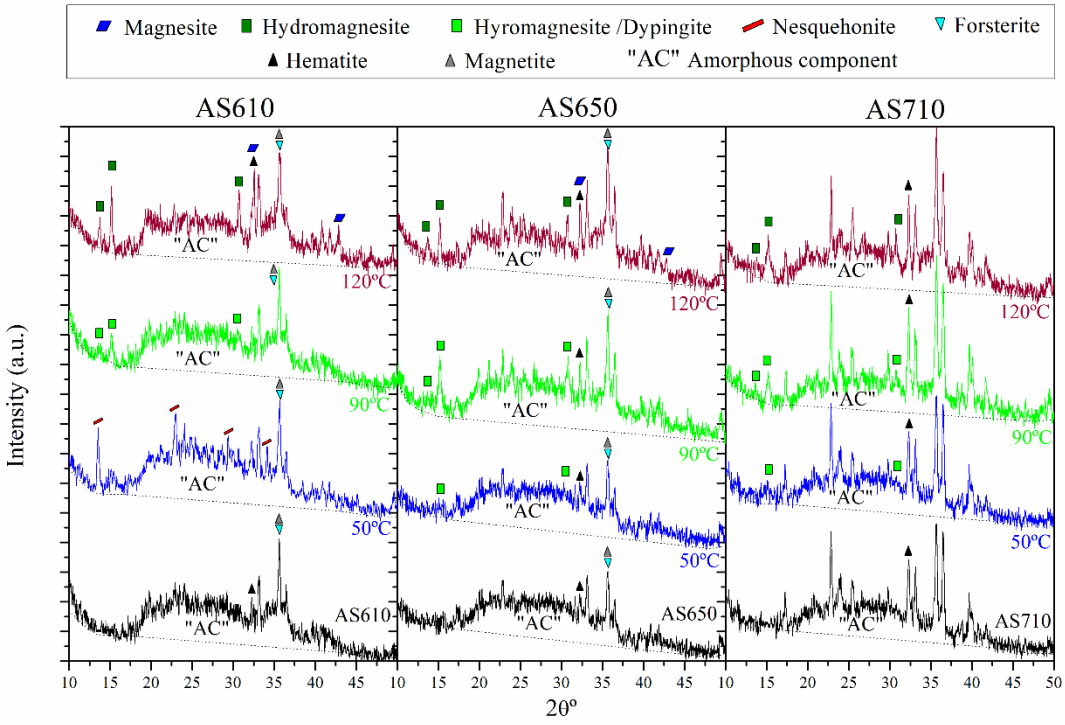

Fig. 6.11. XRD analysis of the activated materials (AS610, AS650 and AS710) and their respective reaction products obtained after 4h of reaction. Unmarked peaks correspond to forsterite. Figure from Rausis et al., 2020 [385].

In order to provide more insights on the differentiation of both carbonate phases and intermediate Mg-rich silicate phases, and XRD analysis of activated and carbonated materials was performed (Fig. 6.11). Hydromagnesite characteristic x-ray scattering [193,203] was observed at 120ºC for all

the activated materials as well as magnesite XRD features [193,198]. However, the x-ray diffraction lines of this latter phase was only observed for the AS610 and AS650 materials. It should be noted that the presence of magnesite in AS710 could be obscured by the XRD data noise. At 90ºC, dypingite-like phases were observed, resembling XRD features observed by Hövelmann et al., 2012 [373] and Rausis et al., 2020a [55]. At 50ºC, characteristic XRD features of nesquehonite were observed only for AS610. Under analogous conditions, dypingite-like phases were observed for AS650 and AS710, in agreement with Raman and FTIR observations. This observation strongly suggest that the reactive material play an important role on the evolution of carbonate phases. The undesired recrystallization of lizardite was not observed upon carbonation.

Moreover, a plateau was observed upon activation and carbonation in the 2θº range between 17 and 43 for all activated materials. Such wide x-ray diffraction suggest the presence of an amorphous component [49,401,405]. The comparison with Raman and FTIR might indicate that the phases responsible for this amorphous component after carbonation might be the observed poorly-reactive amorphous intermediate, amorphous silica and, in some experiments, the presence of a hydrous AMC. The possible amorphous phases upon activation were discussed in section 6.2.1.

Fig. 6.12 shows representative SEM images of the evolution of carbonate phases as the reaction proceeded. Hydromagnesite characteristic plates (≥1μm) [171,194] arranged in a rosette agglomerate are observed upon carbonation of AS610 during 1h at 120ºC (Fig. 6.12a). The progressive formation of rhombohedral magnesite (~1μm) [387] is observed with longer reaction times (2h, Fig. 6.12b; 4h, Fig 6.12c). The aggregation of hydromagnesite and magnesite shown in Figs. 6.14b inset and c, possibly indicate that both minerals were formed by nucleation and crystal growth [198].

Prismatic rod-like structures (~5μm) with similar morphology as nesquehonite [178,376] were observed in AS610 after treatment at 90ºC during 30 min (Fig. 6.12d). Overgrowths of flaky nanocrystals (<100nm) and microcrystals (<1μm) are observed on the surface of the prismatic structure, resembling a well-developed “house of cards” texture, which is characteristic of the transition of nesquehonite to dypingite-like phases [55,179,432,451]. The nano-flaky crystals form also sub-spherical aggregates, as also observed by Zarandi et al., 2017 [376]. Comparison with XRD, FTIR and Raman, where dypingite-like phases probably coexisting with a hydrous AMC were the only identified carbonate phases under these specific conditions and reacting material, suggest that the rod-like structure evidences a rapid formation of prismatic nesquehonite followed by its transformation into dypingite-like phases and possibly AMC. Such transformation is a good example of the Ostwald step rule [393].

The “house of cards” texture is associated with a dissolution-recrystallization self-assembly growth mechanism [452]. This possibly implies the formation of a liquid water interface on the

surface of the reacting material [452]. The condensate water interface might come from the dissolving mineral or from surface condensation of water vapor.

Treatments performed at 90ºC during 1h using AS610 exhibit the formation flaky dypingite crystals arranged in rosette agglomerates (Fig. 6.12e), resembling feature observed by Hopkinson, et al., 2008 [182].

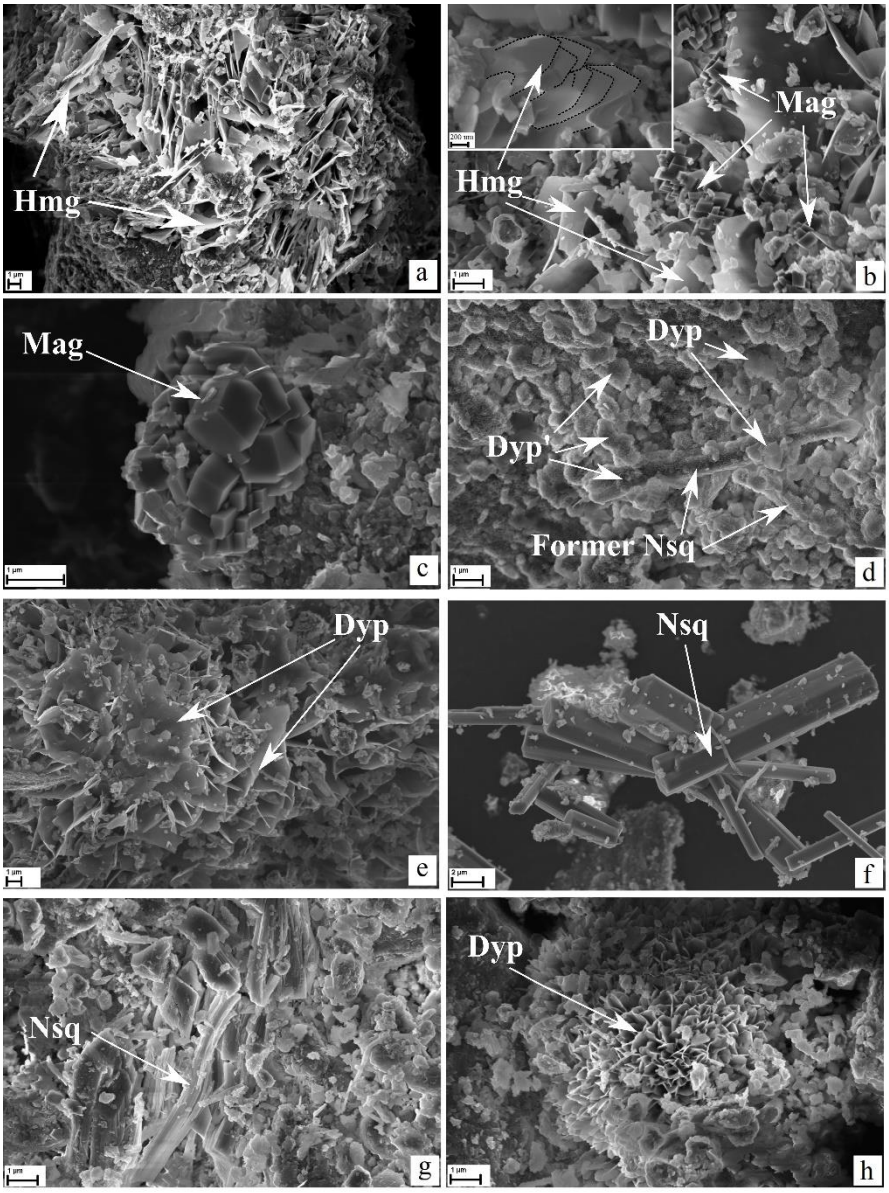

Fig. 6.12. Representative SEM images of carbonate products. AS610 materials carbonated at 120ºC for (a) 1h, (b) 2h and (c) 4h; 90ºC for (d) 30min and (e) 1h. AS650 treated at 50ºC for (f) 4h. AS710 materials carbonated at 50ºC for (g) 2h and (h) 4h. Hmg: hydromagnesite, Mag: magnesite, Dyp': nano-dypingite (<100nm), Dyp: dypingite, Nsq: nesquehonite. Figure from Rausis et al., 2020 [385].

Carbonation of AS650 at 50ºC during 2h shows the formation of massive prismatic nesquehonite crystals (Fig. 6.12f). Analogous treatments using AS710 shows acicular aggregates with morphological features that resembles nesquehonite (Fig. 6.12g) [182]. Comparison with Raman

and XRD indicated that the massive nesquehonite has similar FWHM to the reference mineral. Nonetheless, the acicular aggregation of prismatic crystals is observed to have a significantly higher FWHM while keeping the same peak position as reference nesquehonite. Upon increasing the reaction time (4h) flaky dypingite arranged in rosette crystal arrangement were observed, suggesting that the nesquehonite-like acicular aggregates completely transformed into dypingite, in agreement with Raman, FTIR and XRD observations. The identified carbonate phases in each carried experiment is summarized in Table 3.6.

6.2.3. TPD-CO_2-H_2O analysis

A TPD analysis was carried out in order to quantify the obtained time-resolved carbonation yields (Fig. 6.13). Differentiation of overlapping decomposition behavior among the different Mg-carbonate phases was carried by comparison with Raman, XRD, FTIR and SEM results. Dehydration and decarbonation of hydromagnesite from 120ºC experiments was observed to occur from 165ºC-340ºC and 350-550ºC, respectively, as observed in previous studies [365,394,395]. The decarbonation between 450-570ºC from treatments performed with AS610 at 120ºC for 2 and 4h is significantly increased when compared to lower reaction times (30min and 1h). This observation, together with Raman, XRD, SEM and FTIR data suggest the presence of magnesite. The decomposition behavior of AS650 and AS710 reaction products obtained from 120ºC treatments is similar to those obtained with AS610, but over prolonged reaction times and with a lower peak associated with magnesite decarbonation.

Dehydration of the reaction products obtained from 50 and 90ºC carbonation treatments is observed to occurs from rT to 270ºC and is associate to the dehydration of nesquehonite [396], dypingite-like phases [398–400] and/or possibly a hydrous AMC with dehydration temperature akin to nesquehonite [55,425]. The decarbonation of these phases occurs between 350-550ºC.

The residual OH content from the activated material upon carbonation remained seemingly unchanged. This indicates that undesired recrystallization of lizardite did not occur [353] in agreement with above mentioned observations (see section 6.2.2.). Moreover, it also indicated that a silicate phase containing OH groups (evidenced by the elevated dehydration temperatures >600ºC remained after carbonation. The more plausible explanation might be that the poorly-reactive intermediate and possibly amorphous phase contains OH groups and the highly-reactive intermediate phase is anhydrous. However, there are several scenarios that might explain such observed behavior.

The progressive decomposition of silanol groups were not observed [353]. A possible explanation might be that either such groups are not present upon carbonation of the activated materials or the low abundance of such groups, together with a prolonged dehydration behavior, might be obscured by the He-flow during TPD measurements.

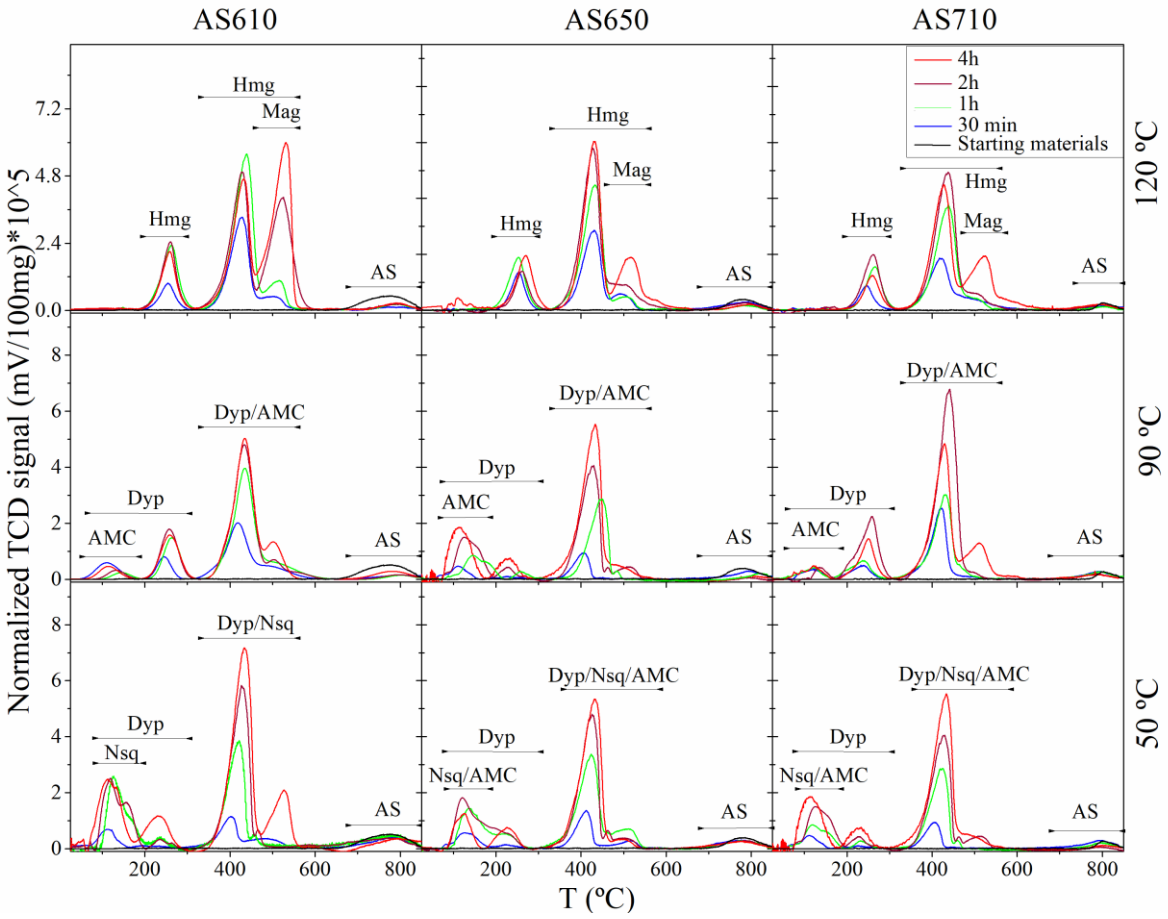

Fig. 6.13. TPD-CO_2-H_2O analysis of the activated materials (AS610, AS650 and AS710) and their respective reaction products. Dehydration and decarbonation temperature ranges of reference Dyp (dypingite), Nsq (nesquehonite), Hmg (hydromagnesite), Mag (magnesite) and AS (activated lizardite) are shown with double ended arrows [203,395–400,453]. Figure from Rausis et al., 2020 [385].

6.2.3.1. CO_2: H_2O ratio of the carbonate products

The CO_2:H_2O ratio was estimated by calculating the areas of the deconvoluted peaks associated with the dehydration and decarbonation of carbonate phases formed upon reaction, respectively. Peak deconvolution of the decarbonation and dehydration of this phases was carried out taking into account the reference decomposition behavior of magnesite [203,453] and hydrated Mg-bearing carbonates [395–400]. Fig. 6.14 shows the calculated CO_2:H_2O ratio of the carbonate products.

The hydration of the carbonate products obtained from reaction of AS710 at 120ºC fits well with stoichiometric hydromagnesite. The reaction products from AS610 and AS650 treatments at 2 and 4h are less hydrated than hydromagnesite, in agreement with the presence of both hydromagnesite and anhydrous magnesite.

The reaction products obtained from carbonation at 90ºC have higher amount of water than stoichiometric dypingite. However, dypingite-like phases have a variable amount of water molecules

per unit [55,180,183,185]. Treatments performed at 50ºC yielded to the formation of hydrated carbonates with a chemical composition similar to stoichiometric nesquehonite during 30min to 1h. Over longer reaction times (2 and 4h), they lose molecular water, resulting in a carbonate product that is more hydrated than nesquehonite and less hydrated than dypingite, in agreement with the presence of dypingite-like phases, as observed with XRD, Raman and SEM.

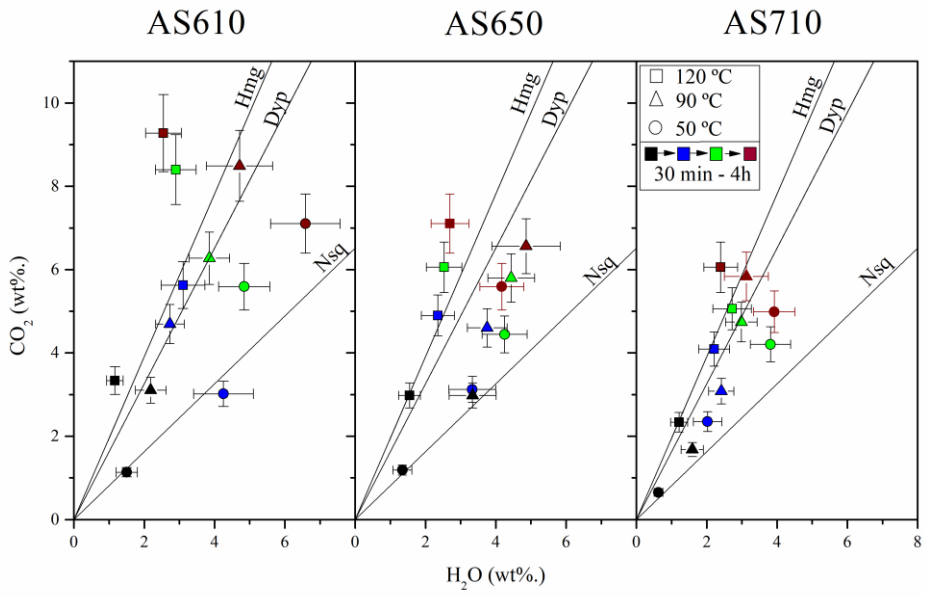

Fig. 6.14. CO_2:H_2O wt%. ratio of carbonate phases formed upon reaction of AS610, AS650 and AS710. Hmg, Dyp and Nsq refers to the CO_2:H_2O composition of stoichiometric hydromagnesite, dypingite and nesquehonite, respectively. Error bars estimate the average between three analogous experiments. Figure from Rausis et al., 2020 [385].

6.2.4. CO_2 sequestration and carbonation yield

The CO_2 wt% sequestered in the reaction products and the estimated Mg wt% fixed by carbonates, estimated by calculating the Mg composition of formed carbonates based on the H_2O and CO_2 contents from Fig. 6.14 (Fig. 6.15). XRF analysis of starting serpentinite exhibit a MgO content of 37wt%., which corresponds to 24,8, 24,9 and 25 Mg wt% for AS610, AS650, AS710, taking into account the increase of oxide composition due to respective partial dehydration of lizardite, which was measured via TPD analysis (Fig. 6.6d).

Reaction products from 120ºC experiments are observed to store more CO_2 than those obtained from 50 and 90ºC for all activated materials. The maximum CO_2 wt% was obtained from the carbonation of AS610 at 120ºC during 4h.

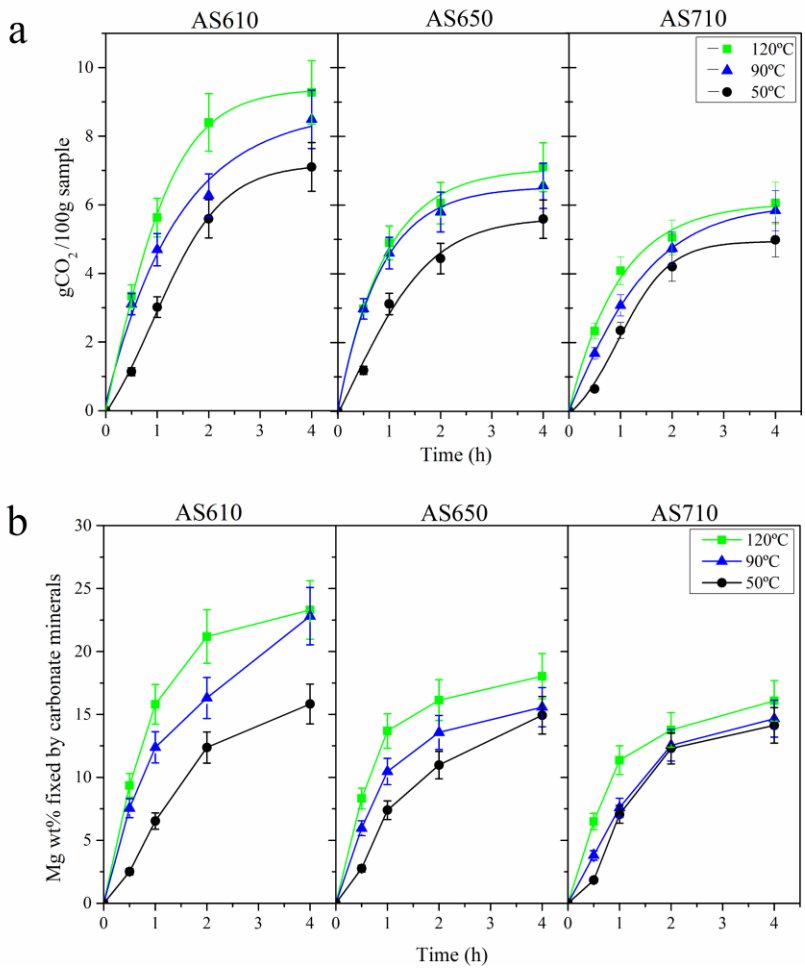

Fig. 6.15. (a) Grams of CO_2 sequestered per 100 grams of sample, as estimated from TPD analysis. **(b)** Amount of Mg fixed by carbonate minerals after carbonation of AS610, AS650 and AS710. Error bars take into account the phase variability and the calculated data from three analogous experiments. Figure from Rausis et al., 2020 [385].

Activation of serpentine minerals induces the formation of highly reactive intermediate phases, particularly the amorphous Mg-rich phases (see section 6.2.1 and 6.2.2) [49,287]. The crystallization of ordered and les-reactive forsterite and enstatite occurs upon gradual increase of activation temperature from 610ºC to 1100ºC. Their formation follows a topotactic, where the rate transition rates decreases with increasing degree of disorder [287]. The undesired nucleation of such phases from intermediate Mg-rich phases significantly decreases the reactivity of such material, particularly the nucleation of enstatite [287]. In this study, a progressive formation of forsterite was observed with increasing activation temperature (Fig. 6.6). This might indicate that the lower carbonate content observed upon carbonation of the activated material at higher temperature (AS710) compared to activated material at lower temperature (AS610) is associated with a gradual nucleation of the intermediate amorphous phases to forsterite. This strongly suggest that there is an optimal combined activation temperature and duration where a complete transformation of lizardite occurs

without the recrystallization of such intermediate phases to forsterite and enstatite, in agreement with previous studies [49,286,287].

The particle size changes upon activation should also be considered, as they play an important role on the carbonation enhancement [145]. In this study, the grain sizes of the different activated materials were found to be very similar (Fig. 6.6). However, higher temperature activated materials (AS710) have slightly bigger grain sizes than those obtained at lower activation temperatures (AS610; Fig. 6.6e). This could contribute to slight decrease on carbonate formation rate for AS650 and AS710 relative to AS650, as less surface area is able to react with CO_2 and H_2O.

Carbonation of AS610 yielded to higher Mg wt% stored by carbonates (accounting to~23.3%) than AS650 and AS710. Carbonate formation reached a steady state after 2h, and therefore, very similar Mg wt% are stored upon 2 and 4 hours of reaction. This low attained Mg wt% strongly suggest that the carbonation reaction have been passivated during the studied timeframe. The concomitant formation of carbonates and silica upon carbonation of intermediate amorphous Mg-rich silicate phases might have played an important role on the passivation of such reaction, as previous studies have suggested [449,450]. Moreover, the presence of magnetite and hematite might also contribute to the passivation of the carbonation reaction, since some studies have suggested that a Fe-rich passivating layer can be formed from the oxidation mechanisms of iron oxides during both activation and carbonation [44,454]. The formation of such passivating layer can be easily avoided by removal of the magnetic fraction by gravimetric separation once the material is grinded [44]. Moreover, relatively pure and profitable magnetite can be obtained from such processes [44,168].

Another factor that might contribute to the low obtained Mg wt% is the formation of forsterite, since the nucleation of this mineral fixes a significant amount of Mg and the concomitant partial loss of the amorphous nature from activated materials. This is in agreement with the lower Mg fraction observed for the higher temperature activated materials (AS710) since they have a significantly higher forsterite yield, compared to materials activated at lower temperature (AS650). Moreover, the slightly bigger grain size for AS710 compared to AS650 and AS610 might also be partially responsible for this behavior.

Moreover, the coexistence of distinct intermediate and amorphous Mg-rich silicate phases with different reactivity might also play a role on the carbonation passivation, since poorly-reactive amorphous phases could have remained partially or fully unaltered upon carbonation, fixing a significant amount of Mg within their disordered structure. Moreover, the formation of a passivating Si/Fe-rich layer and carbonates on the surface of forsterite and poorly-reactive amorphous Mg-rich silicate phases could slow or inhibit their reaction with CO_2 and H_2O.

Undesired reactions, as described in Benhelal et al, 2019 [353], could also play an important role on the passivation of the carbonation reaction. The partial recrystallization of serpentine minerals

upon carbonation not only partially disactivates the highly-reactive materials but also fixes a fraction of Mg. Moreover, a recent study observed that Si-rich phases (such as PMSP) could also retain a fraction of Mg, reducing the available Mg that could be used to form carbonates [353]. The recrystallization of lizardite was not observed in this study. However, the possible formation of Si-rich phases, as observed with FTIR (Fig. 6.10), could have retained a fraction of Mg, reducing the carbonation yield.

Several studies have reported a limited carbonation yield (~ 40%) upon direct carbonation of activated serpentine [196,353,455]. Generally, lower carbonation yields are observed for activated antigorite than lizardite, mainly due to the undesired recrystallization of antigorite upon carbonation [353]. The main discussed factors that passivates the direct carbonation of activated serpentine are: (i) the undesired reactions [353], (ii) unreacted intermediate amorphous Mg-rich phase (this study), (iii) the presence of poorly reactive Q_3 dehydroxylate II [196] (iv) nucleation of forsterite and enstatite [287] and (v) the formation of Si/Fe-rich passivating layers [44,449,450,454]. On basis on this observations, activation processes can be further optimized in order to (i) obtained a complete or almost complete transformation of lizardite as well as a complete transformation of Q_3 dehydroxylate II to amorphous intermediate Mg-rich silicate phases, (ii) increase the proportion of highly-reactive intermediate amorphous phase relative to the poorly reactive amorphous phase and (iii) avoid the nucleation of forsterite and enstatite. Moreover, a combined carbonation and activation processes should be focused on minimizing the passivation effect due to undesired reactions and the formation of passivating layers (if possible).

6.2.5. Magnesite formation

The yield of magnesite and hydromagnesite formation (expressed as the Mg wt% stored in such minerals) was possible to estimate due to the decarbonation of such phases occurs at slightly different temperature ranges observed with TPD and by comparison of Raman, XRD and SEM results. Fig. 6.16 shows the respective Mg wt% fixed within magnesite and hydromagnesite structures upon carbonation of the activated materials at 120ºC from 30 min to 4h.

Hydromagnesite formation reached a steady state after 1h of reaction for the lower temperature activated materials (AS610, AS650) and after 2h for AS710. Moreover, the total Mg wt% stored within hydromagnesite structure once it has reached the steady state was observed to be very similar for all activated materials accounting to ~15%. Such fraction is lower the total obtained after 4h of reaction, which might suggest that the reaction environment is saturated with respect to hydromagnesite, inhibiting further formation of this latter mineral. An analogous behavior can also be observed from 120ºC treatments performed in Farhang et al., 2017 [196].

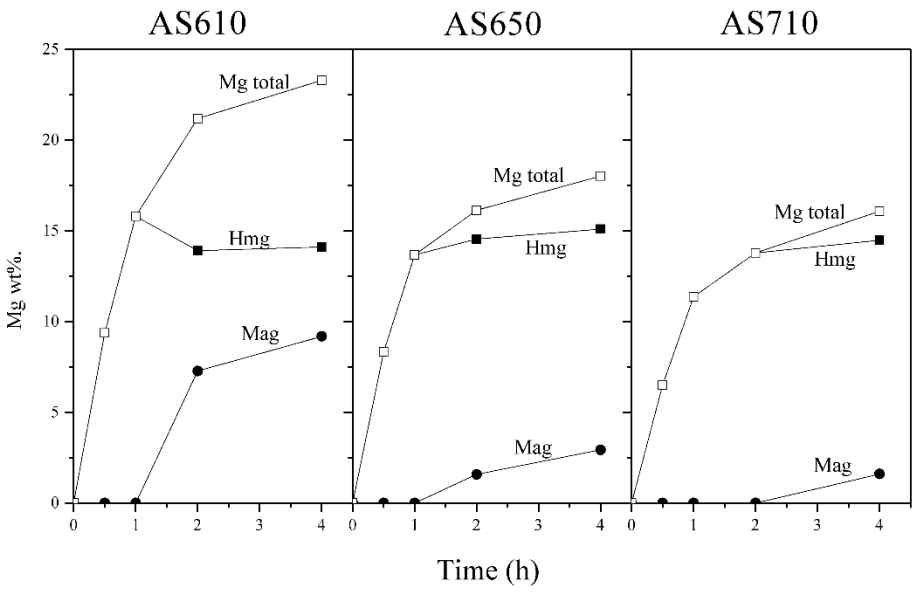

Fig. 6.16. Mg wt% of fixed by hydromagnesite and magnesite upon carbonation of AS610, AS650 and AS710 at 120ºC, from 30 minutes to 4 hours. (Mg total) Mg wt% that has been stored by both (Hmg) hydromagnesite and (Mag) magnesite. Figure from Rausis et al., 2020 [385].

The formation of magnesite was identified after 1h for the AS610 and AS650 materials and it was observed once hydromagnesite formation reached a steady state, which might suggest that magnesite formation is accelerated in a reaction environment saturated with respect to hydromagnesite. Moreover, magnesite content was observed to be lower for the higher temperature activated materials (AS610 > AS650 > AS710). This is in agreement with the slower formation rate of hydromagnesite on AS650 and AS710 compared to AS610, taking longer reaction times to reach the hydromagnesite steady state, thus, delaying the formation of magnesite.

Several studies have observed that the formation of magnesite at moderately low temperatures (<250ºC) often undergoes the transformation of hydrated carbonates (i.e.: hydromagnesite), since the direct formation of magnesite is inhibited by the kinetically preferred formation of hydrated species, mainly due to the high hydration nature of Mg^{2+} [179,193,413]. However direct formation of magnesite (without a hydrated precursor) can also be formed at low temperature, however it is often related to occur over extended times (often involving geological timescales) [194,195]. It remains unclear whether magnesite formation observed in this study underwent a hydrous precursor or if was directly form from activated serpentine.

Magnesite formation often requires elevated temperature and pressures (100ºC, ~100 bar) as well as extended reaction times [178,179,197,200]. Such rapid magnesite formation at this temperature and pressures is often comparable with other studies carried at significantly higher pressures (150 bar). Experiments carried under similar conditions (120ºC, 10 bar) of those reported in this study (120ºC, 6 bar) reported that the transition between hydromagnesite to magnesite

occurred over several days [201]. Our results strongly suggest that magnesite formation is greatly accelerated, as evidence by its appearance at 1h of reaction at 120ºC and 6 bar during steam-mediated carbonation reactions (see also section 2.1.1). This accelerated formation of magnesite might be associated with occur in a reaction environment saturated with respect to hydromagnesite.

6.3. Conclusions

The results from this work provides new insights on the intermediate Mg-rich silicates phases that formed upon activation and the role they individually play during carbonation reactions. Moreover, it also provides new information about the formation of Mg-carbonate phases and their evolution as the reaction proceeds. It was observed that temperature is the dominating factor that controls the hydration level of the formed carbonate species. Treatments performed at 120ºC yielded to the formation of hydromagnesite and magnesite. The accelerated formation of magnesite, particularly for AS610 materials, is observed to occur only after hydromagnesite formation reached a steady state, suggesting that magnesite formation can be accelerated in a reaction environment saturated with respect to hydromagnesite. Reaction carried at 90ºC, exhibit a rapid formation of a nesquehonite-like phase that it transforms in less than 30min to dypingite-like phases and possible and hydrous AMC. On the other hand, nesquehonite remained untransformed from carbonation treatments performed at 50ºC during 2h for AS650 and AS710 and 4h for AS610. The formation and evolution of distinct carbonate phases under analogous experimental conditions between the different activated materials suggest that the reacting material play a key role not only on the formation of carbonate phases but also on the evolution of such phases. This might be partially attributed to the different relative proportion of intermediate Mg-rich phases from different activated materials. Two distinct intermediate and possible amorphous Mg-rich silicate phases were identified upon activation. The phase associated with the 888.1 and 626.3 ± 3.5 cm^{-1} FTIR and Raman peak, respectively, was found to be highly reactive upon carbonation. However, the phase associated with 673 ± 1.1 and 1019 ± 8.5 cm^{-1} FTIR and Raman peak, respectively, remained unreacted upon carbonation.

Results from this work can provide important insights on optimization of the combined thermal activation processes and carbonation treatments of lizardite, including: (i) a complete (or almost complete) transformation of lizardite to intermediate phases as well as the transition between Q^3 Dehydroxylate II to amorphous intermediate phases, without the nucleation of such phases to crystalline forsterite and enstatite, (ii) the increase of the relative proportion of highly-reactive intermediate and possible amorphous Mg-rich silicate phase relative to the poorly reactive amorphous phase, (iii) avoiding (if possible) undesired reactions, such as re-serpentinization and (iv) reduce the formation of Si/Fe-rich passivating layers.

Carbonation of AS610 yielded to higher carbonate contents compared to the higher temperature activated materials (AS650 and AS710). The maximum CO_2 wt%. by formation of carbonates was attained at 120ºC and 4h using AS610, accounting to 9,3 CO_2 wt%, which corresponds to 23.3% of the total available Mg wt% (based on the CO_2:H_2O composition of the combined carbonate products). These results are comparable to those reported for higher pressure treatments (120ºC, 140bar), suggesting that elevated pressures are not strictly required for carbonation of activated lizardite. The lower AS650 and AS710 carbonation yield is mainly attributed to the respective nucleation of forsterite upon activation.

7. Carbonation of brucite-bearing serpentinized dunite as an alternative route to the carbonation of activated serpentine

7.1. Introduction

Mineral carbonation studies at low temperature and pressure conditions are mainly focused on understanding naturally-occurring processes [194,195,456,457]. Nonetheless, research interest in increasing due to the possible application of such processes for CCUS purposes [56,57,270]. An example is the study of passive mineralization in ultramafic mine tailings under atmospheric pressure and temperature conditions [176,376,458]. Carbonation of mine tailing is favored over their natural analogous due to their increased surface area. It has been reported that such processes are able to sequester significant amounts of atmospheric CO_2 through the formation of highly-hydrated hydro-carbonates such as nesquehonite, dypingite and a possible hydrous AMC [371,376,457]. The total sequestered CO_2 if carbonation is accelerated relative to weathering rates throughout the tailing bulk it could significantly exceed the CO_2 emissions of in-situ mining operations [371]. It has been observed that if enriched CO_2 gases (gases with a CO_2 partial pressure above atmospheric) are supplied into the tailings, a significant carbonation acceleration is observed due to the enhance mineral dissolution [459,460].

Brucite is a common but minor alteration product of ultramafic rocks. Different studies have reported the presence of this mineral in chrysotile and nickel tailings as well as in chromite ore processing residue with a total content ranging between 1 to 15wt% [456,461]. The carbonation of brucite offers a significant CO_2 sequestration potential. Several studies have concluded that the presence of brucite in mine tailings plays a key role on both accelerated and natural carbonation of such materials [371,457,458]. The estimated chrysotile tailing mining residues is approximately 2Gt

in Québec, Canada alone. It has been observed that in such tailings, natural brucite occurrences accounts to 1.8wt%. [456]. If this brucite content is scaled to all the chrysotile tailings in Quebec, the estimated CO_2 sequestration capacity of brucite alone is estimated to be approximately 27Mt of CO_2. Carbonation of the total brucite produced annually would significantly offset the CO_2 emissions from mining operations by 22-57% [371]. Mount Keith Nickel Mine (MKM) produces 11 Mt of nickel mine tailing (NiMT) yr^{-1} with contains about 0.11-0.28 Mt of brucite, which is mainly responsible to the sequestered 0.6 kt CO_2 yr^{-1} [371]. It has been suggested that accelerated carbonation processes could significantly increase the carbonation potential of such tailings [371].Tailings produced at Dumont Nickel deposit in Québec contains elevated brucite contents ranging from 10-15wt% [456]. The successful carbonation of this mineral within this tailing with significantly exceed the estimated CO_2 sequestration capacity of MKM tailings. The carbonation of natural occurrences of brucite, despite its relatively low abundance, could provide significant sink for anthropogenic CO_2 emissions [371].

The proposed carbonation reaction between NiMT from Dumont Ni-deposit is shown in Fig. 7.1 [175]. The measured initial pH of the analyzed NiMT was of 9.5. However, upon the introduction of CO_2, a significant pH drop was observed, which lead to the leaching of Mg^{2+} (Fig. 7.1a). The interface between the brucitic regions (taking into account the outer OH layer of serpentine minerals, often referred as “brucite” hydroxyls [101]) has a pH gradient from alkaline (due to the elevated presence of dissolved Mg^{2+} near the brucitic regions) to acidic (CO_2 dissolved in water). The nucleation of carbonates was observed to occur within this pH swing interface (Fig. 7.1b). Formed flaky and poorly crystalline porous carbonates were observed to form aggregates, which is characteristic of dypingite-like phases (see Figs. 4.3, 5.20). Such carbonate agglomerates evolve to form more organized and less porous nesquehonite, which was discussed to limit the diffusion between CO_2 to brucite grain, inhibiting further carbonation (Fig. 7.1c). Moreover, it was also found that dissolution of serpentine minerals thought brucitic regions also contributed to the carbonation reaction, since it was observed the formation of a Si-rich phase upon carbonation (3wt%.) [175]. However, the main responsible for the carbonation reaction is undoubtedly brucite.

The presence of brucite also play an important role on the natural weathering of (ultra)mafic rocks [368]. Such mineral, despite being a common product of the first stages of serpentinization of oceanic and ophiolitic serpentines is only found as a minor phase in such geological settings [163,462,463]. This is mainly associated with a variety of factors, including: (i) increase of silica activity during serpentinization which promotes brucite dissolution by the alteration fluid; (ii) brucite stability is greatly reduced during hydrothermal serpentinization at high temperatures; (iii) the solubility of brucite by low temperature meteoric fluids and seawater, which yields to the formation of hydrous Mg-carbonates [368].

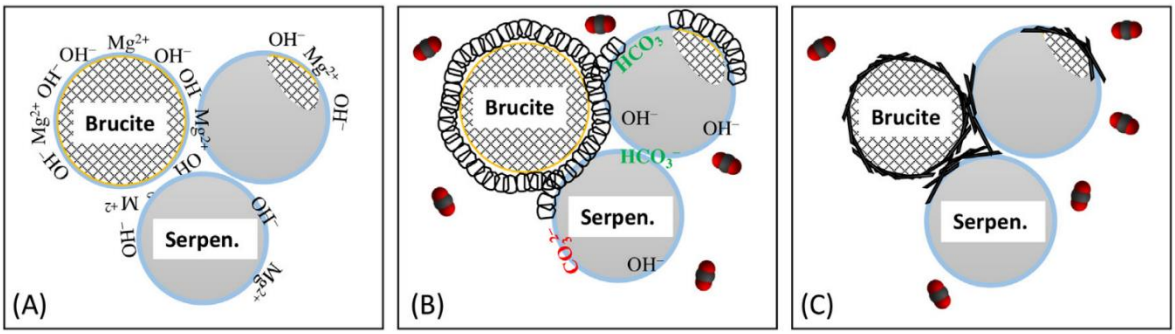

Fig. 7.1. Schematic of NiMT carbonation processes. **(A)** Metal and hydroxyl groups are being leached out of brucitic regions due the acidity caused by the dissolution of CO_2 in water. **(B)** Mg-bicarbonates aggregated in form of flaky dypingite crystals and highly porous hydrous Mg-carbonate structures near the high pH brucite surfaces. **(C)** evolution of Mg-carbonate phases forming nesquehonite prismatic crystals. Figure from Zarandi et al., 2016 [175].

On-going natural carbonation at the Montecastelli ophiolites (in Italy) have proven to provide important insights on the role of brucite upon natural carbonation. It has been observed that brucite-rich serpentinized bodies have underwent and are continuously carbonating [368], yielding the formation of naturally-occurring hydrous carbonate outcrops in selective areas [464]. On the other hand, brucite-free serpentinized harzburgites remained seemingly unreacted [368].

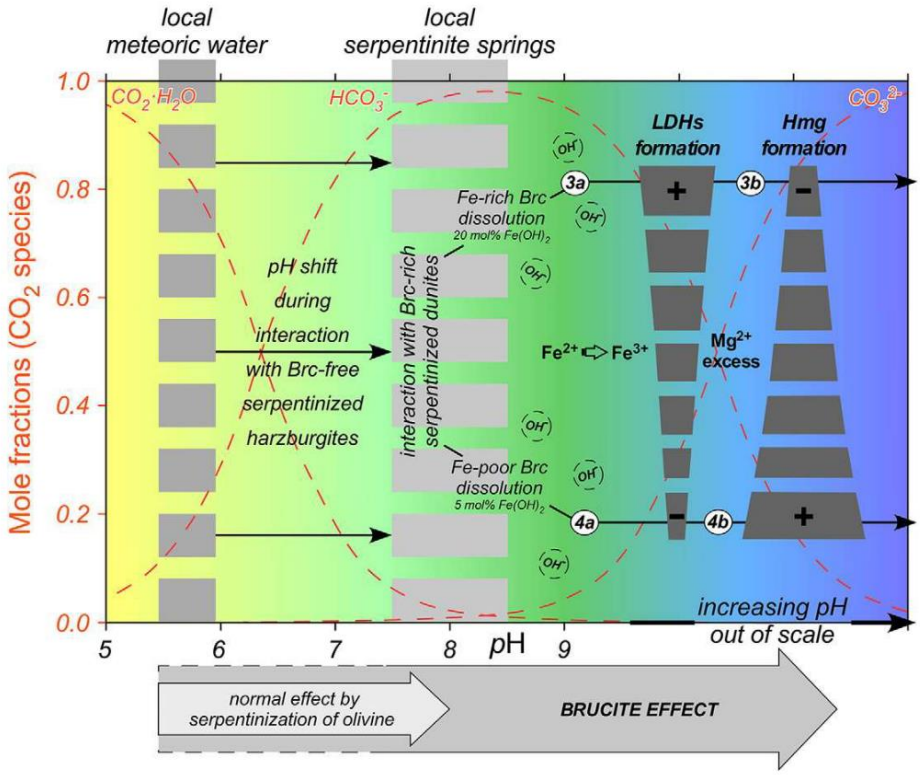

Fig. 7.2. Schematic of the sequence of water-rock interaction at the Montecastelli ophiolites, leading to the dissolution of serpentinized dunites and harzburgites as well as naturally-occurring brucite and precipitation of carbonates (Hmg: hydromagnesite) and LDHs, which is mainly controlled by the Fe-content of dissolving brucite. Figure from Boschi et al., 2017 [368].

Montecastelli meteoric waters are slightly acidic. On the other hand, a variety of spring water have a pH from 7.5-8.5, due to their Mg^{2+} concentration, which is mainly attributed to the dissolution of residual primary silicate relicts (olivine ad pyroxene). The most abundant carbonic species at this pH is HCO_3^-. It was suggested that slightly alkaline spring waters induced serpentine dissolution, increasing further the pH, where CO_3^{2-} species are dominant, leading to the precipitation of carbonates (Fig. 7.2). It was observed that the presence of Fe-rich brucite phases (containing up to 20 Fe mol.%) significantly reduced the carbonation yield due to the formation of layered double hydroxides (LDHs), such as pyroaurite ($Mg_6Fe_2^{3+}(CO_3)(OH)_{16}\cdot 4(H_2O)$. Such minerals fix significant amounts of Mg^{2+} relative to carbonate ions (Mg/C: 6), significantly higher than hydromagnesite (Mg/C: 1.25) and magnesite (Mg/C: 1). Therefore, LDHs have significantly lower CO_2 storage capacity than Mg-carbonates.

Brucite content on such ophiolites was estimated to be in the range of 10-20wt%, which is consistent with the global estimates for other serpentinized dunites [465,466]. Such elevated contents might provide a possible source of highly reactive brucite for MC purposes. However, Fe-rich brucite phases are commonly found in ophiolitic settings. Therefore, LHDs formation should be avoided, which can be accomplished by accelerating the formation of hydrous Mg-carbonate phases [368].

Due to this high carbonation potential of brucite-rich serpentinized dunites, an experimental study on the accelerated carbonation of such materials via steam-mediated direct carbonation was carried in order to assess their reactivity and concomitant CO_2 storage capacity at moderately-low pressures and temperatures (50-185ºC, 10 bar). This could provide insight on the utilization of such materials for mitigating climate change and carbonate synthesis.

7.2. Results and discussion

7.2.1. Role of temperature

Distinct Mg-carbonates phases were formed upon carbonation, where its formation was mainly controlled by reaction temperature. Raman and XRD results of the solid products of reactions at 50-185ºC, 10 bar during 4h are shown in Fig. 7.3. Upon carbonation at 50ºC, the appearance of three distinct peaks are observed within the region of the ν_{1sym} of the carbonate ion (CO_3^{2-}; $\nu_{1symCar}$) [380,381] at 1091.16, 1099.34, 1020.01 cm^{-1} (Figs. 7.4a, 3.6). However, XRD analysis (Fig. 3.5b) shows only the presence of nesquehonite, as evidence by its characteristic X-ray diffraction pattern [193,376]. The presence of this phase is consistent the emergence of its characteristic Raman peak observed at 1099.34 cm^{-1} Raman peak (Fig. 7.3a, 7.4) [182,380,382]. Analogous comparison between FWHM and peak position of $\nu_{1symCar}$ Raman peaks and the two more intense XRD features of each carbonate phase is shown in Fig. 7.5. Despite nesquehonite x-ray diffraction pattern is

consistent with the reference mineral, its characteristic Raman peak has a very similar position but is broader than the reference data of this mineral. This might be attributed to morphological variation among nesquehonite crystals (see section 6.2.2). Calculated data for the broad $\nu_{1symCar}$ band observed at 1020.01 cm^{-1} fits well with reference dypingite, but their respective x-ray scatter was not observed. This might be explained by both the low abundance of this mineral and its highly to semi-ordered structural nature. The level of disorder of such phases influences significantly the intensity and broadness of both Raman and XRD characteristic peaks [55]. Calculated data for the Raman band at 1091.16 cm^{-1} have similar position to magnesite, however the concomitant and characteristic magnesite Raman peak at 328.3 ± 0.1 cm^{-1} is not observed, as well as their XRD features, strongly suggesting that the phase responsible for the 1091.16 cm^{-1} is distinct to magnesite. Moreover, such phase resembles features that might be attributed to the presence of an hydrous AMC (see Chapter 5) [55].

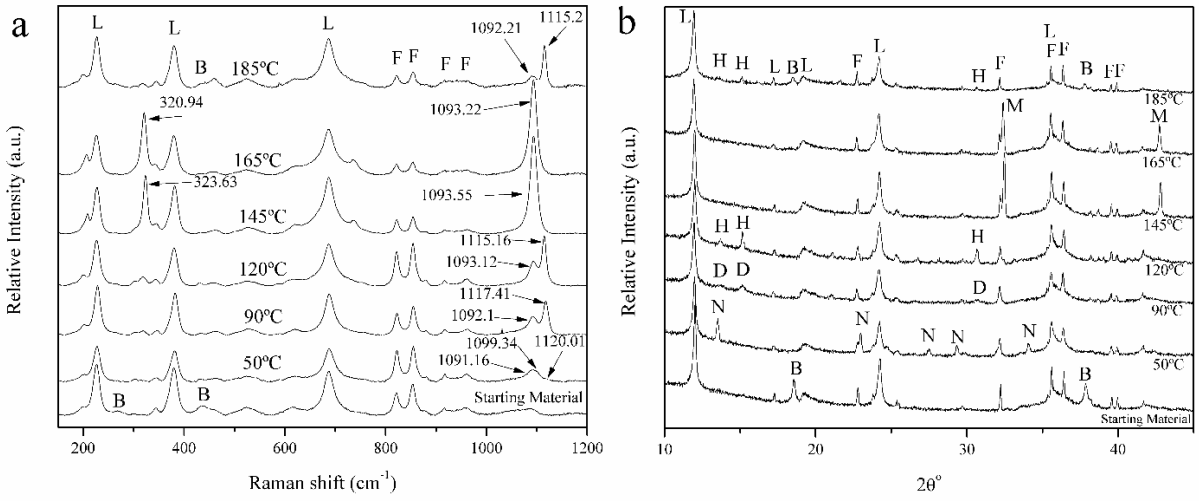

Fig. 7.3. (a) Raman and **(b)** XRD analysis of the solid product of reactions carried at temperature from 50-185ºC during 4h. F, L, B, M, H, D and N shows the XRD peaks associated with forsterite, lizardite, brucite, magnesite, hydromagnesite, dypingite and nesquehonite, respectively.

Reaction products obtained at 90ºC shows the presence of a dypingite-like phase, as evidenced by its characteristic XRD features, which is associated with the emergence of the 1117.41 cm^{-1} $\nu_{1symCar}$ Raman peak. Moreover, an additional $\nu_{1symCar}$ Raman peak at 1092.1 cm^{-1} is also observed. Calculated FWHM vs peak position data suggest that this phase might be a hydrous AMC (see chapter 5). It should be also noted the associated Raman peak to dypingite-like phases is approaching is slightly shifter and has a lower FWHM than such observed from treatments performed at 50ºC, suggesting that the dypingite-like observed at 90ºC has a more ordered structure that at 50ºC [55]. This behavior (dypingite-like phases becomes more structurally ordered upon increasing reaction temperature) is particularly evident at 120ºC, where the level of order is more akin to

hydromagnesite rather than a dypingite-like phases (Figs. 7.3, 7.5). It is known that the level of disorder in hydrous carbonate mineral is mainly controlled by its water content [55,404]. It is likely that the transition between highly disordered dypingite-like phases to hydromagnesite is mainly controlled by cell-shrinkage due to partial dehydration [55]. The slow kinetic of such processes is mainly attributed to the high susceptibly of Mg^{2+} to H_2O [413].

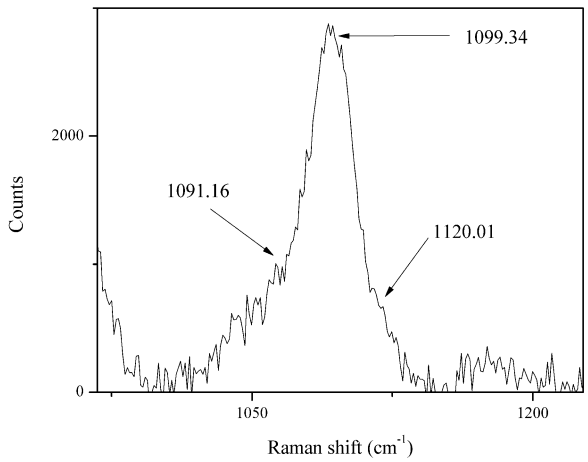

Fig. 7.4. Raman analysis within the $v_{1symCar}$ region of the reaction products obtained at 50ºC, showing the presence of at least three different peak that might be associated with different carbonate phases.

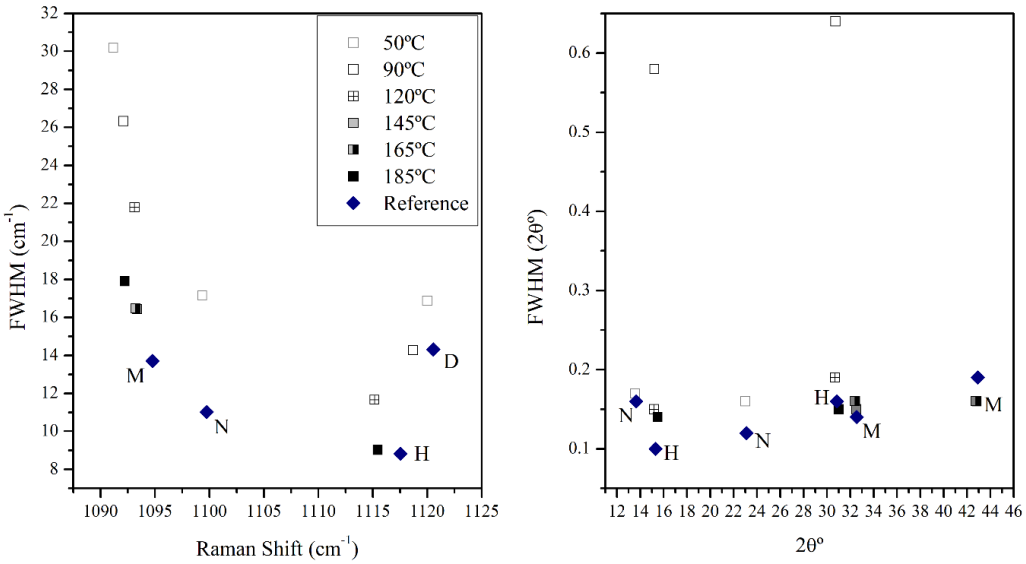

Fig. 7.5. Calculated FWHM vs peak position of the identified $v_{1symCar}$ as well as the two more intense XRD peaks of the observed carbonate phases. M, H, D and N shows the reference data associated with magnesite, hydromagnesite, dypingite and nesquehonite, respectively. The FWHM and peak position of reference minerals were calculated from Lafuente, et al., 2015 [85].

Treatments performed at 145 and 165ºC yielded to the formation of magnesite as evidenced by its characteristic XRD features as well as the emergences of both 322.3 ± 1.3 and 1093.4 ± 0.2 cm^{-1} Raman peaks (Figs. 7.3, 7.5) [203,382]. At 185ºC, hydromagnesite is once again observed as well as a significant decrease on the magnesite yield. The reduced magnesite yield at 185ºC was also observed in section 4.2.1. This behavior might be attributed to the chemical potential that drives diminishes as the temperature approaches the equilibrium boundaries between reacting phases [48,145] (see also section 4.2.4).

In section 6.2.5. it was observed that in a reacting environment saturated with respect to hydromagnesite, the nucleation of magnesite is significantly accelerated [385]. This might explain insights on the appearance of hydromagnesite at 185ºC, as well as the reduced magnesite yield at this temperature when compared to 145 and 165ºC experiments. Hydromagnesite formation occurs slower at 185 than at 165ºC. This increases the required time for hydromagnesite formation to reach a steady state, thus, possibly delaying the formation of magnesite. However, it remains unclear if magnesite formation underwent a precursor hydrated carbonate, such as hydromagnesite [179,193,196] or if it formed directly upon carbonation of the starting material [194,195].

The inexistence of brucite in 50-165ºC experiments suggest that a complete (or almost complete) carbonation of this mineral. At 185ºC, residual brucite is identified, which is likely to be attributed to the slower reaction rates at this reaction temperature. No changes were observed for lizardite and forsterite upon reaction, as evidenced by the seemingly unchanged FTIR absorption features due to the vibrations of Si-O-Si, characteristic of this latter minerals (Fig. 7.6) [356,467].

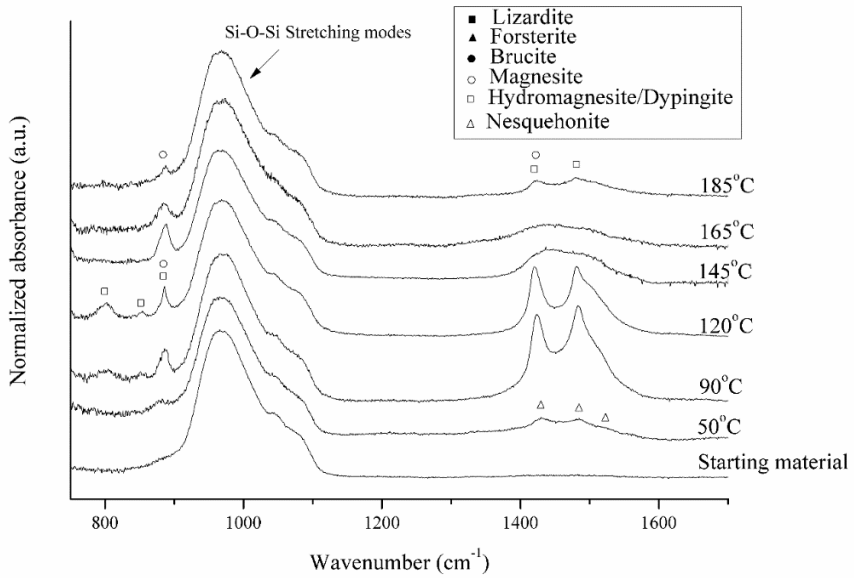

Fig. 7.6. FTIR analysis of the solid products of reactions carried at 50-185ºC and 10 bar during 4h. The reference positions of common Mg-carbonates phases are shown.

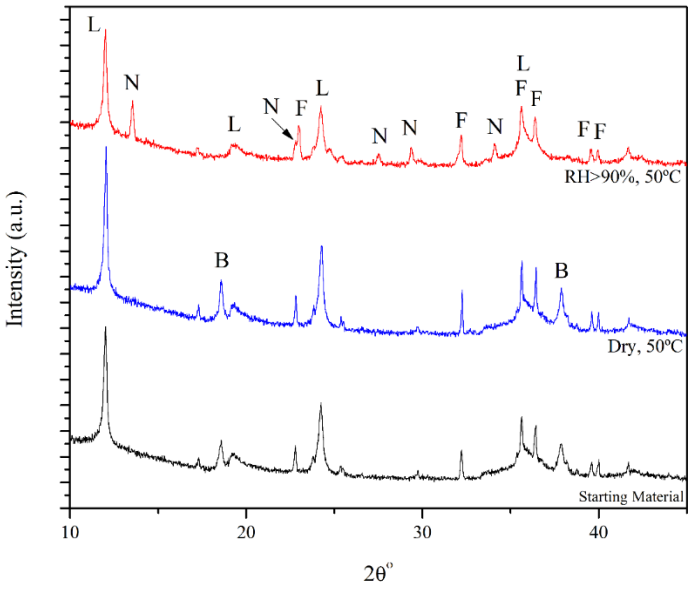

Fig. 7.7. XRD results of the solid products of reactions carried at 50ºC during 4h in the presence and absence of steam. F, L, B and N shows the XRD peaks associated with forsterite, lizardite, brucite and nesquehonite, respectively.

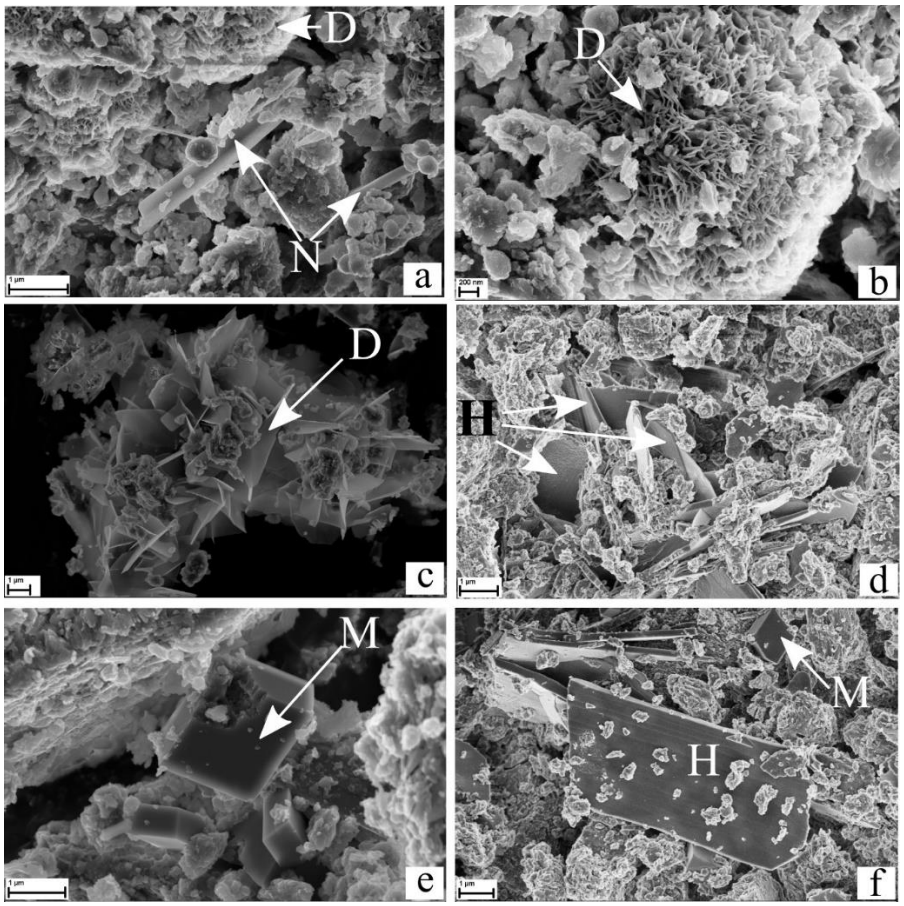

Fig. 7.8. SEM images of the solid products obtained at **(a)** 50, **(b)** 90, **(c)** 120, **(d)** 145, **(e)** 165 and **(f)** 185ºC during 4h and 10bar. N, D, H and M stands for nesquehonite, dypingite, hydromagnesite and magnesite, respectively.

Additionally, carbonation was also performed in the absence of steam (Fig. 7.7). XRD results shows negligible (if any) carbonation of brucite from the starting material. However, with the addition of water vapor, brucite carbonation is almost of fully complete. These results show the critical role of steam in the enhancement of the rate of the carbonation reaction.

The presence of nesquehonite in the 50ºC experiments is also evidence by the appearance of prismatic crystals (Fig. 7.8a) [178,376], characteristic of this mineral. Moreover, flaky crystals organized in rosette-like structures are also observed, often associated with the presence of dypingite-like phases (Fig. 7.8a, b) [55,179]. Significantly bigger flaky crystals (also arranged in rosette-like structures) are observed at 90ºC (Fig. 7.8c). At 120ºC, thicker plates are formed compared to the flaky crystals formed at 50 and 90ºC (≥1 μm; Fig. 7.8d) [171,194]. At 145ºC, only rhombohedral magnesite crystals were observed (~ 1μm; Fig. 7.8e) [387]. At 185ºC, coexisting hydromagnesite plates and rhombohedral magnesite are observed (Fig. 7.8f).

It should be noted that the LDH minerals were not formed upon carbonation. This might indicate either treated brucite had a low Fe content or formation of hydrated carbonated was kinetically preferred over LDH. This provides important insights in the utilization of such materials for mineral carbonation, since naturally-occurring brucite in ophiolites are commonly rich in Fe.

7.2.2. Role of reaction time

Experiments carried at 165 and 185ºC were carried out during 2 to 60h in order to provide more insights in the formation and evolution of magnesite. Raman and XRD results are shown in Fig. 7.9. Results from reactions carried at 165ºC during 2h yielded to the formation of hydromagnesite and magnesite. At this reaction time, brucite is no longer identified. At longer reaction times (≥4h) hydromagnesite is no longer observed and magnesite is the only identified carbonate phase, indicating that hydromagnesite was precursor of magnesite.

Treatments performed at 185ºC also yielded to the formation of hydromagnesite follow by its transformation to magnesite, but over extended reaction times when compared to 165ºC treatments. A complete transformation of hydromagnesite to magnesite is only observed at 60h. It should be also noted that brucite remained partially unreacted even upon 60h of reaction. This is attributed to the slower reaction kinetics at this temperature when compared to 165ºC treatments, as discussed in section 7.2.1.

Comparison between FWHM and peak position of $\nu_{1symCar}$ Raman and the two more intense XRD peaks of the carbonate products shows that the calculated data fits well with hydromagnesite and magnesite (Fig. 7.10). The transition between those phases seemingly underwent without intermediate precursor.

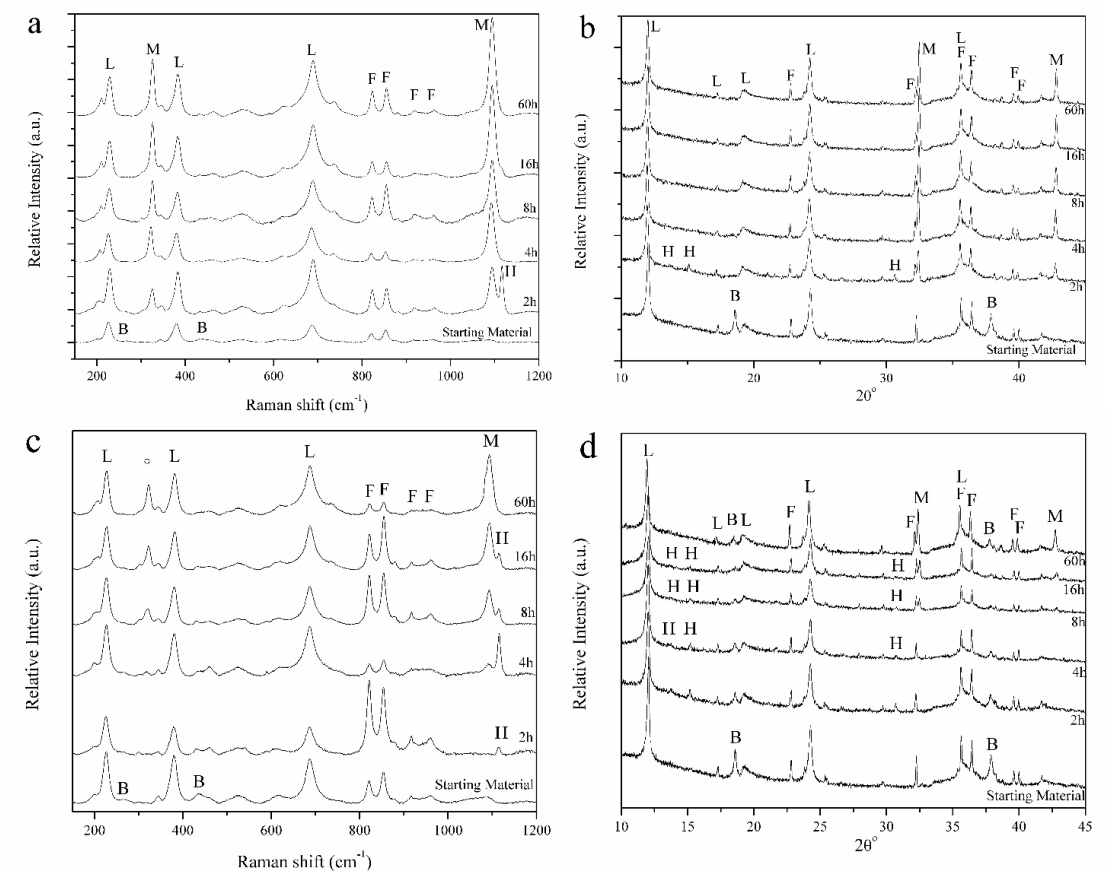

Fig. 7.9. (a, c) Raman and **(b, d)** XRD analysis of the solid products of reactions carried from 2 to 60h at **(a, b)** 165ºC, **(c, d)** 185ºC. F, L, B, H and M shows the Raman and XRD peaks associated with forsterite, lizardite, brucite, hydromagnesite and magnesite

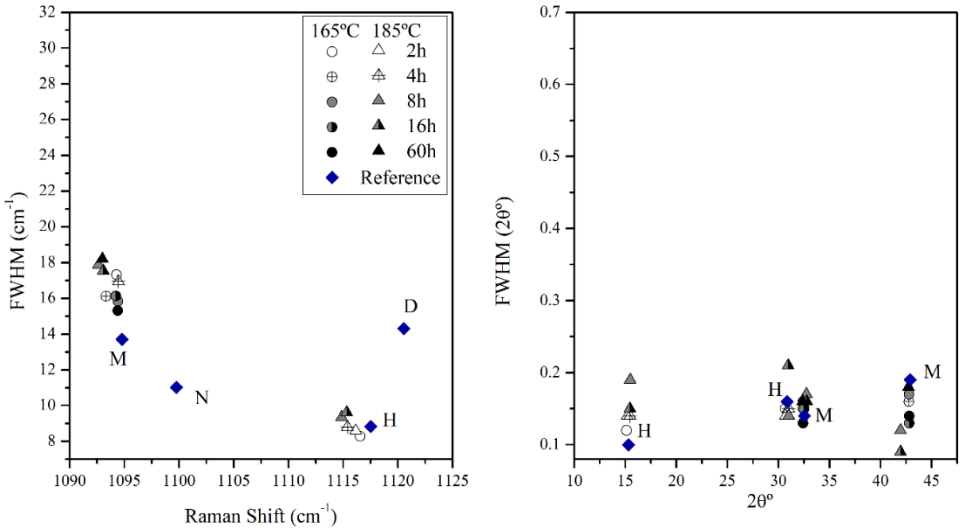

Fig. 7.10. Calculated FWHM vs peak position of the identified **(left)** $v_{1symCar}$ as well as **(right)** the two more intense XRD peaks of the observed carbonate phases obtained at 165 and 185ºC from 2 to 60h. M, H, D and N shows the reference data associated with magnesite, hydromagnesite, dypingite and nesquehonite, respectively. The FWHM and peak position of reference minerals were calculated from Lafuente, et al., 2015 [85].

The slow transition of hydromagnesite to magnesite at 185ºC was monitored with SEM (Fig. 7.11). Hydromagnesite plates (~ 10 μm) are observed at 2h (Fig. 7.11a). At 4h, on a large hydromagnesite plate (~ 10 μm) was observed etch pits and overgrowths of rhombohedral nano-magnesite (< 1 μm; Fig. 7.11b). Such behavior is very similar to such observed during the transformation of nesquehonite to dypingite-like phases (see section 5.2.1.1). Such reaction mechanisms are strongly related to dissolution-recrystallization self-assembly growth mechanism [55,179,432]. The overgrowth of magnesite might act as nucleation points. At 8h, a smaller hydromagnesite plate (~3 μm) is surrounded by magnesite with different crystal sizes (> 2 μm; Fig. 7.11c). A complete transformation of hydromagnesite to magnesite (> 2 μm) is observed at 60h (Fig. 7.11d). Magnesite crystals at 60h are significantly bigger than those observed at lower reaction times, suggesting a nucleation (4h) and growth mechanism (8-60h). This is consistent with previous studies regarding the formation of magnesite, reported to be nucleation-limited and the abundance of this mineral sis mainly increased by crystal growth (see section 2.1.1) [194,197,198].

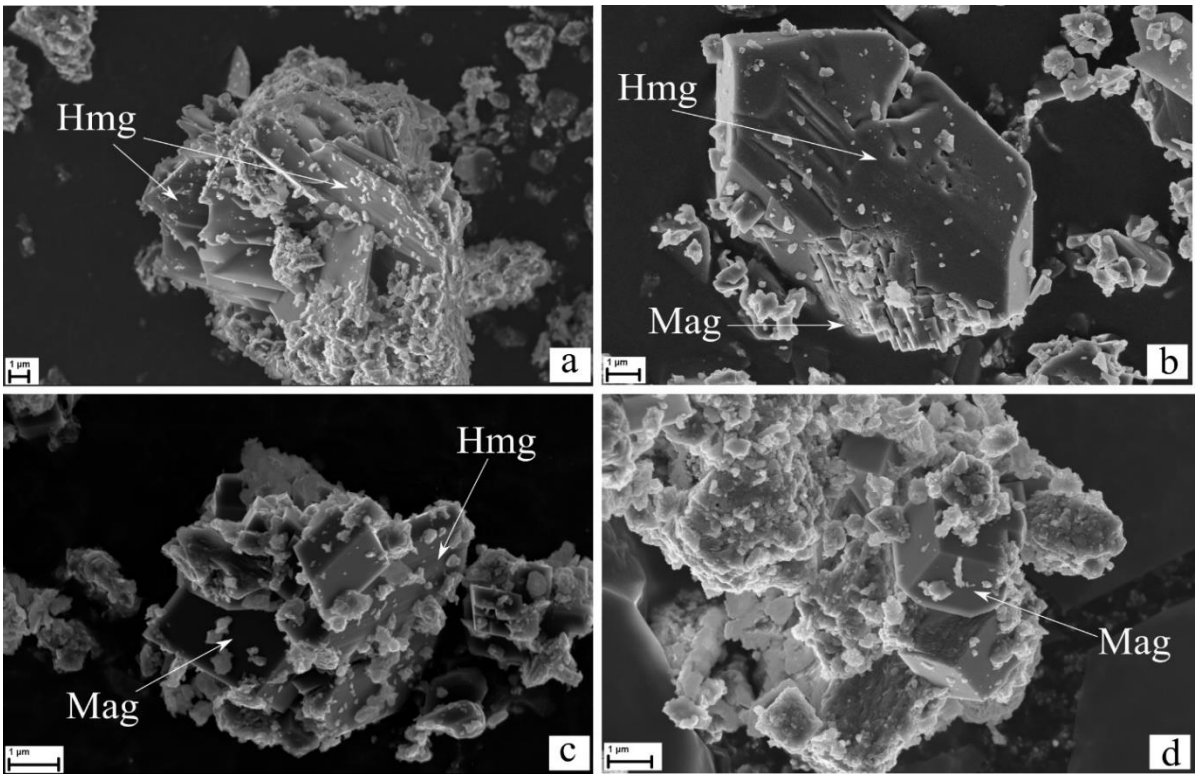

Fig. 7.11. SEM images of the solid products obtained from 185ºC treatments at (a) 2, (b) 4, (c) 8 and (d) 60h. Hmg and Mag stands for hydromagnesite and magnesite, respectively.

The formation of hydromagnesite and its transformation to magnesite is observed to occur in less than 4h for both 165 and 145ºC at 10 bar. Such (at least) two-step reaction is observed to occur significantly faster that such reported for under low pressure and temperature conditions (<10 bar, ≤180ºC). In a recent study it was observed that magnesite formation is significantly accelerated in a reaction environment saturated with respect to hydromagnesite (see section 6.2.5) [385]. This

strongly suggest that the formation of magnesite can be further optimized to achieve reasonable conversion rates at moderately low pressure and temperature conditions. Nevertheless, the dissolution of Mg-rich silicates under such conditions remains kinetically challenging.

7.2.3. TPD analysis

TPD analysis was performed to assess the carbonation yield obtained upon carbonation (Fig. 7.12). The differentiation of overlapping brucite dehydration with the decarbonation of hydrated carbonates was carried taking into account the observed phases based on XRD, Raman and SEM. At 50-90ºC, overlapping dehydration between nesquehonite [396], dypingite [398–400] and possible AMC [55,425] were observed to occur from rT to 340ºC. Decarbonation of such phases occurred between 340 – 550ºC.

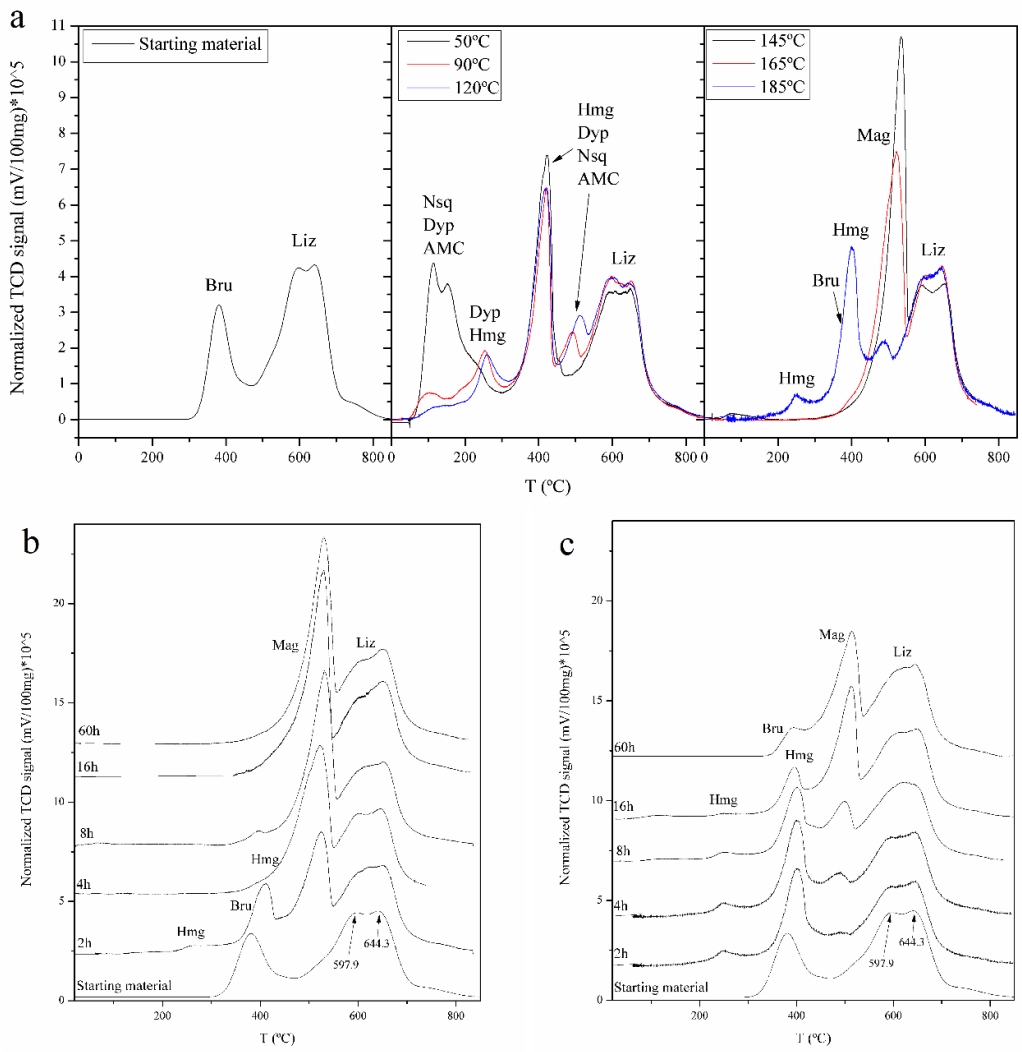

Fig. 7.12. TPD analysis of the reaction products obtained at **(a)** 50-185C during 4h, **(b)** 165ºC from 2-60h and **(c)** 185ºC from 2-60h. Bru, AMC, Dyp, Hmg, Mag and Liz represent the reference decomposition behavior of brucite, hydrous AMC, dypingite, hydromagnesite, magnesite and lizardite, respectively.

Characteristic decomposition of hydromagnesite, and hydrous AMC were observed during TPD analysis of the reaction products obtained at 120ºC. Characteristic decomposition of magnesite [196] is observed from treatments performed at 145 and 165ºC. Coexisting hydromagnesite and magnesite were observed from treatments performed at 185ºC, as well as residual brucite.

The transition between hydromagnesite to magnesite at 165 and 185ºC is also observed in TPD analysis (Fig. 7.12b, d). At 165ºC, partial carbonation of brucite to hydromagnesite as well a partial transition from hydromagnesite to magnesite is observed (Fig. 7.12b). Reaction carried at 4 hour or longer yielded to a complete carbonation of brucite to magnesite via hydromagnesite intermediate. Such transition is also observed from treatments performed at 185ºC over extended reaction times, in agreement with discussion in section 7.2.1 and 7.2.2.

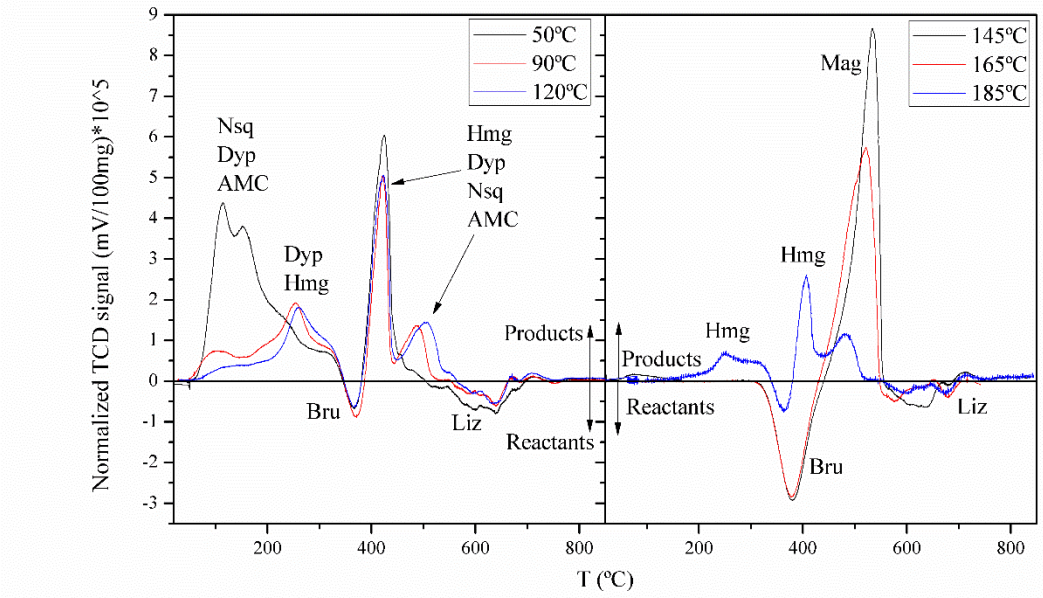

Fig. 7.13. TPD analysis of the reaction products obtained at 50-185ºC, during 4h, after subtracting the TPD acquired data of the starting materials. Bru, AMC, Dyp, Hmg, Mag and Liz represent the reference decomposition behavior of brucite, hydrous AMC, dypingite, hydromagnesite, magnesite and lizardite, respectively.

Changes on the dehydration behavior of lizardite was also observed upon steam-mediated carbonation. Fig. 7.13 shows TPD data of the reaction products after subtraction of TPD analysis of the starting material from reaction from 50-185ºC, during 4h. Overlapped decomposition behaviors between hydrated carbonates with brucite makes difficult the mass balance within the temperature range characteristic of the dehydration of brucite (275ºC – 420ºC) [204,264]. However, the dehydration of lizardite does not overlapped with any decomposition pattern of Mg-bearing carbonates. Therefore, lizardite is either dehydrating or reacting upon carbonation.

Similar behavior is also observed over extended reaction times (2 to 60h) at 165 and 185ºC (Fig. 7.14). Lizardite mass balance is negative upon reaction, particularly evidence by the 598ºC decomposition peak (associated with lizardite inner OH [287,445]), whereas the 644ºC peak (associated with the outer OH) is seemingly increasing as the reaction proceeds. This behavior might indicate that lizardite inner OH are migrating to the outer brucite-like layer, generating more brucitic regions, which might have higher reactivity (see Fig. 7.1) [175].

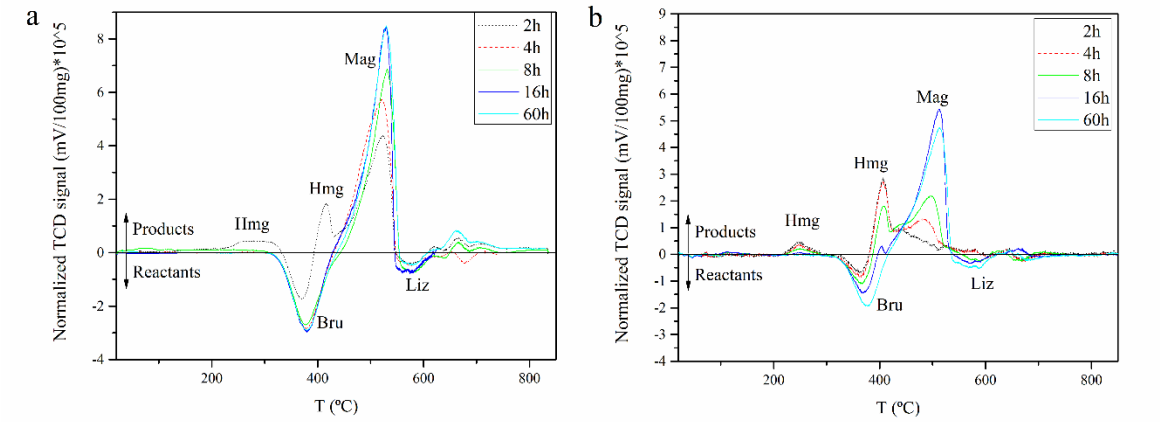

Fig. 7.14. TPD analysis of the reaction products obtained at (a) 165ºC and (b) 185ºC during 2 to 60h, after subtracting the TPD acquired data of the starting materials. Bru, AMC, Dyp, Hmg, Mag and Liz represent the reference decomposition behavior of brucite, hydrous AMC, dypingite, hydromagnesite, magnesite and lizardite, respectively.

7.2.3.1. CO_2:H_2O wt%. ratio of the carbonate products

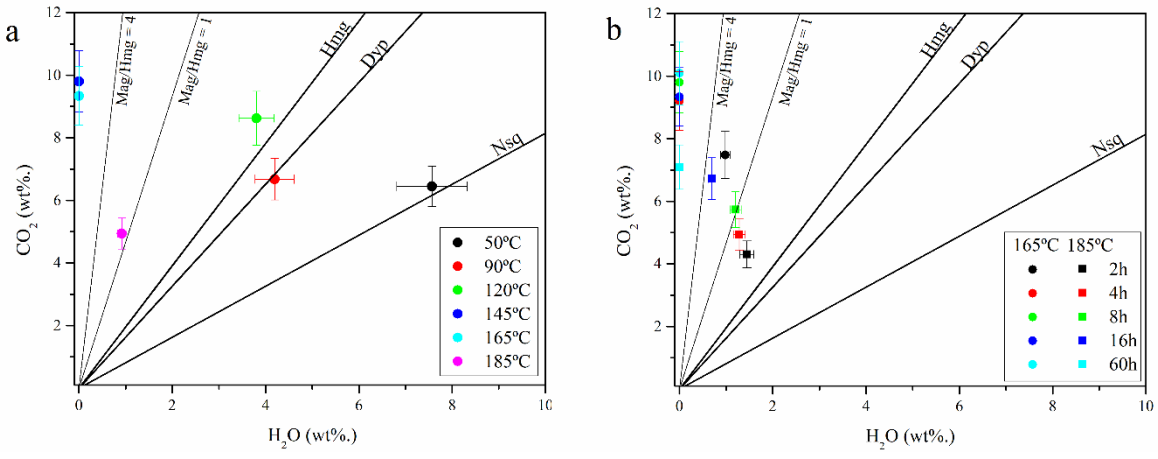

Fig. 7.15. CO2:H2O content of reaction products obtained at **(a)** 50-185ºC, during 4h and **(b)** 165 and 185ºC from 2 to 60h. Mag/Hmg, Hmg, Dyp and Nsq refers to the CO2:H2O of stoichiometric relation of magnesite to hydromagnesite ratio, hydromagnesite, dypingite and nesquehonite, respectively. Error bars estimate the average between three analogous experiments.

Dehydration (rT-340ºC) and decarbonation (350-550ºC) of hydrous Mg-carbonate phases were easily differentiated. When brucite was identified, the associated H_2O released upon dehydration is excluded, since overlaps with the decarbonation of hydrous Mg-carbonates, following the procedure from section 4.2.4.

CO_2:H_2O wt%. of the reaction performed at 50, 90 and 120ºC have similar hydration level to stoichiometric nesquehonite, dypingite and hydromagnesite, respectively (Fig. 7.15). Treatments performed at 145ºC yielded to the formation of anhydrous Mg-carbonate. 165ºC, a rapid dehydration as the reaction proceed is observed. Such behavior is also observed at 185ºC, over extended reaction times.

7.2.4. Carbonation efficiency

Estimated gCO_2 sequestered per 100g of sample (estimated with TPD data, Fig. 7.12) from treatments performed at 50-185ºC during 4h is shown in Figure 7.16. Carbonate contents were calculated considering the CO_2:H_2O composition of the reaction products (Fig.7.15). Treatments performed at 50-165ºC yielded to reaction products with similar carbonate contents. However, different CO_2 sequestration capacities were observed, particularly for 145 and 165ºC treatments, where only magnesite (which is the Mg-carbonate with the highest CO_2 storage capacity) was observed. A maximum of 9.8 CO_2wt%. was successfully sequestered after carbonation at 145ºC. Treatments performed at 185ºC yielded lower carbonation efficiencies (gCO_2 sequestered per 100g of sample) than those obtained at lower temperatures (50-185ºC), mainly attributed to the slower reaction rates at this temperature.

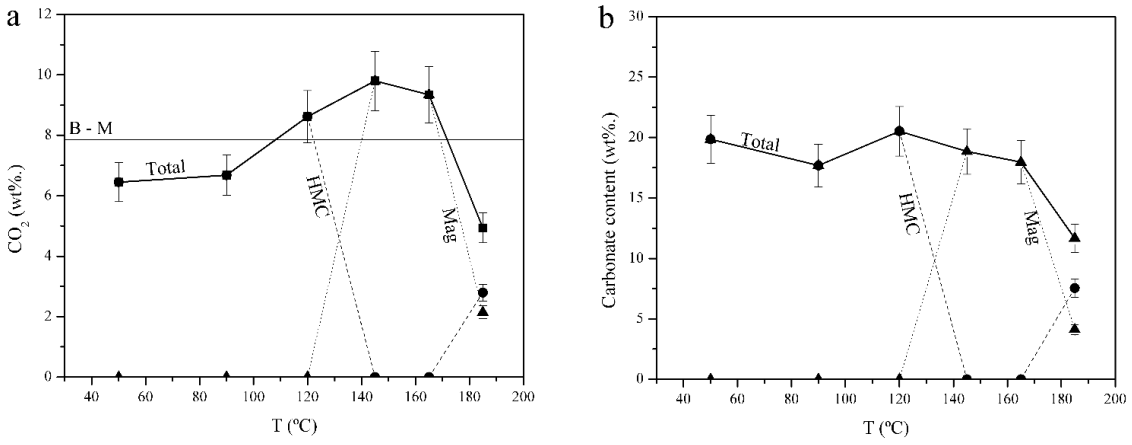

Fig. 7.16. (a) CO_2 wt%. and **(b)** estimated carbonate content of reaction products obtained at 50-185ºC for 4h. HMC: Hydrated Mg-Carbonates, Mag: magnesite, B-M: estimated CO_2 wt%. if all brucite has carbonated to magnesite. Error bars takes into account the phase variability and the calculated data from three analogous experiments.

XRD and Raman results suggested that brucite is the main or only carbonate precursor. Nevertheless, the carbonation efficiency from experiments carried at 120-165ºC exceeds the maximum estimated if all brucite is carbonated. It should also be noted that natural-occurring brucite may have elevated Fe-content, which might lower their CO_2 sequestration capacity [368]. Moreover, lizardite changes were also observed with TPD, indicating that either it underwent partially dehydration or carbonation. Previous studies have suggested that forsterite is significantly more reactive than lizardite [145,281]. Forsterite remained seemingly unreacted upon carbonation, as observed with Raman and XRD analysis. However, it is plausible that it only underwent a very limited carbonation, not detected by standard XRD and Raman measurements.

The Mg wt% that was fixed by carbonates was estimated on the basis of the Mg wt% from the starting materials (Table 6.1), Mg content of 27.8wt%. The maximum Mg wt% extracted from the starting material to form carbonates was obtained at 120ºC, accounting to 21.4%, implying that a large amount of Mg remained fixed within silicate structures (Fig. 7.17). Brucite accounts to 15% of the total available Mg wt% (considering that it does not contain Fe). Therefore, it is estimated that the maximum Mg extracted from silicates accounts to 6.4% (or slightly higher).

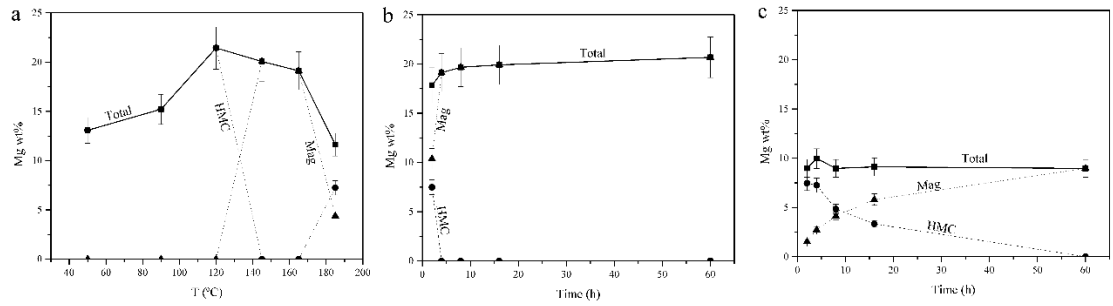

Fig. 7.17. Mg wt% fixed by carbonates after treatments performed at **(a)** 50-185ºC during 4h, **(b, c)** 165 and 185ºC from 2 to 60h, respectively. Hydrated Mg-Carbonates, Mag: magnesite. Error bars were estimated by the results of three analogous experiments and taking into account the different carbonate phases.

The starting material contains 9.4wt%. of brucite (see section 7.2.2). Such brucite content is slightly lower that the estimated global estimates for brucite content in ophiolites (10-20wt%.) [465,466]. Therefore, it should be considered that strategically sourcing serpentinized rocks with higher brucite contents will potentially increase the carbonation potential of such materials even under moderately low pressure and temperature conditions (up to ~20 CO_2 wt%. and 40% Mg fraction). Such carbonation potential is very similar to those reported for activated lizardite under extreme carbonation conditions (150 bar, 150ºC) [196,353,455], without the necessity of heat activating and ultra-grinding pretreatment processes. Results from this work provides a potentially more attractive alternative to the direct carbonation of heat activate serpentine minerals.

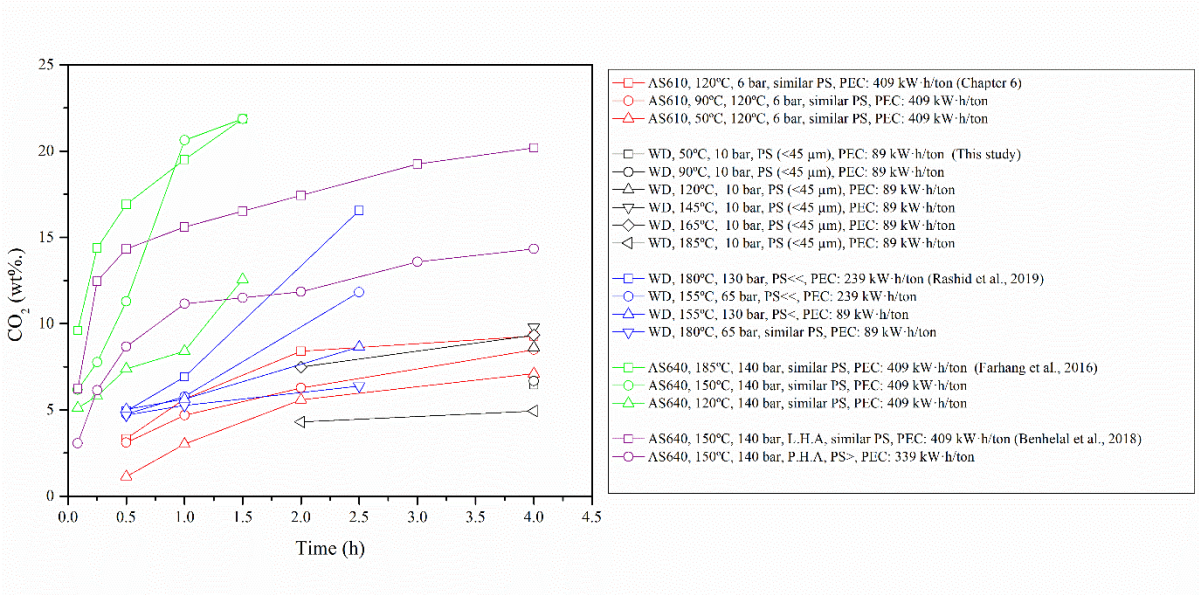

Fig. 7.18. Comparison of the carbonation efficiency obtained in this work and those reported in the literature [196,281,455] and results from chapter 6. AS(TºC): activated serpentine at the specific temperature of activation, WD: weathered dunites, similar PS: similar particle sizes to those observed in this study, PS<: smaller (or greatly smaller, PS<<) particle sizes to those observed in this study. PEC: estimated pretreatment energy consumption as estimated by Gerdemann et al, 2007 of each material.

Higher carbonation efficiencies were observed upon carbonation of brucite-rich serpentinized dunite rather than for the reported using activated lizardite under very similar carbonation conditions (Fig. 7.18). Therefore, not only activated lizardite requires high temperature pretreatments in order to be reactive but less carbonation efficiencies are obtained when compared to brucite-rich serpentinized dunite under moderately-low temperature and pressures (≤10 bar, 150ºC). At elevated pressures (≥130 bar) the carbonation of forsterite and activated lizardite is favored, partially unlocking their carbonation potential [145,260,281]. Reducing the particle plays an important role on the carbonation reaction enhancement [281,468], even more than high pressures and temperatures conditions.

Table 2.5. summarizes the estimated pretreatment energy requirements for grinding and heat activation. Thermal activation of lizardite requires 293 kW·h t^{-1}. Grinding lizardite to grain sizes below 45 µm was estimated to require 85 kW·h t^{-1}[145]. Further grain sizes reduction significantly increases the energy requirements. The estimated pretreatment energy requirements for the materials in this study and those reported in literature is shown in Fig. 7.18. Fig. 7.19 shows the carbonation efficiencies from Fig. 7.18, normalized by the estimated pretreatment energy requirements. Generally, weathered dunites were able to carbonate more efficiently (as defined by the CO_2 wt%. per 100 kW·h/ton of energy consumed during pretreatment) than activated serpentines. The energy penalty associated with decrease the particle size and heat activation reduces significantly the obtained carbonation normalized by pretreatment energy requirements. Moreover, the actual energy

requirements for heat activation will be higher than those represented on Fig. 7.18, since heat treatments from those studies were usually carried at higher temperatures and for longer durations.

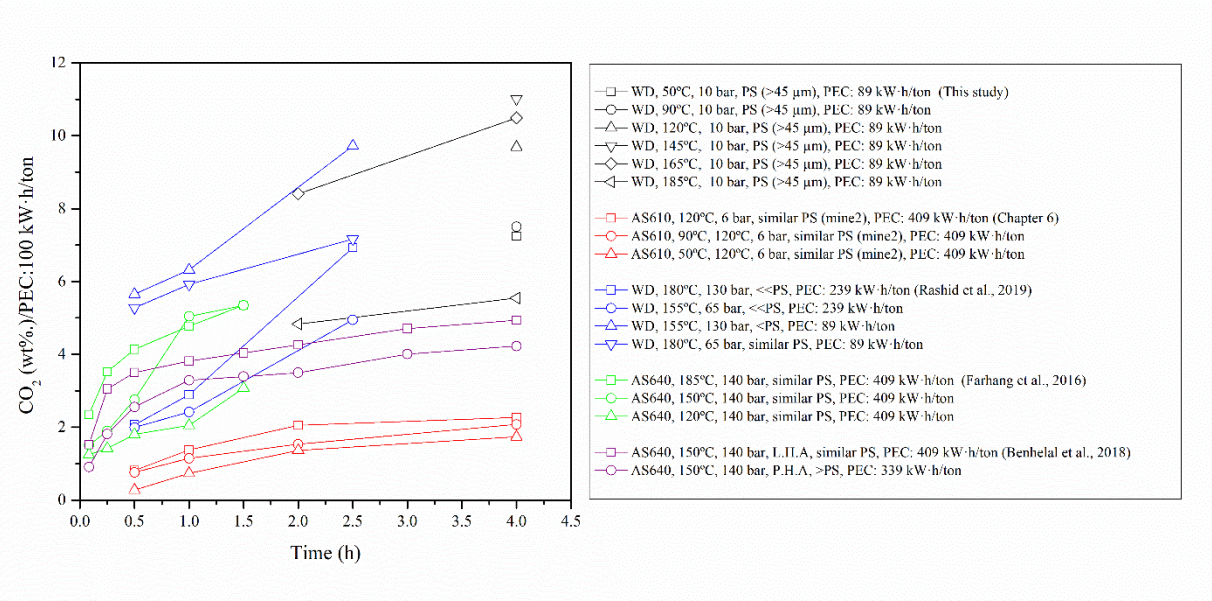

Fig. 7.19. Carbonation efficiencies from this study and those reported in literature [196,281,455] and results from chapter 6 normalized by pretreatment energy consumption (PEC), estimated by Gerdemann et al., 2007 [145]. AS(TºC): activated serpentine at the specific temperature of activation, WD: weathered dunites, PS: particle size PS.

Our results suggest that the accelerated carbonation of weathered dunites is a promising alternative to that of heat activated serpentine. Moreover, similar carbonation efficiencies were obtained during moderately-low (this study) and high-pressure treatments [281] for weathered dunites. However, the studied weathered dunites have a higher content of reactive brucite to those reported by Rashid et al., 2019. In any case, our results indicate an alternative for mineral carbonation at low pressure treatments of widely available weathered dunites, which has carbonation efficiencies similar to those performed at much higher pressures (≥65 bar). The moderately low pressures and temperatures carbonation treatments contribute to overcome the carbonation processing cost [44].

Treatments performed at 165ºC never exceeded 10g of CO_2 sequestered per 100g of samples and 20% of carbonate content during 60 hours of reaction (Fig. 7.20a, b). Similar passivating behavior was also observed from treatments performed at 185º (Fig. 7.20c, d). The maximum Mg fraction stored in carbonates upon reaction was 20.7 and 9 % for 165 and 185ºC treatments, respectively (Fig. 7.17b, c). The carbonate content and the Mg fraction remained relatively unchanged from 4 hours of reaction (Fig. 7.17). The slow reaction kinetics and the uncomplete carbonation of brucite from 185ºC might explain the lower yield of carbonation. At 165ºC, brucite quickly carbonated (≤ 2 hours), and possibly forsterite and/or lizardite were slowly carbonating as the reaction proceeded.

The passivation of the reaction at 165ºC is mainly attributed to the depletion of brucite. However, the possible formation of a Si-rich layer upon liberation of Mg during the probable carbonation for either lizardite and/or forsterite, together with the formation of carbonates might play an important role on the passivation of such reaction, as previous studies have reported [449,450].

Magnetite and/or hematite ($Fe^{3+}_2\ O_3$) were not identified in the starting material. It is probable that such minerals are present in the starting material but in such low abundance that they were not identified with XRD. Their presence might also play a role during the passivation of the reaction, as some studies have discussed that a passivation layer can be formed from the oxidation mechanisms of this latter minerals upon carbonation [44,454].

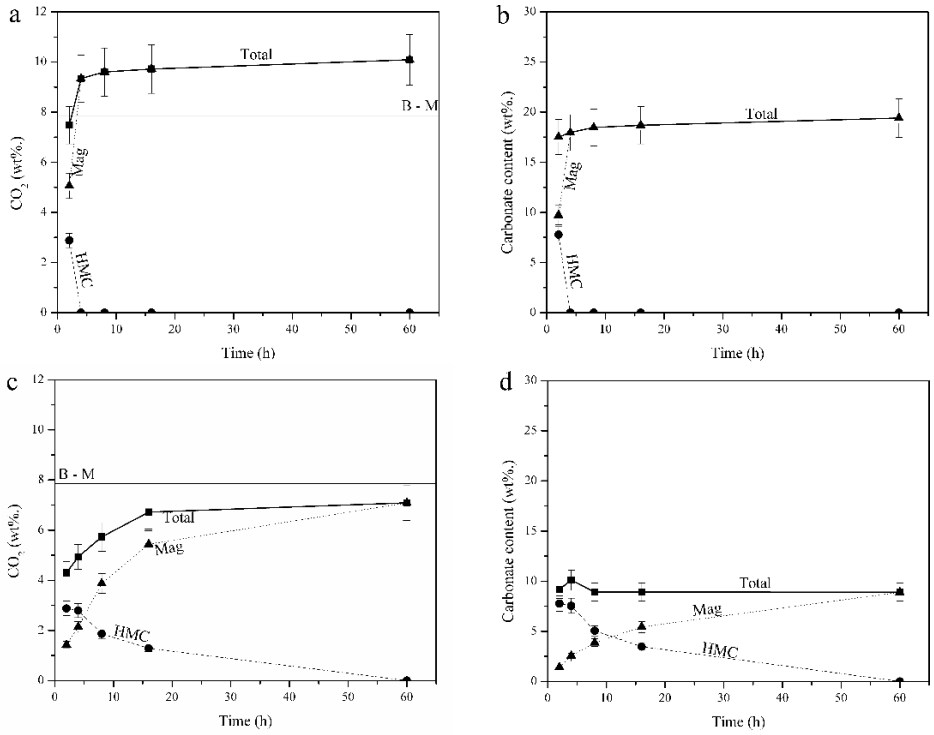

Fig. 7.20. (a, c) Grams of CO_2 sequester per 100 grams of sample and the **(b, d)** estimated carbonate content (wt%.) as estimated with TPD analysis from treatments at **(a, b)** 165ºC and **(c, d)** 185ºC from 2 to 60 hours. HMC: Hydrated Mg-Carbonates, Mag: magnesite, B-M: estimated CO_2 wt%. if all brucite has carbonated to magnesite. Error bars takes into account the phase variability and the calculated data from three analogous experiments.

7.3. Conclusions

The carbonation potential under moderately low pressures (10bar) of brucite-bearing serpentinized dunites was experimentally studied. The reactivity of the material was mainly attributed to the presence of brucite. Lizardite and/or forsterite underwent partial carbonation as evidenced by the exceeding brucite carbonation efficiencies. Moreover, mass balance on lizardite

upon carbonation suggest that inner OH have been either lost or had migrated to lizardite outer OH layer. Such process might create more brucitic regions that might increase lizardite reactivity. The carbonation of such materials yielded to the selective formation of Mg-carbonate phases, as controlled by the reaction temperature. Highly hydrated nesquehonite, dypingite and possibly and amorphous Mg-carbonate were observed at 50ºC. Upon increasing the temperature (145, 165ºC) anhydrous magnesite was observed. The formation of this latter mineral underwent a complete transition of hydromagnesite in less than 4 hours. SEM analysis provided evidence of the dissolution-reprecipitation mechanism occurring in the transition between hydromagnesite to magnesite. After nucleation of nano-magnesite from dissolving hydromagnesite, the increase of magnesite content as the reaction proceeded was observed to occur mainly by crystal growth.

The maximum carbonation efficiency was obtained at 145ºC, accounting to ~10 CO_2 wt%. Reaction carried at 185ºC suffered from slower kinetics, mainly attributed to the lower stability of hydrated carbonates at high temperatures. A passivating effect was observed during 165 and 185ºC treatments, and it is mainly attributed to the depletion of brucite upon carbonation.

Our results suggest that the accelerated carbonation of weathered dunites is a promising alternative to that of heat activated serpentine, as higher carbonation efficiencies per pretreatment energy requirements were obtained. Moreover, it also highlights the importance on the carbonation at moderately low pressures and temperatures, where similar carbonation efficiencies are observed when compared to high pressure treatments. The lower cost associated with low pressure and temperature treatments could contribute to overcome the carbonation processing cost.

8. Raman study of Mg-carbonate minerals: Insights on reaction pathways during accelerated carbonation reactions

8.1. Introduction

Defining unique Raman databases for the recognition of carbonates is increasingly important as several studies have discussed the importance on the correct identification of such materials in order to narrow down the possible reaction mechanisms occurring during transition of metastable phases to ultimately desired magnesite [55,199,380]. This is particularly important for carbonate mineral paragenesis, where often follows the Ostwald step rule [393], as extensively discussed in chapters 4-7. The correct differentiation of naturally-occurring Ca and Mg-carbonates could potentially provide important insights on the formation environment and conditions at which they were formed (see section 2.1) [179].

Moreover, several intermediate precursor, unnamed minerals and highly-disordered materials may play a role on the evolution of metastable carbonate phases [55,179]. The identification of such materials is challenging due to their metastable nature, often are highly-disordered with distinct molecular water per units and are very similar to other known carbonate phases. Raman and FTIR techniques are often very useful for characterizing semi -amorphous an amorphous materials [443,444]. However, overlapping features among the different carbonate phases provides significant challenges regarding the differentiation of carbonate phases (Table 8.1). It has been reported that an unambiguously differentiation among specific carbonate phases is possible using Raman spectroscopy, and has proven to be useful for geological characterization of Ca and Mg-carbonates [380]. However, the differentiation of Mg and Ca-carbonate phases within each group remains challenging and requires additional characterization [380]. This chapter aims to provide additional

insights on the differentiation of Mg-carbonates, particularly referring to semi-amorphous and amorphous Mg-carbonate phases as well as the reaction pathways in the context of accelerated carbonation.

Recently, the kinetics and reaction mechanisms of brucite carbonation to magnesite under elevated CO_2 pressures and moderately temperatures (50 bar, 90ºC) were assessed by means of in-situ Raman monitoring [199].

Several Ca and Mg-carbonates provide suitable habitat for bacterial colonization. The ability to identify such carbonate phases might provide important insights regarding the survival strategies of extremophiles, since it has been reported that such organisms modified the host-geology, particularly Ca and Mg-carbonates (by converting or destroying them) on Earth. Therefore, the correct identification of these phases might provide important insights in the search for evidence of life in the terrestrial geological records as well as for extraterrestrial planetary exploration [380], which Raman spectroscopy have long sought to be considered for the search of life in Mars [469,470].

Table 8.1. Raman main bands for common Ca and Mg-minerals. Table adapted from Edwards et al., 2005 [380].

Phase	$\nu_{1symcar}$ (1200-1000 cm^{-1})	1000-500 cm^{-1} region	Lattice region (500-100 cm^{-1})		
Calcite	1086	713	283	156	
Aragonite	1086	704	208	154	
Dolomite	1098	725	300	177	
Huntite	1123		316	272	253
Magnesite	1094	704	330	213	
Artinite	1094	704	472	173	147
Nesquehonite	1100		228	197	167
Hydromagnesite	1119		232	202	184

8.1.1. Spectroscopic theory

The Raman vibrational activity of an isolated CO_3^{2-} ion with D_{3h} symmetry (symmetry of a tricapped trigonal prism) have the following expression (eq. 7.1):

$$\Gamma = A_1' + A_2'' + 2E' \quad (7.1)$$

Where Γ is the vibrational activity, $A_1' + A_2'' + 2E'$ represent the Raman-active ν_{1sym} (A_1' in D_{3h} symmetry), antisymmetric ν_3 stretching and ν_4 (E') bending modes. In carbonate materials the ν_{1sym} is the strongest band (A_1' in D_{3h} symmetry). Mg-carbonate have higher ν_{1sym} wavenumbers than their Ca-carbonate analogues. This is attributed to a significantly higher polarizing power of Mg^{2+} with respect to Ca^{2+}, which increases the covalent character of the metal-oxygen bonding.

Antisymmetric stretching ν_3 bands of the carbonate ion are significantly less intense than $\nu_{1symcar}$ an it is observed at higher wavenumber (~ 1400 cm^{-1}). Antisymmetric bending ν_4 band occurs near 700 cm^{-1}. Vibrational activity within the lattice region (100-500 cm^{-1}) are associated with ionic

translations and restricted rotations (librations), and it is generally strong in carbonate minerals [380].

8.1.2. Structure of common Mg-carbonate phases

The unequivocal formation of hydrated Mg-carbonate phases upon accelerated carbonation of Mg-silicates and oxides (see chapters 4-7) have justified the increase research interest on the formation mechanisms, kinetics and thermodynamic stability of such phases. Currently, the structure of nesquehonite, hydromagnesite and magnesite are well known (Fig.8.1) [471,472]. Accurate prediction of the crystal structure of a hydrous AMC (Fig. 5.6) and dypingite have also been reported [183,424]. This latter mineral is similar in composition to hydromagnesite, but it has a more disordered structure and variable amount of waters of crystallization [180,183,185].

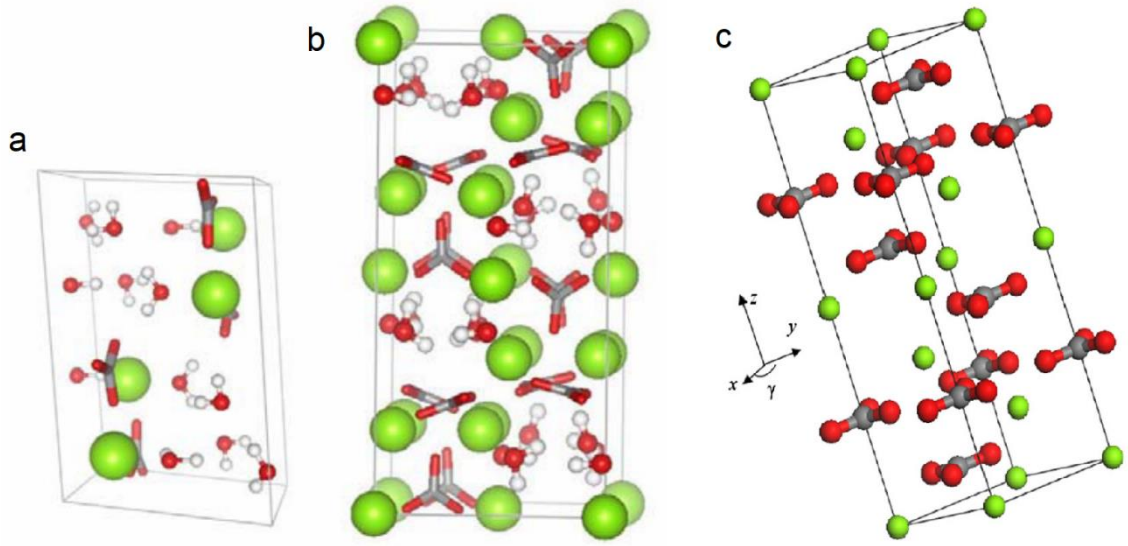

Fig. 8.1. (a) Monoclinic-prismatic2/m unit cell of nesquehonite, **(b)** Monoclinic 2/m unit cell of hydromagnesite and **(c)** Trigonal 32/m unit cell of magnesite. Colored objects represent oxygen (red), carbon (grey), hydrogen (white) and magnesium (green) atoms. Figure adapted from Mckelvy et al., 2006b [471] and Brick, 2011 [472].

Nesquehonite crystal structure is relatively simple when compared to hydromagnesite. CO_3^{2-} ions are all aligned within nesquehonite structure. Those ions have alternating orientations, following a sheet-like arrangement, within hydromagnesite structure. It has been also predicted that bound water in hydromagnesite is structurally coffined by a chain-like hydrogen-bonded arrangement along [010] plane. Therefore, dehydration of such mineral might be plane dependent. Nesquehonite has a similar structure as magnesite and therefore, it has been predicted that such mineral can be transformed to desired magnesite by orderly removal of water molecules. However such transition only occurs at extreme carbonation conditions (150 bar, 100ºC) [471]. This might be attributed to the slow dehydration kinetics of Mg^{2+}[413]. On the other hand, the transformation of

nesquehonite to dypingite-like phases rapidly occurs at temperatures ≥50ºC and higher under moderately low pressures (1-10bar; see chapter 5 and 6) [55,182]. Such transition requires a significant rearrangement of the internal structure, which has been predicted to suffer from slow kinetics [471]. It is also plausible that the slow dehydration kinetics of Mg^{2+} inhibits the direct transformation of nesquehonite to magnesite due to the kinetically preferred reorganization to form hydromagnesite via partial dehydration.

Water molecules are not distributed homogenously within AMC disordered structure, where H_2O-rich regions are interspersed with regions rich in Mg^{2+} and CO_3^{2-} (Fig. 5.6, see section 5.1.1). Moreover, the CO_3^{2-} ions have alternating orientations, similarly to those observed for hydromagnesite. It was suggested by the authors that water molecules from H_2O-rich regions might be relatively easy to remove from hydrous AMC. Such process was proposed to be a formation mechanism of anhydrous AMC, which was expected to be direct precursor of magnesite, analogously as observed for Ca-carbonates (see section 5.1.1) [424,473]. Analogous to the transition of nesquehonite to magnesite or dypingite-like phases, the slow dehydration kinetics of Mg^{2+} might inhibit the formation of either anhydrous AMC or magnesite by the kinetically preferred crystal rearrangement through the nucleation of dypingite-like phases upon partial dehydration. It is also plausible that hydrous AMC will favor nesquehonite nucleation, without losing molecular water, however a significant energy input is expected to start the spontaneous crystal rearrangement (aligning CO_3^{2-} ions and ordering water molecules).

The results presented in this chapter are a compilation of all Raman and XRD results as well as the composition (estimated with TGA and TPD) of the obtained carbonate products in chapters 4-7. Such results provide new insights on the evolution of carbonate phases and their reaction mechanisms under moderately low-pressure conditions (≤10bar). These results might shed light into the preferential nucleation pathways of metastable carbonates from hydrous AMC to ultimately magnesite.

8.2. Compilation of Raman, XRD, TPD/TGA results.

Comparison of the FWHM and peak position of all the $\nu_{1symcar}$ Raman peaks and the two more intense X-ray scattering of carbonate products obtained in chapters 4-7 is shown in Figs. 8.2, 8.3. Five regions withing the $\nu_{1symcar}$ are easily distinguished. Representative Raman and XRD analysis of each of the observed phases are shown in Figs. 8.4, 8.5. Four of the observed Raman regions are in agreement with the calculated data of reference magnesite, nesquehonite, hydromagnesite and dypingite [361]. The last region has been associated with a hydrous AMC with similar composition and thermal dehydration behavior as nesquehonite (see chapter 5) [55]. Peaks located in this region have the same position as magnesite, however, their associated peaks are significantly broader (Figs.

8.2, 8.4). Moreover, the concomitant magnesite characteristic peaks in the lattice region (Table 8.1) is not observed for AMC associated peaks, strongly suggesting that these two phases are distinct (Fig. 8.4). Analogously, nesquehonite and magnesite can be also easily differentiated.

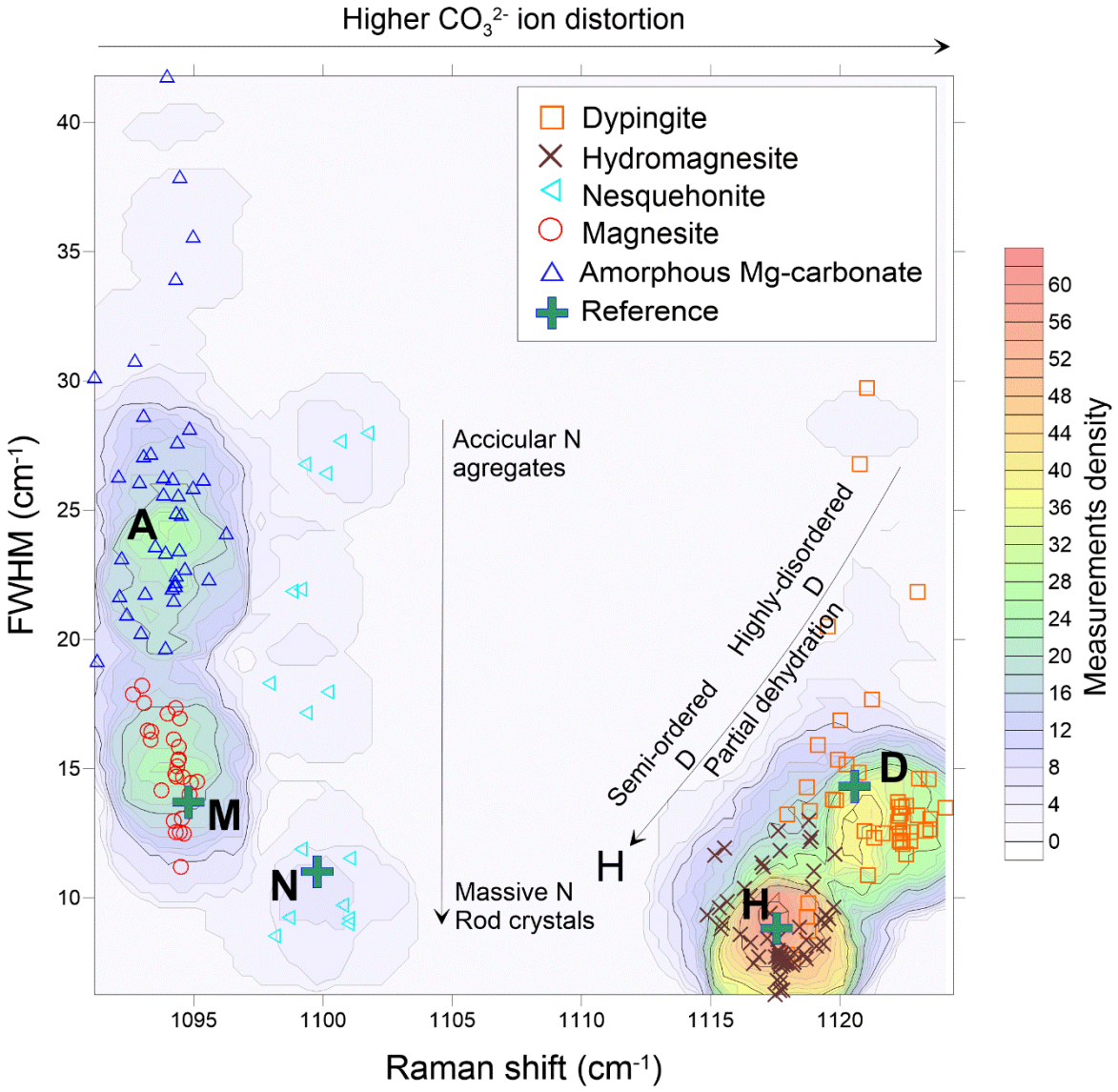

Fig. 8.2. Density map showing the compilation of Raman results obtained in chapters 4-7. Dense regions show coinciding Raman results. Each point represents the average of 40 individual measurements of a specific analyzed sample A: hydrous AMC; M: magnesite; D: dypingite; H: hydromagnesite. The FWHM and peak position of reference minerals were calculated from Lafuente, et al., 2015 [361].

Hydrous AMC have a broad polarizing power, where CO_3^{2-} ions are distorted differently depending on their location in the carbonate matrix. However, their overall CO_3^{2-} ion distortion is similar to that of magnesite. This is in agreement with the disordered structure of a hydrous AMC, where H_2O-rich regions are interspersed with regions rich in Mg^{2+} and CO_3^{2-} (see section 8.1.2) [424]. These latter regions are expected to have similar CO_3^{2-} ions distortion as magnesite, however, CO_3^{2-} ions distortion in the former regions vary depending on the vicinity of CO_3^{2-} ions with respect

to the "small pores", responsible for the peak broadness. This observation is also consistent with nesquehonite structure (Fig. 8.1).

Calculated data for hydromagnesite and magnesite exhibit a very restricted peak position and FWHM. Hydrous AMC and dypingite-like phases have significantly more variability in both FWHM and peak position. Nesquehonite has peaks with similar position, but it has a significant FHWM variability. This latter has been observed to depend on crystal morphology. Massive rod nesquehonite crystals have very similar $\nu_{1symcar}$ peak position and FWHM than reference nesquehonite. However, acicular aggregates with morphologies that resembles nesquehonite has scientifically broader Raman features (see section 6.2.2). Both acicular aggregates and massive rods are structurally well-ordered as evidence by its well-defined x-ray scattering (Fig. 8.3).

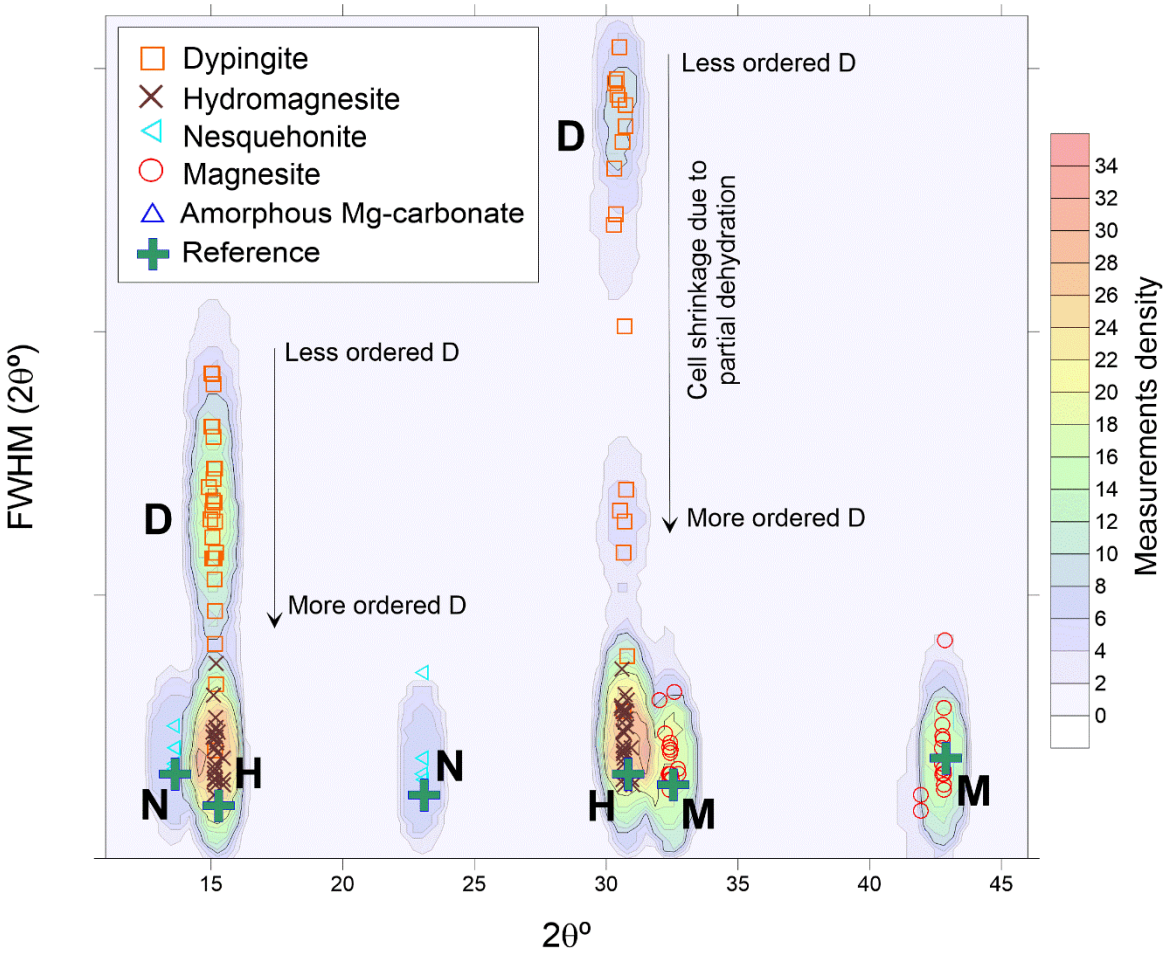

Fig. 8.3 Density map showing the compilation of XRD results obtained in chapters 4-7. Dense regions show coinciding XRD results. M: magnesite; D: dypingite; H: hydromagnesite. The FWHM and peak position of reference minerals were calculated from Lafuente, et al., 2015 [361].

On the other hand, the variability of dypingite-like phases has been attributed to depend on structural order, which depends on its hydration level. Both higher FHWM and peak positions are associated with highly-disordered and hydrated dypingite-like phases, as evidenced by the

significantly broad XRD features (Fig. 8.3; see chapter 6). Dypingite may undergo partial dehydration over extended reaction times as well as increasing temperature (50-90ºC) (see chapter 5 and 6). This induces cell shrinkage, which is the main responsible for the structural ordering. Upon partial dehydration, dypingite calculated Raman and XRD data approaches significantly the estimated data for hydromagnesite, as well as it becomes very similar in composition [55], as evidenced by overlapping Raman and XRD area between hydromagnesite and dypingite in Raman and XRD data (Figs. 8.2, 8.3). Such similarities make difficult the differentiation between semi-ordered dypingite-like phases and hydromagnesite with Raman with the sole observation of Raman spectroscopy. However, the differentiation of highly-disordered dypingite-like phases with hydromagnesite is significantly easier when compared to semi-ordered dypingite. It also indicates that the transition of dypingite-like phases to hydromagnesite follows a progressive partial dehydration process which also defines the structural order of the carbonate phases. Such process includes the transition from highly-disordered to semi-ordered dypingite-like phases, followed by its transition to hydromagnesite (Fig. 8.6). The kinetics of such process is controlled mainly by slow dehydration processes nature of Mg^{2+} [413]. Serval discrepancies are reported in literature among the characterization of dypingite-like phases, particularly regarding its solubility [177] and its dehydration behavior [110–112]. This is likely attributed to the existence of highly-disordered to semi-ordered dypingite-like phases and their similarities with hydromagnesite [179].

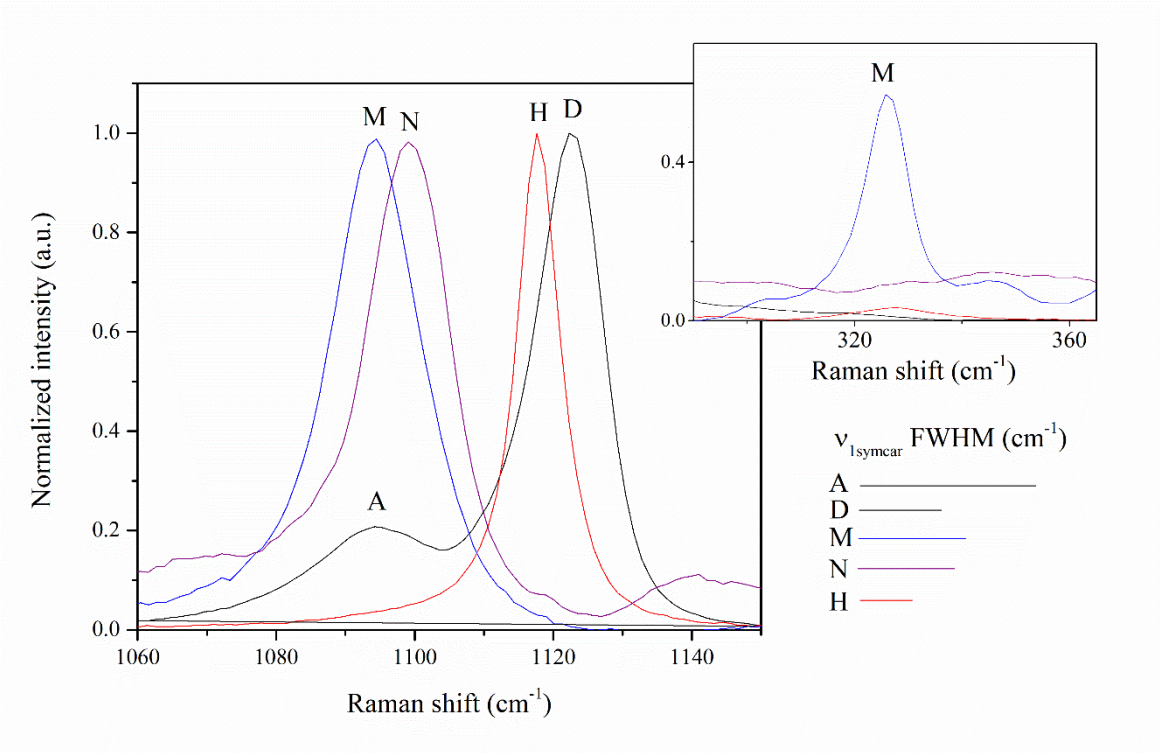

Fig. 8.4. Representative Raman analysis of different carbonate phase as well as a visual representation of the respective $\nu_{1symcar}$ FWHM Raman peaks. A: hydrous AMC; M: magnesite; D: dypingite; H: hydromagnesite.

The CO_3^{2-} ion distortion for hydromagnesite and dypingite-like phases is significantly higher than those observed for magnesite, nesquehonite and a hydrous AMC, particularly higher for highly-disordered dypingite-like phases (Fig. 8.2, 8.6). Upon partial dehydration from highly-disordered dypingite-like phases to hydromagnesite, the polarizing power is reduced as well as it becomes narrower (Fig. 8.6). This might indicate that the carbonate structure becomes homogeneous (crystalline).

Several studies have reported that metastable nesquehonite rapidly transforms to dypingite-like phases at ≥50ºC [55,179–181]. However, the factors that determine such transition are still challenging, particularly regarding the possible presence of amorphous or highly-disordered intermediate precursors [55,179]. The difficulties associated with the characterization of coexisting amorphous with semi-ordered material with very similar composition have limited the characterization of possible intermediate phases occurring during nesquehonite to hydromagnesite transition [55]. Understanding such processes will prove invaluable for understanding the crystallization behavior of hydrous Mg-carbonates [179]. Our results provide important new insights in the differentiation of dypingite-like phases and their progressive transition from highly-hydrated and disordered dypingite-like phases to ordered and less hydrated hydromagnesite.

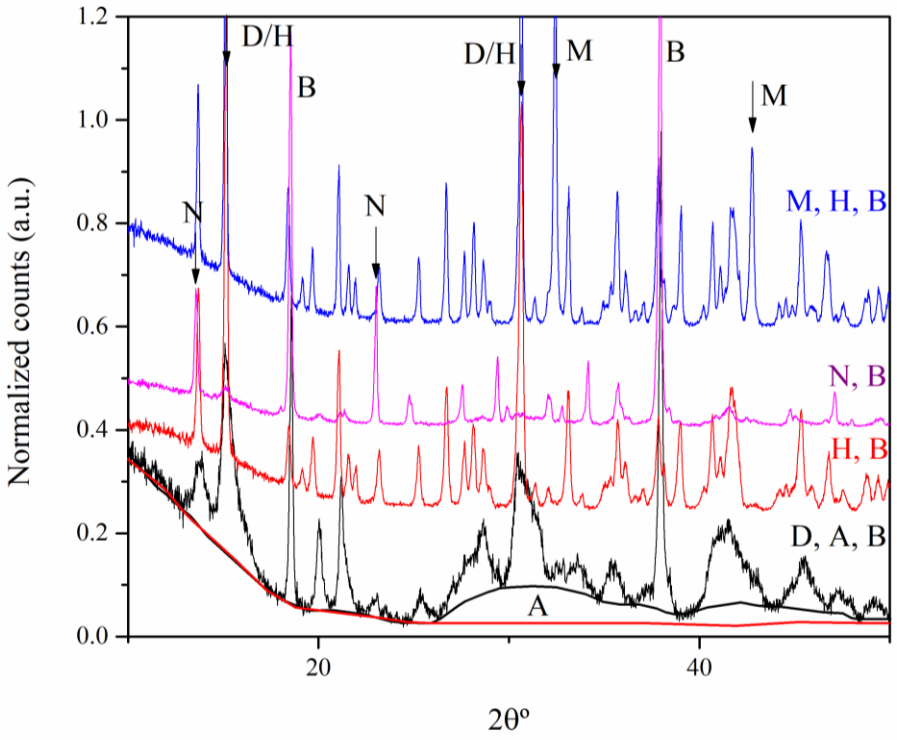

Fig. 8.5. Representative XRD analysis of different carbonate phase. The position of the two more intense XRD features (shown in Fig.8.3) for each carbonate phases is indicated with arrows. The identified phases for each analysis are also shown. A: amorphous component; M: magnesite; D: dypingite; H: hydromagnesite; brucite

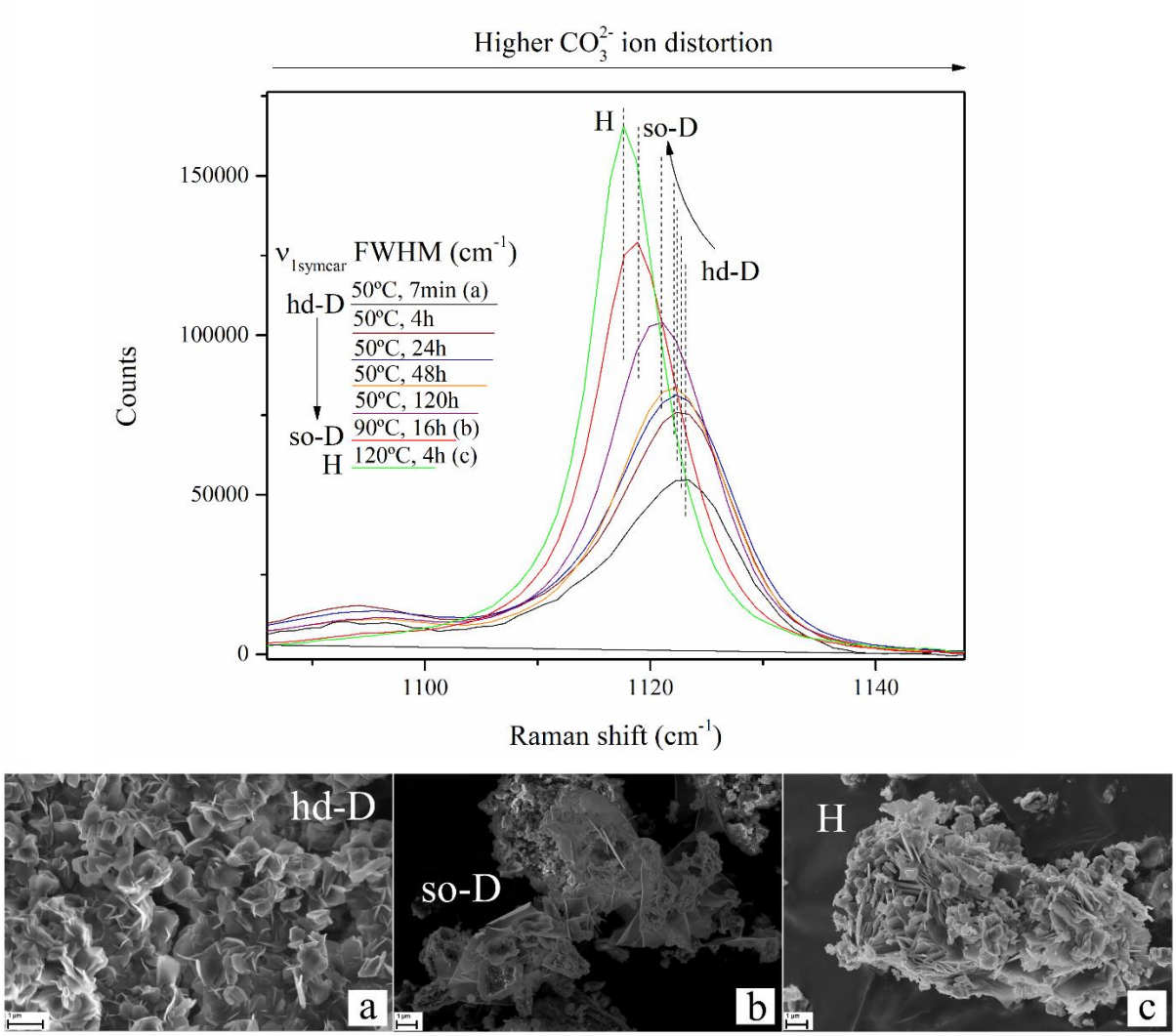

Fig. 8.6. $\nu_{1symcar}$ Raman analysis of reaction products obtained upon brucite carbonation at 10 bar, 50-120ºC during 7min to 120h as well as a visual representation of the respective $\nu_{1symcar}$ FWHM Raman peaks. (a, b, c) SEM imaging of the respective reaction products as specified in Raman spectra. hd-D: highly-disordered dypingite; so-D: semi-ordered dypingite; H: hydromagnesite. Vertical doted lines shows peak position of each peak.

Unfortunately, the decomposition behavior of several hydrous Mg-carbonates have overlapping features, making difficult the quantification of their unique composition (see section 4.2.4) [55,396,398–400,425]. However, CO_2 and H_2O wt% of the obtained mixture of hydrous Mg-carbonates can be obtained as they dehydration and decarbonation of such phases occurs at different temperature ranges (see section 5.2.1.1). MgO wt% was estimated by a linear relation between the different identified carbonate phases (Fig. 8.7, Table 8.2). Fig. 8.8. shows the compilation of the carbonate phases composition obtained in chapters 4-7. A continuous and progressive dehydration of carbonates is observed, following two major trends: (i) progressive dehydration from nesquehonite and/or hydrous AMC and (ii) partial to complete transition of hydromagnesite to magnesite. Phases of relevance to this compilation can be assigned to $Mg_5(CO_3)_4{\cdot}(OH)_2{\cdot}XH_2O$ and

$MgCO_3 \cdot nH_2O$ group minerals ($11 \leq X \leq 4$, $n \geq 0$; Fig. 2.3). The progressive dehydration is mainly or only controlled by the $Mg_5(CO_3)_4 \cdot (OH)_2 \cdot XH_2O$ group. Once the hydration level of hydromagnesite is reached, an abrupt dehydration occurs during dissolution-reprecipitation of hydromagnesite to magnesite (see chapter 7). The abrupt dehydration is evidenced by the sudden changes of CO_3^{2-} ion distortion and their X-ray scattering features upon hydromagnesite to magnesite transition. This process is significantly different from the progressive dehydration of carbonate phases within the $Mg_5(CO_3)_4 \cdot (OH)_2 \cdot XH_2O$ group, where a progressive Raman shift and FWHM is observed (Fig. 8.2, 8.6) as well as progressive reduction of FWHM of XRD features (Fig. 8.3) as partial dehydration occurs (Fig. 8.8).

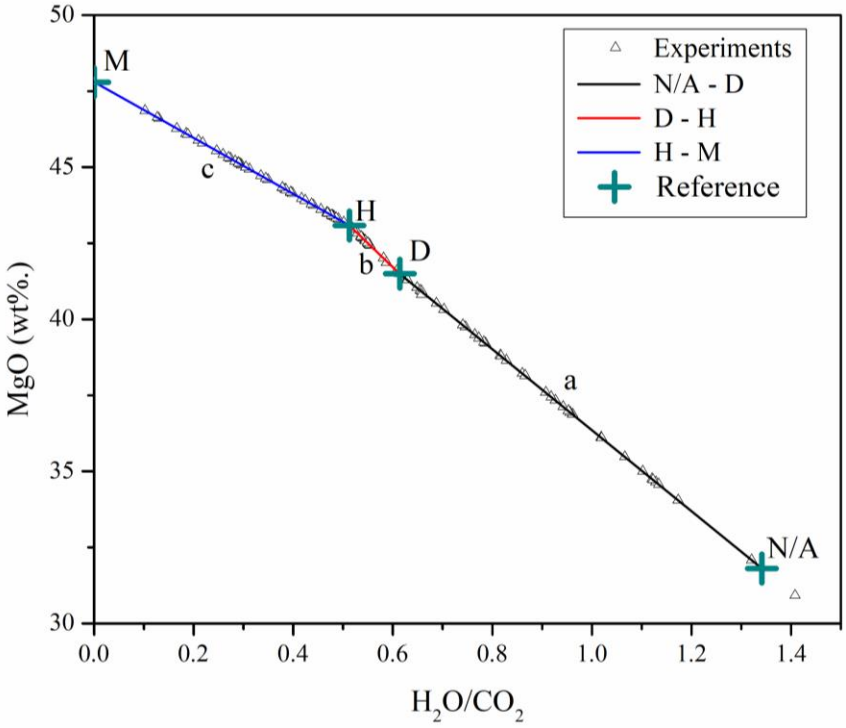

Fig. 8.7. Estimated MgO wt%. based on the H_2O/CO_2 from the obtained carbonate phases following a linear relation between the different identified carbonate phases. N/A: nesquehonite / hydrous AMC; D: dypingite; H: hydromagnesite; M: magnesite. The linear equation for a, b and c is shown in Table 8.2.

Table 8.2. Linear equation (y=mx+b) parameters of lines a, b and c from Fig. 8.7. N/A: nesquehonite / hydrous AMC; D: dypingite; H: hydromagnesite; M: magnesite.

Linear equations	m	b	Range (H_2O/CO_2)
a (N/A – D)	-13.3321	49.68683	1.340886 - 0.614069
b (D – H)	-15.6523	51.11162	0.614069 - 0.512487
c (H – M)	-9.19048	47.8	0.512487 - 0

The evolution of hydrous Mg-carbonate phases is critically controlled by the slow dehydration kinetics of Mg^{2+}, which is known to inhibit the formation of less or anhydrous carbonate phases by the preferential formation of metastable highly-hydrated or less-hydrated phases, respectively [55,413,423]. It is observed that dehydration of hydrous AMC and nesquehonite occurs by the

nucleation and/or transformation of $MgCO_3 \cdot nH_2O$ to $Mg_5(CO_3)_4 \cdot (OH)_2 \cdot XH_2O$ carbonate phase groups. One possible explanation is that carbonate phases of the $Mg_5(CO_3)_4 \cdot (OH)_2 \cdot XH_2O$ group allows a progressive dehydration without a significant re-arrangement of the internal structure, becoming more ordered as cell-shrinkage occurs due to partial dehydration. It is likely that dehydration dypingite-like phases may occur by removal of structurally confined hydrogen bonded water along the [010] plane (sheet-like arrangement), as such dehydration mechanisms was predicted for hydromagnesite [471]. This is consistent with the morphology of such phases, where highly-hydrated dypingite-like phases exhibit flaky crystals (more structurally confined water molecules; Fig. 8.6a), whereas hydromagnesite is characterized to form platy crystals (less structurally confined water molecules; Fig. 8.6c).

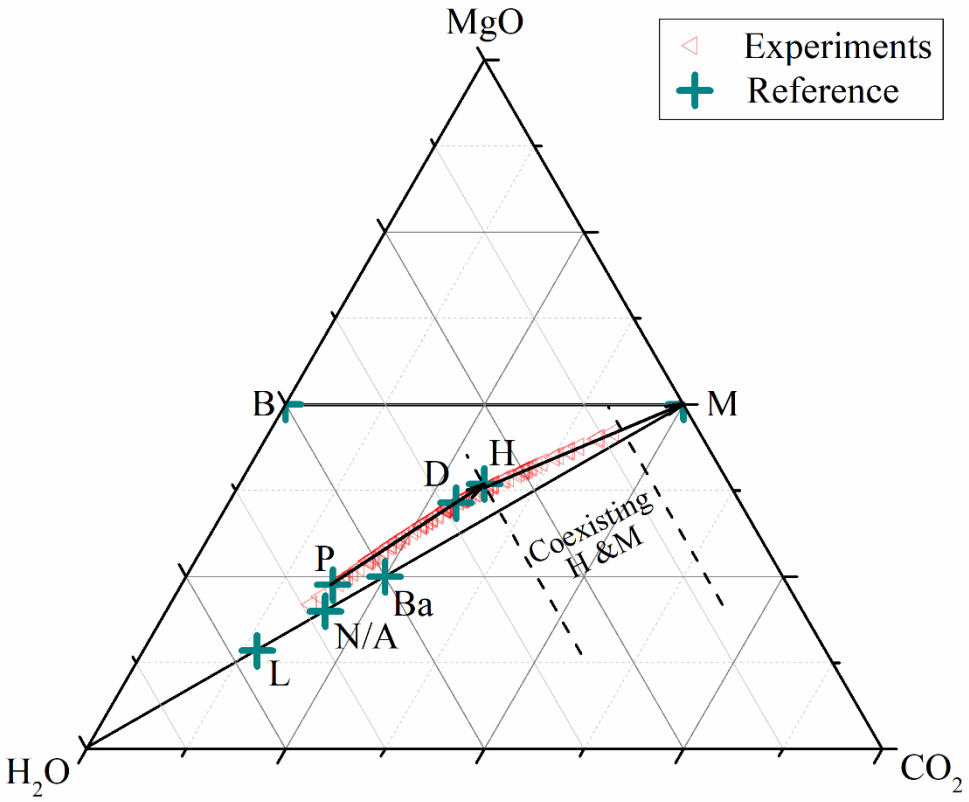

Fig. 8.8. Triangular plot of compositional characteristics of obtained carbonate products in chapter 4-7, as well as reference minerals. L: landsfordite; N/A: nesquehonite / hydrous AMC; Ba: barringtonite; P: protohydromagnesite; D: dypingite; H: hydromagnesite; M: magnesite; B: brucite. Dash lines represent obtained composition of combined carbonate mixtures.

On the other hand, the dehydration from nesquehonite to magnesite via $MgCO_3 \cdot nH_2O$ phase group, despite having similar structure, is only observed at elevated CO_2 partial pressures and temperatures (150 bar, 100ºC) [471]. However, nesquehonite rapidly transforms to dypingite-like phases at temperatures ≥ 50ºC under moderately low pressures (1-10bar) [55,182], despite requiring a significant crystal re-arrangement. Such process is known to occur via dissolution-reprecipitation

[55,179,432]. This strongly indicate that the slow dehydration kinetics of Mg^{2+} is the dominant factor in the evolution of carbonate phases, as the $Mg_5(CO_3)_4 \cdot (OH)_2 \cdot XH_2O$ group allows a progressive partial dehydration. Once the hydration level of hydromagnesite is reached, no significant further dehydration is allowed within the $Mg_5(CO_3)_4 \cdot (OH)_2 \cdot XH_2O$ group, therefore, a significant energy input is required to completely dehydrate Mg^{2+} in order to form magnesite via dissolution-reprecipitation mechanism. Such limiting factor is similar to such observed for the transition of nesquehonite to magnesite via $MgCO_3 \cdot nH_2O$ phase group.

Such behavior might also explain the evolution of hydrous AMC. Partial dehydration is likely to occur from the "small pores" regions of hydrous AMC, since water molecules in this Mg and CO_3^{2-} -deficient regions are less tightly bound to the carbonate matrix [424], where the majority of the water molecules are bound only via hydrogen-bonding interactions [474]. Goodwin et al., 2010 [474] reported that the disordered structure of an hydrous ACC consists of regions rich in Ca^{2+} and CO_3^{2-}interspersed by water-rich channels. Ca^{2+} and CO_3^{2-} rich regions. These latter regions resemble features, with similar Ca-packing density, to those observed for crystalline anhydrous calcium carbonates, analogous to hydrous AMC. It has been predicted that the removal of such H_2O-rich channels within hydrous AMC leads to an straightforward nucleation of anhydrous ACC that eventually transforms to crystalline calcium carbonate [473]. White et al., 2010 [424] predicted a similar straightforward dehydration behavior for hydrous AMC to anhydrous AMC and ultimately magnesite. It should be noted that the presence of Mg^{2+} plays a key role on the formation kinetics of ACC and its enigmatic transition to crystalline phases by inhibiting the formation of anhydrous calcite and vaterite crystallization [414–416] (see section 5.1.1). This behavior is more likely attributed to the slow dehydration kinetics of Mg^{2+} [413]. As observed for the direct transformation of nesquehonite to magnesite (which require extreme pressure conditions and elevated temperatures), the direct dehydration of hydrous AMC to form either anhydrous ACC or magnesite is also predicted to require a significant energy input. However, at moderate pressures and temperatures, the dehydration from "small pores" regions of hydrous AMC are expected to occur gradually, thus, avoiding elevated energy requirements. Upon such partial dehydration, a semi-crystal arrangement is expected, since the stability of amorphous materials is known to depend on size and water content [404]. It should be noted that the carbonate ions within hydrous AMC have alternating orientations, similarly to hydromagnesite and, thereof, dypingite-like-phases [471]. Therefore, we propose that such partial dehydration induces the nucleation of highly-disordered semi-crystalline dypingite-like phases, since such transition might not require a significant re-arrangement of the internal structure and such phases ($Mg_5(CO_3)_4 \cdot (OH)_2 \cdot XH_2O$) allows a progressive dehydration without requiring extreme pressure and temperature conditions.

Ordering of hydrous AMC structure could result in a straightforward formation of nesquehonite, however it does not losses any molecular water in the process. It should be considered that molecular

water might be easily removed from hydrous AMC as predicted by White et al., 2010 [424] when compared to nesquehonite, since it the later phase water is homogeneously distributed within an organized structure, whereas water is heterogeneously distributed with region rich in water molecules (bonded via hydrogen-bonding interactions) in the former phase.

Significant increase of CO_3^{2-} ion distortion is observed during the transition between hydrous AMC to dypingite. This is more likely attributed to the re-arrangement of crystal structure, since, during the nucleation or dissolution-reprecipitation of dypingite-like phases from hydrous AMC, the Mg/C ratio is increased from 1 (hydrous AMC and nesquehonite) to 5/4 (dypingite-like phases, $Mg_5(CO_3)_4 \cdot (OH)_2 \cdot XH_2O$). Thus, carbonate ions are being pulled strongly to Mg cations. It is plausible that such re-arrangement occurs via charge balance after removal of molecular waters, due to the slow dehydration kinetics of Mg^{2+}. Such may also provide insights on the irreversible nature of nesquehonite to dypingite-like phases transition, as previously reported [179]. It is also observed that further dehydration after carbonate phase group transition (from $MgCO_3 \cdot nH_2O$ to $Mg_5(CO_3)_4 \cdot (OH)_2 \cdot XH_2O$) progressively reduces the CO_3^{2-} ion distortion, until the less hydrated known form of Mg-carbonate phases are observed (hydromagnesite). Upon the transition of hydromagnesite to magnesite (see section 7.2.2) via dissolution-reprecipitation, the CO_3^{2-} ion distortion is greatly reduced accounting to very similar distortion as observed during the initial state prior dehydration of AMC and/or nesquehonite.

8.2.1. Role of temperature

Figs. 8.9, 8.10 and 8.11 shows the compilation of Raman and XRD results as well as the estimated composition of carbonate products obtained in chapter 4-7, organized by reaction temperature. A summary of the dehydration-driven reaction pathways from hydrous AMC to magnesite under moderately pressures (1-10bar) and temperatures from 50 to 185ºC is shown in Fig. 8.9.

Generally, less hydrated to anhydrous crystalline carbonate products are observed at higher temperatures (≥120ºC). At lower temperatures (≤90ºC) crystalline, semi-crystalline and highly hydrated carbonate phases with a variable amount of molecular water per unit cell are observed (Fig. 8.9-8.11). Such observation is consistent with the slow dehydration kinetics of Mg^{2+}, where higher temperature are required to obtain less hydrated or anhydrous Mg-carbonate phases, as has been extensively predicted for dolomite and magnesite, commonly referred as “magnesite and dolomite problem” [408,475].

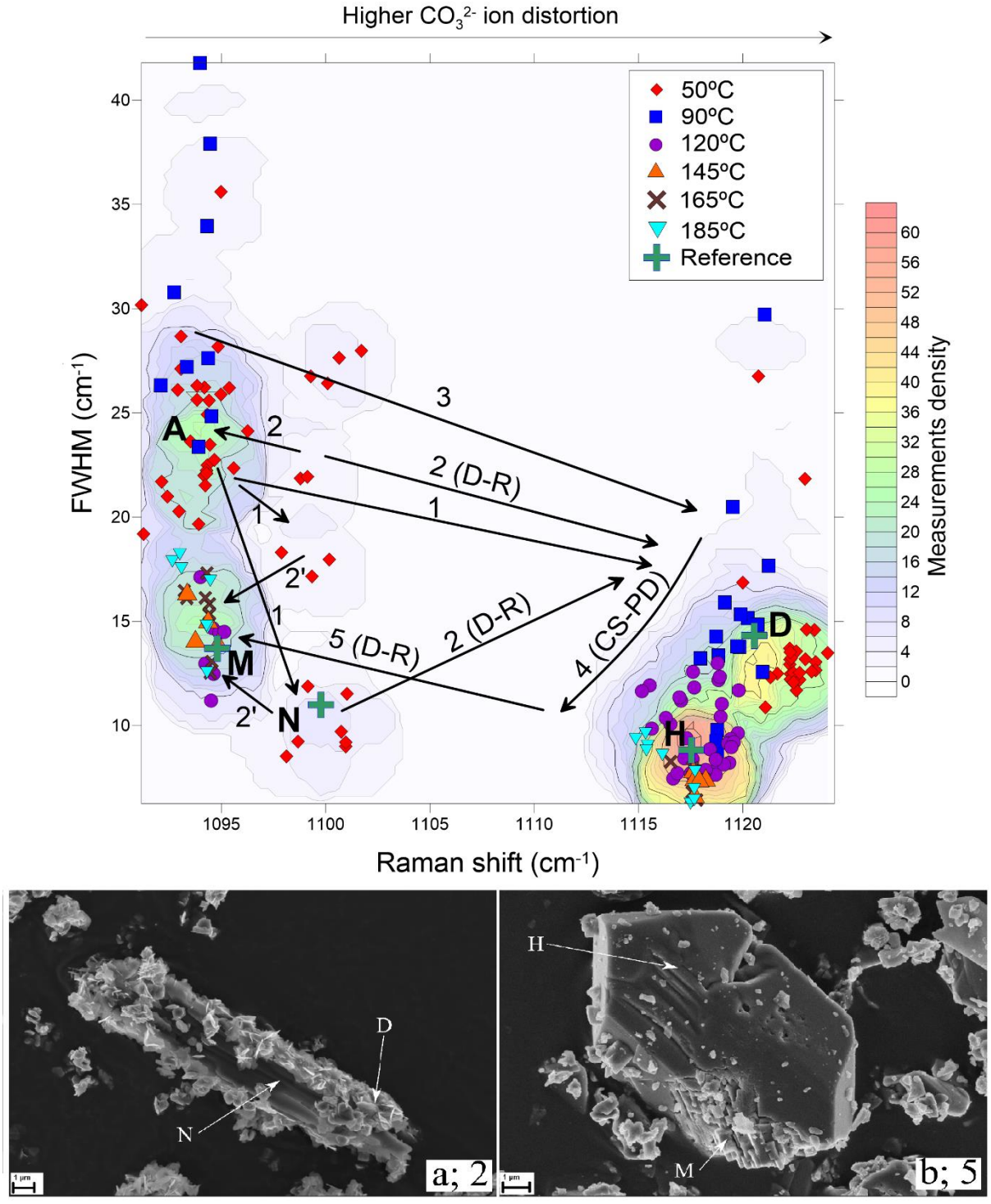

Fig. 8.9. Density map showing the compilation of Raman results obtained in chapters 4-7 organized by reaction temperature (50-185ºC). Dense regions show coinciding Raman results. Each point represents the average of 40 individual measurements of a specific analyzed sample. Arrows indicate the possible dehydration/driven reaction pathways of Mg/carbonate phases. A: hydrous AMC; M: magnesite; D: dypingite; H: hydromagnesite; D-R: dissolution-reprecipitation; CS-PD: cell shrinkage due to partial dehydration. The FWHM and peak position of reference minerals were calculated from Lafuente, et al., 2015 [361]. (a, b) etch pits and overgrowth of flaky dypingite crystals and rhombohedral magnesite on dissolving nesquehonite rod and hydromagnesite plate, respectively.

The reaction pathways from hydrous AMC to ultimately magnesite are described as following (Fig. 8.9): (1) Nucleation or dissolution-reprecipitation of hydrous AMC to highly-disordered dypingite-like phases as well as to nesquehonite (50-90ºC); (2) nesquehonite transition to dypingite-like phases (via dissolution-reprecipitation as evidenced by the "house of cards" texture; Fig. 8.9a [55,179,432]) and possibly to hydrous AMC [55] (50-90ºC); (2') direct transition from nesquehonite to magnesite at extreme carbonation conditions (150 bar, 100ºC) [471]; (3) possible transition from hydrous AMC (formed from dissolution of nesquehonite [55]; 50-90ºC); (4) progressive dehydration and cell shrinkage of highly-disordered dypingite-like phases to hydromagnesite (50-120ºC): (5) hydromagnesite transformation to magnesite via dissolution-reprecipitation, as evidenced by etch pits and overgrowths of rhombohedral nano-magnesite on a large dissolving hydromagnesite crystal (~10 µm; Fig. 8.9b; 120-185ºC).

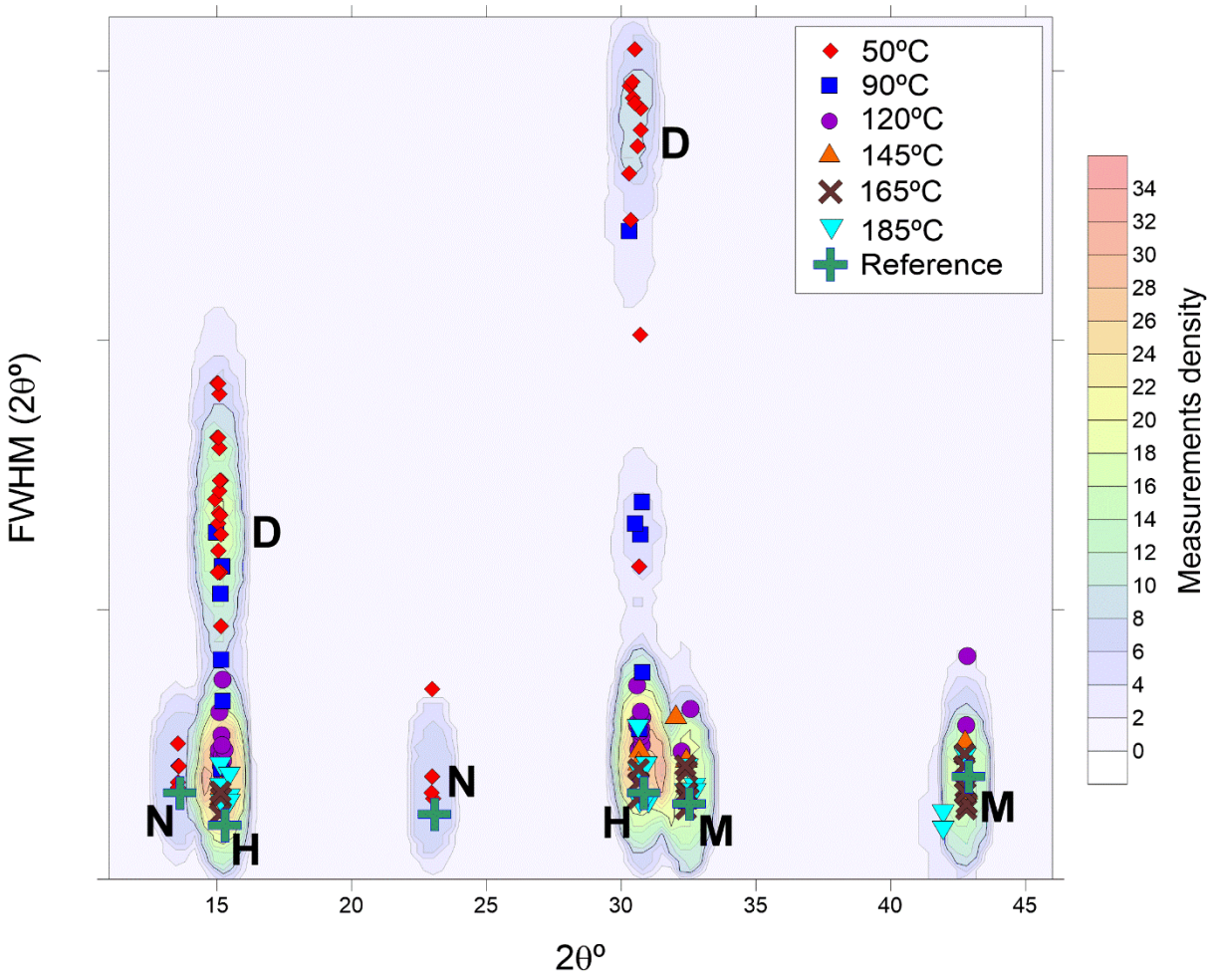

Fig. 8.10. Density map showing the compilation of XRD results obtained in chapters 4-7, organized by reaction temperature (50-185ºC). Dense regions show coinciding XRD results. M: magnesite; D: dypingite; H: hydromagnesite. The FWHM and peak position of reference minerals were calculated from Lafuente, et al., 2015 [361].

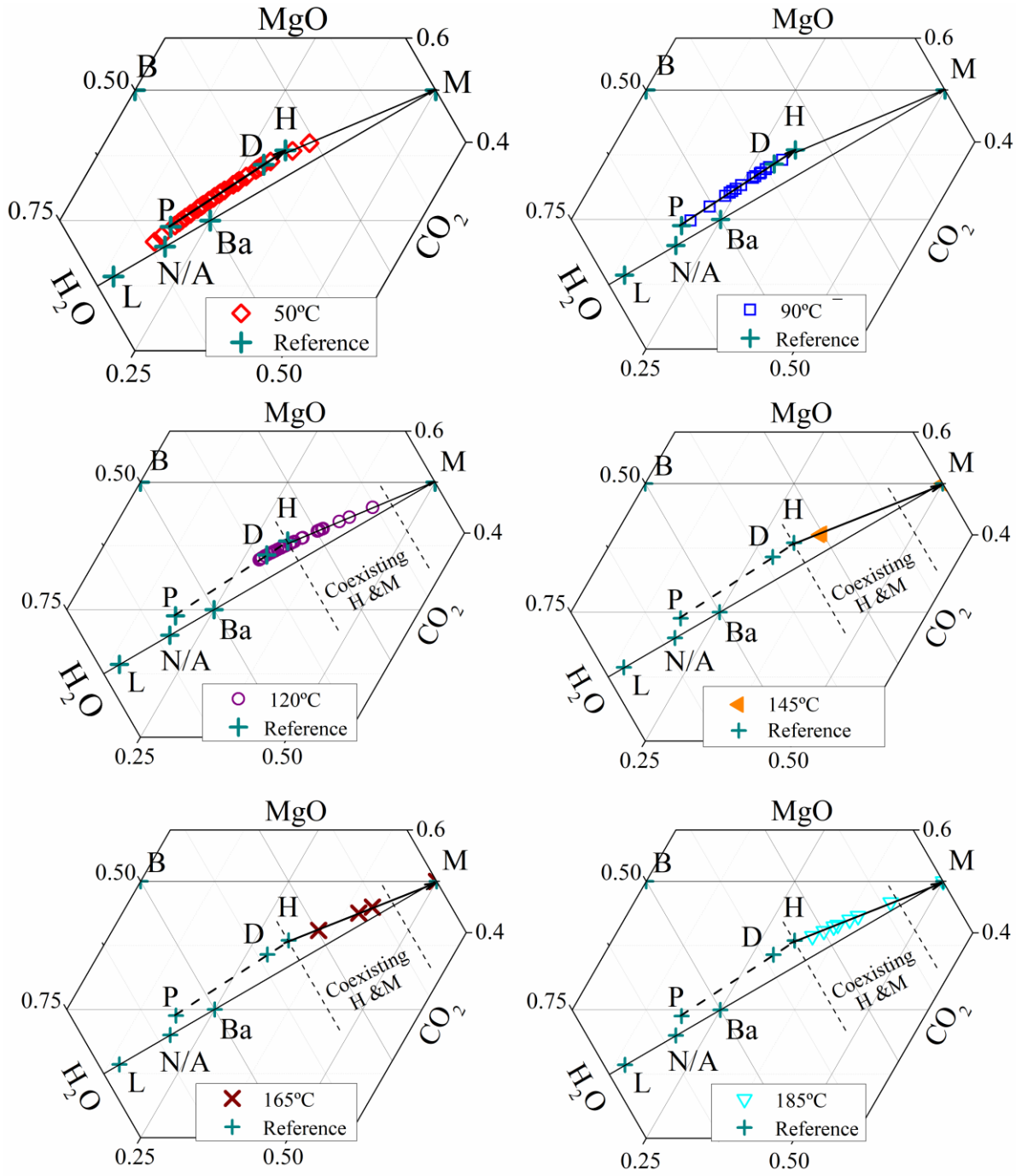

Fig. 8.11. Triangular plot of compositional characteristics of obtained carbonate products in chapter 4-7 (organized by reaction temperatures from 50 to 185ºC, as well as reference minerals. L: landsfordite; N/A: nesquehonite / hydrous AMC; Ba: barringtonite; P: protohydromagnesite; D: dypingite; H: hydromagnesite; M: magnesite; B: brucite. Dash lines represent obtained composition of combined carbonate mixtures.

The dehydration of the carbonated products obtained at 50 and 90ºC occurs gradually following the composition trend of $Mg_5(CO_3)_4{\cdot}(OH)_2{\cdot}XH_2O$ carbonate phase group (Fig. 8.11). A direct correlation is observed as progressive Raman shift and FWHM (Fig. 8.9) as well as a reduction of FWHM of the XRD features (Fig. 8.10) as dehydration occurs (Fig. 8.11). At ≥120ºC, despite a

progressive dehydration is observed from hydromagnesite to magnesite an abrupt change in the respective Raman and XRD features is observed, strongly suggesting that the transition of such phases requires a sudden and complete dehydration. This provides insights into the slow reaction kinetics of such transition (see section 2.1.1), since it has to suddenly remove all the strongly-bonded water molecules within hydromagnesite structure.

It is plausible that the transition of hydromagnesite to magnesite will require less energy input than the direct transition of nesquehonite and/or hydrous AMC to magnesite, as the former transition requires removal of significantly less molecular water per unit cell than the latter transition, taking into account that the slow dehydration of Mg^{2+} is the main factor that controls the Mg-carbonate paragenesis. This is consistent with the energy required for hydromagnesite to magnesite transition, since it has been extensively reported that such transition can occur under moderately low pressures (≤10 bar, ≤ 145ºC) (see chapters 4-7), whereas direct transition of nesquehonite to magnesite requires extreme carbonation conditions (150 bar, 100ºC). It can be also expected that the transition of hydrous AMC to magnesite will also require significant energy input in order to remove its molecular waters. However, the heterogeneous disordered arrangement of hydrous AMC might provide easier and faster dehydration routes than nesquehonite, although it is expected to remain kinetically restricted by the hydration nature of Mg^{2+}.

The reaction kinetics and mechanisms of Mg-carbonates are mainly controlled by the slow dehydration nature of Mg^{2+}. This factor is also responsible for the differences between Ca and Mg carbonates, where Ca-carbonates are able to form anhydrous carbonates significantly faster than Mg-carbonates. Therefore, the transition of hydrous carbonate phases to magnesite could be accelerated if some Mg cations are replaced with Ca. This will lower the high hydration nature of Mg-carbonates which might unlock the desired formation of magnesite under temperature and pressure conditions near to those of flue gas emissions [56,204]. Very similar process has been extensively studied with the opposite purpose, where Ca cations are replaced with Mg cations within ACC-Mg carbonate matrix in order to prevent the rapid dehydration of Ca-carbonates [401,405,407,423].

The progressive dehydration from hydromagnesite to magnesite observed in Fig. 8.11 is due to coexisting hydromagnesite and magnesite as the estimation of carbonate composition was carried out including all coexisting carbonate phases in the analyzed samples.

8.3. Conclusions

A compilation of all the Raman, XRD and TPD/TGA data from chapters 4-7 was carried in order to provide new insights on Mg-carbonate phases paragenesis, where the transition of such phases is mainly controlled by the slow dehydration kinetics of Mg^{2+} rather than evolving to a

thermodynamically more stable or structurally similar phase. This compilation allowed a detailed description of reaction mechanisms in the context of engineered carbonation and might provide new insights into the differentiation of Mg-carbonate phases using Raman spectroscopy

Hydrous AMC was consistently observed to have a $\nu_{1symcar}$ similar to magnesite but unequivocally broader, which is consistent with the estimated disordered structure proposed by White et al., 2010 [424]. This might provide invaluable for the characterization of hydrous AMC. A progressive transition from highly disordered dypingite-like phases to hydromagnesite is observed, indicating that such transition occurs only by partial dehydration and cell shrinkage. This progressive transition might allow a correct characterization of $Mg_5(CO_3)_4{\cdot}(OH)_2{\cdot}XH_2O$ phases ($11 \leq X \leq 4$) via Raman spectroscopy.

The evolution of AMC as it undergoes partial dehydration (from H_2O-rich regions) is likely to occur by progressive structural re-arrangement where Mg/C ratio of the unit cell is increased from 1 (hydrous AMC) to 5/4 (dypingite-like phases). Such re-arrangement significantly increases the $\nu_{1symcar}$ CO_3^{2-} ion distortion as well as allows a progressive partial dehydration from $Mg_5(CO_3)_4{\cdot}(OH)_2{\cdot}11H_2O$ to $Mg_5(CO_3)_4{\cdot}(OH)_2{\cdot}4H_2O$. As dehydration proceeds through removal of structurally confined water molecules along the [010] plane, cell shrinkage occurs reducing the gap between dypingite-like sheets which allows the formation of thicker plates as it dehydrates (from highly-disordered dypingite-like phases to hydromagnesite). Such progressive dehydration makes possible the dehydration-driven evolution of hydrous AMC and nesquehonite without significant energy inputs. Once the hydration level of hydromagnesite is reached, a sudden dehydration occurs forming magnesite. However, this latter transition requires significant energy inputs due to the sudden H_2O removal, taking into account the slow dehydration kinetics of Mg^{2+}. Nevertheless, such transition requires significantly less energy inputs than the required for direct transition from nesquehonite to magnesite, despite both phases having similar internal structures, as this latter transition requires a sudden removal of larger amounts of water molecules when compared to hydromagnesite to magnesite transition. Analogously, it is also predicted that the direct transformation of hydrous AMC to anhydrous AMC or magnesite will also require significant energy inputs. However, those are expected to be lower than for the direct transition from nesquehonite to magnesite, since water molecules from “small pores” in hydrous AMC might be easily removed than structurally-ordered water molecules in nesquehonite.

In order to unlock the kinetically limited transition of hydrated Mg-carbonate phases to magnesite due to the slow dehydration of Mg^{2+}, some Mg cations can be substituted with Ca, thus reducing the strength of hydrogen-bonded water with the carbonate matrix, allowing a faster dehydration of carbonate phases, which might unlock the desired direct transition of nesquehonite or hydrous AMC to magnesite or accelerate hydromagnesite to magnesite transition.

9. Direct-carbonation of enstatite and forsterite single crystals

9.1. Introduction

Carbonation reactions are characterized by diffusion mechanisms, where an exchange of metal cations with carbonate ions allows the formation of carbonates. Such mechanisms occurred at the minerals surface. Therefore, understating the carbonation mechanisms that occurs on the surface of such materials might prove invaluable for the understanding on such mechanisms [449]. Moreover, it has been extensively reported that the carbonation of Mg-rich silicates occurs via solvent-mediated reactions, where a CO_2-rich fluid is responsible for the diffusive-mediated carbonation. Pokrovsky and Schott, 2000 [476] reported that the dissolution of forsterite in acidic or alkaline conditions is controlled occurs via proton exchange reactions including: (i) stoichiometric dissolution of forsterite releasing Mg and Si to the solution, (ii) exchange of $2H^+$ for one Mg^{2+} ion and (iii) absorption of hydroxide and protons into forsterite surface, resulting in a surface precursor complex which increases the molar volume of the crystalline constituents (Fig. 9.1a).

Intergrowth of magnesite and a silica-rich material are often observed from high-pressure (135 bar) aqueous carbonation of olivine (Fig. 9.1b, c). This might indicate that magnesite can nucleate (followed by crystal growth) in association with silica formation or they could be directly forming by dissolution-precipitation mechanisms. However such intergrowth formation mechanisms is often associated with nucleation and growth processes [101], such as: (i) solid state reactions between the CO_2-rich fluids and dissolving olivine and (ii) nucleation an growth mechanisms including the preferential diffusion of dissolved aqueous CO_2 [101]. Surface nucleation of carbonated can be initiated by a surface defect by the precipitation of carbonate grain on dissolving silicate surface. Dissolution-reprecipitation of Mg ions may not be required for magnesite growth if sufficiently high

$CO_{2(aq)}$ concentration in the reacting fluid with sufficient diffusivity to transport Mg ions from dissolving olivine to expanding reacting zone (stem from the surface protonation of olivine, dark gray area in Fig. 9.1b).

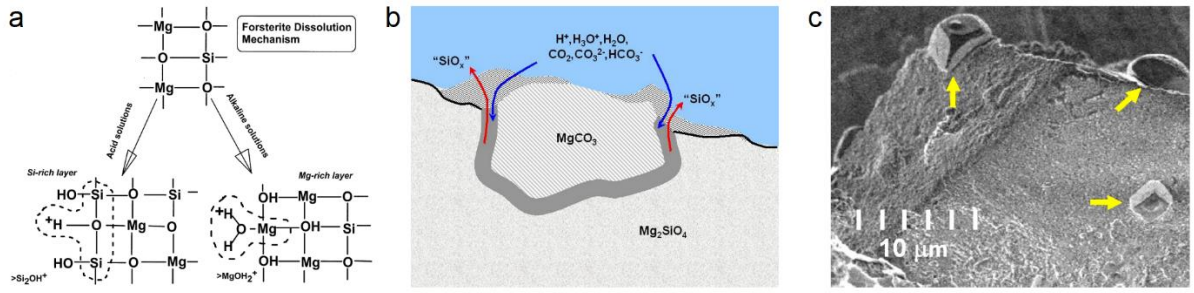

Fig. 9.1. Schematic of **(a)** surface structure upon dissolution in acidic and alkaline conditions and **(b)** a diffusion-mediated growth mode including the expanding reaction zone (gray zone). **(c)** SEM image of intergrowth rhombohedral magnesite with the olivine matrix (showed with yellow arrows). Figure adapted from Pokrovsky and Schott., 2000 [459] and Chizmeshya et al., 2006 [101].

Quantitative nanoscale observations indicate that Si-rich layer contains magnesite nanocrystals. Such observation indicates that CO_2 was able to diffused through the Si-rich layer (Fig. 9.2). During aqueous DC of olivine at elevate pressures (135 bar) a Si-rich layer containing 13 vol% of magnesite nanocrystals has been observed. However, theoretical calculations estimated that magnesite nanocrystals should occupy 67vol% of the Si-rich layer if no ions are diffused into the solution [101,449]. Moreover, it has been postulated that diffusion of Mg is greater than those for silicon upon Mg-rich silicate dissolution, implying an incongruent dissolution [477]. Therefore, a mechanism that is consistent with such observations includes the proton exchange with surface Mg ion. Absorbed protons are bonded to oxygen site forming silanol groups (Si-OH), which generates a glassy-product that is significantly less dense that networked silica glass [449].

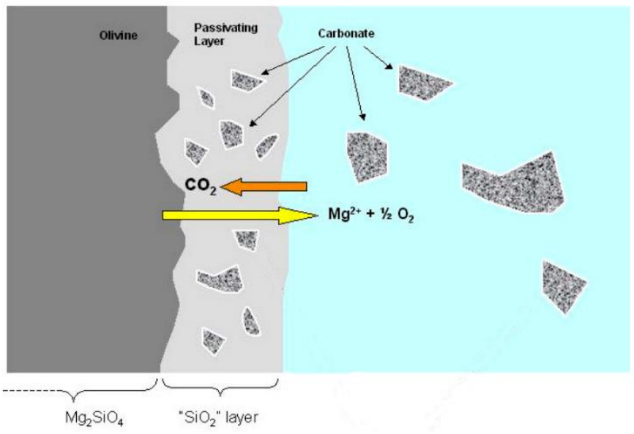

Fig. 9.2. Schematic of the Si-rich layer formed upon olivine dissolution. Solid dark gray: olivine; solid light gray: Si-rich layer; textured gray grains: carbonate nanocrystals; light blue: solution. Figure from Chizmeshya et al., 2006 [101].

Si-rich layer formation is likely associated with occur upon incongruent dissolution of silicates and silica deposition on the reaction surfaces [449,478]. This layer is highly stressed due to the significant molar volume difference between such layer and olivine, which might facilitate facture and exfoliation of such layers.

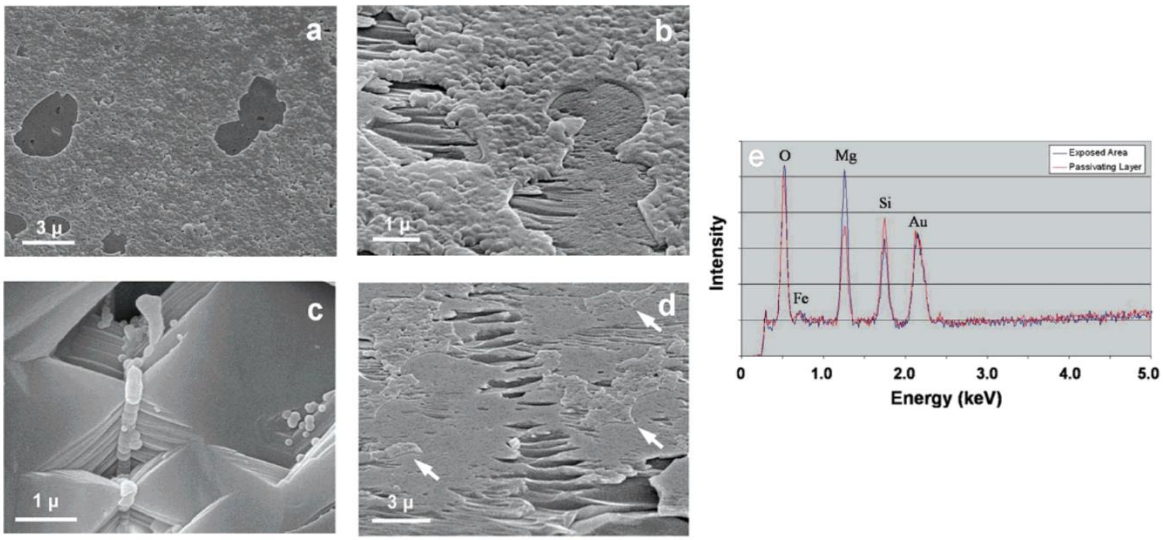

Fig. 9.3. (a, b, c, d) SEM images of reaction surfaces formed upon olivine carbonation. **(a)** Si-rich passivating layer with regions that have experienced fracture and exfoliation. **(b)** Re-growth of Si-rich layer in exfoliated regions. **(c)** occasional silica deposition in regions near etch pits. **(d)** regions were the Si-rich layer have experienced fracture, exfoliation and re-growth. White arrows indicate remnants of Si-rich that have not experienced fracture, exfoliation and regrowth. **(e)** EDS analysis of exposed unreacted olivine grain and Si-rich passivating layer. Figure from Béarat et al., 2006 [449].

Upon olivine carbonation at elevated pressures (135 bar) The formation of such passivating layers is found to cover significantly the surface of olivine (Fig.9.3a, Fig. 9.3e). It has been extensively reported that the formation of such layers play an important role on the inhibition of Ca/Mg-rich carbonation [57,353,449,479]. Fig. 9.3b shows an area that has experienced a glass-like fracture and exfoliation, allowing the depositions of new passivating layers on exposed forsterite. Olivine regions showing etch pits are generally free of Si-rich passivating layers, were only occasional and irregular silica deposition are observed (Fig. 9.3c). Fig. 9.3d shows Si-rich passivating layers that experienced fracture, exfoliation and growth. Residual uncovered Olivine surface appeared partially broken away from the surface.

9.2. Results and discussion

9.2.1. Forsterite single crystal

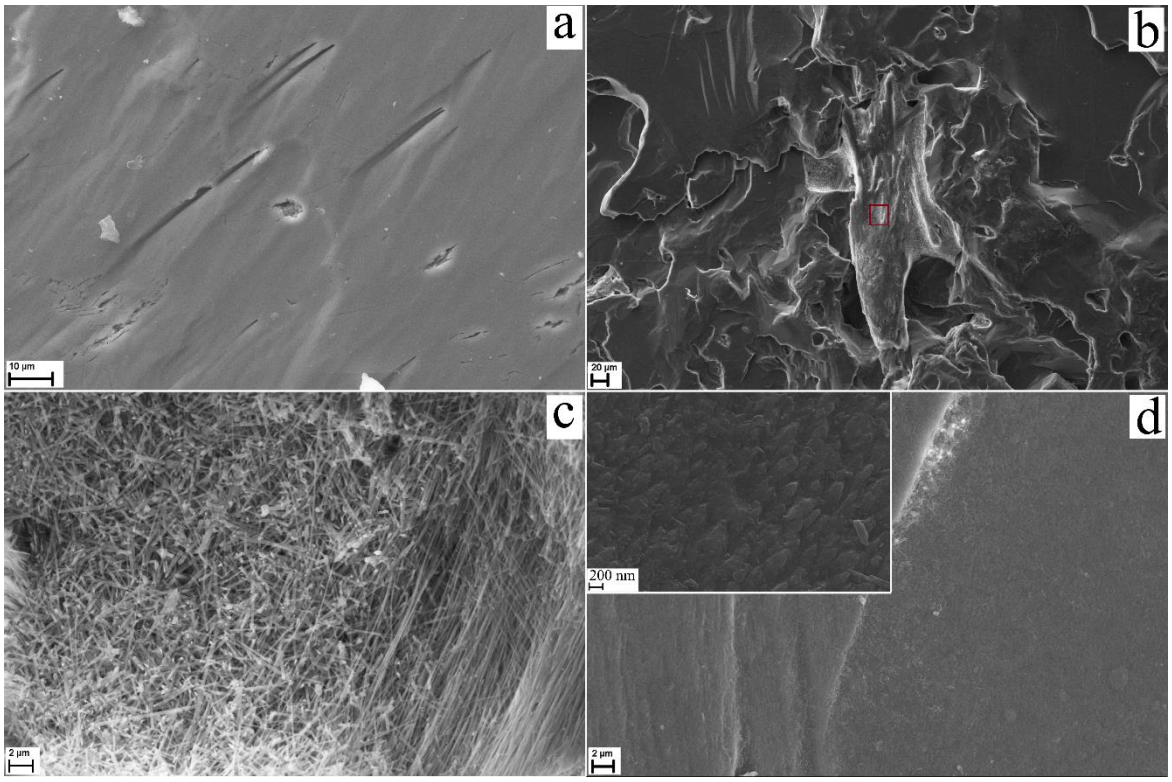

Fig. 9.4. SEM images of **(a)** untreated forsterite single crystal, **(b)** complex structure formed upon carbonation, **(c)** close up image (red square in (b)) showing prismatic-like crystals associated with lizardite; **(d)** surface roughness developed upon surface serpentinization of forsterite.

Fig. 9.4 shows SEM images of untreated and 1-week carbonated forsterite samples. Upon carbonation reactions, complexed prismatic-like structures are developed (Fig. 9.4b), composed of rod micro-crystals, characteristic of lizardite [480] (Fig. 9.4c). Treated-forsterite exhibits a rough surface (different from the crystal plane of untreated forsterite, Fig. 9.4a, d). Such surface roughness is observed to be caused by the nucleation of lizardite-prismatic crystals (Fig. 9.4d inset).

XPS analysis shows negligible C1s chemical changes on forsterite surface, indicating that is more likely that carbonates are absent of the surface of forsterite, since the distinctive binding energies of CO_3^{2-} ion are not observed (289.3 ± 0.6 eV; Fig. 9.5)[266,481]. Quantification of the surface Mg and Si atomic concentration of untreated and carbonated forsterite shows that Mg/Si ratio is greatly decreased upon carbonation (Table 9.1). This is consistent with forsterite serpentinization.

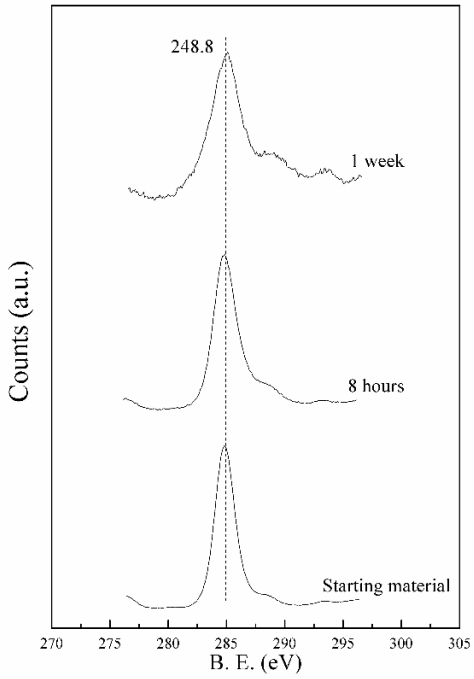

Fig. 9.5. High-resolution XPS analysis of C1S core level spectra of unreacted and carbonated forsterite from 8h to 1-week. The position of adventitious C is shown as reference.

Table 9.1. Surface Mg and Si atomic concentrations of untreated and carbonated forsterite single crystal, estimated based acquired XPS spectra of Mg2p and Si2p core levels.

	Atomic concentration on forsterite surface		
Core level	Clean	8h	1 week
Mg2p	63.6	49.8	50.8
Si2p	36.3	50.1	49.1
Mg2p/ Si2p	1.7	0.9	1

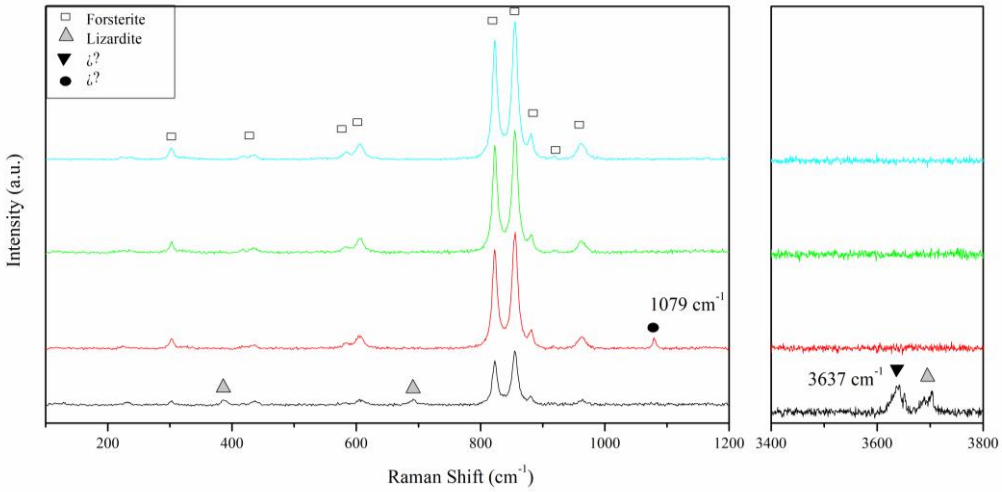

Fig. 9.6. Micro-Raman point analysis of carbonated forsterite during 1 week in different representative areas.

Raman analysis confirmed the presence of lizardite upon carbonation (Fig. 9.6). Two additional and not related Raman features were observed at 1079 and 3637 cm^{-1}. The former peak might be associated with a CO_3^{2-} complex carbonate species [199]. However, such species were not observed during XPS analysis. The latter peak has a lower position than the OH stretching mode of nesquehonite, hydromagnesite, antigorite, lizardite, talc ($Mg_3Si_4O_{10}(OH)_2$) and brucite. Therefore, it remains unknown which is the phase responsible for such peak.

9.2.2. Enstatite single crystal

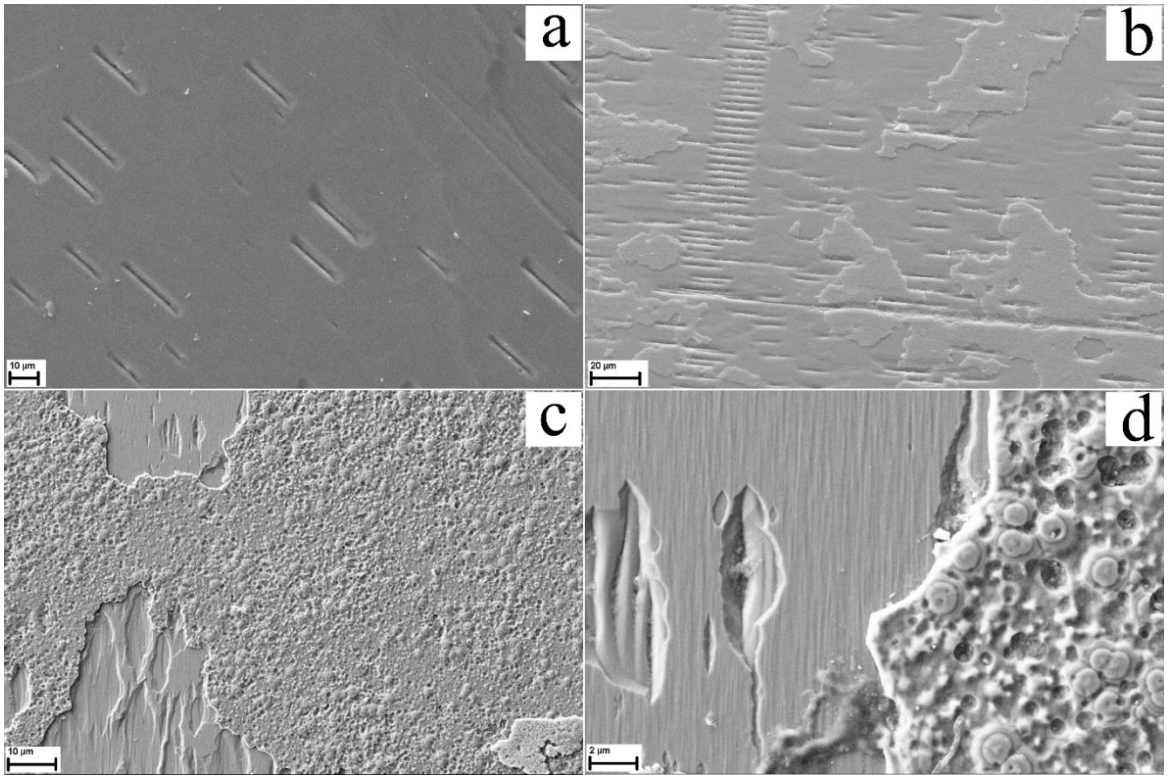

Fig. 9.7. SEM images of **(a)** untreated enstatite single crystal; Si-rich passivating layer formed on enstatite surface upon **(b)** 8h and **(c, d)** 2-weeks carbonation; **(d)** close-up from image (c), showing the broad dislocation and enstatite fragments that appeared partially broken away.

SEM analysis of untreated and carbonated (8h and 2 weeks) enstatite single crystal is shown in Fig. 9.7. Untreated enstatite exhibits a flat and clean surface, showing regular and equally-oriented (following an exfoliation plane) dislocations (Fig. 9.7a). Upon 8h carbonation, an irregular glassy-like layer is observed, partially covering enstatite surface (Fig. 9.7b). Such layer is very similar to a Si-rich layer formed upon olivine carbonation at extreme pressures (135 bar, see section 9.1) observed by Béarat et al., 2006 [449]. Such layer was observed to passivate the carbonation reaction as it limited the diffusion-mediated carbonation. The irregular morphology of this layer resembles feature of individual silica particles as well as hydrothermally deposited silica [478]. EDS analysis confirmed that the observed layer is Si-rich (Fig. 9.8). It should be noted that the Si-distribution across this passivating layer is heterogeneous. After 2 weeks of reaction, the Si-rich layer is almost

covering enstatite surface (Fig. 9.7c). Note that the enstatite dislocations are significantly broader than those observed in untreated enstatite (Fig. 9.8c, d). This strongly suggest that enstatite dissolution occurred, which is responsible for Si-rich layer formation. Some enstatite sections appeared partially broken away from the surface- This might indicate that, upon carbonation, some enstatite fragments are breaking away [449].

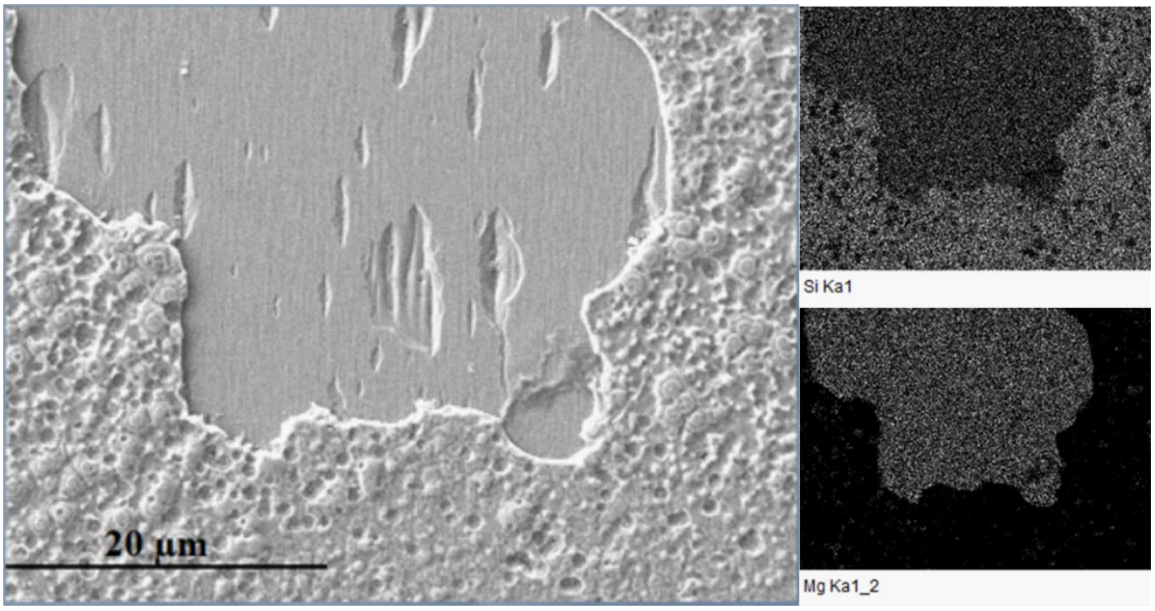

Fig. 9.8. SEM image of 2-weeks carbonated enstatite and elemental EDS analysis. Note that Si-distribution is heterogeneous across the Si-rich layer.

Cross-section SEM images of such Si-rich passivating layer as the carbonation reaction proceeded from 8h to 2 weeks is shown in Fig. 9.9. At 8h of reactions, a thin Si-rich layer is formed (~187 nm; Fig. 9.9b). Generally, the Si-rich layer is observed to be massive, despite its glassy-like appearance. Moreover, morphological differences are clearly observed within the same Si-rich layer (i, ii). Such different morphologies might be associated with the intergrowth formation of Mg-carbonates with Si-rich layers, as previous studies have observed the formation of magnesite within a Si-rich layer upon olivine carbonation under extreme conditions (see section 9.1) [101,449]. This indicates that CO_2 was able to diffused through the Si-rich layer. After 1 week of reaction, this Si-rich layer was observed to be thicker than at 8h (Fig. 9.9c). After 2 weeks of reaction, the Si-rich layer has significantly increased its thickness (from ~ 235nm to ~ 330nm; Fig. 9.9d). Moreover, morphological differences are clearly observed within this Si-rich layer (i, ii), similar to those observed during 8h of reaction (Fig. 9.9b). A depression of the passivating layer is consistent with the presence of phase ii, whereas a semi-spherical shapes surface contour is observed for phase i. This is consistent with the observation of semi-spheres and “holes” across the formed passivating layer (Fig. 9.7, 9.8). EDS analysis clearly shows that such “holes” are rich in Mg and poor in Si (Fig. 9.8). Moreover, phase ii was observed to penetrate within the enstatite crystal, whereas phase i appears to be deposited on enstatite surface. Such observations fit very well with the carbonation

scenario proposed by Chizmeshya et al., 2006 [101] (Figs. 9.1b, 9.10), where the nucleation of magnesite is observed upon olivine dissolution via surface protonation, producing an expanding reaction zone. Silica is driven out from the expanding reaction zone, depositing into enstatite surface [101,476]. Therefore, it is likely that phase i and ii corresponds to deposited silica and nucleated Mg-carbonates upon enstatite carbonation.

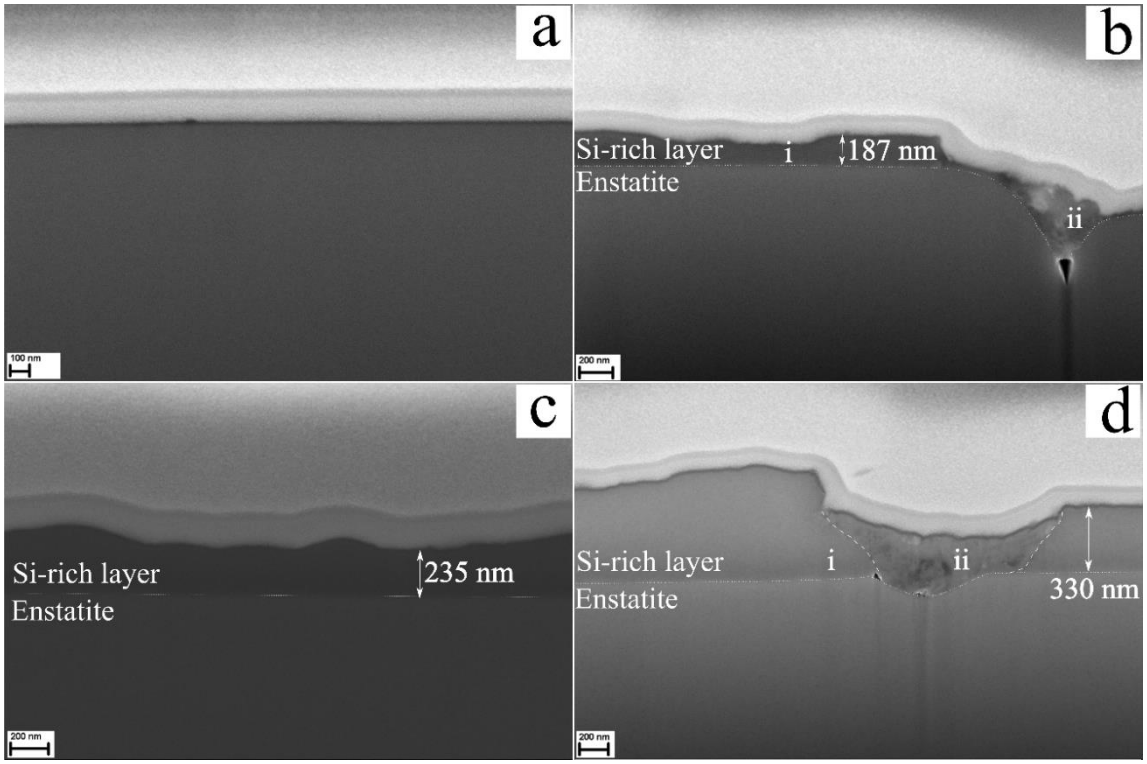

Fig. 9.9. Cross-section FIB imaging of **(a)** untreated and carbonated enstatite during **(b)** 8h, **(c)** 1-week and **(d)** 2-weeks. Note that there are morphological differences within the Si-rich layer, which are shown as phase i and ii, respectively.

XPS analysis shows chemical changes on the C1s core level upon carbonation (Fig. 9.11). After 8h of reaction, XPS C1s spectra is similar to such observed for untreated enstatite, however, a peak with position at 289.6 eV is observed, Such peak might be associated with the presence of carbonate ions (289.3 ± 0.6 eV) in treated enstatite surface [266,481]. The appearance of such carbonate associated peak is particularly evident for 1-week treatments. XPS analysis from 3-days and 2-weeks treatments also exhibit the presence of carbonate ions, however they also exhibit the presence of diverse complex carbon-species, particularly for C-OH and C-O-C species. This might be attributed to the oxidation of adventitious carbon species under carbonation conditions. Comparison with SEM-FIB observations strongly suggest that Mg-carbonates are formed upon dissolving enstatite during carbonation reactions. Such carbonates species might be associated with the presence of phase ii observed with SEM-FIB (Fig. 9.9b, d, Fig. 9.10).

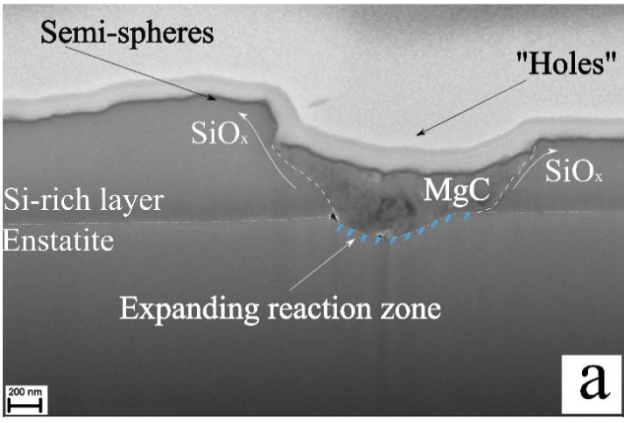

Fig. 9.10. Proposed reaction mechanisms where the nucleation of carbonates occurred upon dissolving enstatite via surface protonation, resulting in an expanding reaction zone.

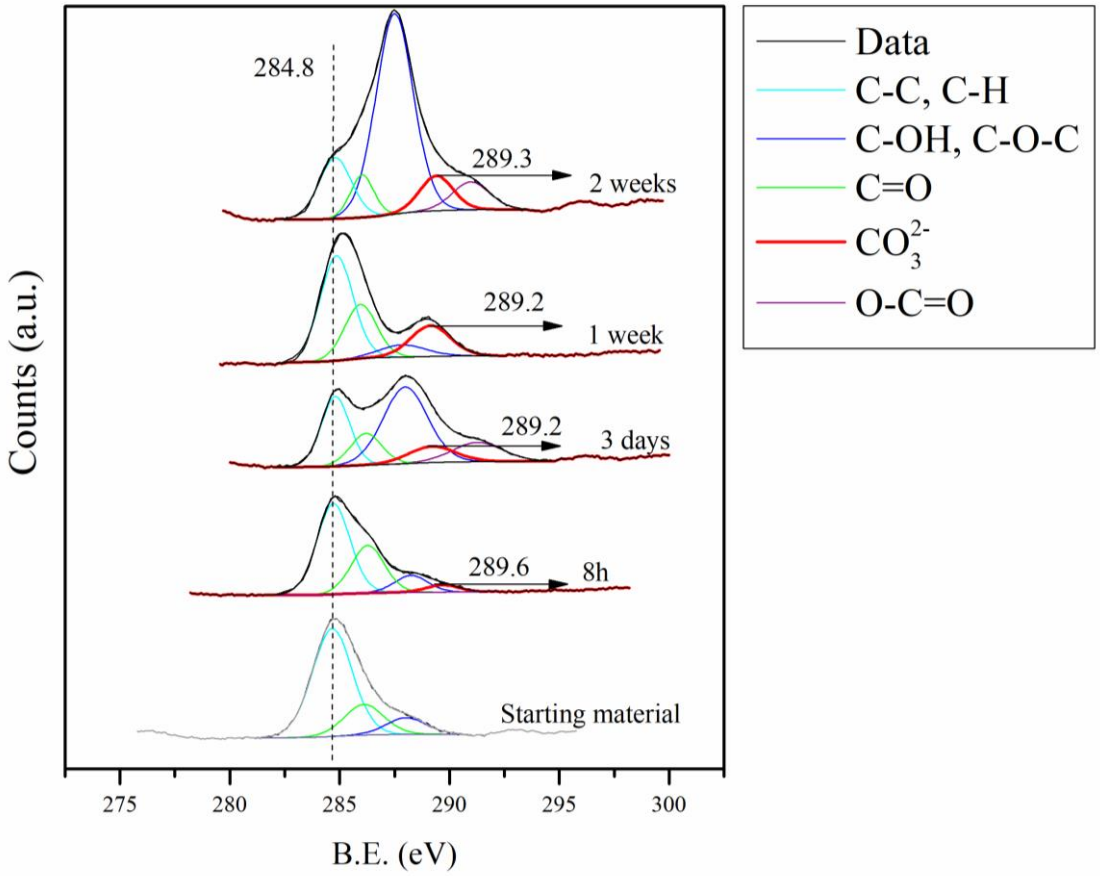

Fig. 9.11. High-resolution XPS analysis of C1S core level spectra of unreacted and carbonated enstatite from 8h to 2-weeks. The position of adventitious C is shown as reference (dashed line).

Quantification of the surface Mg and Si atomic concentration of untreated and carbonated enstatite shows that Mg/Si ratio is increasing as the reaction proceeds from 8h to 3-days (Table 9.2). This might indicate that Mg is being liberated from enstatite matrix upon carbonation, most probably through the nucleation of Mg-carbonate species (Fig. 9.10). At longer reaction times (from 1 to 2 weeks), the Mg/Si ratio decreases, probably indicating that the observed Si-rich layer is partially

covering Mg-carbonate phases. Such observation is similar to that reported in Chizmeshya et al., 2006 [101].

Table 9.2. Surface Mg and Si atomic concentrations of untreated and carbonate enstatite single crystal, estimated based acquired XPS spectra of Mg2p and Si2p core levels.

	Atomic concentration on enstatite surface				
Core level	Clean	8h	3 days	1 week	2 weeks
Mg2p	39.5	39.2	53..1	47.4	42.4
Si2p	60.4	60.7	46.8	52.5	57.5
Mg2p/ Si2p	0.6	0.6	1.1	0.9	0.7

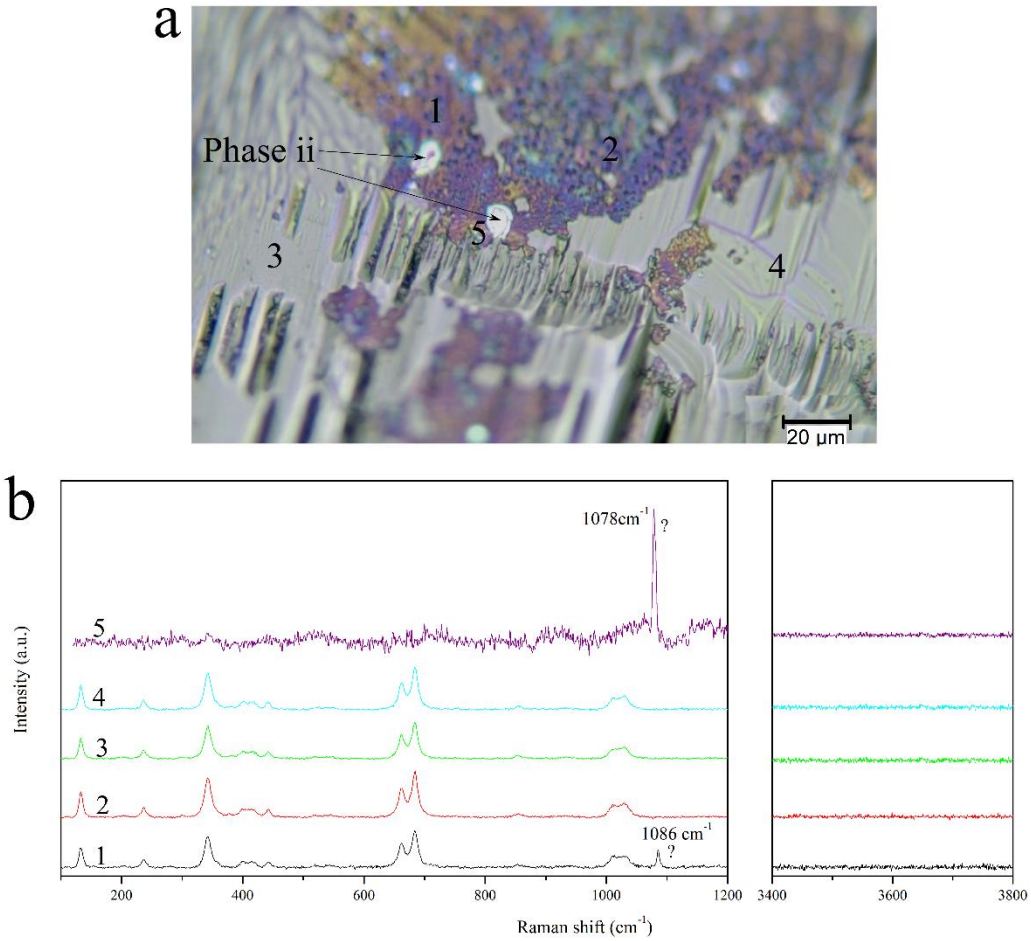

Fig. 9.12. (a) Optical microscope image of carbonated enstatite, showing the position of the Raman analysis shown in (b). **(b)** Micro-Raman point analysis of carbonated enstatite during 2-weeks.

Individual micro-Ramana analysis of the Si-rich layer and in "hole"-like regions (associated with phase ii) of 2-weeks carbonated enstatite shows the presence of two distinct Raman peaks (1078 and 1086 cm^{-1}; Fig. 9.12). The first peak is similar to such observed in carbonated olivine (Fig. 9.6), which might indicate that these phases might be related. The phase responsible for such peaks remains unknown since Mg-carbonate peaks are observed at higher wavenumbers [380]. However, it is plausible that complex carbonate species are responsible for such peaks, since such peak position

are characteristic of the strong $\nu_{1symcar}$ band of several carbonate phases [199,380,382]. Moreover, the reaction products show the absence of OH stretching modes were observed, possibly indicating that they are anhydrous.

The unequivocal enstatite dissolution might be caused by direct interaction of CO_2 and H_2O gas molecules, as such reactions are thermodynamically favored [156]. However, several studies have observed that direct-carbonation mechanisms of Mg-rich silicates is limited to very slow kinetics, if occurring at all (see section 2.3.1.1) [259–261]. However, the presence of water vapor plays a crucial role on accelerating the carbonation reaction [265,266]. Therefore, the presence of water vapor molecules in this study is foreseen to unlock the carbonation of enstatite. However, the dissolution mechanisms remained relatively unconstrained. One possible scenario includes the formation of a liquid water surface film that mediated the dissolution of enstatite, followed by the intergrowth of Mg-carbonates (via precipitation) and silica. Another possibility is that the dissolution of enstatite is driven by gas-solid reactions based on thermodynamic expectations.

9.3. Conclusions

An experimental study of the carbonation of forsterite and enstatite single crystals was carried out under localized near-surface early-Mars conditions in order to provide more insight into the nanoscale process dynamics during Mg-rich silicate carbonation as well as to the depletion of the early CO_2-rich Mars atmosphere. Our nano-scale measurements allowed a detailed description of carbonation surface reactions of Mg-rich silicates, offering new possibilities to investigate mineral carbonation processes.

Forsterite underwent partial serpentinization while no carbonation was observed. On the other hand, the dissolution of enstatite under the presence of water vapor (<1% RH) unequivocally occurred. It is likely that Mg-carbonate phases were formed upon dissolving enstatite. Within such layer, morphological differences were observed, suggesting an intergrowth of carbonates and Si-rich phases. The nucleation of carbonates might occur upon enstatite surface protonation, resulting in an expanding reaction zone that allowed the diffusion of CO_2 species into the expanding reaction zone. Si-rich layer was observed to grow (as evidenced by its increase thickness and covering of enstatite crystal) as the reaction proceeded. Such layer might limit significantly the carbonation reaction, as it covers reactive enstatite surface area. It has been also reported that enstatite dissolution does not require the presence of liquid water. However, the dissolution-mechanisms are yet unknown.

General conclusions

In this experimental work, the direct steam-mediated carbonation of Mg-rich oxides and silicates under moderately low pressure and temperature conditions were studied in order to provide new insights into the formation and evolution of hydrated Mg-carbonates phases as well to assess the carbonation potential of Mg-rich silicates under such conditions. The highlights of this dissertation are summarized in two main sections as:

Formation and evolution of Mg-carbonate phases:

1. Several hydrated Mg-carbonates are formed upon carbonation of Mg-rich oxides and silicates, each having a different amount of water per unit cell, and their formation is selectively dependent of reaction temperature.
2. Observations suggest that an amorphous magnesium carbonate (AMC) coexists with nesquehonite and/or dypingite-like phases at 50ºC. On the other hand, less hydrated dypingite-like phases were observed at 90ºC, and at temperatures ≥120ºC, only hydromagnesite and/or magnesite appeared to be present.
3. The evolution of Mg-carbonate phases is mainly controlled by the slow dehydration kinetics of Mg^{2+} rather than evolving to a thermodynamically more stable or structurally similar phase.
4. A hydrous AMC was observed to have similar decomposition temperatures and chemical composition to nesquehonite.
5. Similar Raman ν_1 symmetric stretching mode of the carbonate ion peak position were observed for magnesite, nesquehonite and hydrous AMC. This is associated with their similar internal structure. However, hydrous AMC have a significantly broader $\nu_{1symcar}$, attributed to its heterogeneous disordered structure.
6. Carbonate phases from the dypingite-like group ($Mg_5(CO_3)_4 \cdot (OH)_2 \cdot XH_2O$, $11 \leq X \leq 4$) allows a progressive dehydration as carbonation proceeds. The structurally disordered nature of dypingite-like phases is caused by the excess of hydrogen-bonded structurally

coffined molecular water along the [010] plane on such phases, forming flaky microcrystals. Upon removal of molecular water, shrinkage of the sheet-like crystal arrangement occurs, resulting into organized hydromagnesite plate crystals.

7. Results obtained from the progressive transition from highly-disordered dypingite-like phases to hydromagnesite allowed the distinction of such phases, shedding light on the enigmatic discrepancies in the solubility and thermal decomposition behavior data of such phases reported in the literature.
8. Despite nesquehonite has a similar internal structure to magnesite, its spontaneous transformation to this latter phase only occurs under extreme carbonation conditions, since such transition requires a complete removal of molecular water. Instead, the preferred reaction pathway includes the dissolution reprecipitation of nesquehonite to form slightly less-hydrated and highly-disordered dypingite-like phases, which then allows a further progressive dehydration.
9. Nesquehonite transition to dypingite-like phases increases the Mg/C ratio of the unit cell from 1 (former phase) to 5/4 (latter phase), evidenced by the increased CO_3^{2-} ion distortion in the latter phase relative to the former.
10. Despite it has been predicted that hydrous AMC might be direct precursor to anhydrous AMC or magnesite (analogous to the prediction of nesquehonite to magnesite), it is strongly argued that such transition will require extreme carbonation conditions and instead, it probably will prefer to evolve through a progressive dehydration via dypingite-like phases.
11. The transition of hydrous AMC to dypingite-like phases remained enigmatic. However, it is likely that upon partial dehydration of hydrous AMC, a partial nucleation of highly-disordered dypingite-like phases occur. It is expected that no significant structural rearrangements are required to obtained such partial transition, since the carbonate ions within hydrous AMC have alternating orientations, similarly to dypingite-like-phases.
12. Straightforward transition of hydrous AMC to nesquehonite is expected to occur with no significant kinetic barriers, since no dehydration occurs in such process.
13. The progressive dehydration of dypingite-like phases is hindered once hydromagnesite hydration level is reached. Further dehydration requires a sudden release of all remaining water molecules (limiting their reaction kinetics) in order to form magnesite. The latter transition was observed to occur via dissolution-reprecipitation mechanism.
14. The transition of hydromagnesite to magnesite is expected to require significantly less energy requirements than the transition of nesquehonite to magnesite, since the former requires significantly less amounts of molecular waters removal than the latter.
15. Magnesite formation is accelerated in a hydromagnesite-saturated environment.

16. A complete hydromagnesite transition to magnesite was observed at 145ºC under RH>90%, however under lower RH~48%, such transition was significantly limited.
17. Magnesite is the preferred Mg-carbonate for mineral carbonation processes, since it has the highest CO_2 sequestration capacity, is the most stable, least soluble and lighter Mg carbonate phase, leading to lower transportation and processing costs. At pressure and temperature conditions near to those of flue gas emission, its formation is kinetically inhibited by the formation of hydrated carbonates. This study shed light into the accelerated formation of magnesite through the evolution of hydrated Mg-carbonate precursors, as well as potential phase transition pathways, under direct moist carbonation of Mg-silicates/oxides at moderately low temperature and pressure conditions (≤10 bar; ≤205ºC).

Carbonation of Mg-rich oxides and silicates

18. Efficient carbonation of brucite was observed at 120ºC and 7-10 bar, due to the high hydromagnesite yield. At higher temperatures (145 and 165ºC), the yield of brucite carbonation is reduced, however, magnesite yield increases, resulting in higher amounts of CO_2 wt% sequestered than those obtained at 120ºC.
19. Brucite carbonation yield is significantly reduced at ≥ 185ºC due to the partial or almost complete inhibition of hydromagnesite formation. This might be attributed to the chemical potential is significantly reduced as the reacting phases approached the equilibrium phase boundaries.
20. Successful carbonation of brucite was obtained when using Simulated Flue Gas (SFG) conditions. However, the obtained results were lower than those obtained when using Concentrated CO_2. This could be attributed to the lower RH on SFG experiments compared to CC. SFG experiments were carried out at lower temperatures and of regular flue gas emissions. An increase of temperature and/or RH could potentially increase the SFG carbonation potential, particularly for atmospheric pressure treatments, without increase the cost associated with carbonation processes.
21. A maximum of 9.3 CO_2 wt%. was sequestered using activated lizardite at 610ºC (AS610) upon carbonation at 120ºC, 6 bar during 4h.
22. Upon lizardite activation two distinct amorphous Mg-rich silicates were identified, each having a significant different reactivity. This sheds light into the yet enigmatic low carbonation efficiency during direct carbonation of heat activated serpentine materials.
23. Highly Reactive Amorphous Mg-rich Silicate phase (HRAS) nourished the growth of carbonates. A complete carbonation of such phase does not require elevated temperature

and pressure conditions. Moreover, it also yielded to the formation of Si-rich passivating phases. Such phases might partially limit the carbonation potential of such materials.

24. Poorly Reactive Amorphous Mg-rich Silicate phase (PRAS) remained seemingly unreacted upon carbonation, fixing a significant amount of unreacted Mg within its disordered structure. The presence of this phase could potentially provide new insights to the yet unanswered question regarding the limited direct carbonation of lizardite.
25. Forsterite nucleation upon activation of lizardite at 710ºC (AS710) relative to AS610 reduced the carbonation yield only by up to 7%. Such carbonation limitation is not significant when compared to such associated with the presence of HRAS.
26. The direct carbonation of activated serpentine is currently prohibited, mainly due to the fate of Si upon activation and carbonation. If no significant optimization of such processes is obtained, alternative indirect carbonation routes should be considered.
27. Brucite-bearing serpentinized dunites were found to have a promising carbonation potential due to their generally high brucite contents.
28. A maximum of ~10 CO_2 wt% was successfully sequestered upon carbonation of serpentinized dunite at 145ºC and 10 bar during 4h (RH: 100%).
29. Changes on the dehydration behavior of un-activated lizardite were observed upon carbonation, where inner OH are generally being removed as the amounts of outer "brucitic" OH are increasing.
30. Forsterite and /or lizardite underwent partial carbonation as evidenced by the obtained carbonation yield significantly exceeded the estimated if only brucite was reacting.
31. Comparison of the obtained carbonation yield normalized by the estimated pretreatment energy requirements shows that brucite-bearing serpentinized dunites have higher carbonation potential than activated serpentines.
32. Partial serpentinization of forsterite single crystal was observed upon carbonation at 5 bar, 185ºC up to 1 week, while no carbonation was observed. Under analogous conditions, dissolution of enstatite single crystal unequivocally occurred in the presence of low humidity (<1%) as evidenced by the formation of a Si-rich passivating layer.
33. XPS analysis strongly suggest the presence of carbonate species on the surface of enstatite upon carbonation. Such observation might indicate that direct gas-solid carbonation of enstatite does not require the presence of liquid water.

Future work

This extensive experimental work provided bleeding edge insights regarding the formation of Mg-carbonates upon accelerated carbonation of Mg-silicates/oxides. There are several ways to possibly extent the current understanding on such processes, particularly in view of the ever-increasing CO_2 concentration in the atmosphere and its concomitant consequences. Ex-situ mineral carbonation processes are foreseen to open the technological pathway for large-scale in-situ processes. Among the different mineral carbonation approaches, the carbonation of alkaline industrial wastes for the formation of highly stable, profitable and CO_2-dense carbonate materials is currently the most successful approach for such technologies. Such reactions should preferably occur via direct gas-solid carbonation, in the presence of water vapor, under relatively low temperature and pressure conditions using simulated flue gas streams instead of concentrated CO_2, integrating both CO_2 capture and utilization within a single process. Some specific guidelines to extent the work performed in the thesis are:

1. Study the relation between Ca and Mg content of ACC-Mg during the formation mechanisms of MHC. Upon the nucleation and crystal growth of this latter phase from the former, only minor amounts of Mg are retained within MHC, resulting in the formation of a hydrous AMC that covers and passivates MHC transition to anhydrous Ca-carbonate phases. Under exceeding Mg contents within AMC-Mg, such passivation effect is expected. However, at low Mg contents might results in the insufficient formation of a hydrated AMC, which might only partially cover MHC, allowing the transition of this latter phase to anhydrous Ca-carbonate phases. It should be considered to analyze the reaction products with Transmission Electron Microscopy (TEM), since it might provide invaluable data regarding the internal structure of such materials.
2. Assess the possibility of substituting some Mg cations for Ca within hydrous AMC in a similar process as detailed in White et al., 2010 [424], in order to reduce the energy required to remove molecular water from hydrated Mg-carbonates, possibly unlocking the direct and desired direct transformation of hydrous AMC to anhydrous AMC and /or magnesite. It

might also provide new insights into the acceleration of the direct transition of hydromagnesite and/or nesquehonite to magnesite. Such process has been extensively studied with the opposite purpose, where Mg cations substituted Ca in ACC-Mg in order to prevent the dehydration of such materials. The author encourages to in-situ analyze such reactions since the emerging intermediate phases might be easier to distinguish as well as the different reaction mechanisms of such materials.

3. Perform an extensive experimental campaign in order to optimize heat activation conditions (temperature and resilience time) on serpentine minerals for increasing the reactivity of such materials. Such optimizations such include to find the "sweet spot" were HRAS/PRAS content ratio is higher, as well as the different optimization parameters extensively discussed in chapter 6 and by Du Breuil et al., 2019 [482].
4. Asses the carbonation of enstatite single crystal under lower temperatures (<185ºC) over extended reaction times (> 2weeks) by detailed surface characterization, including chemical changes on the surface via XPS analysis and morphological changes with SEM-FIB imaging. It is also proposed to perform in-situ XPS analysis with a clean enstatite surface (free of adventitious carbon, via combustion at 500ºC or Ar sputtering) in order to quantify the extent of carbonation. The author suggests to analyze such reaction products with the aid of TEM in order to provide more insights into the internal structure of such products.
5. Study the carbonation potential of Ca/Mg-bearing glass-silicate materials, as they have higher reactivity than their respective crystalline counterparts [217]. An option to consider is to study the carbonation potential of Ca-bearing cenospheres from high Ca- fly ashes (HCFA). Prior studies have suggested that the carbonation of such materials is not only limited to free-lime minerals [82,268]. Moreover Ca-carbonates were observed to form on cenospheres. This might suggest that cenospheres play a key role during carbonation reactions. However, such processes are very difficult to assess due to the several processes that are occurring upon carbonation of all HCFA components. Individually analyzing the carbonation of cenospheres after separation from other HCFA component will provide invaluable new insights into the carbonation processes of HCFA and their valorization if the construction industry.

Achievements of the author

Publications

- **Rausis, K.**, Ćwik, A., Casanova, I., 2020. Insights into the carbonation of activated lizardite: the identification of a poorly-reactive amorphous Mg-rich silicate phase. Int. J. GreenH. Gas Con. Revised Manuscript Submitted
- Ćwik, A., **Rausis, K.**, Casanova, I., Zarębska, K., n.d. Carbonation of high-Ca fly ashes under flue gas conditions: implications for their valorization in the construction industry. J. CO2 Util. Revised manuscript submitted.
- **Rausis, K.**, Ćwik, A., Casanova, I., 2020. Phase evolution during accelerated CO_2 mineralization of brucite under concentrated CO_2 and simulated flue gas conditions. J. CO2 Util. 37, 122–133. ttps://doi.org/10.1016/j.jcou.2019.12.007
- Ćwik, A., Casanova, I., **Rausis, K.**, Zarębska, K., 2019. Utilization of high-calcium fly ashes through mineral carbonation: The cases for Greece, Poland and Spain. J. CO2 Util. 32, 155–162. https://doi.org/10.1016/j.jcou.2019.03.020
- Ćwik, A., Casanova, I., **Rausis, K.**, Koukouzas, N., Zarębska, K., 2018. Carbonation of high-calcium fly ashes and its potential for carbon dioxide removal in coal fired power plants. J. Clean. Prod. 202, 1026–1034. https://doi.org/10.1016/j.jclepro.2018.08.234

Conferences

- **Rausis, K.**, Ćwik, A., Casanova, I. Mg-Carbonate Phase Formation and Evolution during Accelerated Carbonation of Brucite. International Conference on Accelerated Carbonation for Environmental and Material Engineering (ACEME), July 5th-8th, 2020, Tallinn, Estonia.

- **Rausis, K.**, Ćwik, A., Casanova, I. Experimental Study on the Steam-Mediated Carbonation of Activated Lizardite. International Conference on Accelerated Carbonation for Environmental and Material Engineering (ACEME), July 5th-8th, 2020, Tallinn, Estonia.
- **Rausis, K.**, Casanova, I. Experimental evidence for direct gas-solid carbonation of enstatite: implications for CO_2 sequestration in early Mars. Goldschmidt Conference, August 18th-23th, 2019, Barcelona, Spain.
- **Rausis, K.**, Casanova, I., Ćwik, A., CO_2 Sequestration by accelerated carbonation of brucite in moderate pressure and temperatures. Gordon Research Conference (GRC): Carbon Capture, Utilization and Storage – Tackling the Carbon Dioxide Challenge for a Sustainable Future. May 5th-10th, 2019, Les Diablerets, Switzerland.
- **Rausis, K.**, Casanova, I. Carbonation of silicates: An X-ray Photoelectron Spectroscopy study. Gordon Research Conference (GRC): Carbon Capture, Utilization and Storage - Innovative Carbon Management Pathways for a Sustainable Future: June 11th-16th, 2011, New London, United States

References

[1] P. Köhler, R. Bintanja, H. Fischer, F. Joos, R. Knutti, G. Lohmann, V. Masson-Delmotte, What caused Earth's temperature variations during the last 800,000 years? Data-based evidence on radiative forcing and constraints on climate sensitivity, Quat. Sci. Rev. 29 (2010) 129–145. doi:10.1016/j.quascirev.2009.09.026.

[2] A. Berger, Long-Term Variations of Daily Insolation and Quaternary Climatic Changes, J. Atmos. Sci. 35 (1978) 2362–2367. doi:10.1175/1520-0469(1978)035<2362.

[3] B.A. Wielicki, T. Wong, N. Loeb, P. Minnis, K. Priestley, R. Kandel, Changes in earth's albedo measured by satellite, Science (80-.). 308 (2005) 825. doi:10.1126/science.1106484.

[4] X. Qu, A. Hall, Surface contribution to planetary albedo variability in cryosphere regions, J. Clim. 18 (2005) 5239–5252. doi:10.1175/JCLI3555.1.

[5] K.E. Taylor, M. Crucifix, P. Braconnot, C.D. Hewitt, C. Doutriaux, A.J. Broccoli, J.F.B. Mitchell, M.J. Webb, Estimating shortwave radiative forcing and response in climate models, J. Clim. 20 (2007) 2530–2543. doi:10.1175/JCLI4143.1.

[6] J.T. Kiehl, K.E. Trenberth, Earth ' s Annual Global Energy Budget, Bull. Am. Meteorol. Soc. 78 (1997) 197–208.

[7] J.R. Petit, J. Jouzel, D. Raynaud, J.M. Barnola, I. Basile, M. Bender, J. Chappellaz, M. Davis, G. Delaygue, M. Delmotte, V.M. Kotlyakov, M. Legrand, V.Y. Lipenkov, C. Loriu, L. Pepin, C. Ritz, E. Saltzman, M. Stievenard, Climate and atmospheric history of the past 420,000 years from the Vostok ice core, Antarctica, Futur. Nat. Doc. Glob. Chang. (2013) 348–358.

[8] E. Monnin, A. Indermühle, A. Dällenbach, J. Flückiger, B. Stauffer, T.F. Stocker, D. Raynaud, J.M. Barnola, Atmospheric CO2 concentrations over the last glacial termination, Science (80-.). 291 (2001) 112–114. doi:10.1126/science.291.5501.112.

[9] U. Siegenthaler, T.F. Stocker, E. Monnin, D. Luthi, J. Shwander, B. Stauffer, D. Raynaud, J.M. Barnola, H. Fischer, V. Masson-Delmotte, J. Jouzel, Stable Carbon Cycle – Climate Relationship During the Late Pleistocene Stable Carbon Cycle – Climate Relationship During the Late Pleistocene, Science (80-.). 310 (2005) 1313–1317. doi:10.1126/science.1120130.

[10] R. Spahni, J. Chappellaz, T.F. Stocker, L. Loulergue, G. Hausammann, K. Kawamura, J. Flückiger, J. Schwander, D. Raynaud, V. Masson-Delmotte, J. Jouzel, Atmospheric science: Atmospheric methane and nitrous oxide of the late pleistocene from Antarctic Ice Cores, Science (80-.). 310 (2005) 1317–1321. doi:10.1126/science.1120132.

[11] L. Loulergue, A. Schilt, R. Spahni, V. Masson-Delmotte, T. Blunier, B. Lemieux, J.M. Barnola, D. Raynaud, T.F. Stocker, J. Chappellaz, Orbital and millennial-scale features of atmospheric CH4 over the past 800,000 years, Nature. 453 (2008) 383–386. doi:10.1038/nature06950.

[12] D. Lüthi, M. Le Floch, B. Bereiter, T. Blunier, J.M. Barnola, U. Siegenthaler, D. Raynaud, J. Jouzel, H. Fischer, K. Kawamura, T.F. Stocker, High-resolution carbon dioxide concentration record 650,000-800,000 years before present, Nature. 453 (2008) 379–382. doi:10.1038/nature06949.

[13] G. Myhre, E.J. Highwood, K.P. Shine, F. Stordal, New estimates of radiative forcing due to well mixed greenhouse gases, Geophys. Res. Lett. 25 (1998) 2715–2718.

[14] J. Hansen, M. Sato, R. Ruedy, L. Nazarenko, A. Lacis, G.A. Schmidt, G. Russell, I. Aleinov, M. Bauer, S. Bauer, N. Bell, B. Cairns, V. Canuto, M. Chandler, Y. Cheng, A. Del Genio, G. Faluvegi, E. Fleming, A. Friend, T. Hall, C. Jackman, M. Kelley, N. Kiang, D. Koch, J. Lean, J. Lerner, K. Lo, S. Menon, R. Miller, P. Minnis, T. Novakov, V. Oinas, J. Perlwitz, J. Perlwitz, D. Rind, A. Romanou, D. Shindell, P. Stone, S. Sun, N. Tausnev, D. Thresher, B. Wielicki, T. Wong, M. Yao, S. Zhang, Efficacy of climate forcings, J. Geophys. Res. D Atmos. 110 (2005) 1–45. doi:10.1029/2005JD005776.

[15] J. Hansen, M. Sato, P. Kharecha, D. Beerling, R. Berner, V. Masson-Delmotte, M. Pagani, M. Raymo, D. Royer, J.C. Zachos, Targer Atmospheric CO2: Where Should Humanity Aim ?, Open Atmos. Sci. J. 2 (2008) 217–231.

[16] IPCC, Summary for Policymakers. In: Global Warming of 1.5°C, Geneva, Switzerland, 2018. https://doorbraak.be/heibel-om-het-ipcc/amp/?utm_term=Autofeed&utm_medium=Social&utm_source=Twitter&utm_term=Autofeed&utm_medium=Social&utm_source=Twitter&__twitter_impression=true.

[17] R.E. Zeebe, A. Ridgwell, J.C. Zachos, Anthropogenic carbon release rate unprecedented during the past 66 million years, Nat. Geosci. 9 (2016) 325–329. doi:10.1038/ngeo2681.

[18] J.C. Zachos, G.R. Dickens, R.E. Zeebe, An early Cenozoic perspective on greenhouse warming and carbon-cycle dynamics, Nature. 451 (2008) 279–283. doi:10.1038/nature06588.

[19] E.J. Rohling, A. Sluijs, H.A. Dijkstra, P. Köhler, R.S.W. Van De Wal, A.S. Von Der Heydt, D.J. Beerling, A. Berger, P.K. Bijl, M. Crucifix, R. Deconto, S.S. Drijfhout, A. Fedorov, G.L. Foster, A. Ganopolski, J. Hansen, B. Hönisch, H. Hooghiemstra, M. Huber, P. Huybers, R. Knutti, D.W. Lea, L.J. Lourens, D. Lunt, V. Masson-Demotte, M. Medina-Elizalde, B. Otto-Bliesner, M. Pagani, H. Pälike, H. Renssen, D.L. Royer, M. Siddall, P. Valdes, J.C. Zachos, R.E. Zeebe, Making sense of palaeoclimate sensitivity, Nature. 491 (2012) 683–691. doi:10.1038/nature11574.

[20] G.R. Dickens, J.R. O'Neil, D.K. Rea, R.M. Owen, Dissociation of oceanic methane hydrate as a cause of the carbon isotope excursion at the end of the Paleocene, Paleoceanography. 10 (1995) 965–971. doi:10.1029/95PA02087.

[21] P.N. Pearson, E. Thomas, Drilling disturbance and constraints on the onset of the Paleocene-Eocene boundary carbon isotope excursion in New Jersey, Clim. Past. 11 (2015) 95–104. doi:10.5194/cp-11-95-2015.

[22] J.D. Wright, M.F. Schaller, Eèidence for a rapid release of carbon at the Paleocene-Eocene thermal maximum, Proc. Natl. Acad. Sci. U. S. A. 110 (2013) 15908–15913. doi:10.1073/pnas.1309188110.

[23] P. Vervoort, M. Adloff, S.E. Greene, S. Kirtland Turner, Negative carbon isotope excursions: An interpretive framework, Environ. Res. Lett. 14 (2019). doi:10.1088/1748-9326/ab3318.

[24] H. Suess, Radiocarbon Concentration in Modern Wood, Science (80-.). 122 (1955) 415–417.

[25] P. Köhler, Using the Suess effect on the stable carbon isotope to distinguish the future from the past in radiocarbon, Environ. Res. Lett. 11 (2016). doi:10.1088/1748-9326/11/12/124016.

[26] S. Kirtland Turner, P.M. Hull, L.R. Kump, A. Ridgwell, A probabilistic assessment of the rapidity of PETM onset, Nat. Commun. 8 (2017) 1–9. doi:10.1038/s41467-017-00292-2.

[27] A. Ridgwell, D.N. Schmidt, Past constraints on the vulnerability of marine calcifiers to massive carbon dioxide release, Nat. Geosci. 3 (2010) 196–200. doi:10.1038/ngeo755.

[28] K. Caldeira, M.E. Wickett, Anthropogenic carbon and ocean pH, Nature. 425 (2003) 365. doi:10.1038/425365a.

[29] R.E. Zeebe, J.C. Zachos, K. Caldeira, T. Tyrrell, Carbon Emissions and Accidification, Science (80-.). 321 (2008) 51–52.

[30] J. Rockström, W. Steffen, K. Noone, Å. Persson, F. S. Chapin, E. F. Lambin, T. M. Lenton, M. Scheffer, C. Folke, H. J. Schellnhuber, B. Nykvist, C. A. de Wit, T. Hughes, S. van der Leeuw, H. Rodhe, S. Sörlin, P. K. Snyder, R. Costanza, U. Svedin, M. Falkenmark, L. Karlberg, R. W. Corell, V. J. Fabry, J. Hansen, B. Walker, D. Liverman, K. Richardson, P. Crutzen, J. A. Foley, A safe operation space for humanity, Nature. 461 (2009).

[31] R. Cavicchioli, W.J. Ripple, K.N. Timmis, F. Azam, L.R. Bakken, M. Baylis, M.J. Behrenfeld, A. Boetius, P.W. Boyd, A.T. Classen, T.W. Crowther, R. Danovaro, C.M. Foreman, J. Huisman, D.A. Hutchins, J.K. Jansson, D.M. Karl, B. Koskella, D.B. Mark Welch, J.B.H. Martiny, M.A. Moran, V.J. Orphan, D.S. Reay, J. V. Remais, V.I. Rich, B.K. Singh, L.Y. Stein, F.J. Stewart, M.B. Sullivan, M.J.H. van Oppen, S.C. Weaver, E.A. Webb, N.S. Webster, Scientists' warning to humanity: microorganisms and climate change, Nat. Rev. Microbiol. 17 (2019) 569–586. doi:10.1038/s41579-019-0222-5.

[32] R.E. Zeebe, J.C. Zachos, Long-term legacy of massive carbon input to the earth system: Anthropocene versus eocene, Philos. Trans. R. Soc. A Math. Phys. Eng. Sci. 371 (2013). doi:10.1098/rsta.2012.0006.

[33] A. Robinson, R. Calov, A. Ganopolski, Multistability and critical thresholds of the Greenland ice sheet, Nat. Clim. Chang. 2 (2012) 429–432. doi:10.1038/nclimate1449.

[34] R.E. Zeebe, Time-dependent climate sensitivity and the legacy of anthropogenic greenhouse gas emissions, Proc. Natl. Acad. Sci. U. S. A. 110 (2013) 13739–13744. doi:10.1073/pnas.1222843110.

[35] J. Rogelj, M. Den Elzen, N. Höhne, T. Fransen, H. Fekete, H. Winkler, R. Schaeffer, F. Sha, Paris Agreement climate proposals need a boost to keep warming well below 2°C, Nature. (2016). doi:10.1038/nature18307.

[36] C. Le Quéré, R. Moriarty, R.M. Andrew, J.G. Canadell, S. Sitch, J.I. Korsbakken, P. Friedlingstein, G.P. Peters, R.J. Andres, T.A. Boden, R.A. Houghton, J.I. House, R.F. Keeling, P. Tans, A. Arneth, D.C.E. Bakker, L. Barbero, L. Bopp, J. Chang, F. Chevallier, L.P. Chini, P. Ciais, M. Fader, R.A. Feely, T. Gkritzalis, I. Harris, J. Hauck, T. Ilyina, A.K. Jain, E. Kato, V. Kitidis, K. Klein Goldewijk, C. Koven, P. Landschützer, S.K. Lauvset, N. Lefèvre, A. Lenton, I.D. Lima, N. Metzl, F. Millero, D.R. Munro, A. Murata, J.E.M. S. Nabel,

S. Nakaoka, Y. Nojiri, K. O'Brien, A. Olsen, T. Ono, F.F. Pérez, B. Pfeil, D. Pierrot, B. Poulter, G. Rehder, C. Rödenbeck, S. Saito, U. Schuster, J. Schwinger, R. Séférian, T. Steinhoff, B.D. Stocker, A.J. Sutton, T. Takahashi, B. Tilbrook, I.T. Van Der Laan-Luijkx, G.R. Van Der Werf, S. Van Heuven, D. Vandemark, N. Viovy, A. Wiltshire, S. Zaehle, N. Zeng, Global Carbon Budget 2015, Earth Syst. Sci. Data. 7 (2015) 349–396. doi:10.5194/essd-7-349-2015.

[37] M. Fasihi, O. Efimova, C. Breyer, Techno-economic assessment of CO 2 direct air capture plants, J. Clean. Prod. 224 (2019) 957–980. doi:10.1016/j.jclepro.2019.03.086.

[38] P. Smith, S.J. Davis, F. Creutzig, S. Fuss, J. Minx, B. Gabrielle, E. Kato, R.B. Jackson, A. Cowie, E. Kriegler, D.P. van Vuuren, J. Rogelj, P. Ciais, J. Milne, J.G. Canadell, D. McCollum, G. Peters, R. Andrew, V. Krey, G. Shrestha, P. Friedlingstein, T. Gasser, A. Grübler, W.K. Heidug, M. Jonas, C.D. Jones, F. Kraxner, E. Littleton, J. Lowe, J.R. Moreira, N. Nakicenovic, M. Obersteiner, A. Patwardhan, M. Rogner, E. Rubin, A. Sharifi, A. Torvanger, Y. Yamagata, J. Edmonds, C. Yongsung, Biophysical and economic limits to negative CO2 emissions, Nat. Clim. Chang. 6 (2016) 42–50. doi:10.1038/nclimate2870.

[39] H. Geerlings, R. Zevenhoven, CO_2 Mineralization—Bridge Between Storage and Utilization of CO_2, Annu. Rev. Chem. Biomol. Eng. 4 (2013) 103–117. doi:10.1146/annurev-chembioeng-062011-080951.

[40] R.M. Cuéllar-Franca, A. Azapagic, Carbon capture, storage and utilisation technologies: A critical analysis and comparison of their life cycle environmental impacts, J. CO2 Util. 9 (2015) 82–102. doi:10.1016/j.jcou.2014.12.001.

[41] B. Metz, O. Davidson, H. de Coninck, M. Loos, L. Meyer, Editors, Special Report on Carbon Dioxide Capture and Storage. Prepared by Working Group III of the intergovernamental Panel on Climate Change, Cambridge, UK and NY, 2005.

[42] E.R. Bobicki, Q. Liu, Z. Xu, H. Zeng, Carbon capture and storage using alkaline industrial wastes, Prog. Energy Combust. Sci. 38 (2012) 302–320. doi:10.1016/j.pecs.2011.11.002.

[43] P. Styring, D. Jansen, H. de Coninck, H. Reith, K. Armstrong, Carbon Capture and Utilisation in the green economy, 2011.

[44] I. Mouedhen, N. Kemache, L.C. Pasquier, E. Cecchi, J.F. Blais, G. Mercier, Effect of pCO2 on direct flue gas mineral carbonation at pilot scale, J. Environ. Manage. 198 (2017) 1–8. doi:10.1016/j.jenvman.2017.04.048.

[45] K.M.K. Yu, I. Curcic, J. Gabriel, S.C.E. Tsang, Recent advances in CO2 capture and utilization., ChemSusChem. 1 (2008) 893–899. doi:10.1002/cssc.200800169.

[46] G.J.-M. (Ies-J. Jos G.J. Olivier (PBL), J. a. H.W.P. (Pbl) Marilena Muntean (IES-JRC), Trends in Global CO2 Emissions: 2013 Report, 2013. http://edgar.jrc.ec.europa.eu/news_docs/pbl-2013-trends-in-global-co2-emissions-2013-report-1148.pdf.

[47] M. Mazzotti, J. Carlos, R. Allam, K.S. Lackner, F. Meunier, E. Rubin, J.C. Sanchez, Y. Katsunori, R. Zevenhoven, Mineral carbonation and industrial uses of carbon dioxide. IPCC Special Report on Carbon dioxide Capture and Storage, 2005.

[48] P.B. Kelemen, J. Matter, In situ carbonation of peridotite for CO_2 storage, Proc. Natl. Acad. Sci. U. S. A. 105 (2008) 17295–17300. doi:10.1073/pnas.0805794105.

226

[49] M.J. McKelvy, A.V.G. Chizmeshya, J. Diefenbacher, H. Béarat, G. Wolf, Exploration of the role of heat activation in enhancing serpentine carbon sequestration reactions, Environ. Sci. Technol. 38 (2004) 6897–6903. doi:10.1021/es049473m.

[50] K.S. Lackner, A Guide to CO_2 Sequestration, Science (80-.). 300 (2003) 1677–1678.

[51] P. Markewitz, W. Kuckshinrichs, W. Leitner, J. Linssen, P. Zapp, R. Bongartz, A. Schreiber, T.E. Müller, Worldwide innovations in the development of carbon capture technologies and the utilization of CO2, Energy Environ. Sci. 5 (2012) 7281–7305. doi:10.1039/c2ee03403d.

[52] International Energy Agency (IEA), Organisation for Economic Development, United Nations Industrial Development Organization, UNIDO, Technology Roadmap: Carbon Capture and Storage in Industrial Applications, 2011.

[53] G.G. Zaimes, V. Khanna, Microalgal biomass production pathways: Evaluation of life cycle environmental impacts, Biotechnol. Biofuels. 6 (2013) 1–11. doi:10.1186/1754-6834-6-88.

[54] B. Singh, A.H. Strømman, E.G. Hertwich, Comparative life cycle environmental assessment of CCS technologies, Int. J. Greenh. Gas Control. 5 (2011) 911–921. doi:10.1016/j.ijggc.2011.03.012.

[55] K. Rausis, A. Ćwik, I. Casanova, Phase evolution during accelerated CO_2 mineralization of brucite under concentrated CO_2 and simulated flue gas conditions, J. CO2 Util. 37 (2020) 122–133. doi:10.1016/j.jcou.2019.12.007.

[56] L.C. Pasquier, G. Mercier, J.F. Blais, E. Cecchi, S. Kentish, Reaction mechanism for the aqueous-phase mineral carbonation of heat-activated serpentine at low temperatures and pressures in flue gas conditions, Environ. Sci. Technol. 48 (2014) 5163–5170. doi:10.1021/es405449v.

[57] M. Werner, S. Hariharan, M. Mazzotti, Flue gas CO_2 mineralization using thermally

activated serpentine: From single- To double-step carbonation, Energy Procedia. 63 (2014) 5912–5917. doi:10.1016/j.egypro.2014.11.626.

[58] L. Li, N. Zhao, W. Wei, Y. Sun, A review of research progress on CO2 capture, storage, and utilization in Chinese Academy of Sciences, Fuel. 108 (2013) 112–130. doi:10.1016/j.fuel.2011.08.022.

[59] T. Kuramochi, A. Ramírez, W. Turkenburg, A. Faaij, Comparative assessment of CO2 capture technologies for carbon-intensive industrial processes, Prog. Energy Combust. Sci. 38 (2012) 87–112. doi:10.1016/j.pecs.2011.05.001.

[60] M. Pehnt, J. Henkel, Life cycle assessment of carbon dioxide capture and storage from lignite power plants, Int. J. Greenh. Gas Control. 3 (2009) 49–66. doi:10.1016/j.ijggc.2008.07.001.

[61] J. Farla, C. Hendriks, K. Blok, Carbon Dioxide Recovery From Industrial Processes, Clim. Change. 29 (1995) 439–461.

[62] P. Viebahn, J. Nitsch, M. Fischedick, A. Esken, D. Schüwer, N. Supersberger, U. Zuberbühler, O. Edenhofer, Comparison of carbon capture and storage with renewable energy technologies regarding structural, economic, and ecological aspects in Germany, Int. J. Greenh. Gas Control. 1 (2007) 121–133. doi:10.1016/S1750-5836(07)00024-2.

[63] A. Azapagic, R. Clift, C. Duff, Sustainable Development in Practice: Case Studies for Engineers and Scientist (Chapter 3), John Wiley & Sons, Ltd, Chichester, 2004.

[64] M. Pujara, M. Sheth, N. Rachchh, R. Bhoraniya, Chemical Looping Reforming (CLR) System for H2 Production — A Review, Springer, Singapore, 2020. doi:https://doi.org/10.1007/978-981-32-9578-0_24.

[65] M. Najera, R. Solunke, T. Gardner, G. Veser, Carbon capture and utilization via chemical looping dry reforming, Chem. Eng. Res. Des. 89 (2011) 1533–1543. doi:10.1016/j.cherd.2010.12.017.

[66] K.S. Lackner, A.-H.A. Park, B.G. Miller, Chapter 6 - Eliminating CO2 Emissions from Coal-Fired Power Plants, in: F.P.B.T.-G.E. in a C.-C.W. Sioshansi (Ed.), Academic Press, Boston, 2010: pp. 127–173. doi:https://doi.org/10.1016/B978-1-85617-655-2.00006-7.

[67] J. Song, D. Zhang, Comprehensive review of caprock-sealing mechanisms for geologic carbon sequestration, Environ. Sci. Technol. 47 (2013) 9–22. doi:10.1021/es301610p.

[68] W.W. Liu, B. Zhang, Y.Z. Li, Y.M. He, H.C. Zhang, An environmentally friendly approach for contaminants removal using supercritical CO 2 for remanufacturing industry, Appl. Surf. Sci. 292 (2014) 142–148. doi:10.1016/j.apsusc.2013.11.102.

[69] S. Holloway, Storage of fossil fuel-derived carbon dioxide beneath the surface of the earth, Annu. Rev. Energy Environ. 26 (2001) 145–166. doi:10.1146/annurev.energy.26.1.145.

[70] M. Godec, V. Kuuskraa, T. Van Leeuwen, L.S. Melzer, N. Wildgust, CO2 storage in depleted oil fields: The worldwide potential for carbon dioxide enhanced oil recovery, Energy Procedia. 4 (2011) 2162–2169. doi:10.1016/j.egypro.2011.02.102.

[71] National Energy Technology Laboratory, Carbon Dioxide Enhanced Oil Recovery, 2010. http://www.netl.doe.gov/technologies/oil-gas/ publications/EP/CO2_EOR_Primer.pdf.

[72] H. Herzog, B. Eliasson, O. Kaarstad, Capturing Greenhouses Gases, Sci. Am. 282 (2000) 72–79.

[73] K. Mortezaei, A. Amirlatifi, E. Ghazanfari, F. Vahedifard, Potential CO 2 leakage from geological storage sites: advances and challenges , Environ. Geotech. (2018) 1–25. doi:10.1680/jenge.18.00041.

[74] J. Streit, A. Siggins, B. Evans, Predicting and monitoring geomechanical effects of CO_2 injection: Carbon dioxide capture for storage in depp geological formations - Results from the CO_2 capture project. v.2: Geological storage of carbon dioxide with monitoring and , Elsevier, London, 2005.

[75] W. Gunter, E. Perkins, T. McCann, Aquifer disposal of CO2-rich gases: reaction design for added capacity, Enery Convers. Manag. 34 (1993) 941–948.

[76] P. Pogge von Strandmann, K.W. Burton, S.O. Snæbjörnsdóttir, B. Sigfússon, E.S. Aradóttir, I. Gunnarsson, H.A. Alfredsson, K.G. Mesfin, E.H. Oelkers, S.R. Gislason, Rapid CO_2 mineralisation into calcite at the CarbFix storage site quantified using calcium isotopes, Nat. Commun. 10 (2019) 1–7. doi:10.1038/s41467-019-10003-8.

[77] F. Grandia, E. Oelkers, S.O. Snaebjornsdottir, B. Sigfusson, K. Dideriksen, S.R. Gislason, I. Gunnarsson, CarbFix Final Report, 2014.

[78] S. Salvi, F. Quattrocchi, C.A. Brunori, F. Doumaz, M. Angelone, A. Billi, F. Buongiorno, R. Funiciello, M. Guerra, G. Mele, L. Pizzino, F. Salvini, A multidisciplinary approach to earthquake research: Implementation of a Geochemical Geographic Information System for the Gargano Site, Southern Italy, Nat. Hazards. 20 (1999) 255–278. doi:10.1023/A:1008105621134.

[79] J.M. Matter, P.B. Kelemen, Permanent storage of carbon dioxide in geological reservoirs by mineral carbonation, Nat. Geosci. 2 (2009) 837–841. doi:10.1038/ngeo683.

[80] J.M. Matter, M. Stute, S.Ó. Snæbjörnsdóttir, E.H. Oelkers, S.R. Gislason, E.S. Aradottir, B.

Sigfusson, I. Gunnarsson, H.A. Alfredsson, D. Wolff-boenisch, K. Mesfin, K. Dideriksen, W.S. Broecker, Rapid carbon mineralization for permanent disposal of anthropogenic carbon dioxide emissions, Science (80-.). 352 (2016) 10–13.

[81] N. Von Der Assen, J. Jung, A. Bardow, Life-cycle assessment of carbon dioxide capture and utilization: Avoiding the pitfalls, Energy Environ. Sci. 6 (2013) 2721–2734. doi:10.1039/c3ee41151f.

[82] A. Ćwik, I. Casanova, K. Rausis, K. Zarębska, Utilization of high-calcium fly ashes through mineral carbonation: The cases for Greece, Poland and Spain, J. CO2 Util. 32 (2019) 155–162. doi:10.1016/j.jcou.2019.03.020.

[83] E.H. Oelkers, S.R. Gislason, J. Matter, Mineral carbonation of CO2, Elements. 4 (2008) 333–337. doi:10.2113/gselements.4.5.333.

[84] R.S. Norhasyima, T.M.I. Mahlia, Advances in CO2 utilization technology: A patent landscape review, J. CO2 Util. 26 (2018) 323–335. doi:10.1016/j.jcou.2018.05.022.

[85] L. Brennan, P. Owende, Biofuels from microalgae-A review of technologies for production, processing, and extractions of biofuels and co-products, Renew. Sustain. Energy Rev. 14 (2010) 557–577. doi:10.1016/j.rser.2009.10.009.

[86] Y. Li, M. Horsman, N. Wu, C.Q. Lan, N. Dubois-Calero, Biofuels from microalgae, Biotechnol. Prog. 24 (2008) 815–820. doi:10.1021/bp.070371k.

[87] Global CCS Institute, Accelerating the uptake of CCS: industrial use of captured carbon dioxide, 2011.

[88] Advanced Resources International, Optimization of CO2 Storage in CO2 Enhanced Oil Recovery, UK, 2010. https://assets.publishing.service.gov.uk/government/uploads/system/uploads/attachment_data/file/47992/1006-optimization-of-co2-storage-in-co2-enhanced-oil-re.pdf%0Ahttp://www.decc.gov.uk/en/content/cms/what_we_do/uk_supply/energy_mix/c.

[89] P.J.L.B. Williams, L.M.L. Laurens, Microalgae as biodiesel & biomass feedstocks: Review & analysis of the biochemistry, energetics & economics, Energy Environ. Sci. 3 (2010) 554–590. doi:10.1039/b924978h.

[90] L.B. Brentner, M.J. Eckelman, J.B. Zimmerman, Combinatorial life cycle assessment to inform process design of industrial production of algal biodiesel, Environ. Sci. Technol. 45 (2011) 7060–7067. doi:10.1021/es2006995.

[91] R.H. Wijffels, M.J. Barbosa, An outlook on microalgal biofuels, Science (80-.). 329 (2010)

796–799. doi:10.1126/science.1189003.

[92] M.R. Tredici, Photobiology of microalgae mass cultures: understanding the tools for the next green revolution, Biofuels. 1 (2010) 143–162. doi:10.4155/bfs.09.10.

[93] X. Yin, J.R. Moss, Recent developments in the activation of carbon dioxide by metal complexes, Coord. Chem. Rev. 181 (1999) 27–59. doi:10.1016/S0010-8545(98)00171-4.

[94] W. Leitner, The coordination chemistry of carbon dioxide and its relevance for catalysis: A critical survey, Coord. Chem. Rev. 153 (1996) 257–284. doi:10.1016/0010-8545(95)01226-5.

[95] N. MacDowell, N. Florin, A. Buchard, J. Hallett, A. Galindo, G. Jackson, C.S. Adjiman, C.K. Williams, N. Shah, P. Fennell, An overview of CO2 capture technologies, Energy Environ. Sci. 3 (2010) 1645–1669. doi:10.1039/c004106h.

[96] A.P. Steynberg, Chapter 1 - Introduction to Fischer-Tropsch Technology, in: A. Steynberg, M.B.T.-S. in S.S. and C. Dry (Eds.), Fischer-Tropsch Technol., Elsevier, 2004: pp. 1–63. doi:https://doi.org/10.1016/S0167-2991(04)80458-0.

[97] J. Li, Y. He, L. Tan, P. Zhang, X. Peng, A. Oruganti, G. Yang, H. Abe, Y. Wang, N. Tsubaki, Integrated tuneable synthesis of liquid fuels via Fischer–Tropsch technology, Nat. Catal. 1 (2018) 787–793. doi:10.1038/s41929-018-0144-z.

[98] G. Gadikota, A.A. Park, Chapter 8 - Accelerated Carbonation of Ca- and Mg-Bearing Minerals and Industrial Wastes Using CO_2, Elsevier B.V., 2015. doi:10.1016/B978-0-444-62746-9.00008-6.

[99] L.C. Pasquier, G. Mercier, J.F. Blais, E. Cecchi, S. Kentish, Parameters optimization for direct flue gas CO2 capture and sequestration by aqueous mineral carbonation using activated serpentinite based mining residue, Appl. Geochemistry. 50 (2014) 66–73. doi:10.1016/j.apgeochem.2014.08.008.

[100] S. Hariharan, M. Werner, M. Hänchen, M. Mazzotti, Dissolution of dehydroxylated lizardite at flue gas conditions: II. Kinetic modeling, Chem. Eng. J. 241 (2014) 314–326. doi:10.1016/j.cej.2013.12.056.

[101] A.V.G. Chizmeshya, M.J. McKelvy, G.H. Wolf, R.W. Carpenter, D. Gormley, J. Diefenbacher, R. Marzke, Enhancing the atomic-level understanding of CO2 mineral sequestration mechanisms via advanced computational modeling, 2006.

[102] E. Kriegler, N. Bauer, A. Popp, F. Humpenöder, M. Leimbach, J. Strefler, L. Baumstark, B.L. Bodirsky, J. Hilaire, D. Klein, I. Mouratiadou, I. Weindl, C. Bertram, J.P. Dietrich, G.

Luderer, M. Pehl, R. Pietzcker, F. Piontek, H. Lotze-Campen, A. Biewald, M. Bonsch, A. Giannousakis, U. Kreidenweis, C. Müller, S. Rolinski, A. Schultes, J. Schwanitz, M. Stevanovic, K. Calvin, J. Emmerling, S. Fujimori, O. Edenhofer, Fossil-fueled development (SSP5): An energy and resource intensive scenario for the 21st century, Glob. Environ. Chang. 42 (2017) 297–315. doi:10.1016/j.gloenvcha.2016.05.015.

[103] D. Leeson, N. Mac Dowell, N. Shah, C. Petit, P.S. Fennell, A Techno-economic analysis and systematic review of carbon capture and storage (CCS) applied to the iron and steel, cement, oil refining and pulp and paper industries, as well as other high purity sources, Int. J. Greenh. Gas Control. 61 (2017) 71–84. doi:10.1016/j.ijggc.2017.03.020.

[104] C.A. Seipp, N.J. Williams, M.K. Kidder, R. Custelcean, CO2Capture from Ambient Air by Crystallization with a Guanidine Sorbent, Angew. Chemie - Int. Ed. 56 (2017) 1042–1045. doi:10.1002/anie.201610916.

[105] J.C.M. Pires, Negative emissions technologies: A complementary solution for climate change mitigation, Sci. Total Environ. 672 (2019) 502–514. doi:10.1016/j.scitotenv.2019.04.004.

[106] A. Goeppert, M. Czaun, G.K. Surya Prakash, G.A. Olah, Air as the renewable carbon source of the future: An overview of CO 2 capture from the atmosphere, Energy Environ. Sci. 5 (2012) 7833–7853. doi:10.1039/c2ee21586a.

[107] F. Creutzig, N.H. Ravindranath, G. Berndes, S. Bolwig, R. Bright, F. Cherubini, H. Chum, E. Corbera, M. Delucchi, A. Faaij, J. Fargione, H. Haberl, G. Heath, O. Lucon, R. Plevin, A. Popp, C. Robledo-Abad, S. Rose, P. Smith, A. Stromman, S. Suh, O. Masera, Bioenergy and climate change mitigation: An assessment, GCB Bioenergy. 7 (2015) 916–944. doi:10.1111/gcbb.12205.

[108] D.W. Keith, Why capture CO2 from the atmosphere?, Science (80-.). 325 (2009) 1654–1655. doi:10.1126/science.1175680.

[109] R.D. Schuiling, P. Krijgsman, Enhanced Weathering: An Effective and Cheap Tool to Sequester Co2, Clim. Change. 74 (2006) 349–354. doi:10.1007/s10584-005-3485-y.

[110] V.K. Arora, A. Montenegro, Small temperature benefits provided by realistic afforestation efforts, Nat. Geosci. 4 (2011) 514–518. doi:10.1038/ngeo1182.

[111] J.G. Canadell, M.R. Raupach, Managing forests for climate change mitigation, Science (80-.). 320 (2008) 1456–1457. doi:10.1126/science.1155458.

[112] J.L. Sarmiento, N. Gruber, M.A. Brzezinski, J.P. Dunne, High-latitude controls of thermocline nutrients and low latitude biological productivity, Nature. 427 (2004) 56–60.

doi:10.1038/nature02127.

[113] F. Joos, J.L. Sarmiento, U. Siegenthaler, Estimates of the effect of Southern Ocean iron fertilization on atmospheric CO2 concentrations, Nature. 349 (1991) 772–775. doi:10.1038/349772a0.

[114] H.S. Kheshgi, Sequestering atmospheric carbon dioxide by increasing ocean alkalinity, Energy. 20 (1995) 915–922. doi:10.1016/0360-5442(95)00035-F.

[115] D.S. Powlson, C.M. Stirling, M.L. Jat, B.G. Gerard, C.A. Palm, P.A. Sanchez, K.G. Cassman, Limited potential of no-till agriculture for climate change mitigation, Nat. Clim. Chang. 4 (2014) 678–683. doi:10.1038/nclimate2292.

[116] D. Woolf, J.E. Amonette, F.A. Street-Perrott, J. Lehmann, S. Joseph, Sustainable biochar to mitigate global climate change, Nat. Commun. 1 (2010). doi:10.1038/ncomms1053.

[117] J.-F. Bastin, Y. Finegold, C. Garcia, D. Mollicone, M. Rezende, D. Routh, C. Zohner, T.W. Crowther, The global tree restoration potential, Science (80-.). 366 (2019) 76–79. doi:10.1126/science.aay8060.

[118] K.H. Erb, T. Kastner, C. Plutzar, A.L.S. Bais, N. Carvalhais, T. Fetzel, S. Gingrich, H. Haberl, C. Lauk, M. Niedertscheider, J. Pongratz, M. Thurner, S. Luyssaert, Unexpectedly large impact of forest management and grazing on global vegetation biomass, Nature. 553 (2018) 73–76. doi:10.1038/nature25138.

[119] S. Fritz, L. See, I. Mccallum, L. You, A. Bun, E. Moltchanova, M. Duerauer, F. Albrecht, C. Schill, C. Perger, P. Havlik, A. Mosnier, P. Thornton, U. Wood-Sichra, M. Herrero, I. Becker-Reshef, C. Justice, M. Hansen, P. Gong, S. Abdel Aziz, A. Cipriani, R. Cumani, G. Cecchi, G. Conchedda, S. Ferreira, A. Gomez, M. Haffani, F. Kayitakire, J. Malanding, R. Mueller, T. Newby, A. Nonguierma, A. Olusegun, S. Ortner, D.R. Rajak, J. Rocha, D. Schepaschenko, M. Schepaschenko, A. Terekhov, A. Tiangwa, C. Vancutsem, E. Vintrou, W. Wenbin, M. van der Velde, A. Dunwoody, F. Kraxner, M. Obersteiner, Mapping global cropland and field size, Glob. Chang. Biol. 21 (2015) 1980–1992. doi:10.1111/gcb.12838.

[120] E. Kato, Y. Yamagata, BECCS capability of dedicated bioenergy crops under a future land-use scenario targeting net negative carbon emissions, Earth's Futur. 2 (2014) 421–439. doi:10.1002/2014ef000249.

[121] F. Creutzig, Economic and ecological views on climate change mitigation with bioenergy and negative emissions, GCB Bioenergy. 8 (2016) 4–10. doi:10.1111/gcbb.12235.

[122] D. McLaren, A comparative global assessment of potential negative emissions technologies, Process Saf. Environ. Prot. 90 (2012) 489–500. doi:10.1016/j.psep.2012.10.005.

[123] M. Bui, M. Fajardy, N. Mac Dowell, Bio-Energy with CCS (BECCS) performance evaluation: Efficiency enhancement and emissions reduction, Appl. Energy. 195 (2017) 289–302. doi:10.1016/j.apenergy.2017.03.063.

[124] D.P. van Vuuren, E. Stehfest, M.G.J. den Elzen, T. Kram, J. van Vliet, S. Deetman, M. Isaac, K.K. Goldewijk, A. Hof, A.M. Beltran, R. Oostenrijk, B. van Ruijven, RCP2.6: Exploring the possibility to keep global mean temperature increase below 2°C, Clim. Change. 109 (2011) 95–116. doi:10.1007/s10584-011-0152-3.

[125] S. Fuss, J.G. Canadell, G.P. Peters, M. Tavoni, R.M. Andrew, P. Ciais, R.B. Jackson, C.D. Jones, F. Kraxner, N. Nakicenovic, C. Le Quéré, M.R. Raupach, A. Sharifi, P. Smith, Y. Yamagata, Betting on negative emissions, Nat. Clim. Chang. 4 (2014) 850–853. doi:10.1038/nclimate2392.

[126] N.E. Vaughan, C. Gough, Expert assessment concludes negative emissions scenarios may not deliver, Environ. Res. Lett. 11 (2016). doi:10.1088/1748-9326/11/9/095003.

[127] W. Lu, J.P. Sculley, D. Yuan, R. Krishna, H. Zhou, Carbon Dioxide Capture from Air Using Amine-Grafted Porous Polymer Networks, J. Phys. Chem. C. 117 (2013) 4057–4061. doi:10.1021/jp311512q.

[128] K.S. Lackner, H.-J. Ziock, P. Grimes, Carbon Dioxide Extraction From Air: Is It An Option?, in: 24th Annu. Tech. Conf. Coal Util., 1999. http://www.ncbi.nlm.nih.gov/pubmed/21904770.

[129] D.W. Keith, M. Ha-duong, J.K. Stolaroff, Climate Strategy with CO_2 Capture from the Air, Clim. Chang. 74 (2006) 17–45. doi:10.1007/s10584-005-9026-x.

[130] A. Sinha, L.A. Darunte, C.W. Jones, M.J. Real, Y. Kawajiri, Systems Design and Economic Analysis of Direct Air Capture of CO_2 through Temperature Vacuum Swing Adsorption Using MIL-101 (Cr) - PEI-800 and mmen-Mg_2 (dobpdc) MOF adsorbents, Ind. Eng. Chem. Res. 56 (2017) 750–764. doi:10.1021/acs.iecr.6b03887.

[131] K.S. Lackner, Capture of carbon dioxide from ambient air, Eur. Phys. J. Spec. Top. 176 (2009) 93–106. doi:10.1140/epjst/e2009-01150-3.

[132] D.W. Keith, D.S. Angelo, D.W. Keith, G. Holmes, D.S. Angelo, K. Heidel, A Process for Capturing CO 2 from the Atmosphere A Process for Capturing CO 2 from the Atmosphere, Joule. 2 (n.d.) 1573–1594. doi:10.1016/j.joule.2018.05.006.

[133] E. Ping, M. Sakwa-Novak, P. Eisenberger, Lowering the cost of direct air capture: pilot to commercial deployment, in: Int. Conf. Negat. CO2 Emiss., 2018.

[134] A.R. Kulkarni, D.S. Sholl, Analysis of Equilibrium-Based TSA Processes for Direct Capture of CO_2 from Air, Ind. Eng. Chem. Res. 51 (2012) 8631–8645. doi:10.1021/ie300691c.

[135] D.S. Goldberg, K.S. Lackner, P. Han, A.L. Slagle, T. Wang, Co-Location of Air Capture, Subsea fl oor CO 2 Sequestration, and Energy Production on the Kerguelen Plateau, Environ. Sci. Technol. 47 (2013) 7521–7529. doi:10.1021/es401531y.

[136] W. Seifritz, CO2 disposal by means of silicates, Nature. 345 (1990) 486. doi:10.1038/345486b0.

[137] J. Hartmann, A.J. West, P. Renforth, P. Köhler, C.L.D. La Rocha, D.A. Wolf-gladrow, H.H. Dürr, J. Scheffran, Enhanced Chemical Weathering as a Geoengineering Strategy to Reduce Atmospheric Carbon Dioxide, Supply Nutrients, and Mitigate Ocean Acidification, Rev. Geophys. 51 (2013). doi:10.1002/rog.20004.1.Institute.

[138] S. Hangx, C. Spiers, Citation : Coastal spreading of olivine to control atmospheric CO 2 concentrations : a critical analysis of viability, Int. J. Greenh. Gas Control. 3 (2009) 757–767. doi:10.1016/j.ijggc.2009.07.001.

[139] P. Renforth, C.L. Washbourne, J. Taylder, D.A.C. Manning, Silicate production and availability for mineral carbonation, Environ. Sci. Technol. 45 (2011) 2035–2041. doi:10.1021/es103241w.

[140] J. Gaillardet, B. Dupre, P. Louvat, C.J. Allegre, Global silicate weathering and CO 2 consumption rates deduced from the chemistry of large rivers, Chem. Geol. 159 (1999) 3–30.

[141] Geoengineering the climate: Science, Governance and Uncertainty, The Royal Society, London, 2009.

[142] Romero-Mujalli, J. Hartmann, J. Börker, Temperature and CO 2 dependency of global carbonate weathering fluxes – Implications for future carbonate weathering research, Chem. Geol. 527 (2018). doi:10.1016/j.chemgeo.2018.08.010.

[143] N. Moosdorf, J. Hartmann, R. Lauerwald, B. Hagedorn, S. Kempe, Atmospheric CO 2 consumption by chemical weathering in North America, Geochim. Cosmochim. Acta. 75 (2011) 7829–7854. doi:10.1016/j.gca.2011.10.007.

[144] H.H. Schopka, L.A. Derry, C.A. Arcilla, Chemical weathering , river geochemistry and atmospheric carbon fluxes from volcanic and ultramafic regions on Luzon Island , the Philippines, Geochim. Cosmochim. Acta. 75 (2011) 978–1002. doi:10.1016/j.gca.2010.11.014.

[145] S.J. Gerdemann, W.K. O'Connor, D.C. Dahlin, L.R. Penner, H. Rush, Ex situ aqueous mineral carbonation, Environ. Sci. Technol. 41 (2007) 2587–2593. doi:10.1021/es0619253.

[146] G. Gadikota, J. Matter, P. Kelemen, A.A. Park, Chemical and morphological changes during olivine carbonation for CO_2 storage in the presence of NaCl and $NaHCO_3$, Phys. Chem. Chem. Phys. 16 (2014) 4679. doi:10.1039/c3cp54903h.

[147] N. Moosdorf, P. Renforth, J. Hartmann, Carbon Dioxide Efficiency of Terrestrial Enhanced Weathering, Environ. Sci. Technol. 48 (2014) 4809–4816. doi:10.1021/es4052022.

[148] O. Neung-Hwan, P.A. Raymond, Contribution of agricultural liming to riverine bicarbonate export and CO 2 sequestration in the Ohio River basin, Global Biogeochem. Cycles. 20 (2006) 1–17. doi:10.1029/2005GB002565.

[149] P. Köhler, J. Hartmann, D.A. Wolf-gladrow, Geoengineering potential of artificially enhanced silicate weathering of olivine, Proc. Natl. Acad. Sci. 107 (2010) 20228–20233. doi:10.1073/pnas.1000545107/-/DCSupplemental.www.pnas.org/cgi/doi/10.1073/pnas.1000545107.

[150] B. Alloway, Heavy Metals in Soils: Metals and Metalloid in Soil and Their Bioavailability, Springer, New York, 2012.

[151] E. Epstein, Review The anomaly of silicon in plant biology, Proc. Natl. Acad. Sci. 91 (1994) 11–17.

[152] F.P. Massey, A.R. Ennos, S.E. Hartley, Herbivore speci W c induction of silica-based plant defences, Oceologia. 152 (2007) 677–683. doi:10.1007/s00442-007-0703-5.

[153] H.F.M. Berge, H.G. Van Der Meer, J.W. Steenhuizen, P.W. Goedhart, P. Knops, J. Verhagen, Olivine Weathering in Soil , and Its Effects on Growth and Nutrient Uptake in Ryegrass (Lolium perenne L .): A Pot Experiment, PLoS One. 7 (2012). doi:10.1371/journal.pone.0042098.

[154] P. van Straaten, Rocks for Crops: Agrominerals of Sub-Sahran Africa, Nairobi, Kenya, 2002.

[155] K. Hanghòj, P.B. Kelemen, D. Hassler, M. Godard, Composition and Genesis of Depleted Mantle Peridotites from the Wadi T ayin Massif , Oman Ophiolite ; Major and Trace Element Geochemistry , and Os Isotope and PGE Systematics, J. Pet. 51 (2010) 201–227. doi:10.1093/petrology/egp077.

[156] K.S. Lackner, C.H. Wendt, D.P. Butt, E.L. Joyce, D.H. Sharp, Carbon dioxide disposal in carbonate minerals, Energy. 20 (1995) 1153–1170. doi:10.1016/0360-5442(95)00071-N.

[157] W.J.J. Huijgen, R. Comans, Carbon dioxide sequestration by mineral carbonation, 2003.

[158] W.J.J. Huijgen, R.N.J. Comans, G.J. Witkamp, Cost evaluation of CO_2 sequestration by aqueous mineral carbonation, Energy Convers. Manag. 48 (2007) 1923–1935. doi:10.1016/j.enconman.2007.01.035.

[159] P. Linga, R. Kumar, P. Englezos, The Clathrate Hydrate Process for Post and Pre-combustion Capture of Carbon Dioxide, J. Hazard. Mater. 149 (2007) 625–629. doi:10.1016/j.jhazmat.2007.06.086.

[160] Z. Liu, J. Zhao, Contribution of carbonate rock weathering to the atmospheric CO 2 sink, Environ. Geol. 39 (1999) 1053–1058.

[161] H.E. Dunsmore, A geological perspective on global warming and the possibility of carbon dioxide removal as calcium carbonate mineral, Energy Convers. Manag. 33 (1992) 565–572. doi:https://doi.org/10.1016/0196-8904(92)90057-4.

[162] N. Jöns, W. Kahl, W. Bach, Lithos Reaction-induced porosity and onset of low-temperature carbonation in abyssal peridotites : Insights from 3D high-resolution microtomography, LITHOS. 268–271 (2017) 274–284. doi:10.1016/j.lithos.2016.11.014.

[163] P.B. Hostetler, R.G. Coleman, F.A. Mumpton, B.W. Evans, Brucite in alpine serpentinites, Am. Mineral. 51 (1966) 75–98.

[164] P. Renforth, The potential of enhanced weathering in the UK, Int. J. Greenh. Gas Control. 10 (2012) 229–243. doi:10.1016/j.ijggc.2012.06.011.

[165] K.S. Lackner, Carbonate Chemistry for Sequestering Fossil Carbon, Annu. Rev. Energy Environ. 27 (2002) 193–232. doi:10.1146/annurev.energy.27.122001.083433.

[166] S.S. Goldich, A Study in Rock-Weathering, J. Geol. 46 (1938) 17–58. doi:10.1086/624619.

[167] P. Goldberg, Z. Chen, W.O. Connor, R. Walters, H. Ziock, CO2 Mineral Sequestration Studies in US, in: Proc. First Natl. Conf. Carbon Sequestration, 2001: pp. 1–10.

[168] W.K. O'Connor, D.C. Dahlin, G.E. Rush, S.J. Gerdemann, L.R. Penner, D.N. Nilsen, Aqueous mineral carbonation: Mineral availability, pretreatment, reaction parametrics, and process studies, 2005. doi:10.13140/RG.2.2.23658.31684.

[169] K.S. Lackner, D.P. Butt, C.H. Wendt, Progress on binding CO_2 in mineral substrates, Energy Convers. Manag. 38 (1997) 259–264.

[170] A.A. Park, R. Jadhav, L.-S. Fan, CO_2 Mineral Sequestration: Chemically Enhanced Aqueos Carbonation of Serpentine, Can. J. Chem. Eng. 81 (2003) 885–890.

[171] M.M. Maroto-Valer, D.J. Fauth, M.E. Kuchta, Y. Zhang, J.M. Andrésen, Activation of

magnesium rich minerals as carbonation feedstock materials for CO_2 sequestration, Fuel Process. Technol. 86 (2005) 1627–1645. doi:10.1016/j.fuproc.2005.01.017.

[172] W.K. O'Connor, D.C. Dahlin, D.N. Nielsen, S.J. Gerdemann, G.E. Rush, L.R. Penner, R.P. Walters, P.C. Turner, Continuing Studies on Direct Aqueous Mineral Carbonation For CO_2 Sequestration, in: Proc. 27th Int. Tehcnical Conf. Coal Util. Fuel Syst., 2002: pp. 819–830.

[173] W.K. O'Connor, G.E. Rush, D.C. Dahlin, S.P. Reidel, V.G. Johnson, Geologic sequestration of CO2 in the Columbia river balast group, in: 28 IInternational Tehchnical Conf. Coal Util. Fuel Syst., 2003.

[174] G. Gadikota, Morphological and chemical changes during mineral weathering for natural and engineered carbon storage, in: US-Korea Conf., 2013.

[175] A. Zarandi, F. Larachi, G. Beaudoin, B. Plante, M. Sciortino, Multivariate study of the dynamics of CO_2 reaction with brucite-rich ultramafic mine tailings, Int. J. Greenh. Gas Control. 52 (2016) 110–119. doi:10.1016/j.ijggc.2016.06.022.

[176] I.M. Power, A.L. Harrison, G.M. Dipple, S. Wilson, P.B. Kelemen, M. Hitch, G. Southam, Carbon Mineralization : From Natural Analogues to Engineered Systems From Natural Analogues to Engineered Systems, Rev. Mineral. Geochemistry. (2013). doi:10.2138/rmg.2013.77.9.

[177] K. E., K. L., G. H., Low temperature thermodynamic model for the system Na_2CO_3-$MgCO_3$-$CaCO_3$-H_2O, Geochim. Cosmochim. Acta. 63 (1999) 3105–3119.

[178] M. Hänchen, V. Prigiobbe, R. Baciocchi, M. Mazzotti, Precipitation in the Mg-carbonate system—effects of temperature and CO_2 pressure, Chem. Eng. Sci. 63 (2008) 1012–1028. doi:10.1016/J.CES.2007.09.052.

[179] L. Hopkinson, P. Kristova, K. Rutt, G. Cressey, Phase transitions in the system MgO-CO_2-H_2O during CO_2 degassing of Mg-bearing solutions, Geochim. Cosmochim. Acta. 76 (2012) 1–13. doi:10.1016/j.gca.2011.10.023.

[180] P.J. Davies, B. Bubela, The transformation of nesquehonite into hydromagnesite, Chem. Geol. 12 (1973) 289–300. doi:10.1016/0009-2541(73)90006-5.

[181] Z. Zhang, Y. Zheng, Y. Ni, Z. Liu, J. Chen, X. Liang, Temperature and pH-dependent morphology and FT-IR analysis of magnesium carbonate hydrates, J. Phys. Chem. B. 110 (2006) 12969–12973. doi:10.1021/jp061261j.

[182] L. Hopkinson, K. Rutt, G. Cressey, The Transformation of Nesquehonite to Hydromagnesite in the System CaO-MgO-H 2O-CO2 : An Experimental Spectroscopic Study, J. Geol. 116

(2008) 387–400. doi:10.1086/588834.

[183] J. Canterford, G. Tsambourakis, B. Lambert, Some observations on the properties of dypingite, $Mg_5(CO_3)_4(OH)_2 \cdot 5H_2O$, and related minerals, Mineral. Mag. 48 (1984) 437–442.

[184] A. Botha, C.A. Strydom, Preparation of a magnesium hydroxy carbonate from magnesium hydroxide, Hydrometallurgy. 62 (2001) 175–183. doi:10.1016/S0304-386X(01)00197-9.

[185] G. Raade, Dypingite, a new hydrous basic carbonate of magnesium, from Norway, Am. Mineral. 55 (1970) 1457–1465.

[186] J. Suzuki, I. Masahiro, A New Magnesium Carbonate Hydrate Mineral, $Mg_5(CO_3)_4 (OH)_2 \cdot 8 H_2O$, from Yoshikawa, Aichi Prefecture, Japan, J. Japanese Assoc. Mineral. Petrol. Econ. Geol. 68 (1973) 353–361. doi:10.2465/ganko1941.68.353.

[187] R.J. Hill, J.H. Canterford, F.J. Moyle, New data for lansfordite, Mineral. Mag. 46 (1982) 453–457. doi:DOI: 10.1180/minmag.1982.046.341.08.

[188] I.M. Power, S.A. Wilson, J.M. Thom, G.M. Dipple, G. Southam, Biologically induced mineralization of dypingite by cyanobacteria from an alkaline wetland near Atlin, British Columbia, Canada, Geochem. Trans. 8 (2007). doi:10.1186/1467-4866-8-13.

[189] B. Nashar, Barringtonite—A new hydrous magnesium carbonate from Barrington Tops, New South Wales, Australia, Mineral. Mag. J. Mineral. Soc. 34 (1965) 370–372. doi:DOI: 10.1180/minmag.1965.034.268.31.

[190] P. Ballirano, C. De Vito, V. Ferrini, S. Mignardi, The thermal behaviour and structural stability of nesquehonite, MgCO3·3H2O, evaluated by in situ laboratory parallel-beam X-ray powder diffraction: New constraints on CO2 sequestration within minerals, J. Hazard. Mater. 178 (2010) 522–528. doi:10.1016/j.jhazmat.2010.01.113.

[191] M. Hales, R.L. Frost, W.N. Martens, Thermo-Raman spectroscopy of synthetic nesquehonite - implication for the geosequestration of greenhouse gases, J. Raman Spectrosc. 39 (2008) 1141–1149.

[192] F.M. Last, W.M. Last, N.M. Halden, Carbonate microbialites and hardgrounds from Manito Lake, an alkaline, hypersaline lake in the northern Great Plains of Canada, Sediment. Geol. 225 (2010) 34–49. doi:10.1016/j.sedgeo.2010.01.006.

[193] H. Schaef, B. McGrail, J. Loring, M. Bowden, B. Arey, K.M. Rosso, Forsterite [Mg_2SiO_4] Carbonation in wet supercritical CO_2: An in Situ High-Pressure X-ray Diffraction Study, Environ. Sci. Technol. 47 (2013) 174–181.

[194] I.M. Power, A.L. Harrison, G.M. Dipple, S.A. Wilson, S.L.L. Barker, S.J. Fallon, Magnesite

formation in playa environments near Atlin, British Columbia, Canada, Geochim. Cosmochim. Acta. 255 (2019) 1–24. doi:10.1016/j.gca.2019.04.008.

[195] I.M. Power, P.A. Kenward, G.M. Dipple, M. Raudsepp, Room Temperature Magnesite Precipitation, Cryst. Growth Des. 17 (2017) 5652–5659. doi:10.1021/acs.cgd.7b00311.

[196] F. Farhang, T.K. Oliver, M. Rayson, G. Brent, M. Stockenhuber, E. Kennedy, Experimental study on the precipitation of magnesite from thermally activated serpentine for CO_2 sequestration, Chem. Eng. J. 303 (2016) 439–449. doi:10.1016/j.cej.2016.06.008.

[197] E.J. Swanson, K.J. Fricker, M. Sun, A.H.A. Park, Directed precipitation of hydrated and anhydrous magnesium carbonates for carbon storage, Phys. Chem. Chem. Phys. 16 (2014) 23440–23450. doi:10.1039/c4cp03491k.

[198] D.E. Giammar, R.G. Bruant, C.A. Peters, Forsterite dissolution and magnesite precipitation at conditions relevant for deep saline aquifer storage and sequestration of carbon dioxide, Chem. Geol. 217 (2005) 257–276. doi:10.1016/j.chemgeo.2004.12.013.

[199] G. Montes-hernandez, M. Bah, F. Renard, Mechanism of formation of engineered magnesite : A useful mineral to mitigate CO2 industrial emissions, J. CO2 Util. 35 (2020) 272–276. doi:10.1016/j.jcou.2019.10.006.

[200] G. Montes-Hernandez, F. Renard, R. Chiriac, N. Findling, F. Toche, Rapid precipitation of magnesite from $Mg(OH)_2$-H_2O-CO_2 slurry enhanced by NaOH and heat-ageing step (from 20 to 90°C), Cryst. Growth Des. 12 (2012) 5233–5240. http://pubs.acs.org/doi/abs/10.1021/cg300652s.

[201] F. Di Lorenzo, R.M. Rodríguez-Galán, M. Prieto, Kinetics of the solvent-mediated transformation of hydromagnesite into magnesite at different temperatures, Mineral. Mag. 78 (2014) 1363–1372. doi:10.1180/minmag.2014.078.6.02.

[202] G. Gadikota, E.J. Swanson, H. Zhao, A.A. Park, Experimental Design and Data Analysis for Accurate Estimation of Reaction Kinetics and Conversion for Carbon Mineralization, Ind. Eng. Chem. Res. (2014).

[203] K.J. Fricker, A.A. Park, Effect of H_2O on $Mg(OH)_2$ carbonation pathways for combined CO_2 capture and storage, Chem. Eng. Sci. 100 (2013) 332–341. doi:10.1016/j.ces.2012.12.027.

[204] J. Highfield, J. Chen, M. Haghighatlari, J. Abacka, R. Zevenhoven, Low-temperature gas-solid carbonation of magnesia and magnesium hydroxide promoted by non-immersive contact with water, RSC Adv. 6 (2016) 89655–89664. doi:10.1039/C6RA16328A.

[205] D. Goldberg, A.L. Slagle, Energy Procedia A global assessment of deep-sea basalt sites for

carbon sequestration, Energy Procedia. 1 (2009) 3675–3682. doi:10.1016/j.egypro.2009.02.165.

[206] B.P. Mcgrail, H.T. Schaef, A.M. Ho, Y. Chien, J.J. Dooley, C.L. Davidson, Potential for carbon dioxide sequestration in flood basalts, 111 (2006) 1–13. doi:10.1029/2005JB004169.

[207] F. Cipolli, B. Gambardella, L. Marini, G. Ottonello, M. Zuccolini, Geochemistry of high-pH waters from serpentinites of the Gruppo di Voltri (Genova , Italy) and reaction path modeling of CO 2 sequestration in serpentinite aquifers, Geochim. Cosmochim. Acta. 19 (2004) 787–802. doi:10.1016/j.apgeochem.2003.10.007.

[208] D. Kelley, J. Karson, D. Blackman, G. Früh-Green, D. Butterfield, M. Lilley, E. Olson, M. Schrenk, K. Roe, G. Lebon, P. Rivizzigno, An off-axis hydrothermal vent field near the Mid-Atlantic Ridge at 30ºN, Nature. 412 (2001) 145–149.

[209] S.R. Gislason, H.P. Eugster, Meteoric water-basalt interactions. II: A field study in N.E. Iceland, Geochim. Cosmochim. Acta. 51 (1987) 2841–2855. doi:https://doi.org/10.1016/0016-7037(87)90162-1.

[210] C. Dessert, B. Dupré, J. Gaillardet, L. François, C.J. Allegre, Basalt weathering laws and the impact of basalt weathering on the global carbon cycle, Chem. Geol. 202 (2003) 257–273. doi:10.1016/j.chemgeo.2002.10.001.

[211] P.B. Kelemen, G. Hirth, Reaction-driven cracking during retrograde metamorphism : Olivine hydration and carbonation, Earth Planet. Sci. Lett. 345–348 (2012) 81–89. doi:10.1016/j.epsl.2012.06.018.

[212] J.F. Rudge, P.B. Kelemen, M. Spiegelman, A simple model of reaction induced cracking applied to serpentinization and carbonation of peridotite, Earth Planet. Sci. Lett. 291 (2010) 215–227.

[213] D. Blackwell, The Structure and Physical Properties of the Earth's Crust, in: Therm. Struct. Cont. Crust, Geophysica, American Geophysical Union, Washignton, 1971: pp. 169–184.

[214] T. Xu, J.A. Apps, K. Pruess, Numerical Simulation of CO2 Disposal by Mineral Trapping in Deep Aquifers, Appl. Geochemistry. 19 (2004) 917–936. doi:10.1016/j.apgeochem.2003.11.003.

[215] W. Xiong, R.K. Wells, D.E. Giammar, Carbon Sequestration in Olivine and Basalt Powder Packed Beds, Environ. Sci. Technol. 51 (2017) 2105–2112. doi:10.1021/acs.est.6b05011.

[216] M.J. McKelvy, A.V.G. Chizmeshya, K. Squires, R.W. Carpenter, H. Béarat, A novel approach to mineral carbonation: Enhancing carbonation while avoiding mineral

pretreatment process cost, 2005.

[217] D. Wolff-Boenisch, S.R. Gislason, E.H. Oelkers, The effect of crystallinity on dissolution rates and CO_2 consumption capacity of silicates, Geochim. Cosmochim. Acta. 70 (2006) 858–870. doi:10.1016/j.gca.2005.10.016.

[218] S.L. Brantley, A.F. White, M.E. Hodson, Surface area of primary silicate minerals, in: Growth Dissolution and Pattern Fomration in Geosystems, Kluwer Academic Publishers, Rotterdam, 1999: pp. 291–326.

[219] J.L. Palandri, Y.K. Kharaka, A Compilation of Rate Parameters of Water-Mineral Interaction Kinetics for Application to Geochemical Modeling, California, 2004.

[220] M. Hänchen, V. Prigiobbe, G. Storti, T.M. Seward, M. Mazzotti, Dissolution kinetics of fosteritic olivine at 90–150 °C including effects of the presence of CO_2, Geochim. Cosmochim. Acta. 70 (2006) 4403–4416. doi:10.1016/J.GCA.2006.06.1560.

[221] H.T. Schaef, B.P. Mcgrail, Applied Geochemistry Dissolution of Columbia River Basalt under mildly acidic conditions as a function of temperature : Experimental results relevant to the geological sequestration of carbon dioxide, Appl. Geochemistry. 24 (2009) 980–987. doi:10.1016/j.apgeochem.2009.02.025.

[222] S.R. Gislason, E.H. Oelkers, Mechanism, rates, and consequences of basaltic glass dissolution: II. An experimental study of the dissolution rates of basaltic glass as a function of pH and temperature, Geochim. Cosmochim. Acta. 67 (2003) 3817–3832. doi:10.1016/S0016-7037(00)00176-5.

[223] P.B. Kelemen, J. Matter, E.E. Streit, J.F. Rudge, W.B. Curry, J. Blusztajn, Rates and Mechanisms of Mineral Carbonation in Peridotite: Natural Processes and Recipes for Enhanced, in situ CO_2 Capture and Storage, Annu. Rev. Earth Planet. Sci. 39 (2011) 545–576. doi:10.1146/annurev-earth-092010-152509.

[224] A. Sanna, M. Uibu, G. Caramanna, R. Kuusik, A review of mineral carbonation technologies to sequester CO_2, Chem. Soc. Rev. 43 (2014) 8049–8080. doi:10.1039/C4CS00035H.

[225] T.K. Flaathen, S.R. Gislason, E.H. Oelkers, Á. Sveinbjörnsdóttir, Applied Geochemistry Chemical evolution of the Mt . Hekla , Iceland , groundwaters : A natural analogue for CO 2 sequestration in basaltic rocks, Appl. Geochemistry. 24 (2009) 463–474. doi:10.1016/j.apgeochem.2008.12.031.

[226] F. Weise, T. Fridriksson, H. Ármansson, CO2 fixation by calcite in high- temperature geothermal systems in Iceland, 2008.

[227] J.L. Hamilton, S.A. Wilson, B. Morgan, C.C. Turvey, D.J. Paterson, C. MacRae, J. McCutcheon, G. Southam, Nesquehonite sequesters transition metals and CO 2 during accelerated carbon mineralisation, Int. J. Greenh. Gas Control. 55 (2016) 73–81. doi:10.1016/j.ijggc.2016.11.006.

[228] S.R. Gislason, E.H. Oelkers, Carbon storage in basalt, Science (80-.). 344 (2014) 373–374. doi:10.1126/science.1250828.

[229] J.M. Matter, W.S. Broecker, S.R. Gislason, E. Gunnlaugsson, E.H. Oelkers, M. Stute, H. Sigurdardottir, A. Stefansson, H.A. Alfredsson, E.S. Aradóttir, G. Axelsson, B. Sigfússon, D. Wolff-boenisch, The CarbFix Pilot Project – Storing Carbon Dioxide in Basalt, Energy Procedia. 4 (2011) 5579–5585. doi:10.1016/j.egypro.2011.02.546.

[230] H. Alfredsson, B.S. Hardarson, H. Franzson, S. Gislason, CO2 sequestration in basaltic rock at the Hellisheidi site in SW Iceland : Stratigraphy and chemical composition of the rocks at the injection site CO 2 sequestration in basaltic rock at the Hellisheidi site in SW Iceland : stratigraphy and chemical compo, Mineral. Mag. 72 (2008) 1–5. doi:10.1180/minmag.2008.072.1.1.

[231] H.H. Schopka, M. Gudmundsson, H. Tuffen, The formation of Helgafell , southwest Iceland , a monogenetic subglacial hyaloclastite ridge : Sedimentology , hydrology and volcano – ice interaction, J. Volcanol. Geotherm. Res. 152 (2006) 359–377. doi:10.1016/j.jvolgeores.2005.11.010.

[232] S.R. Gislason, D. Wolff-boenisch, A. Stefansson, E.H. Oelkers, E. Gunnlaugsson, H. Sigurdardottir, B. Sigfusson, W.S. Broecker, J.M. Matter, M. Stute, G. Axelsson, T. Fridriksson, Mineral sequestration of carbon dioxide in basalt : A pre-injection overview of the CarbFix project, Int. J. Greenh. Gas Control. 4 (2010) 537–545. doi:10.1016/j.ijggc.2009.11.013.

[233] B. Sigfusson, S.R. Gislason, J.M. Matter, M. Stute, E. Gunnlaugsson, I. Gunnarsson, E.S. Aradottir, H. Sigurdardottir, K.G. Mesfin, H.A. Alfredsson, D. Wolff-boenisch, M.T. Arnarsson, E.H. Oelkers, Solving the carbon-dioxide buoyancy challenge : The design and field testing of a dissolved CO 2 injection system, Int. J. Greenh. Gas Control. 37 (2015) 213–219. doi:10.1016/j.ijggc.2015.02.022.

[234] E.S.P. Aradóttir, E.L. Sonnenthal, G. Björnsson, H. Jónsson, International Journal of Greenhouse Gas Control Multidimensional reactive transport modeling of CO 2 mineral sequestration in basalts at the Hellisheidi geothermal field , Iceland, Int. J. Greenh. Gas Control. 9 (2012) 24–40. doi:10.1016/j.ijggc.2012.02.006.

[235] A.P. Gysi, A. Stefansson, CO_2 – water – basalt interaction. Numerical simulation of low temperature CO_2 sequestration into basalts, Geochim. Cosmochim. Acta. 75 (2011) 4728–4751. doi:10.1016/j.gca.2011.05.037.

[236] I. Clark, P. Fritz, Environmental Isotopes in Hydrogeology, FL: CRC Press/Lewis Publishers, Boca Raton, 1997.

[237] H.A. Alfredsson, D. Wolff-boenisch, In the Field The syringe sampler : An inexpensive alternative borehole sampling technique for CO 2 -rich fl uids during, Greenh. Gases Sci. Technol. 6 (2016) 167–177. doi:10.1002/ghg.

[238] M. Khalilabad, G. Axelsson, S. Gislason, Aquifer characterization with tracer test technique ; permanent CO2 sequestration into basalt , SW Iceland Aquifer characterization with tracer test technique ; permanent CO2 sequestration into basalt , SW Iceland, Mineral. Mag. 72 (2008) 121–125. doi:10.1180/minmag.2008.072.1.121.

[239] N. Assayag, J. Matter, M. Ader, D. Goldberg, P. Agrinier, Water – rock interactions during a CO 2 injection fi eld-test : Implications on host rock dissolution and alteration effects, Chem. Geol. 265 (2009) 227–235. doi:10.1016/j.chemgeo.2009.02.007.

[240] D. Wolff-boenisch, I.M. Galeczka, K.G. Mes, S.R. Gislason, A foray into false positive results in mineral dissolution and precipitation studies, Appl. Geochemistry. 71 (2016) 9–19. doi:10.1016/j.apgeochem.2016.05.011.

[241] S.Ó. Snæbjörnsdóttir, E.H. Oelkers, K. Mesfin, E.S. Aradóttir, K. Dideriksen, I. Gunnarsson, E. Gunnlaugsson, J.M. Matter, M. Stute, S.R. Gislason, The chemistry and saturation states of subsurface fluids during the in situ mineralisation of CO_2 and H_2S at the CarbFix site in SW-Iceland, Int. J. Greenh. Gas Control. 58 (2017) 87–102. doi:10.1016/j.ijggc.2017.01.007.

[242] E.H. Oelkers, R. Butcher, P.A.E. Pogge von Strandmann, J.A. Schuessler, F. von Blanckenburg, S. Snæbjörnsdóttir, K. Mesfin, E.S. Aradóttir, I. Gunnarsson, B. Sigfússon, E. Gunnlaugsson, J.M. Matter, M. Stute, S.R. Gislason, Using stable Mg isotope signatures to assess the fate of magnesium during the in situ mineralisation of CO_2 and H_2S at the CarbFix site in SW-Iceland, Geochim. Cosmochim. Acta. 245 (2019) 542–555. doi:10.1016/j.gca.2018.11.011.

[243] A.P. Gysi, A. Stefánsson, Mineralogical aspects of CO 2 sequestration during hydrothermal basalt alteration — An experimental study at 75 to 250 ° C and elevated p CO 2, Chem. Geol. 306–307 (2012) 146–159. doi:10.1016/j.chemgeo.2012.03.006.

[244] A.P. Gysi, A. Stefa, CO_2 water – basalt interaction . Low temperature experiments and implications for CO_2 sequestration into basalts, Geochim. Cosmochim. Acta. 81 (2012) 129–

152. doi:10.1016/j.gca.2011.12.012.

[245] I. Rigopoulos, A.L. Harrison, A. Delimitis, I. Ioannou, A.M. Efstathiou, T. Kyratsi, E.H. Oelkers, Carbon sequestration via enhanced weathering of peridotites and basalts in seawater, Appl. Geochemistry. 91 (2018) 197–207. doi:10.1016/j.apgeochem.2017.11.001.

[246] S. Snæbjörnsdóttir, S.R. Gislason, I.M. Galeczka, E.H. Oelkers, Reaction path modelling of in-situ mineralisation of CO2 at the CarbFix site at Hellisheidi, SW-Iceland, Geochim. Cosmochim. Acta. 220 (2018) 348–366. doi:10.1016/j.gca.2017.09.053.

[247] I. Gunnarsson, E.S. Aradóttir, E.H. Oelkers, D.E. Clark, M. Þór, B. Sigfússon, S.Ó. Snæbjörnsdóttir, J.M. Matter, M. Stute, B.M. Júlíusson, S.R. Gíslason, The rapid and cost-effective capture and subsurface mineral storage of carbon and sulfur at the CarbFix2 site, Int. J. Greenh. Gas Control. 79 (2018) 117–126. doi:10.1016/j.ijggc.2018.08.014.

[248] S.Ó. Snæbjörnsdóttir, F. Wiese, T. Fridriksson, H. Ármansson, G.M. Einarsson, S.R. Gislason, CO_2 storage potential of basaltic rocks in Iceland and the oceanic ridges, Energy Procedia. 63 (2014) 4585–4600. doi:10.1016/j.egypro.2014.11.491.

[249] D. Wolff-boenisch, S. Wenau, S.R. Gislason, E.H. Oelkers, Dissolution of basalts and peridotite in seawater , in the presence of ligands , and CO 2 : Implications for mineral sequestration of carbon dioxide, Geochim. Cosmochim. Acta. 75 (2011) 5510–5525. doi:10.1016/j.gca.2011.07.004.

[250] D.S. Goldberg, T. Takahashi, A.L. Slagle, Carbon dioxide sequestration in deep-sea basalt, Proc. Natl. Acad. Sci. United States Am. 105 (2008).

[251] R.F. Weiss, Carbon Dioxide in Water and Seawater: The Solubility of Non-Ideal Gas, Mar. Chem. 2 (1974) 203–215.

[252] D.S. Goldberg, D. V Kent, P.E. Olsen, Potential on-shore and off-shore reservoirs for CO 2 sequestration in Central Atlantic magmatic province basalts, Proc. Natl. Acad. Sci. U. S. A. 107 (2010) 1327–1332. doi:10.1073/pnas.0913721107.

[253] D.N. Huntzinger, J.S. Gierke, L.L. Sutter, S.K. Kawatra, T.C. Eisele, Mineral carbonation for carbon sequestration in cement kiln dust from waste piles, J. Hazard. Mater. 168 (2009) 31–37. doi:10.1016/J.JHAZMAT.2009.01.122.

[254] S. Arickx, T. Van Gerven, C. Vandecasteele, Accelerated carbonation for treatment of MSWI bottom ash, J. Hazard. Mater. 137 (2006) 235–243. doi:10.1016/j.jhazmat.2006.01.059.

[255] W. Qiang, Y. Peiyu, Hydration properties of basic oxygen furnace steel slag, Constr. Build. Mater. 24 (2010) 1134–1140. doi:10.1016/j.conbuildmat.2009.12.028.

[256] T.C. Eisele, L.L. Sutter, Carbon Dioxide Sequestration in Cement Kiln Dust through Mineral Carbonation, Environ. Sci. Technol. 43 (2009) 1986–1992.

[257] X. Wang, M.M. Maroto-Valer, Dissolution of serpentine using recyclable ammonium salts for CO_2 mineral carbonation, Fuel. 90 (2011) 1229–1237. doi:10.1016/j.fuel.2010.10.040.

[258] R. Baciocchi, G. Costa, A. Polettini, R. Pomi, Comparison of different reaction routes for carbonation of APC residues, Energy Procedia. 1 (2009) 4851–4858. doi:10.1016/j.egypro.2009.02.313.

[259] K. Soonchul, M. Fan, H.F.M. Dacosta, A.G. Russell, Factor affecting the direct mineralization of CO_2 with Olivine, J. Environ. Sci. 23 (2011) 1233–1239. doi:10.1016/S1001-0742(10)60555-4.

[260] S.P. Veetil, L. Pasquier, J. Blais, Direct gas – solid carbonation of serpentinite residues in the absence and presence of water vapor : a feasibility study for carbon dioxide sequestration, Environ. Sci. Pollut. Res. 22 (2015) 13486–13495. doi:10.1007/s11356-015-4580-x.

[261] R. Zevenhoven, S. Teir, S. Eloneva, Heat optimisation of a staged gas – solid mineral carbonation process for long-term CO_2 storage, Energy. 33 (2008) 362–370. doi:10.1016/j.energy.2007.11.005.

[262] H.F.M. Dacosta, M. Fan, A.G. Russell, Method to sequester CO_2 as mineral carbonate, Pat. Appl. Publ. 1 (2010).

[263] F. Larachi, J. Gravel, B.P.A. Grandjean, G. Beaudoin, Role of steam , hydrogen and pretreatment in chrysotile gas – solid carbonation : Opportunities for pre-combustion CO_2 capture, Int. J. Greenh. Gas Control. 6 (2012) 69–76. doi:10.1016/j.ijggc.2011.10.010.

[264] K.J. Fricker, A.H.A. Park, Investigation of the different carbonate phases and their formation kinetics during $Mg(OH)_2$ slurry carbonation, Ind. Eng. Chem. Res. 53 (2014) 18170–18179. doi:10.1021/ie503131s.

[265] J.H. Kwak, J.Z. Hu, R.V.F. Turcu, K.M. Rosso, E.S. Ilton, C. Wang, J.A. Sears, M.H. Engelhard, A.R. Felmy, D.W. Hoyt, The role of H_2O in the carbonation of forsterite in supercritical CO_2, Int. J. Greenh. Gas Control. 5 (2011) 1081–1092. doi:10.1016/j.ijggc.2011.05.013.

[266] F. Larachi, I. Daldoul, G. Beaudoin, Fixation of CO_2 by chrysotile in low-pressure dry and moist carbonation: Ex-situ and in-situ characterizations, Geochim. Cosmochim. Acta. 74 (2010) 3051–3075. doi:10.1016/J.GCA.2010.03.007.

[267] J. Fagerlund, J. Highfield, R. Zevenhoven, Kinetics studies on wet and dry gas – solid

carbonation of MgO and $Mg(OH)_2$ for CO_2 sequestration, RSC Adv. (2012) 10380–10393. doi:10.1039/c2ra21428h.

[268] A. Ćwik, I. Casanova, K. Rausis, N. Koukouzas, K. Zarębska, Carbonation of high-calcium fly ashes and its potential for carbon dioxide removal in coal fired power plants, J. Clean. Prod. 202 (2018) 1026–1034. doi:10.1016/j.jclepro.2018.08.234.

[269] G.P. Assima, F. Larachi, G. Beaudoin, J.W. Molson, CO_2 sequestration in chrysotile mining residues - Implication of watering and passivation under environmental conditions CO_2 sequestration in chrysotile mining residues - Implication of watering and passivation under environmental co, Ind. Eng. Chem. Res. 51 (2012) 8726–8734. doi:10.1021/ie202693q.

[270] R. Bhardwaj, J.R. Van Ommen, H.W. Nugteren, H. Geerlings, Accelerating Natural CO_2 Mineralization in a Fluidized Bed, Ind. Eng. Chem. Res. 55 (2016) 2946–2951. doi:10.1021/acs.iecr.5b04925.

[271] J. Sipilä, S. Teir, R. Zevenhoven, Carbon Dioxide Sequestration by Mineral Carbonation : Literature Review Update 2005-2007, Turku, Finland, 2008.

[272] T. Haug, R.A. Kleiv, I.A. Munz, Investigating dissolution of mechanically activated olivine for carbonation purposes, Appl. Geochemistry. 25 (2010) 1547–1563. doi:10.1016/j.apgeochem.2010.08.005.

[273] T.A. Haug, I.A. Munz, R.A. Kleiv, Importance of dissolution and precipitation kinetics for mineral carbonation, Energy Procedia. 4 (2011) 5029–5036. doi:10.1016/j.egypro.2011.02.475.

[274] S. Teir, H. Revitzer, S. Eloneva, C. Fogelholm, R. Zevenhoven, Dissolution of natural serpentinite in mineral and organic acids, Int. J. Miner. Process. 83 (2007) 36–46. doi:10.1016/j.minpro.2007.04.001.

[275] S. Kodama, T. Nishimoto, N. Yamamoto, Development of a new pH-swing CO 2 mineralization process with a recyclable reaction solution, Energy. 33 (2008) 776–784. doi:10.1016/j.energy.2008.01.005.

[276] G.J. Stockmann, D. Wolff-boenisch, S.R. Gislason, E.H. Oelkers, Do carbonate precipitates affect dissolution kinetics ? 2 : Diopside, Chem. Geol. 337–338 (2013) 56–66. doi:10.1016/j.chemgeo.2012.11.014.

[277] R.M. Santos, T. Van Gerven, K.U. Leuven, Process intensification routes for mineral carbonation, Greenh. Gases Sci. Technol. 293 (2011) 287–293. doi:10.1002/ghg.

[278] X. Wang, M.M. Maroto-valer, Integration of CO_2 Capture and Mineral Carbonation by Using

Recyclable Ammonium Salts, ChemSusChem. 4 (2011) 1291–1300. doi:10.1002/cssc.201000441.

[279] O.S. Pokrovsky, J. Schott, F. Thomas, Dolomite surface speciation and reactivity in aquatic systems, Geochim. Cosmochim. Acta. 63 (1999) 3133–3143.

[280] M. Fabian, M. Shopska, D. Paneva, G. Kadinov, N. Kostova, E. Turianicová, I. Mitov, R.A. Kleiv, P. Baláz, J. Brianc, The influence of attrition milling on carbon dioxide sequestration on magnesium – iron silicate, Miner. Eng. 23 (2010) 616–620. doi:10.1016/j.mineng.2010.02.006.

[281] M.I. Rashid, E. Benhelal, F. Farhang, T.K. Oliver, M.S. Rayson, G.F. Brent, M. Stockenhuber, E.M. Kennedy, Development of Concurrent grinding for application in aqueous mineral carbonation, J. Clean. Prod. 212 (2019) 151–161. doi:10.1016/j.jclepro.2018.11.189.

[282] W.K. O'Connor, D.C. Dahlin, G.E. Rush, C.L. Dahlin, W.K. Collins, Carbon dioxide sequestration by direct mineral carbonation: Process mineralogy of feed and products, Miner. Metall. Process. 19 (2001) 95–101. http://www.scopus.com/inward/record.url?eid=2-s2.0-0036578302&partnerID=40&md5=4bd8abb93b2ffe30d5e8f0ddbcd0a099.

[283] K. MacKenzie, R. Meinhold, Thermal reactions of chrysotile revisited: A 29Si and 25Mg MAS NMR study, Am. Mineral. 79 (1994) 43–50.

[284] M.J. McKelvy, R. Sharma, A.V.G. Chizmeshya, R.W. Carpenter, K. Streib, Magnesium hydroxide dehydroxylation: In situ nanoscale observations of lamellar nucleation and growth, Chem. Mater. 13 (2001) 921–926. doi:10.1021/cm000676t.

[285] A. Drief, F. Nieto, The Effect of Dry Grinding on Antigorite from Mulhacen, Spain, Clays Clay Miner. 47 (1999) 417–424.

[286] W. Li, W. Li, B. Li, Z. Bai, Electrolysis and heat pretreatment methods to promote CO_2 sequestration by mineral carbonation, Chem. Eng. Res. Des. 87 (2009) 210–215. doi:10.1016/j.cherd.2008.08.001.

[287] B.Z. Dlugogorski, R.D. Balucan, Dehydroxylation of serpentine minerals: Implications for mineral carbonation, Renew. Sustain. Energy Rev. 31 (2014) 353–367. doi:10.1016/j.rser.2013.11.002.

[288] A. Sanna, X. Wang, A. Lacinska, M. Styles, T. Paulson, M.M. Maroto-Valer, Enhancing Mg extraction from lizardite-rich serpentine for CO 2 mineral sequestration, Miner. Eng. 49 (2013) 135–144. doi:10.1016/j.mineng.2013.05.018.

[289] A. Fedorocková, M. Hreus, P. Raschman, G. Sucik, Dissolution of magnesium from calcined serpentinite in hydrochloric acid, Miner. Eng. 32 (2012) 1–4. doi:10.1016/j.mineng.2012.03.006.

[290] R.D. Balucan, B.Z. Dlugogorski, E.M. Kennedy, I. V. Belova, G.E. Murch, Energy cost of heat activating serpentinites for CO_2 storage by mineralisation, Int. J. Greenh. Gas Control. 17 (2013) 225–239. doi:10.1016/j.ijggc.2013.05.004.

[291] G. Brent, US 2009 / 0305378A1, 2009.

[292] A. Sanna, R. Hall, M. Maroto-valer, Post-processing pathways in carbon capture and storage by mineral carbonation (CCSM) towards the introduction of carbon neutral materials, Energy Environ. Sci. 5 (2012) 7781–7796. doi:10.1039/c2ee03455g.

[293] A.-H.A. Park, L.-S. Fan, CO_2 mineral sequestration: physically activated dissolution of serpentine and pH swing process, Chem. Eng. Sci. 59 (2004) 5241–5247. doi:10.1016/J.CES.2004.09.008.

[294] S. Eloneva, A. Said, C. Fogelholm, R. Zevenhoven, Preliminary assessment of a method utilizing carbon dioxide and steelmaking slags to produce precipitated calcium carbonate, Appl. Energy. 90 (2012) 329–334. doi:10.1016/j.apenergy.2011.05.045.

[295] P. Lin, C. Huang, C. Hsiao, H. Teng, Magnesium Hydroxide Extracted from a Magnesium-Rich Mineral for CO_2, Environ. Sci. Technol. 9 (2009) 1–5.

[296] S.C. Krevor, K.S. Lackner, Enhancing process kinetics for mineral carbon sequestration, Energy Procedia. 1 (2009) 4867–4871. doi:10.1016/j.egypro.2009.02.315.

[297] X. Wang, M.M. Maroto-valer, Dissolution of serpentine using recyclable ammonium salts for CO 2 mineral carbonation, Fuel. 90 (2011) 1229–1237. doi:10.1016/j.fuel.2010.10.040.

[298] X. Wang, M.M. Maroto-valer, Optimization of carbon dioxide capture and storage with mineralisation using recyclable ammonium salts, Energy. 51 (2013) 431–438. doi:10.1016/j.energy.2013.01.021.

[299] J. Fagerlund, S. Teir, E. Nduagu, R. Zevenhoven, Carbonation of magnesium silicate mineral using a pressurised gas/solid process, Energy Procedia. 1 (2009) 4907–4914. doi:10.1016/j.egypro.2009.02.321.

[300] K. Bosecker, Bioleaching : metal solubilization by microorganisms, FEMS Microbiol. Rev. 20 (1997) 591–604.

[301] D.W. Schwartzman, T. Volk, Biotic enhancement of weathering and the habitability of Earth, Nature. 340 (1989) 457–460. doi:10.1038/340457a0.

[302] I.M. Power, G.M. Dipple, G. Southam, Bioleaching of ultramafic tailings by Acidithiobacillus spp. for CO_2 sequestration, Environ. Sci. Technol. 44 (2010) 456–462. doi:10.1021/es900986n.

[303] W. Huijgen, G.-J. Witkamp, R. Comans, Mineral CO_2 Sequestration by Steel Slag Carbonation, Environ. Sci. Technol. 39 (2005) 9676–9682. doi:10.1021/es050795f.

[304] S. Eloneva, S. Teir, J. Salminen, C. Fogelholm, R. Zevenhoven, Steel Converter Slag as a Raw Material for Precipitation of Pure Calcium Carbonate, Ind. Eng. Chem. Res. 47 (2008) 7104–7111.

[305] O. Velts, M. Uibu, J. Kallas, R. Kuusik, Waste oil shale ash as a novel source of calcium for precipitated calcium carbonate : Carbonation mechanism , modeling , and product characterization, J. Hazard. Mater. 195 (2011) 139–146. doi:10.1016/j.jhazmat.2011.08.019.

[306] S. Pan, E.E. Chang, P. Chiang, CO_2 Capture by Accelerated Carbonation of Alkaline Wastes : A Review on Its Principles and Applications, Aerosol Air Qual. Res. 12 (2012) 770–791. doi:10.4209/aaqr.2012.06.0149.

[307] G. Montes-Hernandez, R. Pérez-López, F. Renard, J.M. Nieto, L. Charlet, Mineral sequestration of CO_2 by aqueous carbonation of coal combustion fly-ash, J. Hazard. Mater. 161 (2009) 1347–1354. doi:10.1016/j.jhazmat.2008.04.104.

[308] M. Uibu, O. Velts, R. Kuusik, Developments in CO2 mineral carbonation of oil shale ash, J. Hazard. Mater. 174 (2010) 209–214. doi:10.1016/j.jhazmat.2009.09.038.

[309] A. Iizuka, M. Fujii, A. Yamasaki, Y. Yanagisawa, Development of a New CO_2 Sequestration Process Utilizing the, Ind. Eng. Chem. Res. 43 (2004) 7880–7887. doi:10.1021/ie0496176.

[310] M.G. Nyambura, G.W. Mugera, P.L. Felicia, N.P. Gathura, Carbonation of brine impacted fractionated coal fly ash: Implications for CO2 sequestration, J. Environ. Manage. 92 (2011) 655–664.

[311] C. Wang, L. Jia, Y. Tan, E.J. Anthony, Carbonation of fly ash in oxy-fuel CFB combustion, Fuel. 87 (2008) 1108–1114. doi:10.1016/j.fuel.2007.06.024.

[312] X. Li, M. Fernández-Bertos, C.D. Hills, P.J. Carey, S. Simon, Accelerated carbonation of municipal solid waste incineration fly ashes, Waste Manag. 27 (2007) 1200–1206. doi:10.1016/j.wasman.2006.06.011.

[313] A. Uliasz-boche, E. Mokrzycki, Z. Piotrowski, Estimation of CO_2 sequestration potential via mineral carbonation in fly ash from lignite combustion in Poland, Energy Procedia. 1 (2009) 4873–4879. doi:10.1016/j.egypro.2009.02.316.

[314] M. Bauer, N. Gassen, H. Stanjek, S. Peiffer, Carbonation of lignite fly ash at ambient T and P in a semi-dry reaction system for CO_2 sequestration, Appl. Geochemistry. 26 (2011) 1502–1512. doi:10.1016/j.apgeochem.2011.05.024.

[315] E. Rendek, P. Germain, Carbon dioxide sequestration in municipal solid waste incinerator (MSWI) bottom ash, J. Hazard. Mater. (2006) 73–79. doi:10.1016/j.jhazmat.2005.07.033.

[316] R. Baciocchi, G. Costa, E. Di, A. Polettini, R. Pomi, The effects of accelerated carbonation on CO_2 uptake and metal release from incineration APC residues, Waste Manag. 29 (2009) 2994–3003. doi:10.1016/j.wasman.2009.07.012.

[317] G. Cappai, S. Cara, A. Muntoni, M. Piredda, Application of accelerated carbonation on MSW combustion APC residues for metal immobilization and CO_2 sequestration, J. Hazard. Mater. 207–208 (2012) 159–164. doi:10.1016/j.jhazmat.2011.04.013.

[318] M. Uibu, M. Uus, R. Kuusik, CO_2 mineral sequestration in oil-shale wastes from Estonian power production, J. Environ. Manage. 90 (2009) 1253–1260. doi:10.1016/j.jenvman.2008.07.012.

[319] M. Uibu, R. Kuusik, Mineral Trapping of CO_2 via Oil Shale Ash Aqueous Carbonation: Controlling Mechanisms of Process Rate and Development of Continuous-Flow Reactor System, Oil Shale. 26 (2009) 40–58. doi:10.3176/oil.2009.1.06.

[320] M. Radvanec, J. Derco, K. Cechovská, Z. Németh, Change of carcinogenic chrysotile fibers in the asbestos cement (eternit) to harmless waste by artificial carbonatization : Petrological and technological results ˇ, J. Hazard. Mater. 253 (2013) 390–400. doi:10.1016/j.jhazmat.2013.02.036.

[321] S. Teir, S. Eloneva, C. Fogelholm, R. Zevenhoven, Fixation of carbon dioxide by producing hydromagnesite from serpentinite, Appl. Energy. 86 (2009) 214–218. doi:10.1016/j.apenergy.2008.03.013.

[322] R. Pérez-lópez, G. Montes-hernandez, J.M. Nieto, F. Renard, L. Charlet, Carbonation of alkaline paper mill waste to reduce CO_2 greenhouse gas emissions into the atmosphere, Appl. Geochemistry. 23 (2008) 2292–2300. doi:10.1016/j.apgeochem.2008.04.016.

[323] D. Bonenfant, L. Kharoune, R. Hausler, P. Niquette, CO_2 Sequestration Potential of Steel Slags at Ambient Pressure and Temperature, Ind. Eng. Chem. Res. 47 (2008) 7610–7616.

[324] R. Baciocchi, G. Costa, A. Polettini, R. Pomi, Influence of particle size on the carbonation of stainless steel slag for CO_2 storage, Energy Procedia. 1 (2009) 4859–4866. doi:10.1016/j.egypro.2009.02.314.

[325] E. Chang, C. Chen, Y. Chen, S. Pan, P. Chiang, Performance evaluation for carbonation of steel-making slags in a slurry reactor, J. Hazard. Mater. 186 (2011) 558–564. doi:10.1016/j.jhazmat.2010.11.038.

[326] E. Chang, S. Pan, Y. Chen, C. Tan, P. Chiang, Accelerated carbonation of steelmaking slags in a high-gravity rotating packed bed, J. Hazard. Mater. 227–228 (2012) 97–106. doi:10.1016/j.jhazmat.2012.05.021.

[327] E. Chang, S. Pan, Y. Chen, H. Chu, C. Wang, P. Chiang, CO_2 sequestration by carbonation of steelmaking slags in an autoclave reactor, J. Hazard. Mater. 195 (2011) 107–114. doi:10.1016/j.jhazmat.2011.08.006.

[328] S. Khaitan, A.M. Asce, D.A. Dzombak, F. Asce, G. V Lowry, M. Asce, Mechanisms of Neutralization of Bauxite Residue by Carbon Dioxide, J. Environ. Enginnering. 135 (2009) 433–438. doi:10.1061/(ASCE)EE.1943-7870.0000010.

[329] V.S. Yadav, M. Prasad, J. Khan, S.S. Amritphale, M. Singh, C.B. Raju, Sequestration of carbon dioxide (CO_2) using red mud, J. Hazard. Mater. 176 (2010) 1044–1050. doi:10.1016/j.jhazmat.2009.11.146.

[330] C. Gahan, M. Cunha, Å. Sandström, Hydrometallurgy Comparative study on different steel slags as neutralising agent in bioleaching, Hydrometallurgy. 95 (2009) 190–197. doi:10.1016/j.hydromet.2008.05.042.

[331] A. Sanna, M. Dri, M.R. Hall, M. Maroto-valer, Waste materials for carbon capture and storage by mineralisation (CCSM) – A UK perspective, Appl. Energy. 99 (2012) 545–554. doi:10.1016/j.apenergy.2012.06.049.

[332] R.M. Santos, D. François, G. Mertens, J. Elsen, T. Van Gerven, Ultrasound-intensi fi ed mineral carbonation, Appl. Therm. Eng. 57 (2013) 154–163. doi:10.1016/j.applthermaleng.2012.03.035.

[333] F.J. Doucet, Effective CO 2 -specific sequestration capacity of steel slags and variability in their leaching behaviour in view of industrial mineral carbonation, Miner. Eng. 23 (2010) 262–269. doi:10.1016/j.mineng.2009.09.006.

[334] M. Dri, A. Sanna, M.M. Maroto-valer, Mineral carbonation from metal wastes : Effect of solid to liquid ratio on the efficiency and characterization of carbonated products, Appl. Energy. 113 (2014) 515–523. doi:10.1016/j.apenergy.2013.07.064.

[335] G. Costa, R. Baciocchi, A. Polettini, R. Pomi, C.D. Hills, P.J. Carey, Current status and perspectives of accelerated carbonation processes on municipal waste combustion residues, Environ. Monit. Assesment. 135 (2007) 55–75. doi:10.1007/s10661-007-9704-4.

[336] T. Van Gerven, E. Van Keer, S. Arickx, M. Jaspers, Carbonation of MSWI-bottom ash to decrease heavy metal leaching , in view of recycling, Waste Manag. 25 (2005) 291–300. doi:10.1016/j.wasman.2004.07.008.

[337] A. Polettini, R. Pomi, The leaching behavior of incinerator bottom ash as affected by accelerated ageing, J. Hazard. Mater. (2004) 209–215. doi:10.1016/j.jhazmat.2004.06.009.

[338] M. Fernández-Bertos, S.J.R. Simons, C.D. Hills, P.J. Carey, A review of accelerated carbonation technology in the treatment of cement-based materials and sequestration of CO2, J. Hazard. Mater. 112 (2004) 193–205.

[339] H. Ecke, Sequestration of metals in carbonated municipal solid waste incineration (MSWI) fly ash, Waste Manag. 23 (2005) 631–640. doi:10.1016/S0956-053X(03)00095-3.

[340] P.J. Gunning, C.D. Hills, P.J. Carey, Accelerated carbonation treatment of industrial wastes, Waste Manag. 30 (2010) 1081–1090. doi:10.1016/j.wasman.2010.01.005.

[341] M. Back, M. Kuehn, H. Stanjek, S. Peiffer, Reactivity of Alkaline Lignite Fly Ashes Towards CO_2 in Water, Environ. Sci. Technol. 42 (2008) 4520–4526.

[342] K.J. Reddy, S. John, H. Weber, M.D. Argyle, P. Bhattacharyya, Simultaneous capture and mineralization of coal combustion flue gas carbon dioxide (CO_2), Energy Procedia. 4 (2011) 1574–1583. doi:10.1016/j.egypro.2011.02.027.

[343] D.N. Huntzinger, T.D. Eatmon, A life-cycle assessment of Portland cement manufacturing : comparing the traditional process with alternative technologies, J. Clean. Prod. 17 (2009) 668–675. doi:10.1016/j.jclepro.2008.04.007.

[344] D.N. Huntzinger, J.S. Gierke, S.K. Kawatra, T.C. Eisele, Sutter, Carbon Dioxide Sequestration in Cement Kiln Dust through Mineral Carbonation, Environ. Sci. Technol. 43 (2009) 1986–1992.

[345] Y. Katsuyama, A. Yamasaki, A. Iizuka, M. Fujii, K. Kumagai, Development of a Process for Producing High-Purity Calcium Carbonate (CaCO3) from Waste Cement Using Pressurized CO2, Environ. Prog. 24 (2005) 162–170. doi:10.1002/ep.10080.

[346] S.A. Wilson, G.M. Dipple, I.M. Power, J.M. Thom, R.G. Anderson, M. Raudsepp, J.E. Gabites, G. Southam, Carbon dioxide fixation within mine wastes of ultramafic-hosted ore deposits: Examples from the Clinton Creek and Cassiar Chrysotile deposits, Canada, Econ. Geol. 104 (2009) 95–112. doi:10.2113/gsecongeo.104.1.95.

[347] M. Kakizawa, A. Yamasaki, Y. Yanagisawa, A new CO_2 disposal process via artificial weathering of calcium silicate accelerated by acetic acid, Energy. 26 (2001) 341–354.

[348] R. Sahu, R. Patel, B. Ray, Neutralization of red mud using CO2 sequestration cycle, J. Hazard. Mater. 179 (2010) 28–34. doi:10.1016/j.jhazmat.2010.02.052.

[349] H.C. Oskierski, B.Z. Dlugogorski, G. Jacobsen, Sequestration of atmospheric CO<sub>2</sub > in chrysotile mine tailings of the Woodsreef Asbestos Mine , Australia : Quantitative mineralogy , isotopic fi ngerprinting and carbonation rates, Chem. Geol. 358 (2013) 156–169. doi:10.1016/j.chemgeo.2013.09.001.

[350] R. Dilmore, P. Lu, D. Allen, Y. Soong, S. Hedges, J.K. Fu, C.L. Dobbs, A. Degalbo, C. Zhu, Sequestration of CO2 in Mixtures of Bauxite Residue and Saline, Energy & Fuels. 22 (2008) 343–353.

[351] M. Johnston, M.W. Clark, P. Mcmahon, N. Ward, Alkalinity conversion of bauxite refinery residues by neutralization, J. Hazard. Mater. 182 (2010) 710–715. doi:10.1016/j.jhazmat.2010.06.091.

[352] C. Si, Y. Ma, C. Lin, Red mud as a carbon sink : Variability , affecting factors and environmental significance, J. Hazard. Mater. 244–245 (2013) 54–59. doi:10.1016/j.jhazmat.2012.11.024.

[353] E. Benhelal, M.I. Rashid, M.S. Rayson, G.F. Brent, T. Oliver, M. Stockenhuber, E.M. Kennedy, Direct aqueous carbonation of heat activated serpentine: Discovery of undesirable side reactions reducing process efficiency, Appl. Energy. 242 (2019) 1369–1382. doi:10.1016/j.apenergy.2019.03.170.

[354] C. Marchesi, C.J. Garrido, J.A. Proenza, K. Hidas, M.I. Varas-Reus, L. Butjosa, J.F. Lewis, Geochemical record of subduction initiation in the sub-arc mantle: Insights from the Loma Caribe peridotite (Dominican Republic), Lithos. 252–253 (2016) 1–15. doi:10.1016/j.lithos.2016.02.009.

[355] S. Yariv, L. Heller-Kallai, The Relationship between the I.R. Spectra of Serpentines and Their Structures, Clays Clay Miner. 23 (1975) 145–152. doi:10.1346/CCMN.1975.0230210.

[356] W.K. Ryu, H. Jo, S. Hoon, S. Chun, Y. Jang, Changes in mineral assemblages during serpentine carbonation, Appl. Clay Sci. 134 (2016) 62–67. doi:10.1016/j.clay.2016.08.005.

[357] R. Trittschack, B. Gorbèty, M. Koch-Müller, In situ high-temperature Raman and FTIR spectroscopy of the phase transformation of lizardite, Am. Mineral. 97 (2012) 1965–1976.

[358] C. Rinaudo, D. Gastaldi, E. Belluso, Characterization of chrysotile, antigorite and lizardite by FT-Raman spectroscopy, Can. Mineral. 41 (2003) 883–890. doi:10.2113/gscanmin.41.4.883.

[359] J. Hövelmann, H. Austrheim, A. Beinlich, I. Anne Munz, Experimental study of the carbonation of partially serpentinized and weathered peridotites, Geochim. Cosmochim. Acta. 75 (2011) 6760–6779. doi:10.1016/j.gca.2011.08.032.

[360] A. Zarandi, F. Larachi, G. Beaudoin, B. Plante, M. Sciortino, Ambient mineral carbonation of different lithologies of mafic to ultramafic mining wastes/tailings – A comparative study, Int. J. Greenh. Gas Control. 63 (2017) 392–400. doi:10.1016/j.ijggc.2017.06.016.

[361] S.N. (2015) Lafuente B, Downs R T, Yang H, The power of databases: the RRUFF project., 2015. rruff.info.

[362] K.E. Kuebler, B.L. Jolliff, A. Wang, L.A. Haskin, Extracting olivine (Fo-Fa) compositions from Raman spectral peak positions, Geochim. Cosmochim. Acta. 70 (2006) 6201–6222. doi:10.1016/j.gca.2006.07.035.

[363] R. Zucker, S.H. Shim, In situ Raman spectroscopy of MgSiO3 enstatite up to 1550 K, Am. Mineral. 94 (2009) 1638–1646. doi:10.2138/am.2009.3210.

[364] C.A. Myers, T. Nakagaki, K. Akutsu, Quantification of the CO2 mineralization potential of ironmaking and steelmaking slags under direct gas-solid reactions in flue gas, Int. J. Greenh. Gas Control. 87 (2019) 100–111. doi:10.1016/j.ijggc.2019.05.021.

[365] M. Werner, S.B. Hariharan, A. V. Bortolan, D. Zingaretti, R. Baciocchi, M. Mazzotti, Carbonation of activated serpentine for direct flue gas mineralization, Energy Procedia. 37 (2013) 5929–5937. doi:10.1016/j.egypro.2013.06.519.

[366] U.S.P.R. Arachchige, M.C. Melaaen, Aspen plus simulation of CO2 removal from coal and gas fired power plants, Energy Procedia. 23 (2012) 391–399. doi:10.1016/j.egypro.2012.06.060.

[367] P.B. Niles, D.C. Catling, G. Berger, E. Chassefière, B.L. Ehlmann, J.R. Michalski, R. Morris, S.W. Ruff, B. Sutter, Geochemistry of carbonates on Mars: Implications for climate history and nature of aqueous environments, Space Sci. Rev. 174 (2013) 301–328. doi:10.1007/s11214-012-9940-y.

[368] C. Boschi, A. Dini, I. Baneschi, F. Bedini, N. Perchiazzi, A. Cavallo, Brucite-driven CO2 uptake in serpentinized dunites (Ligurian Ophiolites, Montecastelli, Tuscany), Lithos. 288–289 (2017) 264–281. doi:10.1016/j.lithos.2017.07.005.

[369] L. Zhao, L. Sang, C. Jun, J. Ji, H.H. Teng, Aqueous carbonation of natural brucite: Relevance to CO_2 sequestration, Environ. Sci. Technol. 44 (2010) 406–411. doi:10.1021/es9017656.

[370] G.P. Assima, F. Larachi, J. Molson, G. Beaudoin, Emulation of ambient carbon dioxide

diffusion and carbonation within nickel mining residues, Miner. Eng. 59 (2014) 39–44. doi:10.1016/j.mineng.2013.09.002.

[371] A.L. Harrison, I.M. Power, G.M. Dipple, Accelerated carbonation of brucite in mine tailings for carbon sequestration, Environ. Sci. Technol. 47 (2013) 126–134. doi:10.1021/es3012854.

[372] G. Dávila, J. Cama, S. Galí, L. Luquot, J.M. Soler, Efficiency of magnesium hydroxide as engineering seal in the geological sequestration of CO_2, Int. J. Greenh. Gas Control. 48 (2016) 171–185. doi:10.1016/j.ijggc.2016.01.031.

[373] J. Hövelmann, C. V. Putnis, E. Ruiz-Agudo, H. Austrheim, Direct nanoscale observations of CO_2 sequestration during brucite [$Mg(OH)_2$] dissolution, Environ. Sci. Technol. 46 (2012) 5253–5260. doi:10.1021/es300403n.

[374] G.P. Assima, F. Larachi, J. Molson, G. Beaudoin, Accurate and direct quantification of native brucite in serpentine ores New methodology and implications for CO_2 sequestration by mining residues, Thermochim. Acta. 566 (2013) 281–291. doi:10.1016/j.tca.2013.06.006.

[375] G.P. Assima, F. Larachi, J. Molson, G. Beaudoin, Impact of temperature and oxygen availability on the dynamics of ambient CO_2 mineral sequestration by nickel mining residues, Chem. Eng. J. 240 (2014) 394–403. doi:10.1016/j.cej.2013.12.010.

[376] A. Zarandi, F. Larachi, G. Beaudoin, B. Plante, M. Sciortino, Nesquehonite as a carbon sink in ambient mineral carbonation of ultramafic mining wastes, Chem. Eng. J. 314 (2017) 160–168. doi:10.1016/j.cej.2017.01.003.

[377] D.P. Butt, K.S. Lackner, C.H. Wendt, S.D. Conzone, H. Kung, Y.C. Lu, J.K. Bremser, Kinetics of thermal dehydroxylation and carbonation of magnesium hydroxide, J. Am. Ceram. Soc. 79 (1996) 1892–1898. doi:10.1111/j.1151-2916.1996.tb08010.x.

[378] H. Béarat, M.J. McKelvy, A.V.G. Chizmeshya, R. Sharma, R.W. Carpenter, Magnesium hydroxide dehydroxylation/carbonation reaction processes: Implications for carbon dioxide mineral sequestration, J. Am. Ceram. Soc. 85 (2002) 742–748. doi:10.1111/j.1151-2916.2002.tb00166.x.

[379] T.S. Duffy, C. Meade, Yingwei Fei, Ho-Kwang Mao, R.J. Hemley, High-pressure phase transition in brucite, $Mg(OH)_2$, Am. Mineral. 80 (1995) 222–230.

[380] H.G.M. Edwards, S.E.J. Villar, J. Jehlicka, T. Munshi, FT-Raman spectroscopic study of calcium-rich and magnesium-rich carbonate minerals, Spectrochim. Acta - Part A Mol. Biomol. Spectrosc. 61 (2005) 2273–2280. doi:10.1016/j.saa.2005.02.026.

[381] R.L. Frost, Raman spectroscopic study of the magnesium carbonate mineral hydromagnesite

(Mg 5[(CO 3) 4(OH) 2]·4H 2O), J. Raman Spectrosc. 42 (2011) 1690–1694. doi:10.1002/jrs.2917.

[382] G. Montes-Hernandez, F. Renard, Time-Resolved in Situ Raman Spectroscopy of the Nucleation and Growth of Siderite, Magnesite, and Calcite and Their Precursors, Cryst. Growth Des. 16 (2016) 7218–7230. doi:10.1021/acs.cgd.6b01406.

[383] M.L. Frezzotti, F. Tecce, A. Casagli, Raman spectroscopy for fluid inclusion analysis, J. Geochemical Explor. 112 (2012) 1–20. doi:10.1016/j.gexplo.2011.09.009.

[384] A. Spivak, N. Solopova, V. Cerantola, E. Bykova, E. Zakharchenko, L. Dubrovinsky, Y. Litvin, Raman study of MgCO3-FeCO3carbonate solid solution at high pressures up to 55 GPa, Phys. Chem. Miner. 41 (2014) 633–638. doi:10.1007/s00269-014-0676-y.

[385] K. Rausis, A. Ćwik, I. Casanova, Insights into the carbonation of activated lizardite: the identification of a poorly-reactive amorphous Mg-rich silicate phase, Int. J. Greenh. Gas Control. (n.d.) Revised manuscript submitted.

[386] L.S. Shirokova, V. Mavromatis, I.A. Bundeleva, O.S. Pokrovsky, P. Bénézeth, E. Gérard, C.R. Pearce, E.H. Oelkers, Using Mg Isotopes to Trace Cyanobacterially Mediated Magnesium Carbonate Precipitation in Alkaline Lakes, Aquat. Geochemistry. 19 (2013) 1–24. doi:10.1007/s10498-012-9174-3.

[387] V. Prigiobbe, M. Mazzotti, Precipitation of Mg-carbonates at elevated temperature and partial pressure of CO_2, Chem. Eng. J. 223 (2013) 755–763. doi:10.1016/j.cej.2013.03.033.

[388] T.J.B. Holland, R. Powell, An enlarged and updated internally consistent thermodynamic dataset with uncertainties and correlations, J. Metamorph. Geol. 8 (1990) 89–124.

[389] L. Cemič, Thermodynamics in mineral sciences: An introduction, Springer, 2005. doi:10.1007/3-540-28808-2.

[390] R.A. Robie, B.S. Hemingway, Thermodynamic properties of minerals and related substances at 298.15K and 1 bar (10^5 Pascals) pressure and at higher temperatures, Geological, 1995.

[391] B. Morgan, S.A. Wilson, I.C. Madsen, Y.M. Gozukara, J. Habsuda, Increased thermal stability of nesquehonite ($MgCO_3·3H_2O$) in the presence of humidity and CO_2: Implications for low-temperature CO_2 storage, Int. J. Greenh. Gas Control. 39 (2015) 366–376. doi:10.1016/j.ijggc.2015.05.033.

[392] J. Baltrusaitis, J.D. Schuttlefield, E. Zeitler, J.H. Jensen, V.H. Grassian, Surface reactions of carbon dioxide at the adsorbed water-oxide interface, J. Phys. Chem. C. 111 (2007) 14870–14880. doi:10.1021/jp074677l.

[393] J. Morse, W. Casey, Ostwald processes and mineral paragenesis in sediments, Am. J. Sci. 288 (1988) 537–560.

[394] L.A. Hollingbery, T.R. Hull, The thermal decomposition of huntite and hydromagnesite — A review, Thermochim. Acta. 509 (2010) 1–11. doi:10.1016/j.tca.2010.06.012.

[395] V. Vágvölgyi, R.L. Frost, M. Hales, A. Locke, J. Kristóf, E. Horváth, Controlled rate thermal analysis of hydromagnesite, J. Therm. Anal. Calorim. 92 (2008) 893–897. doi:10.1007/s10973-009-0201-6.

[396] V. Vágvölgyi, M. Hales, R.L. Frost, A. Locke, J. Kristóf, E. Horváth, Conventional and controlled rate thermal analysis of nesquehonite $Mg(HCO_3)(OH)•2(H_2O)$, J. Therm. Anal. Calorim. 94 (2008) 523–528. doi:10.1007/s10973-007-8844-7.

[397] L.A. Hollingbery, T.R. Hull, The thermal decomposition of natural mixtures of huntite and hydromagnesite, Thermochim. Acta. 528 (2012) 45–52. doi:10.1016/j.tca.2011.11.002.

[398] B. Maria Foldvari, Handbook of thermo-gravimetric system of minerals and its use in geological practice, 2011.

[399] Y. Jia, T. Luo, X.Y. Yu, B. Sun, J.H. Liu, X.J. Huang, A facile template free solution approach for the synthesis of dypingite nanowires and subsequent decomposition to nanoporous MgO nanowires with excellent arsenate adsorption properties, RSC Adv. 3 (2013) 5430–5437. doi:10.1039/c3ra23340e.

[400] R.L. Frost, S. Bahfenne, J. Graham, W.N. Martens, Thermal stability of artinite, dypingite and brugnatellite-Implications for the geosequestration of green house gases, Thermochim. Acta. 475 (2008) 39–43. doi:10.1016/j.tca.2008.06.007.

[401] K. Fukushi, Y. Suzuki, J. Kawano, T. Ohno, M. Ogawa, T. Yaji, Y. Takahashi, Speciation of magnesium in monohydrocalcite: XANES, ab initio and geochemical modeling, Geochim. Cosmochim. Acta. 213 (2017) 457–474. doi:10.1016/j.gca.2017.06.040.

[402] A.M. Chaka, Ab Initio Thermodynamics of Hydrated Calcium Carbonates and Calcium Analogues of Magnesium Carbonates: Implications for Carbonate Crystallization Pathways, ACS Earth Sp. Chem. 2 (2018) 210–224. doi:10.1021/acsearthspacechem.7b00101.

[403] S. Hild, O. Marti, A. Ziegler, Spatial distribution of calcite and amorphous calcium carbonate in the cuticle of the terrestrial crustaceans Porcellio scaber and Armadillidium vulgare, J. Struct. Biol. 163 (2008) 100–108. doi:10.1016/j.jsb.2008.04.010.

[404] R.T. Devol, C.Y. Sun, M.A. Marcus, S.N. Coppersmith, S.C.B. Myneni, P.U.P.A. Gilbert, Nanoscale Transforming Mineral Phases in Fresh Nacre, J. Am. Chem. Soc. 137 (2015)

13325–13333. doi:10.1021/jacs.5b07931.

[405] C.R. Blue, A. Giuffre, S. Mergelsberg, N. Han, J.J. De Yoreo, P.M. Dove, Chemical and physical controls on the transformation of amorphous calcium carbonate into crystalline $CaCO_3$ polymorphs, Geochim. Cosmochim. Acta. 196 (2017) 179–196. doi:10.1016/j.gca.2016.09.004.

[406] A. Lassin, L. André, N. Devau, A. Lach, T. Beuvier, A. Gibaud, S. Gaboreau, M. Azaroual, Dynamics of calcium carbonate formation: Geochemical modeling of a two-step mechanism, Geochim. Cosmochim. Acta. 240 (2018) 236–254. doi:10.1016/j.gca.2018.08.033.

[407] B. Purgstaller, V. Mavromatis, A. Immenhauser, M. Dietzel, Transformation of Mg-bearing amorphous calcium carbonate to Mg-calcite - In situ monitoring, Geochim. Cosmochim. Acta. 174 (2016) 180–195. doi:10.1016/j.gca.2015.10.030.

[408] J.D. Rodriguez-Blanco, S. Shaw, P. Bots, T. Roncal-Herrero, L.G. Benning, The role of Mg in the crystallization of monohydrocalcite, Geochim. Cosmochim. Acta. 127 (2014) 204–220. doi:10.1016/j.gca.2013.11.034.

[409] C.R. Blue, P.M. Dove, Chemical controls on the magnesium content of amorphous calcium carbonate, Geochim. Cosmochim. Acta. 148 (2015) 23–33. doi:10.1016/j.gca.2014.08.003.

[410] S. Raz, P.C. Hamilton, F.H. Wilt, S. Weiner, L. Addadi, The transient phase of amorphous calcium carbonate in sea urchin larval spicules: The involvement of proteins and magnesium ions in its formation and stabilization, Adv. Funct. Mater. 13 (2003) 480–486. doi:10.1002/adfm.200304285.

[411] J.D. Rodriguez-Blanco, S. Shaw, P. Bots, T. Roncal-Herrero, L.G. Benning, The role of pH and Mg on the stability and crystallization of amorphous calcium carbonate, J. Alloys Compd. 536 (2012) S477–S479. doi:10.1016/j.jallcom.2011.11.057.

[412] P. Raiteri, J.D. Gale, Water is the key to nonclassical nucleation of amorphous calcium carbonate, J. Am. Chem. Soc. 132 (2010) 17623–17634. doi:10.1021/ja108508k.

[413] A. V. Radha, A. Fernandez-Martinez, Y. Hu, Y.S. Jun, G.A. Waychunas, A. Navrotsky, Energetic and structural studies of amorphous Ca 1-xMg xCO 3·nH 2O (0≤x≤1), Geochim. Cosmochim. Acta. 90 (2012) 83–95. doi:10.1016/j.gca.2012.04.056.

[414] K.J. Davis, P.M. Dove, J.J. De Yoreo, The role of Mg2+ as an impurity in calcite growth, Science (80-.). 290 (2000) 1134–1137. doi:10.1126/science.290.5494.1134.

[415] T. Chen, A. Neville, M. Yuan, Assessing the effect of Mg2+CaCO3 scale formation-bulk precipitation and surface deposition, J. Cryst. Growth. 275 (2005) 2–8.

doi:10.1016/j.jcrysgro.2004.11.169.

[416] P. Bots, L.G. Benning, R.E.M. Rickaby, S. Shaw, The role of SO4 in the switch from calcite to aragonite seas, Geology. 39 (2011) 331–334. doi:10.1130/G31619.1.

[417] S.J. Gerdemann, W.K. O'Connor, D.C.D.C. Dahlin, L.R. Penner, H. Rush, W.K. O'Conor, D.C.D.C. Dahlin, L.R. Penner, H. Rush, Ex situ aqueous mineral carbonation, Environ. Sci. Technol. 41 (2007) 2589–2593. doi:10.1021/es0619253.

[418] T. Kimura, N. Koga, Monohydrocalcite in comparison with hydrated amorphous calcium carbonate: Precipitation condition and thermal behavior, Cryst. Growth Des. 11 (2011) 3877–3884. doi:10.1021/cg200412h.

[419] R. Nishiyama, T. Munemoto, K. Fukushi, Formation condition of monohydrocalcite from CaCl2-MgCl2-Na2CO3 solutions, Geochim. Cosmochim. Acta. 100 (2013) 217–231. doi:10.1016/j.gca.2012.09.002.

[420] R. Nishiyama, T. Munemoto, K. Fukushi, Formation condition of monohydrocalcite from CaCl2-$MgCl_2$-Na_2CO_3 solutions, Geochim. Cosmochim. Acta. 100 (2013) 217–231. doi:10.1016/j.gca.2012.09.002.

[421] Y.Y. Wang, Q.Z. Yao, G.T. Zhou, S.Q. Fu, Transformation of amorphous calcium carbonate into Monohydrocalcite in aqueous solution: A biomimetic mineralization study, Eur. J. Mineral. 27 (2015) 717–729. doi:10.1127/ejm/2015/0027-2486.

[422] F. Dejehet, S. Idrissi, R. Debuys, Magnesium and occluded water in calcium carbonate monohydrate, J. Chim. Phys. 96 (1999) 741–753. https://doi.org/10.1051/jcp:1999168.

[423] Z. Zou, W.J.E.M. Habraken, G. Matveeva, A.C.S. Jensen, L. Bertinetti, M.A. Hood, C. Sun, P.U.P.A. Gilbert, I. Polishchuk, B. Pokroy, J. Mahamid, Y. Politi, S. Weiner, P. Werner, S. Bette, R. Dinnebier, U. Kolb, E. Zolotoyabko, P. Fratzl, A hydrated crystalline calcium carbonate phase: Calcium carbonate hemihydrate, Science (80-.). 363 (2019) 396–400. doi:10.1126/science.aav0210.

[424] C.E. White, N.J. Henson, L.L. Daemen, M. Hartl, K. Page, Uncovering the true atomic structure of disordered materials: The structure of a hydrated amorphous magnesium carbonate (MgCO3·3D 2O), Chem. Mater. 26 (2014) 2693–2702. doi:10.1021/cm500470g.

[425] R. Zhang, N. Bassim, D.K. Panesar, Characterization of Mg components in reactive MgO - Portland cement blends during hydration and carbonation, J. CO2 Util. 27 (2018) 518–527. doi:10.1016/j.jcou.2018.08.025.

[426] S.A. Wilson, S.L.L. Barker, G.M. Dipple, V. Atudorei, Isotopic disequilibrium during uptake

of atmospheric CO2 into mine process waters: Implications for CO2 sequestration, Environ. Sci. Technol. 44 (2010) 9522–9529. doi:10.1021/es1021125.

[427] A. V. Radha, A. Navrotsky, Direct experimental measurement of water interaction energetics in amorphous carbonates MCO3 (M = Ca, Mn, and Mg) and implications for carbonate crystal growth, Cryst. Growth Des. 15 (2015) 70–78. doi:10.1021/cg500878w.

[428] A. Orlando, M. Lelli, L. Marini, Production of amorphous hydrated impure magnesium carbonate through ex situ carbonation, Appl. Geochemistry. 27 (2012) 2500–2510. doi:10.1016/j.apgeochem.2012.07.021.

[429] J.Y. Tanaka, J. Kawano, T. Nagai, H. Teng, Transformation process of amorphous magnesium carbonate in aqueous solution, J. Mineral. Petrol. Sci. 114 (2019) 105–109. doi:10.2465/jmps.181119b.

[430] R.L. Frost, S. Bahfenne, J. Graham, Raman spectroscopic study of the magnesium-carbonate minerals - artinite and dypingite, J. Raman Spectrosc. 40 (2009) 855–860. doi:10.1002/jrs.2152.

[431] H. Pang, G. Ning, W. Gong, J. Ye, Y. Lin, Direct synthesis of hexagonal $Mg(OH)_2$ nanoplates from natural brucite without dissolution procedure, Chem. Commun. 47 (2011) 6317–6319. doi:10.1039/c1cc10279f.

[432] Z. Hao, F. Du, Synthesis of basic magnesium carbonate microrods with a “house of cards” surface structure using rod-like particle template, J. Phys. Chem. Solids. 70 (2009) 401–404. doi:10.1016/j.jpcs.2008.11.005.

[433] I. Aouini, A. Ledoux, L. Estel, S. Mary, Pilot Plant Studies for CO_2 Capture from Waste Incinerator Flue Gas Using MEA Based Solvent, Oil Gas Sci. Technol. 69 (2014) 1091–1104. doi:10.2516/ogst/2013205.

[434] F.J. Wicks, Status of the reference X-ray powder-diffraction patterns for the serpentine minerals in the PDF database—1997, Powder Diffr. 15 (2000) 42–50. doi:DOI: 10.1017/S0885715600010824.

[435] M.C. Ball, H.F.W. Taylor, The Dehydration of Chrysotile in Air and under Hydrothermal Conditions, Mineral. Mag. J. Mineral. Soc. 33 (1963) 467–482. doi:DOI: 10.1180/minmag.1963.033.261.04.

[436] G. Brindley, B. Narahari, J. Sharp, Kinetics and mechanism of dehydroxylation of crocidolite, Am. Mineral. 52 (1967) 1697–1705. doi:10.1039/tf9676302051.

[437] C.J. Martin, The thermal decomposition of chrysotile, Mineral. Mag. 41 (1977) 453–459.

doi:DOI: 10.1180/minmag.1977.041.320.05.

[438] E. Benhelal, M.I. Rashid, S.J. Hook, M.S. Rayson, G.F. Brent, M. Stockenhuber, E.M. Kennedy, Si29 Solid State MAS NMR Study on the Fate of Silicon in Mineral Carbonation of Serpentine: A Journey from Mining to End Products, in: ACEME, 2018.

[439] J. Pronost, G. Beaudoin, J.M. Lemieux, R. Hébert, M. Constantin, S. Marcouiller, M. Klein, J. Duchesne, J.W. Molson, F. Larachi, X. Maldague, CO_2-depleted warm air venting from chrysotile milling waste (Thetford Mines, Canada): Evidence for in-situ carbon capture from the atmosphere, Geology. 40 (2012) 275–278. doi:10.1130/G32583.1.

[440] J.G.M. Thom, G.M. Dipple, I.M. Power, A.L. Harrison, Chrysotile dissolution rates: Implications for carbon sequestration, Appl. Geochemistry. 35 (2013) 244–254. doi:10.1016/j.apgeochem.2013.04.016.

[441] S.A. Wilson, A.L. Harrison, G.M. Dipple, I.M. Power, S.L.L. Barker, K. Ulrich Mayer, S.J. Fallon, M. Raudsepp, G. Southam, Offsetting of CO_2 emissions by air capture in mine tailings at the Mount Keith Nickel Mine, Western Australia: Rates, controls and prospects for carbon neutral mining, Int. J. Greenh. Gas Control. 25 (2014) 121–140. doi:10.1016/j.ijggc.2014.04.002.

[442] G. Wang, A.N. Otuonye, E.A. Blair, K. Denton, Z. Tao, T. Asefa, Functionalized mesoporous materials for adsorption and release of different drug molecules: A comparative study, J. Solid State Chem. 182 (2009) 1649–1660. doi:10.1016/j.jssc.2009.03.034.

[443] R.K. Biswas, P. Khan, S. Mukherjee, A.K. Mukhopadhyay, J. Ghosh, K. Muraleedharan, Study of short range structure of amorphous Silica from PDF using Ag radiation in laboratory XRD system, RAMAN and NEXAFS, J. Non. Cryst. Solids. 488 (2018) 1–9. doi:10.1016/j.jnoncrysol.2018.02.037.

[444] J. Ji, Y. Ge, W. Balsam, J.E. Damuth, J. Chen, Rapid identification of dolomite using a Fourier Transform Infrared Spectrophotometer (FTIR): A fast method for identifying Heinrich events in IODP Site U1308, Mar. Geol. 258 (2009) 60–68. doi:10.1016/j.margeo.2008.11.007.

[445] R. Lafay, G. Montes-Hernandez, E. Janots, R. Chiriac, N. Findling, F. Toche, Simultaneous precipitation of magnesite and lizardite from hydrothermal alteration of olivine under high-carbonate alkalinity, Chem. Geol. 368 (2014) 63–75. doi:10.1016/j.chemgeo.2014.01.008.

[446] W.H. Casey, H.R. Westrich, G.W. Arnold, Surface chemistry of labradorite feldspar reacted with aqueous solutions at pH = 2, 3, and 12, Geochim. Cosmochim. Acta. 52 (1988) 2795–2807. doi:https://doi.org/10.1016/0016-7037(88)90147-0.

[447] R. Hellmann, C.M. Eggleston, M.F. Hochella, D.A. Crerar, The formation of leached layers on albite surfaces during dissolution under hydrothermal conditions, Geochim. Cosmochim. Acta. 54 (1990) 1267–1281. doi:https://doi.org/10.1016/0016-7037(90)90152-B.

[448] T.N. Tran, T.V.A. Pham, M.L.P. Le, T.P.T. Nguyen, V.M. Tran, Synthesis of amorphous silica and sulfonic acid functionalized silica used as reinforced phase for polymer electrolyte membrane, Adv. Nat. Sci. Nanosci. Nanotechnol. 4 (2013). doi:10.1088/2043-6262/4/4/045007.

[449] H. Béarat, M.J. Mckelvy, A.V.G. Chizmeshya, D. Gormley, R. Nunez, R.W. Carpenter, K. Squires, G.H. Wolf, Carbon sequestration via aqueous olivine mineral carbonation: Role of passivating layer formation, Environ. Sci. Technol. 40 (2006) 4802–4808.

[450] C. Julcour, F. Bourgeois, B. Bonfils, I. Benhamed, F. Guyot, F. Bodénan, C. Petiot, É.C. Gaucher, Development of an attrition-leaching hybrid process for direct aqueous mineral carbonation, Chem. Eng. J. 262 (2015) 716–726. doi:10.1016/j.cej.2014.10.031.

[451] I.M. Power, A.L. Harrison, G.M. Dipple, Accelerating Mineral Carbonation Using Carbonic Anhydrase, Environ. Sci. Technol. 50 (2016) 2610–2618. doi:10.1021/acs.est.5b04779.

[452] W. Taifan, J. Boily, J. Baltrusaitis, Surface chemistry of carbon dioxide revisited, Surf. Sci. Rep. 71 (2016) 595–671. doi:10.1016/j.surfrep.2016.09.001.

[453] F. Farhang, M. Rayson, G. Brent, T. Hodgins, M. Stockenhuber, E. Kennedy, Insights into the dissolution kinetics of thermally activated serpentine for CO_2 sequestration, Chem. Eng. J. 330 (2017) 1174–1186. doi:10.1016/j.cej.2017.08.073.

[454] D.J. Fauth, J.P. Baltrus, Y. Soong, J.P. Knoer, B.H. Howard, W.J. Graham, M.M. Maroto-Valer, J.M. Andrésen, Carbon Storage and Sequestration as Mineral Carbonates, in: M.M. Maroto-Valer, C. Song, Y. Soong (Eds.), Environ. Challenges Greenh. Gas Control Foss. Fuel Util. 21st Century, Springer US, Boston, MA, 2002: pp. 101–117. doi:10.1007/978-1-4615-0773-4_8.

[455] E. Benhelal, M.I. Rashid, M.S. Rayson, J.D. Prigge, S. Molloy, G.F. Brent, A. Cote, M. Stockenhuber, E.M. Kennedy, Study on mineral carbonation of heat activated lizardite at pilot and laboratory scale, J. CO2 Util. 26 (2018) 230–238. doi:10.1016/j.jcou.2018.05.015.

[456] J. Pronost, G. Beaudoin, J. Tremblay, F. Larachi, J. Duchesne, R. Hébert, M. Constantin, Carbon sequestration kinetic and storage capacity of ultramafic mining waste, Environ. Sci. Technol. 45 (2011) 9413–9420. doi:10.1021/es203063a.

[457] G.P. Assima, F. Larachi, G. Beaudoin, J. Molson, Dynamics of carbon dioxide uptake in chrysotile mining residues - Effect of mineralogy and liquid saturation, Int. J. Greenh. Gas

Control. 12 (2013) 124–135. doi:10.1016/j.ijggc.2012.10.001.

[458] G.P. Assima, F. Larachi, J. Molson, G. Beaudoin, Comparative study of five Québec ultramafic mining residues for use in direct ambient carbon dioxide mineral sequestration, Chem. Eng. J. 245 (2014) 56–64. doi:10.1016/j.cej.2014.02.010.

[459] O.S. Pokrovsky, J. Schott, Forsterite surface composition in aqueous solutions: A combined potentiometric, electrokinetic, and spectroscopic approach, Geochim. Cosmochim. Acta. 64 (2000) 3299–3312. doi:10.1016/S0016-7037(00)00435-X.

[460] O.S. Pokrovsky, J. Schott, Experimental study of brucite dissolution and precipitation in aqueous solutions: Surface speciation and chemical affinity control, Geochim. Cosmochim. Acta. 68 (2004) 31–45. doi:10.1016/S0016-7037(03)00238-2.

[461] M. Chrysochoou, S.C. Fakra, M.A. Marcus, H.M. Deok, D. Dermatas, Microstructural analyses of Cr(VI) speciation in chromite ore processing residue (COPR), Environ. Sci. Technol. 43 (2009) 5461–5466. doi:10.1021/es9005338.

[462] F. Klein, W. Bach, S.E. Humphris, W.A. Kahl, N. Jöns, B. Moskowitz, T.S. Berquó, Magnetite in seafloor serpentinite-Some like it hot, Geology. 42 (2014) 135–138. doi:10.1130/G35068.1.

[463] B.R. Frost, K.A. Evans, S.M. Swapp, J.S. Beard, F.E. Mothersole, The process of serpentinization in dunite from new caledonia, Lithos. 178 (2013) 24–39. doi:10.1016/j.lithos.2013.02.002.

[464] A. Langone, I. Baneschi, C. Boschi, A. Dini, M. Guidi, A. Cavallo, Serpentinite-water interaction and chromium(VI) release in spring waters: Examples from Tuscan ophiolites, Ofioliti. 38 (2013) 41–57. doi:10.4454/ofioliti.v38i1.415.

[465] M. D'Antonio, K.M. B, Serpentine and brucite of ultramafic clasts from the South Chamorro Seamount (Ocean Drilling Program Leg 195, Site 1200): inferences for the serpentinization of the Mariana forearc mantle, Mineral. Mag. 68 (2004) 887. doi:10.1180/0026461046860229.

[466] R.D. Hyndman, S.M. Peacock, Serpentinization of the forearc mantle, Earth Planet. Sci. Lett. 212 (2003) 417–432. doi:10.1016/S0012-821X(03)00263-2.

[467] R. Lafay, G. Montes-Hernandez, E. Janots, R. Chiriac, N. Findling, F. Toche, Mineral replacement rate of olivine by chrysotile and brucite under high alkaline conditions, J. Cryst. Growth. 347 (2012) 62–72. doi:10.1016/j.jcrysgro.2012.02.040.

[468] I. Rigopoulos, K.C. Petallidou, M.A. Vasiliades, A. Delimitis, I. Ioannou, A.M. Efstathiou,

T. Kyratsi, Carbon Dioxide storage in Olivine Basalts : Effect of Ball Milling Process, Powder Technol. 273 (2015) 220–229. doi:10.1016/j.powtec.2014.12.046.

[469] S.E.J. Villar, H.G.M. Edwards, Raman spectroscopy in astrobiology, Anal. Bioanal. Chem. 384 (2006) 100–113. doi:10.1007/s00216-005-0029-2.

[470] A. Steele, M.D. Fries, H.E.F. Amundsen, B.O. Mysen, M.L. Fogel, M. Schweizer, N.Z. Boctor, Comprehensive imaging and Raman spectroscopy of carbonate globules from Martian meteorite ALH 84001 and a terrestrial analogue from Svalbard, Meteorit. Planet. Sci. 42 (2007) 1549–1566. doi:10.1111/j.1945-5100.2007.tb00590.x.

[471] M.J. Mckelvy, A.V.G. Chizmeshya, E. Soignard, R. Marzke, G. Wolf, H. Béarat, B. Doss, Laboratory Investigation of Fluid / Solid Sequestration Reaction Processes under In Situ Sequestration Process Conditions, in: Int. Tech. Conf. Coal Util. Fuel Syst., 2006.

[472] M.G. Brik, First-principles calculations of structural, electronic, optical and elastic properties of magnesite MgCO3 and calcite CaCO3, Phys. B Condens. Matter. 406 (2011) 1004–1012. doi:10.1016/j.physb.2010.12.049.

[473] Y. Politi, R.A. Metzler, M. Abrecht, B. Gilbert, F.H. Wilt, I. Sagi, L. Addadi, S. Weiner, P. Gilbert, Transformation mechanism of amorphous calcium carbonate into calcite in the sea urchin larval spicule (Proceedings of the National Academy of Sciences of the United States of America (2008) 105, 45, (17362-17366) DOI:10.1073/pnas. 0806604105), Proc. Natl. Acad. Sci. U. S. A. 105 (2008) 20045. doi:10.1073/pnas.0811530106.

[474] A.L. Goodwin, F.M. Michel, B.L. Phillips, D.A. Keen, M.T. Dove, R.J. Reeder, Nanoporous structure and medium-range order in synthetic amorphous calcium carbonate, Chem. Mater. 22 (2010) 3197–3205. doi:10.1021/cm100294d.

[475] J. Xu, C. Yan, F. Zhang, H. Konishi, H. Xu, H.H. Teng, Testing the cation-hydration effect on the crystallization of Ca-Mg-CO 3 systems, Proc. Natl. Acad. Sci. U. S. A. 110 (2013) 17750–17755. doi:10.1073/pnas.1307612110.

[476] O.S. Pokrovsky, J. Schott, Kinetics and mechanism of forsterite dissolution at 25°C and pH from 1 to 12, Geochim. Cosmochim. Acta. 64 (2000) 3313–3325. doi:10.1016/S0016-7037(00)00434-8.

[477] R.W. Luce, R.W. Bartlett, G.A. Parks, Dissolution kinetics of magnesium silicates, Geochim. Cosmochim. Acta. 36 (1972) 35–50. doi:https://doi.org/10.1016/0016-7037(72)90119-6.

[478] V. V. Potapov, Formation of solid deposits of amorphous silica in a flow of hydrothermal solution, Glas. Phys. Chem. 30 (2004) 82–89. doi:10.1023/B:GPAC.0000016402.61068.1b.

[479] D. Daval, O. Sissmann, N. Menguy, G.D. Saldi, F. Guyot, I. Martinez, J. Corvisier, B. Garcia, I. Machouk, K.G. Knauss, R. Hellmann, Influence of amorphous silica layer formation on the dissolution rate of olivine at 90°C and elevated pCO2, Chem. Geol. 284 (2011) 193–209. doi:https://doi.org/10.1016/j.chemgeo.2011.02.021.

[480] R. Punturo, A. Bloise, T. Critelli, M. Catalano, E. Fazio, C. Apollaro, Environmental implications related to natural asbestos occurrences in the ophiolites of the gimigliano-mount reventino unit (Calabria, Southern Italy), Int. J. Environ. Res. 9 (2015) 405–418.

[481] R.K. Schulze, M.A. Hill, R.D. Field, P.A. Papin, R.J. Hanrahan, D.D. Byler, Characterization of carbonated serpentine using XPS and TEM, Energy Convers. Manag. 45 (2004) 3169–3179. doi:10.1016/J.ENCONMAN.2004.02.003.

[482] C. Du Breuil, L.C. Pasquier, G. Dipple, J.F. Blais, M.C. Iliuta, G. Mercier, Mineralogical transformations of heated serpentine and their impact on dissolution during aqueous-phase mineral carbonation reaction in flue gas conditions, Minerals. 9 (2019) 1–14. doi:10.3390/min9110680.